MATERIALS RESEARCH SOCIETY
SYMPOSIUM PROCEEDINGS VOLUME 450

Infrared Applications of Semiconductors—Materials, Processing and Devices

Symposium held December 2–5, 1996, Boston, Massachusetts, U.S.A.

EDITORS:

M. Omar Manasreh
U.S. Air Force Phillips Laboratory
Kirtland AFB, New Mexico, U.S.A.

Thomas H. Myers
West Virginia University
Morgantown, West Virginia, U.S.A.

François H. Julien
Université de Paris-Sud
Orsay, France

19980809003 051

MRS

MATERIALS
RESEARCH
SOCIETY

PITTSBURGH, PENNSYLVANIA

DTIC QUALITY INSPECTED 1

Infrared Applications of Semiconductors— Materials, Processing and Devices

CONTENTS

PART I: ANTIMONIDE RELATED MATERIALS AND DEVICES

*Invited Paper

PART II: QUANTUM WELLS AND DEVICES

*Invited Paper

*Invited Paper

*Invited Paper

PART VI: <u>INTERDIFFUSION IN HETEROSTRUCTURES</u>

*Invited Paper

PREFACE

The symposium entitled "Infrared Applications of Semiconductors—Materials, Processing and Devices" was held on December 2-6, 1996, in Boston, Massachusetts, as Symposium O of the 1996 MRS Fall Meeting, and was a joint session with the 1996 International Conference on Electronic Materials. The symposium focused on recent investigations based on III-V, II-VI, and IV bulk semiconductors, quantum wells, and superlattices for infrared detectors, emitters, sources, and materials. Internationally-known experts in the subject presented 86 oral papers covering this diverse field. The resulting 68 papers published in this proceedings are a representative snapshot of the fast-changing field of novel structures and processes that can be used to achieve high-performance infrared detectors, imaging arrays, infrared lasers and sources.

M. Omar Manasreh
Thomas H. Myers
François H. Julien

December, 1996

ACKNOWLEDGMENTS

MATERIALS RESEARCH SOCIETY SYMPOSIUM PROCEEDINGS

MATERIALS RESEARCH SOCIETY SYMPOSIUM PROCEEDINGS

Part I

Antimonide Related Materials
and Devices

InAsSb/InAlAsSb QUANTUM-WELL DIODE LASERS EMITTING BETWEEN 3 AND 4 μm

G.W. TURNER, H.K. CHOI, M.J. MANFRA, AND M.K. CONNORS*
*Lincoln Laboratory, Massachusetts Institute of Technology, Lexington, MA 02173-9108

ABSTRACT

Recently, mid-infrared diode lasers fabricated from the antimonide-based III-V compounds have been receiving increased attention for potential applications in trace gas detection, spectroscopy, pollution monitoring, and military systems. In this paper we will report the growth, fabrication, and modeling of high performance diode lasers with wavelengths longer than 3 μm. Molecular beam epitaxy (MBE) has been employed for the growth of these Type-I, strained quantum-well (QW) laser structures on GaSb and InAs substrates. The lasers consist of compressively strained InAsSb wells, tensile-strained InAlAsSb barriers, and lattice-matched AlAsSb cladding layers. QW lasers grown on GaSb substrates, with emission wavelengths of ~3.9 μm, have operated pulsed up to 165 K. At 80 K, cw power of 30 mW/Facet has been obtained. Ridge-waveguide lasers have operated cw up to 128K. QW lasers grown on InAs substrates have emission wavelengths between 3.2 and 3.55 μm. Broad-stripe lasers on InAs have exhibited cw power of 215 mW/facet at 80 K, pulsed threshold current density as low as 30 A/cm^2 at 80 K, characteristic temperatures (T_o) between 30 and 40 K, and maximum pulsed operating temperature of 225 K. Ridge-waveguide lasers on InAs have cw threshold current of 12 mA at 100 K, and a maximum cw operating temperature of 175 K. In this paper we will present some of the key issues regarding the MBE growth, fabrication, and modeling of such lasers and discuss future directions for improved device performance.

INTRODUCTION

A number of different approaches are presently being investigated with the goal of obtaining mid-infrared (3-5 μm) diode lasers that are capable of high-power cw operation at room temperature. These include laser structures based on conventional electron-hole recombination in quantum-well (QW) and superlattice active regions of either Type I [1] or Type II [2] band alignment, and quantum cascade structures which are based on unipolar intersubband transitions [3]. All of these approaches attempt to overcome parasitic effects, such as nonradiative Auger recombination, that are increasingly important for cw room-temperature operation of diode lasers at long wavelengths. Figure 1 presents a compilation of reported experimental results for cw operating temperature vs. wavelength. It can be readily seen from this figure that it is increasingly difficult to obtain high-temperature cw operation as the emission wavelength is increased [4].
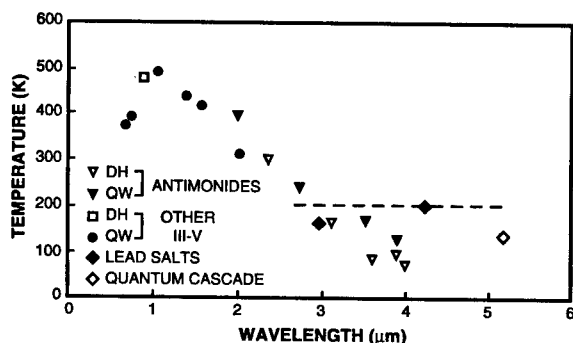
Fig. 1. Maximum cw operating temperature vs. wavelength for a variety of mid-infrared semiconductor lasers. The dotted line indicates the lower limit for thermoelectric cooling.

3

In this paper, we describe our investigation of Type-I strained MQW diode lasers, based on active regions of InAsSb wells/InAlAsSb barriers, and AlAsSb cladding layers, grown by MBE on both GaSb and InAs substrates. These laser structures are grown with epitaxial compositions adjusted to (a) achieve the desired strains and Type I band alignments in the active region materials, and (b) maintain lattice matching of the cladding layers to the GaSb and InAs substrates. The reasons for investigating such QW structures on the two different substrates will be explained and the differences in both growth of the various epitaxial layers and the resultant performance of diode lasers will be discussed below.

EXPERIMENTAL PROCEDURE

The InAsSb QW lasers were grown in a solid-source EPI Gen II 3-inch MBE system, equipped with 2 Sb_4 sources, an EPI valved As cracking source used to provide As_2 flux, and conventional ion pumps. GaSb and InAs (100) n-type substrates were prepared by either (a) solvent cleaning and chemical etching, followed by In-bonding for typical substrate material, or (b) directly loaded into a solderless block containing an Al_2O_3 backing plate for 2-inch epi-ready GaSb and InAs substrates. After careful UHV outgassing and oxide desorption of the GaSb and InAs substrates in an Sb_4 or As_2 flux, respectively, the following layers were grown on GaSb: n^+-GaSb buffer, n-$AlAs_{0.08}Sb_{0.92}$ lower cladding, MQW active region consisting of compressively strained InAsSb wells and tensile-strained InAlAsSb barriers, p-$AlAs_{0.08}Sb_{0.92}$ upper cladding, and p^+-GaSb cap layer. On InAs, an n^+-InAs buffer layer was grown and the cladding composition was changed to the lattice-matched composition of $AlAs_{0.16}Sb_{0.84}$. The design value for composition of the quantum wells was chosen to give approximately ~0.5% compressive strain, with composition in the barriers chosen to give approximately ~0.25% tensile strain, and the well/barrier thicknesses were chosen to produce a nominally strain balanced active region. Be was used as the p-type dopant and GaTe was the source for Te as an n-type dopant for all epitaxial layers. Hall measurements of all nominally undoped InAsSb and InAlAsSb layers grown on semi-insulating GaAs substrates yielded n-type conductivity, for compositions appropriate to both GaSb and InAs substrates. Since the active regions used for this work were nominally undoped, the diode p-n junction was formed at the active-layer/upper-cladding interface. The two Sb_4 effusion cells allowed some optimization of the III/V ratio for each alloy, when used in conjunction with the valved As_2 source. The buffer and cladding layers were grown at ~0.8-0.9 µm/h, and the QW active regions were grown at slightly lower growth rate. The substrate temperature was controlled at 520°C for the lower cladding, 410-430°C for the QW active region, and reduced to 490°C for the upper cladding and GaSb cap layer. As will be shown below, this reduction in upper cladding temperature was necessary to prevent degradation of the active regions. As previously reported [5], the necessity of precise control of composition, strain, and lattice parameter required a number of test growths and calibration procedures for each epitaxial alloy that was used.

After dismounting of the In-bonded samples, the In-alloyed region on the back side of the wafer was removed by etching, making sure that the wafer surface was protected during the etching process. Samples grown on the 2-inch epi-ready substrates did not require this additional step, as there was no apparent degradation of the back side of the substrates at the growth temperatures used. The starting surfaces of the GaSb and InAs substrates were characterized by atomic force microscopy (AFM), and the epitaxial layers were characterized by photoluminescence spectroscopy, double-crystal X-ray diffraction (DCXRD), and Auger microprobe chemical analysis. The complete MBE-grown laser wafers exhibited excellent surface morphology, and especially for the epi-ready InAs substrates, very good yields of laser diodes, with consistent characteristics, were obtained across the entire 2-inch wafer.

To evaluate laser performance, broad-stripe lasers 100-250 µm wide were fabricated by using SiO_2 patterning. For both n and p contacts, nonalloyed Ti/Pt/Au was used. Ridge-waveguide lasers, 8 µm wide, were fabricated from some wafers using reactive ion etching in a BCl_3/Ar plasma to define the ridges. Lasers were mounted junction-side up on Cu heat sinks using In, and loaded into a dewar for low-temperature I-V and L-I measurements.

MATERIALS RESULTS

Because of the desire to grow complete laser structures on large-area, nonbonded substrates, the starting surface of a number commercial epi-ready InAs and GaSb substrates were evaluated by AFM. Figure 2 shows a comparison between conventional GaSb and InAs substrate surfaces, and the corresponding epi-ready surfaces, with the samples taken directly from the vendor's packaging to the AFM apparatus, where the measurements were performed in air. The remarkable smoothness of the epi-ready InAs surface was also confirmed by a comparison of reflection high-energy electron diffraction images obtained before oxide desorption in the growth chamber. In the AFM image of the epi-ready InAs substrates there is some evidence of atomic structure on the as-received surface, and this structure was determined to be crystallographically oriented by AFM scanning in different directions. The GaSb epi-ready surface quality was found to be somewhat inferior to the InAs, with no evidence of atomic structure. Although no laser structures have yet been grown on the epi-ready GaSb, initial test results with GaSb homoepitaxial layers yielded good surface morphologies.
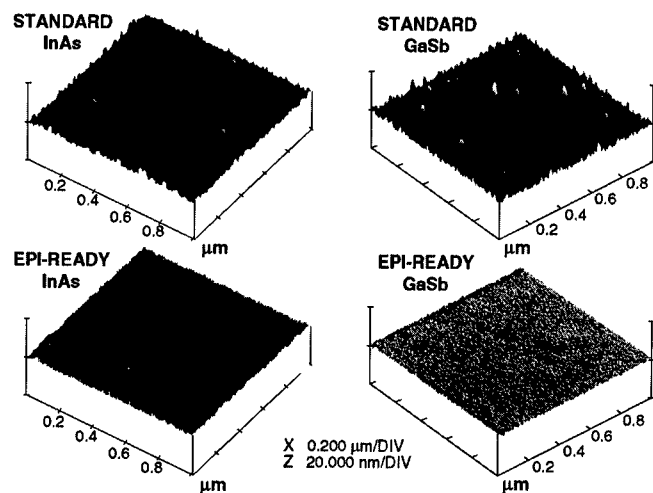
Fig. 2. Atomic force micrograph of conventional and epi-ready substrates.

A key reason for the consideration of the growth of strained InAsSb/InAlAsSb QW active regions on InAs substrates is the presence of a large predicted miscibility gap for the InAlAsSb barrier material [6]. As shown in Fig. 3, changing from GaSb to InAs substrates (a lattice parameter change of only 0.7%) increases the predicted region of stable growth for InAlAsSb from a maximum Al content of less than 6% to approximately 15%. Increasing the Al content in the InAlAsSb barrier material is important to improve both the conduction and valence band offset in the active region, to achieve improved carrier confinement and enhanced laser performance [6].

As an indication of the quality of $InAs_{0.935}Sb_{0.065}/In_{0.85}Al_{0.15}As_{0.9}Sb_{0.1}$ strained MQWs that can be grown on InAs substrates by MBE, Fig. 4 shows a DCXRD scan of a 10-well test structure grown on an InAs buffer layer. The excellent agreement between the actual DCXRD data and the simulated diffraction curve shows high structural perfection in the MQW test structure. For these QW structures the best results were obtained with an As_2 interruption at each well/barrier interface. Although these theoretical predictions of regions of stability of the barrier alloy are only strictly valid for equilibrium growth conditions, our experience with the MBE growth of InAsSb/InAlAsSb QWs on GaSb substrates has confirmed the practical difficulty of increasing the
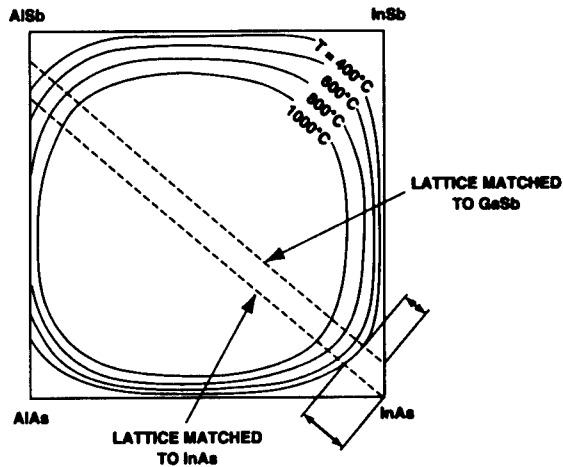
Fig. 3. Calculated alloy stability curves for In-Al-As-Sb system (from Ref. 6). The two dotted lines represent alloys matched to GaSb and InAs.
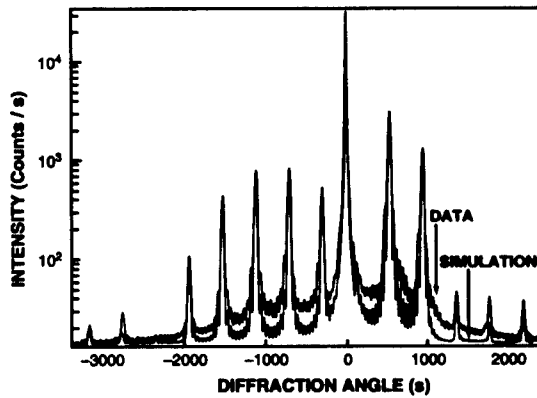
Fig. 4. DCXRD scan and simulation of InAsSb/InAlAsSb QW test structure grown on InAs.

Al content in this barrier alloy, while still maintaining high-quality, stable QWs. As shown in Fig. 5, the DCXRD scan from a MQW structure grown on GaSb showed significant degradation in the interface quality of the active region when the upper cladding layer was deposited at an elevated growth temperature. Even for the more stable MQW active regions grown on InAs, some interface degradation was observed at the higher temperatures used for good quality upper cladding layer growth. To investigate this effect, a MQW test structure on InAs, similar to that in Fig. 4, was furnace annealed in a sealed ampoule containing As for various times, and DCXRD scans were taken after the annealing. Figure 6 shows the results of these experiments, where annealing at 530°C for 3 h (a typical growth time for the upper cladding) completely obliterated the satellite structure, while annealing at 510°C for 3 h resulted in less degradation of the satellite structure. A growth temperature of 490°C for the upper cladding on both GaSb and InAs substrates was chosen

6
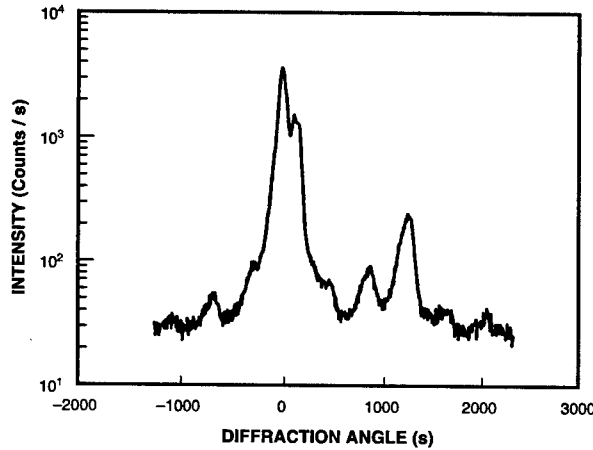
Fig. 5. DCXRD scan of InAsSb/InAlAsSb QW structure grown on GaSb.
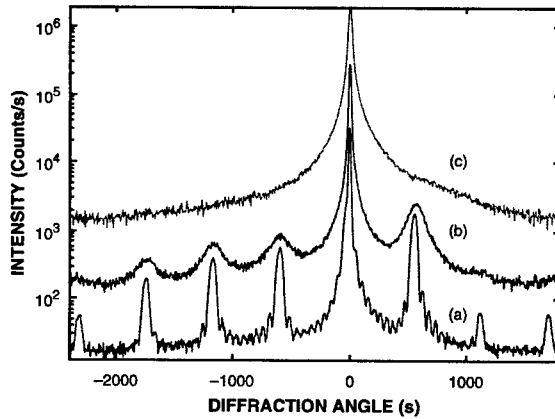
Fig. 6. DCXRD comparison of annealed QW test structures: (a) control sample,
(b) after annealing at 510°C for 3 h, and (c) after annealing at 530°C for 3 h.

as a reasonable compromise between optimizing upper cladding layer electrical and optical quality
and active layer degradation.

While the use of InAs substrates permits the growth of high-quality, stable MQW active
regions, the growth of the $AlAs_{0.16}Sb_{0.84}$ lattice-matched cladding region becomes more
difficult. This alloy contains ~2X as much arsenic as was the case for the lattice-matched cladding
alloy grown on GaSb, and is near a region of alloy miscibility [8]. In spite of this difficulty,
high-quality n- and p-type AlAsSb alloys were grown on InAs, using convention MBE growth
techniques. In addition, as was found with the growth on similar structures on GaSb, the transition
from Sb-dominated growth in the lower cladding to As-dominated growth in the active regions
(and the reverse transition to the upper cladding) was best achieved by enhancing Sb-like interfaces
and suppression of As-like interfaces in these transition regions. This observation has also been
reported for the growth of InAs/AlSb quantum wells [9].

7

DEVICE RESULTS

InAsSb/InAlAsSb QW Lasers on GaSb

The active region of the laser structure on GaSb consisted of ten 15-nm $InAs_{0.85}Sb_{0.15}$ wells and eleven 30-nm $In_{0.85}Al_{0.15}As_{0.86}Sb_{0.14}$ barriers with 3-μm $AlAs_{0.08}Sb_{0.92}$ cladding layers. In order to reduce the additional series resistance due to internal heterobarriers, linearly graded layers of AlGaAsSb were inserted between the n-buffer and n-cladding, as well as between the p-cladding and the p-cap layers.

Broad stripe lasers 100 μm wide were fabricated and tested, using junction side up mounting. Fig. 7 shows a plot of pulsed J_{th} for a 1000-μm cavity length QW device at temperatures between 80 and 165K, and for comparison, data from our best double-heterostructure device, emitting at 3.9 μm, is also plotted in this figure. At 80K the value of J_{th} for the QW device is 78A/cm^2. The value of the characteristic temperature, T_0 is 30K (up to 120K), which is larger
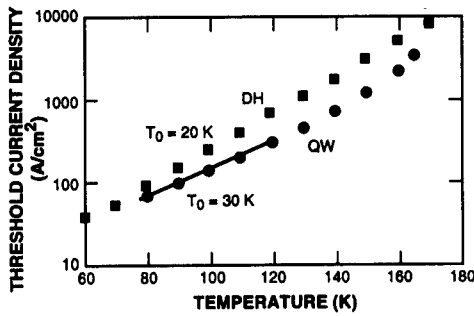
Fig. 7. Pulsed threshold current vs temperature for InAsSb/InAlAsSb QW laser and InAsSb/AlAsSb DH lasers emitting at 3.9 μm.

than the 20K T_0 value obtained for the DH laser emitting at the same wavelength. The lower J_{th} and higher T_0 values obtained for the QW devices indicate that Auger recombination, which is believed to be the limiting non-radiative recombination mechanism for such long-wavelength lasers, has been decreased by the use of the strained QW active region. At the maximum pulsed operating temperature, the value of J_{th} is 3.5 kA/cm^2. Figure 8 shows the cw power vs current for the same device. The maximum cw power at 80K is 30 mW/facet, which is significantly higher than the DH lasers. The highest cw operating temperature is 123K, which is also significantly higher than the best value of 105K obtained for 60-μm-wide DH devices mounted junction-side down. Ridge-waveguide lasers 15 μm wide were also fabricated and tested. Figure 9 shows the cw operation of a 1000-μm-long device at several temperatures. At 80K, the cw threshold current is 35 mA and the maximum cw operating temperature is 128K.
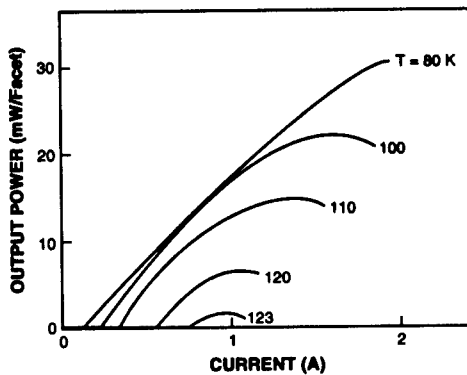
Fig. 8. CW output power vs current of InAsSb/InAlAsSb broad-area QW laser on GaSb.
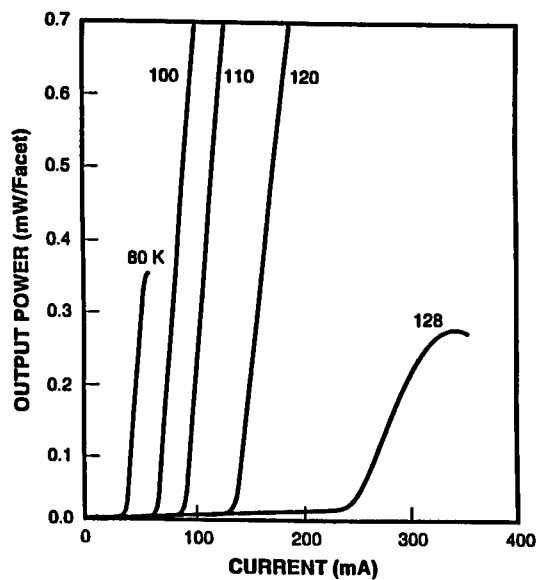
Fig. 9. CW power vs. current of InAsSb/InAlAsSb ridge-waveguide laser on GaSb.

InAsSb/InAlAsSb QW Lasers on InAs

Broad-stripe diode lasers fabricated from these structures and showed emission near 3.4 μm, with pulsed current density as low as 30 A/cm^2 at 80 K, and characteristic temperatures in the range 30-40 K. By measuring devices with cavity lengths of 500, 1000 and 1500 μm the internal quantum efficiency and internal loss coefficient are estimated to be 63% and 9 cm^{-1}, respectively. Figure 10 shows the cw power vs current of a 1500-μm device at several temperatures. At 80 K
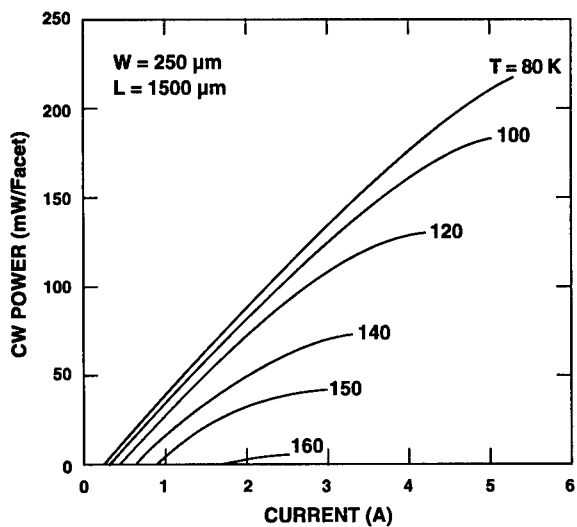
Fig. 10. CW output power vs current for InAsSb/InAlAsSb broad-area QW laser on InAs.

the maximum cw output power is 215 mW/facet, limited by junction heating. The maximum output power decreases with temperature, and at 150 K it is ~ 35 mW/facet. The operating voltage at the maximum power is ~4 V at 80 K. This surprisingly large operating voltage (more than 10 times the photon energy) is caused by the presence of large internal heterobarriers. Unfortunately, for the structures grown on InAs, no easily graded alloy region can be utilized, although superlattice and binary alloy grading regions are being investigated. Substantially higher output power would be expected if these large operating voltages can be reduced by incorporating such graded regions into the laser structure. Lasers with different active layer QW structures have been evaluated and emission wavelengths at 80 K of 3.21 to 3.38 μm have been observed. For a laser with 80-K emission at 3.21 μm, emission wavelength vs temperature is shown in Fig. 11. At low temperatures the wavelength shifts at ~ 1 nm/K, gradually increasing to ~ 2 nm/K at 220 K. Ridge-waveguide lasers 8 μm wide exhibited CW threshold current of 12 mA at 100 K and maximum cw operating temperature of 175 K.
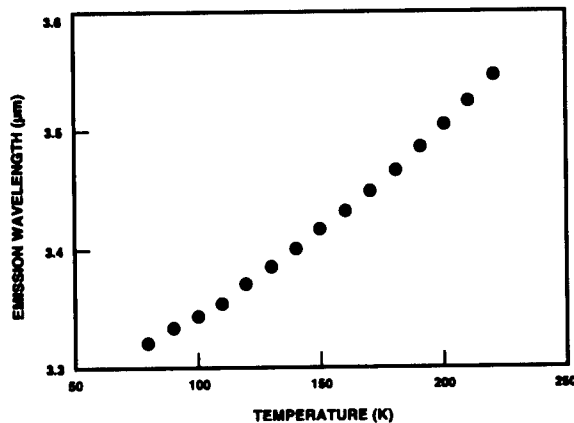
Fig. 11. Emission wavelength vs temperature for broad-area QW laser on InAs.

LASER MODELING and FUTURE LASER STRUCTURES

An important issue for the evolution of high-performance mid-infrared lasers is the development of credible theoretical models which can be effectively utilized to both predict performance of actual laser structures and, more importantly, help design improved laser structures. This has proven to be a challenging task, given the complexity of processes such as Auger recombination and the use of materials whose fundamental properties are often not well known. In addition, as described above, practical limitations in material growth, such as regions of alloy instability, often limit the optimization of potential improved QW laser structures.

In spite of these limitations, we have been utilizing a multi-band k•p theoretical model [11], following the methodology previously reported [11,12] to calculate bandstructure and transition matrix elements for a number of QW configurations. These calculations, together with predictions of carrier occupation probability and some additional simplifying assumptions, can be used to estimate the gain and spontaneous emission threshold as a function of carrier density. By combining the results of these gain calculations with estimates of Auger coefficients determined using a semi-classical model [13], we can estimate the threshold current density as a function of temperature. Figure 12 shows a comparison of our theoretical calculations of threshold current density with actual data taken from one of our 3.4 μm QW lasers grown on InAs. The excellent agreement between the theory and experiment give us confidence that our theoretical approach may be used to predict the performance of other advanced device structures that we are currently investigating.
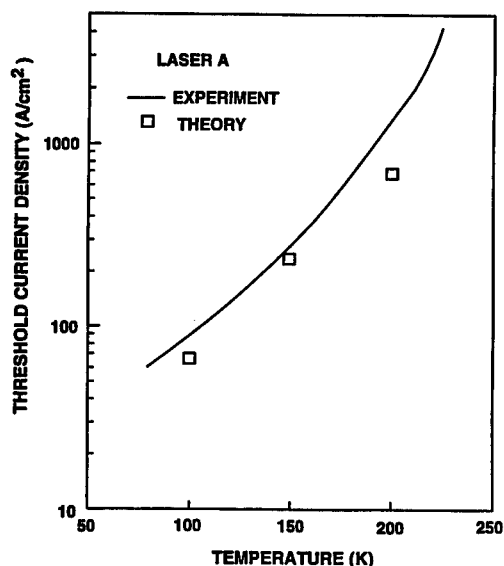
Fig. 12. Comparison of theoretical and experimental data for threshold current density vs temperature of an InAsSb/InAlAsSb QW laser grown on InAs.

DISCUSSION

Impressive diode laser performance has been obtained at 3-4 μm with strained InAsSb/InAlAsSb MQW structures grown on GaSb and InAs substrates. The use of InAs substrates has enabled the growth of InAlAsSb barriers with increased Al content, which in turn lead to the development of improved QW active regions. The use of InAs substrates, however, further complicated the growth of lattice-matched AlAsSb cladding layers. With these complex laser structures, careful attention to growth issues such as strain and lattice matching, thermal effects, and chemistry at interfaces is required for optimum performance. Theoretical models are being developed in an attempt to help predict what QW laser structures will achieve improved performance.

SUMMARY

We have demonstrated that MBE growth on GaSb and InAs substrates is capable of producing high-performance InAsSb/InAlAsSb Type-I QW diode lasers. Further optimization of device structures should lead to even higher performance lasers.

ACKNOWLEDGMENTS

REFERENCES

1. G.W. Turner, H.K. Choi, and H.Q. Le, J. Vac. Sci. Technol. B **13**, p. 699 (1995).

2. T.C. Hasenberg, D.H. Chow, A.R. Kost, R.H. Miles, and L. West, Electron. Lett. **31**, p. 275 (1995).

3. J. Faist, F. Capasso, D.L. Sivco, C. Sirtori, A.L. Hutchinson, and A.Y. Cho, Science **264**, p. 553 (1994).

4. Although lead salt (IV-VI) semiconductor diode lasers have demonstrated 203 K cw operation [Z. Feit, D. Kostyk, R.J. Woods, and P. Mak, Appl. Phys. Lett. **58**, p. 343 (1991)] they are limited to very low power operation.

5. G.W. Turner, H.K. Choi, D.R. Calawa, J.V. Pantano, and J.W. Chludzinski, J. Vac. Sci. Technol. B **12**, p. 1266 (1994).

6. K. Onabe, NEC Res. Dev. **72**, p. 1 (1984).

7. H.K. Choi and G.W. Turner , to be published in Phys. Scripta.

8. H.C. Casey and M.B. Panish, Heterostructure Lasers, Part B, Academic, New York, 1978, p. 25.

9. G. Tuttle, H. Kroemer, and J.H. English, J. Appl. Phys. **67**, p. 3032 (1990).

10. H.K. Choi, G.W. Turner, M.J. Manfra, M.K. Connors, F.P. Herrmann, A. Baliga, and N.G. Anderson SPIE

11. A. Ghiti and E.P. O'Reiley, Semicond. Sci. Technol. **8**, p. 1655 (1993).

12. A. Baliga, F. Agahi, N. G. Anderson, K. M. Lau, and S. Cadambi, *IEEE J. Quantum Electron.* **32**, 29 (1996).

13. J. Wang, P. Von Allmen, J.-P. Leburton, and K. J. Linden, *IEEE J. Quantum Electron.* **31**, 864 (1995).

HIGH POWER InAsSb/InAsSbP LASER DIODES EMITTING at 3 ~ 5 μm RANGE

M. RAZEGHI
J. Diaz, H. J. Yi, D. Wu, B. Lane, A. Rybaltowski, Y. Xiao, H. Jeon[1]
Center for Quantum Devices, Northwestern University, Evanston, Illinois 60208

ABSTRACT

We report metalorganic chemical vapor deposition-grown double heterostructure and multiple quantum well InAsSb/InAsSbP laser diodes emitting at 3 to 4 μm and light emitting diodes up to 5 μm. Maximum output power up to 1 W (from two facets) with differential efficiency above 70 % up to 150 K was obtained from a MQW laser with stripe width of 100 μm and cavity length of 700 μm for emitting wavelength of 3.6 μm at 90 K. Maximum operating temperature up to 220 K with threshold current density of 40 A/cm^2 at 78 K were achieved from the double-heterostructure lasers emitting at 3.2 μm. The far-field beam divergence as narrow as 24° was achieved with the use of higher energy gap barrier layers, i.e., lower effective refractive index, in MQW active region. We also discuss the effect of composition-fluctuation in the InAsSb active region on the gain and threshold current of the lasers.

INTRODUCTION

Mid-infrared laser diodes (λ= 3 to 5 μm) are the attractive source for a wide range of applications ranging from chemical spectroscopy, free-space and optical fiber communication. The first mid-infrared laser operation was demonstrated from Pb-based IV-VI semiconductor lasers [1] and the room temperature operation was achieved for PbSe/Pb$_{1-x}$Sr$_x$Se double heterostructure (DH) lasers at emission wavelength 4 to 5 μm as early as in 1988 [2]. However, the Pb-salt lasers developed to date have been shown problematic in achieving high power, high efficiency, and/or high reliability. These problems presumably originated from weak bonding characteristic of IV-VI (rock-salt structure) semiconductors, resulting in poor mechanical strength and thermal stability.

A number of III-V semiconductor alloys, benefiting from stronger covalent bonding and advanced growth and device processing technology, have been investigated as alternatives. The III-V ternary InAs$_{1-x}$Sb$_x$ is a suitable material for the high power mid-infrared lasers with emission wavelengths of 3 to 5 μm in these reasons. Extensive research has been aimed to the realization of high power, room temperature operation of the lasers based on InAsSb [3,4]. However, to date no satisfactory performance of the Sb-based lasers has been achieved. The major problems are related to the difficulty of growth

---

[1] Permanent address: Semiconductor Physics Research Center, Jeonbuk National University, Jeonju, 560-756, Republic of Korea

of the high-quality cladding and/or barrier layers lattice matched to InAsSb. Initially Al-based higher band gap materials such as AlGaSb, AlInSb have been considered for the cladding layers, but later it was found that they have problems related to unfavorable type II band alignment with InAsSb which prevent efficient carrier confinement.

Unlike Al-based higher band-gap materials, the quaternary InPAsSb material system provides a very favorable condition for the carrier and optical confinement due to its favorable type-I band alignment and lower refractive index of the higher band gap materials, and excellent dopant incorporation [5], thereby providing efficient injection and carriers confinement. However, like other Sb-based alloys, it is well known that the InP(As)Sb is thermodynamically unstable at typical growth temperatures. Sringfellow [6], using his delta lattice theory (DLT), predicted that miscibility gap of $InAs_{1-x}Sb_x$ for growth temperature T ~ 500 °C will be formed between $x = 0.02$ to 0.98. This prediction was later found to be overestimated when realistic strain-stabilization effects related to epitaxial growth are considered [7]. Nevertheless, it is extremely difficult to grow a single phased InPSb system due to spinodal decomposition related to its thermally or unstable metastable phase [8].

After several years extensive research, reasonably high quality of metastable quaternary InPAsSb, AlInAsSb or AlAsSb have been grown either by molecular beam epitaxy (MBE) or metalorganic chemical vapor deposition (MOCVD). [3,4,9] However, for wavelength longer than 3 μm, the optical properties of the devices should be more improved in order to meet the requirements of various applications. To date optical loss larger than 20 cm^{-1}, differential efficiency below 50 %, and optical power below 300 mW are typically obtained. [3,4,9] In this article, we present the recent achievement of the high-power InAsSb/InAsSbP double heterostructure and multiple quantum well laser diodes grown by low-pressure MOCVD (LP-MOCVD) for emission wavelengths of 3 to 5 μm. LP-MOCVD-grown InAsSb/ InPAsSb DH and MQW lasers show the maximum output power (from two facets) up to 600 mW and 1 W, respectively, with differential efficiency of 70 % to 90 % up to 150 K. Maximum operating temperature up to 220K with threshold current density as low as 40 A/cm^{2} at 78 K and the far-field beam divergence as narrow as 24° are obtained.

The dependence of J_{th} on cavity length (or on mirror loss) reveals that the lasers have strong gain saturation. Based on the recent TEM measurements, we have modeled the effect of inhomogeniety of the composition in the active region. This model is shown to explain the steep increase of J_{th} on the increase in mirror loss.

FABRICATION AND EXPERIMENT

Double-heterostructure (DH) [10,11,12] and MQW [13,14] InAsSbP/InAsSb/InAs were grown on (100) oriented Te-doped InAs substrate by LP-MOCVD in an EMCORE MOCVD reactor at a pressure of 60 Torr and a temperature of 490 °C, using trimethylindium (TMIn), trimethylantimony (TMSb), arsine (AsH₃) and phosphine (PH₃) for the group III and V sources, diethylzinc (DEZn) and tetraethlytin (TESn) for p- and n-dopants, respectively. The DH structure consists of a 1.0 μm-thick undoped ternary active region InAsSb centered between two 1.5 μm -thick InAsSbP cladding layers: Sn-

doped (10^{18} cm^{-3}) and Zn-doped (10^{18} cm^{-3}), respectively, and a p^+-doped InAs cap layer. The active region of the MQW lasers consists of 10 compressively strained quantum wells of InAs$_x$Sb$_{1-x}$ embedded in a 1 μm-thick InAs layer which is surrounded by 1.2 μm-thick n- and p-InAs$_x$Sb$_y$P$_{1-x-y}$ cladding layers. All layers except for the compressively strained InAs$_x$Sb$_{1-x}$ layers are lattice-matched to the n^+-InAs substrate. Each quantum well was nominally 100 Å thick and separated by 500 Å InAs barrier layers.

Broad-area laser diodes with a stripe width of 100 μm were fabricated using lift-off process, in which the p^+- InAs cap layer is etched away between the metal contact stripes composed of Ti/Pt/Au. The InAs cap layer between the patterned stripes is chemical etched using H$_2$SO$_4$: H$_2$O$_2$: H$_2$O in order to localize the injection current in the lateral direction. Thermal treatment of the p- and n-ohmic contacts are performed at temperatures between 300 - 320 °C to obtain low-resistance of 0.2 Ω for diodes at cavity length of 700 μm at 78 K. After ohmic contact deposition, individual diodes were cleaved and mounted p-side up on copper heatsinks by indium bonding. Uncoated diodes with cavity length varying from 200 to 1200 μm were prepared. Light-current characteristics were measured in both continuous wave (CW) and pulse-mode (pulse width 4-7 μs, repetition rate 200 Hz) operations with lasers mounted inside a VPF -100 Janis cryostat with temperature varying between 77 K and 300 K using an InSb photodetector.

RESULTS AND DISCUSSION

InAsSb/InPAsSb DH lasers at λ= 3.2 μm

Figure 1 shows the current-light characteristics of the InAsSb/InPAsSb DH lasers. Peak output powers of 540 mW and 240 mW were obtained from the DH lasers at pulsed mode and CW operations, respectively, at λ= 3.2 μm. It shows no significant difference between differential efficiencies η_d in CW and pulse mode operations for the optical power lower than 230 mW. Above 230 mW a very strong thermal-rollover prevents lasing in the CW operation. The CW thermal-rollover is not irreversible damage of the devices, as evidenced by the fact the laser characteristics were recovered when the current is returned below 1.0 A. The differential efficiency η_d for this wavelength was determined by to be 83 %, with *PI* curve showing no sign of any nonlinearities or kinks. The maximum power in most of the devices was limited by our automated current driver. The laser operated up to 220 K with an output power of 1 mW (at I ~ 9.5 A). The internal loss of these InAsSb/InAsSbP DH lasers is determined by measuring the differential quantum efficiency of the diodes at several cavity lengths. Figure 2 shows the measured reciprocal η_d as function of cavity length indicating the optical loss of 3.3 cm^{-1}, which is to the best of our knowledge the lowest ever reported (Fig. 2).

InAsSb/InPAsSb
W=100μm, L=1205μm
— Pulse operation
··· CW operation
540mW/2f
240mW/2f cw
Light power [mW/2facets]
Current [A]
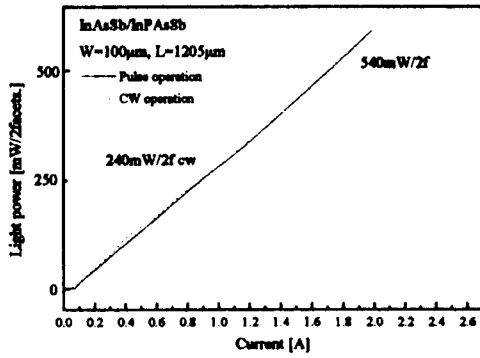
Fig. 1. P-I curve for CW and pulse mode operations of InAsSb/InPAsSb DH lasers (λ= 3.2 μm)

InAsSb/InPAsSb/InAs DH
W=100 μm
pulse=6μs/200Hz
α_{int} ~3.3 cm^{-1}
$1/\eta_d$
Cavity Length [μm]

InAsSb/InPAsSb
W=100 μm
pulse 6μs-200Hz
J_{tr} = 34 A/cm^2
Inhomogeneous media
Homogeneous media
J_{th} [A/cm^2]
1/L [cm^{-1}]
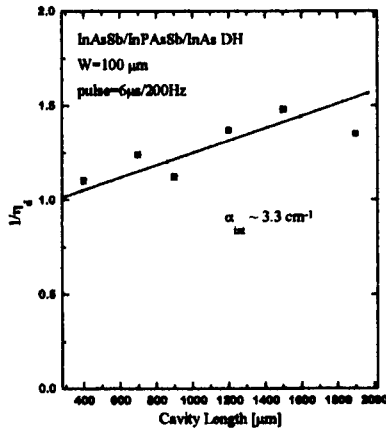
Fig. 2 Dependence of $1/\eta_d$ on cavity length L of InAsSb/InPAsSb DH lasers (λ= 3.2 μm)
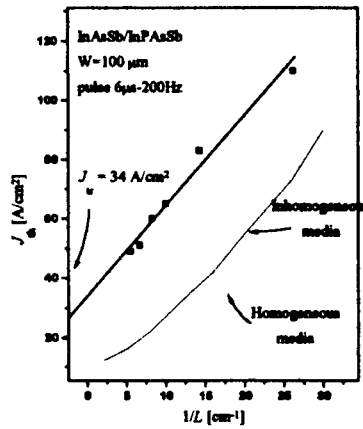
Fig. 3 Dependence of J_{th} on reciprocal cavity length L of InAsSb/InPAsSb DH lasers (λ= 3.2 μm)

The dependence of J_{th} as function of mirror loss α_m (~ 1/L, L is cavity length) (Fig. 3) shows the transparency current density of 34 A/cm^2 and that J_{th} has a very strong dependence on the mirror loss. We made theoretical models to explain the dependence. The dotted line represents the theoretical result when the InAsSb active layer is assumed to form a single-phase alloy with a homogeneous composition.[15] A standard radiative

16

recombination model based on Kane's Hamiltonian is used to calculate the material gain and threshold current density as a function of cavity length.[16] The Auger recombination and minority-carrier leakage current are found negligible in this temperature range through both a recent photoluminescence experiment [12] and our calculation. In this calculation, it was found that the theoretical J_{th} does not significantly depend on the cavity length (Fig. 3 dotted line) and thus cannot explain the strong cavity length dependence of J_{th} observed in our experiment. The small increase of the theoretical values of J_{th} for the decrease in cavity length (i.e. an increase in the mirror loss) is attributed to high differential gain (a rapid increase of material gain g with an increase of carrier density n) (See Fig. 4 solid line).

In recent TEM measurements on InAsSb and InPSb alloys,[8] it was found that the alloys are not stable in forming a single-phase composition as consistent with thermodynamic calculation that predict large miscibility gaps.[6] This led us to consider the effect of the composition inhomogeniety in InAsSb active layer alloys on the radiative recombination model. In the new model, we assumed that alloys have several phases such as ordered and disordered structures with different compositions as observed in TEM.[8] The regions with different compositions have different energy gaps, and therefore have different gain spectrum from other regions. The average material gain spectrum is obtained by summing the gain spectra from each region and the peak gain determined as function of injection current (Fig. 4). As shown in Fig. 4, compared to the homogeneous composition material (solid line), the differential gain (dg/dn, n is injection carrier density) of the inhomogeneous composition material (dotted line) is much lower. The solid line in Fig. 3 represents the results of the new model. A strong gain saturation in the inhomogeneous composition material results in rapid increase of J_{th} with a decree of cavity length, as consistent with experiment. Due to unknown material parameters of the InAsSb alloys, only qualitative modeling is allowed, resulting in some discrepancy shown in Fig. 3. Nevertheless, the above results indicate that the inhomogeniety of the material is significant and may be the governing factor that inhibits the laser operation at high temperature.
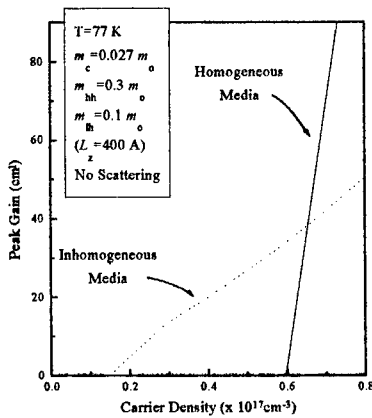
Fig. 4. Theoretical curve of peak gain vs. injection carrier density n
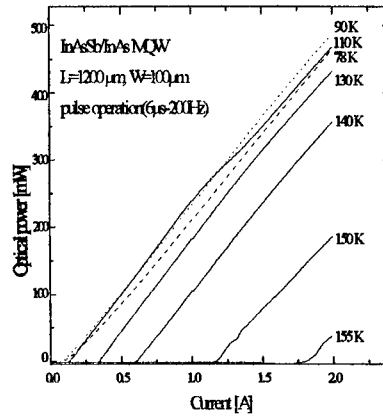
Fig. 5. P-I curves of InAsSb/InAs/InPAsSb MQW lasers (λ= 3.6 μm) for T = 78 to 155 K

17

InAsSb/InPAsSb MQW lasers at λ= 3.6 μm

Figure 5 shows *P-I* curves of the InAsSb/InPAsSb MQW lasers with emission wavelength of 3.6 μm measured between T = 78 and 155 K. The differential efficiency remains above 70 % up to 155 K. Such high values of differential efficiency for the wide range of temperatures up to 155 K, to the best of our knowledge, had not been obtained from lasers based on conventional inter-band transition for λ> 3.5 μm. As shown in Fig. 6, these MQW lasers exhibited multiple longitudinal modes centered at 3.64 μm around 130 K. The most striking feature of Fig. 6 that shows emission spectra vs. operating temperature, is that the spectrum shows two types of temperature dependence: the peak wavelength shifts to longer wavelengths (red-shift) below 130 K with a tuning rate of 0.6 nm/K, while above 130 K, the peak wavelength becomes rapidly shorter as temperature increases with the tuning rate of 7 nm/K. This is a strong indication that below 130 K, the wavelength is determined by the energy gap of InAsSb (energy gaps narrow with the increase in temperature) while above 130 K, the carriers band-filling determines the emission wavelength.
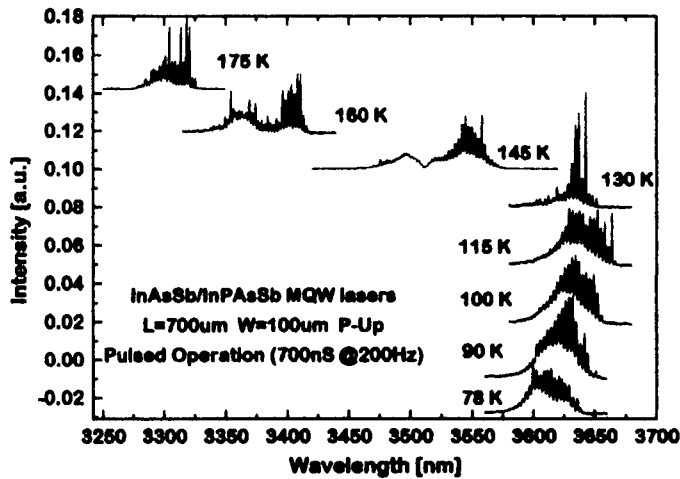
Fig. 6. Laser emission spectra of an InAsSb/InAs/InPAsSb MQW laser (λ= 3.6 μm) for T = 78 to 180 K

Maximum output power (from two facets) up to 1 W was obtained from a MQW laser with stripe width of 100 mm and cavity length of 700 mm for emitting wavelength of 3.65 mm at 90 K (Fig. 7). The output power is, to the best of our knowledge, the highest power reported from laser diodes for the wavelength range. The lasers were bonded p-side-up because of lack of available current confining technologies for low energy gap materials. Current confinement by deposition of SiO_2 layers is expected to enable p-side down bonding and consequently even higher-power and/or higher-temperature operation.

Far-field beam divergence's of the two kinds of MQW structures (#135 and #147) have been compared. MQW active regions of the both structures consist of the same 100 Å-thick InAsSb quantum wells separated by 400 Å-thick barrier layers. The only difference is that one (#135) employs InAs ($\lambda = 3.0$ μm) while the other (#147) uses InPAsSb ($\lambda = 2.7$ μm) as the quantum-well barrier layers. The dotted line and the solid line in Fig. 8 represent the far-field patterns of #135 and #147, respectively. The noise-like small modulations in the far-field patterns are due to experimental artifice due to interference of the lasers with cryostat windows. The far-field beam divergence $\Delta\theta$ is strongly dependent on the structure as shown in Fig. 8. Much narrower $\Delta\theta$ was obtained from #147 (24°) than for #135 (39°). This difference can be explained by the difference in the effective refractive index N_r of the MQW active regions: the higher N_r in MQW active region of #147 than for #135 (since InPAsSb barrier layers (#147) has lower N_r than InAs barrier layers (#135)) makes the confinement of the laser emission light weaker, resulting in narrower far-field beam divergence of #147 as consistent with standard diffraction theory.[17]
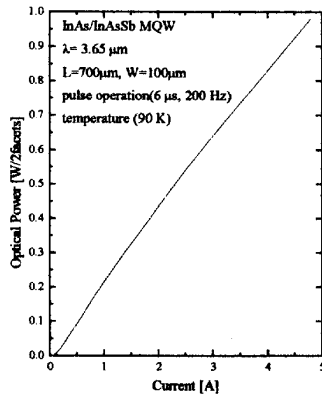
Fig. 7. *P-I* curve of InAsSb/InAs/InPAsSb MQW lasers showing 1 W
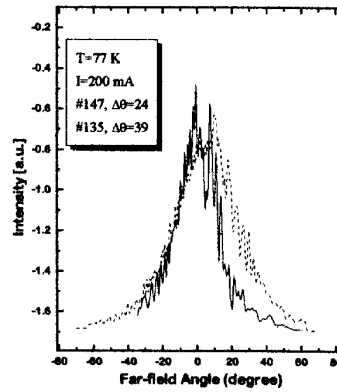
Fig. 8. Far-field pattern of the MQW lasers.

19

InAsSb/InPAsSb MQW light emitting diodes at λ= 4 to 5 µm

Light sources for wavelengths longer than 4 µm are important for detection of important atmospheric gases. For example, H_2O and CO_2, CO have strong absorption bands between 4 to 5 µm wavelength range.[18] We have extended the emission wavelength by increasing Sb composition in the quantum well. The resultant increase in compressive strain of the quantum wells makes the growth of high quality InAsSb active region difficult. Nevertheless, high luminescence-efficiency light sources were grown. Figures 9 and 10 show the electroluminescence spectra of primary MQW InAsSb/InAs/InPAsSb structures with emission wavelengths of 4.2 and 5 µm, respectively with maximum powers of around 1 µW. Very narrow FWHM of 11 meV and 21 meV were obtained at 78 K for λ= 5 µm and λ= 4.5 µm, respectively, which are only 2 to 3 times thermal broadening (*kT*). The bright and narrow-width electroluminescence from the primary MQW structures for beyond 4 µm presents the promising potentials of the MOCVD-grown InAsSb/InPAsSb heterostructures for the mid-infrared lasers for deep mid-infrared ranges.
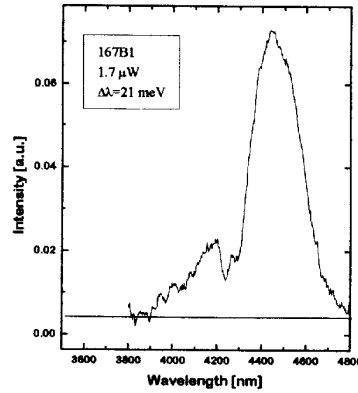
Fig. 9. Electroluminescence spectrum of an InAsSb/InAs MQW structure with center wavelength λ= 4.5 µm
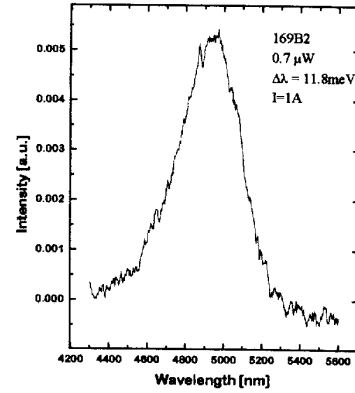
Fig. 10. Electroluminescence spectrum of an InAsSb/InAs MQW structure with center wavelength λ= 5 µm

20

CONCLUSION

In this article, we demonstrated the high power, high temperature operations of the MOCVD-grown DH and MQW lasers based on InAsSb/InPAsSb/InAs heterostructures for the emission wavelengths of 3 to 5 μm. Maximum power up to 1 W has been demonstrated from a MQW laser with differential efficiency over 70 % up to 150 K for $\lambda = 3.2$ μm. Comparison of the measurement on dependence of J_{th} on mirror loss (~ 1/L) with the theoretical calculation indicates that the inhomogeniety may be responsible for the anomalous cavity length (L) dependence of J_{th}. The far-field beam divergence as narrow as 24° is achieved with the use of higher energy gap barrier layers (lower effective refractive index) in MQW active region. Electroluminescence for emission wavelengths up to 5 μm was obtained. The bright and narrow-width electroluminescence from the primary MQW structures for beyond 4 μm presents the promising potentials of the MOCVD-grown InAsSb/InPAsSb heterostructures for the mid-infrared lasers for deep mid-infrared ranges.

REFERENCES

[1] J. N. Walpole, A. R. Calawa, T. C. Harman, and S. H. Groves, Appl. Phys. Lett. **28**, 552 (1976)

[2] B. Spanger, U. Schiessl, A. Lambrecht, H. Bottner, and M. Tacke, Appl. Phys. Lett. **53**, 2582 (1988); Z. Shi, M. Tacke, L. Lambrecht, and H. Bottner, Appl. Phys. Lett. **66**, 2537 (1995)

[3] H. K. Choi, G. W. Turner, M. J. Manfra, and M. K. Connors, "175 K continuous wave operation of InAsSb/InAlAsSb quantum well diode lasers emitting at 3.5 μm", Appl. Phys. Lett. **68**, 2936 (1996)

[4] S. R. Kurtz, R. N. Biefeld, A. A. Allerman, A. J. Howard, M. H. Crawford, and M. W. Pelczynski, "Pseudomorphic InAsSb multiple quantum well injection laser emitting at 3.5 μm", Appl. Phys. Lett. **68**, 1332 (1996)

[5] A. A. Allerman, R. M. Biefeld, and S. R. Kurtz, Appl. Phys. Lett. **69**, 465 (1996); C. A. Wang, K. F. Jensen, A. C. Jones, and H. K. Choi, Appl. Phys. Lett. **68**, 400 (1996)

[6] G. B. Stringfellow, J. Crystal Growth **58**, 194 (1982)

[7] F. Glas, J. Appl. Phys. **62**, 3201 (1987)

[8] D. M. Follstaedt, R. M. Biefeld, S. R. Kurtz, and K. C. Baucom, J. Electron. Mater. **24**, 819 (1995); R. M. Biefeld, K. C. Baucom, S. R. Kurtz and D. M. Follstaedt, J. Cryst. Growth **133**, 38 (1993)

[9] H. K. Choi, G. W. Turner, and Z. L. Liau, Appl. Phys. Lett. **65**, 2251 (1994)

[10] J. Diaz, H. Yi, A. Rybaltowski, B. Lane, G. Lukas, D. Wu, S. Kim, M. Erdtmann, E. Kass, and M. Razeghi, "Aluminium free InAsSbP/InAsSb/InAs laser diodes (λ= 3.2 μm) grown by low-pressure metalorganic chemical vapor deposition", to be published in Appl. Phys. Lett.

[11] D. Wu, E. Kass, J. Diaz, B. Lane, A. Rybaltowski, H. J. Yi, and M. Razeghi, "InAsSbP/InAsSb/InAs diode lasers emitting at 3.2 μm grown by Metalorganic chemical vapor deposition", to be published in IEEE Photon. Technol. Lett.

[12] S. Kim, M. Erdtmann, D. Wu, E. Kass, H. Yi, J. Diaz, and M. Razeghi, "Photoluminescence study of InAsSb/InAsSbP heterostructures grown by low-pressure metalorganic chemical vapor deposition", Appl. Phys. Lett. **69**, 1614 (1996)

[13] B. Lane, D. Wu, H. Yi, J. Diaz, A. Rybaltowki, S. Kim, M. Erdtmann, H. Jeon, and M. Razeghi, "Study on the effects of minority carrier leakage in InAsSb/InPAsSb double heterostructures", to be published in Appl. Phys. Lett.

[14] B. Lane, D. Wu, A. Rybaltowski, H. Yi, J. Diaz, and M. Razeghi, "Compressivly-strained multiple quantum well InAsSb lasers emitting at 3.6 μm grown by metal-organic chemical vapor deposition", to be published in Appl. Phys. Lett.

[15] D. Gershoni, C. H. Henry, and G. A. Baraff, IEEE J. Quantum Electron. **QE-29**, 2433 (1993)

[16] Reisinger, P. Zory, Jr., and R. Waters, IEEE J. Quantum Electron. **QE-23**, 993 (1987)

[17] J. Bulter, J. Zoroofchi, "Radiation Fields of GaAs-(AlGa)As Injection Lasers", IEEE J. Quantum Electron. **QE-10**, 809 (1974)

[18] Monroe Schlessinger, "Infrared Technology fundamentals" (Marcel Dekker, Inc., New York, 1995)

NOVEL MID-INFRARED LASERS WITH COMPRESSIVELY STRAINED InAsSb ACTIVE REGIONS

S. R. Kurtz, R. M. Biefeld, and A. A. Allerman
Sandia National Laboratory, Albuquerque, New Mexico, 87185, USA

ABSTRACT

Mid-infrared lasers grown by MOCVD with AlAsSb claddings and strained InAsSb active regions are reported. A 3.8-3.9 μm injection laser with a pseudomorphic InAsSb multiple quantum well active region lased at 210 K under pulsed operation. A semi-metal layer acts as an internal electron source for the injection laser. An optically pumped laser with an InAsSb/InAsP strained-layer superlattice active region was demonstrated at 3.7 μm, 240 K.

INTRODUCTION

Driven by chemical sensing and infrared countermeasure applications, several mid-infrared (2-6 μm) diode lasers with strained InAsSb active regions have been recently demonstrated. Devices with AlAsSb claddings have been grown by molecular-beam epitaxy,[1,2] and metal organic chemical vapor deposition (MOCVD) lasers with higher index, InPSb claddings have also been reported.[3,4] Although AlAsSb claddings provide superior optical confinement, the large conduction band barriers associated with AlAsSb layers can result in poor electron injection and high turn-on voltages. Also, due to lack of satisfactory aluminum sources and residual carbon resulting in p-type doping of AlSb alloys, MOCVD growth of AlAsSb injection devices had not been reported. In this paper, we report the first MOCVD grown lasers with AlAsSb claddings. First, we describe an electrically injected device which utilizes a GaAsSb (p) / InAs (n) heterojunction to form an internal, semi-metal layer. The semi-metal acts as an internal electron source which can eliminate many of the problems associated with electron injection in these devices, and this novel device is compatible with MOCVD materials and background dopings. Furthermore, the use of an internal electron source enables us to consider alternative laser and LED designs that would not be feasible with conventional, bipolar devices. Initial results for an optically pumped laser with an InAsSb/InAsP strained-layer superlattice (SLS) active region also are presented. Due to a large valence band offset, the light-heavy hole splitting in InAsSb/InAsP SLSs is estimated to be $\approx$ 80 meV, and Auger recombination should be further reduced in this active region.

SEMI-METAL INJECTION LASER WITH PSEUDOMORPHIC InAsSb MULTIPLE QUANTUM WELL ACTIVE REGION

The band alignments[5] for the MOCVD grown, injection laser are shown in Figure 1. As confirmed by x-ray measurements, both the claddings and active region of the laser are nominally lattice matched to the substrate. Following a $GaAs_{0.09}Sb_{0.91}$ buffer, a 2.5 micron thick $AlAs_{0.16}Sb_{0.84}$ cladding is grown on an n-type, InAs substrate. A 200Å, $GaAs_{0.09}Sb_{0.91}$ layer lies between the bottom cladding and a 0.6 μm thick InAs active region containing 10, pseudomorphic $InAs_{0.88}Sb_{0.12}$ quantum wells, each 90Å thick. A 2.5 μm thick $AlAs_{0.16}Sb_{0.84}$ cladding followed by a 200Å, $GaAs_{0.09}Sb_{0.91}$ contact and oxidation barrier layer is grown on top of the active region. AlAsSb and GaAsSb alloys have p-type background doping levels of $\approx 10^{17}/cm^3$, estimated from Hall measurements. The background doping of the InAs/InAsSb active region is n-type, $\approx 10^{15}$-$10^{16}/cm^3$. Details of the MOCVD growth are published elsewhere.[6,7]

For a wide range of Fermi energies, the GaAsSb (p) / InAs (n) heterojunction is a semi-metal, acting as a source/sink for electron-hole pairs. In forward bias (shown in Fig. 1), electrons are generated in the semi-metal and swept into the active region to recombine with holes being injected from the anode (+). The hole flux is replenished by holes generated in the semi-metal and swept away from the active region. Only hole transport is observed in the AlAsSb claddings (labeled points A and B in Fig. 1), and over this segment, the device can be described as unipolar.

Gain-guided, stripe lasers were fabricated with Ti/Au metallizations. The facets were uncoated. Under pulsed operation, lasing was observed in forward bias with 40x1000 or 80x1000 micron stripes. No emission occurred under reverse bias. Devices were tested with 100 nsec pulse widths at 10 kHz (0.1 % duty-cycle). Several longitudinal modes were observed in the 3.8-3.9 μm range, shown in Figure 2 for 80 K and 200 K operation. Characteristic of the pseudomorphic InAsSb lasers, laser emission was blue-shifted by $\approx$ 20 meV from the peak of the InAsSb quantum well photoluminescnce, [3] and consistent with the selection rule for the compressively strained InAsSb quantum well electron ($|1/2,\pm1/2\rangle$) -hole ($|3/2,\pm3/2\rangle$) transition, laser emission was 100% TE polarized. The lasers displayed sharp threshold current characteristics, and lasing was observed through 210 K. (see Figure 3) Under pulsed operation, peak power levels $\geq$ 1 mW/facet could be obtained. A characteristic temperature (T_o) in the 30-40 K range was observed, with the lower value (30 K) being misleading due to degradation of the device at high current density.

These maximum operating temperature and characteristic temperature values are comparable to the highest values reported to date, for injection lasers of this wavelength with either strained InAsSb or InAs/GaInSb active regions.[2,3,8] Previously, a bipolar laser with a similar, pseudomorphic InAsSb multiple quantum well active region displayed the same characteristic temperature.[3] We believe that the characteristic temperature of both devices is limited by design of the active region and the resulting Auger rates.[3] Unlike bipolar lasers, cw operation of the semi-metal laser has not yet been observed. At threshold and 100K, we find that the maximum duration of the semi-metal laser output is $\approx$ 10^{-5} sec, with a comparable recovery time. If the device is driven above threshold with long pulses, lasing ceases and a different, low intensity emission spectrum is observed which indicates extreme band bending and depletion of the semi-metal. Due to capacitive charging within the device, the pulsed threshold current of the semi-metal laser was 10x that reported previously for the pseudomorphic, bipolar laser. Lasing pulse duration, duty-cycle, threshold current, and turn-on voltage of the semi-metal emitters may be improved with modifications in doping and heterojunction design.

OPTICALLY PUMPED, InAsSb/InAsP SLS ACTIVE REGION LASER

To further reduce Auger recombination, we are developing lasers with InAsSb/InAsP SLS active regions. Based on band offsets and light-heavy hole splittings measured in other InAsSb heterostructures,[9,10] we find that InAsSb/InAsP SLSs will exhibit large electron and hole confinement energies, and light-heavy hole splittings as large as 80 meV should be easily realized. (See Figure 4) We constructed a InAsSb/InAsP SLS laser similar to the semi-metal injection laser described previously, except a $InAs_{0.88}Sb_{0.12}/InAs_{0.73}P_{0.27}$ (80 Å / 80Å) SLS was substituted in place of the pseudomorphic active region. The unnecessary carriers in the cladding layers and the semi-metal layer may contribute loss to this optically pumped device.

The InAsSb/InAsP SLS laser was pumped with a Q-switched Nd:YAG (20 Hz, 10 nsec pulse), and emission was detected with an FTIR operated in a step-scan mode. Due to the low rep-rate of the pump, the resolution of the experiment was 2 cm^{-1}. Laser emission was observed from cleaved bars, 1000 μm wide. A sharp lasing threshold and spectrally narrowed stimulated emission was seen from 80 K through 240 K, the maximum temperature where lasing occurred. (See Fig. 5 and Fig. 6(a)) The temperature dependence of the threshold is well described by a characteristic temperature, T_0 = 32 K. (See Fig. 6(b))
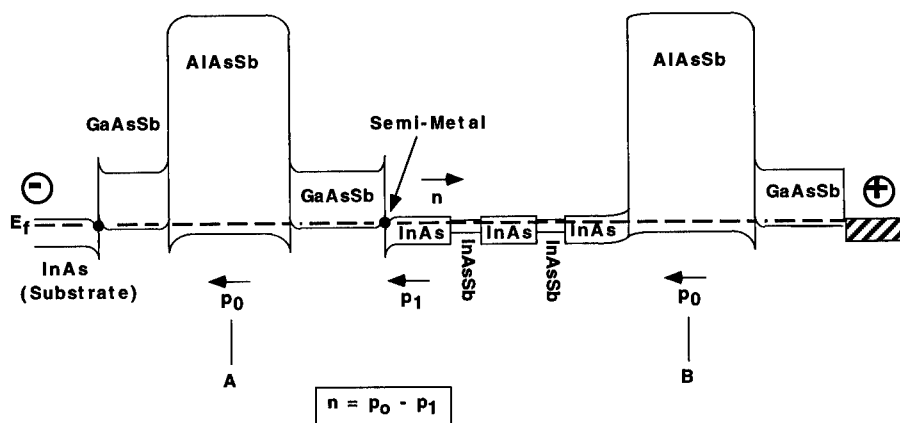
Figure 1 - Heterojunction band alignments for the MOCVD-grown, injection laser with a pseudomorphic InAsSb MQW active region. Forward bias polarity is indicated in the figure.
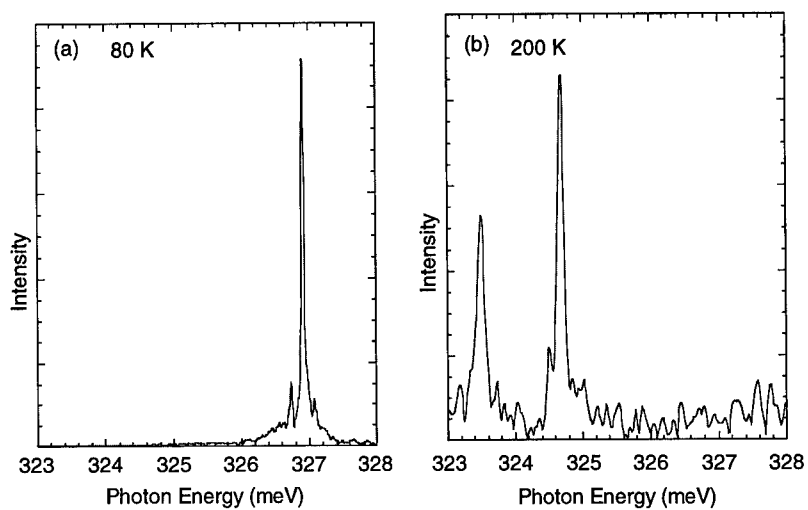
Figure 2 - Injection laser emission spectra at 1.1xIth for (a) 80K and (b) 200K.

25
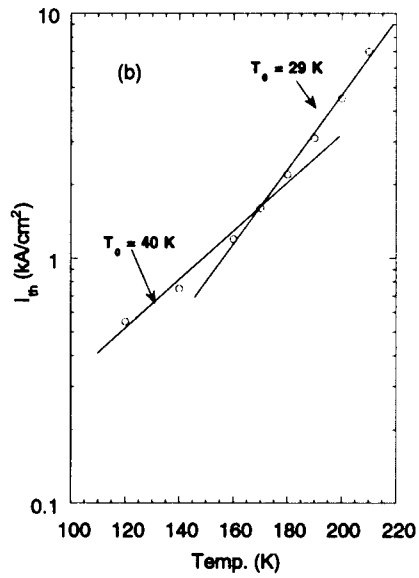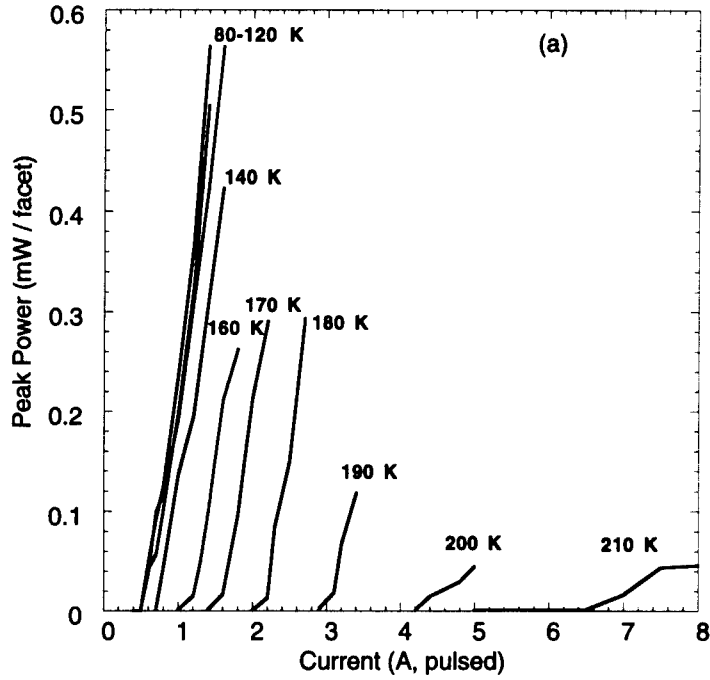
Figure 3 - (a) Injection laser emission intensity versus peak current for various temperatures. (b) Pulsed threshold current density versus temperature. The stripe dimensions were 40x1000 μm.

InP$_{0.29}$As$_{0.71}$
(100 Å)

InAs$_{0.85}$Sb$_{0.15}$
(100 Å)

1e

400 meV

1hh
1lh
2hh
LH
HH

HH
LH
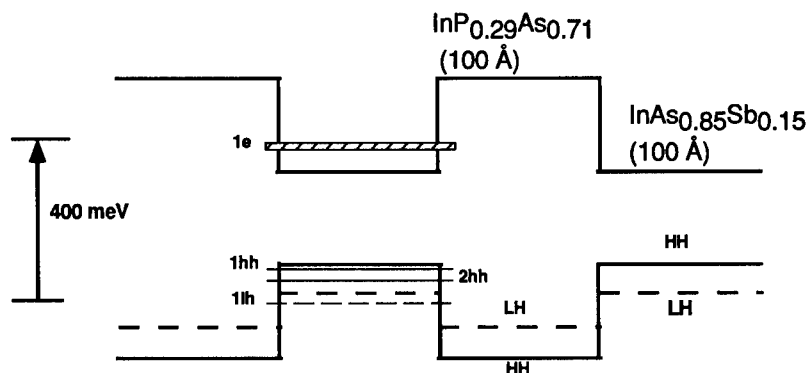
E (1e - 1hh) = 303 meV (4.1 μm)

E (1hh - 1lh) = 86 meV

SLS lattice- matched to InAs

Figure 4 - Band alignments and quantum confinement state energies (drawn to scale) for an InAs$_{0.85}$Sb$_{0.15}$ / In As$_{0.71}$P$_{0.29}$ (100 Å / 100 Å) SLS. The estimated bandgap of the unstrained, MOCVD-grown InAs$_{0.85}$Sb$_{0.15}$ alloy was 218 meV.
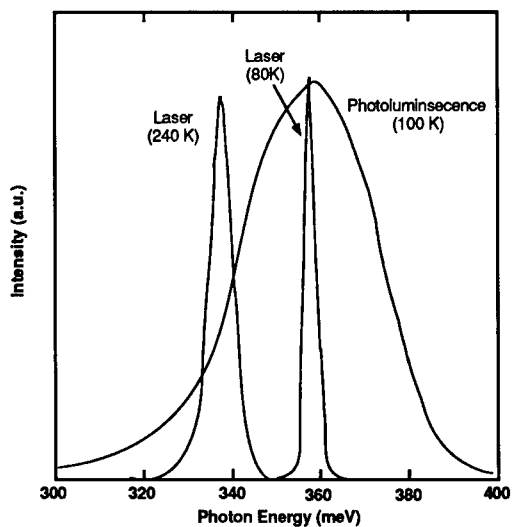
Figure 5 - Photoluminscence and optically pumped laser emission for a device with an InAs$_{0.88}$Sb$_{0.12}$ / InAs$_{0.73}$P$_{0.27}$ (80 Å/ 80 Å) active region.
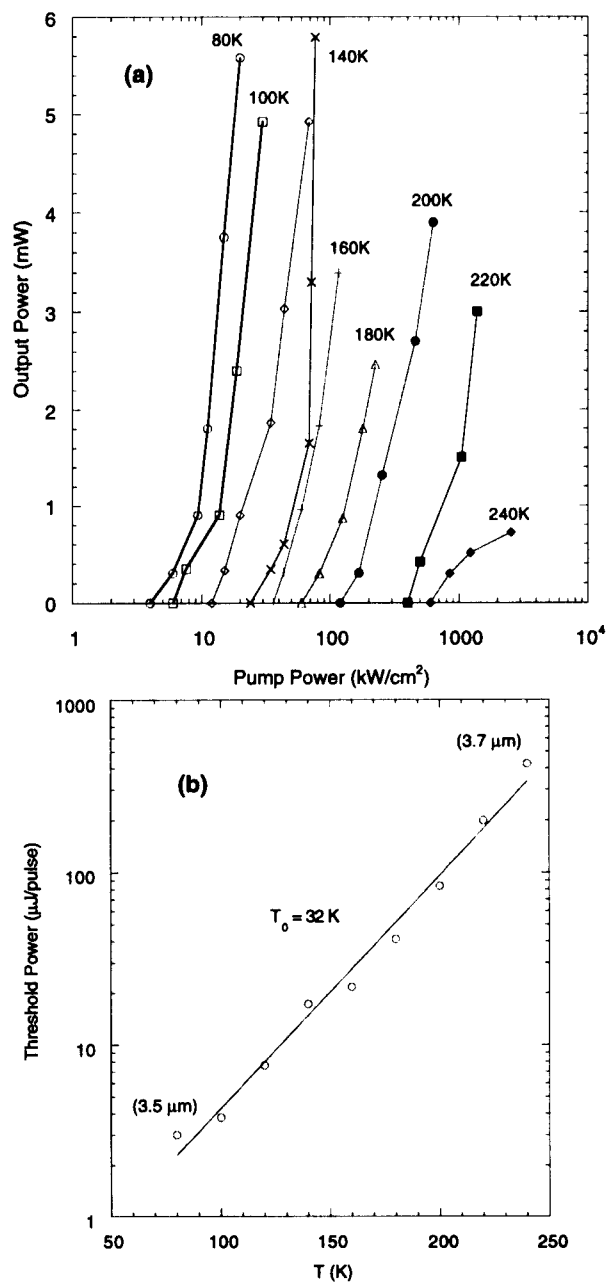
Figure 6 - (a) Peak power output versus temperature and pump power for the InAsSb/InAsP SLS laser. (b) Threshold pump power versus temperature for the SLS laser.

Unlike the pseudomorphic devices, laser emission occurs near the peak of the spontaneous emission, indicated by the photoluminescence sprectrum in Fig. 5. The wavelength of the SLS laser shifts from 3.5 μm to 3.7 μm due to the decrease in bandgap over the 80-240K temperature range. Overall, the performance (output power, threshold power, characteristic temperature, maximum temperature) of the optically pumped type I, InAsSb/InAsP SLS laser is comparable to that initially reported for a 4 μm, InAs/GaInSb type II laser measured under similar conditions.[11]

SUMMARY

In conclusion, we report MOCVD grown, 3.5-3.9 μm lasers with AlAsSb claddings and strained InAsSb active regions. An injection device utilizes an internal semi-metal electron source, and state-of-the-art performance is obtained under pulsed operation. The use of the InAs/GaSb semi-metal for carrier injection, and the compatibility of the semi-metal with InAsSb devices is unique. An analogous concept is being explored for InAs/GaInSb devices where an "InAs/AlSb/GaInSb like" tunnel-barrier is used to internally generate electron-hole pairs and achieve multi-stage or "cascaded" laser operation.[12] In order to further decrease Auger recombination, lasers with InAsSb/InAsP SLS active region are being developed, and an optically pumped device is reported. Measured under pulsed, low rep-rate conditions, emission was observed at 3.8 μm, 240 K for the type I SLS laser.

REFERENCES

[[1] S. J. Eglash and H. K. Choi, Appl .Phys. Lett. 64, 833 (1994).
[2] H.K. Choi and G.W. Turner, Appl. Phys. Lett. 67, 332 (1995)..
[3] S.R. Kurtz, R.M. Biefeld, A.A. Allerman, A.J. Howard, M.H. Crawford and M.W. Pelczynski, Appl. Phys. Lett. 68, 1332 (1996).
[4] R. J. Menna, D. Garbuznov, R. U. Martinelli, and G. H. Olsen, (to be published).
[5] Chris G. Van de Walle, Phys. Rev. B 39, 1871 (1989).
[6] R. M. Biefeld, K. C. Baucom, and S. R. Kurtz, J. Crys. Growth 137, 231 (1994).
[7] A. A. Allerman, R. M. Biefeld, and S. R. Kurtz, Appl. Phys. Lett. 69, 465 (1996).
[8] R. H. Miles (private communication).
[9] S. R. Kurtz and R. M. Biefeld, Appl. Phys. Lett. 66, 364 (1995).
[10] S. R. Kurtz, R. M. Biefeld, and A. J. Howard, Appl. Phys. Lett. 67, 3331 (1995).
[11] J. I. Malin, J. R. Meyer, C. L. Felix, J. R. Lindle, L. Goldberg, C. A. Hoffman, F. J. Bartoli, C. H. Lin, P. C. Chang, S. J. Murry, R. Q. Yang, and S. S. Pei, Appl Phys. Lett. 68, . 2976 (1996).
[12] J. R. Meyer, I. Vurgaftman, R. Q. Yang, and L. R. Ram-Mohan, Elect. Lett. 32, 45 (1996). R. Q. Yang, C. H. Lin, P. C. Chang, S. J. Murry, D. Zhang, S. S. Pei, S. R. Kurtz, A. N. Chu, and F. Ren, Elect. Lett. 32, 1621 (1996).

IR Sources and Modulators Based on InAs/GaSb/AlSb-Family Quantum Wells

J. R. Meyer*, C. L. Felix*, J. I. Malin*, I. Vurgaftman*, C.-H. Lin**, R. Q. Yang**, S.-S. Pei**, and L. R. Ram-Mohan***
*Code 5613, Naval Research Laboratory, Washington, DC 20375
**Space Vacuum Epitaxy Center, University of Houston, Houston, TX 77204
***Worcester Polytechnic Institute, Worcester, MA 01609

ABSTRACT

We review recent applications of *wavefunction engineering* to the design of antimonide quantum heterostructures with favorable properties for infrared devices. Examples include electro-optical and all-optical modulators based on Γ-L intervalley transfer, type-II quantum well lasers with enhanced gain per injected carrier, and type-II interband cascade lasers predicted to combine low thresholds and high output powers.

INTRODUCTION

The InAs/GaSb/AlSb family of materials is particularly well suited for the application of "wavefunction engineering" concepts to the design of new types of optical and electronic devices. In antimonide-based quantum heterostructures, a diverse array of key band structure, electronic, and optical properties may be flexibly tailored to match the needs of a given application.[1] In fact, one may specify either narrow-gap or wide-gap, type-I or type-II band alignment, Γ- or L-point conduction band minimum, large or small interband optical matrix elements, large or small intersubband matrix elements at normal incidence, *etc.*

This paper reviews some recent theoretical and experimental progress toward the development of longwave and mid-wave infrared (LWIR and MWIR) modulators and sources employing antimonide-family quantum wells. Section 2 will consider novel electro-optical (EO) and all-optical IR modulator concepts based on the transfer of electrons from Γ-valley states to L-valley states having much different optical selection rules at normal incidence. IR sources based on type-II quantum wells are discussed in Section 3, along with experimental results displaying the first MWIR lasing from an interband semiconductor device operating at or above room temperature. This is followed in Section 4 by theoretical projections for the type-II interband cascade laser, which combines advantages of both conventional bipolar interband lasers and unipolar intersubband-based cascade lasers.

IR MODULATORS

Intersubband interactions in quantum wells have frequently been suggested as a basis for electro-optical devices operating in the infrared.[2] But despite the experimental confirmation of large EO coefficients,[3] the development of practical IR modulators remains at a relatively primitive stage. In large part this is because normal-incidence intersubband interactions are forbidden for electrons occupying the isotropic conduction band minimum

31

at the center of the Brillouin zone (the Γ point), where coupling requires a component of the optical electric field along the quantization axis. Fortunately, this polarization selection rule breaks down if the electrons populate the highly-anisotropic L or X valleys, as long as the symmetry axes of the elliptical constant-energy surfaces are tilted with respect to the confinement axis.[4] Normal-incidence absorption coefficients of up to 10^4 cm^{-1} have been confirmed by experiments on antimonide-based quantum wells with L-valley conduction-band minima.[5, 6, 7] Several electro-optical and nonlinear optical devices based on the L-valley quantum well properties have been proposed.[8, 9, 10]
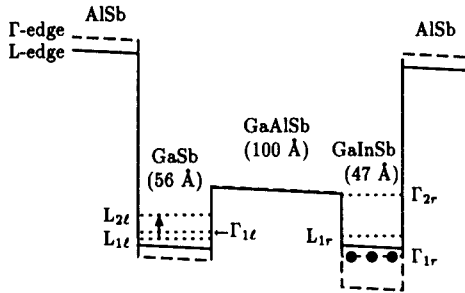
Figure 1. Γ-point (dashed) and L-point (solid) conduction band profiles and quantized energy levels for an AlSb/GaSb/Ga$_{0.6}$Al$_{0.4}$Sb/Ga$_{0.75}$In$_{0.25}$Sb/AlSb asymmetric double quantum well at an applied field of -50 kV/cm.
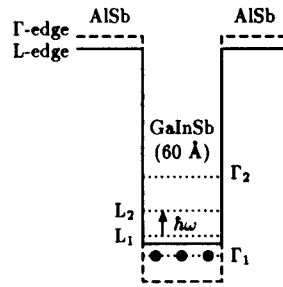
Figure 2. Γ-point and L-point profiles and energy levels for an AlSb/Ga$_{0.80}$In$_{0.20}$Sb/AlSb multiple quantum well at zero applied field for all-optical limiting.

Clearly, one approach to achieving normal-incidence EO modulation is to employ L-valley rather than Γ-valley intersubband interactions in a stepped well or asymmetric double quantum well (ADQW) structure whose transition energies can be shifted by an applied voltage.[8] However, we recently showed the advantages of instead inducing a voltage-controlled competition between Γ-valley and L-valley states having nearly the same energy.[10] A typical Γ-L ADQW EO modulator configuration is illustrated in Fig. 1, which gives the Γ and L band edge profiles and quantized energy levels obtained from a multi-band finite-element method (FEM) formalism. The key feature of this structure is that an applied electric field can transfer virtually the entire electron population from the well at right whose conduction-band minimum is at the Γ-point to the well on the left whose minimum is at the L-point. This transfer occurs rapidly because the Ga$_{1-x}$Al$_x$Sb barrier layer separating the two wells is thin enough to permit sub-nanosecond interwell tunneling times following reversal of the applied voltage from negative (shown in the figure) to positive, or *vice versa*. Thus by varying the field, one can radically alter the polarization selection rules, optical matrix elements, intersubband resonance energies, and the in-plane electron effective mass. The latter enables strong tuning of the plasma contribution to the refractive index, providing an attractive non-resonant mechanism for low-loss phase modulation.[10] In addition, the net available conduction-band offset between GaSb and AlSb is large enough that the same basic scheme may be employed for EO modulators spanning all IR wave-

lengths between 1.5 and 20 μm. A first experimental demonstration of the Γ-L ADQW intensity modulator was recently reported by Du *et al.*[11]

A similar concept may be used to achieve all-optical IR intensity limiting, where in this case the Γ-L electron transfer is in momentum-space only. The required structure consists of a simple $Ga_{1-x}In_xSb/AlSb$ multiple quantum well (MQW), whose Γ and L band profiles and quantized subband minima are illustrated in Fig. 2. The structure is designed such that at the initial lattice temperature, T_L, nearly all of the electrons occupy states in the Γ_1 subband for which normal-incidence absorption is forbidden in lowest order. However, a small thermally-excited L_1 population exists, which weakly absorbs at the $L_1 \rightarrow L_2$ resonance energy. Considering first the case of optical pulses short enough that lattice heating may be ignored, the initially-weak absorption adds heat to the free carrier system, whose temperature T_e then exceeds T_L by an amount proportional to the excitation intensity I. As a consequence of the increased carrier temperature, a larger fraction of the electrons become thermally excited to L_1 states, increasing the normal-incidence absorption. We will model this optically-induced opacity below, and show that it can be quite effective in limiting the intensity of a transmitted IR beam.

Although one can calculate the normal-incidence absorption coefficient α_{12}^N theoretically from first principles,[1, 4] in order to ensure the reliability of the present analysis we have scaled the magnitude to the data of Samoska *et al.*[6] The observed Lorentzian broadening parameter of $\approx$ 12 meV for $\hbar\omega \approx$ 80 meV is assumed to increase linearly with photon energy and as the square root with doping density beyond the experimental value of 1.6×10^{12} cm^{-2} per period. Energy levels, dispersion relations, wavefunctions, and optical matrix elements have been calculated using the multi-band FEM $k \cdot P$ formalism,[12] with Γ-valley states being derived from the full 8-band calculation and L-valley levels from a 1-band version using the quantization effective masses. Populations of the various subbands are then derived using a statistical calculation[1] that numerically incorporates the FEM results for the Γ and L dispersion relations. The high-temperature thermal redistribution of electrons is significantly enhanced by the greater density of states at L, which is approximately 30 times that at Γ due to the 4-fold valley degeneracy and the much larger effective masses along both transverse and longitudinal axes. Furthermore, for thin AlSb barriers the Γ-valley effective mass is also very light along the growth direction, whereas the L-valley electrons remain nearly dispersionless in that dimension.

As an example we consider the MQW illustrated in Fig. 2, assuming a doping density of $N = 1.6 \times 10^{12}$ cm^{-2} per well. The Γ_1 energy minimum lies 96 meV below the L_1 minimum for this structure at 77 K, and the $L_1 \rightarrow L_2$ resonance energy is 125 meV ($\lambda = 9.9$ μm). Figure 3 plots the calculated results for the fraction of carriers populating each of the lowest subbands as a function of carrier temperature. At $T_e = T_L = 77$ K only 7% of the electrons are in the L_1 subband (dash-dot curve), hence the peak normal-incidence absorption coefficient is < 600 cm^{-1} (solid curve). However, with increasing electron temperature the fraction of electrons occupying L_1 increases rapidly, reaching nearly 60% at 300 K. Thus at elevated electron temperatures the intersubband absorption becomes quite strong, e.g., $\alpha_{12}^N \approx 4300$ cm^{-1} at $T_e = 300$ K. The absorption eventually saturates at somewhat higher carrier temperatures (> 500 K), mostly because the L_1 population saturates as it approaches unity but also because an increasing fraction of the L_2 final states are thermally populated at T_e.

We next consider the relationship between the carrier heating that governs the increased opacity and the optical intensity. The magnitude of the carrier heating is obtained by

balancing the rate at which energy is added to the electron system with the rate at which that excess energy relaxes back to the lattice:

$$\Delta T_e = \frac{I\alpha_{12}^N \tau_E}{c_e} \qquad (1)$$

where τ_E is the energy relaxation time (taken to be 1 ps) and c_e is the electronic specific heat. For a single-component 2D system with a parabolic effective mass, $c_e = Nk_B$ in the limit of nondegenerate statistics and $c_e = \pi^2 N k_B^2 T_e / 3 E_F$ in the degenerate limit ($E_F \gg k_B T_e$), where E_F is the Fermi energy relative to the bottom of the band. However, since we wish to consider arbitrary degeneracy in multi-subband systems with nonparabolic masses, the electronic specific heat has instead been obtained numerically using the FEM in-plane and growth-direction dispersion relations in conjunction with the statistical calculation discussed above. By performing this determination self-consistently with Eq. (1), we derive the carrier temperature, and from that the induced absorption corresponding to a given optical intensity.
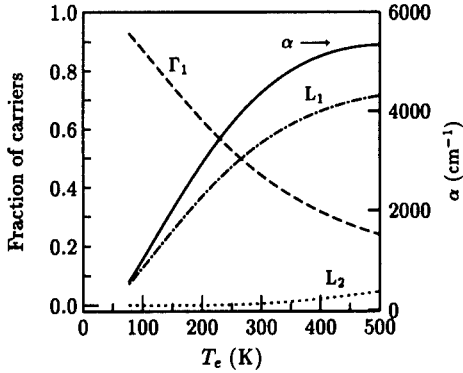
Figure 3. Fraction of carriers in the Γ_1, L_1, and L_2 subbands vs carrier temperature, for the MQW from Fig. 2 with $N = 1.6 \times 10^{12}$ cm^{-2}. Also shown is the resulting absorption coefficient (right scale).
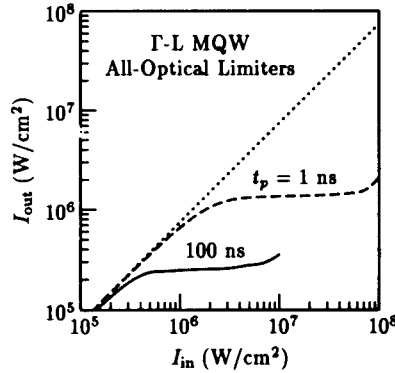
Figure 4. Optical limiting predicted for LWIR pulse lengths of 1 ns and 100 ns.

In modeling device performance, it becomes apparent that the limiting action is more effective if the MQW parameters are varied as a function of depth. For example, near the input surface of the active region, the optical intensity is highest and initiation of the electron heating tends not to be an issue. Since the main goal is then to maximize the induced absorption while minimizing saturation, it is advantageous to have a relatively high doping level and large energy separation between the Γ_1 and L_1 conduction minima (which is accomplished by increasing the alloy composition x in the Ga$_{1-x}$In$_x$Sb quantum wells). On the other hand, the region near the exit surface of the active region experiences much lower excitation intensities, since most of the incident beam has already been absorbed within the limiter. Thus in the exit region the most important consideration

is to maximize the sensitivities of the carrier heating and induced absorption strength to low-intensity excitation. This is best accomplished by employing a lower doping level and much smaller energy difference between the Γ_1 and L_1 subbands (smaller x). At intermediate depths, optimum results are obtained for a digital grading of the doping level and alloy composition. A division of the net active region into 5 uniform MQWs generally gives sufficient modulation of the properties. In view of the practical limitations of MBE growth, we restrict the maximum total active-region thickness to 10 μm.

The dashed curve of Fig. 4 plots output intensity (I_{out}) vs input intensity (I_{in}) calculated for a Γ-L all-optical limiter with doping level and $Ga_{1-x}In_xSb$ alloy composition graded between 4×10^{12} cm^{-2} and $x = 0.3$ at the input surface and 1.6×10^{12} cm^{-2} and $x = 0.2$ at the exit surface. The pulse length is 1 ns (e.g., from an OPO), and the insertion loss due to residual absorption at $T_e = T_L$ is 25%. Whereas the response is nearly linear up to $I_{in} \approx 1$ MW/cm^2, above that value the output is effectively clamped at $I_{out} \approx 1.4$ MW/cm^2. This continues until I_{in} reaches ≈ 100 MW/cm^2, where the I_{in}/I_{out} ratio is roughly a factor of 50. At higher input intensities there is a severe performance degradation due to saturation. We note that the insertion loss may be reduced substantially if the Γ_1-L_1 energy differences in the various regions are increased somewhat. The clamped output intensity at high I_{in} then increases only slightly.

We next consider longer pulse lengths on the order of 100 ns (e.g., the gain-switched spike from a TEA CO_2 laser), for which the net energy absorbed and transferred to the lattice can produce substantial optical heating.[13] This pulse length is nonetheless too short to allow removal of any significant fraction of that heat by thermal conduction. Apart from a small relative lattice-temperature shift of the Γ_1 and L_1 energy minima,[14] the increase of α_{12}^N with increasing T_e is analogous to that in Fig. 3, except that now the carrier heating self-consistently derived from Eq. (1) must be added to the increase in T_L. An additional consideration is the inevitable onset of damage to the limiter due to melting (at ≈ 1000 K) or other thermal degradation at high input intensities. While it is again advantageous to grade the MQW structural parameters, maximization of the damage threshold becomes the dominant consideration governing design of the region near the input surface. The maximum absorption coefficient should therefore be suppressed somewhat in that region.

Imposing the same constraint of a 10-μm total MQW thickness, an optimized structure for the limiting of 100 ns pulses contains doping levels and QW alloy compositions graded between 1×10^{12} cm^{-2} and $x = 0.17$ at the input surface and 1.6×10^{12} cm^{-2} and $x = 0.20$ at the exit surface. This again yields a low-intensity insertion loss of 25%. Results for the output intensity vs input intensity are plotted as the solid curve in Fig. 4. The limiting action turns on somewhat sooner at the longer pulse length, since lattice heating produces a rapid increase of the net electron temperature. For a broad range of inputs, the output intensity is seen to be clamped at ≈ 200 kW/cm^2. The I_{in}/I_{out} ratio exceeds a factor of 20 by the time damage due to melting of the input surface occurs at ≈ 10 MW/cm^2.

Limiting is also expected for still longer pulse lengths, although geometrical considerations then become much more important due to the necessary reliance on thermal transport to remove excess lattice heat. A discussion of that regime is deferred to a later work.

It should be emphasized that the normal-incidence absorption peaks for the two devices discussed above are broad enough to simultaneously provide limiting for the entire CO_2 laser wavelength band. Moreover, analogous optical limiters operating at MWIR wavelengths should also be feasible, although it may be difficult to design a single device to provide protection against threats at all wavelengths between 3 and 5 μm. We finally point out that

the same general principles may be employed in the design of Γ-X all-optical modulators based on GaAs/$Al_x Ga_{1-x}$As/AlAs intersubband systems.

MWIR LASERS

Interband semiconductor lasers have almost always employed active-region constituents with a type-I band alignment, since large optical matrix elements are required if appreciable gain is to be generated. While type-I MWIR lasers have advanced considerably in recent years,[15, 16, 17, 18] it has been pointed out that type-II antimonide structures with thin layers to insure large electron-hole wavefunction overlaps may offer some significant advantages.[12, 19, 20, 21] This is a consequence of such factors as the larger conduction and valence band offsets for improved electrical confinement and the potential for significant suppression of the Auger loss rate.[19, 22] Researchers at Hughes were the first to experimentally demonstrate 3-5 μm type-II antimonide lasers.[23] These diode devices with active regions consisting of 4-1/2-period InAs/$Ga_{0.75}In_{0.25}$Sb superlattices have displayed lasing up to 255 K at an emission wavelength of 3.1 μm, which is equivalent to the highest reported value[24] for type-I interband III-V lasers emitting beyond 3 μm. Here we discuss recent theoretical and experimental progress by the team of NRL and UH/SVEC in the development of type-II quantum well lasers (T2QWLs). This work has produced the first interband semiconductor lasers emitting MWIR wavelengths at and above room temperature.

Design considerations for the T2QWL are discussed in Ref. 21. The active region contains four constituents (e.g., InAs/$Ga_{1-x}In_x$Sb/InAs/AlSb) in each period of the repeated structure. Excellent optical and electrical confinement are provided by the low index of refraction and large conduction and valence band offsets of the AlSb or InAs/AlSb superlattice cladding layers. The gain per injected carrier is large because the AlSb barrier in each period of the active region induces a two-dimensional density of states for both electrons and holes. In addition, the double InAs quantum well significantly enhances the electron-hole overlap integral and hence the optical matrix elements.[21] Finally, a strong suppression of Auger losses is expected due to the small in-plane hole mass, the elimination of resonances between the energy gap and split-off valence band, and the avoidance of resonances with any other low-lying valence subbands.[19, 21]

The first T2QWL devices were recently grown at UH/SVEC and characterized at NRL.[25, 26] Details of the MBE growth may be found in Ref. 27. Broad-area laser bars were lapped and polished to a thickness of ≈ 100 μm, and then cleaved to cavity lengths on the order of 500 μm. The laser bars with uncoated facets were indium heat sunk to a copper cold finger, epitaxial-side-up. These devices were optically pumped by 70 ns pulses from a Q-switched 2.06 μm Ho:YAG laser operating at 1 Hz, focused to a stripe width ranging between 40 and 500 μm.

A series of four T2QWL samples having InAs active layer thicknesses ranging between 17 Å and 24 Å (corresponding to high-temperature lasing wavelengths between 3.2 μm and 4.5 μm) were fabricated and characterized. In all cases, the maximum operating temperature (T_{max}) exceeded any reported previously for either optically-pumped[15] or electrically-pumped interband III-V lasers emitting beyond 3 μm, ranging between 270 K at 4.5 μm and 350 K at 3.2 μm.[26] The latter result is the highest reported to date for any semiconductor laser emitting beyond 2.5 μm, including IV-VI devices (T_{max} = 290 K)[28] and the intersubband-based quantum cascade laser[29] (see below). Figure 5 plots peak output

power as a function of pump intensity for the 3.2-μm device. We observe up to 270 mW at 300 K, which represents a significant step toward the realization of practical MWIR sources. Devices with a 3.4-μm emission wavelength also lased above room temperature (up to 310 K).
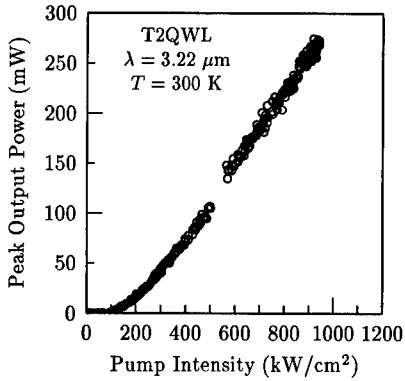
Figure 5. T2QWL peak output power vs optical pump intensity at 300 K, for a stripe width of 90 μm.
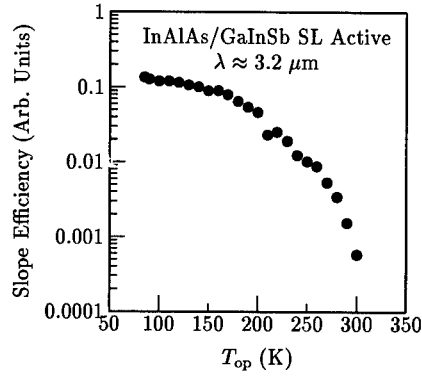
Figure 6. Optical pumping conversion efficiency (normalized to the zero-loss limit) vs temperature for a type-II superlattice laser with cladding layers doped for diode operation.

One of the next goals of this work is to demonstrate diode laser operation. Toward that goal, optical-pumping experiments were recently performed on a structure designed for electrical pumping, but for which the growth was unintentionally halted before the upper optical cladding layer could be completed and a contact layer deposited. The active region was an undoped two-constituent $In_{0.94}Al_{0.06}As/Ga_{0.80}In_{0.20}Sb$ (12Å/33Å) type-II superlattice and the incomplete top cladding layer was an n-type $InAs/In_{0.17}Al_{0.83}Sb$ (15Å/20Å) superlattice, both of which were lattice-matched to the p-type AlSb bottom cladding layer. Because the active region was thinner (0.20 μm) than in most optically-pumped[15, 25, 26] and electrically-pumped[23, 15] MWIR lasers, the structure also contained an n-type $In_{0.94}Al_{0.06}As/Ga_{0.85}In_{0.15}Sb$ (12Å/68Å, 0.25 μm total thickness) high-index region to increase the active-region optical confinement factor to $\approx$ 0.16. The active and high-index regions were separated by an n-type $InAs/In_{0.21}Al_{0.79}Sb$ (14Å/15Å, 0.05 μm total thickness) blocking layer to prevent the escape of holes from the active region. The wavelength of the observed laser emission varied from 2.84 μm at 80 K to $\approx$ 3.2 μm at temperatures approaching ambient. Despite the thinner active region and the presence of doping in the cladding layers, lasing was again observed up to 300 K, with a peak power output of 15 mW at 280 K for a stripe width of $\approx$ 50 μm. Figure 6 illustrates the temperature dependence of the slope efficiency, which has been normalized to the theoretical limit predicted for the case of zero internal loss. Note that the efficiency remains roughly constant for operating temperatures up to $\approx$ 200 K. Although the absolute magnitude of the power conversion efficiency at 86 K is only $\approx$ 0.1%, this value is dominated primarily by such factors as weak coupling to the pump beam (only $\approx$ 4% of the incident energy

is actually absorbed in the active region), the down-conversion photon-energy ratio, and collection inefficiency (including collection from only one of the two facets). If a typical internal loss of ≈ 10 cm^{-1} is assumed, the efficiency observed at 86 K remains approximately a factor of 4 below the theoretical limit. Most of this discrepancy probably resulted from the poor facet quality discussed below.

Despite the record maximum operating temperatures, the low-temperature threshold pump intensities reported in Refs. 25 and 26 were higher than most previous values. While this was originally attributed to short Hall-Shockley-Read recombination lifetimes,[25] it is now realized that the primary cause was actually poor facet quality. Subsequent measurements on additional devices fabricated at both MIT Lincoln Laboratory[30] and NRL from the same wafers but with optimized cleaving procedures have confirmed lasing thresholds an order of magnitude below those reported in Refs. 25 and 26. The revised Hall-Shockley-Read lifetimes estimated from the new thresholds are typical of state-of-the-art values for antimonide quantum heterostructures.

We finally discuss theoretical projections for the type-II interband cascade laser (T2ICL), which is unique to the antimonides and combines advantages of both the bipolar T2QWL and the unipolar quantum cascade laser (QCL) demonstrated by Faist et al.[29] In the QCL, unipolar electron injection into a staircase of coupled quantum wells produces a subband population inversion, and lasing results from stimulated intersubband transitions. In contrast to conventional diode lasers in which a maximum of one photon can be emitted for every electrically-injected electron and hole, in the QCL each electron entering the device can in principle produce an additional photon for each period. Emission wavelengths between 4 μm and 11 μm and operating temperatures up to 320 K have been demonstrated, with characteristic temperatures T_0 often exceeding 100 K.[29] However, the threshold current densities tend to be rather large, owing to a rapid nonradiative phonon relaxation of the population inversion. The T2ICL eliminates this phonon relaxation path, while retaining the advantages of the cascade geometry.

The T2ICL concept, which was originally proposed by Yang,[31] is quite flexible and numerous alternative configurations are possible.[32, 33] Preliminary experimental investigations have led to the observation of mid-IR electroluminescence up to room temperature in an interband cascade device.[34] Detailed active-region design and modeling of device performance have been carried out by Vurgaftman et al.[35] The present discussion will focus on a typical structure illustrated schematically in Fig. 7.[32] The staircase device consists of many active regions separated from one another by injection regions, each of which serves as the collector for one active region and the emitter for the next. With an appropriate bias, electrons are injected from the left and tunnel through the first AlSb barrier into the E1 band of the InAs QW in the active region. Since the subsequent GaInSb, GaSb, and AlSb barriers prevent leakage due to tunneling into the next injection region, the electrons may escape only by making radiative or non-radiative transitions to the valence band, namely the H1 level of the GaInSb hole QW. Note that the non-radiative losses will be relatively low, since phonon relaxation processes have been eliminated and Auger losses can be strongly suppressed as in the T2QWL. Once the electrons have made optical transitions to the valence band, they tunnel into the GaSb QW, whose thickness is such that free carrier absorption due to intervalence transitions is minimized at the lasing wavelength. The electrons finally transfer to the conduction band of the next injection region through elastic interband tunneling[36] or elastic scattering.[35] This crucial step can only be accomplished in systems with a type-II semimetallic band offset, i.e., the antimonides. A cascade of photons

results as the electrons descend the staircase, since a separate radiative transition occurs in each active region of the device.

The operation of a specific 15-period T2ICL structure (964 Å period) surrounded by 1.5-μm-thick n-doped InAs/AlSb optical cladding layers has been simulated in Ref. 35. Using energy dispersion relations and optical matrix elements from the 8-band FEM algorithm and interwell tunneling coefficients from a WKB approximation, Fermi levels and electronic heat capacities were calculated as a function of carrier concentration for each well of a given period. Electron-hole recombination was taken to result from spontaneous and stimulated radiative emission, as well as Hall-Shockley-Read and Auger nonradiative processes. Accounting for the optical confinement factor ($\approx 78\%$), the optical gain was determined as a function of electron and hole densities in the active wells. These dependences were then input to the coupled time-dependent equations for interwell carrier transfer and photon propagation in the presence of carrier and lattice heating. Internal electric fields were self-consistently adjusted according to the spatial build-up of excess charge in the various quantum wells.
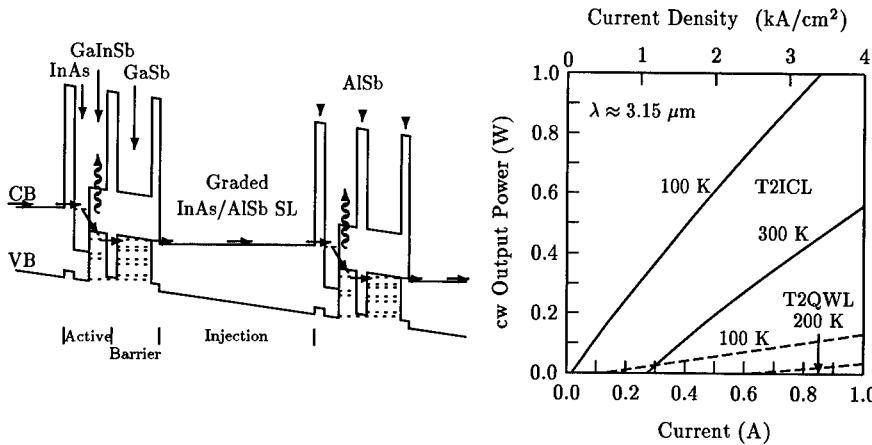
Figure 7. Schematic conduction and valence band profiles and subband minima for a T2ICL structure under bias.

Figure 8. Theoretical output power per facet vs injected current density for a T2ICL[35] (solid curves) and a T2QWL (dashed curves). Cavity lengths are 500 μm and stripe widths are 50 μm.

The simulation was carried out for cw pumping of a T2ICL device ($\lambda = 3.15$ μm) mounted junction-side-down, with one facet coated to achieve a reflectivity of 95%. For threshold conditions at 300 K, the net losses due to mirror transmission, free carrier absorption, and interband absorption at the type-II interface between the active and injection regions was conservatively estimated to be 52 cm^{-1}, although this value can almost surely be reduced in fully-optimized structures. The solid curves of Fig. 8 illustrate the predicted T2ICL output powers as a function of injection current at 100 K and 300 K, which are compared with analogous 100 K and 200 K results from the modeling of a 15-period

T2QWL with the same Auger coefficient (dashed curves). The T2ICL threshold currents are much lower (1.1 kA/cm^2), since for a cascade geometry the contacts need to supply only enough carriers to establish a population inversion in the first period, which then injects the carriers into the next period, *etc*. Furthermore, the differential slope efficiency (with a maximum of 0.9 W/A per facet at 300 K) is far higher due to the generation of 15 photons for every electron injected. Especially encouraging is the prediction that cw output powers exceeding 1 W may be feasible, although the maximum is limited by the carrier and lattice heating at high injection currents as well as nonlinear effects such as filamentation that have not been included in this calculation. When the temperature is decreased from 300 K to 100 K, the threshold current density falls by more than an order of magnitude, to 80 A/cm^2, if the same Auger coefficient is assumed.

By comparison, the T2QWL yields a maximum dP/dI of ≈ 0.12 W/A at 100 K and threshold current densities of 9.5 kA/cm^2 at 300 K (pulsed only) and 550 A/cm^2 at 100 K (cw). Theoretical predictions for the QCL yield threshold cw current densities of ≈ 3 kA/cm^2 and 1 kA/cm^2 at 300 and 100 K, respectively[29] (expected to be relatively independent of wavelength). Thus far, the maximum dP/dI reported for pulsed-mode operation has been ≈ 0.25 W/A at low temperatures,[29] although somewhat higher values will probably be achievable.

These simulations demonstrate that the T2ICL represents a promising approach to achieving high MWIR output powers from single-facet electrical-injection devices. We also emphasize that numerous variations on the interband cascade geometry are possible. For example, while the type-II band alignment at the interface between one period and the next is a defining characteristic that must be present to enable the interband tunneling or scattering step which returns electrons to the conduction band, it is not essential that the active region have a type-II alignment. One may also consider a type-I interband cascade laser (T1ICL),[32] in which the wavefunctions for both electrons and holes taking part in the lasing transitions have their maxima in the same quantum well.

CONCLUSIONS

The inadequacy of current IR optical components has substantially impeded the implementation of high-performance military and commercial systems for such applications as remote chemical sensing (for leak detection, pollution and drug monitoring, chemical process control, etc.), IR spectroscopy, laser surgery, multi-spectral detection, IR illumination, IR countermeasures, and future ultra-low-loss fiber communications. In this review, we have discussed the potential for meeting some of these requirements with novel modulators and sources based on the wavefunction engineering of antimonide-family quantum heterostructures.

We have described QW structures in which virtually the entire electron population can be transfered from Γ states to L states either through the application of an external bias or by optical heating of the carriers and lattice at high excitation intensities. This transfer substantially alters such IR properties as the polarization selection rule governing normal-incidence intersubband transitions. As a consequence, it provides all of the basis elements for MWIR and LWIR EO devices analogous to near-IR modulators based on the excitonic quantum confined Stark effect, as well as for all-optical IR limiters suitable for IR sensor protection. Detailed simulations of short-pulse and intermediate-pulse LWIR

limiters predict an effective clamping of the output intensity over a large range of input intensities.

We have also outlined the prospects for high-performance MWIR lasers based on type-II multiple quantum wells. Some of this potential has already been realized, as optically-pumped T2QWL structures emitting at 3.2 μm have lased up to 350 K, which is nearly 100 K higher than the previous record for III-V interband semiconductor lasers emitting beyond 3 μm. Furthermore, the type-II interband cascade laser is expected to have even more favorable properties, since it retains the photon-recycling advantage of the intersubband-based QCL while eliminating the non-radiative phonon relaxation path. Detailed simulations predict much higher output powers than from conventional bipolar MWIR lasers, coupled with much lower threshold currents than the QCL.

ACKNOWLEDGMENTS

REFERENCES

1. J. R. Meyer, J. I. Malin, I. Vurgaftman, C. A. Hoffman, and L. R. Ram-Mohan, in *Strained-Layer Quantum-Wells and Their Applications*, ed. M. O. Manasreh (Gordon and Breach, Newark, in press).
2. D. A. Holm and H. F. Taylor, IEEE J. Quant. Electron. 25, 2266 (1989).
3. Y. J. Mii, R. P. G. Karunasiri, K. L. Wang, M. Chen, and P. F. Yuh, Appl. Phys. Lett. 56, 1986 (1990).
4. C.-L. Yang and D.-S. Pan, J. Appl. Phys. 64, 1573 (1988).
5. E. R. Brown, S. J. Eglash, and K. A. McIntosh, Phys. Rev. B 46, 7244 (1992).
6. L. A. Samoska, B. Brar, and H. Kroemer, Appl. Phys. Lett. 62, 2539 (1993).
7. Y. Zhang, N. Baruch, and W. I. Wang, Appl. Phys. Lett. 63, 1068 (1993).
8. H. Xie, W. I. Wang, J. R. Meyer, C. A. Hoffman, and F. J. Bartoli, J. Appl. Phys. 74, 1195 (1993).
9. M. J. Shaw and M. Jaros, Phys. Rev. B 50, 7768 (1994).
10. J. R. Meyer, C. A. Hoffman, F. J. Bartoli, and L. R. Ram-Mohan, Appl. Phys. Lett. 67, 2756 (1995).
11. Q. Du, J. Alperin, and W. I. Wang, Appl. Phys. Lett. 67, 2218 (1995).
12. L. R. Ram-Mohan and J. R. Meyer, J. Nonlinear Opt. Phys. Mat. 4, 191 (1995).
13. J. R. Meyer, M. R. Kruer, and F. J. Bartoli, J. Appl. Phys. 51, 5513 (1980).
14. C. Alibert, A. Joullie, A. M. Joullie, and C. Ance, Phys. Rev. B 27, 4946 (1983).
15. H. K. Choi, G. W. Turner, and H. Q. Le, Inst. Phys. Conf. Ser. 144, 1 (1995).
16. H. K. Choi, G. W. Turner, and M. J. Manfra, Electron. Lett. 32, 1296 (1996).
17. A. Popov, V. Sherstnev, Y. Yakovlev, R. Mucke, and P. Werle, Appl. Phys. Lett. 68, 2790 (1996).

18. A. A. Allerman, R. M. Biefeld, and S. R. Kurtz, Appl. Phys. Lett. 69, 465 (1996).

19. C. H. Grein, P. M. Young, and H. Ehrenreich, J. Appl. Phys. 76, 1940 (1994).

20. R. H. Miles, D. H. Chow, T. C. Hasenberg, A. R. Kost, and Y.-H. Zhang, Inst. Phys. Conf. Ser. 144, 31 (1995).

21. J. R. Meyer, C. A. Hoffman, F. J. Bartoli, and L. R. Ram-Mohan, Appl. Phys. Lett. 67, 757 (1995).

22. E. R. Youngdale, J. R. Meyer, C. A. Hoffman, F. J. Bartoli, C. H. Grein, P. M. Young, H. Ehrenreich, R. H. Miles and D. H. Chow, Appl. Phys. Lett. 64, 3160 (1994).

23. R. H. Miles and T. C. Hasenberg, in *Antimonide Related Heterostructures and Their Applications*, ed. M. O. Manasreh (Gordon and Breach, Newark, in press).

24. H. K. Choi, S. J. Eglash, and G. W. Turner, Appl. Phys. Lett. 64, 2474 (1994).

25. J. I. Malin, J. R. Meyer, C. L. Felix, C. A. Hoffman, L. Goldberg, F. J. Bartoli, C.-H. Lin, P. C. Chang, S. J. Murry, R. Q. Yang, and S.-S. Pei, Appl. Phys. Lett. 68, 2976 (1996).

26. J. I. Malin, C. L. Felix, J. R. Meyer, C. A. Hoffman, J. F. Pinto, C.-H. Lin, P. C. Chang, S. J. Murry, and S.-S. Pei, Electron. Lett. 32, 1593 (1996).

27. C.-H. Lin, S. J. Murry, D. Zhang, P. C. Chang, Y. Zhou, S.-S. Pei, J. I. Malin, C. L. Felix, J. R. Meyer, C. A. Hoffman, and J. F. Pinto, J. Cryst. Growth (in press).

28. B. Spanger, U. Schiessl, A. Lambrecht, H. Bottner, and M. Tacke, Appl. Phys. Lett. 53, 2582 (1988).

29. J. Faist, F. Capasso, C. Sirtori, D. L. Sivco, J. N. Baillargeon, A. L. Hutchinson, S.-N. G. Chu, and A. Y. Cho, Appl. Phys. Lett. 68, 3680 (1996).

30. C.-H. Lin, S. J. Murry, D. Zhang, S.-S. Pei, H. Q. Le, C. L. Felix, and J. R. Meyer, to be submitted to Appl. Phys. Lett.

31. R. Q. Yang, Superlatt. Microstruct. 17, 77 (1995).

32. J. R. Meyer, I. Vurgaftman, R. Q. Yang, and L. R. Ram-Mohan, Electron. Lett. 32, 45 (1996).

33. R. Q. Yang and S. S. Pei, J. Appl. Phys. 79, 8197 (1996).

34. R. Q. Yang, C.-H. Lin, P. C. Chang, S. J. Murry, D. Zhang, S. S. Pei, S. R. Kurtz, S.-N. G. Chu, and F. Ren, Electron. Lett. 32, 1621 (1996).

35. I. Vurgaftman, J. R. Meyer, and L. R. Ram-Mohan, IEEE Phot. Tech. Lett. (in press).

36. J. R. Soderstrom, D. H. Chow, and T. C. McGill, Appl. Phys. Lett. 55, 1094 (1989).

Preparation of AlAsSb and Mid-Infrared (3-5μm) Lasers By Metal-Organic Chemical Vapor Deposition

A. A. Allerman, R. M. Biefeld, and S. R. Kurtz
Sandia National Laboratory, Albuquerque, New Mexico, 87185, USA

ABSTRACT

Mid-infrared (3-5 μm) infrared lasers and LEDs are being developed for use in chemical sensor systems. As-rich, InAsSb heterostructures display unique electronic properties that are beneficial to the performance of these midwave infrared emitters. We have grown $AlAs_{1-x}Sb_x$ epitaxial layers by metal-organic chemical vapor deposition using trimethylamine (TMAA) or ethyldimethylamine alane (EDMAA), triethylantimony (TESb) and arsine. We examined the growth of $AlAs_{1-x}Sb_x$ using temperatures of 500 to 600 °C, pressures of 70 to 630 torr, V/III ratios of 1-27, and growth rates of 0.3 to 2.7 μm/hour in a horizontal quartz reactor. The semi-metal properties of a p-GaAsSb/n-InAs heterojunction are utilized as a source for injection of electrons into the active region of lasers. A regrowth technique has been used to fabricate gain-guided lasers using $AlAs_{1-x}Sb_x$ for optical confinement with either a strained InAsSb/InAs multi-quantum well (MQW) or an InAsSb/InAsP strained layer superlattice (SLS) as the active region. Under pulsed injection, the InAsSb/InAs MQW laser operated up to 210K with an emission wavelength of 3.8-3.9 μm. Under pulsed optical pumping, the InAsSb/InAsP SLS operated to 240K with an emission wavelength of 3.5-3.7 μm. LED emission has been observed with both active regions in both p-n junction and semi-metal injection structures.

INTRODUCTION

Driven by chemical sensing and infrared countermeasure applications, several mid-infrared (2-6 μm) diode lasers with strained InAsSb active regions have been recently demonstrated. Devices with AlAsSb claddings have been grown by molecular-beam epitaxy,[1,2] and lasers with higher index, Al free InPSb claddings metal organic chemical vapor deposition (MOCVD) have also been reported.[3] Although AlAsSb claddings provide superior optical confinement, the large conduction band barriers associated with AlAsSb layers can result in poor electron injection and high turn-on voltages. Also, due to lack of satisfactory aluminum sources and residual carbon resulting in p-type doping of AlAsSb alloys, MOCVD growth of AlAsSb injection devices had not been reported. In this paper, we report MOCVD grown lasers with AlAsSb claddings. We describe an electrically injected device which utilizes a GaAsSb(p)/InAs(n) heterojunction to form an internal, semi-metal layer. The semi-metal acts as an internal electron source which can eliminate many of the problems associated with electron injection in these AlAsSb based devices. Furthermore, the use of an internal electron source enables us to consider alternative laser and LED designs that would not be feasible with conventional, p-n junction devices. Initial results for an optically pumped laser with an InAsSb/InAsP strained-layer superlattice (SLS) active region are also presented. Due to a large valence band offset, the light-heavy hole splitting in InAsSb/InAsP SLSs is estimated to be 80 meV, and Auger recombination should be further reduced in this active region.

EXPERIMENT

This work was carried out in a previously described horizontal MOCVD system.[4] TMAA, or EDMAA, TESb, 100% and 10% arsine in hydrogen, and phosphine were the sources for Al, Sb, As and P respectively.

$AlAs_{0.16}Sb_{0.84}$ layers 0.5 - 1 μm thick and lattice-matched to InAs were grown over a range of 500 to 600°C and 76 to 630 torr using a V/III ratio = 1.1 to 27 and a As/V ratio of 0.1 to 0.64 in the gas phase. The growth rate ranged between 0.35 - 2.0 μm/hr. The best morphology was achieved when grown on a buffer layer of InAs or an InAsSb/InAsP strained layer superlattice at a V/III ratio of 7.5 at 500°C and 200 torr at 1.1 μm/hr.

The two active region structures were used for both laser diode and LED devices. The first consisted of a 10 period multi quantum well (MQW) structure of 85Å InSbAs quantum wells with 425Å InAs barriers. The other consisted of a 40 period strained layer superlattice (SLS) with the same InSbAs wells but with 85Å InAsP barriers.

Secondary ion mass spectroscopy (SIMS) was used to determine C and O impurity concentrations. Five crystal x-ray diffraction (FCXRD) of the (004) reflection was used to determine alloy composition and superlattice period. Layer thickness was determined using a groove technique for thicker layers. Photoluminescence was used to characterize the optical quality of the active regions.

RESULTS AND DISCUSSION

The optimum growth conditions for $AlAs_xSb_{1-x}$ occurred at 500 °C and 200 torr at a growth rate of 1.1 μm/hour using a V/III ratio of 7.5 assuming a vapor pressure of 0.75 torr for EDMAA at 19.8°C and an As/V flow ratio of 0.13. Surface morphology was strongly dependent on the InAs substrate. However, the use of a 30 period strain balanced InAsSb/InAsP SLS like that used for the active region greatly improved surface morphology. Surface roughness increased for growth rates of 2 μm/hr. for the same V/III and As/V conditions. Latticed matched GaAsSb cap layers were grown using similar conditions, a V/III of 6.2, and an As/V flow ratio of 0.071. Five crystal x-ray diffraction (FCXRD) measurements of lattice matched AlAsSb films typically exhibited full widths at half of the maximum intensity (FWHM) less than 100 arc seconds. We were also able to reproducibly obtain lattice matching of $AlAs_xSb_{1-x}$ to InAs to within less than 0.015 percent using EDMAA.

The use of other than the above stated growth conditions led to problems in compositional control and reproducibility during the growth of $AlAs_xSb_{1-x}$ layers lattice matched to InAs. Growth at 600 °C resulted in a very broad x-ray peak that extended over hundreds of arc seconds with a constant intensity. Analysis of the x-ray spectra indicated that the large peak width was due to a variation of Sb composition that occurred in the layer as it was grown. Broad x-ray peaks were also observed in films grown using TMAA. The transport of TMAA from the solid source varied during the growth run and changed the V/III ratio resulting in x-ray peaks several hundred arc seconds wide. Sb was also detected by x-ray diffraction in InAs layers grown at 600 °C following previous growths of AlAsSb. We suspect that evaporation of elemental Sb, which has a vapor pressure of 0.1 torr at 600 °C, from deposits on the chamber wall results in the compositional drift observed in the AlAsSb layers grown at 600 °C. Growth at 500 °C greatly reduces this effect as x-ray peaks with FHWM of less than 100 arc seconds were routinely achieved. Likewise Sb was not detected by x-ray diffraction in InAs layers grown on top of AlAsSb. Growth at 70 or 500 torr yielded broader x-ray diffraction peaks (FWHM 300 arc seconds) with less reproducible lattice matching.

SIMS analysis of undoped AlAsSb showed the oxygen level to be 1.2×10^{19} cm^{-3} for a film grown at 500 °C and 200 torr using EDMAA. A similar level of oxygen (1.6×10^{19} cm^{-3}) was found in a film grown at 600 °C and 200 torr using TMAA. The level of carbon found in the film grown at 600 °C was 7.3×10^{17} cm^{-3} and was much lower than the 2.6×10^{18} cm^{-3} found in the sample grown at 500 °C. The source of the oxygen found in these materials is unknown at this time. The oxygen could be coming from contaminants in the organometallic sources, the background O in the MOCVD reactor, or from reaction of the samples with air.

The details of the growth of the InAsSb/InAs multiple quantum well (MQW) structures on InAs have been previously published.[5] An x-ray diffraction pattern of an InAs/InAs$_{0.89}$Sb$_{0.11}$ MQW grown on InAs had sharp satellite peaks out to n=7 indicating good crystalline structure. The structure was grown at 500 °C, 200 torr, a V/III ratio of 25 with an As/V ratio of 0.75 and a growth rate of 2.5 Å/second. A 15 second purge time with reactants switched out of the chamber was used between each layer. The composition, X, of the InAs$_{1-x}$Sb$_x$ quantum wells could be varied between X = 0.1 and 0.2 by changing the As/V ratio between 0.81 and 0.63 using these growth conditions. The composition changes can be explained by the use of a thermodynamic model as previously discussed.[5]

InAsP layers were grown using 10% AsH$_3$ in hydrogen with of V/III ratio of 216 and a As/V ratio of .016. The high V/III and low As/V ratios reflect the low thermal decomposition efficiency of PH$_3$ at 500 °C and 200 torr. The growth rate was 2.5 Å/sec. in the active region.

Low temperature (< 20 K) photoluminescence emission could be controlled between 3.9 to 6.0 µm for Sb compositions between 0.11 to 0.20 in the InAsSb/InAs MQW structures grown on InAs. The long wavelength deviation of these bandgap values from those previously published may be explained by the CuPt-type ordering and phase separation found in these materials.[6, 7] Previous work has shown that the InAs/InAsSb interface band offset in these MOCVD grown materials is type I.[8] PL emission from InAsSb/InAsP SLS structures were blue shifted due to the added confinement provided by the InAsP barriers (Figure 1). PL emission was observed between 3.1 to 4.2 µm for the 20 period SLS shown in Figure 1.

FCXRD of a 20 period InAsSb/InAsP SLS shows sharp SL peaks indicating good structural quality. The n=0 peak is within 10 arc seconds of the substrate indicating the structure is strain balanced. PL emission for the structure grown on InAs is observed at 3.61 µm at 16 K and red shifts to 4.15 µm at 300 K with 8% of the peak intensity at 16 K.

Although the independent growth of the AlAs$_x$Sb$_{1-x}$ layers or the MQW structures gave uniform and reproducible x-ray diffraction patterns, only a very broad x-ray diffraction pattern was observed when the MQW was grown sequentially on top of the AlAs$_x$Sb$_{1-x}$. When a layer of InAs was grown after a layer of lattice matched AlAs$_x$Sb$_{1-x}$, a broad x-ray peak was observed at two theta values greater than the InAs substrate. SIMS measurements indicated the presence of Al in the InAs layer. In order to avoid the incorporation of Al into the quantum well structures, we developed a regrowth technique. Following the growth of the 2.5 µm AlAs$_x$Sb$_{1-x}$ confinement layer capped with 500 Å of GaAs$_{1-x}$Sb$_x$ and a 400 Å layer of InAsSb, the quartz reaction chamber was cleaned before growing the rest of the laser structure. The second growth starts with the active region followed by a second 2.5 µm confinement layer of AlAs$_x$Sb$_{1-x}$ followed by a 1200 Å contact layer of GaAsSb.

None of the layers in the laser structure were intentional doped. The semi-metal nature of the p-GaAsSb / n-InAs interface grown at the end of the first growth is used to inject electrons into the active region. The satellite peaks observed in the first growth are from the InAsSb/InAsP SLS used as a buffer to improve surface morphology (Figure 3). The same structure used in the active region was also used for the buffer. The cladding layer is closely lattice-matched to the substrate.
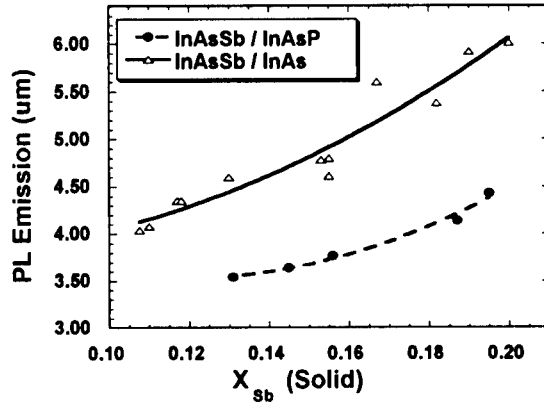
Figure 1. Low temperature photoluminescence (< 20K) from 10 period 85Å $InSb_xAs_{1-x}$ / 425Å InAs MQW's and 40 period 75Å $InSb_xAs_{1-x}$ / 84Å $InAs_{.76}P_{.24}$ SLS's grown on InAs.
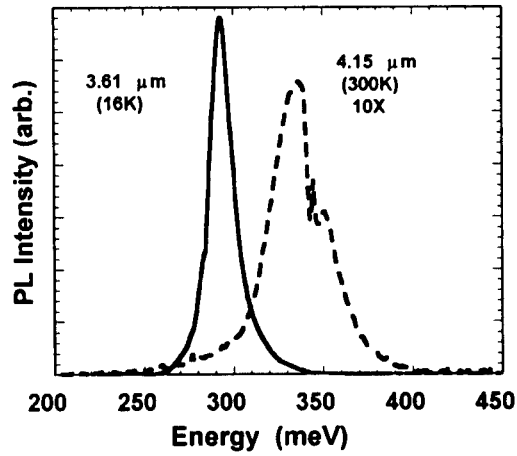
Figure 2. Low temperature photoluminescence from a 40 period 83Å $InSb_{.87}As_{.13}$ / 82Å $InAs_{.73}P_{.27}$ SLS's grown on InAs. The absorption at 350 meV is an artifact in the PL system.

Gain-guided, stripe lasers with a InAsSb/InAs MQW active region and semi-metal electron injection were fabricated. Under pulsed operation with uncoated facets, lasing was observed in forward bias with 40x1000 or 80x1000 micron stripes. No emission occurred under reverse bias. Devices were tested with 100 nsec pulse widths at 10 kHz (0.1 % duty-cycle). Several longitudinal modes were observed in the 3.8-3.9 μm range. The lasers displayed a sharp threshold current characteristic, and lasing was observed through 210K. Under pulsed operation, peak power levels of 1 mW/facet could be obtained. A characteristic temperature (T_o) in the 30-40 K range was observed, with the lower value (30 K) being misleading due to degradation of the device at higher temperatures. These maximum operating temperature and characteristic temperature values are comparable to the highest values reported to date, for injection lasers of this wavelength with either strained InAsSb or InAs/GaInSb active regions [1,2,9,10]. Unlike bipolar lasers, cw operation of the unipolar laser has not yet been observed.

Lasing emission was also observed from optically pumped structures with InAsSb/InAsP SLS active regions. Several longitudinal modes were observed in the 3.5- 3.7 μm range and lasing was observed to 240K. The temperature dependence of the threshold had a characteristic temperature (T_o) of 32 K.
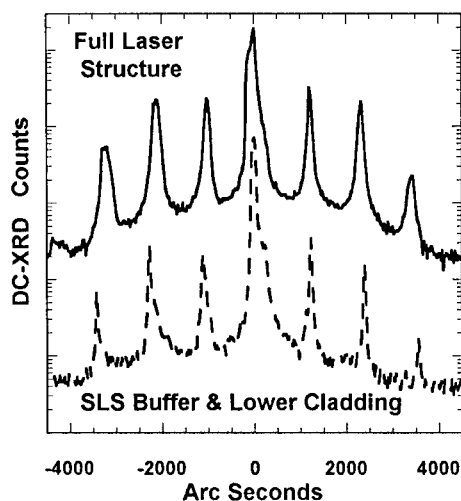
Figure 3. X-ray diffraction pattern of the lower cladding and complete structure following regrowth of the active region and top cladding. An InAsSb / InAsP strain balanced superlattice is used as a buffer to improve surface morphology and as the active region.

LED and laser emission is observed for a variety of forward bias conditions. No emission is observed in reverse bias. The onset of the LED emission coincides with the energy of the InAsSb quantum well photoluminescence. Room temperature LED emission has been observed at 4 μm in excess of 1 μW peak power (10 kHz, 50% duty-cycle). Similar performance has been recorded for LED devices using an InAsSb/InAsP SLS active region. LED emission has been observed from both semi-metal injection and p-n junction structures.

CONCLUSIONS

We have grown $AlAs_xSb_{1-x}$ epitaxial layers by metal-organic chemical vapor deposition (MOCVD) using trimethylamine alane or ethyldimethylamine alane, triethylantimony, and arsine. The growth of high quality $AlAs_xSb_{1-x}$ by MOCVD has been demonstrated and used for optical confinement layers in a 3.8-3.9 μm injection laser with a novel GaSb/InAs semi-metal electron injector. The use of the InAs/GaSb semi-metal for carrier injection, and the compatibility of the semi-metal with InAsSb devices is unique. Diode lasers employing InAsSb/InAs MQW active regions have operated under electrical injection (pulsed) to 210K. Optically pumped laser structures employing strain balanced InAsSb/InAsP SLS active regions have operated to 240K under pulsed conditions.

ACKNOWLEDGEMENTS

REFERENCES

[1] H. K. Choi and G. W. Turner, Appl. Phys. Lett. **67**, 332 (1995).
[2] Y-H. Zhang, Appl. Phys. Lett. **66**, 118 (1995).
[3] S. R. Kurtz, R. M. Biefeld, A. A. Allerman, A. J. Howard, M. H. Crawford, and M. W. Pelczynski, Appl. Phys. Lett. **68**, 1332 (1996).
[4] R.M.Biefeld, C.R. Hills, and S.R. Lee, J. Crys. Growth **91**, 515 (1988).
[5] R. M. Biefeld, K. C. Baucom, and S. R. Kurtz, J. Crystal Growth, **137**, 231 (1994).
[6] D. M. Follstaedt, R. M. Biefeld, S. R. Kurtz, and K. C. Baucom, J. Electronic Mater. **24**, 819 (1995).
[7] S. R. Kurtz, L. R. Dawson, R. M. Biefeld, D. M. Follstaedt, and B. L. Doyle, Phys. Rev. B, **46**, 1909 (1992).
[8] S. R. Kurtz, R. M. Biefeld, and A. J. Howard, Appl. Phys. Lett., **67**, 3331 (1995).
[9] A. A. Allerman, R. M. Biefeld, and S. R. Kurtz, Appl. Phys. Lett., **69**, 465 (1996).
[10] R. H. Miles (private communication).

LPE GROWTH OF MIXED COMPOSITION III-V "VIRTUAL SUBSTRATES" FOR MID-INFRARED OPTOELECTRONIC DEVICES

Y. Mao, A. Krier
Advanced Materials & Photonics Group, School of Physics and Chemistry, Lancaster University,
Lancaster LA1 4YB, UK.

ABSTRACT

Liquid phase epitaxy can be effectively used to grow a thick graded ternary or quaternary buffer layer to provide a "virtual substrate" for subsequent device epitaxy. Grading characteristics of InGaAs, InAsSb and InAsSbP epitaxial layers grown by LPE are discussed. The effects of the principal LPE growth parameters on epilayer thickness, surface morphology and composition, lattice-mismatch and photoluminescence efficiency were investigated and are described.

INTRODUCTION

There is at present considerable interest in the fabrication of semiconductor light emitting diodes, lasers and photodiodes for the mid-infrared region (2-5μm) because of their potential applications in infrared gas sensing instruments, molecular spectroscopy, night vision, thermal imaging, avionics etc. [1,2,3]. But there are some difficulties in obtaining mixed crystal III-V substrates for epitaxial growth [4]. It is therefore not straightforward to readily produce elegant lattice-matched quantum well structures as required for efficient laser, LED and photodetector operation at room temperature and at wavelengths beyond 2μm.

However, liquid phase epitaxy (LPE) yields material of a high crystalline quality in terms of structural perfection owing to the fact that it is a near-equilibrium process [5]. Its growth rates are sufficiently high to permit the growth of layers with thicknesses up to 100μm, which could be effectively used to grow a thick graded ternary or quaternary buffer layer to provide a "virtual substrate" for subsequent device epitaxy. This paper reports on the possibility of growth of such "virtual substrates" using InGaAs, InAsSb and InAsSbP epitaxial layers.

EXPERIMENTAL PROCEDURES

A conventional liquid phase epitaxy (LPE) technique with a horizontal, multiwell sliding graphite boat in a Pd-diffused hydrogen atmosphere was used for the growth of various ternary and quaternary epitaxial layers. The details of the phase equilibria in InGaAs [6], InAsSb [6] and InAsSbP [7] and the LPE procedures used in this work have been described previously elsewhere [8,9,10]. The growth melts were made up using 6N's pure In and Sb metals and undoped polycrystalline InAs and InP. The solid composition of the resulting epitaxial layers was analysed using double crystal x-ray diffraction (DCXD), electron microanalysis (EDAX) and photoluminescence (PL). The surface morphology, interface quality and layer thickness were examined by scanning electron microscopy and Normarski interference microscopy.

RESULTS AND DISCUSSION

By using 3-16°C melt supercooling and a cooling rate of 0.2°C/min, we have obtained high quality reproducible thin epitaxial layers (2-3μm) of $InAs_{0.36}Sb_{0.20}P_{0.44}$ lattice-matched to
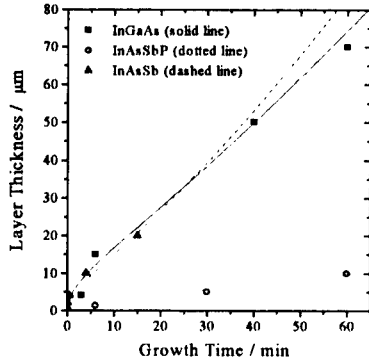
Figure 1. The variation in thickness of epitaxial layers with growth time. Symbols show measured data. The curves are calculated using eqn(1) [15].
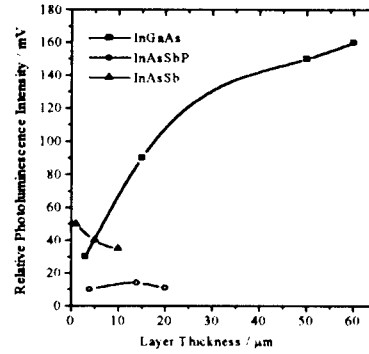
Figure 2. Dependence of photoluminescence intensity on measured layer thickness.

InAs [10], $InAs_{0.91}Sb_{0.09}$ lattice-matched to GaSb [11] and $In_{0.97}Ga_{0.03}As$ lattice-mismatched to InAs [8]. Those materials were successfully used to fabricate efficient 2-5μm LEDs for methane [12], CO_2 [13] and HF [14] gas detection. By using this as a convenient starting point, we investigated the growth of thick graded layers by prolonging the growth time and increasing the cooling rate.

Figure 1 shows the variation in thickness of epitaxial layers with growth time up to 60min for fixed growth temperature, supercooling temperature and ramp rate. This relationship can be explained quite well by the diffusion-limited growth theory presented by Hsieh [15] as follows:

$$d(t) - K(2\Delta T_s t^{1/2} + 3/4Rt^{3/2}) \tag{1}$$

where $d(t)$ is the thickness of the epitaxial layer , t is the growth time, K is a coefficient indicating a growth rate dependent on the intrinsic properties of the solution, for example the diffusion coefficient of the elements, solute concentration and liquidus composition etc., ΔT_s is the supercooling temperature and R is the cooling rate. Table 1 lists the parameters of growth used in our experiments and layer gradient analysed by PL, DCXD and EDAX for $InAs_{1-x-y}Sb_yP_x$, $InAs_{1-x}Sb_x$ and $In_{1-x}Ga_xAs$ alloys. We found K=0.025μm/min$^{1/2}$/°C for $InAs_{1-x-y}Sb_yP_x$, which is much smaller than that of $InAs_{1-x}Sb_x$ and $In_{1-x}Ga_xAs$. It means the growth rate for this quaternary is much slower than the two others and it is probably limited by the small diffusion coefficient

Table1: The parameters of LPE growth and layer grading for 0.2°C/min temperature ramp rate.

Materials	Starting Compositio n	ΔT_s (°C)	K (μm/min$^{1/2}$/°C)	Thickness (μm)	Band-gap shift (from PL)	Lattice Constant Change (DCXD & EDAX)
$InAs_{1-x-y}Sb_yP_x$	x=0.44,y=0.20	16	0.025	10	50meV	0.2%
$InAs_{1-x}Sb_x$	x=0.09	3	0.45	20	26meV	0.05%
$In_{1-x}Ga_xAs$	x=0.03	7	0.32	60	16meV	0.12%

50

of phosphorous. The lattice constant changes are small for all these three alloys grown using a small (0.2°C/min) temperature ramp.

The dependence of photoluminescence intensities on layer thickness are shown in figure 2 for these three materials. The luminescence intensity decreases with increasing layer thickness for both $InAs_{1-x-y}Sb_yP_x$ and $InAs_{1-x}Sb_x$, while PL intensity rises as the layer thickness increases for $In_{1-x}Ga_xAs$. This indicates that the layer qualities for $InAs_{1-x-y}Sb_yP_x$ and $InAs_{1-x}Sb_x$ become poorer, but that of $In_{1-x}Ga_xAs$ gets better as the layers grow. The surface morphology of the relevant samples are shown in figure 3. The Smooth and mirror-like surface of a 4μm $InAs_{0.91}Sb_{0.09}$ is shown in figure 3a, but it becomes rough with a high texture when the layer is grown to 20μm as shown in figure 3b. The same situation is found with the $InAs_{1-x-y}Sb_yP_x$ alloy.

(a)   (b)

(c)   (d)   100μm ———
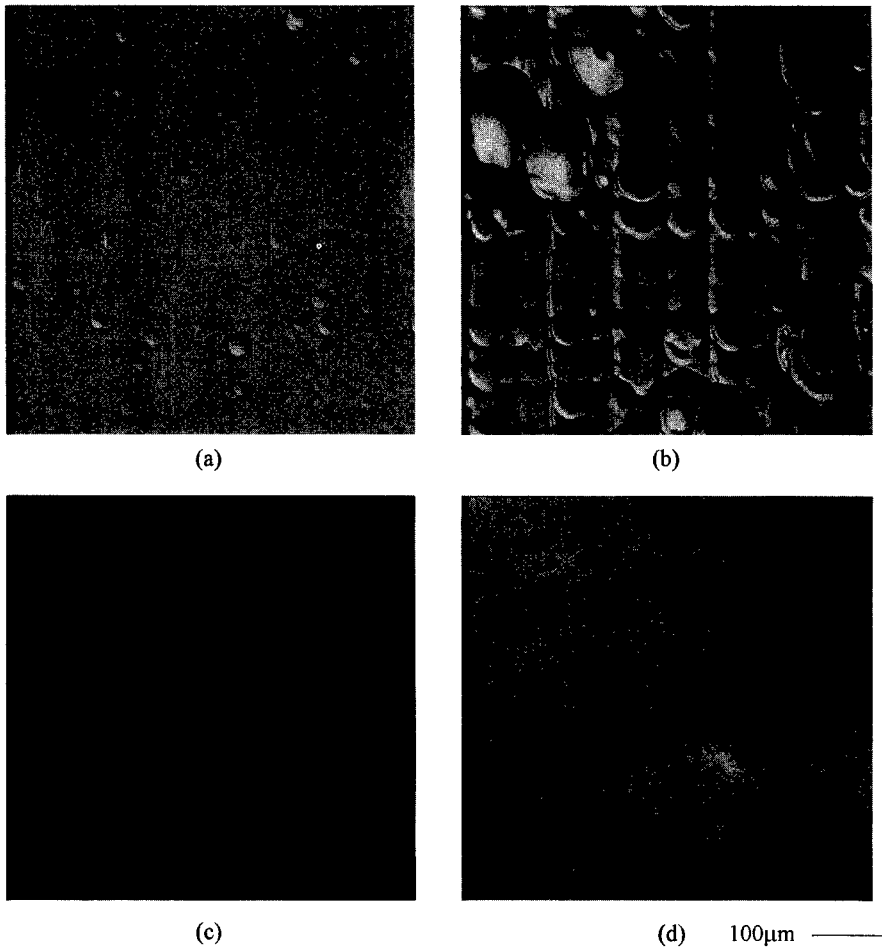
Figure 3. The surface morphology of $InAs_{0.91}Sb_{0.09}$ (4μm) (a) and 20μm (b), $In_{0.97}Ga_{0.03}As$ (4μm) (c) and 60μm (d) epilayers grown by LPE.

The surface morphology of thin (4μm) and thick (60μm) $In_{1-x}Ga_xAs$ samples is shown in figures 3c and 3d, respectively. The 4μm layer has a definite, but fine cross-hatch pattern on the surface along the <011> and <01$\bar{1}$> directions, while the cross-hatch pattern has totally vanished on the 60μm thick sample. It is well known that the cross-hatch pattern arises due to the generation of misfit dislocations in the vicinity of a material heterointerface [16]. The misfit dislocations present in our thin $In_{1-x}Ga_xAs$ layer have disappeared and instead a smooth and shiny surface is now evident for the thick $In_{1-x}Ga_xAs$ sample, which gives stronger PL emission as shown in figure 2a.
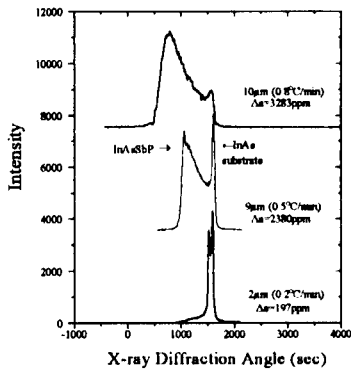
Figure 4. X-ray rocking curves for InAsSbP epilayers grown on InAs by LPE using different growth conditions.

To get larger grading, epitaxial growth with a larger cooling rate was investigated. Figure 4 shows the x-ray rocking curves obtained from the (400) reflection. $InAs_{1-x-y}Sb_yP_x$ grown with three different cooling rates and at the same supercooling temperature. A lattice mismatch of less than 200ppm was obtained from a 2μm sample using a cooling rate of 0.2°C/min as shown in the bottom curve. The two sharp peaks indicate its good crystalline quality in this thin layer. The other two curves with larger lattice mismatch were measured from 9 and 10μm samples with cooling rates of 0.5 and 0.8°C/min, respectively. The cooling rate of 0.8°C/min is the maximum possible value limited by our present LPE temperature control system. The broad peaks on the left of the substrate peak show the presence of grading in these two $InAs_{1-x-y}Sb_yP_x$ epitaxial layers. The measured change in lattice constant is 0.33%, in comparison with 0.20% obtained from the 10μm layer with the cooling rate of 0.2°C/min for $InAs_{1-x-y}Sb_yP_x$.

To get further grading, a very large temperature cooling rate of approximately 80°C/min was obtained by sweeping the furnace off immediately after contacting the substrate with the growth melt. A 50μm $In_{1-x}Ga_xAs$ layer was successfully obtained by growing for 3min using this technique. However, so far we have failed to grow $InAs_{1-x-y}Sb_yP_x$ and $InAs_{1-x}Sb_x$ in this way.

Figure 5 shows the variation in solid composition with the layer thickness for two thick $In_{1-x}Ga_xAs$ samples using the cooling rates of 0.2 and 80°C/min, respectively. The compositions were measured by EDAX from cross-sections of the samples. The gallium composition increases only 10% from 0.045 to 0.050 while the cooling rate increases about 400 times. This is probably due to the temperature of substrate and the growth melt inside the boat not changing as quickly as the outside of the boat during this short (3mins) growth time. The corresponding change of lattice constant in the alloy is about 0.18% (i.e. a_0= 6.0381Å) calculated from the 50μm
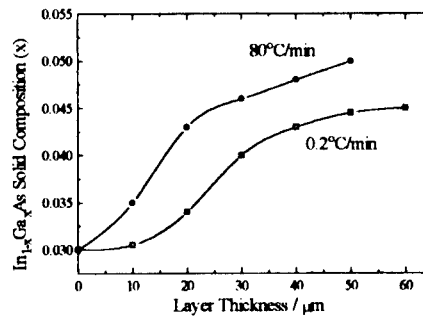
Figure 5. Measured solid composition dependence of the layer thickness for InGaAs grown on InAs by LPE.

52

$In_{1-x}Ga_xAs$ layer grown with a cooling rate of 80°C/min, in comparison with 0.12% (i.e. a_o= 6.0402Å) obtained from the 60μm layer with a cooling rate of 0.2°C/min for $In_{1-x}Ga_xAs$. Gallium in In-rich InGaAs melts has a high segregation coefficient [17] and is therefore rapidly incorporated into the growing solid. If growth continues further, then Ga depletion from the melt occurs and the epitaxial layer composition reverts back towards that of InAs [18]. At room temperature, the lattice parameters of the binaries InAs (6.0584Å) and GaAs (5.6533Å) are different by 6.67%. By using the LPE grading technique we were able to produce an InGaAs virtual substrate having a good surface morphology and with a lattice parameter of 6.0381Å, This represent a shift of approximately 5% of the total range in the InGaAs system away from InAs.

CONCLUSION

The crystalline quality and PL efficiency of lattice-mismatched $In_{1-x}Ga_xAs$ (x=0.03) epitaxial layers grown on InAs by LPE is increased as the layer thickness increases. A 50μm $In_{0.95}Ga_{0.05}As$ epilayer with a smooth and mirror-like surface morphology was successfully obtained using a cooling rate of 80°C/min, which could be used as a "virtual substrate" for subsequent device epitaxy. The gallium concentration could be further increased by growing multiple graded layers. However, $InAs_{1-x-y}Sb_yP_x$ and $InAs_{1-x}Sb_x$ epilayers which were initially lattice-matched to the substrate interface behave differently and the quality of these layers deteriorated as the layer thickness was increased. We conclude that it is necessary to use slightly mismatched epitaxial layers and rather high melt cooling rates in order to obtain a significant grading of lattice parameter. Work is in progress to extend the available range of lattice parameters using these grading techniques for virtual substrates.

ACKNOWLEDGMENTS

REFERENCES

1. C.R.Webster, R.D. May, C.A. Trimble, R.G. Chave and J. Kendall, Appl. Opt., 33, pp.454-471 (1994).

2. P.S. Lee, R.F. Majkovski and R.M. Schreck, 'Method for Determining Fuel and Engine oil consumption using tuneable diode laser spectroscopy', US Patent No. 4,990,780, issued February 5 (1991).

3. P.S. Lee, R.F. Majkovski and T.A. Perry, IEEE Trans., BE-38, 10, pp.966-970 (1991).

4. H. Heineck and E. Veuhoff, Mater. Sci. and Eng., B21, pp.120-129 (1993).

5. E. Kuphal, Appl. Phys., A52, pp.380-409 (1991).

6. G.B. Stringfellow and P. Greene, J. Phys. Chem. Solids, 30, pp.1779 (1969).

7. G.B. Stringfellow, J. Crystal Growth, 27, pp.21 (1974).

8. M.K. Parry and A. Krier, J. Crystal Growth, **139**, pp.238-246 (1994).

9. Y. Mao and A. Krier, J. Crystal Growth, **133**, pp.108-116 (1993).

10. M.R. Wilson, A. Krier and Y. Mao, J. Elect. Mater., 25, pp1439-1445 (1996).

11. A. Krier and Y. Mao, Semicond. Sci. Technol., **10**, pp.930-936 (1995).

12. M.K. Parry and A. Krier, Elect. Lett., **30**, pp1968-1969 (1994).

13. Y. Mao and A. Krier, Elect. Lett., **32**, pp479-480 (1996).

14. Y. Mao and A. Krier, '2.5μm Light Emitting Diodes in InAs$_{0.36}$Sb$_{0.20}$P$_{0.44}$/InAs for HF Detection', to be published.

15. J. Hsieh, J. Crystal Growth, **27**, pp.49 (1974).

16. G.R. Booker, J.M. Titchmarsh, J. Fletcher, D.B. Darby, M. Hockly and M. Al-Jassim, J. Crystal Growth, **45**, pp.407 (1978).

17. M.G. Astles, 'Liquid-phase Epitaxial Growth of III-V Compound Semiconductor Materials and their Device applications', Adam Hilger, P20 (1990).

18. H.J. Gerritsen, Final Report, 'Use of Room Temperature Infrared Diodes for Determining Methane Concentration in Air.' United States Department of Interior, Mine Safety Research Centre Grant N. USBM G0155013 (March 1976), NTIS Number PB-262-649/AS.

GaInAsSb MATERIALS FOR THERMOPHOTOVOLTAICS

C.A. WANG, G.W. TURNER, M.J. MANFRA, H.K. CHOI AND D.L. SPEARS
Lincoln Laboratory, Massachusetts Institute of Technology, Lexington, MA 02173-9108

ABSTRACT

$Ga_{1-x}In_xAs_ySb_{1-y}$ (0.06 < x < 0.18, 0.05 < y < 0.14) epilayers were grown lattice-matched to GaSb substrates by low-pressure organometallic vapor phase epitaxy (OMVPE) using triethylgallium, trimethylindium, tertiarybutylarsine, and trimethylantimony. These epilayers have a mirror-like surface morphology, and exhibit room temperature photoluminescence (PL) with peak emission wavelengths ($\lambda_{p,300K}$) out to 2.4 μm. 4K PL spectra have a full width at half-maximum of 11 meV or less for $\lambda_{p,4K} < 2.1$ μm ($\lambda_{p,300K} = 2.3$ μm). Nominally undoped layers are p-type with typical 300K hole concentration of 9×10^{15} cm^{-3} and mobility ~ 450 to 580 cm^2/V-s for layers grown at 575°C. Doping studies are reported for the first time for GaInAsSb layers doped n type with diethyltellurium and p type with dimethylzinc. Test diodes of p-GaInAsSb/n-GaSb have an ideality factor that ranges from 1.1 to 1.3. A comparison of electrical, optical, and structural properties of epilayers grown by molecular beam epitaxy indicates OMVPE-grown layers are of comparable quality.

INTRODUCTION

Thermophotovoltaic (TPV) power generation involves the conversion of thermal energy to electrical energy through the use of photovoltaic cells. Recent developments of these systems are based on thermal sources which operate in the temperature range 1100 to 1500K [1]. For high conversion efficiency, the cutoff wavelength of the photovoltaic cell should closely match the peak in emissive power of the thermal source, which for this temperature range corresponds to 1.9 to 2.6 μm. Consequently, the cells will be based on low-bandgap semiconductor materials. For example, InGaAs grown on InP substrates has been pursued with some success. However, the alloy composition that satisfies this wavelength range is lattice mismatched to the InP substrate, and the device performance is limited by crystalline defects [2]. Alternatively, the $Ga_{1-x}In_xAs_ySb_{1-y}$ quaternary alloy, with energy gap adjustable in the wavelength range from 1.7 to 4.2 μm, can be grown lattice matched to GaSb substrates. Stable alloys with a cutoff wavelength of 2.39 μm have been grown by liquid phase epitaxy (LPE) [3]. Although this alloy system exhibits a miscibility gap beyond 2.4 μm [4,5], metastable alloys have been grown by organometallic vapor phase epitaxy (OMVPE) [6] and molecular beam epitaxy (MBE) [7,8]. Therefore, the $Ga_{1-x}In_xAs_{1-y}Sb_y$ alloys are of particular interest for TPV's. Unfortunately, there are only limited results of both electrical and optical properties of these alloys grown by either MBE or OMVPE, and no systematic doping studies have been performed.

In this paper, we report the growth of $Ga_{1-x}In_xAs_ySb_{1-y}$ alloys by OMVPE using triethylgallium (TEGa), trimethylindium (TMIn), tertiarybutylarsine (TBAs), and trimethylantimony (TMSb) as precursors. This combination, which is examined for the first time, is selected because of the low pyrolysis temperature of TEGa and TBAs compared to trimethylgallium and AsH₃, which were used in previous studies [6,9]. Doping studies were performed with dimethyzinc (DMZn) as the p-type dopant and diethyltellurium (DETe) as the n-type dopant. The electrical, optical, and structural properties of the $Ga_{1-x}In_xAs_ySb_{1-y}$ alloys are presented. For comparison, a limited number of layers was also grown by MBE, which has been extensively used for the growth of high-performance mid-infrared lasers [10].

55

EPITAXIAL GROWTH, CHARACTERIZATION, AND DIODE FABRICATION

$Ga_{1-x}In_xAs_ySb_{1-y}$ epilayers were grown on Te-doped GaSb or semi-insulating (SI) GaAs substrates oriented 2° off (100) toward (110). A vertical rotating-disk reactor with H_2 carrier gas at a flow rate of 10 slpm and reactor pressure of 150 Torr was used [11]. Solution TMIn, TEGa, TBAs, and TMSb were used as precursors with DETe (50 ppm in H_2) and DMZn (1000 ppm in H_2) as n- and p-type doping sources, respectively. TEGa, TBAs, and TMSb were selected as the organometallic precursors based on their low pyrolysis temperatures and minimal tendency toward adduct formation [12]. The total group III mole fraction was typically 3.5 to 4 x 10^{-4} which resulted in a growth rate of ~2.7 μm/h. The V/III ratio was varied from 0.9 to 1.7. The growth temperature was 575°C for most layers, with some layers grown at 525 or 550°C.

For MBE growth, Ga, In, Sb_4, and As_2 fluxes were used with As_2 provided by a valved As cracker as described previously [8]. Layers were grown on (100) Te-doped GaSb or SI GaAs substrates. The growth temperature was 500 to 510°C, and the growth rate was ~ 1 μm/h. Be was used as the p-type dopant, and GaTe as the n-type dopant.

The surface morphology was examined using Nomarski contrast microscopy. Double-crystal x-ray diffraction (DCXD) was used to evaluate the structural quality and degree of lattice mismatch to GaSb substrates. Photoluminescence (PL) was measured at 4 and 300K. The composition of epilayers was determined from DCXD splitting, the peak emission ($\lambda_{p,300K}$) in PL spectra, and the energy gap dependence on composition based on the binary bandgaps [13]:

$$E(x,y) = 0.726 - 0.961x - 0.501y + 0.08xy + 0.415x^2 + 1.2y^2 + 0.021x^2y - 0.62xy^2,$$

where $y = 0.867(x)/(1 - 0.048x)$, the condition for lattice matching to GaSb.

For electrical measurements, a GaSb buffer layer of various thicknesses was first grown on SI GaAs substrates at 550°C (510°C and 0.5 μm thick for MBE growth), followed by the GaInAsSb epilayer, which was grown at least 3 μm thick. Carrier concentration and mobility were obtained from Hall measurements based on the van der Pauw method. For diode characterization, ohmic contacts to p- and n-GaSb were formed by depositing Ti/Pt/Au and Au/Sn/Ti/Pt/Au, respectively, and alloying at 300°C. The current-voltage (I-V) characteristics were measured on 500 x 500 μm devices which were formed by cleaving.

RESULTS

The surface morphology is sensitive to the V/III ratio, as similarly reported for GaSb layers [12]. Figure 1 shows the effect of V/III ratio on the morphology of 2-μm-thick $Ga_{0.88}In_{0.12}As_{0.1}Sb_{0.9}$ layers grown lattice matched to the GaSb substrate ($\Delta a/a < 1.5$ x 10^{-3}) at 575°C. Below the minimum V/III ratio of 1.05, a metal-rich surface is obtained and the layer is hazy to the eye. Increasing the V/III ratio above this minimum value, the morphology is mirror-like to the eye. However, Nomarski contrast microscopy revealed a wavy texture as the V/III ratio increased to 1.35 and higher, indicating the necessity for precise V/III control. A slightly smoother morphology could be obtained by reducing the growth temperature to 550 or 525°C. For these layers, the minimum V/III ratio increased to 1.15 and 1.25, respectively.

| V/III = 0.9 | V/III = 1.05 | V/III = 1.35 | V/III = 1.65 |
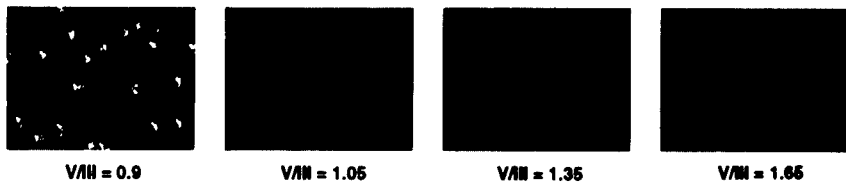
Figure 1. Surface morphology of $Ga_{0.88}In_{0.12}As_{0.1}Sb_{0.9}$ epilayers grown on GaSb substrates at 575°C and various V/III ratios.

20 μm

The lattice mismatch of $Ga_{1-x}In_xAs_ySb_{1-y}$ layers is dependent on the partial pressure ratio TBAs/(TBAs+TMSb). For layers grown at 575°C, Figure 2 shows the x-ray splitting as a function of H_2 flow through the TBAs bubbler. In these experiments, III = 3.9 x 10^{-4} mole fraction, V/III ~ 1.15 and TBAs/(TBAs+TMSb) varied from 0.0830 to 0.1174. The data indicate excellent controllability of lattice-match conditions with the use of TBAs. The DCXD scan shown in Figure 3 for a 2-μm-thick $Ga_{0.9}In_{0.1}As_{0.08}Sb_{0.92}$ layer has a narrow full width at half-maximum (FWHM) of 21 arc sec which is comparable to FWHM = 22 arc sec for the GaSb substrate, indicating the excellent structural quality of this layer.
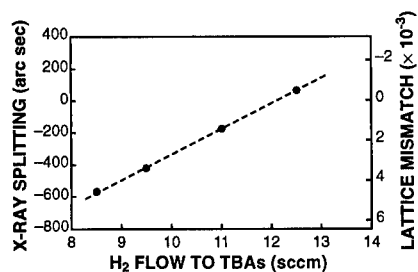
Figure 2. Dependence of lattice mismatch of GaInAsSb epilayers grown at 575°C on GaSb substrates as function of TBAs flow.
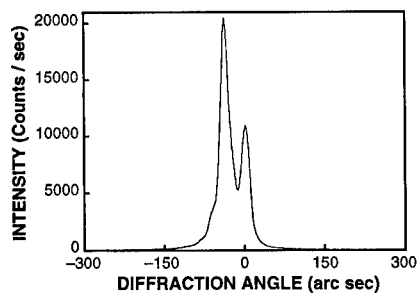
Figure 3. Double-crystal x-ray diffraction scan of $Ga_{0.9}In_{0.1}As_{0.08}Sb_{0.92}$ grown on GaSb.

Figure 4 shows PL spectra measured at 4K for lattice-matched $Ga_{1-x}In_xAs_ySb_{1-y}$ layers of three different compositions. The layers with $\lambda_{p,4K}$ at 1745 and 1860 nm, which were grown at 575°C, have FWHM of 7.8 and 9 meV, respectively. The layer with $\lambda_{p,4K}$ = 2082 nm, grown at 525°C, has FWHM = 11.2 meV which is smaller than previously reported for layers in a similar wavelength range grown by OMVPE [14]. All values are comparable to those for layers grown in this study by MBE, which have FWHM = 8 and 11 meV for $\lambda_{p,4K}$ = 1995 and 2180 nm, respectively. For GaInAsSb grown by LPE, FWHM = 9 meV for $\lambda_{p,4K}$= 2112 nm was reported [15].
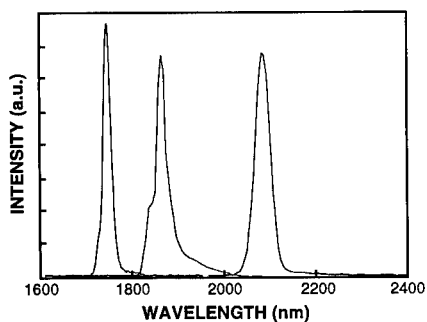
Figure 4. Photoluminescence spectra measured at 4K of GaInAsSb layers grown on GaSb substrates.

The PL spectra measured at 300K of the layers shown in Figure 4 had $\lambda_{p,300K}$ = 1920, 2045, and 2296 nm. The longest $\lambda_{p,300K}$ observed in this study was 2396 nm. However, the surface morphology of this layer exhibited a wavy texture under Nomarski contrast microscopy. In addition, the 4K PL spectra showed emission at a longer wavelength (2432 nm), suggesting that this transition may be impurity- or defect-related.

The electrical properties measured at 300K of nominally undoped $Ga_{0.88}In_{0.12}As_{0.1}Sb_{0.9}$ layers grown on SI GaAs substrates at 575°C and V/III = 1.15 are shown in Figure 5 as a function of GaSb buffer layer thickness. Since the lattice mismatch between $Ga_{1-x}In_xAs_ySb_{1-y}$ (lattice matched to GaSb) and GaAs is 8%, growth was first initiated with a GaSb buffer layer grown at 550°C. All layers are p type and the electrical properties are greatly improved by the GaSb buffer layer. Those layers containing a buffer layer of 0.4 μm or greater have a typical hole concentration of ~9 x 10^{15} cm^{-3} and hole mobility ~ 450 to 580 cm^2/V-s. Nominally undoped GaInAsSb layers grown by MBE in this study were p type with a hole concentration of 2 x 10^{16} cm^{-3} and mobility of ~ 300 cm^2/V-s.
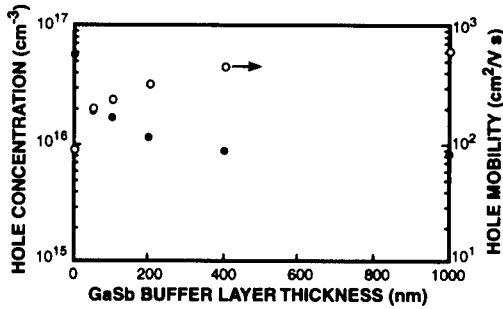
Figure 5   Electrical properties measured at 300K of nominally undoped $Ga_{0.88}In_{0.12}As_{0.1}Sb_{0.9}$ as a function of GaSb buffer layer thickness.

The electrical properties of $Ga_{0.9}In_{0.1}As_{0.08}Sb_{0.92}$ layers grown at 575°C and doped with DETe and DMZn are shown in Figure 6. The electron concentration measured at 300K ranged from 3.4 x 10^{17} to 2.05 x 10^{18} cm^{-3}, with corresponding mobility values of 4640 and 1460 cm^2/V-s, respectively. For p-GaInAsSb, the hole concentration measured at 300K ranged from 7.8 x 10^{16} to 1.5 x 10^{18} cm^{-3} with corresponding mobility values of 430 and 260 cm^2/V-s, respectively. For MBE-grown layers, the maximum electron concentration that has been obtained is 1.9 x 10^{18} cm^{-3} with a mobility of 2280 cm^2/V-s, and the maximum hole concentration is 5.2 x 10^{19} cm^{-3} with a mobility of 50 cm^2/V-s.
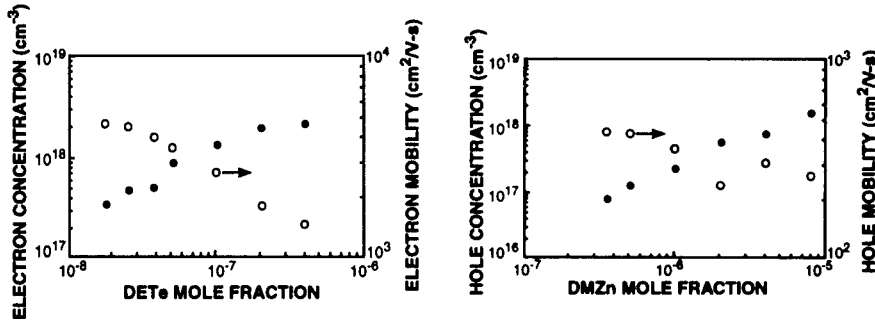
Figure 6. Electrical properties measured at 300K of Te- and Zn-doped $Ga_{0.9}In_{0.1}As_{0.08}Sb_{0.92}$.

Test structures that consist of p-$Ga_{0.9}In_{0.1}As_{0.08}Sb_{0.92}$/n-GaSb substrate were grown to evaluate junction characteristics. With p ≤ 2 x 10^{17} cm^{-3}, the diode ideality factor ranged from 1.1 to 1.3 for a current density of 0.01 to 1 A/cm^2. An increase in the ideality factor was observed for diodes fabricated from structures with higher hole concentrations, which may be related to tunnelling [16].

CONCLUSIONS

GaInAsSb epilayers which span the wavelength range from 1.9 to 2.4 μm were grown lattice matched to GaSb substrates by OMVPE using TEGa, TMIn, TBAs and TMSb. High-quality layers were grown with excellent lattice-matching control with TBAs as the arsenic source. The structural quality is comparable to the GaSb substrate as determined by DCXD. These layers exhibit narrow PL FWHM comparable to MBE-grown layers. A low background concentration of p = 9 x 10^{15} cm^{-3} was obtained for layers grown at 575°C. The first n- and p-doping studies are reported for these quaternary layers grown by OMVPE or MBE. The present results suggest that OMVPE is promising for the growth of TPV structures.

ACKNOWLEDGMENTS

REFERENCES

1. 2nd NREL Conference on the Thermophotovoltaic Generation of Electricity, edited by J.P. Benner, T.J. Coutts, and D.S. Ginley (AIP Conf. Proc. 358, Woodbury, NY, 1995).

2. M.W. Wanlass, J.S. Ward, K.A. Emery, M.M. Al-Jassim, K.M. Jones, and T.J. Coutts, Solar Energy Mater. and Solar Cells 41/42, 405 (1996).

3. E. Tournie, F. Pitard, and A. Joullie, J. Cryst. Growth 104, 683 (1990).

4. K. Onabe, Jpn. J. Appl. Phys. 21, 964 (1982).

5. G.B. Stringfellow, J. Cryst. Growth 58, 194 (1982).

6. M.J. Cherng, H.R. Jen, C.A. Larsen, G.B. Stringfellow, H. Lundt, and P.C. Taylor, J. Cryst. Growth 77, 408 (1986).

7. T.H. Chiu, J.L. Zyskind, and W.T. Tsang, J. Electron. Mater. 16, 57 (1987).

8. H.K. Choi, S.J. Eglash, and G.W. Turner, Appl. Phys. Lett. 64, 2474 (1994).

9. A. Giani, J. Bougnot, F. Pascal-Delannoy, G. Bougnot, J. Kaoukab, G.G. Allogho, and M. Bow, Mater. Sci. and Eng. B9, 121 (1991).

10. H.K. Choi and G.W. Turner, SPIE Proc. Vol. 2382, 236 (1995).

11. C.A. Wang, S. Patnaik, J.W. Caunt, and R.A. Brown, J. Cryst. Gr. 93, 228 (1988).

12. C.A. Wang, S. Salim, K.F. Jensen, and A.C. Jones, J. Cryst. Growth to be published.

13. J.C. DeWinter, M.A. Pollock, A.K. Srivastava, and J.L. Zyskind, J. Electron. Mater. **14**, 729 (1985).

14. M. Sopanen, T. Koljonen, H. Lipsanen, and T. Tuomi, J. Cryst. Growth **145**, 492 (1994).

15. E. Tournie, J.-L. Lazzari, F. Pitard, C. Alibert, A. Joullie, and B. Lambert, J. Appl. Phys. **68**, 5936 (1990).

16. G.W. Charache, J.L. Egley, L.R. Danielson, D.M. DePoy, P.F. Baldasaro, B.C. Campbell, S. Hui, L.M. Frass, and S.J. Wojtczuk, presented at the 26th Photovoltaic Specialist Conf.

OPTICAL CHARACTERIZATION AND MAPPING OF FOUR INCH InSb EPITAXIAL THIN FILMS GROWN ON GaAs BY TURBO DISK METALORGANIC CHEMICAL VAPOR DEPOSITION

Z. C. Feng*, C. Beckham*, P. Schumaker*, I. Ferguson*, R. A. Stall*, N. Schumaker*,
M. Povloski** and A. Whitley**
* EMCORE Corporation, 394 Elizabeth Avenue, Somerset, NJ 08873;
**Renishaw Inc, 623 Cooper Court, Schaumburg, IL 60173Z.

ABSTRACT

A large number of 4 inch (100 mm) diameter 1-2 μm thick InSb films have been grown on GaAs by low pressure metalorganic chemical vapor deposition (MOCVD) turbo disk technology. Raman scattering microscopy was used to study the effects of III-V source ratios on the film crystalline quality and to optimize the growth parameters. Multi-point Raman measurements over the entire 4" wafer were performed to exhibit the uniformity distribution of the film crystalline quality. A FTIR reflectance mapping system has been established to map the film thickness distribution. Good uniformity of the film thickness and crystalline perfection was obtained. Raman and FTIR are showing useful tools for non-destructive characterization of large area wafers for industrial mass production.

INTRODUCTION

InSb has the highest electron mobility and narrowest band gap among III-V compound semiconductors and is attractive for applications in the high speed electronic and optoelectronic devices in the infrared [1,2]. Various growth techniques have been applied to grow InSb on GaAs, including molecular beam epitaxy (MBE) [3,4], liquid phase epitaxy (LPE) [5], magnetron sputter epitaxy [2], plasma-assisted epitaxy [6], atmosphere pressure and low pressure metalorganic vapor phase epitaxy (MOVPE) or metalorganic chemical vapor deposition (MOCVD) [7-17]. Recently, interests in large size and multi-wafer growth of InSb films on GaAs substrates are increasing for industrial infrared applications, and MOCVD is recognized to be a suitable technology for increasing industry mass production of InSb and other III-V materials [10, 14, 17].

Materials characterization for InSb films grown on GaAs substrates is critical. The large lattice mismatch of ~14.5% between InSb and GaAs [18] results in a high density of dislocation near the interface of InSb/GaAs that can propagate throughout the entire InSb film. A great deal of effort has been made to improve the InSb film crystalline quality by optimizing the various growth conditions, such as III-V ratios, pressure, growth temperature, growth rate, film thickness and so on [7-17]. Traditionally, the industry produced InSb films are routinely characterized by Hall measurements, X-ray diffraction, scanning electron microscopy (SEM) etc. [7-17]. More characterization technologies are needed for the routine characterization of InSb films, in particular those non-destructive methods suitable for large diameter wafer, produced in the industry environment.

Raman scattering is an non-destructive and powerful technology for the study of semiconductor materials, and Raman measurements may offer information on the sample crystalline quality, impurity and defects, stress and strain, optimization of crystal growth parameters and other properties [19]. In this study, we applied Raman scattering to assess the effects of III-V ratios in the growth of the MOCVD-grown InSb films on GaAs and the crystalline perfection over 4" (100 mm) InSb film wafers.

The determination of InSb epitaxial film thickness and distribution over the entire layer is critical in the epilayer growth, especially in the case of large diameter wafer production. SEM is usually employed to measure the InSb film thickness in the industry [10,14], which is destructive and not convenient for industry production. Because of the narrow band gap nature of InSb, no reflectance interference fringes appear in the ultra-violet (UV) to visible wavelength range from the InSb/GaAs heterostructure. However, we have found that reflectance interference fringes from InSb/GaAs can be observed in the infrared (IR) wavelength range of 800-8000 cm^{-1}, or 1.2-12 μm. In this study, we present our primary results of using a Fourier transform infrared (FTIR) spectrometer in combination with a mapper to measure the InSb film thickness and map its distribution over the entire 4" wafer.

EXPERIMENT

InSb layers, 1.4-1.6 μm thick, were grown on semi-insulating GaAs (100) substrates with 2° off towards <110> by low pressure (LP) MOCVD utilizing a vertical configuration and a high speed rotating disk (180 mm in diameter) reactor [6,14]. Trimethylindium (TMIn) and Tris(dimethylamino)antimony (TDMASb) were used as In and Sb sources, respectively, both held at 20°C, and with the bubbler pressures of 400 Torr for TMIn and 323 Torr for TDMASb. Hydrogen acted as carrier gas and the pyrolysis growth temperature was 395°C. After growth the samples were first characterized by sheet resistivity and Hall measurements, scanning electron microscopy (SEM) and double crystal x-ray diffraction (DCXRD) to be confirmed with mirror-like surface, good electrical properties with mobility beyond 40,000 cm^2/V·s and carrier concentration around 8×10^{16} cm^{-3}, and high crystalline quality with the DCXRD width better than 200 arc-seconds [10]. These data are not presented in this paper, which is for optical study only, and we will try to set up the correlations between the optical properties and structural/electrical properties in a future paper.

Room temperature (RT) Raman scattering was measured using a Renishaw 1000 Raman microscope. The sample (4" wafer) was placing on a X-Y-Z stage, easily movable for multi-point measurements. The excitation laser beam of He-Ne 633 nm was focusing on the sample surface with a spot size of 1-2 μm. The system spectral resolution was better than 2 cm^{-1}.

A Bio-Rad 175C Fourier transform infrared (FTIR) spectrometer and a Pike *MapplR* wafer testing system were used to perform the FTIR spectral acquisition, mapping and thickness fitting. The spectral range was scanned between 800-7500 cm^{-1} with a resolution of 16 cm^{-1}.

RESULTS AND DISCUSSION

Effects of III/V ratio

III/V source ratio has an important influence on the resulting epitaxial InSb films. Ohshima et al. [6] have studied the effect of Sb/In supply ratio on the electrical properties of

InSb layers grown on (100) semi-insulating GaAs at various substrate temperature and rf powers by plasma-assisted epitaxy technique. Behet et al. [12] studied the dependence of InSb growth rate on V/III ratio in low-pressure (20 hPa) plasma MOVPE with triethylantimony (TESb) as Sb-precursor. We are utilizing Raman scattering to investigate the effect of III-V ratio on the crystalline quality of MOCVD-grown InSb films.

Figure 1 shows Raman spectra of five InSb/GaAs with different III/V ratios of 3.91, 3.98, 4.20, 4.78 and 5.38, respectively. The other growth parameters are the same. For the (100) surface of a zincblende crystal, the longitudinal optical (LO) phonon is allowed and the transverse optical (TO) phonon is forbidden in the backscattering geometry [19]. Therefore, the line shape of the LO mode, and the intensity ratio between TO and LO modes can be adopted as a merit of figure of the crystalline perfection of InSb epitaxial films [18,19]. Also, the appearance and the strength of the second order LO phonon mode are also used to characterize the crystalline quality of InSb [18,20]. Table I lists the main data of these five samples, obtained from measured spectra in Fig. 1, including the phonon frequencies of ω_{LO} for InSb LO mode, ω_{TO} for TO and ω_{2LO} for 2nd order InSb LO, the full width at half maximum (FWHM) for the LO mode, peak intensity ratio between the TO and LO modes, I_{TO}/I_{LO}. It can be seen that all the samples have sharp LO phonon modes with the FWHM values less than 6 cm^{-1} and the second order InSb LO mode clearly detected, implying the good crystalline quality. Poor quality InSb films do not satisfy these two conditions in our practice.

Figure 1   Raman spectra of five MOCVD-grown InSb/GaAs with different III/V ratio, taken at 300 K and excited by 633 nm.

Table I Numerical data from Raman spectra of five InSb/GaAs with different III/V ratios

sample	III/V	ω_{LO}	ω_{TO}	FWHM	I_{TO}/I_{LO}	ω_{2LO}
		(cm^{-1})				(cm^{-1})
IA376	3.91	188.8	178.2	5.60	0.33	379.9
IA380	3.98	188.5	177.8	5.63	0.22	379.6
IA373	4.20	190.7	180.1	5.38	**0.13**	381.9
IA370	4.78	190.9	180.1	**5.03**	0.16	382.0
IA371	5.38	190.9	180.0	5.48	0.15	381.8
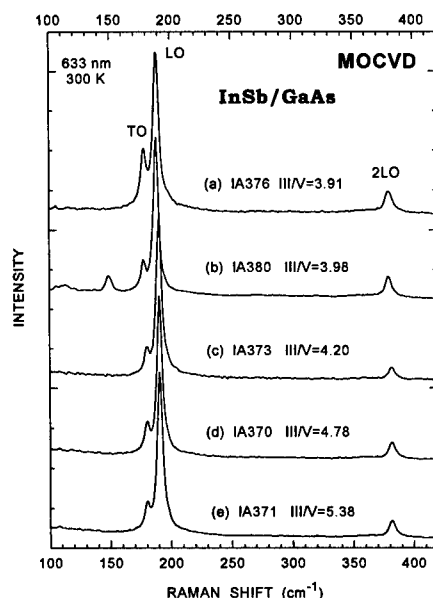
The samples IA376 and IA380 with the lower III/V ratio of 3.91 and 3.98 possess the two strongest forbidden TO mode intensity ratios and widest LO mode widths among these five samples. Fig. 1 (b) for IA380 has also shown extra defect-related features near 150 and 120 cm^{-1}. These facts indicate that the low III/V ratio below 4.0 failed to produce high quality InSb films. IA371 with the high III/V ratio of 5.38 has a low I_{TO}/I_{LO} of 0.15 but also a high LO FWHM value of 5.48 cm^{-1}, only slightly less than that of IA376 and IA380. Therefore, it seems

also not good with a too high III/V ratio. IA373 (III/V=4.20) has a LO FWHM of 5.38 cm^{-1} and a low I_{TO}/I_{LO} of 0.13 while IA370 (III/V=4.78) has a lowest LO FWHM of 5.03 cm^{-1} and a I_{TO}/I_{LO} of 0.16. Because the difference between two FWHM values is more obvious than that between two I_{TO}/I_{LO}, we choose the III/V=4.78 as the optimum value of this set of sample.

Multi-point Raman measurement over the 4" wafer

Figure 2 shows the 9-points Raman spectra of a 4" InSb epitaxial wafer, IA352. The TO mode appears as a shoulder of the InSb LO mode only, and we perform Lorentz fits on the Raman spectra ranging between 170-410 cm^{-1} (not shown) to deconvolute and distinguish well the LO, TO, 2LO and 2TO modes. Table II lists the resulted numerical data, including the mode peak frequency, full width at half maximum (FWHM), integrating intensity ratios between TO and LO, and between 2LO and 1LO, for nine spots over the 4" wafer area. We obtained the following results:

ω_{LO}=190.0±0.1 cm^{-1}, ω_{TO}=179.9±0.2 cm^{-1},   FWHM$_{LO}$=6.9±0.2 cm^{-1},
ω_{2LO}=380.9±0.1 cm^{-1}, I_{TO}/I_{LO}(area)=0.03±0.01, I_{2LO}/I_{LO}(area)=0.073±0.004.

Table II   Numerical data from 9-point Raman spectra of a 4" InSb/GaAs, IA352.

spot	ω_{LO} (cm^{-1})	FWHM$_{LO}$	ω_{TO}	I_{TO}/I_{LO}	ω_{2LO} (cm^{-1})	I_{2LO}/I_{LO}
a)	190.09	6.74	180.22	0.022	380.96	0.070
b)	189.91	7.05	179.99	0.021	380.84	0.075
c)	190.03	6.79	179.69	0.026	380.77	0.073
d)	189.88	7.05	179.81	0.025	380.93	0.077
e)	190.03	6.90	179.78	0.038	380.88	0.073
f)	189.85	7.11	180.00	0.029	380.87	0.068
g)	190.10	6.72	179.82	0.042	380.82	0.070
h)	189.92	6.98	179.80	0.033	380.83	0.073
i)	189.92	6.98	179.93	0.038	380.82	0.073
Average	189.98	6.92	179.89	0.030	380.86	0.073
error bar	0.12	0.20	0.23	0.010	0.10	0.004
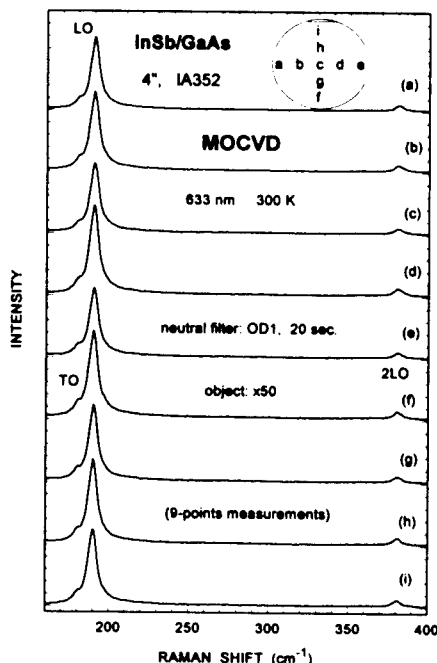
Figure 2   RT Raman scattering spectra over nine points of a 4" MOCVD-grown InSb/GaAs, IA352.

To shorten the data acquisition time, we used a wider spectral slit than in Fig. 1, leading to broader FWHM values. But the resulted uniformity is not affected. These data show that the experimental film is of high quality and high uniformity over the 4" wafer area and they are used as a merit of figure of the crystalline perfection of our MOCVD-grown InSb films. For example, the variation of the LO FWHM, which is an important indication of the crystalline quality similar to the case of PL major peak FWHM, over the 4" wafer is only 0.2 cm^{-1}, indicting a good uniformity.

FTIR map of InSb film thickness

We have also applied the Fourier transform infrared (FTIR) reflectance technology for the non-destructive measurement and mapping of the epitaxial film thicknesses over the entire 4" wafer. Figure 3 shows an example of a 4" InSb film epitaxied on GaAs. The right side in the figure displays the FTIR reflectance spectra in the wavenumber range of 800-6500 cm^{-1}. Although signals from water vapor, C-H and O-C-O bands were observed, all the spectra showed clear interference fringes, the peak or valley positions were used to calculate the film thickness by computer. The left side in Fig. 3 shows the obtained thickness distribution over 25 points of the wafer. Over the 4" (100 mm) diameter wafer area with a 5 mm edge exclusion, we obtain: the average film thickness = 1.43 μm, standard deviation = 0.02 μm, and uniformity = 1.4%.
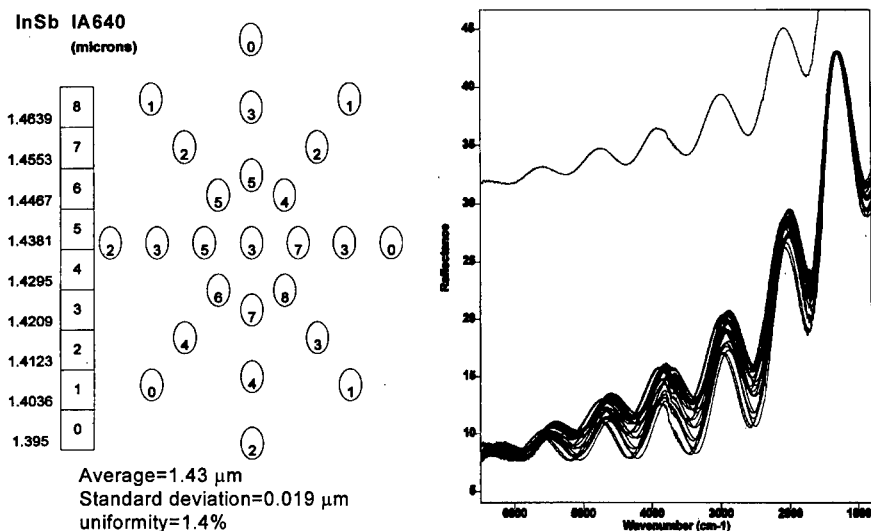
Figure 3   FTIR spectra of 25 points and calculated film thickness map over a 4" (100 mm) InSb/GaAs, IA640, with an edge exclusion of 5 mm.

CONCLUSIONS

We have demonstrated our results on the optical characterization and mapping of 4" InSb films epitaxied on GaAs. Raman spectroscopy was used successfully to study the effects of III/V

source ratios and to optimize the growth parameters. Multi-point Raman measurements was utilized to assess the InSb crystalline perfection over the 4" wafer area. The obtained distribution values of the InSb LO phonon mode frequency, full width at half maximum (FWHM), relative integrated intensity ratio between the forbidden and defect-related TO phonon and the allowed LO mode are adopted as figures of merit for the quality of the InSb films. We have set up a FTIR reflectance mapping system to measure the film thickness distribution and our InSb films possess good uniformity with differences less than ~1.4% over 4" area, by 25 points mapping. Our results show that MOCVD turbo disk technology is capable to produce high quality and high uniformity large area (4") far infrared InSb epitaxial materials, and that Raman and FTIR are very useful tools for non-destructive characterization of large size wafers in industrial mass production. Further improvement of the production of large diameter compound semiconductor materials with high quality and excellent uniformity, and the exploration and developments on the non-destructive and whole wafer characterization are in progress.

REFERENCES

[1]   R. F. C. Farrow and A. J. Noreika, in *Characterization and Behavior of Materials with Submicron Dimensions*, edited by J. T. Waber (World Scientific, Singapore,1993), p. 130.

[2]   J. Webb and R. Rousina, in *Semiconductor Interfaces and Microstructures*, edited by Z. C. Feng (World Scientific, Singapore, 1992), p. 199.

[3]   G. M. Williams, C. R. Whitehouse, C. F. McConville, A. G. Cullis, T. Ashley, S. J. Courtney and C. T. Elliott, Appl. Phys. Lett. **53**, 1189 (1988).

[4]   E. Michel, G. Singh, S. Slivken, C. Besikci, P. Bove, I. Ferguson and M. Razeghi, Appl. Phys. Lett. **65**, 3338 (1994).

[5]   D. E. Holmes and G. S. Kamath, J. Electron. Mater. **9**, 95 (1980).

[6]   T. Ohshima, S. Yamuchi and T. Tariu, Inst. Phys. Conf. Ser. **106**, 241 (1990).

[7]   R. M. Biefeld and G. A. Hebner, Appl. Phys. Lett. **57**, 1563 (1990).

[8]   D. K. Gaskill, G. T. Stauf and N. Bottka, Appl. Phys. Lett. **58**, 1905 (1991).

[9]   C. H. Chen, Z. M. Fang and G. B. Stringfellow, Appl. Phys. Lett. **58**, 2532 (1991).

[10]   M. A. McKee, B.-S. Yoo and R. A. Stall, J. Crystal Growth **124**, 286 (1992).

[11]   R. M. Graham, N. J. Mason, P. J. Walker, D. M. Frigo and R. W. Gedridge, Jr., J. Crystal Growth **124**, 363 (1992).

[12]   M. Behet, B. Stoll, W. Brysch and K. Heime, J. Crystal Growth **124**, 377 (1992).

[13]   Y. H. Choi, R. Sudharsanan, C. Besikci, E. Bigan and M. Razeghi, MRS. Res. Soc. Symp. Proc. **281**, 375 (1993).

[14]   B.-S. Yoo, M. A. McKee, S.-G. Kim and E.-H. Lee, Solid State Commun. **88**, 447 (1993).

[15]   K. C. Baucom and R. M. Biefeld, Appl. Phys. Lett. **64**, 3021 (1994).

[16]   J. Shin, Y. Hsu, T. C. Hsu, G. B. Stringfellow and R. W. Gedridge, J. Electron. Mater. **24**, 1563 (1995).

[17]   E. Woelk, H. Jurgensen, R. Rolph and T. Zielinski, J. Electron. Mater. **24**, 1715 (1995).

[18]   Z. C. Feng, S. Perkowitz, T. S. Rao and J. B. Webb, J. Appl. Phys. **68**, 5363 (1990).

[19]   F. H. Pollak, in *Analytical Raman Spectroscopy*, edited by J. G. Grasselli and B. J. Bulkin (Willey, New York, 1991), p. 137.

[20]   J. Wagner, P. Koidl and R. C. Newman, Appl. Phys. Lett. **91**, 1729 (1991).

FORMATION OF DOUBLE-CHANNEL MESA STRUCTURE FOR GaSb-BASED MID-INFRARED LASER

ANNA PIOTROWSKA, MAREK GUZIEWICZ, ELIANA KAMIŃSKA, AND EWA PAPIS
Institute of Electron Technology, Al. Lotników 32/46, Warszawa, Poland, ania@ite.waw.pl

ABSTRACT

Semiconducting antimonide compounds have received increasing attention as the alternative materials for mid-infrared photonic devices, with a variety of applications such as remote sensing, pollution monitoring, and molecular spectroscopy. For many, if not all these devices it is necessary to pattern antimonide films into mesa or line structures. While plasma etching techniques have played an increasing role in producing such features, little was reported until now on dry etching of GaSb- and AlSb-containing alloys. In this paper we present the results of our recent work towards the development of the technology for GaSb-based ridge wave-guide laser emitting at 2-2.3 μm at RT. Specifically, we discuss the fabrication of double-channel mesa structure in $Al_xGa_{1-x}As_ySb_{1-y}$/GaSb (x=0.2-0.5) heterostructure materials by RIE technique. The effects of gas and material composition, rf power, pressure and temperature on etching characteristics were studied with special attention paid to surface quality, etching rate and etching profile, which are crucial for obtaining a single mode waveguide. CCl_2F_2/H_2 and CCl_4/H_2 process chemistries were investigated which shows the latter to provide vertical sidewalls and residue free etch surfaces at controllable etch rates.

INTRODUCTION

Semiconducting antimonide compounds continue to increase in importance for the development of mid-infrared photonic devices [1-11] and thermophotovoltaics [12,13]. Much of the recent progress in the technology of these devices has occurred on the materials side. In particular, low threshold current density heterostructure materials for mid-infrared lasers have been demonstrated [3-5, 8-11]. In order to realize this potential, it is important to develop an etching technology for device fabrication.

In recent years plasma etching techniques have played an increasing role in device fabrication technology, mainly due to feature profile control of the etch process and the possibility of low etch rate dependence on material composition - the characteristics required for making waveguides or laser mirrors. However, few studies have been published on dry etching of antimonide compounds. Werking et al. [14] reported the use of RIE in CH_4/H_2 plasma to etch GaSb with slow about 20 nm/min., well-controlled etch rates. Electron cyclotron resonance (ECR) plasma etching of GaSb in Cl_2/Ar or BCl_3/Ar with etch rate up to 450 nm/min. and 250 nm/min., respectively was performed by Pearton et al. [15]. BCl_3/Ar plasma was used to fabricate single mode ridge waveguide lasers either with GaInAsSb/InGaAsSb QW heterostructure emitting at λ = 2.1.μm [8] or InAsSb/InAlAsSb QW heterostructure with AlAsSb cladding and GaSb contact layers emitting, at λ = 3.8 μm [11]. However, no details were reported on ridge waveguide etching processes.

In this paper we present the results of our recent work towards the development of the technology for GaSb-based ridge wave-guide laser emitting at 2-2.3 μm at RT. Specifically, we will discuss the fabrication of double-channel mesa structure in $Al_xGa_{1-x}As_ySb_{1-y}$/GaSb

(x=0.2-0.5) heterostructure materials by RIE technique. CCl_2F_2/H_2 and CCl_4/H_2 process chemistries were investigated which shows the latter to provide vertical sidewalls and residue free etch surfaces at controllable etch rates.

EXPERIMENTAL PROCEDURE

Our experiments were performed on (100) oriented p-type GaSb substrates doped with Ge to a concentration of $1.3-5\times10^{18}$ cm^{-3}, single epilayers $GaSb/Al_xGa_{1-x}As_ySb_{1-y}$ (x=0.2-0.5) grown by LPE either at IET Warsaw or at Ioffe Physico-Technical Institute St. Petersburg, and LPE-grown DH laser diode structures $GaSb/In_{0.12}Ga_{0.88}As_{0.10}Sb_{0.90}/Al_{0.47}Ga_{0.53}As_{0.04}Sb_{0.96}$ fabricated both, at Université de Montpellier and IET Warsaw.

Based on our previous experience with the RIE etching of GaAs, CCl_2F_2/H_2 and CCl_4/H_2 process chemistries were chosen to produce features in GaSb and AlGaAsSb alloys. Prior to RIE experiments, the samples were degreased in hot organic solvents, and etched in a solution of $HCl+HNO_3=30+1$, T=5 °C, t=20 s, followed by a rinse in H_2O DI, etching in 5% HCl for 10 s, final rinse in H_2O DI, and blow dry in N_2.

Photolithographic technique was used to pattern 4 μm wide channels separated by a 8 μm gap for RW lasers, as well as 100 μm diameter circular mesas, typical for light emitting diodes.

The mask pattern was fabricated with a trilevel technique. 200 nm thick sputter-deposited SiO_2 film was used as the bottom layer, while 80 nm thick sputter-deposited Cr film and 1.5 μm thick AZ 1375 photoresist were applied as middle and top layers, respectively. The top layer pattern was defined with a conventional photolithography and transferred to the middle Cr layer by RIE in CCl_4/O_2, while the Cr pattern was transferred to the bottom SiO_2 layer by RIE in CF_4/O_2.

The etching investigations were performed in a commercial Secon Mark 4 system which has a diode configuration RIE chamber with a 13.56 MHz power supply. The témperature of both top and bottom electrodes was controlled by a closed-loop heat exchanger. During the loading of the wafers the chamber was floated with argon to prevent contamination. Roots and two stage rotary pump were used for evacuating the reactor and for exhausting the gases. The flow rates of etching gases were controlled with mass flow meters. The process gas pressure was measured by a capacitance manometer and controlled independently of the gas flow rate by an automatically driven throttle valve in the downstream line.

The etch depth, profile and surface roughness were measured using TENCOR ALPHA-STEP profiler and both, optical (with Nomarski contrast) and SEM (JOEL 6400) techniques. Etch rates were determined by measuring the heights of the mesas (depth of the channels) both before and after removing the masks.

RESULTS AND DISCUSSION

Etching in CCl_2F_2/H_2 plasma was characterized by very low etch rates ($\leq$ 100 nm/min.) and poor surface morphology. Much more promising results were obtained with RIE in CCl_4-based plasmas. In general, etch rate of GaSb and AlGaAsSb in CCl_4/H_2 plasma increased with rf power, pressure, and concentration of CCl_4.

Fig. 1. shows a plot of the etch depth as a function of rf power and gas flow for RIE of GaSb in CCl_4/H_2 plasma. As expected, etch rate increases with an increase of rf power and gas flow presumably due to the enhancement of ion bombardment energy and reactive species concentration.

Fig. 2 presents the dependence of GaSb etch depth on feed gas composition at a constant rf power. A pure CCl_4 plasma gave relatively high etch rates, however it produced very rough surfaces. Addition of H_2 at a fraction 1.2 - 1.6 was necessary to ensure smooth etched surface. At H_2 fraction greater than 1.6 the etch rates decreased rapidly and required long etch time for
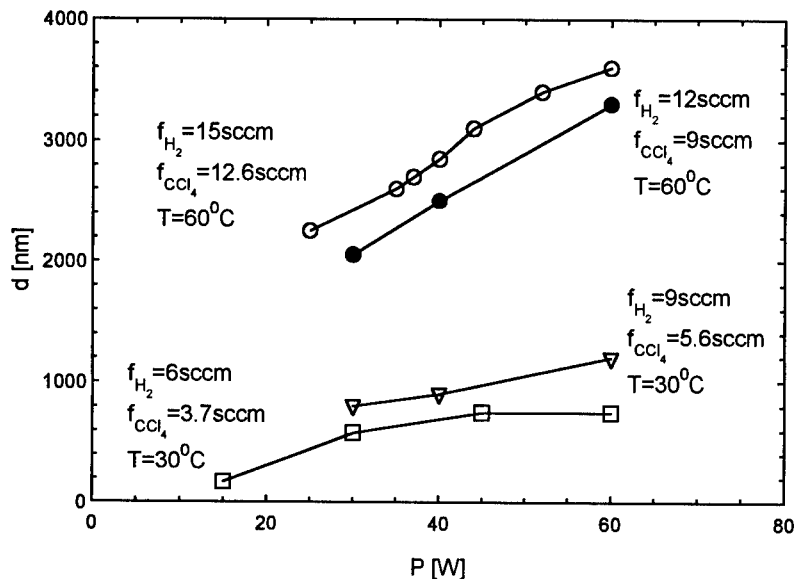
Fig.1. Etch depth of GaSb as a function of rf power for etching time 10 min.

device structures. On the other hand, etch rate increased by a factor of 5 with an increase of processing pressure from 62.5 to 170 μbar (Fig. 3), which is likely the result of an increasing generation of radicals.

Etching investigations of $Al_xGa_{1-x}As_ySb_{1-y}$ (x=0.2-0.5) for varying rf powers have shown some difficulty in anisotropic etching of $GaSb/Al_xGa_{1-x}As_ySb_{1-y}$ heterostructures when high rf power was applied. However, when keeping the rf power below 50 W similar etch rate for GaSb and $Al_xGa_{1-x}As_ySb_{1-y}$ were obtained (Fig.4). Careful analysis of the obtained results suggested that optimum etch conditions were obtained at rf power of 30 W, a pressure of 150 μbar, and gas flow rate $f_{CCl4}/f_{H2} = 9/12$.

The formation of double-channel mesa structure in $GaSb/In_{0.12}Ga_{0.88}As_{0.10}Sb_{0.90}/Al_{0.47}Ga_{0.53}As_{0.04}Sb_{0.96}$ DH by etching in CCl_4/H_2 discharge is shown in Fig. 5. Here the etch was timed to expose the active region of the heterostructure. Smooth sidewalls can be seen though some roughness of the surface morphology was observed. This is believed to be caused by the initial morphology of the as-grown material.
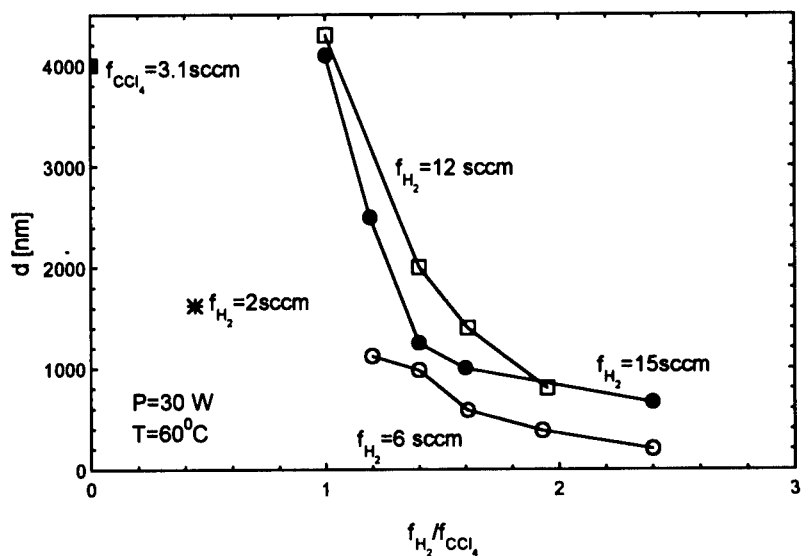
Fig.2. Etch depth of GaSb as a function of CCl_4 concentration for etching time 10 min.
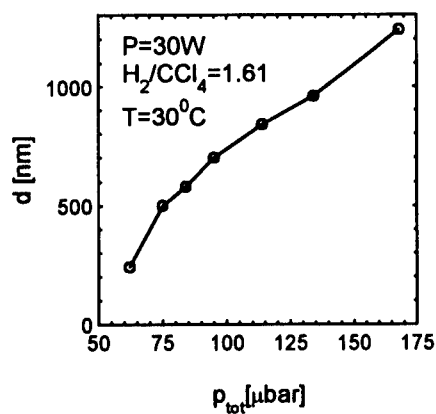
Fig.3. Etch depth of GaSb as a function of process pressure for etching time 10 min.
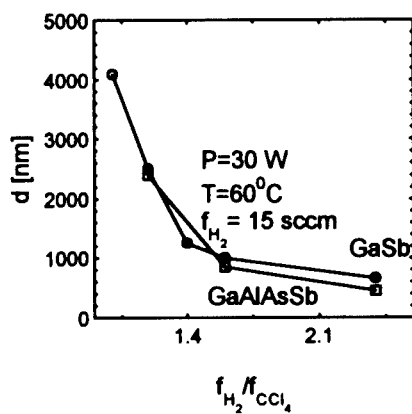
Fig.4. Etch depth of GaSb and GaAlAsSb as a function of CCl_4 concentration for etching time 10 min.
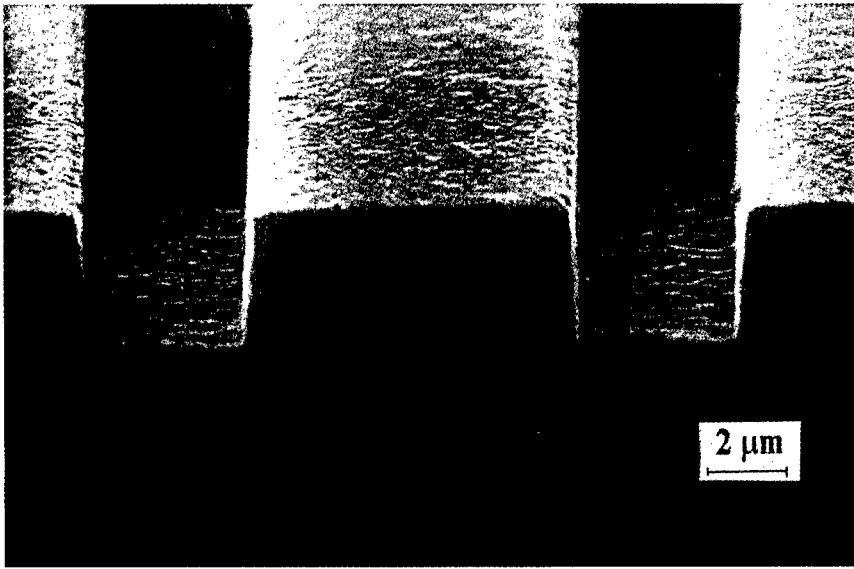
a)
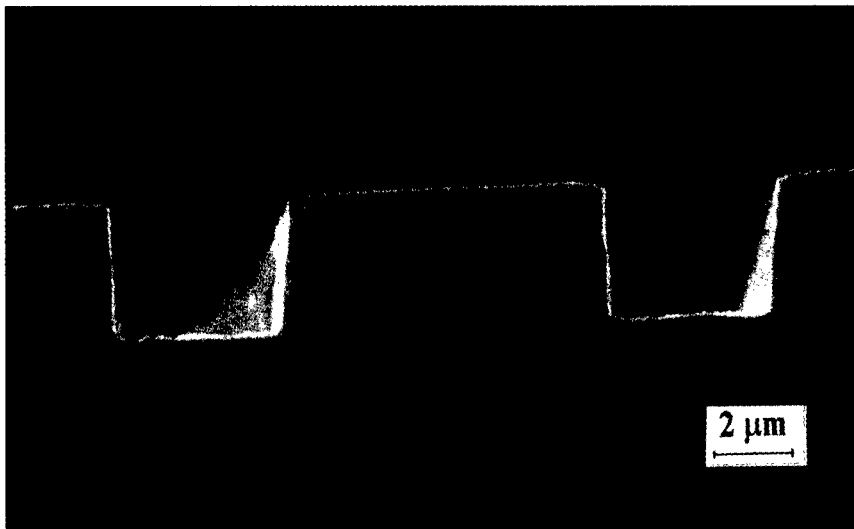
b)

Fig. 5. SEM micrographs of $Ga_{1-x}Al_xAs_ySb_{1-y}/In_xGa_{1-x}As_ySb_{1-y}/GaSb$ double channel mesa structure obtained with in CCl_4/H_2 ($f_{H2}/f_{CCl4} = 1.3$, $P = 30$ W) RIE. Channel depth 3 μm, mesa 8 μm: a) top view, b) cross sectional profile.

CONCLUSIONS

We have shown that CCl_4-based RIE can be used for processing III-V antimonide semiconductor devices. The fabrication of double channel mesa structure in $GaSb/Al_xGa_{1-x}As_ySb_{1-y}$ /$In_xGa_{1-x}As_ySb_{1-y}$ DH have been demonstrated.

The optimum etch conditions providing vertical side walls and residue free etch surfaces, at etch rate of 200 nm/min. were obtained with CCl_4/H_2 plasma at a pressure of 150 μbar, rf power of 30 W, and gas flow rate $f_{CCl_4}/f_{H_2} = 9/12$.

REFERENCES

1. H.D. Law, K. Nakano, and L.R. Tomasetta, IEEE J. Quantum Electron. QE-15, 549, (1979).
2. J.E. Bowers, A.K. Srivastava, C.A. Burrus, J.C. de Winter, M.A. Pollack, and J.L. Zyskind, Elector. Lett. 22(3), 137 (1986).
3. A.E. Bochkarev, L.M. Dolginov, A.E. Drakin, P.G. Eliseev, and B. N. Svierdlov, Sov. J. Quantum Electron. 18, 1362 (1988).
4. A.N. Baranov, T.N. Danilova, B.E. Dzurtanov, A.N. Imenkov, S.G. Konnikov, A.M. Litvak, and Yu. P. Yakovlev, Sov. Tech. Phys. Lett. 14, 727 (1988).
5. S.J. Eglash and H.K. Choi Appl. Phys. Lett. 57, 1292 (1990).
6. E. Tournie, J.-L. Lazzari, E. Villemain, A. Joullie, L. Gouskov, M. Karim, and I. Salesse, Electron. Letters 27(14), 1237 (1991).
7. M. Chyi and C.Chen, J. Appl. Phys. 71(12), 6116 (1992).
8. H. K. Choi, S.J. Eglash, and M.K. Connors, Appl. Phys. Lett. 63, 3271 (1993).
9. A.N. Baranov, C. Fouollant, P. Grunberg, J.L. Lazzari, S. Gaillard, and A. Joullie, Appl. Phys. Lett. 65, 616 (1994).
10. H. Lee, P.K. York, R.J. Menna, R.U. Martinelli, D.Z. Garbuzov, S.Y. Narayan, and J.C. Connolly, Appl. Phys. Lett. 66, 1942 (1995).
11. H.K. Choi, G.W. Turner, M.J. Manfra, and M.K. Connors, Appl. Phys. Lett. 68, 2936 (1996).
12. T.J. Coutts and M. Lunstrom, J. Electron. Mater. 22, 57 (1993).
13. L.Fraas, R. Ballantyne, J. Samaras, and M. Seal, Proc. 1994 IEEE First World Conf. on Photovoltaic Energy Conversion, vol. II, p.1713, 1994.
14. J. Werking, J. Schramm, C. Nguyen, E.L. Hu, and H. Kroemer, Appl. Phys. Lett. 58, 2003 (1991).
15. S.J. Pearton, C.R. Abernathy, and F. Ren, J. Vac. Sci. Technol. A 13(3), 849 (1995).

ROOM TEMPERATURE LED'S FOR THE MID-INFRARED BASED ON IN(AS,SB) STRAINED LAYER SUPERLATTICES

C.C. Phillips*, P.J.P. Tang*, M.J. Pullin*, H R Hardaway*, S.J. Chung*, W.T. Yuen*, R.A. Stradling*, Y.B. Li*, and L. Hart**

*Solid State Group, Physics Department, Imperial College, London SW7 2BZ
**Interdisciplinary Research Centre for Semiconductor Materials, Imperial College, London SW7 2BZ

ABSTRACT.

Arsenic-rich InAs/InAs$_{1-x}$ Sb$_x$ strained-layer superlattices (SLS's) are studied in time-resolved optical, and CW magneto-optical spectroscopies. A pronounced type-II offset, with electrons confined to the alloy layers, is found. High radiative efficiencies at wavelengths well into the mid-IR, and the suppression of Auger recombination yield LED's operating at 3-10 μm. Present room temperature powers are ~30 μW, probably limited by inadequate carrier confinement.

INTRODUCTION.

Recently much progress has been made towards 300K lasers operating in the mid-IR spectral range where a wide variety of gases have strong absorption lines. Current interest centres on λ= 3.3 μm and 4.2μm for CH_3 and CO_2 detection at high sensitivities and specificities, although longer λ sources would allow the detection of other important pollutants, for example NH_3 and O_3 and the "acid-rain" gases NO_x and SO_x.

III-V interband devices typically employ InAs-based active layers with small alloy fractions of Sb (for bandgap lowering) and/or Ga (for lattice matching). Lasers have been demonstrated at λ~3-3.5 μm [1-5] but so far Auger recombination has prevented 300K operation beyond λ~3.2 μm [6]. Very recently intersubband "Quantum Cascade" (QC) lasers, have improved spectacularly and given 320K pulsed 5.2 and 8μm output [7] in the wide-gap (InGa)As/(AlIn)As materials system. The ingenious MBE epilayer design used though is very demanding technologically.

In comparison the epitaxial growth technology of narrow gap III-V's is immature but developing rapidly. Bandstructure engineering techniques, such as strain-lightening the valence-bands and using systems with type-II band offsets for Auger suppression are just being explored [8]. For gas-sensing, output stability rather than spectral intensity is often the dominant engineering criterion and a narrow-line laser output drifting through a sharply resonant gas absorption line can cause severe systems engineering headaches. LED sources suffer from a much lower spectral density but their broad output spectra (some of which can be used in a stabilising reference channel) and good manufacturability, may make them the preferred choice for many practical gas sensing applications.

Growth details.

All samples were grown by MBE at T_g~450° on either InAs substrates or on InAs$_{1-x/2}$Sb$_{x/2}$ buffer layers on GaAs substrates [9]. Growth parameters were checked by numerically modelling

the XRD data and corroborated with TEM, Raman and PL (fig.1), magneto-PL and magneto-absorption methods.
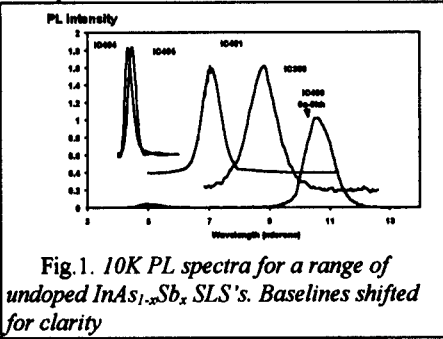
The bandgaps of bulk alloy samples, measured in magneto-absorption [10], were all found to be consistent with literature data [11,12]. For a 10% Sb alloy for example the data of in refs. 10,11 and 12 give 10K bandgaps of 335, 336.5 and 331 meV respectively, all mutually consistent but at odds with the ~270 meV deduced [2] from "optical studies of bulk ternary alloy". The latter was attributed to an "order induced bandgap reduction" (OIBGR) caused by Cu-Pt ordering on the alloy sublattice in T$_s$~475° MOCVD material.

It should be noted though that low temperature photoluminescence spectra from bulk samples commonly feature defect-related transitions [13,14] and can lead to underestimates of the bandgap unless carefully interpreted. On the basis of the above considerations we conclude that the "OIBGR" effect is absent in our samples and model the SLS bandstructures with the bandgap data of ref.10.

Sample number	SLS (~2μm thick)	SLS period (nm)	Substrate	Doping type
IC 208	bulk InAs$_{0.812}$ Sb$_{0.188}$	3μm	GaAs	Undoped
IC 210	bulk InAs$_{0.905}$ Sb$_{0.095}$	2.5μm	GaAs	Undoped
IC 372	bulk InAs control	3μm	GaAs	Undoped
IC 389	InAs/InAs$_{0.68}$ Sb$_{0.32}$	20	GaAs	Undoped
IC 481	InAs/InAs$_{0.73}$ Sb$_{0.27}$	23.5	GaAs	Undoped
IC 494	InAs/InAs$_{0.86}$ Sb$_{0.14}$	16	GaAs	Undoped
IC 495	InAs/InAs$_{0.86}$ Sb$_{0.14}$	24.8	GaAs	Undoped
IC 499	InAs/InAs$_{0.61}$ Sb$_{0.39}$	21.5	GaAs	Undoped
IC 500	InAs/InAs$_{0.905}$ Sb$_{0.095}$	24.2	GaAs	p-n diode
IC 501	InAs/InAs$_{0.897}$ Sb$_{0.103}$	16.4	GaAs	p-n diode
IC 506	InAs	3μm	InAs	p-n diode
IC 516	InAs/InAs$_{0.875}$ Sb$_{0.125}$	24	GaAs	p-n diode
IC 523	InAs (+20nm In$_{0.85}$ Al$_{0.15}$ As)	2.5μm	InAs	p-n diode
IC 527	InAs/InAs$_{0.875}$ Sb$_{0.125}$ (+20nm In$_{0.85}$ Al$_{0.15}$ As)	24	InAs	p-n diode
IC 536	bulk InAs control	5μm	InAs	Undoped
IC 583	triple InAs$_{0.90}$Sb$_{0.10}$/ InAs/ InAs$_{0.90}$Sb$_{0.10}$ QW	1μm/16/60/11 .5/60/8.3/100	InAs	Undoped
IC 587	InAs/InAs$_{0.871}$ Sb$_{0.129}$	25	InAs	Undoped
IC 595	InAs/ InAs$_{0.83}$ Sb$_{0.17}$ SQW	16nm	GaAs	p-n diode

Table 1. Design parameters for the various MBE wafers cited.

Epilayer Materials and Bandstructure Studies.

a) Optical band structure determination.

74
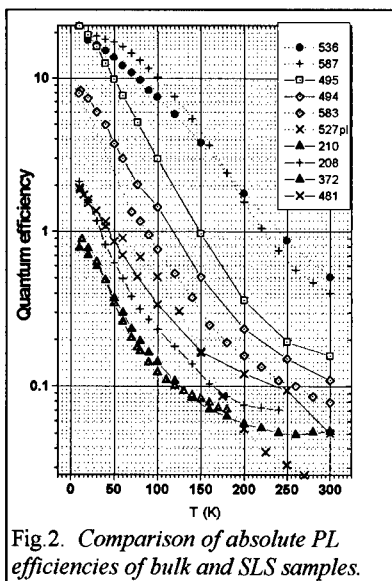
Fig.2. *Comparison of absolute PL efficiencies of bulk and SLS samples.*

10K PL spectra for a number of SLS's (fig.1) all evidence SLS bandgaps well below either of the strained SL constituents and, in the absence of an OIBGR effect, are consistent only within a type-II band offset interpretation. Magneto-absorption spectra [15] of the undoped SLS's show the same transitions, arguing that our PL is genuinely band-to-band and not defect-related.

Magneto-PL spectra from a pair of triple QW In($As_{1-x}Sb_x$)/InAs samples, designed according to the alternative assumptions about the sign of the type-II offset i.e. type-IIA (electrons in the alloy) vs. type-IIB (electrons in the binary), provide strong evidence [16] for a type-IIA assignment. As in previous studies of similar samples [17] the energy separations of the PL peaks between the different QW's in one of this pair are so large that they can be due only to differences in electron (as opposed to hole) confinement energies. Given the sample designs this immediately implies, that the electron wells are in the alloy.

In both studies [16,17] the magnetic-field shifts of the QW transition energies yield *lighter* in-plane reduced masses for the ground-state QW transitions than the bulk values for either of the QW constituents. Again this argues that the PL transitions are band-to-band because defect related transitions have weaker magnetic field dependencies, yielding an apparent *increase* in the reduced mass when it is extracted from the slope of the transition energy in a fan diagram. In [17] it was argued that these light reduced masses implied that the holes were also confined in the (compressively strained) alloy. i.e. the offsets had a type-I character. To fit the observed PL energies with this type-I scheme though requires the assumption of a large "OIBGR" effect, invoking a 30% reduction of the x=0.135 Sb alloy bandgap below its accepted value.

In reality however "valence band mixing" (VBM) by the QW potential gives a complex in-plane dispersion for both valence bands and dramatically modifies the in-plane reduced masses. VBM is absent at the in-plane zone centre, leaving the above B=0 transition energy calculations unaffected, but including it, in an 8x8 k.p calculation [15] which includes the effects of strain and conduction-band non-parabolicity, we find we can accurately reproduce all the experimental transition energy and reduced mass data of refs. 16 and 17 without having to invoke any "OIBGR" effect. This yields an unstrained type-IIA valence band offset estimate of ~800x meV, in good agreement with the values extracted previously [15] from SLS magneto-absorption data.

b) Evidence for Auger suppression.

Fig.2 summarises the calibrated PL efficiencies (PLη's) of a number of SLS and bulk "control" samples. To generalise: i) Homoepitaxial InAs has the best 300K PLη but is closely matched by the best SLS (IC587, 13nm InAs/13nm In $As_{0.85}Sb_{0.15}$ on InAs) even though the heteroepitaxial SLS has the higher dislocation density and a 25% lower bandgap. ii) Bulk alloys [IC210 and IC 208 , x= 9.5% and 18.8%] have PLη's 15 - 40 times lower than SLS's with equivalent bandgaps. iii) The PLη sensitivity to substrate type is more pronounced in the bulk

75

epilayers [e.g. the ~20 factor between IC372, UD InAs:GaAs and IC536, homoepitaxial InAs] than in the SLS's [e.g. the ~10 factor between IC 587, 13nm InAs/ 13nm InAs$_{0.85}$Sb$_{0.15}$ SLS on InAs and IC 494, a 8nm InAs/ 8nm InAs$_{0.86}$Sb$_{0.14}$ SLS on GaAs].

Although the heteroepitaxial InAs has excellent bulk electrical characteristics (N_A,N_D ~ 2 x 10^{14} cm^{-3}, μ_e ~2 x 10^5 cm^{2}V^{-1}sec^{-1}) and IR picosecond laser measurements show carrier diffusion lengths [18] of some μm, no effort has gone into strain-relief schemes as yet. The PLη figures in at least in the bulk samples, are thus determined by non-radiative recombination at the heavily dislocated substrate/ epilayer interface, and this may partially account for the PLη improvements of SLS's over the bulk samples.

Fig. 3.. *Typical physical and electronic structure of the SLS LED's.*

Nevertheless the SLS samples preserve their PLη much better than bulk alloys as the bandgap narrows, consistent with Auger suppression in the SLS's, due to the type-II offset and valence band modifications. Auger suppression (by a factor of ~100), in an SLS sample compared with a control InSb epilayer with a similar effective bandgap, has also recently been demonstrated [19] in psec pump-probe measurements of the total carrier recombination rates at high excess carrier densities.

Fig. 4 . *LED EL efficiency as a function of Temperature.*

Device studies.

EL device wafers, with the SLS's included in p-i-n junctions with, occasionally, thin (~20nm) electron-confining In$_{0.85}$Al$_{0.15}$As barriers (fig.3), were processed into ~300-600μm diameter mesas. Due to photocarrier separation by the diode field the PLη's were low, but in forward bias the SLS electroluminescence efficiency (ELη) typically corresponded (Fig.4) to internal quantum efficiencies of ~0.8% at 300K. The main EL emission matches the PL peak of the equivalent undoped test SLS's but occasionally extra higher energy substrate/buffer layer related features were seen in EL, implying poor electron confinement (fig.5) and diffusion of the injected carriers to the doped regions before recombination.

A single 16nm x=0.17 QW LED, IC595, grown pseudomorphically on a GaSb/AlSb SL buffer(fig.6) also gave a very promising 300K ELη figure of ~1%. All the radiative recombination occurred in the well for T<200K, evolving into a broad spectral output centred on the CO_2 absorption line at 300K (fig.7). This result has particular implications on the design of necessarily thick laser cavities, where strain considerations may limit the allowable mole fraction of Sb.

Under bias the excess carrier concentration profile is determined by a complex and non-linear drift-diffusion-recombination equation which, for practical purposes is insoluble, precluding a meaningful analysis of the ELη data in terms of Auger recombination.

Nevertheless the ELη's are similar to a range of bulk "control" homoepitaxial InAs devices of superior crystal quality, and the 300K SLS outputs now reach 30 μW peak and 15 μW equivalent CW @I=500 mA. The best SLS LED's have superior output than the homoepitaxial InAs devices, in spite of the former's lower bandgaps, and may be close to being Auger limited. Qualitatively speaking, Auger recombination may also account for the unusual ELη temperature characteristics seen in some of the LED's (e.g. IC 527 in Fig.4) as various Auger channels come in and out of resonance as the bandstructure evolves with increasing temperature.

CONCLUDING REMARKS.
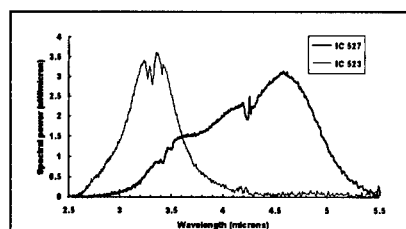
Fig. 5. 300K EL from SLS and InAs "control" LED's, I=60 mA.
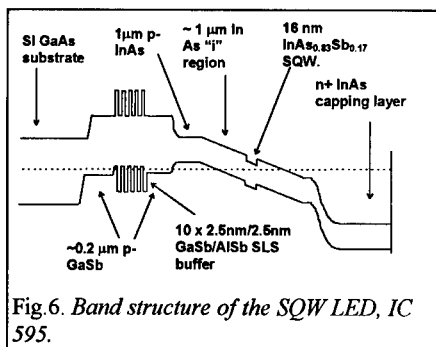
Fig.6. *Band structure of the SQW LED, IC 595.*

Fig. 7. *EL spectra from the SQW LED at various temperatures.*

A large body of experimental evidence briefly summarised here indicates that InAs/InAs$_{1-x}$ Sb$_x$ SLS's have a pronounced type-IIA band offset character and that this may be an important route to high efficiency room temperature mid-IR sources. Existing evidence is that Auger suppression is a real effect but that inadequate carrier confinement, leading to carrier escape to the damaged hetero-interface, is the present limiting factor in LED efficiency.

References

1. Y H Zhang, H Q Le, D H Chow and R H Miles. Inst. Phys. Conf. Series **144**, 36-40 (1995).

2. S R Kurtz, R M Biefield, L R Dawson, K C Baucom and A J Howard. Appl. Phys. Lett. **64** (7), 812-814 (1994).

3. Yu. P Yakovlev, A N Baranov, A N Imendov, A A Popov and V V Sherstnev. J.de Physique III **4,** C4-671-676, (1994).

4. H Q Le, G W Turner, S J Eglash, H K Choi and D A Coppeta. Appl. Phys. Lett. **64** (2),152-154, (1994).

5. M Adaraliev, M S Bresler, O B Guslev, S A Karandashov, B A Matveev, M N Stus', G N Talalakin and N V Zotova. Semicon. Sci. Tech. **10** 151-156 (1995).

6 . J I Malin, C L Felix, J R Meyer, C A Hoffman, J F Pinto, C.-H. Lin, P.C. Chang, S. J. Murray and S.-S. Pei. Electron. Lett. **32**, (17), 1593-1595. (1996)

7. J Faist, F Capasso, C Sirtori, D L Sivco, J N. Baillargeon, A L Hutchinson, S-N G Chu, and A Y Cho. App. Phys. Lett. **68** (26), 3680-3682, (1996).

8. J I Malin, J R Meyer, C L Felix, J R Lindle, L Goldberg, C A Hoffman, F J Bartoli, C-H Lin, P C Chang, S J Murry, R Q Yang and S-S Pei. Appl. Phys. Lett. **68** (21), 2976-2978 (1996).

9. P J P Tang, M J Pullin, S J Chung, C C Phillips, R A Stradling, A G Norman, Y B Li and L Hart. Semicond. Sci. and Technol. **10**, 1177-1180 (1995).

10. S N Smith, C C Phillips, R H Thomas, R A Stradling B N Murdin and C R Pidgeon. Semicond. Sci and Technol. 7, 900-906 (1992).

11. Z M Fang, K Y Ma, D H Jaw, R M Cohen and G B Stringfellow. J. Appl. Phys. **67** (11) 7034-7039 (1990).

12. A Rogalski, Prog. Quant. Electr. **13**, 191-231 (1989).

13. P J P Tang, A Norman, R A Stradling and C C Phillips. Semicond. Sci. and Tech. **8**, 2135-2142 (1993).

14. P J P Tang, M J Pullin and C C Phillips Accepted for Phys. Rev. B. **55**, (7) (15th Feb 1997)

15. Y B Li, D J Bain, L Hart, M Livingstone, C M Ciesla, M J Pullin, P J P Tang, W T Yuen, I Galbraith, C C Phillips, C R Pidgeon and R A Stradling. Accepted for Phys. Rev. B.**55**, (7), (15th Feb.1997).

16. P.J.P. Tang, M.J. Pullin, Y.B. Li, C.C. Phillips, R.A.Stradling, S.J. Chung, W.T. Yuen, L. Hart, D.J. Bain and I Galbraith. App. Phys. Lett. **69**, (17), 2501-2503 (1996).

17. S R Kurtz and R M Biefield. Appl. Phys. Lett. **66**,(3), 364-366, (1995).

18. K L Vodopyanov, H Graener, C C Phillips and T J Tate. J. Phys.D: Appl. Phys. **73**, (2) 627-632 (1993).

19. C M Ciesla, B N Murdin, C R Pidgeon, R A Stradling, C C Phillips, M Livingstone, I Galbraith, D A Jarosznyski, C J M Langerak, P Tang and M Pullin. J. Appl. Phys. **80**, (5), 2994-2997. (1996).

InSb Detectors and Focal Plane Arrays on GaAs, Si, and Al$_2$0$_3$ Substrates

E. Michel, H. Mohseni, J. Wojkowski, J. Sandven, J. Xu, and M. Razeghi
Center for Quantum Devices, Electrical and Computer Engineering Department
Northwestern University, Evanston, IL 60208

P. Vu and R. Bredthauer
Lockheed Martin Fairchild Systems, Tustin, CA

W. Mitchel and M. Ahoujja
Wright Laboratory, Materials Directorate, WPAFB, OH

ABSTRACT

In this paper, we report on the growth and fabrication of InSb detectors and Focal Plane Arrays (FPA's) on (100) Si, Al$_2$O$_3$, and (100) and (111) GaAs substrates for infrared (IR) imaging. Several advantages result from using GaAs, Si, or Al$_2$O$_3$. First, InSb FPA's on these materials do not require thinning as with detectors fabricated from bulk InSb. In addition, these substrates are available in larger sizes, are semi-insulating (GaAs and sapphire), and are less expensive than InSb.

Optimum growth conditions have been determined and discrete devices have been fabricated on each substrate material. The structural, electrical, and optical properties were verified using x-ray, Hall, photoresponse, and photoluminescence (PL) measurements. Measured x-ray Full Widths at Half Maximum (FWHM) were as low as 55 and 100 arcsec for InSb epilayers on GaAs and Si, respectively. Hall mobilities were as high as 128,000, 95,000 and 72,000 cm^2/V-sec at 200 K, 77 K, and room temperature, respectively. In addition, 77 K PL linewidths were as low as 18, 20 , and 30 meV on GaAs, Si, and sapphire substrates respectively, well below the 48 meV value previously reported in the literature.

In collaboration with Lockheed Martin Fairchild Systems (LMFS), IR thermal imaging has been obtained from InSb FPA's on GaAs and Si substrates. This is the first successful IR thermal imaging from heteroepitaxially grown InSb. Because of the high quality substrates, larger areas, and higher yields, this technology is very promising for challenging traditional InSb FPA hybrid technology.

INTRODUCTION

InSb is a well established material system for mid-IR detector applications. These applications include IR thermal imaging, environmental gas monitoring, and free space communications. The work described in this paper is directed toward IR thermal imaging using FPA's. InSb FPA's have been well researched, but only on InSb substrates. These substrates have several drawbacks and limitations. First, InSb substrates are limited in size because the quality is not uniform as the wafer diameter increases. In addition, InSb substrates are expensive, non semi-insulating, and are of lower quality than GaAs or Si. And most importantly, InSb substrates used for FPA's must be thinned to $\approx$ 10 μm due to absorption in the substrate. This thinning is a major yield-limiting step in the FPA fabrication process, and this problem is only exacerbated by the limited substrate size.

Thus, the use of a suitable alternative to InSb substrates is very attractive to InSb FPA technology. GaAs, Si, and Al$_2$O$_3$ are possible candidates despite having large lattice mismatch (4-15 %). For these materials to be viable, the devices fabricated on them must have performance comparable to that of bulk arrays with the advantage of larger area arrays with excellent uniformity. Considering the large mismatch these materials have with InSb, especially GaAs, it would seem impossible that device performance could be anywhere near that of existing

technology. However, in this paper we report on the first IR imaging obtained from InSb FPA's fabricated on GaAs or Si substrates with performance comparable to that of bulk InSb detectors.

EXPERIMENT

InSb on GaAs and Si

The growth of InSb on GaAs and Si substrates was optimized using an EPI/Intevac Modular Gen II MBE system with elemental uncracked sources (7N pure). Si and Be were used as n- and p-type dopants, respectively. Substrates were epi-ready GaAs and GaAs coated Si which were cleaved into ~ 1 cm^2 pieces and In-mounted to molybdenum blocks before being loaded into the system. The oxide was desorbed by heating the sample under an As flux.

Static and dynamic Reflection High Energy Electron Diffraction (RHEED) surface characterization was used to accurately control the growth conditions as reported previously [1-3]. The Sb/In incorporation ratio was calibrated at 1.2/1.0 using dynamic RHEED oscillations, and the substrate temperature was calibrated by monitoring the c(4x4) to a(1x3) transition which occurs at ~390 °C, T_T, for typical Sb fluxes. Growth on (100) GaAs showed the highest quality when grown slightly above the transition temperature, T_T. For growth on (111) GaAs, however, the optimum growth temperature was higher, ~ 420 °C. This higher required growth temperature has been attributed to the different bonding characteristics of the two surfaces. In growth on (100) surfaces, there are two bonds available for both In and Sb. But on the (111) surface, there are three bonds for each Sb atom and one for each In atom [4]. Thus, for a given Sb/In ratio, a higher temperature is needed to obtain stoichiometric growth on the (111) surface.

A difficulty in growing (111) InSb was that there was no transition in the RHEED pattern when the substrate temperature was varied above or below growth temperature under an Sb flux. For this reason, the substrate surface temperature had to be measured with an IR pyrometer which was calibrated using the transition temperature on a (100) InSb sample. However, this measurement technique could only determine temperatures with an accuracy of +/- 10 °C because of the difference in thickness of the (111) GaAs and the (100) GaAs used for the pyrometer calibration, and differences between block emissivity and In mounting of the samples.

Even with the difficulty in accurate temperature control, the material quality was essentially identical on (100) and (111) GaAs. The material quality was assessed structurally, electrically, and optically using x-ray diffraction, Hall, photoluminescence, and photoresponse measurements.

Structural characterization was performed on a five-crystal x-ray diffractometer. Figure 1 a) below shows the x-ray rocking curve FWHM for both (100) and (111) material versus epilayer thickness on GaAs substrates. It should be noted that the (100) and (111) FWHM are essentially equal indicating that the growth conditions have been optimized for both surfaces. The crystallinity shows a large dependence on substrate temperature as shown in Figure 1 b). As indicated in the figure, the optimum substrate temperature is ~ 420-430 °C. The optimum (100) growth temperature is ~ 395, well under that of (111) InSb.

Electrical characterization was obtained with a Hall system and samples etched with standard Van der Pauw patterns. The room temperature mobility versus epilayer thickness is shown for both (100) and (111) InSb in Figure 2 a). As the epilayer is increased past ~ 1 μm, the mobility levels off near that of bulk InSb. The (100) curve is for a single layer which was step-and-etched using a lactic/nitric acid etching solution, whereas the (111) points are from separate samples. Figure 2 b) shows InSb on (100) GaAs mobility versus temperature for a 3.3 μm thick epilayer. Peak mobilities of ~ 92,000 cm^2/V-sec were obtained on samples of 5 μm thickness. The curve shows typical n-type mobility for a sample grown with 6N pure Sb source material resulting in a background concentration of 10^{16} cm^{-3}.
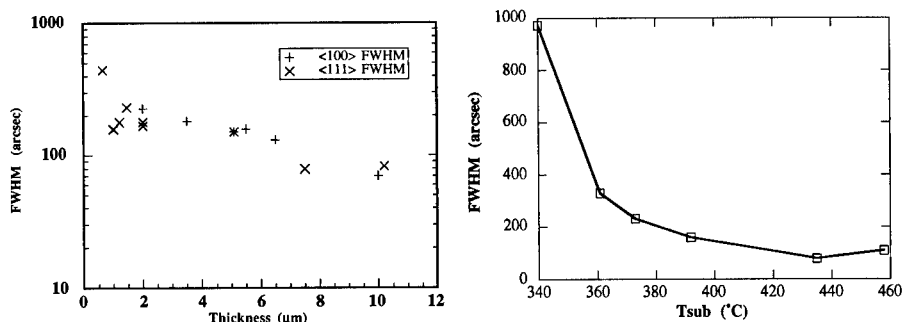
Figure 1.   a) X-ray FWHM versus Thickness for InSb on (100) and (111) GaAs
             b) X-ray FWHM versus Substrate Temperature for InSb on (111) GaAs
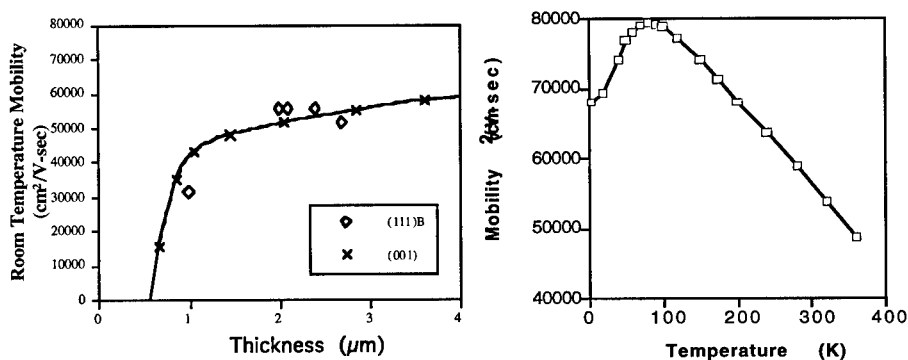
Figure 2.   a) 300 K Mobility versus Thickness for InSb on (100) and (111) GaAs
             b) Hall Mobility versus Temperature for a 3.3 μm InSb Epilayer on (100) GaAs

An interesting effect was discovered when higher purity (7N) source material was installed in the reactor. The room temperature mobility increased slightly, but the 77K mobility dropped drastically from ~ 92,000 cm²/V-sec to ~ 3,000 cm²/V-sec. This effect was also noted by Thompson et al [5]. By doping the material n-type in the range of ~ 5 x 10^{15} cm^{-3}, the mobility would again be back up to values obtained with the 6N source material. This low 77K mobility has been attributed to the interface which dominates the Hall measurements in this temperature range. The epilayer can be considered to be composed of three layers: a surface inversion (or depletion) layer, a bulk-like layer, and a highly dislocated interface layer as described by Besikci et al [6]. When the material had a 10^{16} cm^{-3} background, the 77K Hall measurement was not dominated by the interface layer because the bulk-like layer had a high enough conductivity. However, with the background at 10^{15} cm^{-3}, the bulk-like layer is at least an order of magnitude less conductive, and the interface layer dominates Hall measurements.

This theory was supported by Hall measurements made on samples after the substrate had been etched off and by field-dependent Hall measurements. Samples were epoxied to glass slides epi-side down, and were then placed in a H_2O_2:NH_4OH:H_2O solution which etched off the substrate and left a mirror-like surface. The samples were then characterized using Hall measurements, and exhibited very high mobilities at 77 K. A 5 μm sample exhibited 65,000

cm^2/V-sec at 300 K, and 95,000 cm^2/V-sec at 77 K. Before removing the substrate, this same sample had mobilities of 60,000 cm^2/V-sec at 300 K and 4,230 cm^2/V-sec at 77 K.

Field-dependent measurements were performed at Wright-Patterson Air Force Base (WPAFB) on three samples with thickness of 2.0, 5.0, and 9.2 μm. Figure 3 shows the electron mobility and concentration versus temperature for these samples under a 5.0 kG field. It is evident from the mobility curves that the mobility is being limited by a thickness independent mechanism at low temperatures as indicated by the drastic drop in mobility around 200 K and because the sheet concentration at low temperature for these three samples is constant (~ 1 x 10^{12} cm^{-2}). The mobility measurement made with the substrate etched off is indicated in Figure 3 a). Mobility spectra obtained by WPAFB show several conduction channels - specifically a high mobility n-type channel and a low mobility n-type layer with a mobility of a few thousand cm^2/V-sec. These measurements taken together indicate that Hall measurements made on these samples are dominated by the interface especially at low temperatures (< 200 K).
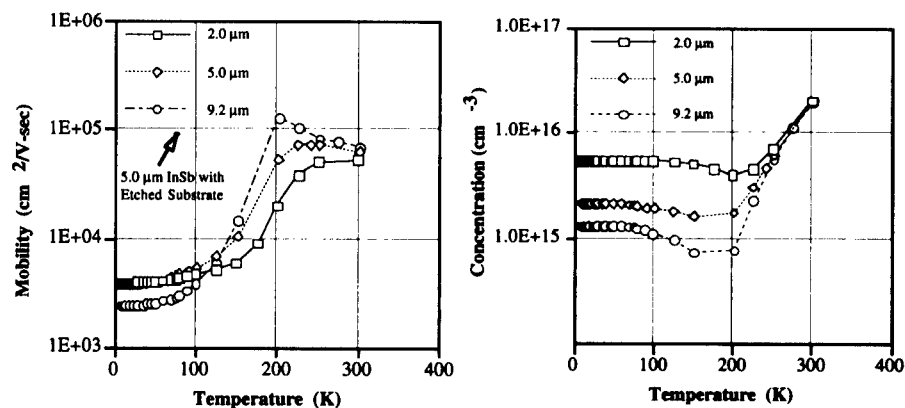
Figure 3 a) Electron Mobility versus Temperature b) Electron Concentration versus Temperature

Optical characterization was performed on these samples using photoluminescence (PL), transmission, and photoresponse measurements. PL linewidths of 18 and 20 meV were obtained at 77 K for InSb on GaAs and Si, respectively. Transmission measurements were performed using a Fourier Transform Infrared (FTIR) spectrometer. Relative photoresponse of photoconductor samples was also measured using the FTIR system with a preamplifier and bias voltage circuit. Photodiode response measurements were made on p-i-n detector structures.

Photodiodes were fabricated using standard photolithography and wet chemical etching techniques. p-i-n photodiodes were realized by etching 400 x 400 μm mesas using a lactic:nitric etching solution, and contacts were made using e-beam evaporated Au/Ti. The detector structure consisted of a 1.5 μm n^+ region, a 6 μm undoped active region, and a 0.5 μm p^+ contact region. This structure was grown on both GaAs and Si substrates.

The relative photoresponse of these devices was measured using the FTIR system. The absolute responsivity was obtained by measuring the signal using a calibrated blackbody source and a lock-in amplifier system. The absolute responsivity for p-i-n detectors on Si and (111) GaAs are shown in Figure 4 a) and b), respectively.

These devices showed excellent response, comparable to that of bulk detectors, with detectivities of ~ 3 x 10^{10} cm-$Hz^{1/2}$/W at 77K. Note that the detectors operate up to room temperature, even though these devices were not optimized for room temperature operation.
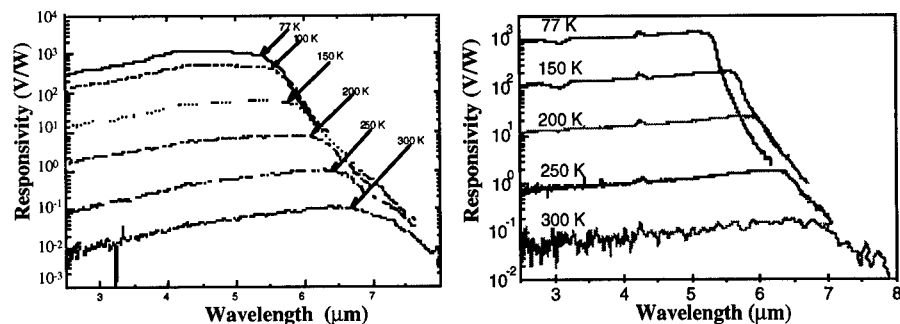
Figure 4.   Absolute Responsivity of a p-i-n Photodiode on a) Si and b) (111) GaAs

In collaboration with LMFS, 256 x 256 InSb FPA's were fabricated from InSb epilayers on GaAs and Si substrates. Starting from an undoped 10 μm InSb epilayer, the p-type regions were ion implanted, the structures were then chemically etched to form mesas, and finally In bump-bonded to Si CMOS readout circuitry. This readout circuitry resulted in standard video output which was then sent to a workstation equipped with a frame grabber and processing capability. Two images from the device are shown in Figure 5.

Figure 5.   IR Images obtained from an InSb on GaAs FPA

InSb on Sapphire

Sapphire has been investigated as a substrate for InSb FPA's. Sapphire is highly insulating, high in mechanical strength, transparent through mid-IR, has a good thermal expansion coefficient match with InSb, and has ~ 4 % lattice mismatch with InSb. Growth on sapphire results in (111) material which has lower surface recombination than (100) material providing it is properly passivated. Preliminary results obtained from MBE growth on sapphire show good morphology and crystalline material with x-ray FWHM of ~ 400 arcsec. 300 K electron mobility of 35,000 cm^2/V-sec has been obtained and 2,000 cm^2/V-sec p-type mobility was obtained at 77 K. PL measurements resulted in a 30 meV linewidth but of lower intensity than that from InSb on GaAs or Si. Good photoresponse was measured from an InSb on sapphire photoconductor as

shown in Figure 6. These results are promising, but more work needs to be done investigating the initial surface during InSb nucleation, as this is extremely important to the quality of the layer.
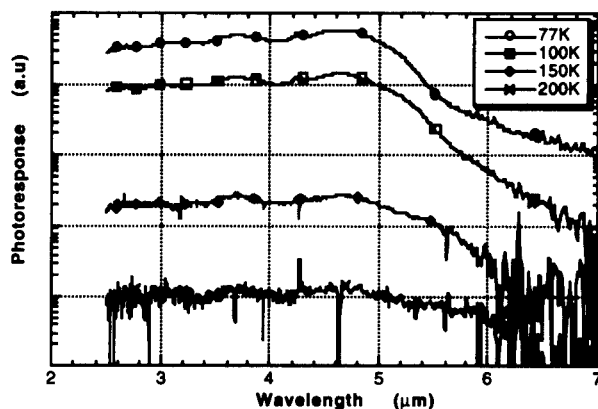
Figure 6.   Relative Photoresponse from an InSb on Sapphire Photoconductor

CONCLUSION

In this paper, we have reported on the growth of high quality InSb on GaAs, Si, and sapphire substrates as well as the first demonstration of InSb photodiodes on GaAs and Si substrates. Material quality was confirmed using structural, electrical, and optical characterization. Photoresponse comparable to that of bulk InSb has been obtained, with response even up to room temperature. In addition, IR thermal imaging has been obtained for the first time from an InSb FPA on GaAs or Si. This technique has the potential to revolutionize InSb FPA technology.

REFERENCES

1. E. Michel, G. Singh, S. Slivken, C. Besikci, P. Bove, I. Ferguson, and M. Razeghi, *Appl. Phys. Lett.*, **65**, 3338 (1994)

2. G. Singh, E. Michel, C. Jelen, S. Slivken, J. Xu, P. Bove, I. Ferguson, and M. Razeghi, *J. Vac. Sci. Technol. B*, **13**, 782 (1995)

3. E. Michel, R. Peters, S. Slivken, C. Jelen, P. Bove, J. Xu, I. Ferguson, and M. Razeghi, *Proceedings of the SPIE*, **2397**, 379 (1995)

4. A. Chin, P. Martin, P. Ho, J. Ballingall, T. Yu, and J. Mazurowski, *Appl. Phys. Lett.*, **65**, 3338 (1994)

5. P.E. Thompson, J.L. Davis, J. Waterman, R.J. Wagner, D. Gammon, D.K. Gaskill, and R. Stahlbush, *J. Appl. Phys.*, **69**, 7166 (1991)

6. C. Besikci, Y.H. Choi, R. Sudharsanan, and M. Razeghi, *J. Appl. Phys.*, **73**, 5009 (1993)

THEORETICAL PERFORMANCE OF MID-IR BROKEN-GAP SUPERLATTICE QUANTUM WELL LASERS

MICHAEL E. FLATTÉ*, C.H. GREIN**, J.T. OLESBERG*, AND T.F. BOGGESS*
* Department of Physics and Astronomy, University of Iowa, Iowa City, IA 52242
** Department of Physics, University of Illinois, Chicago, IL 60607

ABSTRACT

We will present calculations of the ideal performance of mid-infrared InAs/InGaSb superlattice quantum well lasers. For these systems several periods of an InAs/InGaSb type-II superlattice are grown in quantum wells. Calculations of the non-radiative and radiative lifetimes of the carriers utilize the full non-parabolic band structure and momentum-dependent matrix elements calculated from a semi-empirical multilayer $K \cdot p$ theory. From these lifetimes, threshold current densities have been evaluated for laser structures. We find serious problems with the hole and electron confinement in the superlattice quantum wells grown to date, and propose a four-layer superlattice structure which corrects these problems.

INTRODUCTION

Commercial and military interest in mid-infrared lasers has spawned research efforts focusing on a few promising strategies for constructing a laser active region. These include quantum well[1] and superlattice[2,3] active regions in which light is created during an interband recombination event, and quantum cascade structures[4], in which the radiative transition is between conduction subbands. For the first two categories, the dominant non-radiative carrier loss mechanism near the maximum operating temperature is carrier-carrier (Auger) scattering, while in the quantum cascade lasers it is electron-phonon scattering.

Design strategies to reduce the Auger recombination rate have been developed for superlattice active regions based on InAs/InGaSb[5]. These include attempts to lower the density of states at the valence edge, thereby decreasing the threshold carrier concentration, and to eliminate final states for Auger processes within the conduction and valence bands. Figure 1 shows two Auger processes, one involving two non-equilibrium holes (a), and one involving two non-equilibrium electrons (b). The processes are shown on the calculated band structure of a superlattice of 16.7Å thick InAs layers alternating with 35Å thick $In_{0.25}Ga_{0.75}Sb$ layers. This structure appears to have a relatively light in-plane mass for the top valence band and to lack final states at resonant energies for Auger processes.

Unfortunately the above superlattice cannot be grown as is, since it is not lattice-matched to a useful substrate. The strategy adopted for growing structures approximating the above system is to alternate several periods of the superlattice with a strain-relaxing barrier material. If the superlattice material can be approximated as a bulk semiconductor with the band structure of the superlattice, one could consider such a structure to be a multiple quantum well (MQW). We will show that this structure has several unfavorable unintended effects on the electronic structure of the active region. We will then propose a new family of structures, strain-balanced on a GaSb substrate, which not only eliminate
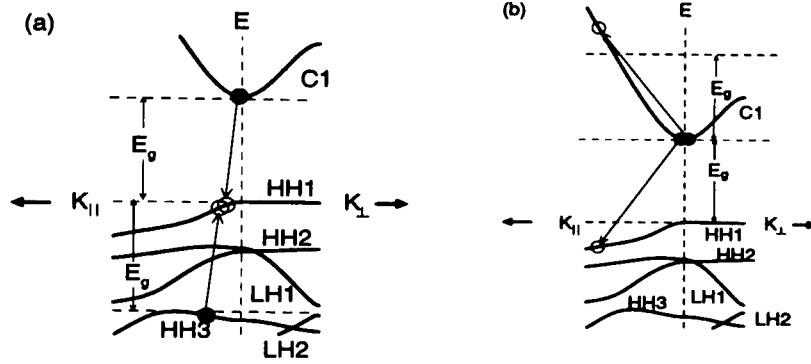
Figure 1: Schematic of Auger process involving (a) two non-equilibrium holes and one non-equilibrium electron, and (b) two non-equilibrium electrons and one non-equilibrium hole. The band structure shown is for 16.7Å InAs/35Å In$_{0.25}$Ga$_{0.75}$Sb at low temperature. $K_\perp$ is in the growth direction and $K_\parallel$ is in the in-plane direction.

the problems with the MQW arrangement, but should perform better than the ideal two-layer superlattices as well.

THEORY

Calculations of the band structure including non-parabolicity, and the K-dependent optical matrix elements, were performed with a superlattice $\mathbf{K} \cdot \mathbf{p}$ technique similar to that used for the two-layer superlattices[5] but generalized to an arbitrary number of layers in the unit cell. The radiative and non-radiative recombination rates were then calculated with the procedure described in Ref. 6. Carrier lifetimes and threshold current densities were computed from these rates.

RESULTS

In Figure 2(a) we show a representative band-edge alignment for a superlattice multiple quantum well. This structure was grown for the benefit of optical investigations of carrier dynamics[7], and so the barrier material was chosen to have a high conduction edge. Unfortunately the heavy-hole confinement is weak. Since the quantum wells terminate with In$_{0.25}$Ga$_{0.75}$Sb layers, and the barrier layer does not confine holes as well as the InAs layers, the top two heavy-hole states are localized in the outer wells. As shown in Figure 2(b) the HH1 state does not have a significant overlap with the C1 state — it is the HH3 state which has a large overlap. The HH1-HH3 splitting is approximately 10meV, so the five top heavy-hole subbands (one for each ternary layer) are approximately equally occupied at room temperature. Carriers in the HH1 or HH2 states will not contribute efficiently to the gain, but will degrade laser performance through enhancing the possibilities for non-radiative recombination. This type of problem also applies to the barrier materials used in laser structures[2], which also have problems with electron confinement.
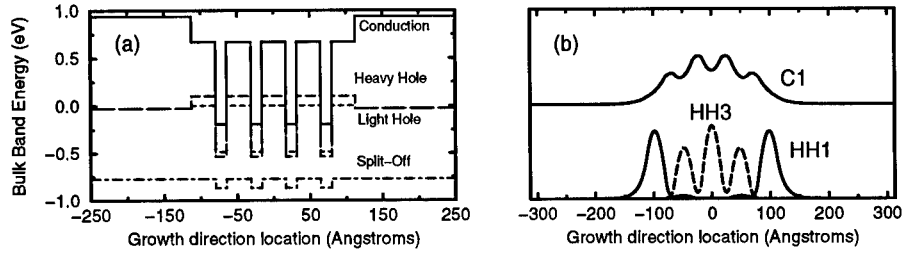
Figure 2: (a) Band alignment and (b) envelope functions for a 4.5 period 15Å InAs/33Å In$_{0.25}$Ga$_{0.75}$Sb superlattice with 400Å Al$_{0.2}$Ga$_{0.8}$Sb barriers.

We show in Figure 3 a comparison of the band structure for a two-layer superlattice (3(a)), and the band structure for this superlattice MQW (3(b)). Two undesirable features are evident in the latter: the five low-energy heavy-hole states (one for each ternary layer) are rather heavy in the in-plane direction, and there is no evident gap in the MQW band structure except for a small one just below HH5. Within $K \cdot p$ theory a small C1-HH1 overlap implies a heavy HH1 mass. The design strategy for optimizing hole-hole Auger recombination is predicated on the heavy hole having a light in-plane mass. Furthermore the gap in the final states, which is another element of Auger optimization, is eliminated due to the multitude of subbands in the MQW. We therefore do not expect Auger recombination to be suppressed in the superlattice MQW.

We propose a new four-layer superlattice to eliminate these problems. It has tensile strain when grown on GaSb and thus the overall superlattice unit cell (from 60Å to 110Å) can be lattice matched. Strain balancing over this size unit cell should provide better conditions for MBE growth than attempting to strain-balance over ~500Å (as in Ref. 2). The new four-layer superlattice is shown in Figure 4(a). The design is somewhat similar to the four-layer structures proposed earlier[3] for optically-pumped active regions with an AlSb fourth layer.
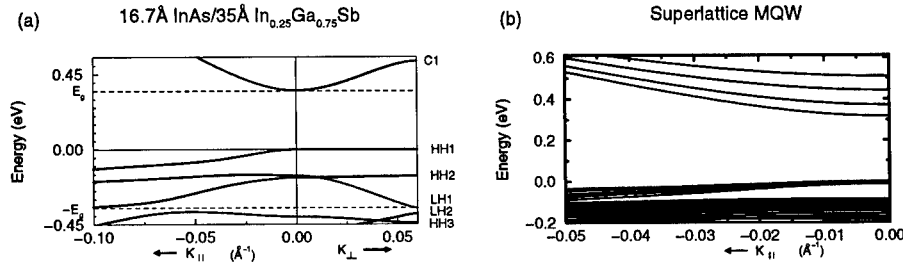
Figure 3: Comparison of the band structure of an optimized two-layer superlattice (a) and a two-layer superlattice in a quantum-well arrangement. The optimized features of the band structure evident in (a), including a light in-plane heavy-hole mass and an absence of states at the resonant energy (dashed line) are eliminated when the structure is placed in a quantum well in (b).
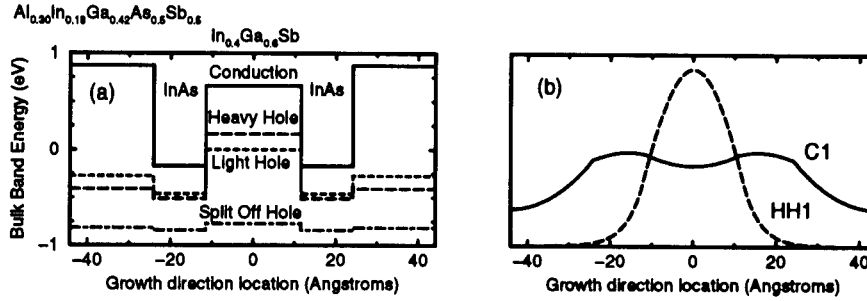
Figure 4: (a) Band alignment for the new four-layer superlattice. (b) C1 and HH1 envelope functions for the four-layer superlattice showing the extension of the C1 envelope function over the entire unit cell.

Use of strained $Al_{0.30}Ga_{0.42}In_{0.18}As_{0.5}Sb_{0.5}$ also allows us to use $In_{0.4}Ga_{0.6}Sb$ as the ternary layer. The increase in compressive strain in the ternary layer increases the heavy-light hole splitting, which pushes the light hole farther down in energy. The heavy-hole band offset between the ternary layer and the quinternary is estimated to be 573meV, and the conduction band offset between the InAs and the quinternary is estimated to be 1.045eV. The large heavy-hole offset clears out final heavy-hole states from around the resonant energy. Unlike the "quantum well"-like four-layer structures[3] proposed for optical pumping, the conduction state is spread over the entire unit cell, as shown in Figure 4(b). Thus the transport properties of this structure may be superior to those grown with an AlSb barrier.

The band structure of the four-layer superlattice is shown below in Figure 5. The bandwidth of the C1 state is approximately 40meV in the growth direction. In contrast to the superlattice MQW shown in Figure 3(b) the heavy-hole state has a light in-plane mass. The gap in the final states (140meV) in Fig. 5 is even larger than that found in the two-layer superlattice (30meV) shown in Fig. 3(a). Since half this gap, 70meV, is more than two optical phonon energies, placing the resonant energy in the middle of this gap might also suppress phonon-assisted Auger processes.

This gap in the final states within the valence band should have an identifiable signature in the intersubband absorption. We show in Figure 6 a representative intersubband absorption calculation for such a system at the lasing threshold density (defined as 25cm^{-1} gain) at room temperature[8]. The intersubband absorption feature, which exceeds 500 cm^{-1} at its peak, should be visible in pump-probe measurements. The gain region should be placed midway between the two intersubband absorption features, as shown in Figure 6. By locating the intersubband absorption peaks experimentally one can determine how close the grown structure approaches the calculated structure, and also how well the Auger optimization procedure is working.

We find that the threshold carrier concentration for this structure at 25cm^{-1} gain, 4.9×10^{17}cm^{-3}, is smaller than that calculated for the two-layer superlattice. The calculated carrier lifetime at threshold is 5.2ns, yielding a threshold current density per unit thickness of active region of 1500A/cm$^2\mu$m.

12.6Å InAs/23Å $In_{0.4}Ga_{0.6}Sb$/12.6Å InAs/40Å $Al_{0.30}In_{0.28}Ga_{0.42}As_{0.50}Sb_{0.50}$
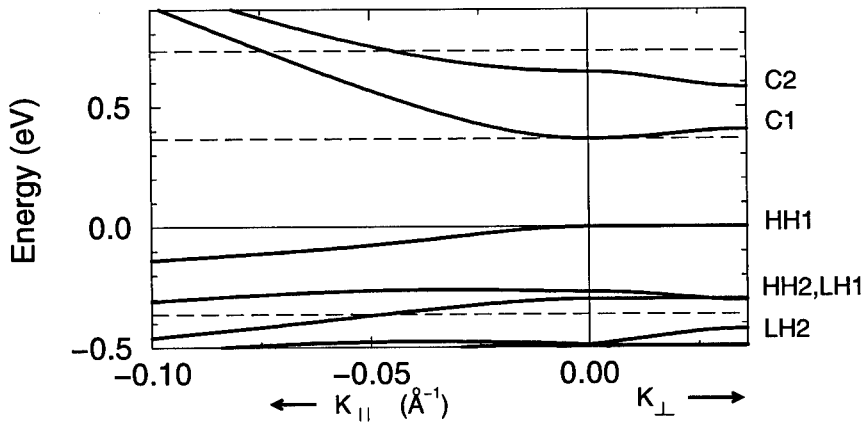
Figure 5: Band structure for new four-layer superlattice showing a light in-plane heavy-hole mass and a 140meV gap in the valence band structure centered at the resonant energy for Auger transitions (dashed line). The other two dashed lines indicate the resonant energy in the conduction band for Auger transitions and the energy gap itself.
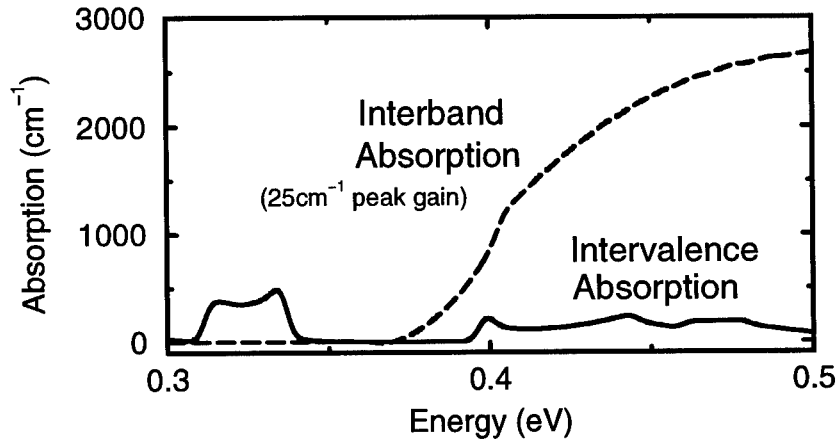
Figure 6: For an Auger-optimized structure the intersubband absorption (here dominated by that coming from the valence subbands) has a gap at the lasing energy due to the absence of final valence states. Hence the Auger optimization procedure also optimizes intersubband absorption. The large intersubband features (here shown for the calculated threshold carrier density) should be visible in a pump-probe experiment.

CONCLUSIONS

We find that the procedure of growing optimized two-layer superlattices in an MQW structure for strain balancing does not preserve the optimized features of the band structure. We propose a new four-layer, lattice-matched, structure which has even better calculated properties than the original two-layer structures. Strain balancing over a shorter unit cell should also improve conditions for MBE growth.

ACKNOWLEDGMENTS

REFERENCES

1. H.K. Choi, G.W. Turner and M.J. Manfra, Electron. Lett. **32**, 1296 (1996); H.K. Choi, G.W. Turner, M.J. Manfra and M.K. Connors, Appl. Phys. Lett. **68**, 2936 (1996).

2. D.H. Chow, R.H. Miles, T.C. Hasenberg, A.R. Kost, Y.H. Zhang, H.L. Dunlap and L. West, Appl. Phys. Lett. **67**, 3700 (1995); T.C. Hasenberg, D.H. Chow, A.R. Kost, R.H. Miles and L. West, Electron. Lett. **31**, 275 (1995).

3. J.I. Malin, J.R. Meyer, C.L. Felix, J.R. Lindle, L. Goldberg, C.A. Hoffman, and F.J. Bartoli, Appl. Phys. Lett. **68**, 2976 (1996); J. R. Meyer, C.A. Hoffman, F.J. Bartoli, and L.R. Ram-Mohan, Appl. Phys. Lett. **67**, 757 (1995).

4. J. Faist, F. Capasso, D.L. Sivco, C. Sirtori, A.L. Hutchinson, and A.Y. Cho, Science **264**, 553 (1994). J. Faist, F. Capasso, C. Sirtori, D.L. Sivco, A.L. Hutchinson, and A.Y. Cho, Electron. Lett. **32**, 560 (1996).

5. M.E. Flatté, C.H. Grein, H. Ehrenreich, R.H. Miles and H. Cruz, J. Appl. Phys. **78**, 4552 (1995). C.H. Grein, P.M. Young, and H. Ehrenreich, J. Appl. Phys. **76**, 1940 (1994).

6. C.H. Grein, P.M. Young, M.E. Flatté, and H. Ehrenreich, J. Appl. Phys. **78**, 7143 (1995).

7. S.W. McCahon, S.A. Anson, D.-J. Jang, M.E. Flatté, T.F. Boggess, D.H. Chow, T.C. Hasenberg, and C.H. Grein, Appl. Phys. Lett. **68**, 2135 (1996).

8. The apparent gap (60meV) is smaller than that seen in Figure 5 since there are transitions for momenta not shown on Figure 5 which somewhat narrow the gap.

Low-Loss, Broadened-Waveguide, High-Power 2-μm
AlGaAsSb/InGaAsSb/GaSb Separate Confinement Quantum-Well Lasers

R. J. Menna, D. Z. Garbuzov, R. U. Martinelli, H. Lee, P. K. York,
J. C. Connolly, and S. Y. Narayan

David Sarnoff Research Center, CN5300, Princeton, NJ 08543

ABSTRACT

(Al, In)GaAsSb/GaSb MQW lasers with a broadened waveguide have been used to fabricate 2-μm diode lasers with CW output power of 1.2 W. 2-μm linear arrays have output powers of 11 W and an efficiency of 0.13 W/A.

INTRODUCTION

Semiconductor lasers with emission wavelengths of 2 μm or longer are being developed for low-cost, high-sensitivity gas sensing[1] and LIDAR instruments. In addition, optically pumped lasers at λ = 4 μm have been reported using a 2 μm laser as the excitation source[2]. 2-μm lasers are fabricated using active regions of InGaAs on InP substrates[3] or InGaAsSb on GaSb substrates[4]. The applications cited above favor the latter case since they would benefit from wavelengths longer than 2 μm[1], a wavelength range currently inaccessible from strained InGaAs on InP.

This report describes the use of broadened waveguide (BWG) technology to fabricate discrete 2-μm (Al, In)GaAsSb/GaSb lasers with output powers greater than 1 W and linear arrays with output powers of 11 W. A BWG structure reduces optical loss by confining the transverse mode mainly to the thick (~1 μm), undoped waveguide portion of the laser structure. The low optical loss realized in the BWG laser allows a long Fabry-Perot cavity length (≥ 2 mm) to be used without significantly reducing the laser efficiency.

EXPERIMENT

Broadened Waveguide Design

Figure 1 illustrates the broadened waveguide concept. The standard design is based on maximizing the overlap of the optical mode with the quantum wells. As a result, a significant portion of the optical mode extends into the doped cladding layers where the optical loss is higher than in the undoped waveguide. By broadening the waveguide the fraction of the optical mode in

91

the cladding layers and the optical loss of the structure is reduced. The overlap of the optical mode and the quantum wells is also reduced, but this factor is more than compensated for by increasing the cavity length.
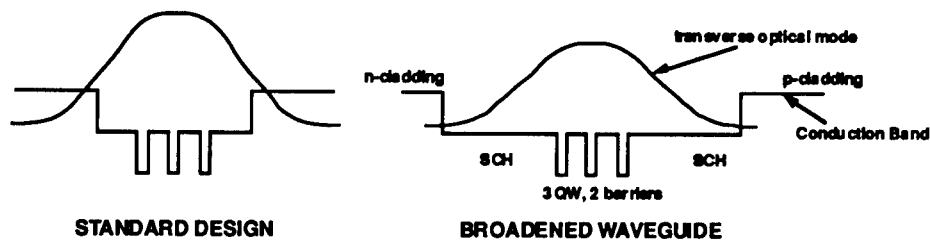
Figure 1. Schematic diagram illustrating the broadened waveguide concept.

The structure used to fabricate 2-μm lasers is shown in Fig. 2 and has been described in detail in reference 5. Briefly, the array uses 5 $In_{0.19}Ga_{0.81}As_{0.02}Sb_{0.98}$ quantum wells sandwiched inside a 880 nm wide $Al_{0.25}Ga_{0.75}As_{0.02}Sb_{0.98}$ waveguide. The waveguide layers are undoped. The cladding layers are $Al_{0.90}Ga_{0.10}As_{0.07}Sb_{0.93}$. All layers except the quantum wells are lattice matched to the GaSb substrate. The quantum wells have are compressively strained by 1%.
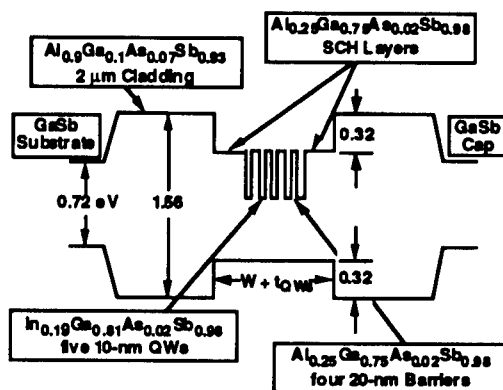
Figure 2. Band structure of 2-μm (Al, In)GaAsSb/GaSb multi-quantum well laser

Diode Laser Results

The increase in differential quantum efficiency effected by broadening the waveguide is shown in Fig. 3. (Al, In)GaAsSb/GaSb laser structures with waveguide thicknesses of W = 0.12, 0.32, and 0.88 μm were tested for output power and efficiency. The highest efficiency, η_d = 36%, and output power, P_o = 1.2 W are obtained from the laser with the widest waveguide layer, 0.88 μm.
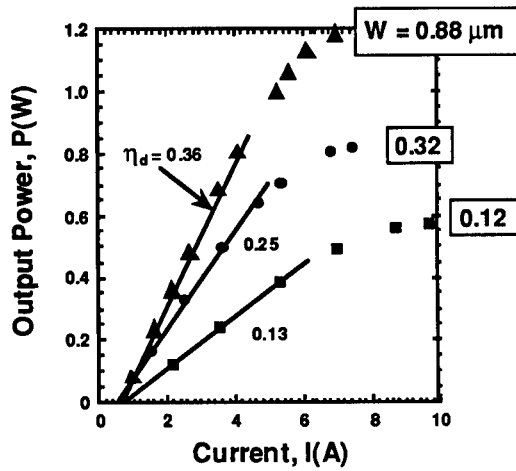
Figure 3. Output characteristics of 2-μm MQW lasers with waveguide thicknesses of 0.12, 0.32, and 0.88 μm.

Figure 4a indicates the decreasing optical mode overlap with the cladding layers as the waveguide thickness is increased. Also in Fig. 4a, it should be noted that the mode overlap with the quantum wells varies by only 25%. Decreasing internal loss with increasing waveguide thickness is shown in Fig. 3b. The calculated values[5] are based on the fraction of the mode in the cladding layer and a free-carrier-absorption value of 87 cm^{-2}. The broadest waveguide laser structure has a measured internal loss value of 2 cm^{-1}.

Array Fabrication

Arrays of stripe lasers were fabricated by depositing a layer of SiO$_2$ onto the p-cap layer and patterning it with 100-, 200-, or 300-μm-wide stripe openings. Electrical contact was made to the GaSb p$^+$ cap and n$^+$ substrate using Cr, Au, and Sn, Ni, Au, respectively. Prior to depositing the n-contact metal, the

substrate is thinned to 100 μm. 2-mm-long bars were cleaved from the wafer. Front and back facets were coated to achieve reflectivities of 3% and 95%, respectively. Arrays with up to 20 elements were chipped from the cleaved bars and mounted, p-side down, onto a Cu heat sink using In solder. A few individual lasers were also chipped from each bar for testing.
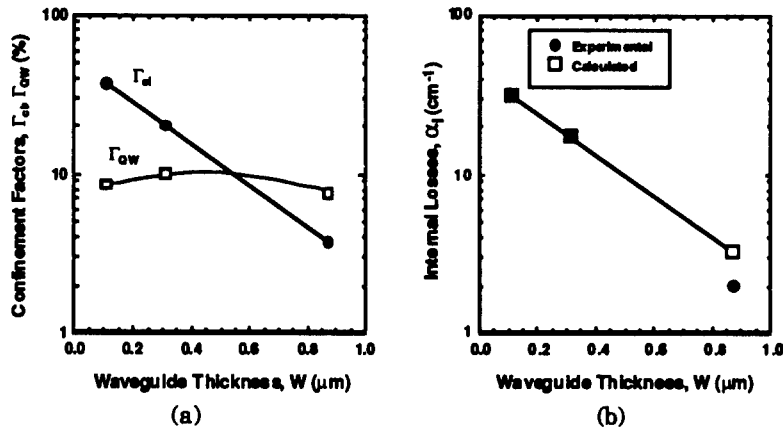
Figure 4 Confinement factors for cladding and quantum well layers (a) and internal loss values (b) as a function of waveguide thickness.

The packaged arrays were mounted onto a separate Cu block cooled by a recirculating water-ethylene glycol solution. Thermocouples were attached to the heat sink and to the array itself to monitor their respective temperatures during operation.

ARRAY RESULTS

A 7-element array of 0.2 x 2.0 mm^2 lasers on a 500 μm pitch was tested. P-I characteristics shown in Fig. 5 indicate a maximum output power of 5 W at a CW drive current of 34 A and an array temperature of 32 °C. The array operated up to a temperature of 62 °C. The threshold current temperature dependence over the range of 32-62 °C yields a characteristic temperature of 87 K.

At the maximum power of 5 W (Fig. 5), the amount of power dissipated as heat is 38 W. With a temperature difference between the array and the cooling fluid of 36 °C, the thermal resistance of the array is 0.95 °C/W.
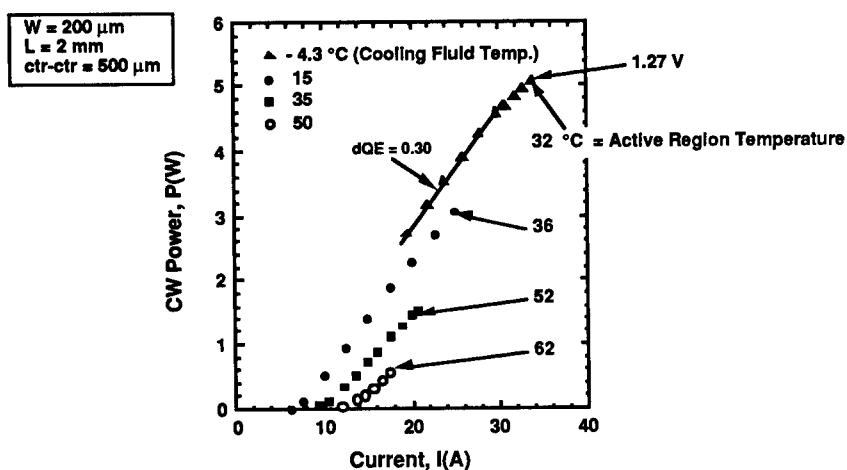
Figure 5. P-I characteristics of a 2-µm, 7-element laser array in the temperature range 32 °C to 62 °C.
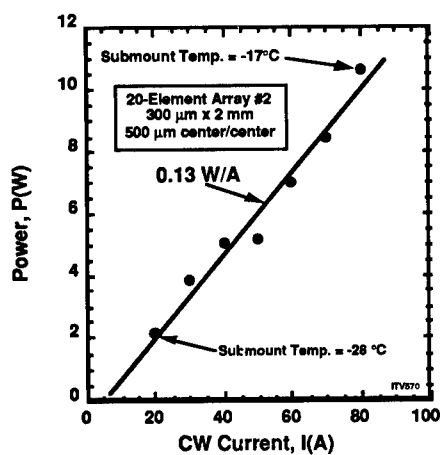
Figure 6. P-I Characteristic of a 20-element, 2-µm laser array with an output power of 11 W CW.

Figure 6 shows the P-I characteristic of a 20-element array of 0.3 x 2.0 mm^2 stripe lasers. An output power of 11 W was achieved at a drive current of 80 A and a heat sink temperature of -17 °C. The 20-element array was operated for 100 hours at a power level of 2.5 W and retested. There was no significant change in operating characteristics.

CONCLUSIONS

We have demonstrated a discrete (Al, In)GaAsSb/GaSb, 2-μm laser using a broadened waveguide design with a CW output power of 1.2 W CW. The broadened waveguide is shown to produce higher efficiency and lower internal loss compared to the standard laser design. A 20-element array of stripe lasers has achieved a CW output power of 11 W at a temperature of -17 °C.

ACKNOWLEDGMENTS

REFERENCES

1. R. U. Martinelli, R. J. Menna, D. E. Cooper, C. B. Carlisle, and H. Riris, SPIE Proceedings 2148, (1994).
2. H. Q. Le, G. W. Turner, J. R. Ochoa, and A. Sanchez, Elect. Lett. 30, 1944, (1994).
3. S. Forouhar, A. Ksendzov, A. Larsson, and H. Temkin, Elect. Lett, 28, 1431, (1992).
4. H. K. Choi and S. J. Eglash, Appl. Phys. Lett. 61, 1154, (1992).
5. D. Z. Garbuzov, R. U. Martinelli, H. Lee, P. K. York, R. J. Menna, J. C. Connolly, and S. Y. Narayan, Appl. Phys. Lett. 69, 2006, (1996).

MBE GROWTH AND CHARACTERIZATION OF
InSb/Al$_x$In$_{1-x}$Sb STRAINED LAYER STRUCTURES

K.J. GOLDAMMER[*], W.K. LIU[*], W. MA[*], M.B. SANTOS[*],
R.J. HAUENSTEIN[**] and M.L. O'STEEN[**]

[*]Department of Physics and Astronomy and Laboratory for Electronic Properties of Materials,
University of Oklahoma, Norman, Oklahoma 73019, kjgoldam@phyast.ou.edu
[**]Department of Physics, Oklahoma State University, Stillwater, Oklahoma 74078

ABSTRACT

Three types of structures were fabricated using molecular beam epitaxy. High-resolution x-ray diffraction measurements demonstrated the high structural quality of InSb/Al$_x$In$_{1-x}$Sb superlattices grown on InSb and GaAs substrates. Hall effect data revealed the effect of substrate temperature on autocompensation in InSb δ-doped with Si. Two-dimensional electron systems with a high mobility were realized in InSb quantum wells with Al$_x$In$_{1-x}$Sb barriers δ-doped with Si.

INTRODUCTION

InSb has the narrowest bandgap, the smallest effective mass, and the highest intrinsic electron mobility of all binary III-V semiconductors. These characteristics make InSb an attractive material both for industrial applications, such as infrared detectors and magnetoresistive sensors [1], and for studying the physics of electrons in semiconductors. Incorporation of an electron barrier material can lead to improved device performance [2] and allows the fabrication of InSb quantum wells. However, these heterostructures are difficult to realize since no III-V binary or ternary compounds are lattice matched to InSb. An attempt was made in 1990 using the II-VI compound CdTe as the barrier material. However, cross doping between the III-V and II-VI compounds led to poor interface quality and a correspondingly low carrier mobility [3]. Attention has since been turned to Al$_x$In$_{1-x}$Sb as a potential barrier material. AlSb has a ~5% smaller lattice constant than InSb, but it also has a much larger energy gap. In 1994, Saker *et al.* demonstrated quantum confinement in InSb quantum wells with Al$_x$In$_{1-x}$Sb barriers [4].

To further investigate the potential of these materials, we have grown a variety of InSb/Al$_x$In$_{1-x}$Sb strained layer structures on GaAs(001) and InSb(001) substrates. In this paper, data is reported on three types of structures. First, high-resolution x-ray diffraction (HRXRD) performed on InSb/Al$_x$In$_{1-x}$Sb superlattices characterize their structural quality. Second, Hall effect measurements made on InSb layers δ-doped with Si reveal the effect of substrate temperature on Si autocompensation. Third, Hall effect measurements demonstrate that two-dimensional electron systems with high mobility can be realized in InSb quantum wells with δ-doped Al$_x$In$_{1-x}$Sb barriers.

EXPERIMENT

All samples were grown in an Intevac Modular Gen II molecular beam epitaxy system. Effusion cells were loaded with In (7N RASA), Al (6N Ulvac), Sb (6.5N Dowa), and Si (Silicon Sense). An EPI Sb cracker was used with a cracking zone temperature of 900°C. Growth rates for InSb and AlSb were calibrated and Al$_x$In$_{1-x}$Sb composition was deduced from temporal oscillations in the intensity of reflection high energy electron diffraction (RHEED) patterns.

Substrate temperatures were calibrated through changes in the RHEED pattern upon crossing the transition temperature, $T_{tr} \approx 390°C$, at which the InSb surface reconstruction changes between c(4×4) and pseudo(1×3). The $Al_xIn_{1-x}Sb$ and InSb layers were grown at substrate temperatures of $\sim T_{tr}+30\pm5°C$, an Sb/group-III flux ratio slightly larger than unity, and an InSb growth rate of ~0.8ML/s.

HRXRD was performed using a Philips Materials Research Diffractometer with a four-reflection Ge (220) monochrometer. Dynamical simulations were carried out using Philips PC-HRS Simulation Software. Hall effect measurements at magnetic fields up to 0.5T were performed on square samples with ~4mm edges. Electrical contact was made at each corner of a sample by alloying In at ~210°C in a $H_2(15\%)/N_2(85\%)$ atmosphere for 2-5 minutes. Ohmic contact was checked through observation of linear current-voltage characteristics. Resistivity and Hall resistances were determined from measurements at 300K, 77K, and 4.2K using the van der Pauw geometry.

EXPERIMENTAL RESULTS AND DISCUSSION

Abrupt interfaces are required for many device structures. To characterize interfacial quality, an $Al_xIn_{1-x}Sb$/InSb superlattice was grown on an InSb substrate with a 3μm-thick InSb buffer. The HRXRD data (solid line) is shown in Figure 1a for the superlattice structure shown in Figure 1b. The ω-2θ scan reveals a large number of sharp satellite peaks ($m = \pm 1, \pm 2$, etc.) on either side of the central peak ($m = 0$). The prominent peak at $\theta = 28.394°$ is due to the InSb substrate and buffer layer. From the separation between the satellite peaks and from the location of the central peak, we deduce a period of 364Å and an alloy composition of 12.7%, respectively. The simulation (dashed line) shows very good agreement with our data, indicating that the superlattice has interfaces of very high quality. A HRXRD map of the $(\bar{1}\,\bar{1}\,5)$ reciprocal lattice points verifies that the superlattice barriers are strained to the lattice constant of the InSb substrate.

Growth on semi-insulating GaAs substrates is desirable in order to minimize parallel conduction paths at room temperature, as well as to allow for potential integration with GaAs devices. Figure 2a shows the results of a HRXRD ω-2θ scan (solid line) of an $Al_xIn_{1-x}Sb$/InSb superlattice grown on a GaAs substrate, which is shown in Figure 2b. GaSb, AlSb, and $Al_xIn_{1-x}Sb$ buffer layers were inserted to help alleviate the effects of the 14.6% lattice mismatch between InSb and GaAs. The series of peaks between $\theta = 27.5-29°$ arise from the superlattice and adjacent $Al_{0.125}In_{0.875}Sb$ buffer layer. From the location of the central peak ($m = 0$), we calculate the average lattice parameter of the superlattice and thereby determine an aluminum alloy composition of 14.5%. We observe several satellite peaks ($m = -1, \pm 2$, etc.); the $m = +1$ satellite peak is obscured by the dominant peak at $\theta = 28.549°$, which is attributed to the $Al_{0.125}In_{0.875}Sb$ buffer layer. From the spacing between satellite peaks, we deduce a superlattice period of 340Å. A HRXRD reciprocal space map of the $(\bar{1}\,\bar{1}\,5)$ reflections indicates that the superlattice structure is strained to the lattice constant of the $Al_xIn_{1-x}Sb$ buffer layer.

The dashed line in Figure 2 shows the simulated data. The simulation software only allows for strained layers, so we performed the simulation defining the 3μm $Al_{0.125}In_{0.875}Sb$ layer as the substrate. As a result, the broad peak, which arises from the 1μm $Al_{0.25}In_{0.75}Sb$ layer and which washes out the +5 and +7 satellite peaks, is not modeled. The widths of the satellite peaks we observe here are larger than for the superlattice grown on InSb, presumably due to the large lattice mismatch between the substrate and the superlattice and the lack of optimization in the
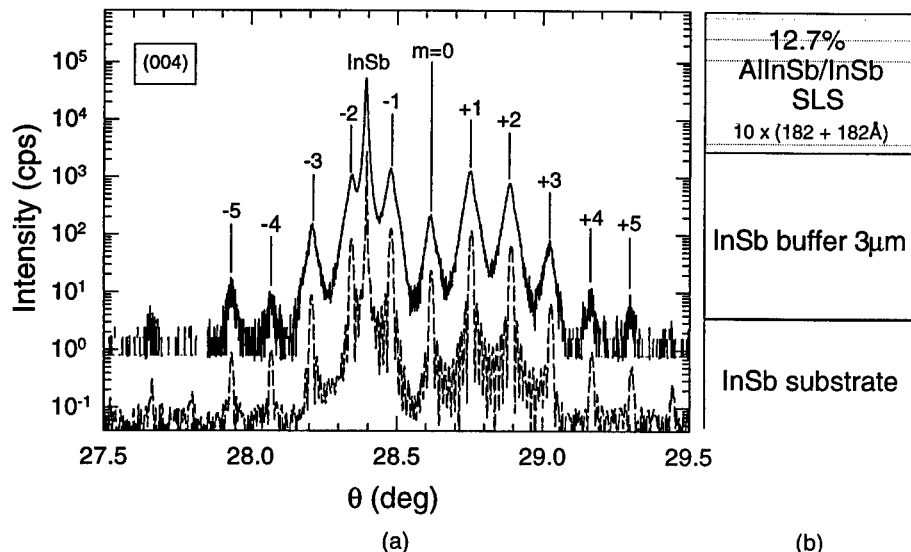
Figure 1: (a) (004) HRXRD ω-2θ scan (solid) and simulation (dashed) for a 10 period $Al_xIn_{1-x}Sb/InSb$ strained-layer superlattice (SLS) grown on an InSb substrate. An Al alloy concentration of 12.7% was obtained from the simulation. FWHM= 90 arcsec for the m=0 peak, and FWHM=27arcsec for the InSb peak. (b) Structure of the $Al_xIn_{1-x}Sb/InSb$ SLS sample.
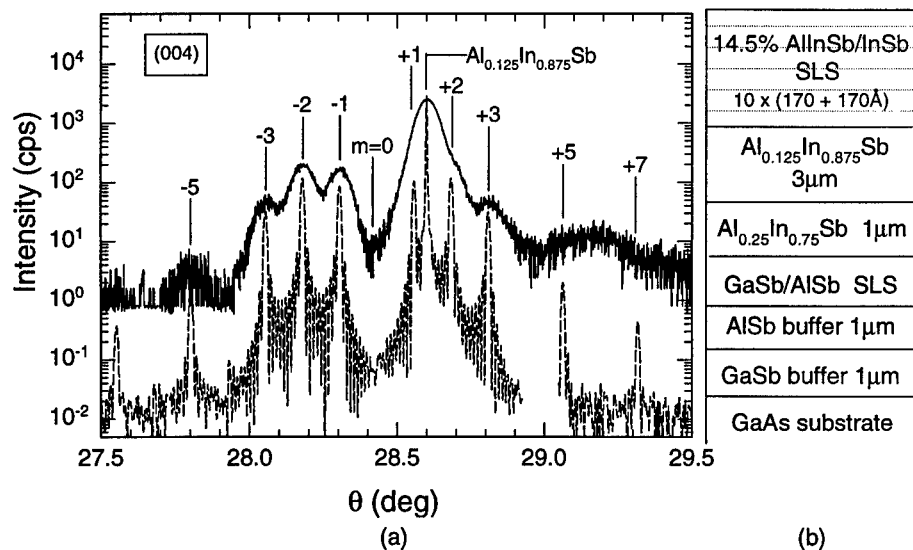
Figure 2: (a) (004) HRXRD ω-2θ scan (solid) and simulation (dashed) for a 10 period $Al_xIn_{1-x}Sb/InSb$ SLS grown on a GaAs substrate. An Al alloy concentration of 14.5% was obtained from the simulation. FWHM= 274 arcsec for the $Al_{0.125}In_{0.875}Sb$ peak. The broad peak obscuring the m=+5 and +7 satellite peaks was not modeled. (b) Structure of the $Al_xIn_{1-x}Sb/InSb$ SLS sample.

buffer layers. However, good agreement is still seen between the experimental and simulated data, indicating that the interfaces in the superlattice are of high quality.

Well behaved dopants are also important for many device structures. The use of Si as a donor in InSb has been motivated by its low vapor pressure and its successful use as a donor in GaAs. However, Si atoms (column-IV in the periodic table) can be either donors or acceptors in InSb, depending on whether they occupy In or Sb atomic sites. Bulk doping of InSb does result in n-type conduction across a range of growth conditions, but the number of donors for a given Si concentration decreases with increasing substrate temperature [5]. Since fewer Sb sites are available during δ-doping (In shutter closed, Sb shutter open), n-type material with less autocompensation is expected in δ-doped structures.

A series of δ-doped samples was grown to explore the effect of substrate temperature on Si autocompensation. Each sample consists of an InSb epilayer with a Si δ-doped layer located 3100Å below the surface. A high doping density ensures that electrical conduction at low temperature will be dominated by the δ-doped layer. The only difference among the samples is the substrate temperature, T_δ, used both during the δ-doping and the growth of the 3100Å InSb cap layer. Figure 3 is a plot of carrier density, from Hall effect measurements at 77K, as a function of T_δ. For T_δ well below T_{tr}, the carrier density maintains a roughly constant value of ~4×10^{12} cm^{-2}. However, for temperatures above T_{tr}, the carrier density decreases strongly with increasing T_δ.

An additional sample was grown to compare the relative importance of the substrate temperature during doping and the substrate temperature during cap layer growth. Doping was performed at a high temperature, T_{tr}+30°C, while the cap layer was grown at a low temperature, T_{tr}−20°C. The measured carrier concentration of 3.0×10^{12}cm^{-2} was six times higher than in sample S317, where both the doping and cap layer temperatures were T_{tr}+30°C, but only 25% lower than in sample S314, where both the doping and cap layer temperatures were T_{tr}−20°C. We therefore conclude that temperature-dependent autocompensation occurs primarily during growth of the cap layer.

To determine whether autocompensation occurs due to simple diffusion, a sample identical to S314 (δ-doping and cap layer growth at T_{tr}−20°C) was grown but with an *in situ* anneal performed after growth. The sample was annealed at T_{tr}+40°C for a time interval equal to that needed to grow the δ-doped and cap layers. The measured carrier density of 3.70×10^{12}cm^{-2} was only slightly lower than what was obtained for the same growth parameters without annealing. Hence, simple diffusion is not the dominant mechanism for autocompensation. We therefore attribute the temperature dependent carrier concentration predominantly to surface segregation of Si atoms through hopping on to Sb sites. Recent images of InSb surfaces obtained from scanning tunneling microscopy support the plausibility of this interpretation. The c(4×4) surface is observed to be completely Sb terminated while one third of the sites on the pseudo(1×3) surface are Sb sites [6].

The ability to form abrupt interfaces and to control n-type doping makes possible the growth of remotely-doped InSb quantum well structures [7]. A typical such structure contains a 300Å InSb quantum well with $Al_{0.07}In_{0.93}Sb$ barriers on a GaAs substrate. The electrons in the quantum well are supplied by a δ-doped $Al_{0.07}In_{0.93}Sb$ layer located 300Å above the quantum well. Hall effect measurements indicate that the carrier density decreases from 6.63×10^{11}cm^{-2} at room temperature to 1.9×10^{11}cm^{-2} at 77K and 4.2K, and the mobility increases monotonically from 19,800cm^{2}V^{-1}s^{-1} at room temperature to 77,000cm^{2}V^{-1}s^{-1} at 77K to 97,000cm^{2}V^{-1}s^{-1} at 4.2K. Both of these behaviors are qualitatively similar to what is seen in GaAs quantum wells, but are distinctly different from what is observed for transport through either δ-doped layers [8] or undoped InSb [9]. As such, our transport data serves as evidence that a two-dimensional electron system exists in the InSb quantum well.
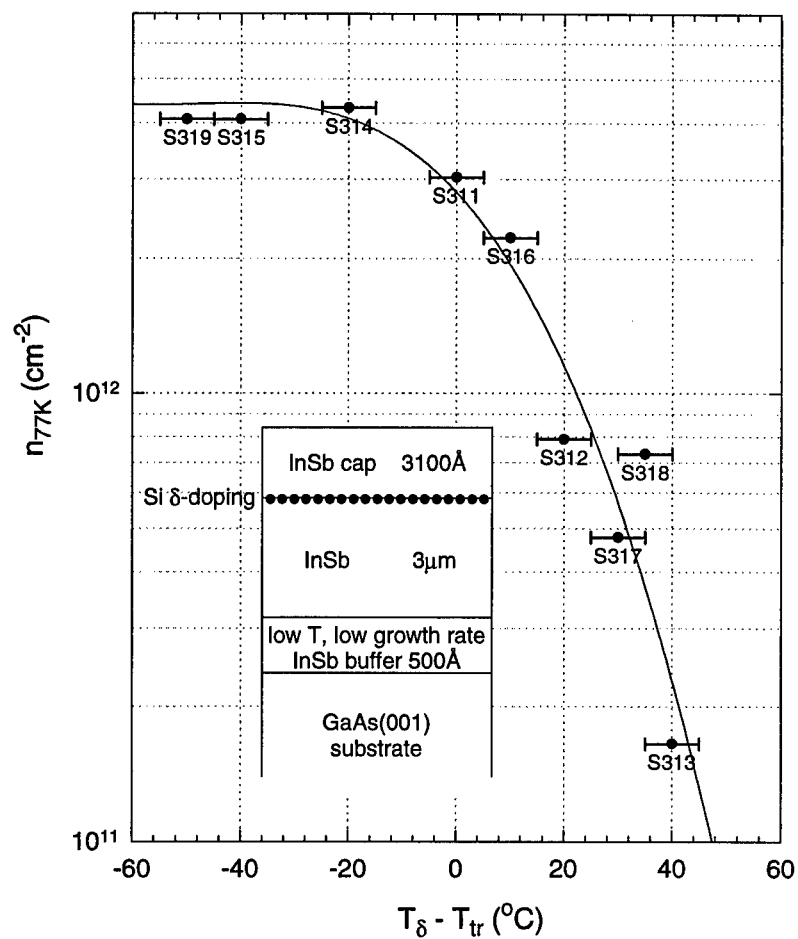
Figure 3: Plot of carrier density, measured at 77K, vs. substrate temperature during δ-doping and subsequent cap layer growth. The structure is shown in the inset.

CONCLUSIONS

HRXRD data indicates that strained $InSb/Al_xIn_{1-x}Sb$ structures with good interface quality can be obtained on either InSb or GaAs substrates. Silicon can be used for δ-doping of InSb, but low substrate temperatures must be used to avoid autocompensation due to Si segregation with the growth front. Two-dimensional electron systems with a high mobility can be realized in InSb quantum wells with remotely-doped $Al_xIn_{1-x}Sb$ barriers.

REFERENCES

1. J. Heremans, D.L. Partin, C.M. Thrush, and L. Green, Semicond. Sci. Technol. **8**, S424 (1993).
2. T. Ashley, C.T. Elliot, N.T. Gordon, R.S. Hall, A.D. Johnson, and G.J. Pryce, Appl. Phys. Lett. **64**, 2463 (1994).
3. T.D. Golding, S.K. Greene, M. Pepper, J.H. Dinan, A.G. Cullis, G.M. Williams, and C.R. Whitehouse, Semicond. Sci. Technol. **5**, S311 (1990).
4. M.K. Saker, D.M. Whittaker, M.S. Skolnick, C.F. McConville, C.R. Whitehouse, S.J. Barnett, A.D. Pitt, A.G. Cullis, and G.M. Williams, Appl. Phys. Lett. **65**, 1118 (1994).
5. S.D. Parker, R.L. Williams, R. Droopad, R.A. Stradling, K.W.J. Barnham, S.N. Holmes, J. Laverty, C.C. Philips, E. Skuras, R. Thomas, X. Zhang, A. Staton-Bevan, and D.W. Pashley, Semicond. Sci. Technol. **4**, 663 (1989).
6. C.F. McConville, T.S. Jones, F.M. Leibsle, S.M. Driver, T.C.Q. Noakes, M.O. Schweitzer, and N.V. Richardson, Phys. Rev. **B50**, 14965 (1994).
7. W.K. Liu, Xuemei Zhang, Weiluan Ma, J. Winesett, and M.B. Santos, J. Vac. Sci. Technol. **B14**, 2239 (1996).
8. J. Heremans, D.L. Partin, D.T. Morelli, C.M. Thrush, G. Karczewski, and J.K. Furdyna, J. Appl. Phys. **74**, 1793 (1993).
9. J.R. Meyer and F.J. Bartoli, Phys. Rev. **B32**, 1133 (1985).

MBE GROWTH OF InSb BASED DEVICE STRUCTURES ONTO InSb(111)A,(111)B AND InGaSb(111)A SUBSTRATES

A D JOHNSON, R JEFFERIES, G J PRYCE, J A BESWICK, T ASHLEY, J NEWEY,C T ELLIOT & T MARTIN
DRA Malvern, St. Andrews Road, Great Malvern, WR14 3PS, UK.

ABSTRACT

We report on the optimum growth conditions for Molecular Beam Epitaxy (MBE) growth of InSb onto InSb (111)A and (111)B substrates. It was found that for (111)A substrates the optimum epilayer morphology was obtained for growth temperatures above 385°C and with a Sb:In ratio of 1.5:1. In contrast, for the (111)B surface, best morphology was found for growth temperatures above 385°C but with V:III ratio of ~7.0:1. In both cases the dopant incorporation was found to be the same as the (100) surface and did not particularly depend either on V:III ratio or substrate temperature. We also describe the device characteristics of InAlSb light emitting diodes (LEDs) grown lattice matched onto ternary InGaSb(111)A substrates using the optimized growth conditions obtained.

INTRODUCTION

InSb has recently attracted a lot of attention due to its unique material properties which are a result of its narrow energy gap. A low electron effective mass and very high saturation velocity offer the opportunity of very high speed, low power and low noise electronic devices [1]. In addition, it has a cutoff wavelength of ~7μm at room temperature and so has found particular applications in infrared detectors. Recently we have reported on room temperature InSb/InAlSb heterostructure LEDs grown by MBE which show both positive and negative luminescence with a peak spectral output at ~5.8μm [2,3] and also the first InSb diode lasers with emission wavelengths of 5.1μm and operation up to 90K [4]. To enable these lasers to achieve operation at ambient temperatures we plan to utilize strain effects to reduce Auger recombination mechanisms in quantum well structures. As InSb has the largest lattice parameter of the III-V compounds, it does not lattice match to any wider gap III-V material which could be used for optical and electrical confinement. We therefore have initiated a programme of work aimed at producing InGaSb ternary substrates for lattice matching to InAlSb using a novel double crucible Czochralski technique [5]. So far, since we have been using InSb seed crystals, the Ga composition varies along the length of the crystal. As the crystals are pulled on the (111) axis, wafers therefore have to be cut on (111) to maintain Ga composition and hence lattice parameter across the slice. The growth conditions for MBE growth onto (111) substrates have been found to be significantly different to those necessary for growth onto (100) surfaces for other material systems such as GaAs [6]. We have therefore investigated the MBE growth of InSb onto InSb(111)A and (111)B substrates as a function of substrate temperature and V:III ratio and studied the resulting surface morphologies and dopant incorporation.

Most previous InSb MBE work has been based on (100) growth [7], although growth onto (110) [8] and (111) [9] has been reported. One such paper [9] reported Reflection High Energy Electron Diffraction (RHEED) patterns for (111)A, (111)B and (100) surfaces as a function of V:III ratio but made no comment about epilayer morphology or doping. A more recent publication [10] has investigated MBE growth of InSb onto GaAs(111)B substrates. This work concentrated on full width half maximum (FWHM) of X-ray diffraction peaks as a function of growth temperature and epilayer thickness. No comment was made about epilayer morphology, but presumably the 14% mismatch in this material system precludes very high quality epitaxy.

Having obtained optimum growth conditions for these InSb(111) surfaces, we have been able to produce InAlSb LED diodes nominally lattice matched to InGaSb ternary substrates and report here on their room temperature operation.

EXPERIMENTAL

All the layers were grown in a modified VG V80H MBE reactor equipped with elemental Sb, In and Al effusion sources and Si and Be sources for n and p type doping respectively. (111)A and (111)B wafers were supplied by MCP Wafer Technology Ltd and doped n-type with Te at $\sim 2 \times 10^{15} cm^{-3}$. Prior to insertion into the reactor the wafers were degreased in acetone, trichloroethylene and iso-propyl alcohol and etched in a modified CP4 etch described previously [11]. Native surface oxide was removed using atomic hydrogen produced by an Astex AX4300 Electron Cyclotron Resonance (ECR) plasma source, using conditions which have been shown to provide and oxide free, atomically flat surface [11]. InSb growth rates were measured by In induced RHEED oscillations from the (100) surface and nominally set to $0.5 \mu m/hr$. The Sb:In ratio was measured by using Sb induced RHEED oscillations from the same sample and varied as described below in the text. For InAlSb barrier layers and layers grown lattice matched to ternary substrates, the Al composition was calibrated by use of AlSb RHEED oscillations from a GaSb(100) surface cleaned with the ECR plasma source.

Substrate temperature during growth was calibrated for the (111)A surface with reference to the c(4x4)→1x3 surface phase transition from a (100) InSb sample mounted alongside the (111)A wafer on the sample block. The substrate temperature for (111)B growth was calibrated by a surface phase transition described below. InSb diode layers were grown at V:III ratios of 1.5, 4.0, 7.0 and 13.0:1 and at substrate temperatures of T_t+50, T_t, T_t-25 and $T_t-50°C$. The epilayer structure studied was the same in each case: a p-i-n diode comprising $1\mu m$ p+ InSb/$0.02\mu m$ p+ $In_{0.85}Al_{0.15}Sb$/$0.75\mu m$ undoped InSb/$1\mu m$ n+ InSb. The chemical Be doing level for all layers was nominally $3 \times 10^{18} cm^{-3}$, and the Si level nominally $2 \times 10^{19} cm^{-3}$, based on calibrations achieved previously using InSb(100) epitaxy.

a)

RESULTS

b)

a)InSb(111)B
The (111)B surfaces were cleaned for ten minutes using the ECR hydrogen plasma under an Sb overpressure. The RHEED pattern of the cleaned surface at $\sim 350°C$ exhibited a 6x2 reconstruction which changed to 2x2 on increasing the substrate temperature. On cooling, the pattern changed to a 1x1 even down to $\sim 150°C$. This is in contrast to the (100) surface where a spotty RHEED pattern is obtained below $\sim 250°C$ due to Sb condensation [12]. Figure 1 shows RHEED patterns obtained from the (111)B surface along the [010]

Figure 1) RHEED patterns of the [010] azimuth of InSb(111)B. a)6x pattern at T=460°C and b) 2x pattern at T+470°C

azimuth. Figure 1a) shows the 6x pattern at an indicated substrate temperature of 460°C and figure 1b) shows the same azimuth at 470°C, exhibiting a 2x symmetry. To enable substrate temperature calibration, a transition temperature T_t was defined as the point where the 1/6th order streaks in figure 1a) disappeared, at a Sb:In ratio of 7.0:1. To estimate the true temperature of this T_t, (111)B and (100) samples were mounted side by side on a single substrate block. Comparison of the (111)B 6x2→2x2 transition temperature (V:III = 7.0) with our usual (100) c(4x4)→1x3 transition (V:III = 1.50) showed that the two temperatures were equivalent to within a few °C. The transition temperature on the (001) surface has previously been estimated to be $\sim 385-390°C$ [7]. All layers

subsequently grown on (111)B were thus referenced to T_t.

InSb(111)B layers were first grown as a function of Sb:In ratio at a fixed substrate temperature of T_t. At V:III=1.5 the surface morphology was mirror-like and when examined with a Nomarski microscope the surface appeared smooth apart from a number inclusions at a density of ~10^3-10^4 cm$^{-2}\mu$m^{-1}. These inclusions were similar to features seen in (100) epitaxy (we have examined them in the past and they appear to be InSb), although at a higher density. On increasing the V:III ratio to 4.0 the number of inclusions fell, and the density fell again on increasing the ratio to 7.0 (~500 cm$^{-2}\mu$m^{-1}). However, on increasing the Sb:In ratio to 12.0, the surface remained mirror-like to the naked eye but showed a uniform 'orange-peel' structure under Nomarski. The V:III ratio of 7.0:1 was thus chosen as the optimum to study morphology as a function of growth temperature.

(111)B growth as a function of temperature was much more critical than versus V:III ratio. Figure 2 a) shows a Nomarski micrograph of a layer grown at T_t+50°C. It can be seen that the surface is featureless apart from a small number of the inclusions described above. Figure 2b) shows a similar micrograph for a layer grown at T_t-50°C. In this case the wafer surface was matt to the eye and, as can be seen from the figure, the layer comprised a very high density of triangular pyramids. Growth at T_t-25°C yielded a similar result with a lower density of islands. In summary, (111)B growth gives optimum epilayer morphology with a V:III ratio of ~7.0 at growth temperatures >T_t, with morphology improving with increasing substrate temperature.

a)

a)

b)
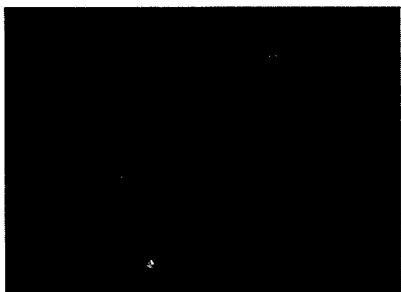
b)
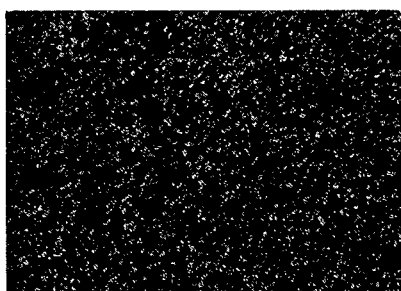
Figure 2) Nomarski micrographs (x80) of InSb(111)B diodes grown at a substrate temperature of **a)** T_t+50 and **b)** T_t-50°C.
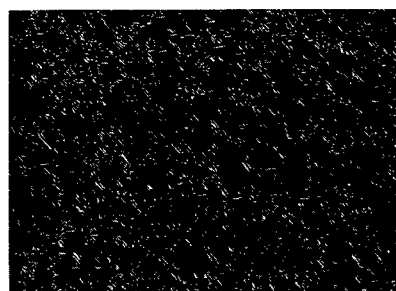
Figure 3) Nomarski micrographs (x80) of InSb(111)A diodes grown at an Sb:In ratio of **a)** 1.50:1 and **b)** 4.0:1

As every layer grown was a p-i-n diode, Secondary Ion Mass Spectrometry (SIMS) measurements were carried out to determine the chemical doping level in each case. All layers exhibited the same Be and Si level as would be expected for epitaxy onto InSb(100) i.e. V:III ratio and growth temperature did not affect chemical doping level. We are currently investigating the effect of these parameters on dopant activation as it has been shown previously that Si activation is highly dependent on substrate temperature in InSb(100) MBE [13].

b) InSb(111)A
After hydrogen ECR plasma cleaning for ten minutes, the (111)A surface displayed a 2x2 RHEED pattern at all substrate temperatures and V:III ratios. Therefore it was necessary to mount a small piece of (100) InSb to enable substrate temperature calibration as described above. The (111)A surface was found to be much more sensitive to V:III ratio than the 'B' face. At Sb:In = 1.50 and a growth temperature of T_t, the resulting surface was mirror-like with a density of inclusions, as seen on the (111)B surface, of ~$10^4 cm^{-2} \mu m^{-1}$. A Nomarski micrograph of such a surface can be seen in Figure 3a). On increasing the Sb:In ratio to 4.0 the epilayer surface became misty and Nomarski indicated a surface characterized by triangular island growth, as shown in Figure 3b). Increasing the V:III ratio to 7.0 only succeeded in increasing the density of these islands and making the wafer appear more misty to the eye.

Thus having chosen Sb:In =1.50 as the optimum for (111)A epitaxy, layer morphology as function of growth temperature was investigated. Results were found to be remarkably similar to those for the 'B' face. On reducing the temperature below T_t, the surface became misty and was made up of triangular pyramid-like islands, the density of these islands increasing with decreasing substrate temperature. Raising growth temperature above T_t caused a reduction in the number of inclusions visible and generally the surface morphology improved with increasing substrate temperature. Thus the optimum growth conditions for InSb(111)A were found to be a V:III ratio=1.50 (as for InSb(100) epitaxy), and growth temperatures >T_t. SIMS measurements again could find no variation in Si and Be doping level with Sb:In ratio or growth temperature. The chemical doping levels were also similar to those found on the (100) and (111)B InSb surfaces.

c) InAlSb/InGaSb(111)A
Having obtained optimum growth conditions for epitaxial growth onto InSb(111)A surfaces, the knowledge gained was used to facilitate lattice matched growth of $In_{1-x}Al_xSb$ onto $In_{1-y}Ga_ySb(111)A$ substrates. A sample was grown with Al composition of x=0.067 to lattice match with the substrate Ga composition of y=0.06 as determined by double crystal X-ray diffraction measurements. The layer was identical to the p-i-n diodes grown on InSb substrates described above, with a 200Å p+ barrier layer of Al composition x=0.217 above the p+ layer. Mesa diodes ranging from 100μm to 400μm square in size were fabricated from both layers using conventional lithographic techniques and Cr/Au contacts sputtered onto their tops. The room temperature (294K) current vs. voltage characteristics were measured and compared with a pseudomorphic InSb/InAlSb diode grown onto InSb(100). The ternary device had a significantly lower reverse bias leakage current (I_{sat}) and higher zero bias resistance (R_o) than the InSb diode. he room temperature results are summarized in the following table:-

Layer	$I_{sat}(\mu A)$	$R_0(\Omega)$
InSb/InAlSb/InSb(100)	470	55
InAlSb/InGaSb(111)A	100	550

Although the ternary substrate diode had a higher zero bias resistance at room temperature, on cooling to 77K it was found be several orders of magnitude below that of the InSb grown diode i.e it did not increase as much as the temperature was reduced. This indicates that the ternary grown device had a higher defect density, presumably due to the ternary InGaSb(111)A substrate being of poorer quality in comparison with the InSb(001) substrate.

Electroluminescence from the devices was measured at 294K. The emission spectra for the InSb and InGaSb grown diodes are shown in Figure 4). Under low forward bias (100mA), the InSb device peaked at a wavelength of 6.2μm with maximum spectral output power of 4μWμm-1. Under the same bias conditions, the ternary device displayed a peak positive emission at a wavelength of 4.1μm, with a spectral power of approximately 11μWμm-1. The dip in the output that can be seen in the figure at a wavelength of 4.2μm is due to absorption of atmospheric CO_2 (one application of these mid-IR LEDs is for gas detection). Thus the peak emission was shifted to shorter wavelengths by an amount expected from the increased energy gap of the ternary InAlSb active region. The negative going region of the spectrum from the ternary diode is referred to as negative luminescence and represents a reduction in the emitted intensity below that of the normal ambient level. It is believed to be due to the reverse bias applied between the p+ region of the epilayer and the n-type substrate (the InGaSb substrates were doped with Sn to harden the lattice and reduce microcracks). The InGaSb has a slightly higher energy gap than InSb, which is why the negative luminescence 'peaks' at a slightly shorter wavelength then the InSb LED.
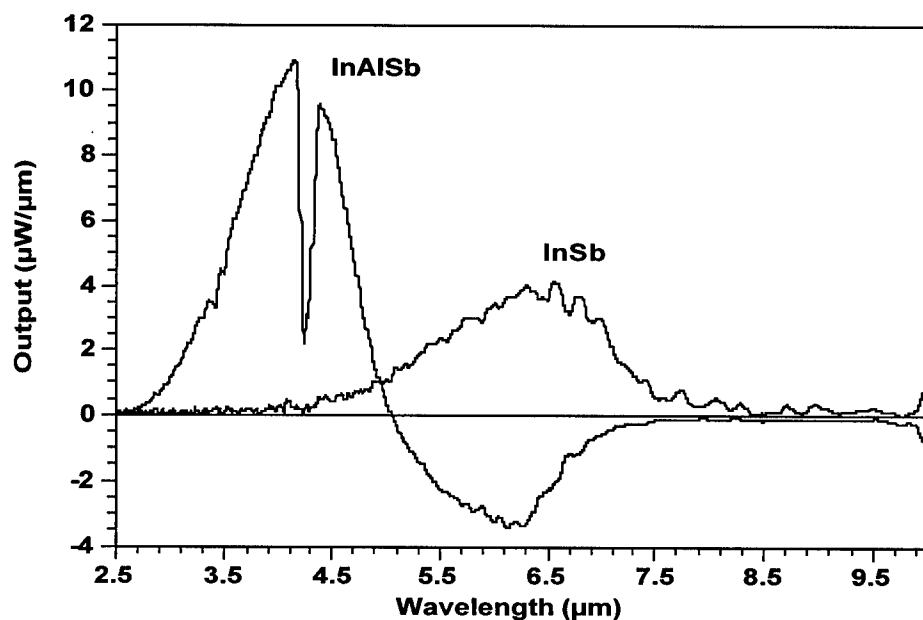
Figure 4) Spectral emission from $In_{0.933}Al_{0.067}Sb$/InGaSb(111)A and InSb/InSb(100) diodes under 100mA forward bias at 294K.

SUMMARY AND CONCLUSIONS

We have optimized the MBE growth conditions for successful epitaxy of InSb onto InSb(111)A and (111)B surfaces. Using Nomarski microscopy and SIMS, we have shown that, in the case of (111)B epitaxy, optimum growth conditions are a Sb:In ratio of~ 7.0 and growth temperature >T_t (~380°C). For (111)A growth the optimum V:III ratio is 1.50:1 and substrate temperature must also be above T_t for good layer morphology. The information obtained on growth conditions was applied to the growth of InAlSb LEDs lattice matched to InGaSb(111)A substrates.
Electrical characterization at 77K of the ternary LEDs indicated a higher defect density than a similar InSb diode. Room temperature electroluminescence from the ternary diodes gives peak emission at a shorter wavelength than InSb diodes, as expected from the wider energy gap of the InAlSb active

layer of such a device. This work demonstrates the feasibility of tailoring the lattice constant of the substrate to match the desired epilayer structure and possibly offers a viable route to the production of mid-IR lasers based on strained quantum well structures, operating at near ambient temperatures.

Immediate future work will concentrate on investigating dopant activation and electrical and optical characteristics of InSb(111)B and (111)A diodes in comparison with similar InSb(100) structures. The resulting information will be applied to ternary diodes and quantum wells grown onto InGaSb substrates.

ACKNOWLEDGEMENTS

REFERENCES

[1]   T Ashley, A B Dean, C T Elliott, G J Pryce, A D Johnson & H Wills, Appl. Phys. Lett. **66**, No.4, pp481-3, (1995).

[2]   T Ashley, C T Elliott, N T Gordon, R S Hall, A D Johnson & G J Pryce, Appl. Phys. Lett. **64**, No. 18, pp2433-5, 1994.

[3]   T Ashley, C T Elliott, N T Gordon, R S Hall, A D Johnson & G J Pryce, Infrared Physics & Technology, **36**, pp1037-44, 1995.

[4]   T Ashley, C T Elliott, R Jefferies, A D Johnson, G J Pryce & A M White, Accepted for Publication, Appl. Phys. Lett.

[5]   T Ashley, J A Beswick, B Cockayne & C T Elliott, Inst. Phys. Conf. Ser. No. 144, Section 4, pp209-13, 1995.

[6]   T Shitara, E Kondo & T Nishinaga, J. Cryst. Growth **99**, p530, (1990).

[7]   G M Williams, C R Whitehouse, T Martin, N G Chew, A G Cullis, T Ashley, D E Sykes, K Mackay & R H Williams, J. Appl. Phys. **63**, p1526, 1988.

[8]   A J Bosch, R G van Welzenis & O F Z Schannen, J. Appl. Phys. **58**, No. 9, pp3434-9, 1985.

[9]   Kunishige Oe, Seigo Ando & Koichi Sugiyama, Jap. Journ. Appl. Phys. **19**, No. 7, ppL417-20, 1980.

[10]   E Michel, J D Kim, S Javadpour, J Xu, I Ferguson & M Razeghi, Appl. Phys. Lett. **69**, No. 2, pp215-7, 1996.

[11]   A D Johnson, G M Williams, A J Pidduck, C R Whitehouse, T Martin, C T Elliott & T Ashley, Inst. Phys. Conf. Ser. No. 144, Section 4, pp204-9, 1995.

[12]   M B Santos & W K Liu, Inst. Phys. Conf. Ser. No. 144, Section 4, pp199-203, 1995.

[13]   S D Parker, R L Williams, R Droopad, R A Stradling, K W J Barnham, S N Holmes, J Laverty, C C Phillips, E Skuras, R Thomas, X Zhang, A Staton-Bevan & D W Pashley, Semicond. Sci. Technol. **4**, pp663-76, 1989.

Part II

Quantum Wells and Devices

SPONTANEOUS AND STIMULATED INTERSUBBAND EMISSION
UNDER OPTICAL PUMPING

P. Boucaud*, S. Sauvage*, O. Gauthier-Lafaye*, Z. Moussa*, F.-H. Julien*, R. Prazeres**, F. Glotin**, J.-M. Ortega**, R. Planel***, J. P. Leburton****, V. Berger*****, J. Nagle*****

* IEF, Université Paris XI, Bat 220, 91405 Orsay, FRANCE, phill@ief.u-psud.fr
** CLIO/Lure, Université Paris XI, Bat 209, 91405 Orsay, FRANCE
*** L2M, 196 Av. H. Ravera, 91220 Bagneux, FRANCE
****Beckman Institute, University of Illinois, Urbana-Champaign IL 61801, USA
***** LCR, Thomson CSF, Domaine de Corbeville, 91404 Orsay, FRANCE

ABSTRACT

We have investigated the mid-infrared spontaneous and stimulated emission between confined subbands in the conduction band of GaAs/AlGaAs quantum wells. The carriers which give rise to the intersubband emission are excited in the upper subbands using an intersubband optical pumping in coupled asymmetric quantum wells. The quantum wells are designed using phonon engineering in order to obtain population inversion between the second and first excited subband. This is obtained by adjusting the subband energy spacing between E_2 and E_1 close to the optical phonon energy which in turn allows an efficient relaxation. We have first observed intersubband spontaneous emission between E_3 and E_2 at 14 µm using an intersubband pumping with a CO_2 laser in resonance with the E_1-E_3 transition. In a second set of experiments, the quantum wells are embedded in an infrared waveguide. We have measured the stimulated intersubband gain using a picosecond two-color free electron laser. The first color bleaches the E_1-E_3 transition and provides the population inversion. The intersubband stimulated gain is measured versus the waveguide length and photon energy. Stimulated gains ≈ 80 cm^{-1} are reported thus demonstrating that laser emission under optical pumping appears feasible in optimized structures. Finally, we show that intersubband emission can also be observed in quantum wells using an interband optical pumping.

INTRODUCTION

Since the seminal proposal of Karazinov and Suris in 1971 [1], the experimental evidence for intersubband emission in semiconductor quantum wells or superlattices

has been difficult to obtain. In 1989, Helm and co-workers [2] have reported the observation of intersubband spontaneous emission in the far-infrared region. The superlattices were excited by sequential resonant tunneling. The first observation of spontaneous emission in the mid-infrared region (5-10 μm) has only been reported in 1993 [3]. The quantum efficiency of the intersubband emission is given by the balance between the non-radiative relaxation time τ_{nr} and the radiative relaxation time τ_r. The radiative relaxation time exhibits a λ^2 dependence for intersubband transition. One expects that the efficiency will be larger at shorter wavelengths. On the other hand, the non-radiative relaxation rate becomes very large above the optical phonon energy (36 meV in GaAs) due to the efficient interactions of electrons with longitudinal optical (LO) phonons. The intersubband relaxation times are typically in the ps range for energies larger than the LO-phonon energies. The quantum efficiency of spontaneous emission is therefore very low, of the order of 10^{-4} - 10^{-6}, in the mid-infrared spectral region. In the far-infrared spectral range, the non-radiative relaxation is dominated by interactions with acoustic phonons which occur typically on a 100 ps time scale. Nonetheless the intersubband radiative lifetime is larger and the quantum efficiency for spontaneous emission remains weak. The realization of efficient spontaneous light emitting devices with intersubband transitions is therefore not achievable. However, a careful engineering of the quantum wells can provide population inversion between the subbands along with large optical gains. In quantum wells, the relaxation is governed by interactions between carriers with slab and interface phonon modes [4]. Basically, the relaxation rate between two subbands exhibits a $1/q_{//}^2$ dependence where $q_{//}$ is the phonon momentum transfer during the relaxation. When the subband energy spacing is close to the optical phonon energy, the relaxation time between two subbands is very short, typically 0.5 - 0.7 ps. When the subband energy is much larger than the optical phonon energy, the relaxation rate will involve emission of phonons with large in-plane momentum and the intersubband lifetimes are typically of the order 1 - 1.5 ps. A careful engineering of the subbands spacing in the quantum wells can therefore lead to population inversion. Intersubband lasing at 4.5 μm under electrical injection has been first reported in 1994 [5]. Quantum cascade lasers appear now as challenging competitors to low band-gap materials in the mid-infrared spectral region. Due to their inherent conception, the intersubband lasers are unipolar components which exhibit high T_0 characteristic temperatures. The high T_0 value can in particular be explained by the origin of the emission which occurs between nearly parallel subbands, the lack of Auger recombinations, and the weak dependence of the non-radiative relaxation times with temperature. Quantum cascade lasers can be operated either continuous wave up to 140 K [6] or in pulsed mode at room temperature in the 4-8 μm spectral range [7].

An alternate approach to observe intersubband emission has been recently proposed. It relies on the optical pumping of the electrons with intersubband transitions [8]. The design of samples for optical pumping is much more easier than the conception of samples operated under electrical injection since it does not require superlattice injectors in the active region. Two types of optical pumping can be considered : intersubband or interband pumping. In the case of intersubband pumping, a CO_2 laser operated around 10.6 μm is a practical source to excite intersubband transitions. The intersubband emission will therefore occur at longer wavelengths, typically 12.5 - 15 μm. One can notice that under optical pumping,

intersubband lasing can be expected in a three-bound states system as long as $\tau_{32} > \tau_{21}$. In the case of interband pumping, carriers are optically generated from the valence band to the conduction band. The intersubband emission wavelength is not limited by the pump energy but rather by the composition and thickness of the quantum wells. The efficiency of interband pumping is not as large as intersubband pumping since one cannot excite HH_3-E_3 without exciting HH_2-E_2. However, it is possible to show that population inversion can also be achieved as long as the condition $\dfrac{\Gamma_p^3}{\Gamma_p^2} > \dfrac{\tau_{21}}{\tau_3(1 - \frac{\tau_{21}}{\tau_{32}})}$ is

fulfilled [9], where $\Gamma_p{}^i$ is the generation rate from the valence band to the ith conduction subband under optical pumping. Interband pumping exhibits a greater potential in terms of applications since monolithic integration of an interband laser diode and an intersubband emitter can be easily envisaged.

RESULTS

Spontaneous emission under intersubband optical pumping

The conduction band diagram of coupled asymmetric quantum wells which are designed for intersubband pumping is shown in figure 1. Three subbands are bound in the conduction band. An intersubband pumping excites carriers from the ground subband to the second excited subband where they can recombine radiatively to the first excited subband. The design of the quantum wells requires the three following conditions to be fulfilled : asymmetric structures to allow both intersubband transitions between E_1-E_3 and E_2-E_3 ; a subband energy spacing between E_1-E_2 close to the optical phonon energy and a trade-off between the E_1-E_3 and the E_2-E_3 oscillator strength to enhance both absorption and emission.
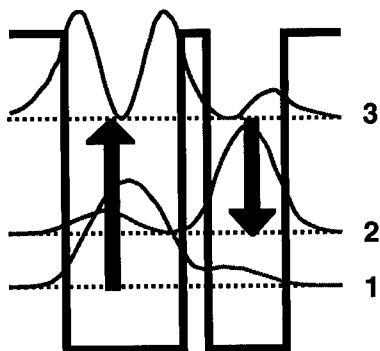
Figure 1 : principle of intersubband emission (3-2) under intersubband optical pumping (1-3) in the conduction band of GaAs quantum wells.

A sample satisfying to these prerequisites has been grown by molecular beam epitaxy [8](sample A): it consists of 100 asymmetric quantum wells separated by 20 nm $Al_{0.22}Ga_{0.78}As$ barriers. The quantum well consists of two GaAs wells of 7.5 nm and 5 nm respective thickness separated by 1.7 nm $Al_{0.22}Ga_{0.78}As$ barriers. The doping in the quantum wells is $1x10^{11}$ cm^{-2}. At room temperature, the quantum well exhibits two intersubband absorption lines at 124 meV (E_1-E_3) and 84.2 meV (E_2-E_3) with similar amplitudes. The energy spacing E_1-E_2 (39.8 meV) is close to the optical phonon energy (36 meV). The dipole moment z_{31} and z_{32} are respectively found equal to 1.3 nm and 2.5 nm [8].

The intersubband spontaneous emission spectrum of sample A is reported on figure 2. The experiments have been carried out at liquid helium temperature, the spontaneous emission being collected by an He-liquid cooled bolometer. The intersubband pumping is provided by a CO_2 laser in resonance with the E_1-E_3 transition (9.8 μm). The emission spectrum is resonant with a maximum at 88 meV and a full width at half maximum of 4 meV. We have reported on the same spectrum the room-temperature intersubband absorption spectrum associated with the E_2-E_3 transition. The emission spectrum is shifted by ≈ 4 meV to high energy as compared to the absorption spectrum, this blue-shift being characteristic of intersubband transitions.
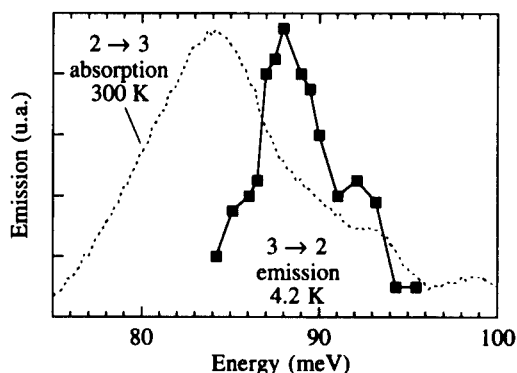
Figure 2 : Low-temperature intersubband emission spectrum (sample A, squares) under intersubband optical pumping compared with room temperature intersubband absorption.

Figure 3 shows the dependence of the intersubband emission at 14 μm on the pumping energy. This excitation spectrum is compared to the 77 K E_1-E_3 intersubband absorption spectrum. The 14 μm intersubband emission is directly proportional to the incident pump power absorbed in the quantum wells and therefore follows the E_1-E_3 intersubband absorption since all the pump is not absorbed in the sample. The efficiency of spontaneous emission is estimated around 60 nW for 1 W incident pump power. These first experiments clearly demonstrate that intersubband spontaneous emission can be observed under intersubband optical pumping.
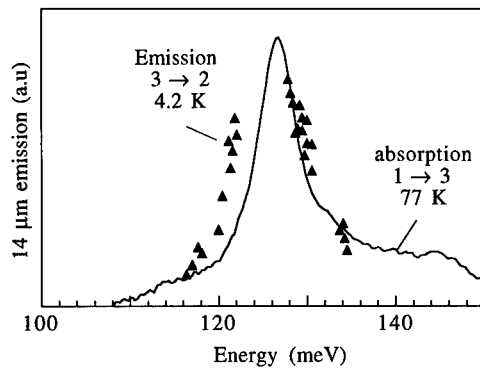
Figure 3 : Excitation spectrum of the 14 μm spontaneous emission (triangles) compared to the E_1-E_3 intersubband absorption (full line).

Spontaneous emission under interband optical pumping

We now turn to the interband optical pumping case. Two situations can be considered : in the first case, the carriers are resonantly pumped from the valence subband to the excited levels in the conduction band and can recombine afterwards radiatively through intersubband emission. This mechanism is illustrated on figure 4. In the second case, the carriers are generated on the ground subband and subsequently thermally excited on the upper levels. Although population inversion can not be obtained in the second case, it provides an infrared emission spectroscopy of the intersubband transitions in the mid-infrared spectral range. We will first describe the emission measurements performed at room temperature. For these experiments, the sample is set on the emission port of a Fourier transform infrared spectrometer which is operated in step-scan mode with a lock-in amplifier. The interband optical pumping is mechanically chopped at 3 kHz.

When the carriers are injected on the ground subband by an interband pumping, part of the carriers are thermally excited on the upper levels where they can recombine radiatively. This emission can be analyzed as the blackbody emission of a two-dimensional electron gas [10]. This is illustrated on figure 5 which reports the infrared emission in asymmetric quantum wells. The investigated structure consists of 100 coupled quantum wells separated by 150 Å $Al_{0.3}Ga_{0.7}As$ barriers grown on GaAs by molecular beam epitaxy (sample C). The coupled quantum well active region is formed by two GaAs quantum wells with respective thickness of 62 and 52 Å separated by 8.5 Å $Al_{0.3}Ga_{0.7}As$ intermediate barrier. The structure is nominally undoped. The excitation is provided by a Ti:sapphire laser at 1.62 eV, an energy lower than the HH_3-E_3 transition, i.e electrons are excited in the E_1 and E_2 subbands but not on the E_3 subband.

115
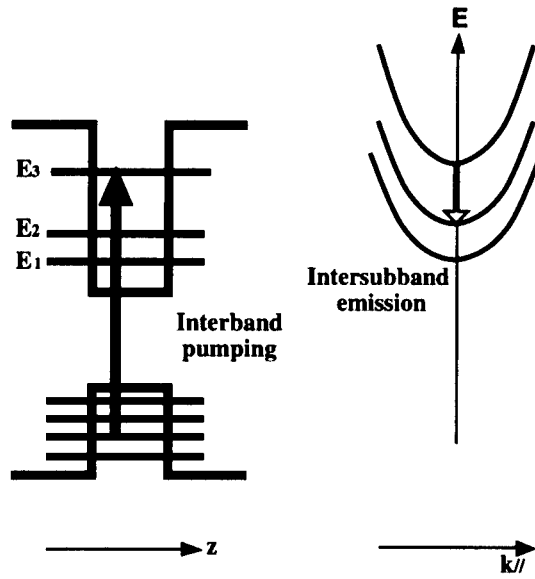
Figure 4 : Principle of interband optical pumping for intersubband emission.
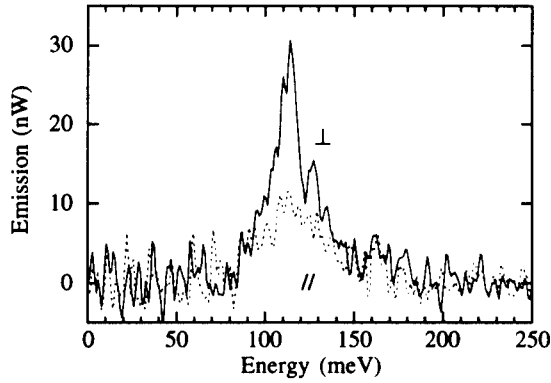
Figure 5 : Room temperature intersubband emission of sample C under interband
optical pumping.

The full and dotted curves are the emission spectra for a polarization
respectively perpendicular and parallel to the layer plane of the quantum wells. We
observe an emission peak which is strongly p-polarized and attributed to the
radiative intersubband spontaneous emission between E_3 and E_2. The energy
position and FWHM of the emission are similar to those measured for the E_2-E_3
intersubband absorption. The intersubband spontaneous emission scales with the

number of injected carriers. The collected intersubband optical power is estimated around ≈ 22 nW for 400 mW pump power. The collected power P_{isb} is given by :

$$P_{isb} = \alpha_{ib}P_{ib}\frac{h\nu_{isb}}{h\nu_{ib}}\frac{\tau_{ib}}{\tau_{rad}}e^{-E_{31}/kT}\eta_{coll}$$
(1)

where α_{ib} and P_{ib} are the interband absorption efficiency (%) and the interband optical power, $h\nu_{isb}$ and $h\nu_{ib}$ the intersubband and interband energy respectively, τ_{ib} and τ_{rad} the interband relaxation times and the intersubband relaxation time and η_{coll} the collection efficiency of the subband luminescence which is coupled out of the sample [11]. From the magnitude of the photo-induced intersubband absorption, we have deduced $\tau_{ib} \approx 65$ ns. Assuming $\eta_{coll} \approx 2\ 10^{-3}$, $\alpha_{ib} \approx 0.81$ and $\tau_{rad} \approx 76$ ns, we effectively expect an intersubband power at 115 meV of about 57 nW for 1 W interband pump power at 1.62 eV.
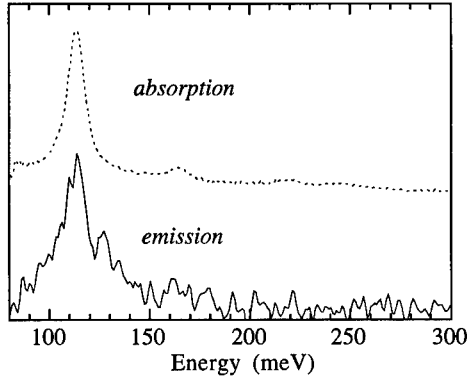
Figure 6 : Room temperature infrared absorption and emission of sample C under interband optical pumping.

Figure 6 shows a comparison between the photo-induced infrared absorption spectrum of sample C and the intersubband emission spectrum obtained under interband optical pumping. As seen, the energy position and broadening of the two spectra are similar. This similitude is the consequence of the design of the quantum wells where intersubband transitions are vertical in the real space, i.e interface roughness is minimized. It demonstrates that this new photoluminescence technique is a sound spectroscopic tool to study intersubband transitions in the mid-infrared spectral range.

The experimental evidence of intersubband spontaneous emission under resonant interband optical excitation is however a key issue for the realization of optically pumped intersubband lasers. Unlike thermal population, only resonant pumping allows to keep the population inversion betwen subbands which could in turn lead to lasing action. We have therefore investigated the intersubband spontaneous emission under resonant optical pumping. These measurements are however not a straightforward task since the emitted power is expected to be much lower (factor of

100) than the room temperature intersubband emission. This lower efficiency can be explained by the short non-radiative lifetime as compared to the interband lifetime. Moreover, the measurement of weak emission signals is difficult due to the coupling of the blackbody generated by the spectrometer which is modulated by the interband pumping. The emission signals are therefore superimposed on an absorption signal. In order to discriminate the emission, we have performed the following experiments : at low temperature ($\approx$ 20 K), sample C is pumped with an interband source set below the E_3-HH_3 transition. In a second set of experiments, the quantum wells are pumped above E_3-LH_3 transition. The ratio of the two spectra is presented on figure 7. As seen, we clearly observe the E_3-E_2 intersubband emission at an energy (120 meV) in agreement with the energy measured by absorption spectroscopy [12]. One can notice that the spontaneous collected power is weak ($\approx$ 0.2 nW for 0.5 W interband pump power).
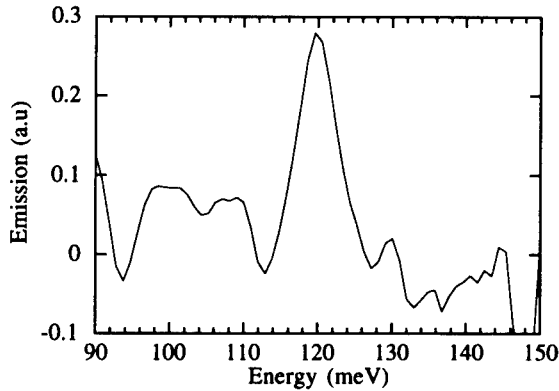
Figure 7 : 20 K emission spectrum of sample C under optical pumping at 660 nm normalized by the emission spectrum under optical pumping at 760 nm. The curve has been smoothened.

Stimulated emission under intersubband optical pumping

In order to check if population inversion can be effectively obtained under optical pumping in 3-level asymmetric quantum wells, we have investigated the stimulated emission in a structure similar to sample A. For this purpose, the active region was buried in an infrared waveguide [13] (sample B). The index profile of the waveguide and the fundamental TM optical propagating mode are reported on figure 8. The structure is grown on a GaAs doped substrate and consists of a 5 μm $Al_{0.9}Ga_{0.1}As$ cladding layer and a 5.4 μm GaAs layer for the core of the waveguide. 30 asymmetric quantum wells separated by 21 nm $Al_{0.3}Ga_{0.7}As$ barriers are grown in the central region of the waveguide. The asymmetric quantum wells consist of two GaAs wells respectively 7.7 nm and 4.7 nm thick separated by a 1.1 nm thick $Al_{0.3}Ga_{0.7}As$ intermediate barrier. The quantum wells are nominally doped with a 3×10^{11} carrier density. The room-temperature infrared absorption spectrum exhibits two resonances

at 133 meV and 93 meV which are respectively attributed to the E_1-E_3 and E_2-E_3 intersubband absorptions. The confinement factor of the TM fundamental mode with the quantum wells is estimated around 7.5 %. However, we have observed an unexpected roughness of the GaAs layer after the growth of the quantum wells. The confinement factor is therefore most probably overestimated. The intersubband non-radiative relaxation times have been found equal to $\tau_{21} = 0.7$ ps, $\tau_{31} = 1.2$ ps, $\tau_{32} = 1.5$ ps. Population inversion is therefore achievable in this system since $\tau_{32} > \tau_{21}$.
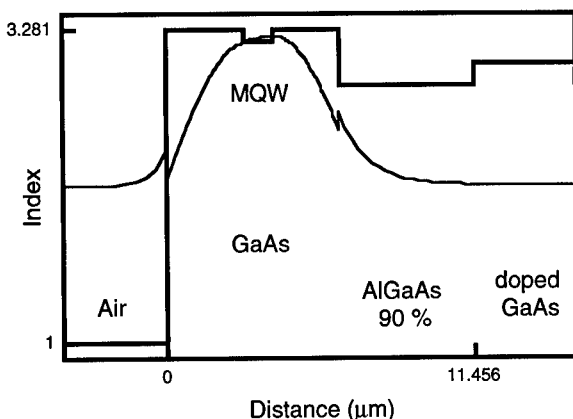
Figure 8 : Infrared waveguide and optical TM mode profile

In order to probe the intersubband stimulated gain, we have used a picosecond infrared two-color free-electron laser (CLIO). This laser can emit simultaneously at two wavelengths which can be independently tuned [14]. The laser delivers macropulses of about 10 μs which contains picosecond micropulses. Typical peak power of 10 MW can be obtained on the picosecond pulses. The experimental set-up is depicted on figure 9.
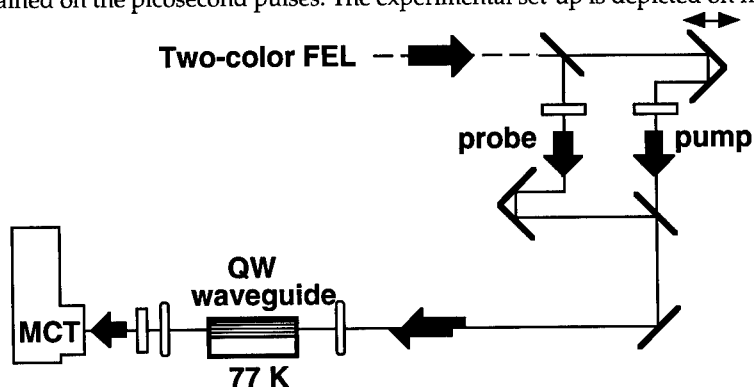
Figure 9 : Experimental set-up involving the two-color free-electron laser.

The experiment is performed at liquid nitrogen temperature in order to eliminate the thermal population of the first excited subband. The first color of the laser bleaches the E_1-E_3 transition while the second color probes the transmission around the E_2-E_3 intersubband transition. The two colors of the laser are delayed using a standard Michelson set-up. The intensity of the pump is larger than the saturation intensity thus implying that population inversion is achieved over the waveguide length. The probe transmission at 12.5 μm versus the time delay between pump and probe is presented on figure 10.
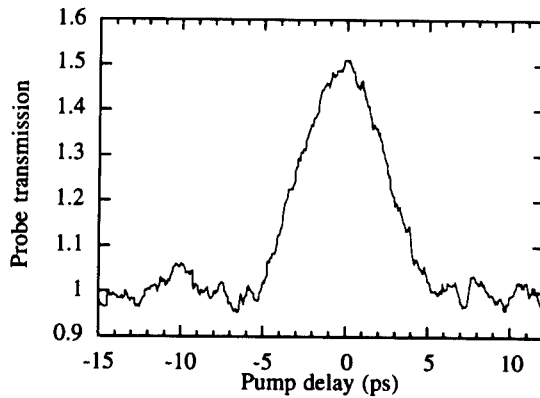
Figure 10 : Probe transmission at 12.5 μm versus time delay between pump (9.2 μm) and probe. The waveguide length is 0.7 mm.

As seen, the transmission is constant when the pump and probe are not synchronized. However, the transmission increases when both pump and probe beams are synchroneously incident on the sample. This transmission increase demonstrates that intersubband stimulated emission is observed under intersubband optical pumping. For a 0.7 mm waveguide length, the amplification is found equal to 1.5. This amplification increases up to 3.5 in a 2 mm long waveguide. These values are found in agreement with the intersubband oscillator strengths which are deduced from the absorption measurements [15]. The 3.5 amplification gain measured in the 2 mm long waveguide corresponds to a 6 cm^{-1} amplification in the structure. If one accounts for a 7.5 % confinement factor of the infrared mode with the quantum wells, the stimulated gain in the quantum wells is found around 80 cm^{-1}.

The energy dependence of the stimulated gain is presented on figure 11. The measurement has been performed in the 2 mm long waveguide with the pump beam set at 9.2 μm. The stimulated gain exhibits a resonance at 99 meV which is close to the E_2-E_3 intersubband energy. The FWHM of the stimulated gain is also consistent with the broadening of the intersubband absorption. The results reported in figure 11 clearly demonstrate the resonant enhancement of the stimulated gain which is attributed to the intersubband resonance.

120
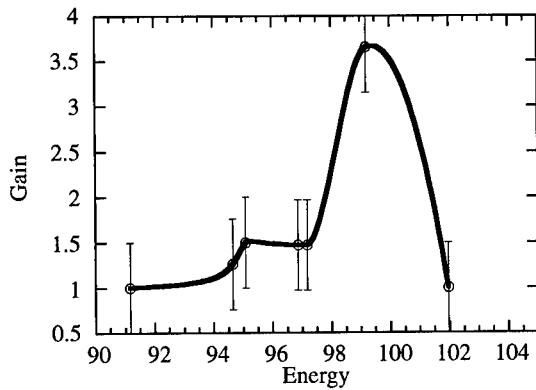
Figure 11 : Energy dependence of the stimulated gain measured in the 2 mm long
waveguide. The pump is set at 9.2 μm. The full line is a guide to the eye.

We have therefore demonstrated that intersubband stimulated gain can be observed
under intersubband optical pumping. The question is to know if intersubband lasing is
possible under intersubband optical pumping. The conditions required for lasing is
given by $\Gamma g - \alpha_{pr} + \ln(R)/L = 0$, where Γ is the confinement factor, g the stimulated
gain, α_{pr} is the propagation loss coefficient, L is the waveguide length and R ≈ 0.27 is
the reflection coefficient at the waveguide cleaved facets. If one accounts for
propagation losses ≈ 5 cm^{-1} which include the losses in the doped substrate as well as
the losses due to free carrier absorption, we see that lasing could be observed in a
structure similar to the one we have used. Besides, optical gains as large as 500 cm^{-1}
have been predicted in asymmetric quantum wells with optimized intersubband
oscillator strengths and for reasonable pumping intensities [16]. Intersubband lasing
under intersubband optical pumping should therefore be achievable with an
appropriate pump source.
  In the case of interband pumping, we have reported intersubband spontaneous
emission. One can notice that the intersubband transition energy is not limited by the
pumping energy : intersubband emission can therefore be investigated at shorter
wavelengths (4-5 μm) where the quantum efficiency is larger. Besides, the waveguide
losses vanish at these wavelengths since free carrier absorption remains weak. For
these reasons, intersubband lasing under interband optical pumping appears also
possible.

ACKNOWLEDGEMENTS

REFERENCES

[1] R. F. Karazinov, and R. A. Suris, Sov. Phys. Semicond. **5**, 707 (1971).

[2] M. Helm, P. England, E. Colas, F. DeRosa, and S. J. Allen, Jr, Phys. Rev. Lett. **63**, 74 (1989).

[3] J. Faist, F. Capasso, C. Sirtori, D. L. Sivco, A. L. Hutchinson, and A. Y. Cho, Electron. Lett. **29**, 2230 (1993).

[4] J.-L. Educato, J.-P. Leburton, P. Boucaud, P. Vagos, and F. H. Julien, Phys. Rev. B. Brief Report **47**, 12949 (1993).

[5] J. Faist, F. Capasso, D. Sivco, C. Sirtori, A. L. Hutchinson, S. N. G. Chu and A. Y. Cho, Science, **264**, 553 (1994).

[6] C. Sirtori, J. Faist, F. Capasso, D. L. Sivco, A. L. Hutchinson, S. N. G. Chu, and A. Y. Cho, Appl. Phys. Lett. **68**, 1745 (1996).

[7] J. Faist, F. Capasso, C. Sirtori, D. L. Sivco, A. L. Hutchinson, and A. Y. Cho, Electron. Lett. **32**, 560 (1996).

[8] Z. Moussa, P. Boucaud, F. H. Julien, Y. Lavon, A. Sa'ar, V. Berger, J. Nagle, and N. Coron, Electron. Lett. **31**, 912 (1995).
Y. Lavon, A. Sa'ar, Z. Moussa, F. H. Julien, and R. Planel, Appl. Phys. Lett. **67**, 1984 (1995).

[9] Z. Moussa, Ph.D thesis, Université Paris XI, November 1996.

[10] H. Hirakawa, M. Grayson, D. C. Tsui, and C. Kurdak, Phys. Rev. B **47**, 16651 (1993).

[11] S. Sauvage, Z. Moussa, P. Boucaud, F. H. Julien, V. Berger, and J. Nagle, submitted to Appl. Phys. Lett.

[12] S. Sauvage, P. Boucaud, O. Gauthier-Lafaye, F. H. Julien, V. Berger, and J. Nagle, unpublished.

[13] F. H. Julien, P. Vagos, J.-M. Lourtioz, D. D. Yang, and R. Planel, Appl. Phys. Lett. **59**, 2645 (1991).

[14] D. A. Jaroszynski, R. Prazeres, F. Glotin, and J.-M. Ortega, Phys. Rev. Lett. **72**, 2387 (1994).

[15] O. Gauthier-Lafaye, S. Sauvage, P. Boucaud, F. H. Julien, R. Prazeres, F. Glotin, J.-M. Ortega, V. Thierry-Mieg, R. Planel, J.-P. Leburton, V. Berger, submitted to Phys. Rev. Lett.

[16] F. H. Julien, A. Sa'ar, J. Wang, and J. P. Leburton, Electron. Lett. **31**, 838 (1995).
J. Wang, J.-P. Leburton, Z. Moussa, F. H. Julien, and A. Sa'ar, J. Appl. Phys. **80**, 1970 (1996).

INTERSUBBAND TRANSITIONS IN MICROCAVITIES WITH A GRATING: COUPLED OSCILLATORS

J.-Y. DUBOZ
Laboratoire Central de Recherches, Thomson-CSF, 91404 ORSAY Cedex, France

ABSTRACT

We theoretically study the absorption in grating coupled quantum wells in a cavity. We describe the coupling between the three oscillators present in the structure: The intersubband transition, the grating and cavity modes. We show that optical mode anticrossings should be observed. The splitting between the cavity mode and the intersubband transition is calculated but its experimental observation would require electronic coherence times longer than what was measured.

INTRODUCTION

During the last ten years, two important fields in the physics of semiconductor heterostructures have experienced spectacular developments in large part owing to the improvement of crystalline growth methods such as molecular beam epitaxy.

The first field deals with intersubband transitions (ISBT) in quantum wells[1,2]. Many infrared devices have been proposed and fabricated for modulation[3,4] detection[5] and emission[6]. In n-doped structures and in large bandgap materials, the polarization selection rule prevents any coupling between the light and the wells at normal incidence (only the electric field E_z perpendicular to the well is coupled with it, z being the growth axis). The coupling can be obtained by increasing the incidence angle thereby creating a z electric field component. However, due to the refraction, the coupling remains weak. A grating can also be used which diffracts photons along directions where the E_z may be important. The grating coupling has been introduced first for detectors[5,7] and then extended to the case of modulators[8].

The second rapidly growing field is related to microcavity effects[9]. The recent developments of deposition techniques have allowed the fabrication and the accurate control of microcavities, and many resonant cavity enhanced devices have been realized. A good review of these devices was published recently[10]. As far as light emission is concerned, microcavities in VCSEL's have allowed to drastically reduce semiconductor laser thresholds and the spectral width of LED's[9]. Cavity finesses as high as 5000 have been obtained thanks to the high quality of the MBE growth[11]. These microcavities are planar and use materials which are optically active at normal incidence. They will be called regular microcavities hereafter.

At the mergence of these two fields, the possibility of obtaining microcavity effects with intersubband transitions was remained unexploited up to now because of the polarization selection rule. Recently[12], it has been proposed to introduce a grating inside the cavity in order to get both the cavity field enhancement and the grating coupling. From the point of view of the photons oscillating in the cavity, the grating and well regions may thus be simply considered as a lossy region and are equivalent to the active region in a regular microcavity device. The electromagnetic field in a cavity and the electronic transition (band-to-band in general, intersubband transition here) can be viewed as two oscillators that are broadened by the finite photon lifetime in the cavity and the coherence time T_2 respectively. In a regular cavity, the coupling between these oscillators has led to the observation of the absorption enhancement[10], modifications of the spontaneous emission[9] or even Rabi splittings[13]. In grated cavities, the enhancement of the absorption or emission has been calculated[12]. We discuss here more specific features that may arise from the coupling between oscillators: anticrossings and intersubband Rabi oscillations. In this regards, we recall here that the analysis of the coupling from the transmission or the reflection may be ambiguous[9] so that we study the coupling from the absorption. All calculations are performed at normal incidence.

123

WEAK COUPLING REGIME

In the calculations presented in this paper, the active region is made of 40 GaAs/AlGaAs quantum wells. The 4 nm GaAs well is doped to 10^{10} cm^{-2}. The 40% Al rich barrier is 35 nm thick. The transition wavelength is 5.5 μm and the Full Width at Half Maximum is 10 meV unless otherwise stated. This active region is in between two doped (10^{17} cm^{-3}) GaAs regions as in a regular detector based on ISBT. A transparent phase grating is defined in the top GaAs layer. These layers define a $3\lambda/2$ active region and are placed in between two Bragg mirrors. The optical indices for top mirror are $n_1 = 1.4$ and $n_2 = 2.43$ (as for CaF$_2$ and ZnSe respectively). In this part, the top mirror is CaF$_2$/ZnSe/CaF$_2$ while the bottom one is made of 5 GaAs/AlAs periods. These parameters were chosen as they describe a cavity that can realistically be fabricated. The number of periods is small and the overall layer thickness remains compatible with growth techniques. The reflection coefficient of both mirrors is 0.5. We calculated the field in this planar cavity and found an enhancement of the electromagnetic energy density (Q factor) close to 22, in agreement with the width of the transmission specrum. The finesse is equal to 4.45. We first calculated the absorption α in the active region with the grating but without the cavity and found 1%. Then we calculated the absorption in the complete structure. Fig. 1 shows that the absorption increases with the bottom mirro reflectivity and exceeds 45% for R=0.5 (5 AlAs/GaAs periods). At this point, it is important to clarify the double role played by the low index layers of the mirror. They first constitute the mirror that partially reflects the non diffracted order and gives the cavity mode. Second, because of their low optical index, they totally reflect the diffracted orders propagating in the active layer. The modes propagating in the latter non planar optical guide defined on one side by the bottom mirror and on the other side by the grating will be called grating modes. In Fig. 1, part of the absorption enhancement is due to the guiding effect that increases with the low index layer total thickness. We calculated that this guiding effect can lead to an absorption as large as 20%. We observe that the absorption is peaked at the electronic transition wavelength independent of the mirror reflectivity. We recall here that three oscillators are present in this structure: the cavity field, the grating resonance and the electronic transition. The grating parameters (see Fig. 1) and the cavity length were chosen in order to give resonances at the same wavelength as the ISBT. However, we do not observe any special feature due to the coupling between oscillators: We are thus in a weak coupling regime. It means that the coupling energy $h\Omega$ is small compared with the width of individual transitons h/T_2 or hv/Q for the ISBT and the cavity respectively.
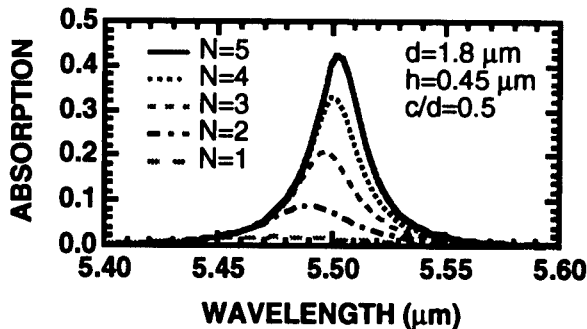
Figure 1: Calculated absorption in a 40 quantum well structure in a grated cavity at normal incidence. The top mirror indices are $n_1/n_2/n_1$ with $n_1=1.4$ and $n_2=2.43$. The bottom mirror indices are $n_3=2.75$ and $n_4=3.27$. The number of pairs in the bottom mirror varies from 1 to 5. The grating parameters are (d, c/d, h)=(1.8 μm, 0.5, 0.45 μm). The FWHM of the intersubband transition is 10 meV. The doping density is equal to 10^{10} cm^{-2}.

This can be translated in terms of mirror reflectivity R and total absorption in the structure α[14]: $\alpha < \pi$ /finesse $= (1-R)/\sqrt{R}$. The latter relation is verified with an absorption with guiding effects of 20% and R=0.5.

STRONG COUPLING REGIME

We now use a symmetric cavity with both top and bottom mirrors made of 3 CaF_2/ZnSe periods. The reflectivity is close to 90%. The finesse is now close to 30. The cavity length L is around mλ/2 with m = 3. The Q factor reaches 130 indicating a penetration of the light in the mirrors equal to $m_0 \lambda$/2 with $m_0 = 1.3$ (Q= $(m+m_0) \times$ finesse). We first calculated the absorption without any cavity. We took the guiding effect into account by placing the active region in between two CaF_2 thick layers. For the following grating parameters: (d=1.865 μm, c/d=0.5, h=0.1 μm), the absorption without cavity was found to be around 35%, weakly dependent on the cavity length. We also noted that the peak wavelength of the grating mode increases from 5.46 μm for L=2.57 μm to 5.49 μm for L=2.75 μm. Then, we calculated the transmission spectrum of the cavity without any grating, replacing it by a layer of the same thickness and with an optical index equal to an average of the grating optical indices. As expected, we found that the transmission peak was increasing from 5.35 μm for L=2.57 μm up to 5.64 μm for L=2.75 μm, in agreement with the cavity order (4.3) and the cavity average optical indices. Finally, we calculated the absorption spectrum in the whole structure as a function of the cavity length. The result is presented in Fig. 2. We observe the grating and cavity modes as they were described above. The interesting phenomenon occurs when these two modes are resonant for the same wavelength: We observe a clear anticrossing, with a splitting between modes. We now have $(1-R)/\sqrt{R}=0.1 < \alpha= 0.35$ which states that we are in the strong coupling regime. It is important to note that the electronic transition remains spectrally broad and we do not observe here the splitting between the ISBT and an optical mode but the splitting between two optical modes.
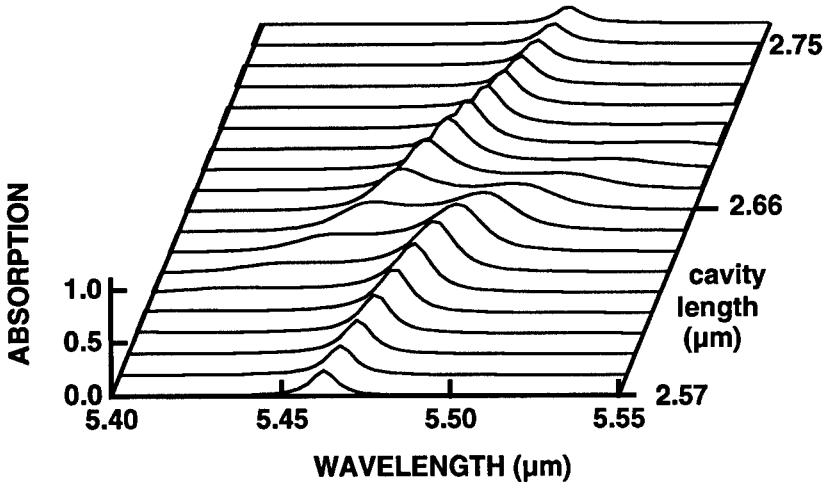
Figure 2: Calculated absorption spectrum in a grated cavity as a function of cavity length. Top and bottom mirrors are made of 3 n_1/n_2 periods with n_1=1.4 and n_2=2.43. The grating parameters are (d, c/d, h)=(1.865 μm, 0.5, 0.1 μm). Other parameters are as in Figure 1.

INTERMEDIATE COUPLING REGIME

The coupling between the cavity and the active region can be tuned in different ways. The relation describing the strong coupling regime ($\alpha > \pi$/finesse) can be obtained by increasing either the absorption or the cavity finesse. For brevity, we choose here to increase the absorption with the grating diffraction efficiency.

We calculated the absorption in the active region (grating and quantum wells) placed between two CaF_2 layers. Hence, there is no cavity but guiding effects are taken into account. We performed this calculation for the same grating period and profile as above but the height is varied from 0 to 0.4 μm. We found that the absorption increases roughly linearly from h= 0 to 50% for h=0.15 μm. It equals 35% for h= 0.1 μm as already mentioned, and 13% for h=0.05 μm. For h>0.15 μm it saturates and finally decreases for h>0.3 μm. Then, we calculated the absorption in the whole structure, with the same mirror as above (R=0.90) with a grating height that varies from zero to 0.2 μm. The result is presented in Fig. 3. For a weak diffraction efficiency, we observe a single peak. As the coupling increases, this peak is split in two peaks and the splitting varies almost linearly with the grating height and thus with the coupling. The splitting becomes visible for h around 0.05 μm. We thus verify that we go from the weak coupling to the strong coupling regime for $(1-R)/\sqrt{R} = 0.1 \approx \alpha = 0.13$.

Let us recall here that the ISBT remains broad compared to the optical resonances studied here and the observed splittings are between optical modes. Experimentally, it should be possible to observe these features as the structures and the parameters used for the simulation are very realistic.
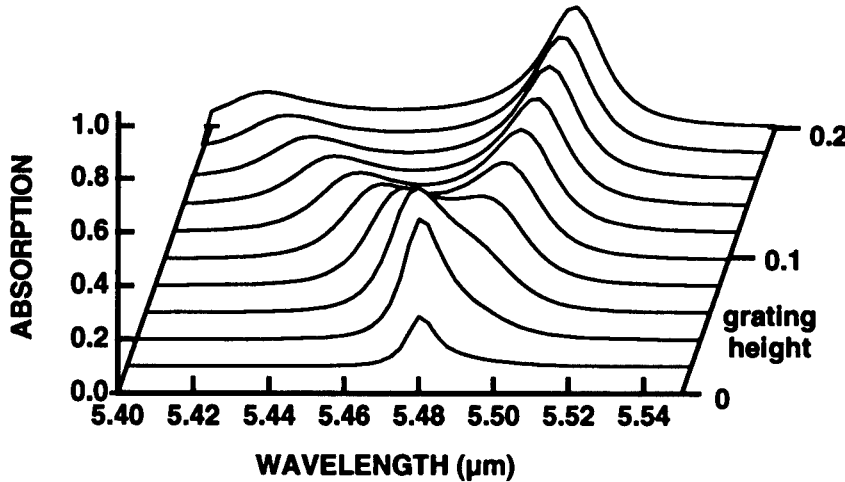
Figure 3: Calculated absorption spectrum in a grated cavity as a function of grating height. The mirrors are the same as in Fig. 2. The grating parameters are (d, c/d) = (1.865 μm, 0.5). The cavity length equals 2.65 μm. Other parameters are as in Figure 1.

RABI SPLITTING

Let us now push the parameters to make splittings between optical modes and the ISBT observable. It is necessary that the FWHM of the electronic transition be equal to or smaller than that of optical modes and smaller than the coupling energy. Choosing a geometry where we observe a splitting between optical modes, the latter condition will be satisfied if the former

one is. We thus have to satisfy the condition that the electronic FWHM is smaller than the cavity mode width. A mirror reflectivity of 0.9 gives a finesse of 30 and a Q factor of 130. The cavity mode width thus equals $\lambda/130=0.042$ μm or 1.7 meV. As a result, a Rabi splitting involving the ISBT and the cavity mode should be observed if one could reduce the FWHM of the ISBT to 1.7 meV. This implies a long coherence time, longer than what has ever been observed for ISBT in quantum wells. At present, it seems unrealistic that an ISBT Rabi splitting could be observed in the grated microcavity. For the simulation, let us suppose that a FWHM as small as 1 meV can be reached. We calculated the absorption in the cavity described above. We increased the doping to 2×10^{10} cm^{-2}. The grating parametrs are d= 1.865 μm, c/d= 0.5 and h= 0.1 μm. Three CaF$_2$/ZnSe periods are used. The cavity length varies from 2.61 to 2.70 μm. We present the result in Fig. 4. As the cavity length increases, the cavity mode resonance wavelength increases from 5.4 to 5.55 μm. The grating mode is around λ= 5.45 μm, almost independent of the cavity length, while the ISBT peaks at λ= 5.50 μm. When L increases, we first observe an anticrossing of the grating and cavity modes that occurs for L $\approx$ 2.65 μm. Then, we observe the splitting between the cavity mode and the ISBT for L $\approx$ 2.68 μm. This one is a Rabi splitting. In other words, for these cavity parameters, one would observe an oscillatory energy transfer from the quantum wells to the cavity mode. This transfer is not direct as it implies the transfer via the grating mode.
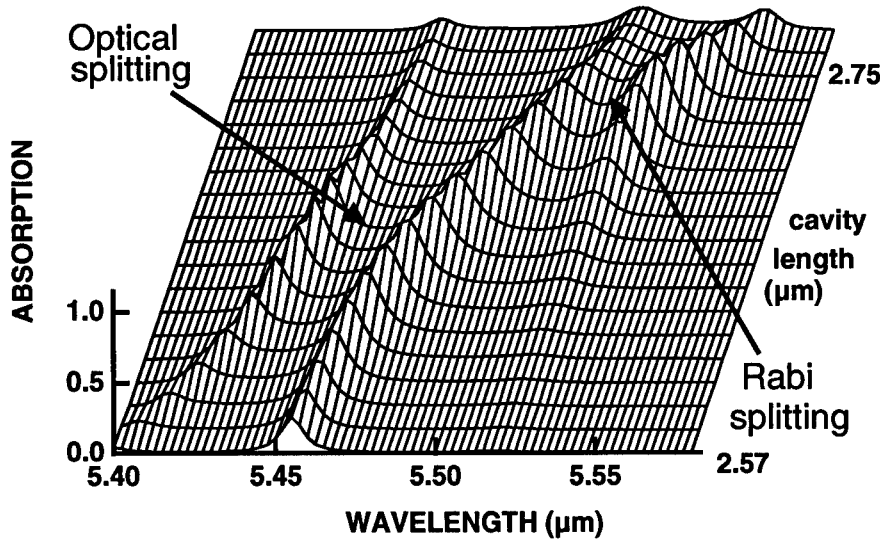
Figure 4: Calculated absorption spectrum in a grated cavity as a function of cavity length. Top and bottom mirrors are made of 3 n$_1$/n$_2$ periods with n$_1$=1.4 and n$_2$=2.43. The grating parameters are (d, c/d, h)=(1.865 μm, 0.5, 0.1 μm). The FWHM of the intersubband transition is 1 meV. The doping density is equal to 2×10^{10} cm^{-2}.

CONCLUSION

The use of grated microcavities for ISBT had been proposed previously[12]. In this paper, we have discussed specific features associated with the coupling between cavity, grating and electronic modes. We have calculated splittings between optical modes that should be observable experimentally. We have verified the criteria for the strong coupling regime where the mode anticrossing appears. In this anticrossing region, quantum wells will absorb or emit photons that are bouncing back and forth from the cavity to the grating mode. In the case of emission for instance, the spontaneous emission lifetime can be reduced. However, it still remains in the regime of a damped oscillator. On the other hand, for ideal unrealistic ISBT parameters, we also calculated a splitting between the ISBT and the cavity modes. In this case, the ISBT considered as an oscillator is not in a damped regime anymore but energy should be transfered between the wells and the cavity at the Rabi frequency. With the present day values of ISBT coherence time, this cannot be experimentally observed.

ACKNOWLEDGMENTS:

REFERENCES

[1] E. Rosencher, B. Vinter, and B. F. Levine, eds., *Intersubband Transitions in Quantum Wells* (Plenum, New York, 1992).
[2] H. C. Liu, B. F. Levine, and J. Y. Andersson, *Quantum Well Intersubband Transitions: Physics and Devices* (Kluwer, Dordrecht, 1994).
[3] V. Berger, N. Vodjdani, B. Vinter, D. Delacourt, E. Dupont, E. Costard, D. Papillon, E. Böckenhoff, and J. P. Schnell, in *Intersubband Transitions in Quantum Wells* E. Rosencher, B. Vinter, and B. F. Levine, eds. (Plenum, London, 1992) p. 133.
[4] R. P. Karunasiri, Y. J. Mii, and K. L. Wang, IEEE Electron Device Lett. **EDL-11**, 227 (1990).
[5] B. F. Levine, J. Appl. Phys. **74**, R1 (1993).
[6] J. Faist, F. Capasso, D. L. Sivco, C. Sirtori, A. L. Hutchinson, and A. Y. Cho, Science **264**, 553 (1994).
[7] J. Y. Andersson and L. Lundqvist, J.Appl.Phys. **71**, 3600 (1992).
[8] J. Y. Duboz and V. Berger, submitted to Appl. Phys. Lett. (1996).
[9] E. Burstein and C. Weisbuch, eds., *Confined Electrons and Photons* (Plenum, New York, 1995).
[10] M. S. Ünlu and S. Strite, J. Appl. Phys. **78**, 607 (1995).
[11] R. P. Stanley, R. Houdré, U. Oesterle, M. Gailhanou, and M. Illegems, Appl. Phys. Lett. **65**, 1883 (1994).
[12] J. Y. Duboz, J. Appl. Phys. **to be published**, (1996).
[13] C. Weisbuch, M. Nishioka, A. Ishikawa, and Y. Arakawa, Phys. Rev. Lett. **69**, 3314 (1992).
[14] Y. Zhu, D. J. Gauthier, S. E. Morin, Q. Wu, H. J. Carmichael, and T. W. Mossberg, Phys. Rev. Lett. **64**, 2499 (1990).

EMISSION EFFICIENCY IN InAs LEDs CONTROLLED BY SURFACE RECOMBINATION

M J Kane, G Braithwaite[*], M T Emeny, D Lee, T Martin and D R Wight
Defence Research Agency, St Andrews Rd Malvern Worcs, WR14 3PS U.K.
[*]AMG Systems Ltd Biggleswade SG18 8QB U.K.

ABSTRACT

In this paper, light emitting diodes (LEDs) are used to study the recombination dynamics of minority electrons in p type InAs. The LEDs operate through injecting electrons into p type material with a free surface. When surface recombination is dominant, the output of the LEDs is shown to depend only on the strength of the radiative recombination and not on its efficiency. When surface recombination is not dominant, the dependence of the LED efficiency on the thickness of the active layer is analysed to give the minority carrier diffusion lengths and recombination efficiencies. The electron diffusion length is shown to be 3 ± 0.5 μm in 5×10^{18} cm^{-3} p type InAs and 6 ± 1 μm in 2×10^{18} cm^{-3} p type material. An upper limit of $\sim2.1\times10^{-28}$ cm^{6}s^{-1} is deduced for the total Auger recombination rate constant in p type material.

INTRODUCTION

Light emitting diodes (LEDs) in the visible and near infra-red have been available as cheap commodity products for many years, after extensive research and development.[1] This research has led to their operation being well understood. In contrast, the operation of LEDs in the mid infra-red (λ>2μm) is much less well understood. One of the reasons that this understanding is poorer is that the recombination dynamics in the relevant materials have been studied in far less detail than in the wider gap materials. A major issue with narrow gap materials is that there are intrinsic non radiative (Auger) processes which may limit their radiative recombination efficiency.

This paper presents an analysis of the recombination dynamics in p type InAs which is obtained from an experimental study of InAs LEDs (λ_{peak}~3.45 μm). Before details of the physics of bulk radiative and non radiative processes can be studied in LEDs, effects such as surface recombination and re-absorption of the emitted light must analysed and accounted for. The major part of this paper is an analysis which shows how to account for these effects and extract quantitative details of the underlying physics.

THEORY

Bergh and Dean[1] described a model for the output efficiency of an LED where the effects of surface recombination were taken in to account, but were relatively minor. In this paper we will present a model for the operation of an LED with strong surface recombination. This full teatment of surface recombination shows up some unexpected consequences, not described in reference 1, for the way in which the output power of the LED depends on its materials parameters.

The LED model considers the diffusive flow of minority carriers injected into an active region extending in the x direction, with injection at x=L and a free surface at x=0. The injected electron (or hole) density $n(x)$ is governed by the diffusion equation

$$D\frac{d^2n}{dx^2} = \frac{n}{\tau} \qquad (1)$$

where D is the diffusion constant and τ is the bulk carrier lifetime. The boundary conditions are (i):

$$D\frac{dn}{dx} = Sn \qquad (2)$$

at x=0, where S is the surface recombination velocity and (ii):

$$D\frac{dn}{dx} = J \tag{3}$$

at x=L, where J is the rate of carrier injection. The solution to equation (1) has the form

$$n(x) = A\exp\left(\frac{x}{L_D}\right) + B\exp\left(-\frac{x}{L_D}\right) \tag{4}$$

where A and B are determined from the boundary conditions in the usual manner.

The rate at which photons are generated in the structure is $\eta n(x)/\tau$ where η is the radiative recombination efficiency of the active region. η can be written as τ/τ_{rad} where τ_{rad} is the radiative lifetime. If light is extracted through the junction plane at x=L and there is re-absorption of the light with absorption coefficient α, the total output quantum efficiency of the LED (at the junction plane), E, is given by

$$E = \int_0^L \frac{\eta n(x)\exp(-(L-x)\alpha)}{J\tau}dx \tag{5}$$

(The InAs active layer has a refractive index ~3.5 (θ_c~18°) so that the implicit assumption in (5) that all light travels through the active layer normal to the surface is justified. The model also assumes that all light is emitted towards the junction. The correction factor that allows for front and back emission is included below with the factor that allows for the critical angle

The full expression for E is straightforward to derive and the derivation will not be presented here. Instead we will consider the results obtained in two illustrative special cases.

(i) No absorption, active layer thickness << minority carrier diffusion length and infinite surface recombination velocity.

Boundary condition (2) reduces to n(0)=0 and the injected electron density is given by

$$n(x) = \frac{JL_D\sinh\left(\frac{x}{L_D}\right)}{D\cosh\left(\frac{L}{L_D}\right)} \tag{6}$$

The efficiency is then given by

$$E = \eta\left(1 - \text{sech}(\frac{L}{L_D})\right) \tag{7}$$

When L_D>>L (7) reduces to

$$E = \frac{\eta L^2}{2L_D^2} = \frac{L^2}{2D\tau_{rad}} = \frac{L^2}{2L_{D,rad}^2} \tag{8}$$

where $L_{D,rad}=L_D/\eta^{\frac{1}{2}}=(D\tau_{rad})^{\frac{1}{2}}$. (From hereon this quantity will be called the radiative diffusion length.) In this case, the efficiency depends only on the radiative rate constant ($1/\tau_{rad}$) and not on the radiative efficiency. (Changes in the radiative efficiency of the material are met by changes in the surface recombination rate and not by changes in the radiative recombination rate.)

(ii) Active layer thickness much greater than the diffusion length

The surface recombination does not influence the carrier distribution and

$$n(x) = \frac{JL_D}{D}\exp\left(\frac{x-L}{L_D}\right) \tag{9}$$

the efficiency E is given by

$$E = \eta(1 + \alpha L_D)^{-1} \qquad (10)$$

when $\alpha L \gg 1$. The absorption coefficient in InAs at the peak of the LED generation spectrum (3.42 μm) is[2,3] ~0.21 μm^{-1}. The output efficiency will be half the bulk generation efficiency if the diffusion length is <~5 μm and the active layer thickness significantly thicker than 5 μm.

These two special cases are the limits of the situations considered in detail in the experimental results section below. When analysing experimental results, the active layer thicknesses and absorption coefficients are known, so that the full expression for equation (5) will have two unknown parameters; the diffusion length L_D and internal radiative efficiency η. Analysis of the dependence of the output efficiency on thickness allows L_D and η to be determined provided that the range of thicknesses extends to ~2L_D. Knowledge of L_D and η and their dependences on the doping density allows some deductions to be made about the radiative and non radiative recombination mechanisms.

EXPERIMENTAL DETAILS

The device structures studied here are grown on n type InAs substrates, doped to 2x10^{18} cm^{-3} and 500 μm thick. The band gap of the substrates is up-shifted by ~150 meV by the Moss-Burstein Shift. The diodes consist of a 1 μm thick n-type region Si doped to 10^{18} cm^{-3} and a top Be doped p-type region with a doping density which is varied between 5x10^{16} and 5x10^{18} cm^{-3}. (See table 1 below.) The structures were grown by molecular beam epitaxy. The junction configuration (high n and moderate to high p) ensures that the forward bias current is essentially carried by electrons injected in to the p type material. This sense of junction also ensures that these electrons have a clearly positioned boundary that terminates the minority carrier flow, which would not be the case, if electrons were injected into p type material grown on a p type substrate.

Table 1 Details of the InAs p-n junctions

Structure	p doping level (cm^{-3})	p layer thickness (μm)	Output efficiency (μW/A)	Radiative diffusion length (μm)
A	5x10^{16}	6	3	87
B	1.5x10^{17}	6	10	47
C	5x10^{17}	6	32	26.3
D	10^{18}	6	40	23.5
E	2x10^{18}	6	60	-
F	2x10^{18}	12	94	16.3
G	5x10^{18}	10	55	13.4

Structures C D E and F have a 2000 Å top contact layer doped to 5x10^{18} cm^{-3}. Structures G also has an additional 1 μm thick p layer doped at 5x10^{16} cm^{-3} between the n layer and the heavily doped p layer in order to suppress tunnel currents.

The epitaxial junctions are processed into mesa diodes with diameters varying between 100 and 400 μm using conventional semiconductor technology. The top surface of the mesa is completely covered in a metallic contact. The light output of the diodes is measured through the substrate and corrected for substrate absorption. The metal contact is assumed to give a large (essentially infinite) surface recombination velocity. No evidence to contradict this assumption was found in any of the experiments.

Absolute output powers were obtained by integrating the LED's polar diagram. This was measured at a single current using a calibrated detector and no other optics, in order to eliminate systematic errors. Detailed light-current characteristics were measured over a wide range of currents in an uncalibrated system with fast optics which give a higher dynamic range. The relative values obtained in this way were converted to absolute measurements using this single reference point.

RESULTS AND ANALYSIS

The output efficiency of devices made from all of the structures were measured for currents varying between 10^{-5}A and 10^{-1}A in the 100 to 400 μm devices. The output efficency was found to be essentially independent of current, except for the smallest devices and largest currents. The fourth column in table 1 shows the output efficiency measured through the substrate in the low drive limit for all of the device structures.

Figure 1 shows the output powers of structures E and F, and G as a function of active layer thickness. The active layer thickness was varied after the structures were grown by wet chemical etching. The solid lines in figure 1 are fits to equation (5) obtained using L_D and η as fitting parameters as described above.
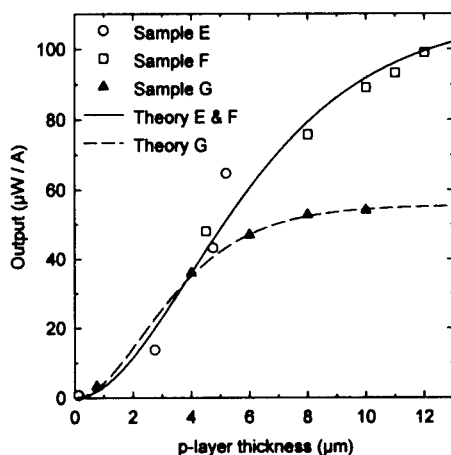
Figure 1 Ouput efficiency versus active layer thickness for InAs LEDs with p type active layer doping densities of 2×10^{18} (structures E and F) and 5×10^{18} cm^{-3} (structure G).

The three other, fixed, inputs needed to obtain the fits are as follows:

(i) InAs has a refractive index[4], n_r, of 3.5 which results in a correction factor between the internal and external quantum efficiencies[5] of $\sim 1/(n_r(n_r+1)^2)$ ($\sim 1/71$ in this case). This factor relates the power extracted from a single face to the total internally generated power.

(ii) The 500 μm thick substrate doped n type to a level of 2×10^{18} cm^{-3} has a cut off wavelength of 3 μm because of the Moss-Burstein shifted band edge and a maximum transmision of 50% because of free carrier absorption. A detailed integration of the spectrum measured through the substrate and the surface spectrum obtained from a thin device, which is taken to be the generated spectrum, indicates that the output (in W/A) must be divided by a factor of 0.13 to give the quantum efficiency at the junction plane of the LED. (This factor must be used with the factor of 1/71 above.)

(iii) The correction for reabsorption in the active layer is applied at the peak of the generated spectrum, 3.42 μm. At this wavelength the absorption coefficient[2,3] is 0.21 μm^{-1}.

132

The best fits are obtained with $L_D=6\pm1$ μm and $\eta=0.135$ when $[p]=2\times10^{18}$ cm^{-3} (structures E &F) and $L_D=3.1\pm0.5$ μm and $\eta=0.05$ when $[p]=5\times10^{18}$ cm^{-3} (Structure G).

The results obtained for structures E to G, suggest that in structures A to D the minority carrier diffusion lengths will be much greater than the thickness of the active layers (6 μm) and that the output of the LED will be determined solely by the radiative diffusion length and not by the internal efficiency. The active layers in these devices have thicknesses comparable to the absorption length at the peak of the emission and an expression derived from equation (5) that is rather more complicated than equation (8) must be used to analyse the data fully. The radiative diffusion lengths that are deduced in this way are shown in the fourth column of table 1.

The sensitivity of the LED output to the radiative efficiency of the active layer has been calculated for structure D, with the assumption of infinite surface recombination velocity and a constant radiative diffusion length of 23.5 μm. The output of the LED decreases by about 10% as the internal efficiency of the active material drops from 1 to 0.2, verfying the statement that the LED output is essentially independent of the internal efficiency.

It is estimated that about 65% of the light generated at the emission spectrum peak escapes from a 6 μm thick active layer so that photon recycling cannot cause a major perturbation of the analysis of such devices whatever the internal efficiency. In the thicker devices, the internal efficiency is sufficiently low, <14%, so that photon re-cycling will again not be of major significance.

Figure 2 shows the diffusion lengths and radiative equivalent diffusion lengths derived from the LED analysis as a function of doping density.
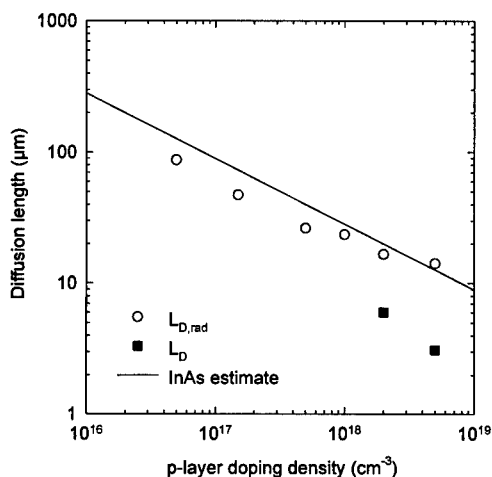
Figure 2 Diffusion lengths (L_D) and radiative diffusion lengths ($L_{D,rad}$) in p type InAs.

DISCUSSION

The radiative equivalent diffusion length in InAs can be estimated using an argument based on: the diffusion lengths measured in GaAs[6]; van Roosbroeck and Shockley's treatment of radiative lifetimes in semiconductors and a scaling argument for the variation of minority carrier diffusion constant from material to material. In GaAs[6] the diffusion lengths of minority electrons in p type material is given by an expression of the form $A_L/p^{\frac{1}{4}}$ where A_L is $\sim1.26\times10^{10}$ μmcm$^{-3/2}$ so that L_D is in microns if p is in cm^{-3}. The diffusion length scales as the square root of the product of the diffusion

constant and the carrier lifetime. Using the band edge absorption data of Dixon and Ellis[2] the radiative recombination rate constant (B) for electrons in p type InAs is estimated to be 5.7×10^{-11} $s^{-1}cm^{-3}$ compared to 10^{-10} $s^{-1}cm^{-3}$ in GaAs. The diffusion constant is estimated from the mobility using the Einstein relation. The minority electron mobility is taken to scale inversely with the electron mass. (The masses of the heavy holes in InAs and GaAs are similar so that the screening of electron scattering by the holes is taken to have the same magnitude in InAs as in GaAs.) The ratio of the electron masses in InAs and GaAs is ~3. Taken together, these arguments give a value of 2.82×10^{10} $\mu m cm^{-3/2}$ for A_L in InAs. This estimate of the radiative diffusion length is shown as a solid line in figure 2. Reasonable agreement is obtained between the experimental values and estimated values. Figure 2 also shows the diffusion length at the two doping densities where this was determinable.

The internal efficiencies of the InAs active material allow an upper limit for the rate constant of Auger recombination in p type material to be estimated. In the presence of radiative recombination and hole Auger processes only, the internal efficiency is given by an expression of the form

$$\eta = \left(1 + \frac{C_p p}{B}\right)^{-1} \qquad (11)$$

where C_p is the total hole Auger recombination rate constant (defined[7] such that the Auger limited recombination time is $1/C_p p^2$) and B is the radiative rate constant. C_p is the sum of the rate constants for all Auger processes involving two holes in the initial state. The most important of these are expected to be the CHLH and CHSH processes using the notation defined in reference 8. Using the value for B of given above with the measured values of η, a value of $(2.1 \pm 0.2) \times 10^{-28}$ $cm^6 s^{-1}$ is deduced for C_p. The occurrence of other non radiative processes occurring simultaneously with the Auger recombination cannot be excluded so that this value of the rate constant must be regarded as an upper limit. The value of C_p has previously been calculated from first principles by Takeshima[7] who obtained a value of 2×10^{-27} $cm^6 s^{-1}$. The measured value is much smaller than this calulated value.

CONCLUSIONS

Radiative recombination in p type InAs has been studied through an analysis of InAs LEDs. It is found that when the LED is dominated by surface recombination, the efficiency of the LED depends only on the strength of the radiative recombination and not on the bulk recombination efficiency. The experimentally determined strength of this recombination is compared with estimates based on the known properties of InAs and found to agree well. LEDs that are sufficiently thick not to be dominated by surface recombiation are also studied and the bulk recombination efficiency deduced. These values of efficiency are found to indicate that the combined strengths of the CHHS and CHHL Auger processes are much weaker than would be indicated from the previously available theoretical estimates.

REFERENCES

1 A A Bergh and P J Dean, Light Emitting Diodes (Clarendon Press, London 1976)
2 J. R. Dixon and J. M. Ellis, J. Appl. Phys. 123 1560 (1960)
3 Measurements on p type InAs indicate that the absorption in p InAs at ~3.45 μm is little changed by doping densities up to 5×10^{18} cm^{-3}.
4 Landolt-Bornstein, Numerical Data and Functional relationships in Science and Technology 17a (Springer Verlag Heidelberg 1982)
5 T. S. Moss, G. J. Burrell and B. Ellis, Semiconductor Opto-electronics (Butterworths, London 1973) p 244
6 D R Wight Chapter 1 in M. J. Howes and D. V. Morgan ed. Gallium Arsenide Materials, Devices and Circuits (Wiley Interscience Chichester 1985).
7 M Takeshima, Jap. J. Appl. Phys. 22 491 (1983)
8 A Sugimura J. Appl. Phys. 51 4405 (1980)

CAVITIES FOR INTERSUBBAND TRANSITIONS

V. BERGER*, J-Y DUBOZ*, E. DUCLOUX*, F. LAFON* , I. PAVEL*, P. BOUCAUD**,
O. GAUTHIER-LAFAYE**, F. JULIEN**, A. TCHELNOKOV**, R. PLANEL* * *.
* Laboratoire Central de Recherches, THOMSON-CSF, Domaine de Corbeville, 91400 OR-
SAY Cedex, FRANCE.
** Institut dElectronique Fondamentale, URA CNRS 22, Batiment 220, Université Paris-
Sud, 91405 ORSAY Cedex, FRANCE.
* * * Laboratoire de Microstructures et Microélectronique, CNRS, 196 Av. H. Ravera, 92220
BAGNEUX, FRANCE.

ABSTRACT

The different possible geometries for intersubband transitions in microcavities are dis-
cussed. A consequence of the selection rule governing intersubband transition is the vanish-
ing interaction with the electromagnetic field inside a usual vertical cavity. The geometry
of vertical planar cavities which has been used extensively with interband transitions is
therefore useless in the case of intersubband transitions. Different solutions are reviewed
to overcome this problem. The breakdown of the selection rule in a vertical cavity is first
discussed. This can be done with the use of vertical quantum wells, or thanks to intracavity
diffraction gratings. Second, the use of in plane cavities is discussed. Two solutions are here
envisaged: Whispering gallery modes in microdisk cavities, and efficient etched air/GaAs
Bragg mirrors. Concerning the latter attractive solution, the losses by diffraction into the
substrate are evaluated theoretically and experimentally. The solution of the Maxwell equa-
tions by a finite element method in this three dimensional system shows the great importance
of diffraction. These results are confirmed by waveguided Fourier transform spectroscopy.
To overcome this difficulty, we propose the use of lower refractive index substrates, such as
oxidized AlAs.

INTRODUCTION

The latest developments of efficient light emitters or detectors, modulators or non lin-
ear optical devices, have been achieved largely thanks to the realization of cavities. Let us
quote for example resonant cavity enhanced photodetectors and light emitting diodes[1, 2],
lasers[3, 4, 5] or modulators[6, 7]. Microcavity concepts have also been studied in more
fundamental solid state physics, in atomic physics[8, 9], and quantum optics[10]. As far as
semiconductor heterostructures are concerned, these two aspects of applied and more fun-
damental physics have benefited from cavities and especially from microcavities, which have
been improved with the progress of heterostructure growth techniques. For example, the
vertical cavity surface emitting lasers [3, 4, 5] (VCSELs) have lowered the semiconductor
laser thresholds by several orders of magnitude, reaching now the μA range thanks to the
technological development of oxidized AlAs[11, 12]. On the other hand, vacuum Rabi split-
ting has been observed with cavity polaritons[13, 14], opening the exciting field of strongly
coupled exciton-photon interactions[10]. These two aspects are closely linked since the ulti-

mate performances of the devices will be limited by the quantum nature of light. Enhanced photon confinement for improved efficiencies or spontaneous emission control are also aimed for by more complex structures as whispering gallery cavities[15, 16, 17, 18] or photonic band gap materials(PBGs)[19], which can be viewed as a three-dimensional generalization of planar microcavities[20].

Up to now, the field of intersubband transitions(ISBTs)[21, 22]has not interacted a lot with the community of microcavities. The reason for this is that the selection rule governing ISBTs forbids the interaction between the intersubband dipoles and the resonant electromagnetic field in a planar cavity, since in a conventional planar cavity the electric field is parallel to the layer, and then cannot induce ISBTs. New devices such as quantum well infrared photodetectors[23] or quantum cascade lasers (QCLs)[24] could highly improve their efficiencies by using high Q microcavities. This is particularly important for QCLs which do not present any transparency current[25]. Low threshold and low consuming devices need small cavity volumes and low losses, especially low mirror losses, as in the case of VCSELs. Optically pumped intersubband emitters are in the same situation, since population inversion is also thresholdless at low temperature.[26]. New solutions and new geometries have to be found, more complex than the regular planar microcavity, to overcome the problem of the selection rule. In this article, we review different solutions, and analyze their pros and cons.

VERTICAL CAVITIES

Vertical quantum wells

Originating from the growth developments of quantum wires on nonplanar substrates[27, 28], Vertical Quantum Wells(VQWs) have been fabricated by metalorganic vapor phase epitaxial growth of a single-doped AlGaAs layer on a submicron grating[29]. An example of such VQWs is shown in figure 1. Thanks to this irregular orientation of the QWs, ISBT at normal incidence was demonstrated[29]. This "rotation" of the selection rule opens the possibility of inserting the VQWs in a planar microcavity. Both mirrors could be grown by molecular beam epitaxy; however in that case the very thick $\frac{\lambda}{4}$ layers need a very long growth time. Another possibility is the growth of the bottom mirror only in the GaAs/AlAs system, the top mirror being obtained by the deposition of dielectric stacks.

The drawbacks of this geometry are:
- the impossibility of band gap engineering,
- the poor crystalline quality of the quantum layers.

As a consequence of the simplicity of the self-organized growth of the VQWs, fine control of the band structure is not possible as in the case of the usual planar growth. The ISBT energy can be controlled by changing the growth parameters (Al content of the AlGaAs alloy, temperature and V/III ratio). Apart from this control, complex structures such as asymmetric step or double quantum wells used for non linear frequency conversion[30, 31] or for modulation[32, 33] are not possible. Under special growth conditions, coupled VQWs have been grown, but without control of the exact band structure[34, 35]. It is thus clear that sophisticated structures such as the biased electronic Bragg mirrors used in the QCLs are impossible to grow with this technique. QW infrared photodetectors have a simple band structure, but require good transport properties of the layers, especially the barriers. The growth of the VQWs is obtained in a corner between two [111A] planes, and this results
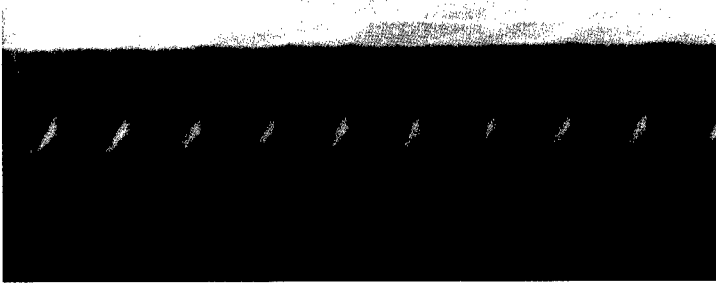
Figure 1: Vertical quantum wells obtained by self-organized growth of a single AlGaAs layer on a V-groove substrate. From [29].

in a great number of dislocations in the vicinity of the VQW, so that very bad transport performances are foreseen. In addition, the two dimensional shape of the barriers (due to the shape of the GaAs grating inside the AlGaAs barriers) is not well suited for the transport between the different VQWs, the carriers being trapped in the substrate, which presents a lower potential than the VQWs themselves.

The conclusion of our analysis is thus that the VQWs cannot be used either for emission or detection. The only possibility is their use in intracavity modulation. The population of the VQWs can be tuned by a Schottky diode[36]. Benefiting from the increase of the optical field inside the microcavity, efficient modulators with a modulation depth near 100% at room temperature seem to be obtainable.

Diffraction gratings in microcavities

The problems due to the selection rule have been overcome by using diffraction gratings, especially for infrared photodetectors[37], where normal incidence was imposed by the focal plane array geometry. Normal incident light is diffracted by the grating in a direction such that ISB absorption is optimized. It was recently shown by one of us that the use of diffraction gratings is not restricted to photodetectors[38]. Indeed, the concept of normal incidence ISBT coupling was generalized to the cases of modulators or emitters. An experimental demonstration of this concept was given with the realization of a grating coupled infrared modulator at normal incidence[39]. Opposite to the case of photodetectors, a transparent phase grating was used and the modulation was observed in the non diffracted order transmitted by the modulator[39]. The coupling with the ISBT was provided through the diffracted modes. The overall effect of the association between the grating and the quantum wells is then essentially a variation of the normal incidence dielectric function. In this experiment, modulation depths were increased by a factor of three compared with the same structure used without grating at Brewster angle. Moreover, these experiments showed the validity of this concept of normal incidence ISBT, which was the basic idea of using ISBTs in microcavities, introduced by Duboz[38]. In the microcavities pictured schematically in figure 2, the grating and the quantum wells are inserted in a planar microcavity, and both
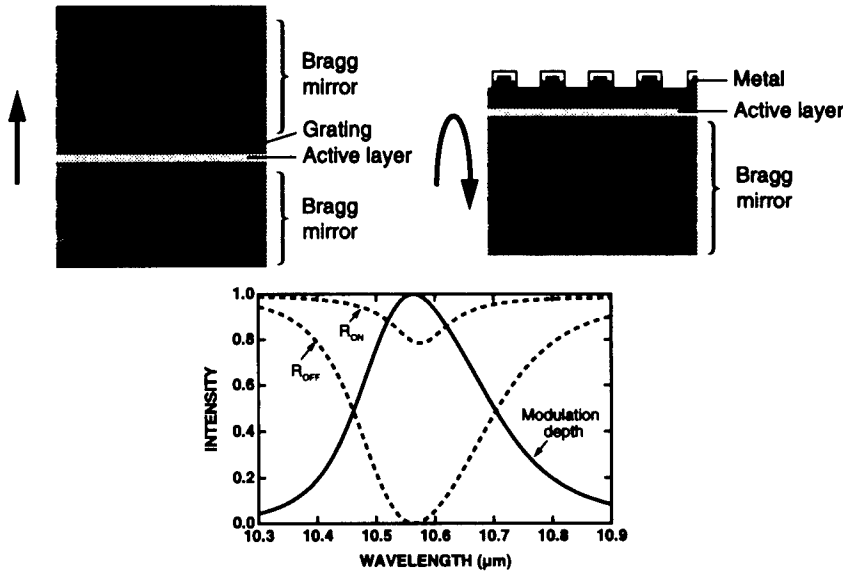
Figure 2: Schematic picture of the diffraction gratings in microcavities. Top left: All di-electric microcavity with two Bragg mirrors. Top right: Metal-dielectric microcavity, used in reflection. Bottom: Calculated modulation depth in a metal-dielectric microcavity. From [38].

the grating and the cavity are resonant with the ISB energy. Calculations were performed for various configurations, for dielectric or metallic gratings, and for infrared detection, emission, or modulation[38]. A simple and efficient structure is obtained for example in a reflection geometry with a metallic grating, the other cavity mirror being an AlAs/GaAs epitaxial Bragg mirror grown below the quantum wells (see figure 2). An example of the efficiency of such a structure is also given in figure 2. It is shown that a modulation depth near 100% is easily obtained, with only 4 $\frac{\lambda}{4}$ layers.

It is clear that this concept is more useful than the insertion of VQWs in a planar cavity, since we can benefit from the possibility of growing complex structures by standard molecular beam epitaxy. However, this solution has also some limitations: The growth of the thick Bragg mirrors, especially for the middle infrared wavelengths, leads to a degradation of the quality of the quantum layers, and the control of their parameters (widths, Al contents) is also decreased[40]. For example, the structure of figure 2 needs a Bragg mirror of 6.7μm total thickness, containing 4 AlAs layers of thickness 0.9μm, which is a challenge for a good quality molecular beam epitaxy. The second and major limitation of this concept is the low possible quality factor of these cavities. As a consequence of the growth difficulties of these very thick structures, only a few Bragg pairs can be grown and the very high finesses that have been realized in the near infrared for exciton photon strong coupling are impossible

in the middle infrared, even with the use of dielectric coatings on one side. The use of a metallic mirror for one side of the cavity adds losses which limit also the maximum possible finesses. The finesses which seem to be feasible in this system are of the order of a few tens[41], which is about two orders of magnitude below what has been realized in the near infrared[42]. This has bad consequence for the use of diffraction gratings in microcavities as far as a VCSEL is concerned, and also for the strong ISB dipole-photon interaction studies.

In a VCSEL, the mirror loss factor in a round trip $\frac{1}{2L}ln(R_1R_2)$ becomes very large due to the short cavity length L. As a consequence, the mirror reflectivities have to be increased by a huge factor to lower the thresholds to values similar to those of edge emitting lasers. This was done with the epitaxial growth of Bragg mirrors of reflectivity greater than 0.999 in the near infrared, but this is impossible in the middle infrared due to the prohibitive growth thicknesses.

In addition, numerical simulations showed that strong coupling régime with ISBTs is also very difficult to achieve in this system[41]. There are two reasons for that: First, the ISBT linewidth has to be smaller than the Rabi frequency, or equivalently the coherence time T_2 of the ISBT has to be greater than the Rabi oscillation time. The Rabi oscillation frequency associated to the ISBT in intracavity square quantum wells is given by:

$$\Omega = \sqrt{\frac{e^2 \rho_s N_{QW} f_{osc} \alpha_g}{\pi^2 \epsilon_0 m^* n^2 L_{cav}}} \tag{1}$$

In this equation, n is the refractive index medium of the cavity, L_{cav} its length. $N_{QW}.\rho_s$ is the total carrier surface density in the system, N_{QW} is the number of QWs and ρ_s their doping density. f_{osc} is the oscillator strength containing the effective mass and α_g describes the non perfect coupling between the quantum wells and the normal incident light through the grating. In practice, $0 \leq \alpha_g \leq 1$ and this factor lowers the oscillator strength. (For example in the structure of reference [39], we have $\alpha_g \approx 0.16$). For a square quantum well, with $f_{osc} \approx 1$, and for a standard value of $\rho_s = 5.10^{11}cm^{-2}$, we get $\hbar\Omega = 0.57\sqrt{N_{QW}\alpha_g}$ meV for a λ cavity. For the observation of the Rabi splitting in an absorption experiment, this Rabi frequency has to be greater than the transition linewidth[43]. Since for modulation doped QWs, the smaller observed linewidths are of the order of 4meV, this requires a number of QWs greater than one hundred. However, with such a high number, the coupling α_g between the grating and the QWs decreases, because of the poor grating efficiency at a long distance for the diffracted modes. In other words, the Rabi frequency depends on N_{QW} in a square root law only for small N_{QW}, and saturates for high N_{QW}. Due to this saturation and to the large ISBT linewidths, the first necessary condition for strong coupling régime ($\Omega > \Gamma_{ISBT}$) is very hard to achieve in these microcavities including diffraction gratings.

A second necessary condition is that the photon lifetime in the cavity be long enough to allow the Rabi oscillations. This is not easy with such large wavelength microcavities with low index contrasts. With a GaAs/AlAs mirror, a quality factor equal to 30 leads to a photon lifetime $\frac{Q}{\omega} = 0.16$ps for a $10\mu m$ wavelength, or equivalently to a cavity linewidth equal to $\Gamma_{cav} = \frac{\hbar\omega}{Q} = 4$meV. In this case, the conclusion is the same as in the above discussion about the ISBT linewidth. Note that slightly larger theoretical Q (of the order of 100) seem to be obtainable with two dielectric Bragg mirrors. It could be sufficient for the condition $\Omega > \Gamma_{ISBT}$. However, in this case, the complexity of the technological process, particularly the planarization of the grating for the top mirror, will make it difficult to realize such high Q cavities. Not high enough Q cavities and not sharp enough transitions, with a Rabi frequency

which cannot be easily increased due to the local nature of the grating coupling: For all these reasons, diffraction gratings in microcavities are not well suited for strong coupling effects.

In conclusion, diffraction gratings in microcavities are certainly a very powerful concept as far as low Q devices are concerned, especially detectors and modulators. However, the requirements for the observation of strong coupling between intersubband dipoles and the mid infrared electromagnetic field as well as the realization of QCLs VCSELs need higher quality factors. They can be obtained only by taking into account the specificity of ISBTs, that is to say the in-plane character of the emission.

IN PLANE CAVITIES

Whispering gallery cavities

Microdisk structures have been demonstrated, resulting in very low thresholds microdisk lasers using electrical or optical pumping[44, 17, 18]. They consist of micron size disk resonators, on a post which provides thermal coupling to the substrate and then avoids heating of the structure. The small size of these devices results in a very small number of guided modes, with only a few high Q modes propagating around the perimeter of the disk. These low loss modes have been called "whispering gallery" modes by analogy to the efficient propagation of sound waves along the walls of the circular whispering gallery of St. Paul Cathedral in London. As a consequence of the high quality factor of these modes and the small cavity volume, the proportion of the total spontaneous emission which is emitted into this mode (the well-known parameter β) is highly enhanced, resulting in low threshold lasers[16]. Microdisk structures are well suited for ISBTs since the optical mode propagates in the plane of the layers. Some of the difficulties that arise for the microdisk structures for interband transitions are much easier to overcome when we deal with ISBTs. First, the losses due to scattering on the edges will be lower thanks to the larger wavelength (in the $5-10\mu m$ range), for a given edge roughness. The difficulty of the technological process is reduced as the wavelength and hence the dimensions are increased, which is important to achieve electrical pumping. The confinement factor is also increased thanks to the air "substrate" for the whispering gallery mode, and the losses are reduced. Recently, Faist et al. realized a quantum cascade microdisk laser with a quality factor $Q \approx 3300$, with a threshold as low as 2.85mA for a $17\mu m$ diameter[18].

These devices are very interesting structures for studying new effects which arise when β approaches the limit of the thresholdless laser, such as nonequilibrium carrier dynamics, anomalous laser linewidth, or photon statisctics[45]. However, as far as a device is concerned, the problem of the extraction efficiency remains very difficult. There is no directional coupling of light out from these microdisks. The attempts of breaking the symmetry of the structure by introducing a defect in the circular disk have increased the amount of light emitted in a given direction[46], however the brillance of these structures remains very poor. This problem is very similar to the problem of coupling between a defect mode (a localized mode) in a photonic band gap material, and an external plane wave, which is the desired output for a device. The transmission spectra of defect modes in photonic band gap materials have always been very low (<-10dB), due to this very bad coupling. All the photonic microstructures need to solve this problem of coupling between a highly localized mode inside the structure and an outside wave well suited for applications, with a large spatial coherence. This is why microdisk lasers have not been integrated in a device up to now. The

last section will deal with the geometry of standard semiconductor lasers, where the light is propagating inside a linear waveguide. This is the case of QCLs, where the mirrors are the cleaved facets of the sample, except the very recent realization of a DFB structure[25]. We will discuss the alternative and exciting solution of etching air/semiconductor Bragg mirrors.

Etched Bragg mirrors cavities

Several groups have tried to produce air/semiconductor Bragg mirrors in waveguides by a simple etching of the waveguide structures[47, 48, 49, 50]. If we compare with a DFB structure (which is essentially the same structure but with a low index contrast in the Bragg mirrors), this geometry has the advantage that the high index contrast gives a large band gap, and therefore the possibility to increase the ratio of spontaneous emission into a single mode, thanks to the inhibition of all other modes in the gain spectrum. In addition, very high reflection coefficients are expected with a small number of etched holes. These structures were therefore studied for reduced threshold possibilities. The etching process is a technological challenge since the required aspect ratios are large for these tiny holes (a quarter wavelength). Up to now, the experimental realizations are not very convincing, diffraction in the substrate dominating the system. In particular, transmission spectra do not show a high transmission inside the "conduction" transmission band (i.e. the high energy side of the Bragg band gap). In addition, the measured cavities always exhibit low transmission levels. This bad coupling between outside and inside the structure could be due to reflection (due to poor mode matching between the outside incident mode and the intracavity localized mode, which is analogous to the problems discussed for microdisks), but also to leakage to the substrate. Useful high Q cavities, with high transmission levels, seem then very difficult to realize due to these losses. It is therefore essential to evaluate the diffraction in a corrugated waveguide.

The perturbation assumptions used in coupled mode theory are not valid in our case, because of the high corrugation (the waveguide can be completely etched through). A complete three-dimensional resolution of Maxwell equations is necessary here. We have developed a code for this purpose, in the frequency domain. In a first step, the two-dimensional fundamental mode of the unetched waveguide is calculated, and then this mode is extrapolated on a three-dimensional mesh of the complete structure. The complete calculation of the
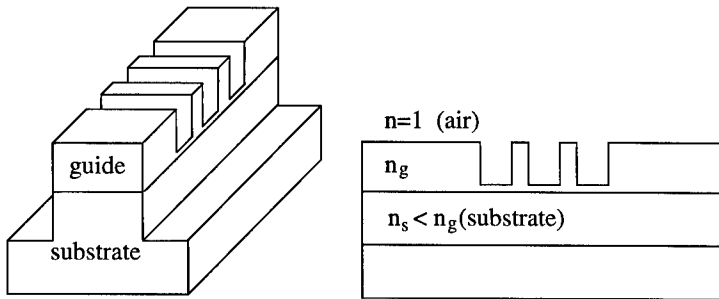
Figure 3: Schematic picture of the Bragg-etched waveguide structures studied numerically.

Figure 4: Left: Incident (from the right) waveguided mode on the etched Bragg mirror, in the weak guiding case. The diffraction in the substrate is very important. (The limit between the substrate and the waveguide core is the horizontal white line in the middle of the figure). Right: Incident waveguided mode on the etched Bragg mirror, in the strong guiding case. The diffraction in the substrate has been highly reduced.

electromagnetic field is then performed in the whole structure by a finite element method. The three-dimensional harmonic Maxwell equations are solved using the combined E-field variational formulation, with first order edge elements. We have observed that the scale of the mesh has to be of the order of one tenth of the wavelength to lower numerical noise to a few percent. This very stringent condition on the mesh period limits the size of the structures that can be studied in a reasonable computing time, the typical limits of size of the studied structures are of the order of $(5\lambda)^3$.

We have estimated the importance of diffraction of the guided modes incident on an etched Bragg structure. Figure 3 shows schematically the structures. Two cases were analyzed: In the first case (the weak guiding case), the structure is a waveguide with a low index contrast between the guiding layer and the substrate. This structure corresponds typically to a GaAs guiding layer (index taken equal to 3.3 in the mid infrared) on an AlAs cladding layer (index equal to 2.9). In the second case (the strong guiding case), the index contrast is high, as for example with a GaAs guiding layer on an oxidized AlAs layer of index 1.6. Indeed, oxidized AlAs (Alox), obtained by lateral oxidation of an epitaxial AlAs layer, is a very low index material which is completely compatible with QW structures, as it was shown with the latest developments of Alox based VCSELs[11, 12].

Our calculations show that the diffraction losses are very important in the weak guiding case, because the confinement of the electromagnetic wave is too shallow. In the case of incomplete etching through the waveguide, (for example figure 4 shows the propagation of the electromagnetic field in a waveguide with a Bragg mirror etched through 3/5 of the waveguide), the transmission bands transmit always less than 10%. In the case of a deep etch (through the substrate), the bad coupling between the different waveguide zones separated by an air layer is sufficient to diffract more than 50% of the electromagnetic field, in the air or in the substrate. It is thus clear that the realization of microcavities using weak waveguides will certainly lead to very poor quality factors.

In the strong guiding case, we have observed that the diffraction into the substrate is considerably reduced. Figure 4(right) is an illustration of the quality of the Bragg reflection. The depth of the etching is identical to that of the weak guiding case also pictured in figure 4(left) (3/5 of the waveguide). We now see that the diffracted intensity is very low, and was
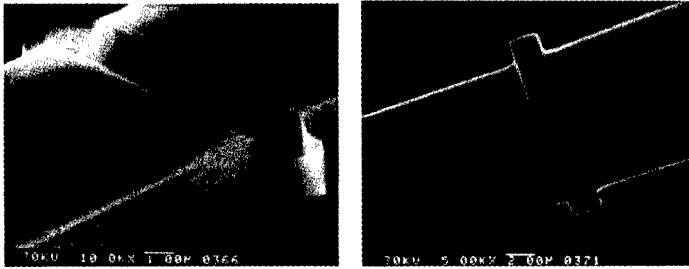
Figure 5: SEM picture of the $\frac{\lambda}{4}$ etched layer across the infrared waveguide.
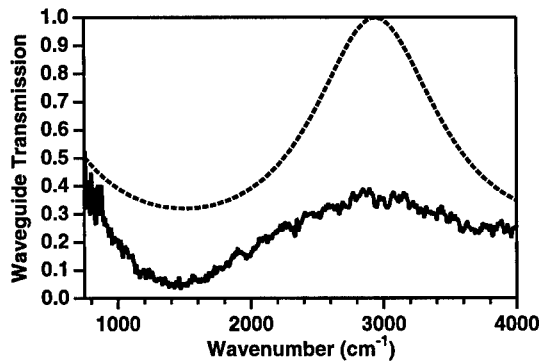
Figure 6: Waveguided Fourier transform infrared spectroscopy of the sample of figure 5. Dotted line: Theoretical transmission using a simple effective index model.

limited to the numerical noise of our computed calculations. We have also calculated the transmission of these Bragg mirrors in the "valence" and in the "conduction" transmission bands, and in both cases the diffraction outside the waveguide was negligible. However, in the case of a deep etch, even in the strong guiding case the diffraction was important. We can now express the following empirical rule: If the width of the etched waveguide is still large enough to allow a guided mode (situation of under cut-off etching), then the mode can be transmitted from one waveguide layer to the next one with a low diffraction and the resulting Bragg mirror presents low diffraction losses. In the other case, if no guided mode exists inside the etched layer (situation of over cut-off etching), the diffraction is important and the Bragg mirrors are useless for high Q cavity applications. In the favorable case of under cut-off etching, it is clear that the bandwidth of the Bragg mirror will be decreased with respect to an ideal Air/GaAs Bragg mirror, because of the decrease of the index contrast. Indeed, in that case, the effective index theory is found to give good results for the spectral position and width of the forbidden bands: this width is given by the ratio between the two

143

effective indexes, in the unetched and etched layers.

We have checked experimentally the importance of the diffraction in the weak guiding case. Mid infrared waveguides were realized by reactive ion etching of a $5\mu m$ waveguide on a $3\mu m$ $Al_{0.9}Ga_{0.1}As$ cladding layer. A simple etch was realized in the middle of the waveguide, providing a $2\mu m$ air opening, as shown in figure 5. This layer was defined by electron beam lithography, whereas the waveguide was defined by optical lithography, in a second technological step. Figure 6 shows the transmission of the final structure together with the simulated transmission in the "non diffracting" case. The latter transmission is calculated with a simple effective index model. The position of the maxima and minima are in good agreement and are characteristic of a $\frac{\lambda}{4}$ layer[51]. However, in the experiment, the level of transmission is low with respect to the theoretical expectations. These losses are due to diffraction, and confirm our theoretical discussion.

CONCLUSION

The realization of high Q microcavities for intersubband transitions is not an easy task, due to:

 - the stringent selection rule which makes the intersubband transitions not well suited for usual vertical cavities,

 - the large wavelengths in the mid infrared, which are not compatible with large numbers of Bragg pairs.

The possibilities of vertical quantum wells are limited, since no band gap engineering is possible in these structures. Intracavity diffraction gratings are interesting for low Q device applications; however neither vertical cavity surface emitting lasers nor strong coupling dipole-field interactions are possible. In opposite, the highest Q are obtained with whispering gallery modes in microdisks; however the coupling between the electromagnetic field inside these structures and usable optical beams outside is very inefficient. We have theoretically and experimentally studied the diffraction losses in etched Bragg mirrors in waveguides. We have shown this diffraction to be very important and to prevent the production of high Q cavities in the weak guiding case. We propose the use of a very low index confining layer such as Alox (strong guiding case), to suppress diffraction losses, together with a partial etch of the guiding layer. However, few outstanding problems have to be studied to validate such a structure: We have neglected the absorption losses in oxidized AlAs. The mid infrared properties of this new material are not well known and have to be measured. A second problem may arise from additional losses introduced by the technological defects coming from the oxidation step. These two problems are under investigation.

ACKNOWLEDGMENTS

References

[1] M. S. Ünlü, J. Appl. Phys. **78**, 607 (1995).

[2] N. Hunt and E. F. Schubert, in *Microcavities and Photonic bandgaps: Physics and Applications*, edited by J. Rarity and C. Weisbuch (Kluwer Academic Publishers, 1996).

[3] J. L. Jewell *et al.*, IEEE J. of Quant. Elec. **27**, 1332 (1991).

[4] J. L. Jewell, J. P. Harbison, and A. Scherer, Scientific American **November 91**, 56 (1991).

[5] E. Hadji, J. Bleuse, N. Magnea, and J. Pautrat, Appl. Phys. Lett. **68**, 2480 (1996).

[6] R. H. Yan, R. J. Simes, and L. A. Coldren, IEEE Photonics Tech. Lett. **1**, 273 (1989).

[7] M. Whitehead, A. Rivers, and G. Parry, El. Lett. **26**, 1588 (1990).

[8] P. Berman, *Cavity Quantum Electrodynamics* (Academic Press, Boston, 1994).

[9] S. Haroche and J. Raimond, in *Advances in Atomic and Molecular Physics Vol XX*, edited by D. Bates and B. Bederson (Academic Press, New York, 1985).

[10] *Microcavities and Photonic Band Gaps: Physics and Applications*, edited by J. Rarity and C. Weisbuch (Kluwer Academic Publishers, Dordrecht, 1996).

[11] Y. Hayashi *et al.*, El. Lett. **31**, 560 (1995).

[12] G. M. Yang, M. H. MacDougal, and P. Dapkus, Electron. Lett. **31**, 886 (1995).

[13] C. Weisbuch, M. Nishioka, A. Ishikawa, and Y. Arakawa, Phys. Rev. Lett. **69**, 3314 (1992).

[14] R. Houdré *et al.*, Phys. Rev. Lett. **73**, 2043 (1994).

[15] S. L. McCall *et al.*, Appl. Phys. Lett. **60**, 289 (1992).

[16] Y. Yamamoto and R. E. Slusher, Phys. Today **june 93**, 66 (1993).

[17] U. Mohideen *et al.*, Appl. Phys. Lett. **64**, 1911 (1994).

[18] J. Faist *et al.*, Appl. Phys. Lett. **69**, 2456 (1996).

[19] J. D. Joannopoulos, R. D. Meade, and J. N. Winn, *Photonic Crystals* (Princeton University Press, Princeton, 1995).

[20] E. Yablonovitch, Nature **383**, 665 (1996).

[21] E. Rosencher, B. Vinter, and B. Levine, *Intersubband Transitions in Quantum Wells* (Plenum, New York, 1992).

[22] H. C. Liu, B. F. Levine, and J. Y. Andersson, *Quantum Well Intersubband Transition Physics and Devices* (Plenum, Dordrecht, 1994).

[23] B. F. Levine, J. of Appl. Phys. **74**, R1 (1993).

[24] J. Faist *et al.*, Science **264**, 553 (1994).

[25] C. Sirtori, private communication.

[26] O. Gauthier-Lafaye *et al.*, submitted to Phys. Rev. Lett. .

[27] M. Walther *et al.*, Appl. Phys. Lett. **60**, 521 (1991).

[28] G. Vermeire *et al.*, J. of Crystal Growth **124**, 513 (1992).

[29] V. Berger, G. Vermeire, P. Demeester, and C. Weisbuch, Appl. Phys. Lett. **66**, 218 (1995).

[30] E. Rosencher and P. Bois, Phys. Rev.B **44**, 11315 (1991).

[31] C. Sirtori, F. Capasso, D. L. Sivco, and A. Y. Cho, Appl. Phys. Lett. **68**, 1010 (1992).

[32] R. P. Karunasiri, Y. J. Mii, and K. L. Wang, IEEE Electron Device Lett. **11**, 227 (1990).

[33] V. Berger *et al.*, Appl. Phys. Lett. **61**, 1898 (1992).

[34] G. Biasiol *et al.*, Appl. Phys. Lett. **69**, 2710 (1996).

[35] E. Martinet and E. Kapon, private communication.

[36] V. Berger, N. Vodjdani, D. Delacourt, and J. Schnell, Appl. Phys. Lett. **68**, 1904 (1996).

[37] J. Y. Anderson and L. Lundqvist, J. Appl. Phys. **71**, 3600 (1991).

[38] J. Y. Duboz, J. of Appl. Phys. to be published (1996).

[39] J. Y. Duboz *et al.*, Appl. Phys. Lett. to be published (1997).

[40] J. Nagle, private communication.

[41] J. Y. Duboz, in this volume .

[42] R. P. Stanley *et al.*, Appl. Phys. Lett. **65**, 1883 (1994).

[43] R. P. Stanley *et al.*, in *Microcavities and Photonic bandgaps: Physics and Applications*, edited by J. Rarity and C. Weisbuch (Kluwer Academic Publishers, 1996).

[44] R. E. Slusher *et al.*, Appl. Phys. Lett. **63**, 1310 (1993).

[45] U. Mohideen and R. Slusher, in *Microcavities and Photonic bandgaps: Physics and Applications*, edited by J. Rarity and C. Weisbuch (Kluwer Academic Publishers, 1996).

[46] D. Y. Chu *et al.*, Appl. Phys. Lett. **65**, 3167 (1994).

[47] K.-C. Shin *et al.*, IEEE Photon. Technol. Lett. **7**, 1119 (1995).

[48] T. Baba *et al.*, in *Int. Conf. Solid State Devices and Materials* (Osaka, 1995).

[49] R. P. Espinolada *et al.*, Appl. Phys. Lett. **68**, 241 (1996).

[50] T. F. Krauss and R. M. D. L. Rue, Appl. Phys. Lett. **68**, 1613 (1996).

[51] M. Born and E. Wolf, *Principle of Optics* (Pergamon Press, Oxford, 1980).

SINGLE MODE OPERATION OF IMPURITY-INDUCED DISORDERING LARGE AREA VERTICAL CAVITY SURFACE EMITTING LASERS

C.W. Lo and S.F. Yu
The University of Hong Kong, Department of Electrical and Electronic Engineering, Pokfulam Road, Hong Kong.

ABSTRACT

Vertical-cavity surface-emitting lasers (VCSELs) with suitable interdiffusion quantum wells profile by the use of selective impurity-induced disordering is proposed for high power single mode operation in large area devices. It is shown that the transverse optical confinement in the quantum well active region formed by the diffusion profile counteracts the influence of carrier spatial hole burning for VCSELs biased at high injection current. Results indicate that a single mode operation can be maintained in VCSELs with the diameter of core region equal to 50μm.

INTRODUCTION

VCSELs are becoming one of the promising devices for various applications in high bit-rate optical fiber communication system, optical parallel processing and optical interconnections. This is because of their unique features such as small circular output beam divergence, single longitudinal mode operation with low threshold currents less than 1mA and high relaxation oscillation frequency [1-3]. However, the excitation of higher order transverse modes degrades VCSELs' performance in high speed optical communication systems and should be avoided. To achieve the above applications, a single fundamental transverse mode operation is essential due to the elimination of noise and instability and the ease of higher coupling efficiency with optical fibers [4]. In index guided VCSELs, the number of modes depends on their transverse dimensions and the refractive index profile between the core and cladding regions. In gain guided VCSELs, the fundamental transverse mode operation can be maintained for large area devices. However, higher order transverse modes are excited with high injection currents due to spatial hole burning effect within the core region [5]. Therefore, it is necessary to suppress the multiple transverse modes in VCSELs at high output power for large area devices.

Concentration of impurity varies the refractive index and carrier diffusion rate of diffused quantum well (DFQW) material [6]. A defined pattern of refractive index profile can be obtained by selective area disordering of quantum well materials and this technique can be utilized for the fabrication of optical devices such as lasers and modulators [7]. In this paper, single mode operation of large area VCSELs using selective disordering of quantum well active region is studied theoretically.

LASER STRUCTURE

The schematic of VCSEL after selective impurity-induced disordering is shown in figure 1. It is assumed that the active layer consists of 20 $Al_{0.3}Ga_{0.7}As$/GaAs quantum wells with well width and barrier thickness of 100Å and 100Å, respectively. In order to achieve a single mode operation of VCSELs, the transverse optical confinement in the quantum well active region is produced by the use of selective impurity-induced disordering technique. The selective injection of impurities can be done by using a circular mask located at the center of the core region to

shelter from the ion implantation. A suitable distribution of impurity along the transverse direction of impurity can be obtained with appropriated annealing time and temperature. Therefore, dimension of mask, implantation energy, annealing temperature and time are the parameters to optimized the gain margin of VCSELs.

LASER MODEL

The multimode rate equation model of VCSEL used in our analysis are given as follows [8]

$$\frac{\partial N(r,t)}{\partial t} = \frac{J(r,t)}{qd_k} - \frac{N(r,t)}{\tau} + D\frac{1}{r}\frac{\partial}{\partial r}\left(r\frac{\partial N(r,t)}{\partial r}\right) - v_g\Gamma_z G(r,t)\sum_i |E_i(r)|^2 S_i(t) \qquad (1)$$

$$\frac{\partial S_i(t)}{\partial t} = v_g(\Gamma_z G_i - \alpha_i)S_i(t) + R_{sp}(t) \qquad (2)$$

where N is the transverse distribution in the radial direction, r of carrier concentration inside the active layer and S_i is photon density of the ith mode. d_k is the thickness of the active layer, q is the electron charge, τ is the carrier lifetime, Γ_z is the longitudinal confinement factor, v_g ($=c/n_g$, where n_g is the group index and c is the velocity of light in free space) is the group velocity and D is the ambipolar diffusion coefficient. α_i is the scattering loss in the active layer for ith mode and Rsp is the spontaneous emission rate. J(r, t) is the current density distribution along the transverse direction.

In the photon rate equation, the effective optical gain G_i of the ith mode is given by

$$G_i = \frac{2}{w^2}\int_0^\infty g(N)|E_i(r,t)|^2 \, r dr, \qquad (3)$$

where g is the optical gain of the quantum well's active layer to be determined.

The symbol E_i represents the normalized slowly varying complex field intensity (i.e. $1 = 2\int_0^\infty |E_i|^2 \, r dr/w^2$) for the ith mode with S_i as the corresponding photon density. The field intensity ,E_i, can be determined by solving the complex scalar Helmholtz equation. It is expected that the active layer supports the transverse modes which can be expressed in terms of linearly-polarized (LP_{lp}) modes where the indexes l and p denote the azimuthal and radial order of modes respectively. The LP_{01} mode is dominated due to its maximized overlapping with the optical gain profile, however, the LP_{11} mode can also be excited for the reasons of non-uniform current injection and spatial hole burning effects. Therefore, the influence of modes competition (between LP_{01} and LP_{11} modes) is also taken into calculation. The subscript i=1 and i=2 of the above equations represent the case of LP_{01} and LP_{11} mode respectively.

The threshold and above threshold behavior of VCSELs with selective disordering is obtained from equation (1) and (2) by setting the time-derivatives equal to zero. These non-linear and time independent simultaneous rate equations can be solved in a self-consistent manner. The lateral variation along carrier concentration of the active layer is also solved by using finite difference method subject to the condition that N and its derivative are continuous everywhere. If we assume the circular symmetry of carrier concentration, at r=0, the first and second derivative of N take the form as follow :

$$\left.\frac{\partial N}{\partial r}\right|_{r_1} = 0, \qquad (4)$$

$$\left.\frac{\partial^2 N}{\partial r^2}\right|_{r_1} = \frac{2(N(r_2,t) - N(r_1,t))}{\Delta r^2} \qquad (5)$$
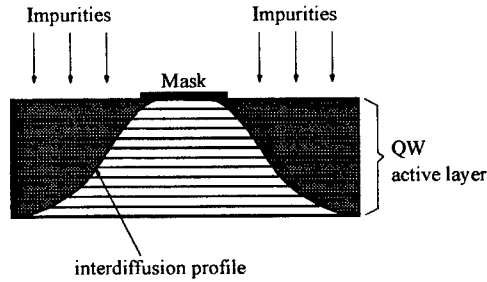
Figure 1. Schematic of a VCSEL after selective disordering
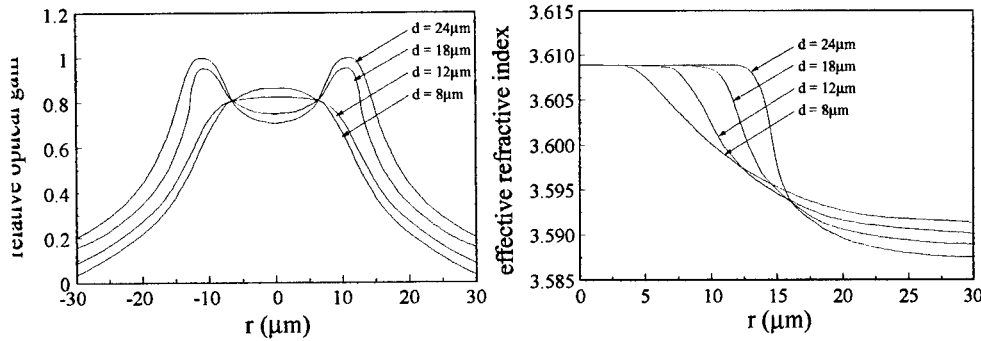
Figure 2. The optical gain and refractive index distribution of VCSEL with the diameter of mask, d varied between 8 to 24 μm.

where Δr is the separation between two successive points in the radial direction, r. It is also required that as r → very large, the carrier concentration change N → 0. The field intensity E_i is also solved simultaneously with the carrier concentration such that the time–dependent transverse field intensity variation can also be considered into investigation.

MODEL FOR QUANTUM WELL MATERIAL

The refractive index and optical gain of quantum wells material under the influence of impurities induced disordering are also considered in our analysis. The models given in references [9,10,11] are utilized to calculate the optical and electrical properties of DFQW's which are summarized in Appendix A. It is defined that the extent of interdiffusion into the quantum wells material is characterized by a diffusion length, L_d, where L_d=0Å represents the as-grown quantum wells and the diffusion strength of impurity is described by the magnitude of L_d. The corresponding magnitude of L_d between the mask and non-mask region are equal to 0 and 10Å, respectively. In the following calculation, the values of DFQW's parameters vary with L_d and device parameters used in the laser model are given in Table I and II, respectively.

149

Table I. Material Parameters in Laser Structure

(at operating wavelength of 0.85μm)	Diffusion Length (L_d)	
	0 Å	10 Å
Fitted parameters (a_N) cm^{-1}	1780.0121	468.6990
Transparency carrier density (N_0)x10^{18}cm^{-3}	2.1996	2.4092
Fitted parameters (e)	-0.02824	-0.02521
Fitted parameters (N_r)x10^{18}cm^{-3}	2.0673	1.9809
Refractive index (n_B)	3.627	3.5880

Table II. Parameters Used in Model

Parameters (symbol)	Magnitude
Thickness of active region (d)	1 μm
Carrier lifetime (τ)	4 ns
Effective group refractive index (n_a)	3.70
Longitudinal confinement factor (Γ_z)	0.16
Velocity of light in free space (c)	3×10^{10} cms^{-1}
Ambipolar diffusion coefficient (D)	15 cm^{2}s^{-1}

RESULTS & DISCUSSIONS

It is assumed that the laser is initially biased at threshold and modulated by a step current of 2 times its threshold value. The operating wavelength of the VCSEL is chosen to be $\lambda_o = 0.85\mu m$ and the diameter of core region is equal to 50μm. The diameter of circular mask, d is varied between 8 and 24μm to shelter from the ion implantation. In order to ensure the current is effectively injected in the laser, the current confinement structure is needed. It is observed that the relative optical gain at the center of core region of DFQW-VCSEL is suppressed for the increasing diameter of circular mask. With the cases of the diameter of circular mask equal to 8μm and 12μm, the transverse optical confinement in the quantum well active region is produced. This is because a gaussian distribution of permittivity along the active layer is produced by the impurities andthe transverse field is guided. The gain margin can also be enhanced if the overlapping integral between the optical gain and the fundamental transverse mode is maximized.

Figure 3 shows the near field profile of DFQW-VCSEL with the diameter of circular mask varied between 8 and 24μm. It is found that the fundamental mode of optical field can not be maintained for large size of circular mask. This is because the active layer of DFQW-VCSEL with large circular mask no longer supports the LP_{01} transverse mode. Moreover, the excitation of higher-order transverse mode is observed due to the spatial hole burning effects. Therefore, the dimension of the circular mask can affect the performance of DFQW-VCSEL.
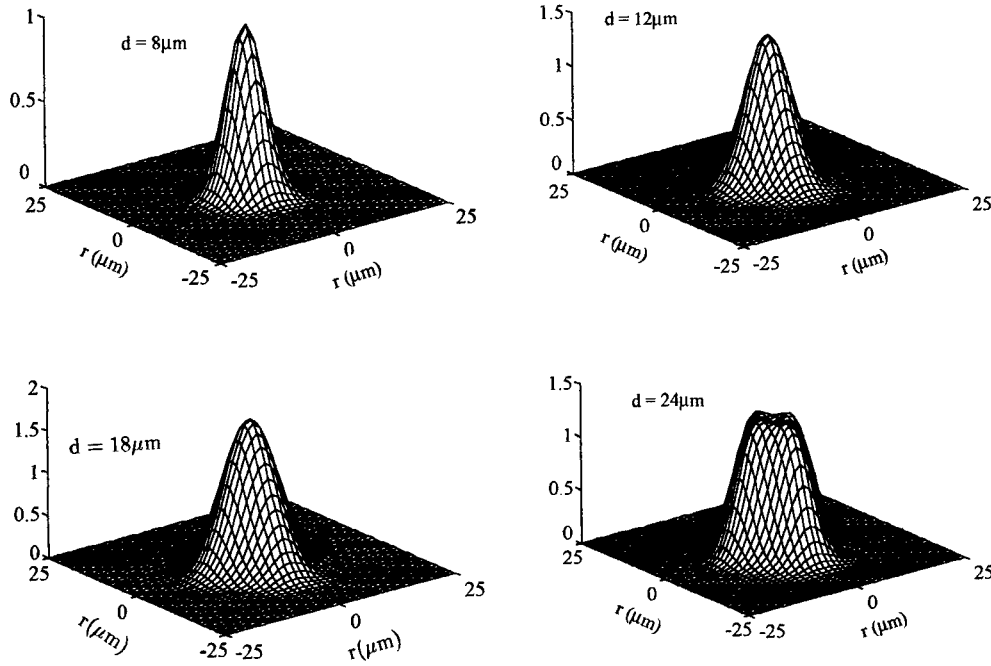
Figure 3. The near field profile with the diameter of mask, d, varied between 8 to 24 μm.

CONCULSION

In conclusion, the selective impurity-induced disordering vertical-cavity surface-emitting lasers with the diameter of the core region equal to 50μm is investigated. These devices are designed to achieve a high power single mode opearion at 0.85μm. Results show that the single mode operation with the diameters of the circular mask varied between 8 and 18μm are obtained. The confinement of the transverse optical field is produced by using selective IID technique can reduce the influence of the carrier spatial hole burning at high injection current. Therefore, the behaviour of the DFQW-VCSEL is affected by the size of the circular mask. Besides, the implanation energy, annealing temperature and time are also the important parameters to determine the modal behaviour of DFQW-VCSEL.

APPENDIX A

The refractive index, n_{DFQW}, of diffused quantum wells active layer is given by [9]

$$n_{DFQW}(\omega) = \left(\tfrac{1}{2}\varepsilon_1^T(\omega) + \tfrac{1}{2}\left\{ \left[\varepsilon_1^T(\omega)\right]^2 + \left[\varepsilon_2^\Gamma(\omega)\right]^2 \right\}^{1/2} \right)^{1/2} \qquad (A1)$$

where ω is the angular frequency, $\varepsilon_1^\Gamma(\omega)$ and $\varepsilon_2^\Gamma(\omega)$ are the real and imaginary parts of the total dielectric function for the Γ valley, respectively.

151

Using density matrix approach, the optical gain with photon generated in the direction perpendicular to the surface of quantum well layers is given as [11]

$$g(\omega) = \frac{e^2 M_b^2}{\pi c \varepsilon m_o^2 \omega L_z} \sum_{p,q} \int \left| \langle \psi_{Cp} | \psi_{Vq} \rangle \right|^2 \mathbf{P}_{pq}(k)$$

$$\times L \left[E_p(k) - E_q(k) - \eta\omega \right] \left\{ f^c \left[E_p(k) \right] - f^v \left[E_q(k) \right] \right\} dk \qquad (A2)$$

where m_0 is the rest mass of electron and M_b is the optical matrix. E_p and E_q are the pth-electron and qth-hole sub-band-edge energy, respectively, ψ_C and ψ_V are the envelope wavefunctions for the electrons and holes, respectively. L is the Lorentzian broadening factor with HWHM of 5meV and k is the wavevector. The summation in (A2) is over all the conduction and valence sub-bands and P(k) is the TE-polarization factor. f^c and f^v are the quasi-Fermi for the electrons in the conduction and valance bands, respectively.

It is noted from our calculation that at a particular L_d and at an external carrier injection level, N, the TE net optical gain spectrum at room temperature is found to have a simple expression, $g(\omega) = a_N \ln(N/N_0)$, where a_N is the fitted parameter and N_0 is the carrier concentration at transparency. The parameters a_N and N_0 at particular frequency vary with L_d are given in Table I.

The carrier induces refractive index change, Δn, which varies with the background refractive index profile of active region, can be obtained from the change of gain coefficient, $\Delta g(\omega) = g(\omega) - g_0(\omega)$, through the Kramers-Kronig dispersion relation [10]

$$\Delta n(\omega) = \frac{\pi}{c} PV \int_0^\infty \frac{\Delta G(\omega')}{\omega'^2 - \omega^2} d\omega' \qquad (A3)$$

where $g_0(\omega)$ is the optical gain at transparency. The symbol PV stands for the Cauchy principle value. We can also show that at a particular L_d the relation between Δn and N can be expressed as, $\Delta n = e \ln(N/N_r)$, where e and N_r are fitted parameters vary with L_d and also given in Table II.

REFERENCES

[1] Y. H. Lee, B. Tell, K. Brown-Goebeler, J. L. Jewell and J. V. Hove, Electron. Lett., **26**, 710 (1990).

[2] R. S. Geels and L. A. Coldren, Appl. Phys. Lett., **57**, 1605 (1990).

[3] D. Tauber, G. Wang, R. S. Geels, J. E. Bowers, and L. A. Coldern, Appl. Phys. Lett., **62**, 325 (1993).

[4] C. J. Chang-Hasnain, M. Orenstein, A. Von Lehmen, L. T. Florez, J. P. Harbison and N.G. Stoffel, Appl. Phys. Lett., **57**, 218 (1990).

[5] A. Valle, J. Sarma and K. A. Shore, IEEE J. Quantum Electron., **31**, 1423 (1995).

[6] E. H. Li and B. L. Weiss, IEEE J. Quantum Electron., **29**, 311 (1993).

[7] R. P. Bryan, J. J. Coleman, L. M. Miller, M. E. Givens, R. S. Averback and J. L. Klatt, Appl. Phys. Lett., **55**, 94 (1989).

[8] G. Ronald Hadley, K. L. Lear, M. E. Warren, K. D. Choquette, J. W. Scott and S. W. Corzine, IEEE J. Quantum Electron., **32**, 607 (1996).

[9] E.H. Li, B.L. Weiss, K.S. Chan and J. Micallef, Appl. Phys. Lett. **62**, 550, (1992).

[10] C.H. Herny, R.A. Logan and K.A. Bertness, J. Appl. Phys. **52**, 4457, (1981).

[11] E.H. Li and K.S. Chan, Electron. Lett., **29**, 1233, (1993).

GROWTH AND CHARACTERIZATION OF InAs$_x$P$_{1-x}$/InP STRAINED MULTIPLE QUANTUM WELLS BY GAS SOURCE MOLECULAR BEAM EXPITAXY

H. C. Kuo*, S. Thomas*, A. P. Curtis*, G. E. Stillman*, C. H. Lin** and H. Chen**
*Dept. of Electrical and Computer Engineering, Microelectronics Laboratory. University of Illinois at Urbana-Champaign, Urbana, IL 61801, U. S. A. h-kuo1@students.uiuc.edu
**Dept. of Material Science and Engineering, Materials Research Laboratory, University of Illinois at Urbana-Champaign, Urbana, IL 61801, U. S. A.

Abstract

InAs$_x$P$_{1-x}$/InP (10 period 50/100Å with x=0.25-0.79) pseudomorphically strained multiple quantum wells (SMQWs) were grown by gas source molecular beam expitaxy (GSMBE) at 470°C and characterized by cross-sectional transmission electron microscope (XTEM), double crystal x-ray diffraction (DCXRD), and optical spectroscopy. The structural analysis demonstrates that excellent control of the sharp interface and limited As-P interdiffusion can be achieved by GSMBE growth. XTEM images of these SMQWs display no misfit dislocations, and DCXRD scans reveal high order superlattice satellite peaks. Photoluminescence (PL) and transmission measurements were performed for all SMQWs to evaluate crystal quality. Only slight degradation in luminescence was observed as the As composition increased. Based on the three-band Kane model which includes the lattice strain, the transition energies of SMQWs were calculated using the conduction-band offset ($Q_c = \Delta E_c / \Delta E_g$) as an adjustable parameter. The best fit of measured and calculated interband transition energies suggests that Q_c is independent of As composition and is 0.70±0.05. Finally, a growth kinetics model based on the Langmuir equation was derived to realize the As/P incorporation ratio in the InAsP materials. Theoretical results show good agreement with experimental data.

Introduction

InAs$_x$P$_{1-x}$ ternary compounds have a number of advantages over Ga$_x$In$_{1-x}$As$_y$P$_{1-y}$ quaternary materials: 1) the fundamental bandgap of this material is the same as GaInAsP[1] 2) InAsP quantum wells (QWs) have a larger conduction band offset compared to GaInAsP QWs.[2-5] This large conduction band discontinuity can reduce the hot electron overflow and improve the temperature characteristics of a laser diode 3) The composition control of InAsP is better than that of GaInAsP and the growth rate is governed only by the In beam flux under normal growth conditions (V/III>1). Thus, InAsP has great potential for opto-electronic devices operating in the 0.9~1.5μm range, such as lasers[4,6-9] and modulators[10-12]. However, InAsP has received less attention than the quaternary GaInAsP system, with the result that there are only a few experimental reports on the material parameters of the InAsP system.

In this paper, we report a comprehensive study of InAsP/InP (10 period 50/100Å with x=0.25-0.79) pseudomorphically strained multiple quantum well (SMQWs) grown by gas source MBE (GSMBE). The crystal quality of InAsP/InP SMQWs were characterized by double crystal x-ray diffraction (DCXRD), cross-sectional transmission electron microscopy (XTEM), photoluminescence (PL) and absorption measurements. The band offset ratio of InAsP/InP heterostructures with arsenic in the range of 0.25-0.79 was determined by analyzing the transmission spectra of InAsP/InP MQWs. Finally, the growth kinetics, derived from Langmuir's isotherm model, were used to correlate the As/ P incorporation behavior with the flow rate of group V sources.

Experimental Details

Epitaxial growth was performed in a modified Perkin-Elmer 430P GSMBE/CBE system. The growth chamber was equipped with a 5000 l/s cryopump and a 2200 l/s turbomolecular pump. Cracked AsH$_3$ and PH$_3$ (100%) were used as the group V sources, while elemental solid source effusion cells were used for the group III sources. The operating temperature of the cracker was 950~1100°C for maximum As$_2$:As$_4$ and P$_2$:P$_4$ ratios. All InAs$_x$P$_{1-x}$/InP SMQWs in this studies were grow on InP SI substrates at 470°C and the AsH$_3$ flow rate was varied from 0.3 to 1.2 sccm (0.3, 0.6, 0.9, 1.2 sccm for samples A, B, C and D, respectively) while the PH$_3$ flow rate was kept constant (3 sccm). The source switching sequence InP/InAsP was: 1 sec for AsH$_3$ introduction time, 20 sec for AsH$_3$ residual source evacuation time (RSE). The critical number (before being relaxed) for InAsP/InP SMQW is 25>n>20 for 75Å InAs$_{0.44}$P$_{0.56}$ and ~15 for 50Å InAs$_{0.79}$P$_{0.21}$ at a growth temperature of 470°C[13].
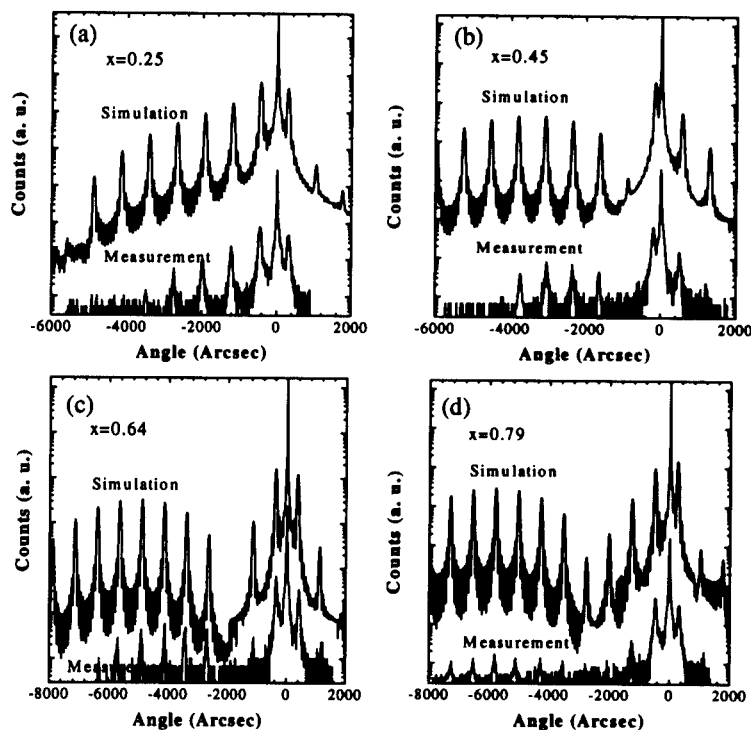
Fig. 1 (a)-(d) Experimental and simulated double crystal x-ray rocking curve of 10 period $InAs_xP_{1-x}/InP$ SMQW. Simulated spectrum using a two-layer model of the dynamical theory.

A Phillips x-ray diffractiometer with double crystal geometry was used to measure the (004) rocking curve of each sample. The cross-sectional transmission electron microscopy (XTEM) micrograghs were taken by a Hitachi H800 electron microscope operated at 200kV. Photoluminescence measurements were taken at 300K using the 5145Å line of an argon-ion laser as excitation source and detection with a LN_2 cooled Ge detector used in a lock-in configuration. All transmission spectra were taken in a surface normal configuration at room temperature with a tungsten-halogen lamp and monochromator combination used as the light source.

Results and Discussion

I. Microstructure characterization

Fig 1-4(a) shows the x-ray rocking curve taken for all samples. Satellite peaks from diffraction of all of the SMQW's can be observed up to the 5th-7th order, demonstrating excellent periodicity and crystalline quality. A simulation of experimental data, shown in Fig 1-4(b), was performed by means of the dynamical theory[14]. The best fit of the well and barrier thickness listed in table I are in good agreement with the nominal values 50/200Å. The As concentration in the InAsP well was measured using the out of plane strain ($\varepsilon_\perp$) listed in table I. Compared with simulation results, the slight broadening of the actual rocking curve may be attributed to As carryover into the InP layer at the interface during the growth interruption.

154

A cross-sectional transmission electron microscopy image taken from sample D (strain~2.6%) is shown in Fig. 2. The layer thickness deduced from the DXCRD spectrum of all samples agree with the corresponding TEM measurements. TEM measurements were performed on all samples and show that the structures are free of dislocations and are clearly defined for both normal (InAsP on InP) and inverted (InP on InAsP) interfaces. The TEM micrographs also verified that the As-P interdiffusion at the InAsP/InP interface is limited to 1~2 ML even for strain up to 2.6 % (sample D). Tweet *et al.*[15] observed a strong strain-enhanced As-P interdiffusion at the InAsP/InP interface for MOCVD grown materials. As the strain increases, an unusual island growth mode begins to appear. Furthermore, These islands penetrate deeply into the substrate, resulting in phase separation[15,16]. In our materials, the As-P interdiffusion at both normal and inverted interfaces is limited which can be attribute to the relatively low growth temperature for GSMBE (~470°C) compared with MOCVD (~600 °C). Thus, GSMBE or CBE could be more suitable growth technique than MOCVD in the growth of highly-strained $InAs_xP_{1-x}$ materials on InP.
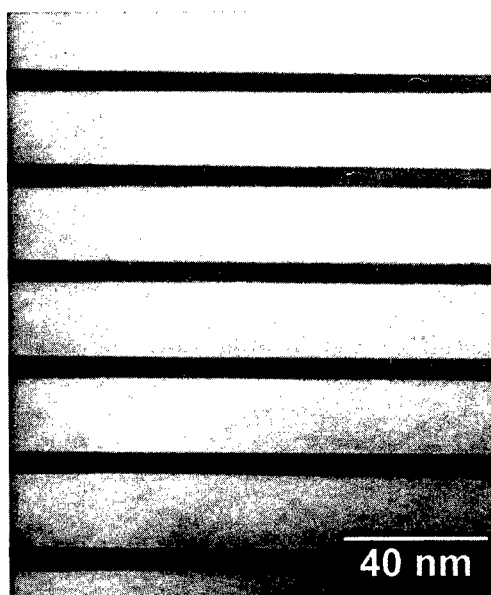
Fig. 2 Cross-sectional TEM image of InAsP/InP strained MQWs, show that the structures are free of dislocations and are limited interdiffusion for both normal (InAsP grown on InP) and inverted (InP grown on InAsP) interfaces.

II. Photoluminescence and Absorption Measurements

(1) Photoluminescence

Fig. 3 shows PL curves for samples A to D. Intense, sharp excitonic transition range form 1.1 to 1.6 μm were observed for all SMQW samples. Only a slight degradation in PL efficiency was observed with increasing As composition. A small increase in linewidth of these excitonic emissions was also observed with increasing As composition from 35 to 45 meV which was attributed to the increase in strain[17]. The excellent PL efficiency as well as sharp excitonic peaks indicate high quality GSMBE grown MQWs which are suitable for 1.1~1.6 μm optoelectronic applications.
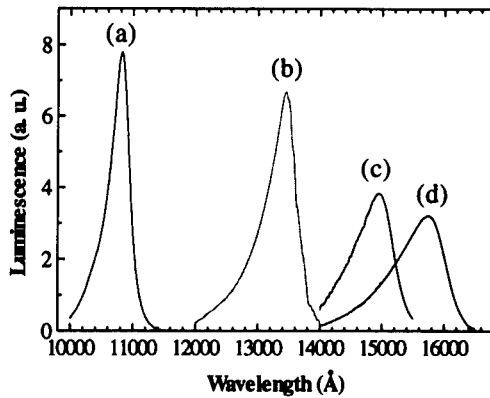
Fig. 3(a)-(d). 300K PL spectra of the InAsP/InP MQWs.

(2) Absorption measurements and band off-set

Fig. 4 (a)-(d) shows low temperature absorption spectra for samples A to D. The notation nC-$mH(L)$ is used to indicate the transitions related to the nth conduction and mth valence heavy (light) hole subbands. Sharp excitonic transitions up to $3C$-$3H$ were observed below the InP continuum edge. Both allowed, $\Delta n=0$, and dipole-forbidden/parity-allowed transitions, $\Delta n=2$, can be resolved in the spectrum. The experimental absorption spectra were used to extract the energies of the excitonic transition peaks and the exciton binding energy of the $1C$-$1H$ transitions. The $1C$-$1H$ excitonic resonances were fitted by using Gaussian line shapes. The continuum of the quantum well density of states was simulated using a step function with the same Gaussian broadening function used to reproduce the exciton absorption feature, with the inclusion of the Coulomb enhancement factor at the edge[18]. The binding energy for different samples was obtained from the energy separation between the Gaussian absorption feature and the broadened continuum edge and the data are listed in table I.

A three band $k \cdot p$ model [19,20] was used to calculate the strained quantum-well transition energies at k=0, with the band-offset value used as a fitted parameter. The input parameters included the well (InAsP) and barrier (InP) thickness as well as the composition of InAsP, which was determined by rocking curve simulation and TEM measurements. The material parameters for InAsP were obtained by linear interpolation of the parameters for InAs and InP, except for the deformation potentials and the unstrained $InAs_xP_{1-x}$ bandgap and the spin-orbit splitting. The material parameters used for InAs and InP and the interpolation formulas used for $InAs_xP_{1-x}$ are from reference [21-22]. The best fit suggest conduction band offset ratio (Q_c) of 0.7. The uncertainty in our experimental value of Q_c lies in both the experimental accuracy and theoretical model. The theoretical uncertainity originates from the unknown temperature dependent stiffness tensor and deformation potentials for InAsP. The uncertainties in the composition and thickness in QW region can also complicate the analysis. Thus the accuracy of Q_c is estimated to be within ± 0.05. Nevertheless, our results show excellent agreement between the experimental and theoretically determined value. The largest deviation between the experimental and the calculated energy is 5 meV, but most deviations from experimental data are less which gives us confidence in our assignments.

Fig. 4(a)-(d) Low temperature absorption spectra of the InAsP/InP MQWs. The notation mC-$nH(L)$ is used to indicate the transitions related to the mth conduction and nth valence heavy (light) hole subbands. Vertical bars indicate the calculated transition energies.

TABLE I. Parameters extracted from the x-ray dynamical theory and absorption measurements

sample #	As composition	well/barrier thickness	exciton binding energy
A	0.25	52/200 Å	10 meV
B	0.45	50/200 Å	11 meV
C	0.64	49/200 Å	11.5 meV
D	0.79	51/200 Å	11.8 meV

III. Kinetics of As/P incorporation in $InAs_xP_{1-x}$

In GSMBE, the growth rate and composition may be controlled by three steps, 1) beam flux, 2) absorption and desorption , and 3) surface reactions. For mixed group V ternary compound such as GaAsP, InAsP or quaternary GaInAsP, although the growth rate is controlled by the group III beam flux, the composition is affected by surface reactions between group III atoms and group V species and adsorption and desorption of group V species on the growth surface. This means that there is a competition between As and P incorporation during the growth of InAsP, GaAsP or GaInAsP. Here we will use the simple kinetic model to explain the As and P incorporation behavior in InAsP grown on InP[23]. In this model, the solid composition ratio of P/As in $InAs_xP_{1-x}$ can be solved analytically:

$$\frac{1-x}{x} = 2 f_P \left[k f_{As} - f_P - (k-1) f_{In} m + \sqrt{(k f_{As} - f_P - (k-1) f_{In} m)^2 + 4 k f_{As} f_P} \right]^{-1} . (1)$$

where f_{As} and f_P are the flow rates of AsH_3 and PH_3 in SCCM, f_{In} is the In flux rate in ML/s(0.716 ML/s in this study), and m is the flux rate to flow rate conversion factor which has the value 1.5 (determined by RHEED oscillation). The only fitted parameters is k, which describes the influence between the desorption time constant and the reaction rate constants of As and P monomers with In adtoms. Therefore, k can be a good indicator for the reactive incorporation ability of As and P.

Fig. 5 shows the experimental and simulated arsenic solid composition as a function of AsH_3 flow rate. Solid squares were obtained from DCXRD measurement, while the open circles were inferred from secondary ion mass spectrometry(SIMS) depth profiling. The best fit to the experimental results gives k=42 which implies that the incorporating probability of As atoms on the surface migration state is 42 times larger than that of P atoms. As shown in Fig. 5, the As concentration in the epitaxial solid phase is much greater than the AsH_3/ PH_3 flow-rate ratio. With the k factor determined, we can predict the solid composition of InAsP for various AsH_3 and PH_3 flow rates.

Conclusion

In conclusion, high quality InAsP /InP SMQW structures were grown by GSMBE at 470°C and characterized by DCXRD, XTEM, PL and absorption measurements. The band offset ratio (Q_c=0.70±0.05) of $InAs_xP_{1-x}$/InP heterostructures with x=0.25~0.79 were obtained by analyzing the absorption spectra and determined to be independent of the As composition. Finally, the As and P incorporation behavior for GSMBE grown $InAs_xP_{1-x}$ is successfully explained using kinetic model. The solid compositions of $InAs_xP_{1-x}$ can be accurately controlled by adjusting the gas flow rate.

Acknowledgments
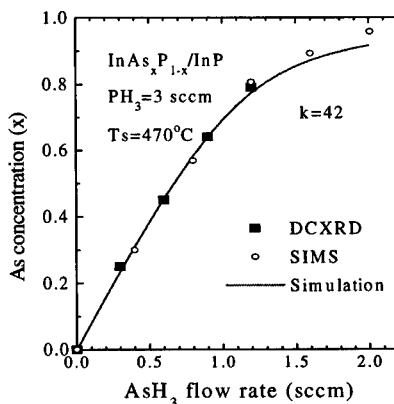
Fig. 5.   Experimental and simulated arsenic composition as a function of AsH_3 flow rate.

References

1. E.C. Wood, in GaInAsP Alloy Semiconductors, edited by T. P. Pearsall (Wiley, New York, 1982), 87–106.

2. P. Schneider, and B. W. Wessels, *J. Electron. Mater.* **20**, 1117 (1991).

3. E. A. Montie, P. J. A. Thijs, and G. W. 't Hooft, Appl. Phys. Lett. **53**, 1611 (1988).

4. H. Oohashi, T. Hirono, S. Seki, H. Sugiura, J. Nakano, M. Yamamoto, Y. Tohmori, and . K. Yokoyama, *J. Appl. Phys.* **77**, 4119(1995).

5. H. Q. Hou and C. W. Tu, *J. Appl. Phys.* **75**, 4673 (1994) and the references therein.

6. H. Sugiura, *J. Cryst. Growth* **164**, 434 9(1996) and the references therein.

7. Thiagarajan, A. A. Bernussi , H. Temkin, G. Y. Robinson, A. M. Sergent, R. A. Logan, *Appl. Phys. Lett.* **67**, 3676 (1995).

8. M. Yamamoto. N. Yamamoto and J. Nakano. *IEEE QE* **30** 554 (1994).

9. Sugiura. M. Mitsuhara. H. Oohashj. T. Hirono and K. Nakashima. J. Crystal Growth **147** (1995).

10. H. Q. Hou, A. N. Cheng, H. H. Wieder, W. S. C. Chang, and C. W. Tu, Appl. Phys. Lett. **63**, 1833 (1993).

11. H. Chiu. J.E. Cunningham. T.K. Woodward and T. Sizer II. *Appl. Phys. Lett.* **62** (1993) 340.

12. X. Jiang and P.K.L. Yu. *Appl. Phys. Lett.* **65** 2536(1994).

13. H.C. Kuo, S. Thomas, A.P. Curtis, G.E. Stillman, unpublished data.

14. B. K. Tanner, Adv. X-ray Anal. **33**, 1 (1990).

15. D. Tweet , H. Matsuhata , R. Shioda, H. Oyanagi, H. Kamei, *Appl. Phys. Lett.*, **67**, 1286(1995).

16. Y. H. Xie, G. H. Gilmer, C. Roland, P. J. Silverman, S. K. Buratto, J. Y. Cheng, E. A. Fitzgerald, A. R. Kortan, S. Schuppler, M. A. Marcus, and P. H. Citrin, Phys. Rev. Lett. **73**, 3006 (1994).

17. M. Sato, and Y. Horikoshi *J. J. Appl. Phys.* **27**, L2192(1988).

18. M. Beaudoin , A. Bensaada, R. Leonelli, P. Desjardins, R. A. Masut, L. Isnard, A. Chennouf, G. L'Espérance *Phys. Rev. B53* 1990 (1996).

19. E. O. Kane, *J. Phys. Chem. Solids* **1**, 249 (1957).

20. G. E. Pikus and G. L. Bir, Fiz. Tverd. Tela(leningrad) **1**, 154 (1959)[Sov. Phys. Solid State **1**, 136 (1959)]; **1**, 1642 (1959)[**1**, 1502(1960)].

21. V. Swaminathan and A. T. Macrander, *Materials Aspects of GaAs and InP Based Structures* (Prentice Hall, Englewood Cliffs, NJ, 1991).

22. *Physics of Group IV Elements and III-V Compounds*, edited by O. Madelung, Landolt-Bornstein, New Series, Group III, Vol. **17**, Pt. a (Springer, Berlin, 1982).

23. T.-L. Lee, J.-S. Liu and H.-H. Lin J. Crystal Growth **155**, 16-22(1995).

1.5 μm $In_{0.53}Al_{0.14}Ga_{0.33}As/In_{0.52}Al_{0.48}As$ DISTRIBUTED BRAGG REFLECTOR AND SINGLE CAVITY ACTIVE LAYER GROWN WITH IN-SITU DOUBLE BEAM LASER REFLECTOMETRY

Jong-Hyeob Baek, Bun Lee, Jin Hong Lee, Won Seok Han*, and El-Hang Lee,
Electronics and Telecommunications Research Institute,
Yusong P.O. BOX 106,Taejon 305-600, Republic of Korea
*Physics Department, Chungnam National University, Taejon 305-600, Republic of Korea

ABSTRACT

We report the highly reflecting (>99.9%) $In_{0.53}Al_{0.14}Ga_{0.33}As/In_{0.52}Al_{0.48}As$ 30.5 pairs distributed Bragg reflector (DBR) and the $In_{0.53}Ga_{0.47}As/In_{0.52}Al_{0.48}As$ active cavity layer grown at high temperature by low pressure metal organic chemical vapor deposition with in-situ double beam laser reflectometry. One of the laser wavelengths selected for in-situ measurement was same as the DBR wavelength. The growth temperature was 750 °C. Good surface morphology of the multi-layer stacks was achieved by the temperature ramping of the InP buffer layer at the beginning of a multi-layer stacks. The width of stop band edge of the DBR reflectivity spectrum was found to be 1000Å.

INTRODUCTION

There has been growing interest in vertical cavity surface emitting lasers (VCSEL) [1-2] due to the many advantages that surface emitting geometry holds over edge emitting geometry. These include the ease of fabrication of integrated laser arrays, wafer scale testing, self aligned optical fiber coupling, and chip-to-chip communication via micro-optic components. For high bit rate optical fiber transmission, 1.3 - 1.55 μm emission [3-5] is desired due to the low loss and small dispersion penalty. Operating wavelengths have been primarily limited to the near-infrared (NIR) owing to the materials used. Extension to longer wavelengths (near 1.55 μm), for long distance telecommunication applications, has been achieved with InGaAsP/InP heterostructures.[6] Many reports have been published concerning heterostructures of AlAsSb/GaAsSb[4], AlAsSb/InGaAsP[5], and InAlGaAs/InP[7] for Bragg reflector tuned at 1.55 μm, but the relatively low contrast in refractive indices of these system ($\Delta n \sim 0.3$), as compared to GaAs/AlGaAs ($\Delta n \sim 0.6$), leads to very thick structural layers. Hence the fused technology was proposed to overcome this problem by making mirrors with other materials and fusing them to the cavity.[8] Nevertheless, up to now, no practical VCSEL has been realized continuously operated at a wavelength of 1.55 μm at room temperature due to several physical and technological difficulties. In this work, we report a highly reflecting (>99.9%) InAlGaAs/InAlAs distributed Bragg reflector (DBR), lattice matched to InP tuned at 1.5 μm, grown by low pressure metal-organic chemical vapor deposition. The highly reflecting DBR layer is followed by an InGaAs/InAlAs multiple quantum well as a cavity layer emitting at a wavelength of 1.5 μm. The heterostructure of $In_{0.53}Al_{0.14}Ga_{0.33}As/In_{0.52}Al_{0.48}As$ ($\Delta n \sim 0.4$) has an applicable advantage as compared with the other materials mentioned above. The VCSEL fabricated with this heterostructure can be fabricated as an uncooled laser continuously operated at room temperature because the structure has an excellent electron confinement. However, a previously reported $In_{0.52}Al_{0.48}As$ epitaxial layer grown at optimal growth temperature[9] showed anomalous optical behavior due to the ordering or phase separation.[10] To prevent similar effects in this

159

work, the growth temperature of the Bragg reflector layer and subsequently grown cavity layer was raised to 750 °C. In-situ double beam laser reflectometry was employed to determine the growth rate of the epitaxial layer in real time. The laser reflectometry technique has been successfully applied as an in-situ growth monitoring tool for MOCVD grown AlAs/GaAs Bragg reflectors by measuring the oscillatory signals of buffer layers at the beginning of a run.[11] A diode laser operating at 1.5 μm was used so that quarter wavelength optical thickness of each layer could be directly determined in real time without previous measurement of thickness.

EXPERIMENT

The epitaxial layer of $In_{0.53}Al_{0.14}Ga_{0.33}As/In_{0.52}Al_{0.48}As$ Bragg reflector including cavity layer was grown in a vertical flow, low pressure (20 torr) MOCVD chamber. Trimethylindium (TMIn), Trimethylaluminum (TMAl), and Trimethylgallium (TEGa) were used as a metal-organic precursor. 100% Pure gas of arsine (AsH_3), phosphin (PH_3) were used as hydride sources. The growth temperature of the multi-layer stacks was 750 °C and the V/III ratio was about 80. The layers were grown on a (100) Fe-doped InP substrate rotating at a speed of 1400 rpm. All the layers were undoped. Figure 1 shows a structural diagram of the multi-layer stacks. The grown structure consists of an initial 0.3 μm undoped InP buffer layer followed by 0.5 μm

$In_{0.53}Ga_{0.47}As/ In_{0.52}Al_{0.48}As$ 3QW cavity layer

$In_{0.52}Al_{0.48}As/ In_{0.53}Al_{0.14}Ga_{0.33}As$ 30.5 pairs DBR

$In_{0.52}Al_{0.48}As$ buffer layer

$In_{0.53}Al_{0.14}Ga_{0.33}As$ buffer layer

InP

λ
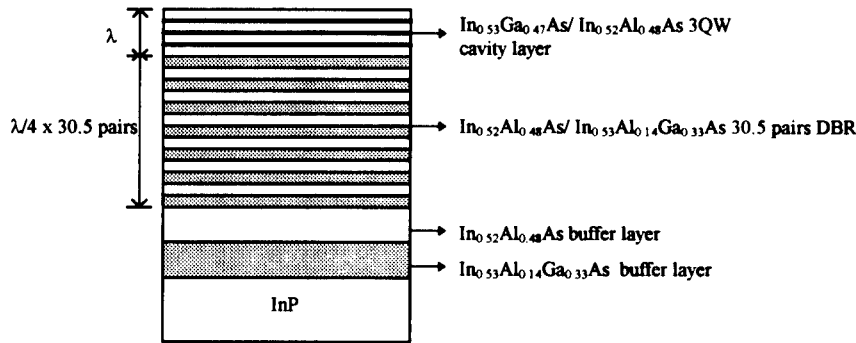
λ/4 x 30.5 pairs

Figure 1. Layer sequence for the 1.5 μm $In_{0.52}Al_{0.48}As/ In_{0.53}Al_{0.14}Ga_{0.33}As$ 30.5 pairs DBR and cavity active layer grown on the InP substrate.

$In_{0.53}Al_{0.14}Ga_{0.33}As$ and $In_{0.52}Al_{0.48}As$ buffer layers. The Bragg reflector and cavity layers were subsequently grown on the two buffer layers. During the growth of $In_{0.53}Al_{0.14}Ga_{0.33}As$ and $In_{0.52}Al_{0.48}As$ buffer layers, the growth rate of each layer was determined by in-situ laser reflectometry. We used two different wavelength laser beams: One was 5 mW He-Ne laser operating at 0.633 μm and the other was 2 mW diode laser operating at 1.5 μm, and they were detected by Si and Ge photovoltaic detectors, respectively. Two laser beams were simultaneously entered and exited the reactor chamber, at an angle of 71° with respect to the substrate surface normal, through optical ports, which remained clear during the epitaxial growth. To avoid the effects of laser power fluctuations, the intensity of the reflected beams was normalized to the intensity of a laser beam that was split by a 1:1 beam splitter located in front of the laser. Only the S-polarized laser beam (TE mode) was injected to the growth chamber through polarizing filter. The period of a complete oscillatory signal, T_p, is given by $λ/2n_{eff}G$,

where λ_i is the wavelength of the laser i, n_{eff} is the effective index of refraction of the layer, which takes into account the growth temperature and 71° incidence angle, and G is the epitaxial growth rate. We determined the quarter wavelength optical thickness ($\lambda/4$) of the Bragg reflector by using a diode laser operating at 1.5 μm. The optical thickness of each layer ($\lambda/4$) is given by ($t_g \cdot T_p / 2$), where t_g is the growth rate and T_p is the period of the oscillatory reflectance signal by 1.5 μm diode laser. The photoluminescence of the $In_{0.53}Ga_{0.47}As / In_{0.52}Al_{0.48}As$ cavity active layer was measured at room temperature by using an Ar^+ ion laser.

RESULTS AND DISCUSSION

Epitaxial growth of buffer, Bragg reflector and cavity layer

The $In_{0.52}Al_{0.48}As/In_{0.53}Al_{0.14}Ga_{0.33}As$ buffer layers were grown prior to growth of the DBR layer to determine the growth rate by in-situ laser reflectometry. In order to obtain the good surface morphology of the $In_{0.52}Al_{0.48}As/In_{0.53}Al_{0.14}Ga_{0.33}As$ at a temperature of 750 °C, a high quality InP buffer layer is essential. An InP buffer layer with good surface morphology was achieved by a temperature ramping technique. The initial growth temperature was 500 °C and the temperature was slowly increased to 750 °C at a rate of 0.4 °C/second. As soon as the temperature reached to 750 °C, the $In_{0.53}Al_{0.14}Ga_{0.33}As$ buffer layer was subsequently grown after a PH_3 purge. The $In_{0.52}Al_{0.48}As$ buffer layer was grown on the $In_{0.53}Al_{0.14}Ga_{0.33}As$ layer after an AsH_3 purge due to the arsenide surface. The optimal PH_3 and AsH_3 purge times were 3 seconds in both cases. Then the quarter wavelength DBR layer was grown after growth of ternary and quarternary buffer layers with an AsH_3 purge at each interface. We had previously decided the Al composition of the InAlGaAs layer lattice matched to InP should be 14 % in order to avoid the absorption at the stop band edge of the Bragg reflector. The Al composition was measured by Rutherford backscattering spectroscopy (RBS). The band edge of the $In_{0.53}Al_{0.14}Ga_{0.33}As$ layer measured by the room temperature photoluminescence (PL) was found to be 1.46 μm. The active cavity layer consists of 3 quantum wells of $In_{0.53}Ga_{0.47}As$ of 100 Å thickness with barrier layers of $In_{0.52}Al_{0.48}As$ of 200 Å thickness. The quarter wavelength thickness ($\lambda/4$) of the Bragg reflector for the 1.5 μm wavelength can be determined by in-situ laser reflectometry.

In-situ laser reflectometry

Figure 2 shows the in-situ oscillatory signal of the reflection intensity of the $In_{0.52}Al_{0.48}As/In_{0.53}Al_{0.14}Ga_{0.33}As$ buffer layer and subsequently grown DBR layer without cavity layer as a function of the growth time, simultaneously monitored by 0.633 μm and 1.5 μm lasers. The reflection intensity is in arbitrary units and has been controlled with a bias voltage applied to the photodetector. We previously reported the detailed technique of the double beam laser reflectometric method.[12] During growth of $In_{0.53}Al_{0.14}Ga_{0.33}As$ and $In_{0.52}Al_{0.48}As$ buffer layers, the period of the oscillatory signal (T) for each laser is determined. Since the wavelength of the diode laser (1.5 μm) corresponds to the designed wavelength of the DBR, we can directly determine the growth time of each layer for DBR structure as $T_1/2$ and $T_2/2$, where T_1 and T_2 are oscillation periods for the $In_{0.53}Al_{0.14}Ga_{0.33}As$ and $In_{0.52}Al_{0.48}As$ buffer layer, respectively. The thickness of the alternative multi-stack layer corresponds to the quarter wavelength optical thickness of the layer at the laser wavelength. If the refractive index of the layer at one wavelength laser is known, the refractive indices of the layer at other laser wavelength can be determined as follow ;

161
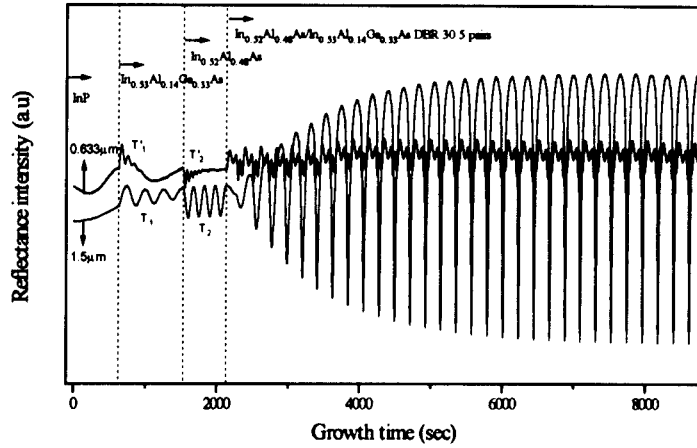
Figure 2. In-situ oscillatory reflectance signal of the $In_{0.52}Al_{0.48}As/In_{0.53}Al_{0.14}Ga_{0.33}As$ buffer layer and subsequently grown DBR layer on InP substrate as a function of the growth time by two lasers.

$$ G = \frac{\lambda_1}{2\,n_{1,eff}T_1} = \frac{\lambda_2}{2\,n_{2,eff}T_2} , \qquad (1) $$

where G is the growth rate of the layer and λ_1 and λ_2 are laser wavelengths. During growth of the DBR layer in this work, the oscillation period at the 0.633 μm was more than two times larger than that at the 1.5 μm wavelength. Since the complete oscillation period could be determined using 0.633 μm in this case, we could confirm the real thickness of the alternative multi-stack layer by using equation (1). As is shown in Figure 1, the reflection intensity monitored by 1.5 μm reached plateau after the growth of 25 periods of DBR layer, indicating a reflectivity of unity.

Reflectivity and photoluminescence measurement

The reflectivity of the 30.5 pairs $In_{0.52}Al_{0.48}As/In_{0.53}Al_{0.14}Ga_{0.33}As$ DBR layer grown on the ternary and quaternary buffer layers without an active cavity layer is shown in Figure 3(a). Since the reflectivity of the DBR layer was so high that no effect was observed on the reflectivity of the DBR layer by growth of buffer layers of $In_{0.53}Al_{0.14}Ga_{0.33}As$ and $In_{0.52}Al_{0.48}As$. The reflectivity has been calibrated using a gold mirror. The DBR structure showed a maximum reflectivity of more than 99.9 % at 1.56 μm and the width of stop band was found to be about 1000 Å. A shift from the design wavelength (1.5 μm) determined by the half period of the oscillatory signal from the 1.5 μm laser is presumably due to the changes in refractive indices between growth temperature room temperature. Since the effective index of refraction at growth
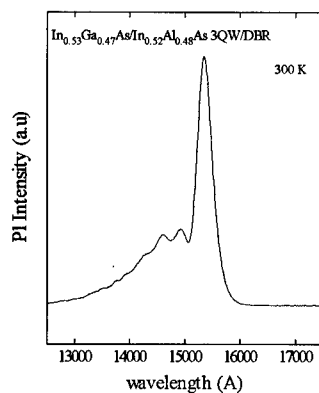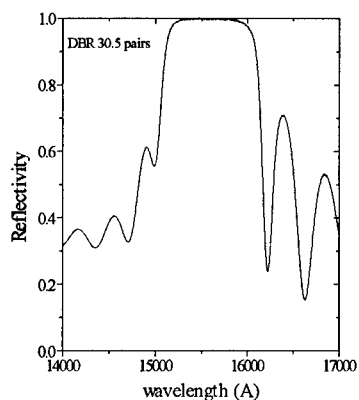
Figure 3(a). Reflectivity spectrum of the $In_{0.53}Al_{0.14}Ga_{0.33}As$ and $In_{0.52}Al_{0.48}As$ 30.5 pairs DBR structure.

Figure 3(b). Photoluminescence spectra of a $In_{0.53}Ga_{0.47}As/$ $In_{0.52}Al_{0.48}As$ 3QW cavity layer grown on DBR layer

temperature and incident angle is larger than that at the room temperature, the reflectivity spectrum which is measured at room temperature shifted to the longer wavelength position. Figure 3(b) shows the photoluminescence spectrum of the $In_{0.53}Ga_{0.47}As$ 3 quantum wells each - of 100 Å thickness with barrier layers of $In_{0.52}Al_{0.48}As$ of 200 Å thickness subsequently grown on a DBR layer. The peak position is correlated with the stop band structures of DBR and the cavity length of active quantum wells. The peak intensity is extremely strong due to the presence of the DBR layer, which reflects the emission peak within the stop band towards the active layer.

CONCLUSIONS

A highly reflecting (>99.9 %) DBR of 30.5 pairs $In_{0.52}Al_{0.48}As/In_{0.53}Al_{0.14}Ga_{0.33}As$ lattice matched to an InP substrate and operating at 1.5 μm was grown by low pressure metal organic chemical vapor deposition. The quarter wavelength optical thickness ($\lambda/4$) of the DBR layer was determined by in-situ laser reflectometry with a laser of equal wavelength. A high quality InP buffer layer was achieved by temperature ramping technique. The reflection spectrum of the DBR structure showed a maximum reflectivity at 1.56 μm and the width of the stop band was found to be 1000 Å.

REFERENCES

1. P. L. Gourley, I. J. Fritz, T. M. Brennan, B. E. Hammons, A. E. MaDonald, and D. R. Myers, Appl. Phys. Lett. 60, 2057 (1992).

2. F. Koyama, H. Uenohara, T. Sakaguchi, and K. Iga, Jpn. J. Appl. Phys. 26, 1077 (1987).

3. K. Tai, F. S. Chao, W. T. Tsang, S. N. G. Chu, J. D. Wynn, and A. M. Sergent, Electronic Lett. 27, 1540 (1991).

4. B. Lambert, Y. Toudic, Y. Rouillard, M. Gauneau, and M. Baudet, Appl. Phys. Lett. 66, 442 (1995).

5. K. Tai, R. J. Fischer, A. Y. Cho, K. F. Huang, Electronics Lett. 25, 1160 (1989).

6. C. H. Lin, C. L. Chua, Z. H. Zhu, F. E. Ejeckam, T. C. Wu Y. H. Lo, and R. Bhat, Appl. Phys. Lett. **64**, 3395 (1994).

7. A. J. Moseley, J. Thompson, D. J. Robbins, and M. Q. Kearley, Electronics Lett. 25, 1718 (1989).

8. D. I. Babic, J. J. Dudley, K. Streubel, R. P. Mirin, J. E. Bowers, and E. L. Hu, Appl. Phys. Lett. 66, 1030 (1995).

9. R. Bhat, M. A. Koza, K. Kash, S. J. Allen, W.P Hong, S. A. Schwarz, G. K. Chang, and P. Lin, J. Crystal Growth, 108, 441 (1991).

10. J. H. Lee, B. Lee, J.-H. Baek, W. S. Han, H. M. Kim, E.-H. Lee, T. Y. Sung, submitted in Appl. Phys. Lett.

11. N. C. Frateschi, S. G. Hummel, and P. D. Dapkus, Electronics Lett. 27, 157 (1991).

12. J.-H. Baek, B. Lee, S. W. Choi, J. H. Lee, and E.-H. Lee, Appl. Phys. Lett. 68, 2355 (1996).

STARK SHIFT AND FIELD INDUCED TUNNELING
IN DOPED QUANTUM WELLS
WITH ARBITRARY POTENTIAL PROFILES

S. PANDA, B. K. PANDA, S. FUNG and C. D. BELING
Department of Physics, The University of Hong Kong, Hong Kong

ABSTRACT

The energies and resonance widths of single doped quantum wells consisting of Al-GaAs/GaAs with rectangular and annealing induced diffusion modified shapes are calculated under an uniform electric field using the stabilization method. The electronic structure is calculated without an electric field in the finite temperature density functional theory with exchange-correlation potential treated in the local density approximation. Our scheme for solving the Schrödinger and Poisson equations is based on the Fourier series method. The electric field is added to the self-consistent potential and energies are obtained as a function of the combined width of the well and barriers. This yields us the stabilization graph from which the energies and resonance widths at different field strengths are extracted using the Fermi Golden rule.

INTRODUCTION

There has been growing interest in using quantum wells (QWs) for optoelectronic device applications such as quantum well lasers, infrared detectors, wave guides and modulation doped field effect transistors[1,2]. The details of the electronic structures of the subband levels under the uniform electric field are necessary to understand the device performance. In an undoped sample the electronic structure of the subbands are described in the single particle picture where electron wave functions and the energy levels are completely decided by the barrier height and the well width. In a modulation doped QW the electrons flow from the barrier region into the well to bring the system to equilibrium. As a result of the higher density of electrons in the well, the Coulomb interaction between electrons becomes very important needing a complete many-body approach to this problem. In this case the subband energies and wave functions are dependent on the two-dimensional electron density and temperature.

Density functional theory (DFT) is a popular scheme for solving many-body problem. In this method the ground-state property of interacting electrons is determined by its charge density[3]. The many-body effects are taken in the exchange-correlation potential treated in the local density approximation (LDA). The single particle energies and wavefunctions are calculated using self-consistent Kohn-Sham equations[3]. This method has been applied to get energies and wave functions in the modulation doped rectangular QW[4]. However, the effect of the electric field on the electron subband energies and wave functions has not been addressed. A suitable method of extracting the mean tunneling times of the electrons under the applied electric field is not yet formulated. This paper attempts to use Fourier series technique[5] for the calculation of the energies, wave functions and mean tunneling lifetimes in the modulation doped rectangular and annealing induced diffusion modified QWs. For simplicity the conduction band shift due to the strain effect, nonparabolicity, depolarisation and exciton shifts[1] are not considered in this work.

THEORY

The self-consistent Kohn-Sham equation for calculating the energy E_n and wave function $\Psi_n(z)$ within the effective mass approximation in the Rydberg unit ($\hbar=1$, $m_0=0.5$

165

and $e^2=2$) is given by

$$\left[-\frac{\hbar^2}{2}\frac{\partial}{\partial z}\frac{1}{m^*(z)}\frac{\partial}{\partial z} + V_{eff}(z) + eFz\right]\Psi_n(z) = E_n\Psi_n(z) \qquad (1)$$

The effective potential (V_{eff}) is given by

$$V_{eff}(z) = V_{QW}(z) + V_H(z) + V_{XC}(z) \qquad (2)$$

where V_{QW}, V_H and V_{XC} are the quantum confined potential, the Hartree potential and the exchange-correlation potential respectively. The Hartree potential is obtained from the Poisson equation

$$\frac{\partial}{\partial z}\epsilon_r(z)\frac{\partial}{\partial z}V_H(z) = 4\pi e^2\rho(z) \qquad (3)$$

where $\epsilon_r(z)$ is the relative dielectric constant along the z-direction and $\rho(z) = [n(z) - N_D^+(z)]$ with $n(z)$ and $N_D^+(z)$ as the carrier density and the ionised dopant density respectively. The carrier charge density at some finite temperature is given as

$$n(z) = 2\sum_{n=1}^{n_b}\frac{k_BTm^*(z)}{\pi\hbar^2}ln\left[1 + \exp\left(\frac{\mu - E_n}{k_BT}\right)\right]\mid\Psi_n(z)\mid^2 \qquad (4)$$

where μ is the chemical potential. Integrating Eqn. (3) twice we obtain the Hartree potential as

$$V_H(z) = 4\pi e^2\int_{-\infty}^{z}\frac{dz'}{\epsilon_r(z')}\int_{-\infty}^{z'}\rho(z'')dz'' \qquad (5)$$

The boundary condition in this equation is that $V_H(\pm\infty) = 0$. The zero temperature exchange-correlation potential (V_{XC}^0) in the LDA using parametrised form of Hedin and Lundqvist[6] is given by

$$V_{XC}^0(z) = -2\left[\frac{9}{4\pi^2}\right]^{\frac{1}{3}}\frac{1}{r_s}\left[1 + \frac{0.7734}{21}r_s\left(1 + \frac{21}{r_s}\right)\right]R_y \qquad (6)$$

where $r_s = [3/4\pi a_0^3(z)n(z)]^{1/3}$, $a_0(z) = \epsilon_r(z)/m_r^*(z)$ and $R_y = m_r^*(z)/\epsilon_r^2(z)$ with $m_r^* = m^*/m_0$ The temperature is incorporated into the $V_{XC}^0(z)$ through[7]

$$V_{XC}(z) = \begin{cases} V_{XC}^0(z), & \gamma \leq 0.15; \\ V_{XC}^0(z)\left[1 + (a_1r_s^2 + b_1r_s + c_1)\gamma^e/(a_1^*r_s^2 + b_1^* + \gamma^d)\right], & 0.15 < \gamma < 12. \end{cases} \qquad (7)$$

where $\gamma = k_BT/\mu$, $a_1 = -0.00388$, $b_1 = 0.04544$, $c_1 = -0.443$, $a_1^* = 1.5460$, $b_1^* = 0.7023$, $e = 2.04258$ and $d = 1.80518$. The chemical potential(μ) is obtained from the charge neutrality and depletion approximation conditions[4].

We have adopted the Fourier series method to solve the Kohn-Sham equation to obtain energies and envelope functions. Since the envelope function $\Psi_n(z)$ is a continuous function of z, it can be expanded into a truncated Fourier series of the form

$$\Psi_n(z) = \sqrt{\frac{1}{d}}\sum_k C_n(k)\exp\left(j\frac{2\pi k}{d}z\right) \qquad (8)$$

where $j = \sqrt{-1}$ and d is the total length obtained by combining the width of the QW and barriers. Similarly $V_{eff}(z)$ and $1/m^*(z)$ and eFz are expanded in terms of the Fourier Series with coefficients $V_{eff}(k)$, $m(k)$ and $f(k)$ respectively. In terms of these coefficients the Eqn.(1) is derived as

$$\sum_i \left[-\frac{\hbar^2}{2} \left(\frac{2\pi}{d} \right)^2 m(k-i)ik + V_{eff}(k-i) + f(k-i) \right] C_n(i) = E_n C_n(k) \qquad (9)$$

The calculation of the chemical potential under the applied electric field is a complex problem to solve. It involves detailed knowledge of the field induced drift current and the tunneling current at the applied bias. For simplicity we have solved the DFT without electric field to obtain the quantum confined well shape and have then applied electric field on the well to study the Stark shift and resonance width.

The calculation of the energy shift and resonance width in a rectangular QW under uniform electric field by the stabilization method was developed by Borondo and Sánchez-Dehesa[8]. In the QW the energy levels calculated and plotted as a function of d show avoided crossings between stable and unstable eigenvalues at some points. The stable eigenvalues correspond to the energies representing the resonance position and the unstable eigenvalues correspond to the discretized continuum states. As an example, in Fig. 1 we present the stabilisation graph (SG) for a rectangular well at 100 kV/cm.
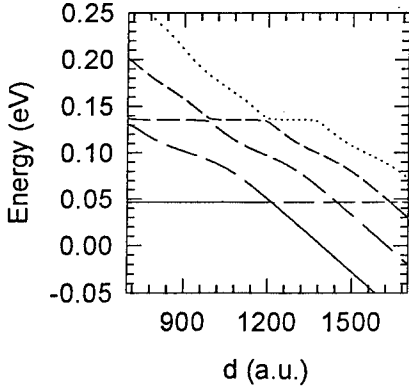
Fig.1
Stabilization graph of the rectangular quantum well with well width 100Å and $x = 0.3$ at the applied field strength 100 kV/cm. The energy levels for the ground, first, second, third, fourth and fifth excited states are denoted by solid, long-dashed, middle-dashed, short-dashed and dotted lines respectively. The avoided crossings are clearly seen here.

This graph presents avoided crossings between stable and unstable eigenvalues at different d_c for both ground state and first excited state energy levels. In the standard Fermi-golden-rule-type formula the resonance width (Γ)[8,9] is given by

$$\Gamma = 2\pi \rho(E_n) V_c^2 \qquad (10)$$

where the interaction term V_c is taken to be half the energy splitting at the pseudo-crossing (d_c) of the SG and $\rho(E_n)$ is the density of the continuum states. If E_n is the discretized continuum eigenvalue interacting with the stable one, a good approximation for $\rho(E_n)$ is[8,9].

$$\rho(E_n) = \frac{2}{E_{n+1} - E_{n-1}} \qquad (11)$$

To demonstrate its potentiality of the SG technique. We have applied it to two different types of well structures, namely the rectangular and the diffusion modified QW structures.

RESULTS AND DISCUSSIONS

I. Rectangular Single Quantum Well

The potential profile for a rectangular QW is given by

$$V(z) = \begin{cases} V_0, & |z| \geq L/2; \\ 0, & |z| < L/2. \end{cases} \tag{12}$$

where $V_0 = B_{off}(E_g(x) - E_g(0))$ with $E_g(x)$ and $E_g(0)$ the band gaps of $Al_xGa_{1-x}As$ and GaAs respectively. B_{off} is the band offset usually taken to be 0.7 and L is the width of the rectangular QW. The expressions for $E_g(x)$ and $m^*(x)$ have been given in our earlier work[5]. The width of the well is taken to be 100Å and $x = 0.3$ which corresponds to the barrier height of 295.6 meV. This well contains three bound states corresponding to energies of 32.07 meV, 126.51 meV and 267.88 meV. The barrier is doped with Si donors with binding energy 20 meV and concentration $2.5 \times 10^{20} cm^{-3}$. We have taken five eiteration to get full convergence in energy eigenvalues. The effective potential V_{eff} with and without the effect of the manybody terms is shown in Fig. 2. The chemical potential is found to be 107 meV. The concentration of the ionised donors corresponding to this chemical potential is found to be $9.3 \times 10^{16} cm^{-3}$. The energy levels are 54.59 meV and 133.44 meV.
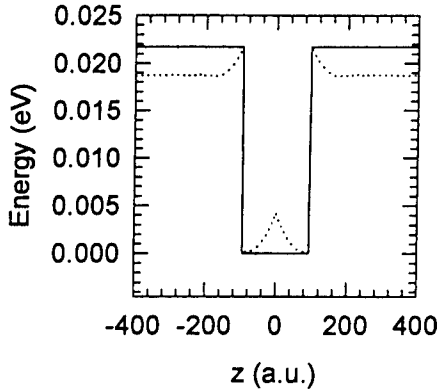
Fig.2
Potential profiles of the rectangular quantum well with and without modulation doping. The dotted line and solid line are the potential profiles with and without doping

The effect of the electric field on the energy levels with their resonance widths are given in Table 1.

Table I

Comparison of the energies and resonance widths with and without doping in a single rectangular QW. Energies with and without doping are denoted as $E_r^{(d)}$ and $E_r^{(w)}$ respectively. Similarly the resonance widths with and without doping are denoted as $\Gamma^{(d)}$ and $\Gamma^{(w)}$ respectively.

F (kV/cm)	$E_r^{(w)}$ (eV)	$\Gamma^{(w)}$ (eV)	$E_r^{(d)}$ (eV)	$\Gamma^{(d)}$ (eV)
50	0.03167	1.252×10^{-22}	0.05248	1.308×10^{-18}
100	0.02718	1.934×10^{-11}	0.04631	1.482×10^{-8}
150	0.02010	2.869×10^{-7}	0.03708	1.502×10^{-5}
200	0.01075	1.278×10^{-5}	0.02581	3.653×10^{-3}

From this table it is clear that energy levels and resonance widths are increased in the doped well compared to the undoped well. This happens because the barrier height is lowered as a result of the modulation doping in the rectangular QW.

II. Diffusion Modified Quantum Well

When the rectangular QW is subject to annealing above 800°C, intermixing starts at the heterojunction and the formation of the Ga vacancy induces Al atoms to diffuse into the GaAs layer from the AlGaAs [10]. The interdiffusion process is therefore characterized by the Al diffusion length ($L_d = \sqrt{Dt}$) which can be obtained from the diffusion constant (D) at the annealing temperature and the annealing time (t). Taking the diffusion constant to be isotropic, the position dependent Al concentration from the diffusion equation is found as[10,11]:

$$w(z) = x \left[1 - \frac{1}{2} \left\{ erf \left(\frac{L + 2z}{4L_d} \right) + erf \left(\frac{L - 2z}{4L_d} \right) \right\} \right] \tag{13}$$

where erf is the error function[12] and L is the width of the rectangular QW. The potential profile is expressed as

$$V(z) = B_{off}[E_g(w(z)) - E_g(w(0))] \tag{14}$$

We have taken $x = 0.3$, $L=100$Å. The binding energy and concentration of Si dopants are the same in this case as in the rectangular QW. The diffusion length L_d=20Å. The chemical potential and the concentration of ionised donors calculated in the doped QW are found to be 52 meV and 4.17×10^{16} cm^{-3} respectively. The potential profiles with and without doping are shown in Fig. 3.
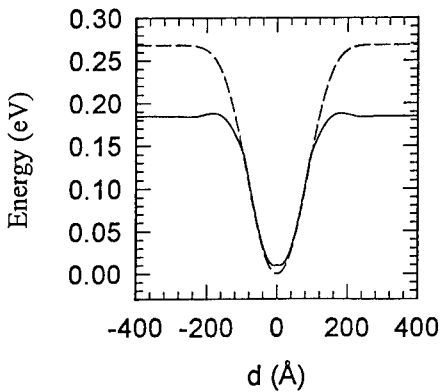
Fig. 3
Potential profiles of the diffusion modified quantum well with and without modulation doping. The solid line and dashed line are the potential profiles with and without doping.

The modulation doping has increased the effective width of the well and decreased the barrier height. The well before doping contains two energy levels at 55.63 meV and 160.46 meV. Since the barrier height is decreased in the doped well there is a single level in the well at 60.89 meV. The ground state energies and resonance widths for different field intensities are presented in Table II.

Table II
Comparison of the energies and resonance widths for a single diffusion modified quantum well with and without doping. The notations are the same as in Table I.

F (kV/cm)	$E_r^{(w)}$ (eV)	$\Gamma^{(w)}$ (eV)	$E_r^{(d)}$ (eV)	$\Gamma^{(d)}$ (eV)
25	0.028176	2.214×10^{-15}	0.060518	8.754×10^{-13}
50	0.027180	1.934×10^{-13}	0.059392	1.928×10^{-11}
75	0.020100	2.869×10^{-7}	0.057545	6.639×10^{-6}

As in the rectangular QW the energy levels and resonance widths are increased in the doped well compared to the undoped well. This happens because the barrier height is lowered as a result of the modulation doping.

CONCLUSION

In the present work we have extended the Fourier series method to calculate both the ground state quasi-bound energy levels with their resonance widths in the rectangular and diffusion modified modulation doped QWs. Although we have studied only two types of QW structures, this method can be applied to single, double and multiple QWs with arbitrary potential profiles. However, we would like to mention that this method cannot be used to study energies and lifetimes in QWs under a high electric field as the SG in this case cannot be obtained. We have not addressed the nature of quasi-Fermi level in the presence of the applied electric field in this work. The absorption coefficient in doped QWs under an applied electric field needs the temperature dependence of the Fermi level, wavefunctions, energies and mean tunneling lifetimes. Therefore our present work will be useful in calculating the absorption coefficients accurately in QW structures.

REFERENCES

[1] J. P. Loehr and M. O. Manasreh, Semiconductor quantum wells and superlattices for long wave length infrared detectors (Artech House, C1993, Ed. M. O. Manasreh)p-19
[2] G. Bastard, *Wave mechanics applied to semiconductor heterostructures* (Les Editions de Physique, c1988)
[3] W. Kohn and L. J. Sham, Phys. Rev. **140**, A1133 (1965)
[4] D. Huang, G. Gumbs and M. O. Manasreh, Phys. Rev. **B52**, 14126 (1995)
[5] S. Panda, B. K. Panda, S. Fung and C. D. Beling, Solid State Commun. **99**, 299 (1996)
[6] L. Hedin and B. I. Lundqvist, J. Phys. C **4**, 2064 (1971)
[7] D. G. Kanhere, P. V. Panat, A. K. Rajgopal and J. Callaway, Phys. Rev. A **33**, 490 (1986)
[8] F. Borondo and J. Sánchez-Dehesa, Phys. Rev. **B33**, 8758 (1986)
[9] A. Mácias and A. Riera, J. Chem. Phys. **96**, 2877 (1992)
[10] L. L. Chuang and A. Koma, Appl. Phys. Lett. **29**, 138 (1976)
[11] K. Mukai, M. Sugawara and S. Yamazaki, Phys. Rev. **B50**, 2273 (1994)
[12] M. Abramowitz and I. A. Stegun, *Handbook of Mathematical Function*, Washington DC (National Bureau of Standards, Washington, DC, 1964) p. 446

Part III

Quantum Infrared Detectors

THEORETICAL STUDIES OF ELECTRONIC INTERSUBBAND TRANSITIONS IN n-TYPE DOPED QUANTUM WELLS FOR INFRARED PHOTODETECTOR APPLICATIONS

DANHONG HUANG AND M. O. MANASREH
Phillips Laboratory (PL/VTMR), 3550 Aberdeen Avenue Southeast, Building 426
Kirtland Air Force Base, New Mexico 87117

ABSTRACT

A self-consistent (8×8)-$\mathbf{k} \cdot \mathbf{P}$ model based on the Kohn-Sham density-functional formalism is used to calculate the quasi-particle wave functions and energy levels in n-type doped quantum wells. The self-energy from electron-electron, electron-impurity, and electron-phonon scattering was included in the calculation. The electronic intersubband absorption was calculated using a generalized self-consistent-field method including the vertex correction. The theoretical approach was applied to explain the variation of the intersubband transition peak energies as the temperature or the electron density is changed. Good agreement between the theory and experiment was achieved. The present theoretical model was also applied to design two-colors quantum well infrared photodetectors and was found to agree with the experimental measurements. Based on the numerical calculation, an approach to realize the three-colors infrared photodetectors in the triple-coupled quantum wells was proposed.

INTRODUCTION

One way to monitor the changes in the material optical response is using a weak probe light that induces the intersubband transitions in the materials studied. Optical absorption technique has been proven to be one of the simplest and most applicable methods [1-4] to characterize materials. A full understanding of their optical properties is necessary because of their potential use as opto-electronic devices such as photodetectors, modulators, and lasers. Early work [5-10] on the intersubband transitions in Si-doped quantum wells showed that the exchange energy has a nontrivial contribution to the subband structure. The design of these photo-devices requires an accurate theory for the purpose of device modeling.

Quantum well intersubband photodetectors based on III-V semiconductors have been investigated in recent years as alternative structures to replace II-VI semiconductor materials in the infrared focal-plane arrays technology. Multi-band spectra are needed for many applications and image recognitions. In fact, one can extract many useful details from images obtained using the infrared focal-plane arrays with multi-band spectra.

There has been increasing interest in multi-band infrared detectors for simultaneous

imaging in separate wavelength bands. [11-13] One possible design for a two-colors photodetector is a quantum well with at least three confined states to generate large oscillator strengths for all possible intersubband transitions. To achieve this goal, one can increase either the barrier height or well width. In case of doping in well region, the two-dimensional electron density (n_{2D}) is increased as the well width (L_W) increases assuming that the three-dimensional doping concentration remains constant. For fixed n_{2D} and barrier material $Al_yGa_{1-y}As$, one can still increase the barrier height by choosing the well material as a ternary alloy $In_xGa_{1-x}As$ instead of $GaAs$. In a single-particle picture, the electron wave functions and energy subbands are completely decided by the barrier height and well width. When the quantum well is doped with electrons to obtain intersubband transition optical absorption spectra, the Coulomb interaction between electrons becomes very important, which leads to the wave functions and energy levels as being dependent on n_{2D} and temperature (T).

There have been many efforts devoted to the fabrication of multi-colors infrared photodetectors. The simplest method is to construct an image with multi-infrared focal-plane arrays each covers a different spectral band. Another method is to grow multi-stacks of different quantum well infrared photodetector structures separated by thick doped layers for different electrical contacts. [14-17] This approach can be applied to design more than two colors since each quantum well infrared photodetector can be tailored independently for certain wavelength regions. However, the existence of too many electrodes greatly complicates the device processing and the read-out electronics. Two-terminal devices have also been tested, [18,19] where the detected wavelength can be switched by applying different bias voltages. Due to the in-series electrical connections in this structure, a spectral crosstalk occurs when different stacks are illuminated simultaneously at different wavelengths. The quantum confined Stark-shift has been used to tune the detection wavelength by varying the bias voltage; [20-23] The bias electric field changes the electron energy-level separations leading to a shift in the intersubband absorption peaks. In order to get sufficient tuning range, different quantum-well structures such as stepped quantum well and asymmetric coupled-double quantum wells have been tried. [20-23] Unfortunately, the operation of these structures usually requires a relatively high bias voltages causing a large dark current and noise. Recently, Schneider, et al. [24] have proposed to stack a quantum well infrared photodetector and a photodiode together. As a result, by applying a forward or a reverse bias voltages, the device will operate at a long wavelength absorption quantum well infrared photodetector mode or at a short wavelength absorption photodiode mode. However, this structure depends on the bias voltage and requires three electrical contacts layers. It again complicates the device processing and introduces image distortions in the continuous operation mode. The same idea which makes use of the amorphous silicon materials was also proposed to fabricate multi-colors visible photodetectors. [25,26] The asymmetric or symmetric multi-subband quantum well infrared photodetector is thought of as another approach to the multi-colors infrared photodetectors [27-29] where there are more than one occupied subband. In this structure, the multi-intersubband transitions take place between two occupied subbands below the

Fermi energy or between one occupied subband and another empty subband close to the top of barrier height. However, it is very difficult to design more than two colors in this kind of structures since the conduction band offset is limited by the semiconductor materials. In addition, this structure requires a short-period superlattice barrier to collect the photo-generated carriers through a miniband transport.

In this paper, instead of using a single-band model for the electronic intersubband transitions we adopt a (8×8)-$\mathbf{k} \cdot \mathbf{P}$ multi-band model based on the Kohn-Sham density-functional formalism, which includes the band-mixing effect. Using this approach, we calculate the self-consistent quasi-particle wave functions and energy levels. Further, we have included the Coulomb self-energy correction to the quasi-particle energy levels. The electron-impurity and electron-phonon scattering is also considered in a self-consistent way to give rise to the lifetime of the quasi-particles and their energy shifts. The optical absorption coefficient has been calculated using the self-consistent-field method modified by the vertex correction in the ladder-diagram approximation. Very good agreement between our theoretical calculation and the experimental measurement is achieved.

This paper is organized as follows. In Sec. II, our model and theory for the calculation of electronic intersubband absorption in the n-type doped quantum wells are presented. In Sec. III, we apply our theory to explain the experimental results for the blue- and red-shifts in the absorption spectra as the temperature and electron density are changed. We also use our theory to design a two-colors quantum well infrared photodetector, which agrees with the experimental measurement. Moreover, a new way to realize the three-colors infrared photodetectors in the triple-coupled quantum wells is proposed based on our numerical calculation. Finally, the conclusion is presented in Sec. IV.

MODEL AND FORMALISM

In this section, we will present the formula for calculating the self-consistent quasi-particle wave functions and energy levels as well as the absorption coefficient in the n-type doped quantum wells.

Self-Consistent (8×8)-$\mathbf{k} \cdot \mathbf{P}$ Model

The quasi-particle wave functions $\phi_{j,k_\parallel}^{p}(z)$ and energy levels $E_j^p(k_\parallel)$ in the n-type doped quantum wells is determined by the Schrödinger equation in the (8×8)-$\mathbf{k} \cdot \mathbf{P}$ model [30]

$$\sum_{p'=1}^{8} \left[\underline{\mathcal{H}}_{p,p'} \left(k_\parallel, k_z \to -\frac{d}{dz} \right) + (V_{\mathrm{H}}(z) + V_{\mathrm{xc}}[n(z)]) \, \underline{I}_{p,p'} \right] \phi_{j,k_\parallel}^{p'}(z) = E_j^p(k_\parallel)\phi_{j,k_\parallel}^{p}(z) \quad (1)$$

for $j = 1,\ 2,\ \cdots,\ N$. The single-particle Hamiltonian matrix in Eq. (1) reads [31]

$$\underline{\mathcal{H}}(k_\parallel, k_z) = \underline{\mathcal{H}}^{\mathbf{k} \cdot \mathbf{P}}(k_\parallel, k_z) + \underline{\mathcal{H}}_1^{\mathrm{S.O.}}(k_\parallel, k_z) + \underline{\mathcal{D}}^{\mathbf{k} \cdot \mathbf{P}}(k_\parallel, k_z) + \underline{\mathcal{D}}_1^{\mathrm{S.O.}}(k_\parallel, k_z) \ , \quad (2)$$

where $\underline{\mathcal{H}}^{\mathbf{k} \cdot \mathbf{P}}(k_\parallel, k_z)$ is the usual Kane (8×8) unstrained Hamiltonian matrix including the k-independent part of the spin-orbit interaction, $\underline{\mathcal{H}}_1^{\mathrm{S.O.}}(k_\parallel, k_z)$ is the k-dependent part

of the spin-orbit interaction, $\underline{\mathcal{D}}^{\mathbf{k}\cdot\mathbf{P}}(k_{\parallel}, k_z)$ is the strained part of the Hamiltonian matrix including the k-independent part of the spin-orbit interaction, and $\underline{\mathcal{D}}_{i}^{\mathrm{S.O.}}(k_{\parallel}, k_z)$ is the k-dependent part of the spin-orbit interaction in the strained part of the Hamiltonian matrix. Since we are only concern the electronic intersubband transitions within the conduction band, we label $p = 1$ and 2 for the up-spin and down-spin states, respectively. The electron density function, $n(z)$, in Eq. (1) is written as

$$n(z) = \frac{1}{2\pi} \sum_{p=1}^{2} \sum_{j=1}^{N} \int_{0}^{+\infty} k_{\parallel} \, dk_{\parallel} \, \left| \phi_{j,k_{\parallel}}^{p}(z) \right|^2 \, f_0[E_j^p(k_{\parallel})] \; . \tag{3}$$

Moreover, the Hartree potential in Eq. (1) is determined from the Poisson's equation

$$\frac{d}{dz} \left[\epsilon_{\mathrm{b}}(z) \frac{d}{dz} V_{\mathrm{H}}(z) \right] = \frac{e^2}{\epsilon_0} [N_{\mathrm{D}}(z) - n(z)] \; , \tag{4}$$

and the exchange-correlation potential in the local-density approximation is written as [32]

$$V_{\mathrm{xc}}[n(z)] = -\frac{e^2}{8\pi\epsilon_0\epsilon_{\mathrm{b}}(z)a_0^*(z)} \left\{ 1 + \frac{0.7734 r_{\mathrm{s}}(z)}{21} \ln\left[1 + \frac{21}{r_{\mathrm{s}}(z)} \right] \right\} \left[\frac{2}{\pi\alpha r_{\mathrm{s}}(z)} \right] \; . \tag{5}$$

The following notations were introduced for the parameters appeared in Eqs. (3) and (5).

$$\alpha = \left(\frac{4}{9\pi} \right)^{\frac{1}{3}} \; , \tag{6}$$

$$f_0[E_j^p(k_{\parallel})] = \left[\exp\left(\frac{E_j^p(k_{\parallel}) - E_{\mathrm{F}}}{k_{\mathrm{B}}T} \right) + 1 \right]^{-1} \tag{7}$$

is the Fermi-Dirac distribution function of electrons in the quantum well with Fermi energy E_{F} and electron temperature T,

$$a_0^*(z) = \frac{4\pi\epsilon_0\epsilon_{\mathrm{b}}(z)\hbar^2}{m^*(z)e^2} \tag{8}$$

is the effective Bohr radius of electrons, and

$$r_{\mathrm{s}}(z) = \left\{ \frac{4}{3}\pi \, [a_0^*(z)]^3 \, n(z) \right\}^{-\frac{1}{3}} \tag{9}$$

is the dimensionless electron density parameter. Besides, $N_{\mathrm{D}}(z)$ in Eq. (4) is the doping profile, $\epsilon_{\mathrm{b}}(z)$ in Eqs. (4) and (5) is the position-dependent dielectric constant in the well ($\epsilon_{\mathrm{b}}^{\mathrm{W}}$) and the barrier ($\epsilon_{\mathrm{b}}^{\mathrm{B}}$) materials, $m^*(z)$ in Eq. (8) is the position-dependent effective mass of electrons. Eqs. (1) - (9) will be solved simultaneously in a self-consistent way.

Coulomb Self-Energy Correction

If the band gap of the semiconductor materials studied is not narrow, the spin splitting of the electronic states in the conduction band can be neglected. In this case, we adopt the spin-degenerate model for the electrons and drop the spin index p from now on. It is known that the local-density approximation can neglect the local non-neutrality, band-structure, and temperature effects in the exchange-correlation energy. Since the self-consistent wave functions obtained above are good approximations of the true wave functions, the subband energies will be improved by calculating the Coulomb self-energy correction to the energy levels $E_j(k_\parallel)$, which brings in an additional modification to the electron energy dispersion. This correction is real and found to be [33]

$$\delta\Sigma_j^c(k_\parallel) = -\int_{-\infty}^{+\infty} dz \; \left|\phi_{j,k_\parallel}(z)\right|^2 \; V_{\text{xc}}[n(z)] \; - \sum_{i,\mathbf{k}_\parallel'} f_0[E_i(k_\parallel')] \; \left[\frac{e^2}{2\epsilon_0\epsilon_b(|\mathbf{k}_\parallel - \mathbf{k}_\parallel'| + q_i^{\text{TF}})}\right]$$

$$\times \left[\int_{-\infty}^{+\infty} dz \int_{-\infty}^{+\infty} dz' \; \phi_{j,k_\parallel}^*(z)\phi_{i,k_\parallel'}(z)\exp(-|\mathbf{k}_\parallel - \mathbf{k}_\parallel'||z - z'|) \; \phi_{i,k_\parallel'}^*(z')\phi_{j,k_\parallel}(z')\right] \;, \quad (10)$$

where $\epsilon_b = (\epsilon_b^{\text{W}} + \epsilon_b^{\text{B}})/2$ is the average dielectric constant for the quantum well system. Here, q_j^{TF} in Eq. (10) is the inverse of the Thomas-Fermi screening length [29]

$$q_i^{\text{TF}} = \frac{e^2}{8\pi\epsilon_0\epsilon_b k_B T} \int_0^{+\infty} dk_\parallel \; k_\parallel \; \cosh^{-2}\left[\frac{E_i(k_\parallel) - E_F}{2k_B T}\right] \quad (11)$$

Scattering Correction

Although the Coulomb self-energy has been included, it produces an infinite lifetime of the quasi-particles. The electron-impurity and electron-phonon scattering introduce an additional complex self-energy term $\Sigma_j^s(k_\parallel)$. This self-energy is expressed as the sum of two contributions

$$\Sigma_j^s(k_\parallel) = \Sigma_{j,k_\parallel}^{\text{im}}(E)\Big\|_{E=E_j(k_\parallel)+\delta\Sigma_j^c(k_\parallel)} + \Sigma_{j,k_\parallel}^{\text{ph}}(E)\Big\|_{E=E_j(k_\parallel)+\delta\Sigma_j^c(k_\parallel)} \;, \quad (12)$$

where in the self-consistent Born approximation [34] we get the following two self-consistent equations for the electron-impurity and electron-phonon self-energies, namely,

$$\Sigma_{j,k_\parallel}^{\text{im}}(E) = \frac{1}{2\pi}\sum_{j'} \left[\int_0^{+\infty} k_\parallel' \, dk_\parallel' \; \left[\Gamma_{j,j'}^{\text{im}}(\mathbf{k}_\parallel, \mathbf{k}_\parallel')\right]^2 \left(\frac{1}{E - E_{j'}(k_\parallel') - \delta\Sigma_{j'}^c(k_\parallel') - \Sigma_{j',k_\parallel}^{\text{im}}(E)}\right)\right]$$

$$(13)$$

is for the electron-impurity scattering, and

$$\Sigma_{j,k_\parallel}^{\text{ph}}(E) = \sum_{j'} \sum_{\mathbf{q}_\parallel, q_z} \left|M_{j,j'}(k_\parallel; q_\parallel, q_z)\right|^2$$

$$\times \left[\frac{n_{\mathrm{ph}}(\omega_{\mathrm{LO}}) + f_0[E_{j'}(|\mathbf{k}_\| + \mathbf{q}_\||) + \delta\Sigma^c_{j'}(|\mathbf{k}_\| + \mathbf{q}_\||)]}{E + \hbar\omega_{\mathrm{LO}} - E_{j'}(|\mathbf{k}_\| + \mathbf{q}_\||) - \delta\Sigma^c_{j'}(|\mathbf{k}_\| + \mathbf{q}_\||) - \Sigma^{\mathrm{ph}}_{j',|\mathbf{k}_\| + \mathbf{q}_\||}(E + \hbar\omega_{\mathrm{LO}})} \right.$$

$$\left. + \frac{n_{\mathrm{ph}}(\omega_{\mathrm{LO}}) + 1 - f_0[E_{j'}(|\mathbf{k}_\| + \mathbf{q}_\||) + \delta\Sigma^c_{j'}(|\mathbf{k}_\| + \mathbf{q}_\||)]}{E - \hbar\omega_{\mathrm{LO}} - E_{j'}(|\mathbf{k}_\| + \mathbf{q}_\||) - \delta\Sigma^c_{j'}(|\mathbf{k}_\| + \mathbf{q}_\||) - \Sigma^{\mathrm{ph}}_{j',|\mathbf{k}_\| + \mathbf{q}_\||}(E - \hbar\omega_{\mathrm{LO}})} \right] \tag{14}$$

is for the electron-phonon scattering. In Eqs. (13) and (14), we have defined the scattering vertex as follows:

$$\left[\Gamma^{\mathrm{im}}_{j,j'}(\mathbf{k}_\|, \mathbf{k}'_\|)\right]^2 = \left[\frac{e^2}{2\epsilon_0\epsilon_b(|\mathbf{k}_\| - \mathbf{k}'_\|| + q_{j'}^{\mathrm{TF}})}\right]^2 \int_{-\infty}^{+\infty} dz' \; N_{\mathrm{D}}(z')$$

$$\times \left| \int_{-\infty}^{+\infty} dz \; \phi^*_{j,k_\|}(z) \; \exp(-|\mathbf{k}_\| - \mathbf{k}'_\|| |z - z'|) \; \phi_{j',k'_\|}(z) \right|^2 \tag{15}$$

is for the electron-impurity scattering vertex, and

$$\left| M_{j,j'}(k_\|; q_\|, q_z) \right|^2 = \frac{\hbar\omega_{\mathrm{LO}}}{2} \left(\frac{1}{\epsilon_\infty} - \frac{1}{\epsilon_s} \right) \left[\frac{e^2}{\epsilon_0(q_\|^2 + q_z^2 + 2q_{j'}^{\mathrm{TF}}/L_{\mathrm{W}})} \right]$$

$$\times \left| \int_{-\infty}^{+\infty} dz \; \phi^*_{j,k_\|}(z) \; \exp(iq_z z) \; \phi_{j',|\mathbf{k}_\| + \mathbf{q}_\||}(z) \right|^2 \tag{16}$$

is for the electron-phonon scattering vertex. Moreover, L_{W} in Eq. (16) is the width of quantum well, $\hbar\omega_{\mathrm{LO}}$ is the frequency of the longitudinal-optical phonons for the well material, and

$$n_{\mathrm{ph}}(\omega_{\mathrm{LO}}) = \left[\exp\left(\frac{\hbar\omega_{\mathrm{LO}}}{k_{\mathrm{B}}T} \right) - 1 \right]^{-1} \tag{17}$$

is the phonon distribution factor. In Eq. (16), we have also introduced the static dielectric constant, ϵ_s, and the optical-frequency dielectric constant, ϵ_∞.

Absorption Coefficient

When an external z-polarized probing field is applied, the resulting perturbation in the electron density function will produce an optical response from a normal mode of density fluctuation. In the long wavelength limit, only the vertical intersubband transitions need to be considered. For a probing field interacting weakly with the electrons in the quantum wells, the absorption coefficient is defined as the ratio of the energy absorbed per unit volume and per unit time to the incident flux. A straightforward calculation yields [29]

$$\beta_{\mathrm{abs}}(\omega) = \frac{\omega\sqrt{\epsilon_b}}{cn(\omega)} \left[\rho_{\mathrm{ph}}(\omega) + 1 \right] \; Im \; \alpha_{\mathrm{L}}(\omega) \,, \tag{18}$$

where ω is the frequency of the probing field, $\rho_{\mathrm{ph}}(\omega) = [\exp(\hbar\omega/k_{\mathrm{B}}T) - 1]^{-1}$ is the photon distribution factor. In Eq. (18), $\alpha_{\mathrm{L}}(\omega)$ is the complex Lorentz ratio, which is given by

$$
\alpha_{\mathrm{L}}(\omega) = -\frac{e^2}{\pi\epsilon_0\epsilon_{\mathrm{b}} L_{\mathrm{W}}} \sum_{j<j'} \int_0^{+\infty} k_\parallel \, dk_\parallel \, F_{j',j}(k_\parallel)
$$

$$
\times \left[F_{j,j'}(k_\parallel) + D_{j,j'}(k_\parallel,\omega) \right] \chi_{j,j'}^{(0)}(k_\parallel,\omega) \, \Gamma_{j,j'}(k_\parallel,\omega) \,, \tag{19}
$$

and $n(\omega)$ is the scaled frequency-dependent refractive index function, which is give by

$$
n(\omega) = \frac{1}{\sqrt{2}} \left\{ 1 + Re\ \alpha_{\mathrm{L}}(\omega) + \sqrt{[1 + Re\ \alpha_{\mathrm{L}}(\omega)]^2 + [Im\ \alpha_{\mathrm{L}}(\omega)]^2} \right\}^{\frac{1}{2}} \,. \tag{20}
$$

In Eq. (19), the susceptibility of non-interacting quasi-particles, $\chi_{j,j'}^{(0)}(k_\parallel,\ \omega)$, is for $j < j'$

$$
\chi_{j,j'}^{(0)}(k_\parallel,\omega) = \frac{n_j(k_\parallel) - n_{j'}(k_\parallel)}{\hbar\omega - \Delta_{j'}(k_\parallel) + \Delta_j(k_\parallel) + i\gamma_{j,j'}(k_\parallel)} + \frac{n_{j'}(k_\parallel) - n_j(k_\parallel)}{\hbar\omega + \Delta_{j'}(k_\parallel) - \Delta_j(k_\parallel) + i\gamma_{j,j'}(k_\parallel)} \,,
$$
$$
\tag{21}
$$

where

$$
\Delta_j(k_\parallel) = E_j(k_\parallel) + \delta\Sigma_j^{\mathrm{c}}(k_\parallel) + Re\ \Sigma_j^{\mathrm{s}}(k_\parallel) \tag{22}
$$

is the renormalized quasi-particle energy levels,

$$
\gamma_{j,j'}(k_\parallel) = -2 \left[Im\ \Sigma_j^{\mathrm{s}}(k_\parallel) + Im\ \Sigma_{j'}^{\mathrm{s}}(k_\parallel) \right] \tag{23}
$$

is the energy level broadening due to the electron-impurity and electron-phonon scattering, and $n_j(k_\parallel)$ in Eq. (21) cab be obtained by replacing $E_j^{\mathrm{p}}(k_\parallel)$ in Eq. (7) with $\Delta_j(k_\parallel)$. The vertex part, $\Gamma_{j,j'}(k_\parallel,\ \omega)$, in Eq. (19) is due to the excitonic interaction and can be calculated by summing over all the ladder diagrams. The result of this summation is the following Bethe-Salpeter's equation [35] for $j < j'$

$$
\Gamma_{j,j'}(k_\parallel',\omega) = 1 - \frac{1}{(2\pi)^2} \int d^2\mathbf{k}_\parallel \, \chi_{j,j'}^{(0)}(k_\parallel,\omega) \, \Gamma_{j,j'}(k_\parallel,\omega) \left[\frac{e^2}{2\epsilon_0\epsilon_b(|\mathbf{k}_\parallel' - \mathbf{k}_\parallel| + q_{j'}^{\mathrm{TF}})} \right]
$$

$$
\times \left[\int_{-\infty}^{+\infty} dz \int_{-\infty}^{+\infty} dz' \, \phi_{j,k_\parallel'}^*(z)\phi_{j',k_\parallel}(z) \exp(-|\mathbf{k}_\parallel' - \mathbf{k}_\parallel||z - z'|) \, \phi_{j',k_\parallel}^*(z')\phi_{j,k_\parallel'}(z') \right] \,, \tag{24}
$$

where we need to replace $E_j(k_\parallel)$ with $\Delta_j(k_\parallel)$ in evaluating q_j^{TF} in Eq. (11) for the Thomas-Fermi dielectric-function matrix above. In Eq. (24), the small exciton-coupling effect is neglected. Moreover, in Eq. (19) the quasi-particle dipole moment, $F_{j,j'}(k_\parallel)$, and the collective dipole moment, $D_{j,j'}(k_\parallel,\omega)$, are calculated according to

$$
F_{j,j'}(k_\parallel) = \int_{-\infty}^{+\infty} dz \, \phi_{j,k_\parallel}^*(z) \, z \, \phi_{j',k_\parallel}(z) \,, \tag{25}
$$

and [36]

$$\sum_{\mathbf{k}_{\parallel}} \sum_{j<j'} D_{j,j'}(k_{\parallel},\omega) \left[\delta_{n,j}\delta_{n',j'}\delta_{\mathbf{k}_{\parallel},\mathbf{k}'_{\parallel}} - 2\, \chi^{(0)}_{j,j'}(k_{\parallel},\omega)\Gamma_{j,j'}(k_{\parallel},\omega) \right.$$

$$\times \left. \int_{-\infty}^{+\infty} dz \int_{-\infty}^{+\infty} dz' \phi^{*}_{n,k'_{\parallel}}(z)\phi_{n',k'_{\parallel}}(z)\left(-\frac{e^2}{2\epsilon_0\epsilon_b}\,|z-z'|\right)\phi^{*}_{j',k_{\parallel}}(z')\phi_{j,k_{\parallel}}(z') \right]$$

$$= 2 \sum_{\mathbf{k}_{\parallel}} \sum_{j<j'} \chi^{(0)}_{j,j'}(k_{\parallel},\omega)\Gamma_{j,j'}(k_{\parallel},\omega)$$

$$\times \int_{-\infty}^{+\infty} dz \int_{-\infty}^{+\infty} dz' \phi^{*}_{n,k'_{\parallel}}(z)\phi_{n',k'_{\parallel}}(z)\left(-\frac{e^2}{2\epsilon_0\epsilon_b}\,|z-z'|\right)\phi^{*}_{j',k_{\parallel}}(z')\phi_{j,k_{\parallel}}(z') . \tag{26}$$

We can see from Eq. (26) that the screening effect has been included in the dielectric-function which is shown as a coefficient matrix.

APPLICATIONS TO INFRARED PHOTODETECTORS

In this section, we will apply our theory to explain the variation of the intersubband transition peak energies as the temperature or the electron density is changed. We will also use the present theoretical model to design two-colors quantum well infrared photode-tectors. Motivated by the numerical calculation, we will propose a new way to realize the three-colors infrared photodetectors in the triple-coupled quantum wells. The following numerical results shown in Figs. 1-5 are obtained by using the single-band self-consistent Hartree-Fock approximation. However, the results using (8×8)-$\mathbf{k} \cdot \mathbf{P}$ theory only display a little change compared with the Hartree-Fock calculations.

Blue- and Red-Shifts of Intersubband Transition Peak Energies

First, we compare our theoretical calculations of the optical absorption spectra with the experimental measurements in a $Al_{0.3}Ga_{0.7}As/GaAs$ quantum well with well width $L_W = 75$ Å. The n-type doping is in the well region. There are two confined states in the quantum well and the intersubband transition is between these two states.

In Fig. 1, we present the absorption coefficient $\beta_{abs}(\omega)$ from both our calculated results and experimental data (recorded at the Brewster angle using a FTIR spectrometer) for two electron densities n_{2D} at $T = 5$ K. The peak energy increases with n_{2D}. The positive Hartree energy, depending on n_{2D}, shifts both subbands upward, while leaving their separation almost unchanged. The negative exchange energy shifts the first subband down more than the second subband, thereby increasing their separation. For an increased n_{2D}, the exchange energy becomes dominant. Therefore, the peak position moves to the right.

In addition, we find that the calculated peak positions coincide well with those from experiment for both the low- and high-density samples. The peak strength of the low-density peak is slightly lower than that observed in the experiment. The line shapes show slight deviations at energies away from the peak energy and a small peak width is obtained in comparison with the measurement. For high n_{2D}, the second subband begins to be populated. The collective dipole moment $D_{j,j'}(k_{\parallel}, \omega)$ due to the Hartree interaction is found to shrink the peak width, while the exchange interaction expands the peak width. We attribute the asymmetrical line shape to the ω-dependence in $n(\omega)$, strong non-parabolic energy dispersion at large k and the exchange interaction.
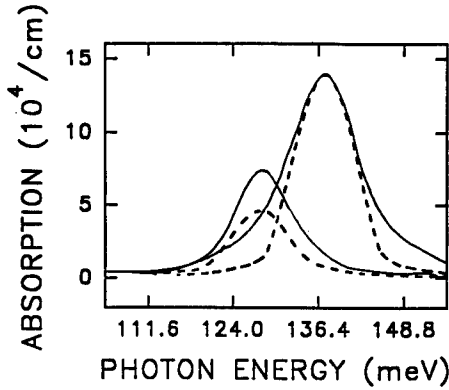
FIG. 1: Comparison between the calculated $\beta_{abs}(\omega)$ (dashed lines) with the measurements (solid lines) at $T = 5$ K for $Al_{0.3}Ga_{0.7}As/GaAs$ samples with $L_W = 75$ Å, $n_{2D} = 7.5$ and 37.5×10^{11} cm^{-2}. The high-energy peak is for the high-density sample.
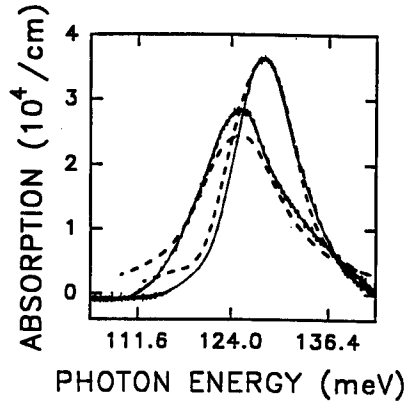
FIG. 2: Comparison between the calculated $\beta_{abs}(\omega)$ (dashed lines) of the $Al_{0.3}Ga_{0.7}As/GaAs$ sample with $L_W = 75$ Å and $n_{2D} = 7.5 \times 10^{11}$ cm^{-2} at $T = 5$ K and 300 K with the experimental measurements (solid lines). The high-energy peak is for $T = 5$ K.

In Fig. 2 we present a quantitative comparison between $\beta_{abs}(\omega)$ from our numerical simulations and experimental data for the low-density sample at $T = 5$ K and 300 K. The peak energy increases with reducing T, shown as a blue-shift. The crucial negative exchange energy brings down the first subband more than the second subband, and increases the separation between them. With an increase in T, the exchange interaction becomes weaker, and then, the peak energy decreases. Moreover, we find that the calculated peak positions also coincide with those measured at low and high temperatures. The peak strength of the high-temperature peak seems a little bit smaller than that observed. The asymmetrical line shape of both curves displays very small deviations on the lower energy side.

Design of Two-Colors Quantum Well Infrared Photodetectors

Second, we apply our theory to design a two-colors quantum well infrared photodetector. The structure we consider in a $In_{0.07}Ga_{0.93}As/Al_{0.40}Ga_{0.60}As$ strained quantum well with doping concentration 2.0×10^{18} cm^{-3} in the well region. There are three confined states in the quantum well. The intersubband transitions studied include from the ground energy level to the middle energy level E_{12} and from the middle energy level to the top energy level E_{23}.
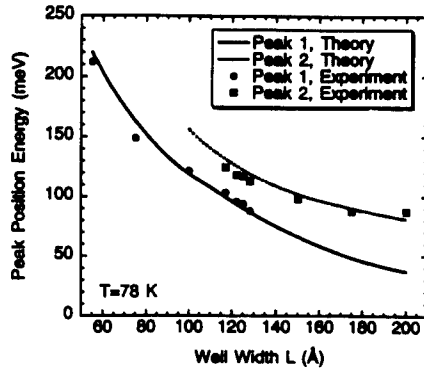
FIG. 3: Comparison of the calculated (lines) and measured (symbols) peaks position energies of the two intersubband transitions related to E_{12} (peak 1) and E_{23} (peak 2) at 78 K as a function of the well width L_W in the $In_{0.07}Ga_{0.93}As/Al_{0.40}Ga_{0.60}As$ multiple quantum wells with doping concentration 2.0×10^{18} cm^{-3} in the well region.

For direct comparison between our design and experimental measurement, we plotted the peak position energies of E_{12} and E_{23} transitions in Fig. 3 as a function of the well width L_W at $T = 78$ K. It is clear from this figure that good agreement between our theoretical prediction (solid and dashed lines) and experimental measurement (solid squares and circles) is achieved. It is also noted in Fig. 3 that the separation between two intersubband transitions is increased as L_W increases. Thus far we are able to show the following. First, the optical absorption measurements of the intersubband transitions show that one transition related to E_{12} is observed in samples in which the Fermi energy E_F lies between the ground and middle energy levels. Second, two intersubband transitions related to E_{12} and E_{23} transitions are observed for samples in which E_F is above

the middle energy level. Third, the strength of the E_{12} transition is decreased as E_F is raised above the middle energy level, which is achieved by increasing L_W. In fact, we are unable to observe the E_{12} transition in samples with L_W larger than 175 $\mathring{A}$ which can be explained by the phase blocking. The phase blocking is a result of the Pauli's exclusion principle for electrons. Considering that the electrons are excited from the ground energy level to the middle energy level, we know that it can happen only when the initial state is occupied and the final state is empty, or partially empty, at the same time. If E_F is above the middle energy level, the population of the middle energy level would block out the electron transition from the ground energy level to the middle energy level. Since the peak strength (intensity) depends strongly on the number of the allowed transitions from the ground energy level to the middle energy level, it is then easy to explain the suppression of the E_{12} transition as E_F is raised above the middle energy level.

Realization of the three-Colors Infrared Photodetectors

Third, we use our numerical calculation as a guide to propose an approach of realizing the three-colors infrared photodetectors in the triple-coupled quantum wells (TCQW).
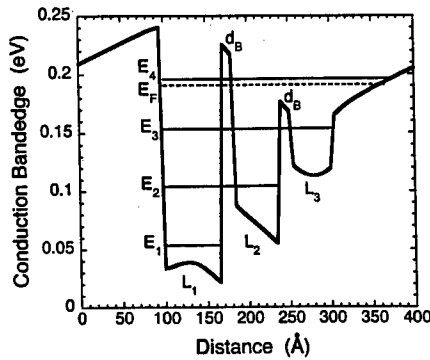
FIG. 4: Plot of the calculated conduction band edge of the tripled-coupled quantum wells structure. The energy levels E_1, E_2, E_3, E_4 and the Fermi energy E_F are also shown. In this figure, d_B is the thickness of the inner barriers and L_1, L_2, L_3 are the well widths for three quantum wells.
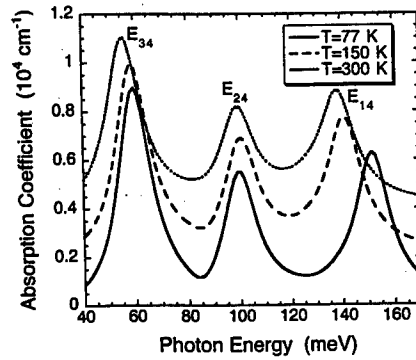
FIG. 5: The optical absorption coefficient, $\beta_{abs}(\omega)$, as a function of photon energy at three different temperatures for the structure shown in Fig. 4. The three peaks represent the E_{14}, E_{24}, and E_{34} transitions. The spectra were displayed for clarity.

The structure we consider is shown in Fig. 4, where all the barrier layers are composed of $Al_{0.25}Ga_{0.75}As$ material, the first well from left is composed of $GaAs$ material, the

second well is composed of $Al_{0.10}Ga_{0.90}As$ material, and the third well is composed of $Al_{0.20}Ga_{0.80}As$ material. The width of these three wells are 70, 60 and 55 $\mathring{A}$, respectively. The thickness of two middle barrier layers is $d_B = 10$ $\mathring{A}$. The doping is in the well regions with the same concentration 4×10^{18} cm^{-3}. We have set $T = 77$ K in this calculation. Because we assume that the doping concentration is the same for the three wells, then resulting n_{2D} is different in each well since they have different well widths. This causes a built-in space charge electric field, opposite to the z direction, inside the TCQW structure due to the imbalance of n_{2D}. The built-in space charge electric field introduces the band bending effect as shown in Fig. 4. The band bending is usually affected by varying T and/or increasing/decreasing the well widths assuming the same doping concentration for the three wells. Additionally, this type of band bending can be compensated by applying an electric field in the opposite direction to the built-in space charge electric field. The structure is designed such that the Fermi energy E_F lies between E_3 and E_4. The final state E_4 is slightly below the top of the barriers, which implies the intersubband transitions to E_4 is a bound-to-bound transitions. The transitions we studied here take place from the three initial states E_1, E_2, E_3 to the same final state E_4 and they are denoted here as E_{14}, E_{24} and E_{34}. Because of the Pauli exclusion principle, the oscillator strength of the transitions between any pair of occupied energy levels E_1, E_2, and E_3 are expected to be negligible. Therefore, we only need to consider E_{14}, E_{24} and E_{34} intersubband transitions.

The temperature effect on the optical absorption coefficient $\beta_{abs}(\omega)$ of the intersubband transition is studied and the results are shown in Fig. 5. It is clear from this figure that $\beta_{abs}(\omega)$ associated with E_{14} and $_{34}$ transitions exhibit a blue-shift as the temperature decreases, while the E_{34} transition remains approximately independent of temperature. This behavior could be explained as follows: the energy levels E_1 and E_3 are occupied and therefore they are shifted downward due to various many-body effects. On the other hand E_4 is almost empty and it is affected slightly by the many-body effects. It is worth mentioning here that E_{24} transition is almost independent of temperature as shown in Fig. 5. This is due to the fact that the band bending and many-body effects in the middle quantum well are opposite in sign and approximately equal in magnitude. The resultant of the competition between these effects in the middle quantum well is negligible in a way that E_2 remains unaffected as T is increased/decreased leading to an almost constant E_{24} peak position energy as a function of T.

CONCLUSIONS

In conclusion, we used a (8×8)-$\mathbf{k} \cdot \mathbf{P}$ multi-band Hamiltonian model with the Kohn-Sham density-functional formalism to include many-body, space-charge, and band-mixing effect. Based on this self-consistent approach, we calculated the wave functions and energy levels of the quasi-particles. By using these self-consistent quasi-particle wave functions, we further computed the Coulomb self-energy correction to the quasi-particle energy levels. Both the electron-impurity and electron-phonon scattering was included in our calculation

in the self-consistent Born approximation, which provided a finite lifetime to the quasi-particles and and a energy-level shift. The intersubband optical absorption coefficient was calculated using the self-consistent-field method to include the electron screening and modified by the vertex in the ladder-diagram approximation correction to include the excitonic interaction. Very good agreement between our theoretical calculation and the experimental measurement was achieved for the blue-shift and red-shift in the intersubband transition peak energies as the temperature and electron density are varied. The current theory was also applied to design a two-colors quantum well infrared photodetector. Our theoretical prediction was to found to agree with the experimental measurement. Furthermore, based on our numerical calculation a new approach to realize the three-colors infrared photodetectors in the triple-coupled quantum wells was proposed.

ACKNOWLEDGEMENTS

REFERENCES

1. M. O. Manasreh, F. Szmulowicz, D. W. Fischer, K. R. Evans, and C. E. Stutz, Appl. Phys. Lett. **57**, 1790 (1990).

2. M. O. Manasreh and J. P. Loehr in *Semiconductor Quantum Wells and Superlattices for Long Wavelength Infrared Detection*, (Artech, Boston, 1993), Chap. 2.

3. M. O. Manasreh, F. Szmulowicz, T. Vaughan, K. R. Evans, C. E. Stutz, and D. W. Fischer, Phys. Rev. **B43**, 9996 (1991).

4. P. von Allmen, et al., Semi. Sci. and Technol. **3**, 1211 (1988); Superlattices and Microstructures **5**, 259 (1989).

5. K. Bandara, D. D. Coon, O. Byungsung, Y. F. Lin, and M. H. Francombe, Appl. Phys. Lett. **53**, 1931 (1988).

6. F. Szmulowicz, M. O. Manasreh, C. E. Stutz, and T. Vaughan, Phys. Rev. **B50**, 11618 (1994).

7. G. Gumbs, D. Huang, and J. P. Loehr, Phys. Rev. **B51**, 4321 (1995).

8. M. Za /użny, Solid State Commun. **82**, 565 (1992).

9. M. Za /użny, Phys. Rev. **B43**, 4511 (1991).

10. D. H. Huang, G. Gumbs, and M. O. Monasreh, Phys. Rev. **B52**, 14126 (1995).

11. Kim, S. R. Forrest, M. J. Lange, G. H. Olsen, and M. J. Cohen, IEEE Photon. Technol. Lett. **PFL-6**, 235 (1994).

12. M. C. Chen and M. J. Bevan, J. Appl. Phys. **78**, 4787 (1995).

13. Y, Huang and C. Lien, J. Appl. Phys. **77**, 3433 (1995).

14. A. Köck, E. Gornik, G. Abstreiter, G. Böhm, M. Walther, and G. Weimann, Appl. Phys. Lett. **60**, 2011 (1992).

15. M. C. Chen and M. J. Bevan, J. Appl. Phys. **78**, 4787 (1995).

16. C. J. Chen, K. K. Choi, M. Z. Tidrow, and D. C. Tsui, Appl. Phys. Lett. **68**, 1446 (1996).

17. Y. Zhang, D. S. Jiang, J. B, Xia, L. Q. Cui, C. Y. Song, and Z. Q. Zhou, Appl. Phys. Lett. **68**, 2114 (1996).

18. I. Gravé, A. Shakouri, N. Kuze, and A. Yariv, Appl. Phys. Lett. **60**, 2362 (1992).

19. K. L. Tsai, K. H. Chang, C. P. Lee, K. F. Huang, J. S. Tsang, and H. R. Chen, Appl. Phys. Lett. **62**, 3504 (1993).

20. S. R. Parihar, S. A. Lyon, M. Santos, and M. Shayegan, Appl. Phys. Lett. **55**, 2417 (1989).

21. K. K. Choi, B. F. Levine, C. G. Bethea, J. Walker, and R. J. Malik, Phys. Rev. B **39**, 8029 (1989).

22. V. Berger, N. Vodjdani, P. Bois, B. Vinter, and S. Delaitre, Appl. Phys. Lett. **61**, 1898 (1992).

23. Y. Huang and C. Lien, J. Appl. Phys. **77**, 3433 (1995).

24. H. Schneider, C. Schönbeinm, and Bihlmann, Appl. Phys. Lett. **68**, 1832 (1996).

25. H. Stiebig, J. Giehl, D. Knipp, P. Rieve, and M Böhm, Mat. Res. Soc. Symp. Proc. **377**, 815 (1995).

26. J. Giehl, Q. Zhu, P. Rieve, and M. Böhm, "Transient Behavior of Color Diodes", Mat. Res. Soc. Symp. Proc., 1996 (to be published).

27. K. Kheng, M. Ramsteiner, H. Schneider, J. D. Ralston, F. Fuchs, and P. Koidl, Appl. Phys. Lett. **61**, 666 (1992).

28. Y. H. Wang and S. S. Li, Appl. Phys. Lett. **62**, 93 (1993).

29. D. H. Huang and M. O. Manasreh, Phys. Rev. B **54**, 5620, 1996.

30. W. Kohn and L. J. Sham, Phys. Rev. **140**, A1133 (1965).

31. T. B. Bahder, Phys. Rev. B **41**, 11992, 1990.

32. L. Hedin and B. I. Lundqvist, J. Phys. C **4**, 2064 (1971).

33. A. Tomita, Phys. Rev. B **54**, 5609, 1996.

34. T. Ando, A. B. Fowler, and F. Stern, Rev. Mod. Phys. **54**, 437 (1982).

35. G. D. Mahan, *Many-Particle Physics* (Plenum, New York, 1981), Chap. 5.

36. A. C. Tselis and J. J. Quinn, Phys. Rev. B **29**, 3318 (1984).

INFRA-RED TUNNELING ABSORPTION IN SEMICONDUCTOR DOUBLE QUANTUM WELLS IN TILTED MAGNETIC FIELDS

S. K. LYO
Sandia National Laboratories, Albuquerque, N. M. 87185

ABSTRACT

Using a linear response theory, interwell-tunneling absorption of infra-red photons is calculated in a double-quantum-well structure with a wide center barrier in tilted magnetic fields. Tunneling occurs between the ground sublevels of the two quantum wells, with an energy difference that is tunable. The absorption intensity depends strongly on the temperature and the carrier densities. The resonance width is narrow even at high temperatures due to the two-dimensional phase restriction for tunneling. In magnetic fields, both the in-plane and perpendicular components of the field sensitively control and tune the absorption lineshape in very different ways, affecting the absorption threshold, the resonance energy of absorption, and the linewidth.

INTRODUCTION

Long-wavelength infra-red (IR) detectors are currently receiving increasing attention for chemical sensing, thermal detection, and other applications. In this paper, we present theoretical studies of IR tunneling absorption in weakly tunnel-coupled n-type semiconductor double quantum wells (DQWs) (e.g., GaAs/AlGaAs) in tilted magnetic fields $\mathbf{B} = (\mathbf{B}_{\parallel}, \mathbf{B}_{\perp})$. The QWs are separated by a wide barrier and have a tunable energy mismatch Δ between the two ground sublevels. Inter-QW IR absorption is one of many interesting phenomena caused by tunneling between two quasi-two-dimensional (2D) electron layers [1]. Recently, Simmons pointed out that the absorption linewidth is narrow for tunneling in two dimensions and proposed to use tunneling-DQW structures for IR detectors [2]. In this structure, the two QWs have independent ohmic contacts [3]. In DC and AC tunneling transport and photoconductance, electrons flow in through one end of a QW, undergo resonant or photon-assisted tunneling through the barrier between the two QWs, and then flow out of the other end of the second QW. The in-plane conductances in the QWs are much larger than the tunneling conductance, yielding negligible potential drop along the current paths inside each QW. The linear driving electric field is in the direction perpendicular to the plane of the two QWs. The QWs are in equilibrium. The present study does not apply to strongly-coupled DQWs with a thin center barrier, where entirely different physical phenomena occur [1].

Our theory is valid for tunneling absorption of IR photons between the sublevels of one QW and those of the other QW. However, applications are made only to the typical situation where tunneling occurs between the two ground sublevels. The effect of spin splitting is neglected. In $\mathbf{B} = 0$, the absorption intensity decreases significantly as the line width increases with increasing temperature (T). The absorption intensity depends strongly on the electron density. In magnetic fields, the in-plane ($B_{\parallel}$) and perpendicular ($B_{\perp}$) components of the field are found to sensitively control and tune the absorption line shape in very different ways. The perpendicular component of the field $B_{\perp}$ tunes the cyclotron energy, relative positions of the two Landau ladders for asymmetric QWs, and the interwell spectral overlap of the density of states of the Landau levels. On the other hand, for $B_{\perp} = 0$, the in-plane field $B_{\parallel}$ merely shifts the relative separation of the energy-dispersion paraboloids of the two QWs in k-space, tuning the absorption maxima, minimum, and the absorption edges. For $B_{\perp} > 0$, however, the in-plane field also modulates the effective tunneling strength by displacing the centroid of the initial- and final-state Landau-level wave functions.
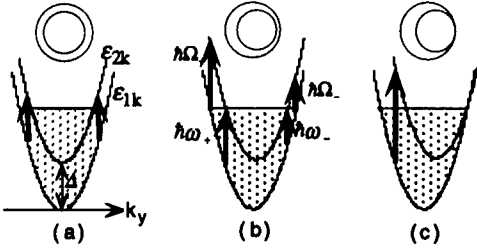
Fig.1 Relative positions of the dispersion parabolas of QW1 and QW2, with their Fermi circles, for increasing $B_\parallel$ from (a) to (c). The upper parabola slides further relative to the lower one for larger $B_\parallel$. The vertical arrows indicate tunneling absorptions. The arrows in (b) signify the transitions responsible for the absorption edges at $\hbar\Omega_\pm$ and the cusps at $\hbar\omega_\pm$.

TUNNELING ABSORPTION WITH IN-PLANE MAGNETIC FIELDS ($B_\perp = 0$)

For $\mathbf{B} = 0$ and in the effective mass (m^*) approximation, the energy-dispersion paraboloids of the two QWs are concentric, offset by Δ, as shown in Fig. 1(a) for the $k_x = 0$ plane. For nonzero Δ, DC resonant tunneling is impossible because momentum-energy conservations cannot be achieved simultaneously on the Fermi surface, owing to the fact that the two concentric Fermi circles in Fig. 1(a) do not intersect [4]. However, tunneling can occur through the absorption of photons as illustrated schematically by the vertical arrows, which originate from the occupied states of the lower parabola of QW1 and terminate at the vacant states of the upper parabola of QW2. The shaded area indicates occupied 2D electron states. The absorption lineshape is sharply peaked at the photon energy $\hbar\omega = \Delta$, yielding possible applications to IR-detector devices. The energy mismatch Δ can be tuned by applying a bias either between the two QWs or to a surface gate. As will be shown later, the absorption decreases with T due to the thermal depopulation and population of the lower and upper levels, respectively.

In $B_\parallel$ applied in the x-direction, the in-plane wave vector $\mathbf{k} = (k_x, k_y)$ is still a good quantum number at low $B_\parallel$ when the classical magnetic length $\ell_\parallel = (\hbar c/eB_\parallel)^{1/2}$ is much larger than the QW widths. However, the two paraboloids are shifted in $\mathbf{k}$ space relative to each other in the k_y-direction by an amount $\Delta k_y = d/\ell_\parallel{}^2$. This is shown for $k_x = 0$ in Fig. 1(b) - 1(c) for increasing $B_\parallel$ [1]. Here d is the center-to-center distance of the QWs. Inspection of Fig. 1 implies that the absorption lineshape should change dramatically with increasing $B_\parallel$, as will be shown below.

Using a linear response theory [5], the absorption is given for $B_\perp = 0$, *with or without $B_\parallel$* and to the lowest order in the zero-field tunneling integral J_0, by the real part of the tunneling conductance of the QWs:

$$G(\omega) = \frac{2\pi J_o{}^2 e^2}{\hbar} \sum_k \int_{-\infty}^{\infty} \frac{f(z) - f(z + \hbar\omega)}{\hbar\omega} \rho_{1k}(z)\rho_{2k}(z + \hbar\omega)dz + (1 \leftrightarrow 2), \qquad (1)$$

where $f(z)$ is the Fermi function and $\rho_{ik}(z)$ is the spectral density in the i-th QW:

$$\rho_{ik}(z) = \frac{1}{\pi} \frac{\Gamma_{ik}(z)}{(z - \varepsilon_{ik})^2 + \Gamma_{ik}(z)^2}. \qquad (2)$$

The energies are given by

$$\varepsilon_{1k} = \varepsilon(k_x) + \varepsilon(k_y),$$

$$\varepsilon_{2k} = \varepsilon(k_x) + \varepsilon(k_y - \Delta k_y) + \Delta, \quad (\Delta k_y = \frac{deB_\parallel}{\hbar c}) \qquad (3)$$

where $\varepsilon(q) = \hbar^2 q^2/(2m^*)$. In (2), $\Gamma_{1k}(z)$ is the imaginary part of the self-energy given in the Born approximation by $\Gamma_{1k}(z) = \Gamma_1 \theta(z)$ and $\Gamma_{2k}(z) = \Gamma_2 \theta(z - \Delta)$ for short-range (i.e., delta-function)
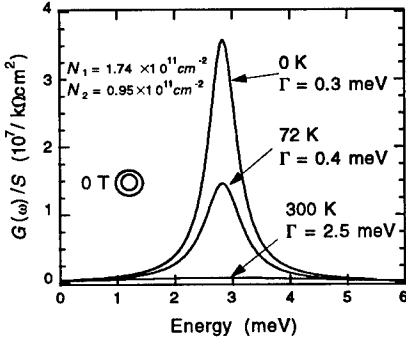
Fig. 2 The temperature dependence of G of sample 1 at $\mathbf{B} = 0$.
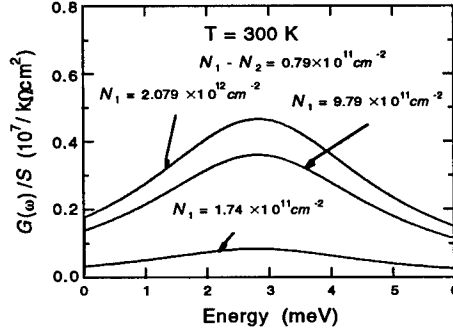
Fig. 3 The density (N_1) dependence of G of sample 1a for a fixed value of N_1 -N_2 at $\mathbf{B} = 0$.

scattering potentials. Here $\theta(z)$ is a unit step function and Γ_1 and Γ_2 are constants.

In zero magnetic field (i.e., $\mathbf{B} = 0$), $G(\omega)$ in (1) can be approximated as

$$G(\omega) = \frac{J^2 e^2 \rho_{2D}}{\hbar^2 \omega} \frac{\Gamma}{(\hbar\omega - \Delta)^2 + \Gamma^2} \left\{ \frac{1}{\beta} \ell n \frac{e^{\beta\hbar\omega} + e^{\beta(\Delta, -\mu)}}{1 + e^{\beta(\Delta, -\mu)}} \right\}, \tag{4}$$

where $\Gamma = \Gamma_1 + \Gamma_2$, $\beta = (k_B T)^{-1}$, $\rho_{2D} = m^*S/(\pi\hbar^2)$ is the 2D density of states, S is the QW area, and $\Delta_>$ is the larger of Δ and $\hbar\omega$. Eq. (4) is exact in the limit $\Gamma_1 \to 0$ or $\Gamma_2 \to 0$. The lineshape is peaked at $\hbar\omega = \Delta$. The chemical potential μ is a function of the 2D densities N_1, N_2, and T. In Fig. 2, we show zero-field G for n-type GaAs/AlGaAs DQWs (sample 1) with $N_1 = 1.74$, $N_2 = 0.95$ ($\times 10^{11}$ cm^{-2}), $\Delta = 2.83$ meV, $m^* = 0.067m_0$ (m_0 is the free electron mass), $d = 21.5$ nm, and $J = 0.04$ meV [5, 6]. The $T = 0$ K value of $\Gamma = 0.3$ meV corresponds to the mobility of 57.4×10^3 cm^2/Vsec. T-dependent phonon contributions Γ_{ph} are added to $\Gamma = 0.3$ meV for $T = 72$ K and 300 K. Here Γ_{ph} is obtained from mobility data [7]. At $T = 300$ K, the absorption is weak due to the depopulation (population) of the lower (upper) level but has a width much smaller than $k_B T$ due to phase restrictions unique to 2D-2D tunneling. The absorption improves significantly for large N_1. This is seen in Fig. 3 where we show the absorption for sample 1a for increasing N_1 with a constant resonance energy Δ (i.e., constant N_1 - N_2). Sample 1a is identical to sample 1 except that it has $\Gamma = 2.2$ meV at 300 K, corresponding to the phonon-limited mobility of 8×10^3 cm^2/Vsec.

In an in-plane magnetic field, the field-induced broadening of the absorption lineshape arising from the relative displacement of the dispersion parabolas of QW1 and QW2 is much larger than Γ in a *high-mobility* structure. In this limit (i.e., in the limit $\Gamma_1 \simeq \Gamma_2 \simeq 0$), we reduce (1) to

$$G(\omega) = \frac{J^2 e^2 S}{2\pi\hbar^2 \omega \ell d\varepsilon(\ell^{-1})} \left(F(\varepsilon^*) - F(\varepsilon^* + \hbar\omega) \right), \tag{5}$$

where $\varepsilon^* = \varepsilon(k_y^*)$, $k_y^* = [(\Delta - \hbar\omega)/\varepsilon(\ell^{-1}) + (d/\ell)^2]/2d$, and

$$F(z) = \ell \int_0^\infty \frac{dk_x}{\exp[\beta(\varepsilon(k_x) + z - \mu)] + 1}. \tag{6}$$

At $T = 0$, G in (5) can be evaluated exactly [8]. Its sensitive $B_{\parallel}$-dependence is seen in Fig. 4 for sample 1. The $B_{\parallel} = 0$ T lineshape is for $\Gamma = 0.3$ meV. DC tunneling is turned on at $B_{\parallel} = 0.84$ T, where the two Fermi circles touch tangentially from inside as illustrated in the inset. The absorp-

191
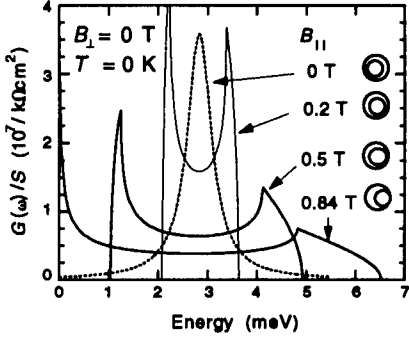
Fig. 4 The $B_{\parallel}$-dependence of G of sample 1 with $\Gamma = 0$ meV for $B_{\parallel} > 0$ T, and $\Gamma = 0.3$ meV for $B_{\parallel} = 0$ T.
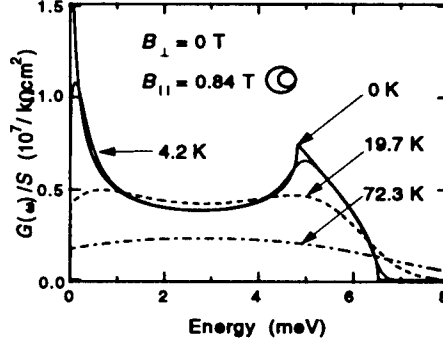
Fig. 5 The temperature dependence of G of sample 1 at $B_{\parallel} = 0.84$ T with $\Gamma = 0$ meV.

tion diverges as $\omega^{-1/2}$ for $\omega \rightarrow 0$. $B_{\parallel}$-dependent behavior of the DC tunneling conductance has been studied earlier in detail and will not be discussed here [4 - 6, 9]. The deep minimum in the $B_{\parallel}$ - dependent absorption, with sharp cusps at both edges, arises from the forbidden absorption into the Fermi sea of QW2. The sharp cusps and absorption edges are rounded for $\Gamma > 0$. The absorption minimum is absent for sample 2 in Fig. 6. The parameters of sample 2 are the same as those of sample 1 except that QW2 is empty (i.e., $N_2 = 0$) and $\Delta = 6.7$ meV. The physical origin for the absorption edges ($\hbar\Omega_{\pm}$) and the cusps ($\hbar\omega_{\pm}$) in Fig. 4 are illustrated in Fig. 1. The sharp edges of G are rounded at finite T as shown in Fig. 5 at $B_{\parallel} = 0.84$ T for sample 1.

TUNNELING ABSORPTION IN TILTED MAGNETIC FIELDS ($B_{\perp} > 0$)

When a perpendicular component $B_{\perp}$ // z is added to an in-plane field $B_{\parallel}$, Landau levels are formed and the plane wave picture above is no longer valid. The interwell tunneling integral
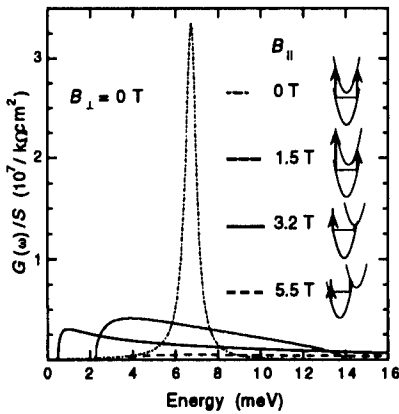
Fig. 6 Absorption per area of sample 2 with $N_2 = 0$, $\Gamma = 0.3$ meV for $B_{\parallel} = 0$ T, and $\Gamma = 0$ meV for $B_{\parallel} > 0$ T.
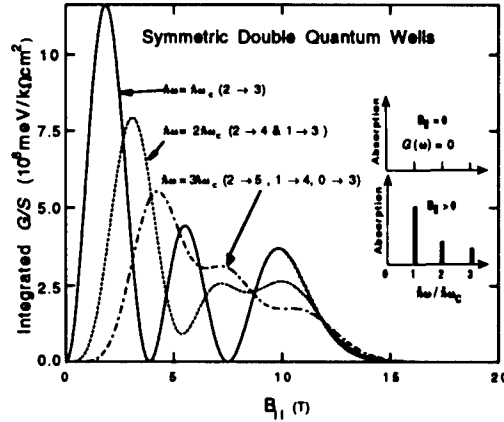
Fig. 7 Integrated absorption per area of sample 3 for $B_{\perp} = 2.8$ T. The inset illustrates the absorption spectra.

between Landau levels n and n' is given by [10]

$$J_{n,n'} = (-1)^{n_> - n_<} J_0 e^{-x/2} (n_<!/n_>!)^{1/2} x^{(n_> - n_<)/2} L_{n_<}^{n_> - n_<}(x), \qquad (7)$$

where $n_>$ ($n_<$) is the larger (lesser) of (n, n'). $L_n^m(x)$ is the associated Laguerre polynomial and $x = \alpha^2/2 = (d/\ell_{\parallel})^2 B_{\parallel}/2B_{\perp}$. Note that $J_{n,n'} = J_0 \delta_{n,n'}$ for $B_{\parallel} = x = 0$, namely, only the $n \to n' = n$ interwell transitions are allowed in the absence of $B_{\parallel}$.

The absorption is given by

$$G = \frac{2\pi e^2 g}{\hbar} \sum_{n,n'} J_{n,n'}^2 \int_{-\infty}^{\infty} \frac{f(z) - f(z + \hbar\omega)}{\hbar\omega} \rho_{1n}(z) \rho_{2n'}(z + \hbar\omega) dz + (1 \leftrightarrow 2), \qquad (8)$$

where $g = S/(2\pi\ell_{\perp}^2)$ is the Landau level degeneracy per spin, $\ell_{\perp} = (\hbar c/e\, B_{\perp})^{1/2}$ and

$$\rho_{in}(z) = \frac{1}{\pi} \frac{\Gamma_{in}(z)}{(z - \varepsilon_{in})^2 + \Gamma_{in}(z)^2}. \qquad (9)$$

Here $\Gamma_{in}(z)$ is the imaginary part of the self-energy for the Landau level energies given by

$$\varepsilon_{1n} = (\tfrac{1}{2} + n)\hbar\omega_c, \qquad \varepsilon_{2n'} = (\tfrac{1}{2} + n')\hbar\omega_c + \Delta, \qquad (10)$$

where $\omega_c = eB_{\perp}/m^*c$. Eqs. (8) - (10) can be reduced to Eqs. (1) - (3) by using asymptotic expressions for $L_n^m(x)$ in the limit $B_{\perp} \to 0$ (i.e., $x \to \infty$) [11].

According to (7), tunneling can occur only between the Landau levels with same quantum numbers n in the absence of $B_{\parallel}$. With nonvanishing $B_{\parallel}$, the intensities of $n \to n$ transitions diminish while those of $n \to n'$ ($\neq n$) transitions grow from zero initially and then oscillate with increasing $B_{\parallel}$. This is illustrated in Fig. 7 for symmetric DQWs (sample 3) for $\Gamma \to 0$. Here, resonant photon energies are given by $\hbar\omega = \delta n \hbar\omega_c$ where $\delta n = n' - n = 1, 2, \cdots$. The parameters of sample 3 are given by $N_1 = N_2 = 4 \times 10^{11}$ cm^{-2}, $J_0 = 0.04$ meV, and $d = 17.5$ nm. Three Landau levels are filled at $B_{\perp} = 2.8$ T, where $\hbar\omega_c = 4.9$ meV. Resonant DC (i.e., $n \to n$) tunneling is negligible because the Fermi level is halfway between the Landau levels $n = 2$ and $n = 3$, where the density of states is zero. The intensities for the $\hbar\omega = 2\hbar\omega_c$ and $\hbar\omega = 3\hbar\omega_c$ absorption arise from the superpositions of two and three transitions respectively as indicated in Fig. 7. As a result, their minima do not become zero.

In Fig. 8, we plot the integrated absorption from sample 4 where only QW1 has carriers. For sample 4, $N_1 = 2 \times 10^{11}$ cm^{-2}, $N_2 = 0$, $\Delta = 5.0$ meV, $J_0 = 0.04$ meV, and $d = 17.5$ nm at $B_{\perp}$
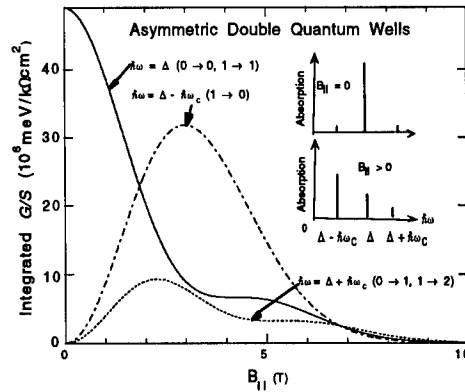
Fig.8 Integrated absorption per area of sample 4 for $B_{\perp} = 2.1$ T with $N_2 = 0$. The inset illustrates the absorption spectra.

= 2.1 T, where $\hbar\omega_c$ = 3.6 meV and two Landau levels n = 0, 1 of QW1 are filled. Note, however, that some electrons migrate back to QW2 from QW1 (i.e., $N_2 > 0$) at $B_\perp = 0$ since the Fermi energy (at $B_\perp = 0$ T) is larger than Δ. In this sample, transitions $0 \to \delta n$ (δn = 0, 1,··) and $1 \to 1 + \delta n$ (δn = -1, 0, 1,··) from QW1 to the empty levels of QW2 yield resonant absorption of photons of energy $\hbar\omega = \delta n \hbar\omega_c + \Delta$ as shown in Fig.8. The intensity for the $\hbar\omega = \Delta$ transition drops with increasing $B_\parallel$, while that of $\hbar\omega = \delta n \hbar\omega_c + \Delta$ ($\delta n \neq 0$) transition grows from zero and oscillate.

CONCLUSIONS

We have employed a linear-response theory to study the interwell-tunneling absorption in tilted magnetic fields in weakly-coupled n-type symmetric and asymmetric double QWs with a tunable energy mismatch between the two ground sublevels. Photon-assisted tunneling occurs between the ground sublevels of the QWs. We have shown that applied magnetic fields sensitively alter the threshold energy, the resonance energy, and the linewidth. In zero magnetic field, the absorption intensity decreases significantly as the linewidth increases with the temperature. The absorption intensity depends strongly on the electron density. In magnetic fields, both the in-plane and per-pendicular components of the field are found to sensitively control and tune the absorption line shape in very different ways. The perpendicular component of the field tunes the cyclotron energy, relative positions of the two Landau ladders for asymmetric QWs, and the interwell spectral over-lap of the density of states of the Landau levels. In the absence of a perpendicular component of the field, the in-plane field merely shifts the relative separation of the energy-dispersion parbo-loids of the two QWs in k-space, tuning the absorption maxima, minimum, and the absorption edges. In the presence of a finite perpendicular component of the field, however, the in-plane field also modulates the effective tunneling strength by displacing the centroid of the two Landau-level wave functions involved in the transition.

ACKNOWLEDGMENTS

REFERENCES

1. See S. K. Lyo, J. A. Simmons, N. E. Harff, T. M. Eiles, and J. F. Klem, Inst. Phys. Conf. Ser. No 145, p 845 (IOP Publishing Ltd, 1996) and references therein.
2. J. A. Simmons, unpublished.
3. J. P. Eisenstein, L. N. Pfeiffer, and K. W. West, Appl. Phys. Lett. 57, 2324 (1990).
4. J. P. Eisenstein, T. J. Gramila, L. N. Pfeiffer, and K. W. West Phys. Rev. B 44, 6511 (1991).
5. S. K. Lyo and J. A. Simmons J. Phys.: Condens. Matter 5, L299 (1993).
6. J. A. Simmons, S. K. Lyo, J. F. Klem, M. E. Sherwin, and J. R. Wendt Phys. Rev. B 47, 15741(1993).
7. J. H. English, A. C. Gossard, H. L. Stormer, and K. W. Baldwin, Appl. Phys. Lett. 50, 1826 (1987).
8. S. K. Lyo, Superlattices and Microstructures, Vol. 20, No. 3 (1996), in press.
9. L. Zheng and A. H. MacDonald Phys. Rev. B 47, 10619(1993).
10. J. Hu and A. H. MacDonald, Phys. Rev. B 46, 12554 (1992).
11. S. K. Lyo (unpublished).

GaAs/GaInP QUANTUM WELL INTERSUBBAND PHOTODETECTORS FOR FOCAL PLANE ARRAY INFRARED IMAGING

C. JELEN*, S. SLIVKEN*, G.J. BROWN**, M.RAZEGHI*
*   Center for Quantum Devices, Department of Electrical and Computer Engineering,
    Northwestern University, Evanston, IL 60208.
** Wright Laboratory, Materials Directorate, WL/MLPO, Wright-Patterson AFB, Ohio
   45433

ABSTRACT

We demonstrate long wavelength quantum well infrared photodetectors (QWIP) with GaAs quantum wells and GaInP barriers grown using gas-source molecular beam epitaxy. Wafers were grown with varying well widths. The optimum well width was 75 Å, which resulted in a detection peak at 13 µm and a cutoff wavelength of 15 µm. Dark current measurements of the samples with 15 µm cutoff wavelength show low dark current densities. Preliminary focal plane array imaging is demonstrated.

INTRODUCTION

Very long wavelength infrared detectors with response in the 12-20 µm regions are needed for atmospheric observation and space astronomy focal plane array imaging applications[1] Quantum well infrared photodetectors (QWIPs) have a number of advantages over conventional mercury cadmium telluride (MCT) or silicon blocked impurity band (BIB) detectors in the very long wavelength infrared spectral region. In comparison to MCT, these include more mature materials growth and processing technology with greater uniformity and larger substrate areas available, possibility of monolithic integration with GaAs signal processing electronics (and even Si electronics with GaAs on Si growth), improved thermal stability, radiation hardness, and inherent high speed with advantages for heterodyne detection and ranging. These advantages are particularly desirable for large area imaging arrays. Background limited detectivities of 5×10^{11} cm $\sqrt{Hz}$ W^{-1} at 52K with a 15 µm cutoff wavelength have been reported in GaAs/AlGaAs detectors[2] which is a higher temperature then the ~10 K required for BLIP detection using Si(BIB) detectors.

In this paper we concern ourselves with GaAs/GaInP MQW detectors with cutoff wavelengths near 15 µm. Lattice-matched GaAs-GaInP heterostructures have the advantages of an ultralow surface recombination velocity[3], very low interface roughness[4] an absence of the deep level traps associated with DX centers and oxygen defects in AlGaAs, and an order of magnitude higher electron mobility than AlGaAs[5] The excellent optical and electrical properties of GaAs/GaInP and GaAs/GaInAsP heterostructures have been demonstrated in such diverse devices as solid-state lasers, heterojunction bipolar transistors, and tandem solar cells[6]. Aluminum-free GaInAsP based QWIPs have been reported with peak response wavelengths from 3 to 10 µm.[7-10] In this paper, we report new results for n-type GaAs/GaInP QWIPs with cut-off wavelengths greater than 10 µm.

195

Mat. Res. Soc. Symp. Proc. Vol. 450 ®1997 Materials Research Society

EXPERIMENT

We have made measurements on GaAs/GaInP samples grown by gas-source molecular beam epitaxy (GSMBE) on (100) semi-insulating GaAs substrates. Three different wafers were grown with GaAs well widths of 30Å, 65Å, and 75Å respectively. Each sample superlattice had 20 periods. The silicon doping in the quantum wells was 5×10^{17} cm^{-3}. The barriers were undoped. The QWIPs were grown on a 1 μm thick buffer layer of n+ GaAs and had a 0.5 μm thick n+ cap layer (both doped to n=3×10^{18} cm^{-3}) which served as ohmic contacts to the active photodetection region. The structural quality and parameters of the grown layers were verified by double-crystal x-ray diffraction and simulation. The key sample parameters are given in Table I. The material was processed into 400 μm square mesa geometry detectors with individual top and bottom AuGe/Ni/Au ohmic contacts. Prism coupled devices, in which the light was incident on a 45° bevel polished on the substrate were fabricated. Small arrays of these mesas were indium bonded on a copper heat sink and mounted in a cryostat with a ZnSe window providing a 60° field of view.

Table I. Nominal sample parameters: well width L_w, barrier width L_b, well electron density N_e.

Sample	L_w	L_b	$N_e (10^{17} cm^{-3})$
A	40	500	5.0
B	65	500	5.0
C	75	500	5.0

RESULTS

Relative responsivity measurements were made using a Fourier transform spectrometer with the sample as detector biased in series with a low noise current amplifier. Absolute responsivity measurements were made using a Mirkon infrared blackbody source chopped at 40 Hz together with phase sensitive detection. Representative responsivity curves for the three samples are shown in Fig. 1. The spectral response characteristics of the detectors are summarized in Table II.

The I-V characteristics of the QWIP were measured using an HP 4155A Semiconductor Parameter Analyzer. The measurement was made at several temperatures from 40 K to 300 K
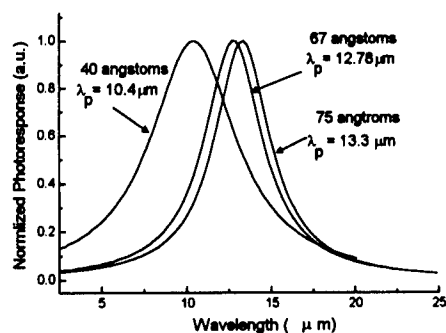
Figure 1.Normalized Optical Response at 77K

Table -II. Responsivities in A/W (-4 V, 78K) for the three samples as well as the peak and cutoff wavelengths and FWHM.

Sample	A	B	C
λ_p	10.4	12.78	13.3
λ_c	13.4	14.85	15.34
FWHM	6μm	4.25μm	4.1μm
	185 meV	37 meV	42 meV
Rp (A/W)	0.004	0.08	0.140

by using a variable flow liquid helium cryostat. Figure 1 shows the dark currents measured at different temperatures. A cold shield is used to shield the 300K black body radiation from the cooling chamber. The observed asymmetry with bais may be due to an asymmetric QW potential profile or doping impurity segregation. The dark current density at 77K as a function of electic field is shown in Figure 3. The results of Levine[2] for a GaAs/AlGaAs QWIP with similar well doping density, and cutoff wavelength is shown for comparison. The smaller dark current may be due to GaInP's larger mobility, smaller surface recombination velocity, or smaller interface roughness by comparison to AlGaAs.
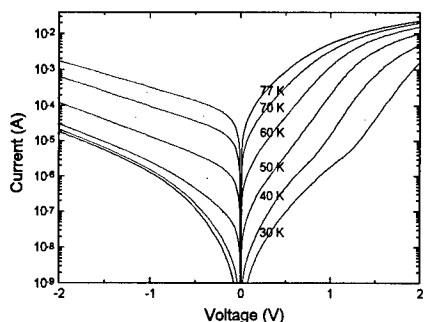
Figure 2. Measured QWIP dark current from 30 to 77 K with a cold shield for the wafer with 65 Å wells.
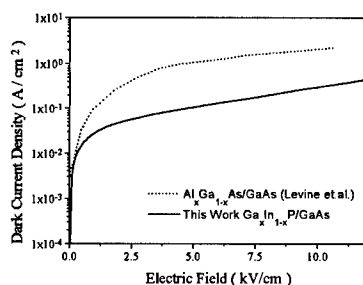
Figure 3. Measured dark current density for sample C compared to GaAs/AlGaAs results in reference 2.

In order to evaluate the specific detectivity D* of these detectors we have directly measured the noise voltage using a spectrum analyzer at T=77K. D* is defined as

$$D^* = R_p \sqrt{A \Delta f} / i_n \qquad (1)$$

(where A = 1.6 x 10^{-3} cm^2 is the detector area). For example, for sample C at T=77K, i_n = 1.7 pA/$\sqrt{Hz}$ and R_p = 0.01 A/W at V_b = 0.75 V, resulting in a D* of 2.4 x 10^8 cm $\sqrt{Hz}$ W^{-1}. The detectivity of sample C as a function of bias is shown in Figure 4. A comparision of these GaAs/GaInP results with published results for GaAs/AlGaAs QWIPs[11] is shown in Figure 5.
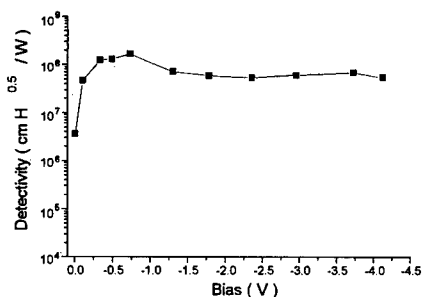
Figure 4. Detectivity versus bias voltage for sample C measured at T=77K.
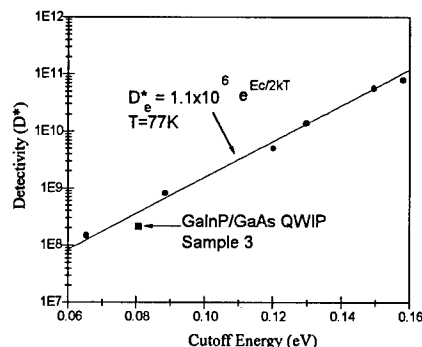
Figure 5. Detectivity of sample C compared with the GaAs/AlGaAs data of reference 11.

Preliminary fabrication of infrared focal plane array staring cameras has been carried out using GaAs/GaInP QWIPs. Shown in Figure 6 is an infrared image collected with the array. It is an image of the hottest tip area of a soldering iron. Complete characterization of the array has not been completed and will be reported elsewhere.
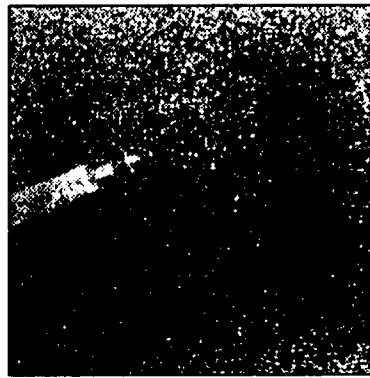
Fig.6. Infrared image of the tip of a hot soldering iron.

CONCLUSION

In summary, we have demonstrated 15 μm cut-off wavelength quantum well infrared photodetectors fabricated using n-doped GaAs/GaInP quantum wells. Dark currents for these samples are smaller than equivalent GaAs/AlGaAs QWIPs. Preliminary infrared focal plane imaging has been demonstrated.

ACKNOWLEDGEMENTS

REFERENCES

1. R.Rosen and G.Johnston in Proceedings of the 43rd Congress of the International Astronautical Federation, (IAF, 1992), p. 751.
2. A.Zussman, B.Levine, J.Kuo, J.de Jong, J.Appl.Phys. 70, 5101 (1991).
3. J.Olson, R. Ahrenkiel, D.Dunlavy, B.Keyes, and A.Kibbler, Appl.Phys.Lett.55, 1208 (1989).
4. W.Mitchel, G.Brown, K.Lo, S.Elhamri, M.Ahoujja, K.Ravindran, R.Newrock, X.He, M.Razeghi, Appl.Phys.Lett.65, 1578 (1994).
5. M.Razeghi, M.Defour, F.Ohmnes, M.Dobers, J.Vieren, Y.Guldner, Appl.Phys.Lett. 55, 457 (1989).
6. M.Razeghi, MOCVD Challenge V.2 (IOP Press, Bristol UK) 1995.
7. S.Gunapala, B.Levine, D.Ritter, R.Hamm, M.Panish, Appl.Phys.Lett.57,1802 (1990).
8. J.Hoff, C.Jelen, S.Slivken, E.Bigan, G.Brown, M.Razeghi, Superlatt. & Microstruct. 18, 249 (1995).
9. J.Hoff, G.Brown, M.Razeghi, Phys.Rev.B 54, 11033 (1996).

10. C.Jelen, S. Slivken, J.Hoff, G.Brown, M.Razeghi, to be published in Appl.Phys.Lett. (Jan. 20, 1997).
11. B.Levine, J.Appl.Phys. 7 4 R1 (1993).

INTERSUBBAND TRANSITIONS, INFRARED DETECTORS, AND OPTICAL NONLINEARITIES IN SiGe MULTIQUANTUM WELLS

M. HELM*, P. KRUCK*, T. FROMHERZ*, M. SETO*, G. BAUER*, J.F. NÜTZEL**,
AND G. ABSTREITER**
*Institut für Halbleiterphysik, Universität Linz, A-4040 Linz, Austria
**Walter Schottky Institut, TU München, D-85748 Garching, Germany

ABSTRACT

A survey is given about the potential use of Si/SiGe heterostructures for applications in the mid-infrared spectral range. We discuss theoretical foundations and experiments of intersubband absorption in p-type Si/SiGe quantum wells and show that due to the complex valence-band structure, normal-incidence absorption can be observed. On the basis of these quantum wells, mid-infrared detectors were fabricated and characterized in terms of responsivity, dark current and detectivity. In asymmetric, compositionally stepped quantum wells second harmonic generation of CO_2 laser radiation has been demonstrated.

INTRODUCTION

Traditionally, narrow-gap III-V and II-VI semiconductors such as InSb and HgCdTe have been the materials of choice for infrared applications, since their band gap of a few hundred meV corresponds to wavelengths of a few microns. Recently, however, a dramatic change has occurred through the availability of MBE grown quantum wells (QWs) and superlattices based on a variety of different material systems. In such structures infrared (IR) radiation can interact with with the quantized energy levels (subbands) in semiconductor quantum wells, the resonant wavelength being determined by the well thickness and the effective mass, but not by the fundamental energy gap [1]. Based on this concept of intersubband transitions, both IR lasers (Quantum Cascade Lasers) [2] and IR detectors (Quantum Well Infrared Photodetectors, QWIPs) [3] have already been demonstrated using the the (Al)GaAs [3] and the InGaAs/InAlAs [2] system, respectively. Also nonlinear optical effects [4,5] have been reported. Owing to the great progress in epitaxial growth techniques, intersubband transitions have also been observed in Si/SiGe structures, which are of special interest due their compatibility with standard Si technology and electronics.

In the present paper we will discuss the general features of intersubband absorption in p-type Si/SiGe quantum wells and present experimental data on a series of samples with different parameters. As an application we describe the realization of a Si/SiGe quantum well infrared photodetector (QWIP) and its performance. Finally we present some results on a nonlinear optical process, the infrared second-harmonic generation in an asymmetric, compositionally stepped quantum well structure.

GENERAL CONSIDERATIONS

The major part of works on intersubband transitions in quantum wells has employed the confinement of electrons in the conduction band, which are located at the Γ-point in many semiconductors. Due to the symmetry and the simplicity of the respective band structure, in this case intersubband transition are only allowed for radiation containing a polarization component along the growth axis (z-direction). In order to couple the IR radiation to the electronic transition, a multipass waveguide geometry is frequently used, where the light is coupled into

the sample at a wedged facet and subsequently undergoes several total internal reflections [6]. The s-polarization contains only an electric-field component in the layer planes (xy direction), whereas the p-polarization contains both xy and z components and, therefore, couples to the intersubband transition. In addition, if the active multiquantum well (MQW) layer is close to the sample surface and its thickness is much smaller than the resonant wavelength of the radiation, the electromagnetic boundary conditions require a metal layer to be deposited on the sample surface in order to make the z polarized transitions observable [7].

In Si/SiGe heterostructures significant electron confinement (in Si) can only be achieved when the QWs are grown on a thick, relaxed SiGe alloy buffer (often with graded Ge content). When grown pseudomorphically on Si, which is preferred because of its simplicity, most of the band offset occurs in the valence band leading to confinement of holes in the SiGe layers. Due to the coupling of heavy-hole (HH), light-hole (LH), and spin-orbit split-off (SO) bands, such p-type quantum wells exhibit a much more complex band structure. However, as a consequence of this coupling, some optical transitions are also allowed for xy-polarized radiation [8-15]. This is why p-type quantum wells are well suited for normal-incidence infrared detectors [13-15] and SiGe quantum wells grown pseudomorphically on Si are a good candidate for IR device applications.

SAMPLES

All the investigated samples were grown by molecular beam epitaxy (MBE) in a commercial chamber (Riber SIVA 32) at the Walter Schottky Institute on n-type ($\rho = 1500\ \Omega$cm) Si (001) substrates. They typically consist of 10-30 periods of $Si_{1-x}Ge_x$ quantum wells with a thickness of 20 - 70 Å and a Ge content of 20 - 60%. The thickness of the Si barrier varies between 150 Å and 500 Å. Boron doping was introduced either into the barriers (modulation doping) or into the wells, resulting in areal hole densities of 0.4 - 3 x 10^{12} cm^{-2} per quantum well. Routine characterization was performed by high-resolution triple-axis x-ray diffraction and reciprocal space mapping [16].

INTERSUBBAND ABSORPTION

Intersubband absorption in quantum wells was first reported by West and Eglash [17] in n-type GaAs, and later on in many other material systems, both n- and p-type. Hole intersubband absorption in SiGe quantum wells has been observed by several groups [12,13,15,18-20], initially on very highly doped structures [13], where the absorption spectra were dominated by free-carrier [18] and plasma [12] effects. Only recently has a coherent picture emerged about the various transitions involved in the absorption process.

The intersubband absorption experiments reported here were performed with a Bruker Fourier transform spectrometer (FTS). The samples were prepared in the waveguide geometry discussed above with a metal layer deposited on top and were placed in a liquid-He flow cryostat. Most measurements were performed at T = 10 K.

Fig. 1 shows absorption spectra of several quantum well samples obtained by dividing the p-polarized transmission by the s-polarized transmission, and further normalized to the same transmission ratio of an undoped Si substrate prepared in the same manner. Any possible s-polarized absorption is shorted out by the metal layer on the surface. The experimental spectra are represented by the solid lines.

In order to understand the position and the shape of the absorption lines, we have performed a self-consistent 6-band Luttinger-Kohn type envelope function calculation [20], which takes into account the band bending due to charge transfer, the exchange-correlation correction within the local density approximation, the strain in the quantum well and the in-
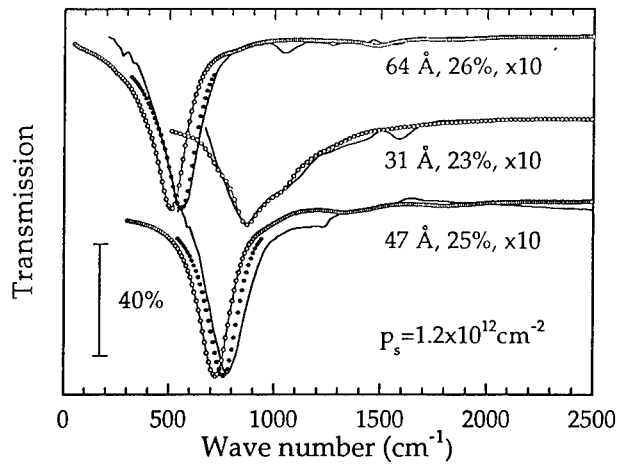
Fig. 1: Transmission spectra (T = 10 K) of three modulation doped Si/SiGe MQWs with a Ge content of approximately 25 % and various well widths as indicated. Solid curves: experiment. Open (full) dots: theory without (with) depolarization shift (for details see text).
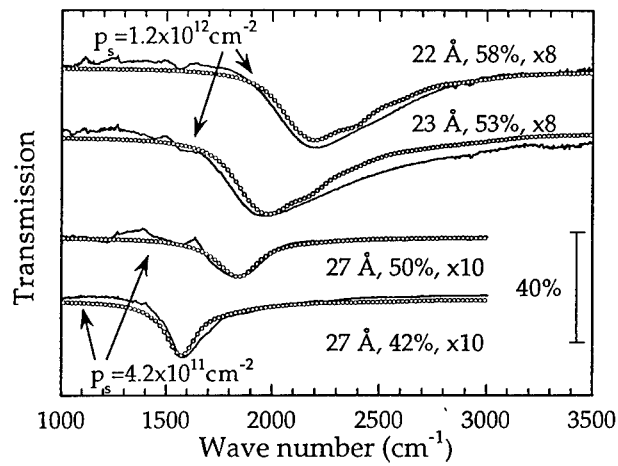
Fig. 2: Same as Fig. 1, for MQWs with higher Ge content and narrower wells.

plane dispersion of the subbands. The resulting band structure was used as an input for a dielectric simulation of the waveguide structure [20] (including the multilayer stack and the electromagnetic boundary conditions). The results of this calculation are plotted by the open symbols in Fig. 1. For the two widest quantum wells also the depolarization shift [21] turns out to be significant and has been calculated in a one band model. The final result is represented by the full symbols. For all the narrower QWs, whose main intersubband absorption occurs at higher energies, the depolarization shift is a negligible correction. The main conclusions from the calculation are as follows [20]. For most samples the strong absorption line is due to the HH1-HH2 intersubband transition and follows the usual intersubband selection rule, i.e., it is only allowed for z-polarized radiation. In the sample with 31 Å well width and 23% Ge content, the HH2 level is localized in the barriers and the absorption goes to the HH3, HH4 and HH5 states, which are located very close to each other and are actually miniband states in the continuum. This is why the absorption line is quite broad and shows some fine structure on the high-energy side. A similar situation occurs for the very narrow wells (22-23 Å) with large Ge content (Fig. 2). Here, however, some additional line broadening has to be assumed due to the diminished material quality at these high Ge contents (x > 50%). We would like to point out that the only fitting parameters in the calculation are a single line broadening parameter and a correction factor for the absolute magnitude of the absorption, which is between 0.5 and 1 for each sample. This is not surprising, since the hole concentrations are not known very accurately. The above samples are relatively low doped ($\leq 1.2 \times 10^{12}$ cm^{-2}), resulting in a typical Fermi energy of only 10 meV. As a consequence, the observed absorption lines are quite narrow, since only k-values near zero participate in the absorption. For the same reason xy-polarized transitions cannot be observed in these samples (even when there is no metal layer on the surface); calculations show that most of these transitions become significant only at much larger k-values.

Therefore another sample was grown in order to study the polarization dependence of the absorption. It consisted of 30 Si/Si$_{0.71}$Ge$_{0.29}$ quantum wells of 30 Å thickness, separated by 150 Å wide Si barriers. The p-type (modulation) doping was increased to 2.8×10^{12} cm^{-2}. In addition, a 1.25 μm undoped Si cap layer was grown on top. Because of this set-back of the MQW sequence from the surface and the large number of 30 periods, both polarization components couple effectively to the respective transitions and the polarization dependence of the absorption can be investigated on the same sample piece [22].

The results are shown in Fig. 3 by the solid lines. Here the p- (s-) polarized sample transmission is normalized by the p- (s-) polarized transmission of an undoped Si substrate. The s-polarized spectrum shows a narrow absorption line at 400 cm^{-1} and a broad feature between 1200 and 2500 cm^{-1}, which can be remarkably well reproduced by the calculations (lines with open symbols). Detailed analysis of the band structure shows [22] that the line at 400 cm^{-1} corresponds to the HH1-LH1 transition, which is allowed only for k≠0. The broad absorption band consists of the HH1-SO2 transition (between 1800 and 2400 cm^{-1}) and a transition to a subband which has a mixed HH/LH/SO character (1200 - 1800 cm^{-1}), the latter one again only at k≠0. All the final states of the broad absorption feature are continuum bands well above the barriers. The p-polarized spectrum shows a strong line at 1000 cm^{-1}, which can be identified as the "usual" HH1-HH2 intersubband transition. In order to understand the additional features, one must keep in mind that the p polarization contains both z and xy components of the electric field, so these features are the same as in the s-polarized spectrum. Finally note that the data between 550 and 650 cm^{-1} are very noisy (and therefore not shown), and that the experimental spectra contain a background which can mostly be ascribed to free-carrier absorption [18].
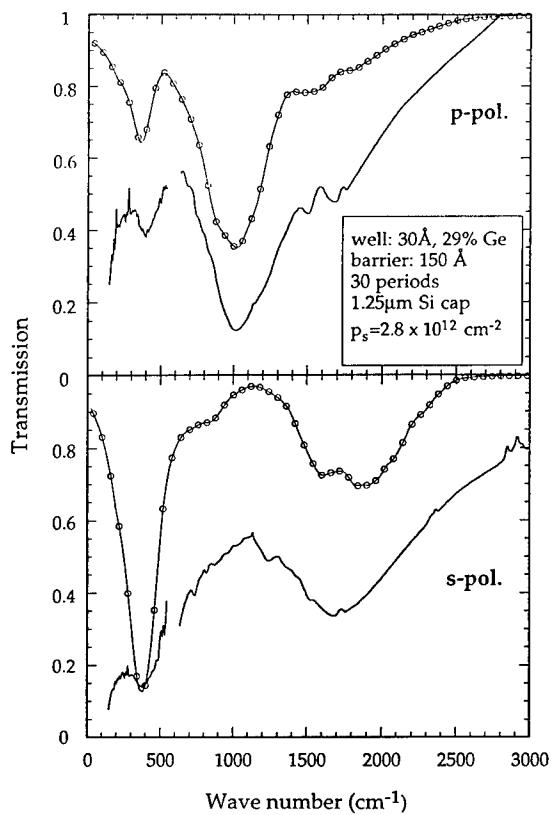
Fig.3: Polarization dependent transmission spectrum (at T = 10 K) of a Si/SiGe MQW with parameters as indicated. Solid curves: experiment. Lines connected by open dots: calculation. Note that the s- polarization contains only xy electric-field components, whereas the p-polarization contains both z and xy components.

INFRARED DETECTORS

Efforts for the development of infrared detectors based on quantum wells were started to provide an alternative for the most frequently employed HgCdTe. Many investigations were focused on GaAs based devices [3], but recently also SiGe QWIPs have been reported [15], which have the advantage of being compatible with standard Si technology and electronics. A SiGe based QWIP structure utilizes transitions from the ground state (HH1) to excited states which are close to or above the barriers, so the photo-excited holes can give rise to a photocurrent [3]. Furthermore the Si barriers have to be thick in order to minimize the dark current (i.e., make the tunneling contribution to the dark current negligible) and the MQW layers have to be enclosed between heavily doped p-type contacts. For recent volumes on QWIP's (both Si/SiGe and other) see Ref. 23.

The detector structure presented here [24] consists of 10 periods of 30 Å thick Si/Si$_{0.65}$Ge$_{0.35}$ quantum wells which are separated by 500 Å thick Si barriers. For detector structures it appears more appropriate to introduce the doping directly into the quantum wells (1.5 x 10^{12} cm^{-2} in the present case), since modulation doping would lead to band bending and

thus to an effective decrease of the barrier width and height. Also photo-excited carriers could get trapped in the barriers.

The samples were processed into 200 μm x 200 μm square mesas by reactive ion etching. Standard metallization was applied to the contact layers. The photoresponse measurements were performed both under direct normal incidence and by coupling through a wedged facet. The latter geometry allows one to analyze the polarization dependence. Fig. 4 shows the results of these measurements at T = 77 K. A peak responsivity of 50 mA/W is observed at a wavelength of λ_p = 5 μm and a bias voltage of V_b = 3 V (increasing to 75 mA/W at V_b = 4 V), a value comparable to p-type GaAs QWIPs [14], but smaller than for n-type GaAs QWIPs [3]. Quite surprisingly, the response is higher in s-polarization than in p-polarization [25], which is in contrast to the transmission results on similar samples. A reason for this may be the influence of the final state in the absorption process on the photo-excited carrier transport [26]. z-polarized radiation excites holes mainly into the HH2 state, wheras xy polarized radiation excites them into the LH and SO states; since the latter are higher in energy and have a smaller effective mass, transport may be more efficient here. Also note that the p-polarized spectrum contains both z and xy electric-field components. This is why the spectral shape for s- and p-polarization is quite similar except for the long-wavelength cut-off, where the p-absorption is dominated by the HH1-HH2 transition.

For further characterization the dark current was measured as a function of temperature, which is shown in Fig. 5. The dashed lines indicate the contribution of the 300 K background radiation to the photocurrent. From the intersection points it can be concluded that background limited performance (BLIP) is achieved at temperatures as high as 85 K for V_b = 0.8 V. Combining the responsivity and dark current results we obtain a detectivity of D^* = 2x10^{10} cm√Hz/W at T= 77 K and V_b = 0.8 V. At higher bias D^* of course drops due to the increasing dark current. The activation energy which can be extracted from the dark-current curves agrees very well with the p-polarized cut-off wavelength [24].
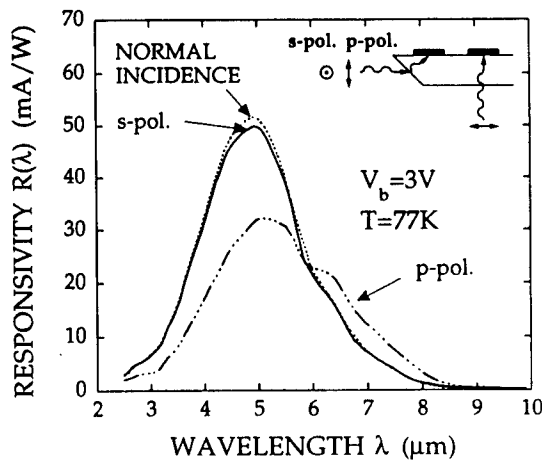
Fig. 4: Spectral photoresponse of the Si/SiGe detector (at T = 77 K) for a bias voltage of V_b = 3 V. Shown are the spectra taken at normal incidence, with s polarization, and p polarization. The corresponding experimental geometries are shown in the inset.
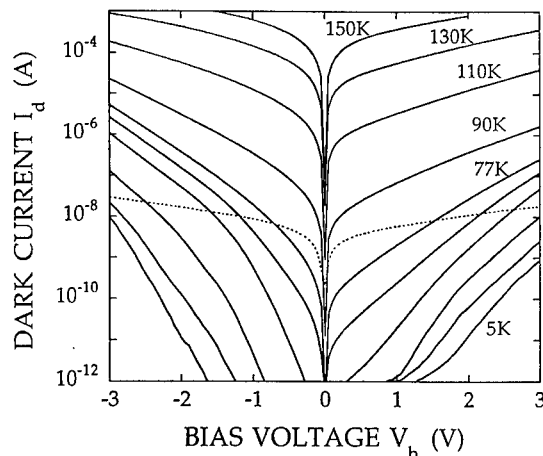
Fig. 5: Detector dark current as a function of bias voltage for temperatures T = 5, 10, 30, 50, 70, 77, 90, 110, 130, and 150 K. The dashed line is the photocurrent generated by the room-temperature background radiation entering through the dewar window.

SECOND HARMONIC GENERATION

Intersubband optical transitions cannot only be utilized for linear absorption processes, but also for nonlinear optical phenomena. However, in order to make second-order nonlinear processes possible, the inversion symmetry of the quantum well has to be broken. This can be done by growing asymmetric coupled quantum wells or compositionally stepped quantum wells, as has been demonstrated for several III-V semiconductor systems [4,5]. We have used the latter type to investigate the frequency doubling of 10.6 μm CO_2 laser radiation. The Si/SiGe system is different from the III-V's, since the substrate is inversion symmetric and does not posses a second-order nonlinear susceptibility.

The sample consisted of 15 stepped quantum wells with 36 Å $Si_{0.75}Ge_{0.25}$, 19 Å $Si_{0.57}Ge_{0.43}$, separated by 200 Å Si barriers. The doping was placed in the quantum wells with an areal hole concentration of p = 2.2×10^{12} cm^{-2}. This structure is designed in a way that the HH1, HH2 and HH3 levels are separated by approximately 120 meV each, the photon energy of the CO_2 laser. Thus the nonlinear susceptibility responsible for second harmonic generation (SHG) can be expected to be enhanced due to the near-resonant conditions.

First the linear absorption was measured in a similar way as described in section 1. (Fig. 6). A strong absorption peak is observed at approximately 150 meV, which can be assigned to the HH1 - HH2 transition. The shoulder visible at ≈ 230 meV is due to the HH1 - HH3 transition, which is allowed because of the broken symmetry. The relative strength of the two absorption lines compares reasonably well with the calculation, which yields a 3:1 ratio for the HH1-HH2 and HH1-HH3 oscillator strengths, respectively. The absolute line positions deviate somewhat from the theoretical values; this can be ascribed to a deviation of the actual sample parameters

from the nominal values (due to the complicated layer structure X-ray analysis does not permit a unique determination of the individual layer thicknesses and compositions).

The SHG experiment [27,28] was performed using a grating tunable, rotating-mirror Q-switched CO_2 laser yielding 150 ns pulses with a peak power of 2 kW. The radiation was focused onto the long edge of the rectangular shaped sample (focal spot 170 μm diameter) covered with a metal layer to enhance the coupling of the z-polarized radiation. A part of the laser was diverted into a pyroelectric detector and used as a power reference and a trigger signal. The frequency doubled signal after the sample was collected and focused with two ZnSe lenses into a liquid-nitrogen-cooled InSb detector. The transmitted 10 μm laser radiation was blocked using a sapphire window and a 5 μm band-pass filter, the latter to block all thermal radiation which might result from heating effects. Two polarizers before the sample were used to vary the laser power and a polarizer after the sample to analyze the polarization of the second-harmonic signal. The polarization of the incoming radiation could be rotated from vertical to horizontal with a λ/2 plate (only at 10.6 μm).

Fig. 7 shows the second-harmonic power as a function of input power recorded at room temperature. Both the polarization of the pump beam and the SHG radiation were polarized along the growth axis, which implies that the (zzz) component of the nonlinear optical susceptibility tensor $\chi^{(2)}$ is responsible for the SHG. A quantitative analysis of previous results obtained in Brewster-angle geometry [27] gave a numerical value of $\chi^{(2)}_{zzz} = 5 \times 10^{-8}$ m/V, in rough agreement with a theoretical estimate. In the present measurement a much better coupling efficiency is achieved, however, for a quantitative evaluation a mode propagation analysis appears to be necessary.

In a similar manner as xy polarized absorption can be observed in p-type quantum wells, also other $\chi^{(2)}$ components are expected to be finite, as has been demonstrated for p-GaAs quantum wells [29]. To clarify this issue for Si/SiGe quantum wells, more experimental work is required using different sample geometries.
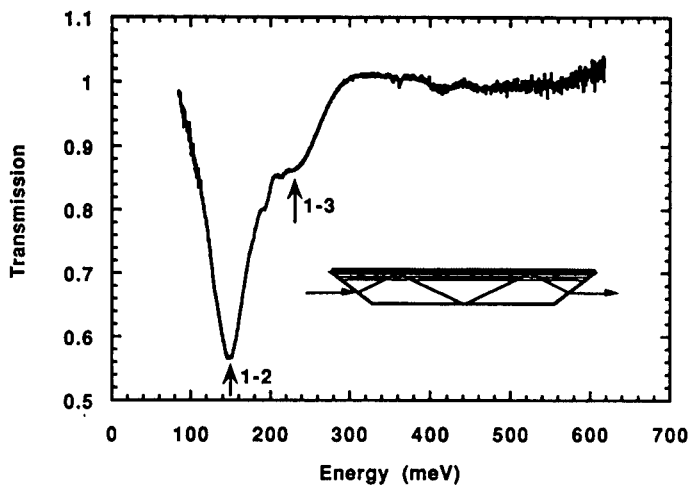
Fig. 6: Transmission spectrum of the compositionally stepped Si/SiGe MQW structure recorded at T = 10 K. The HH1-HH2 and HH1-HH3 transitions are indicated.
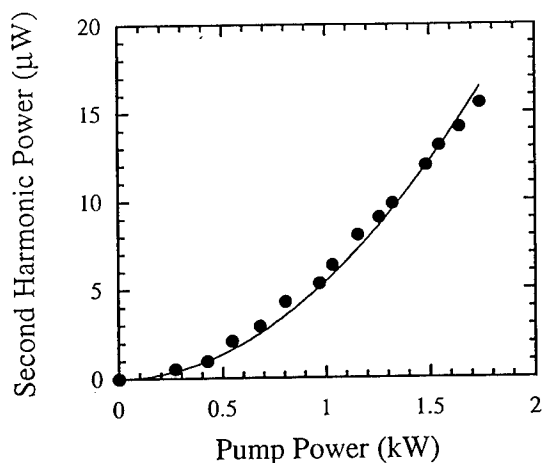
Fig. 7: Second-harmonic power vs input pump power. The solid line is a quadratic fit to the experimental points.

SUMMARY

We have presented a number of experiments which show that, due to the matured growth techniques and the resulting material quality, Si/SiGe quantum wells can be engineered as a material system useful for infrared applications. We have shown that a basic understanding of intersubband absorption can be obtained in Si/SiGe quantum wells and that this knowledge can be exploited for the development of devices such as infrared detectors or for nonlinear optical phenomena such as second-harmonic generation. A great challenge for the future remains the possible realization of a Quantum Cascade Laser based on Si/SiGe [30].

ACKNOWLEDGMENTS

REFERENCES

1. for a recent survey, see *Quantum Well Intersubband Transition Physics and Devices*, ed. H. C. Liu, B. F. Levine, and J. Y. Andersson (Kluwer Academic Publishers, Dordrecht, 1993).

2. J. Faist, F. Capasso, D. L. Sivco, C. Sirtori, A. L. Hutchinson, and A. Y. Cho, Science **264** (1994) 553; J. Faist, F. Capasso, C. Sirtori, D. L. Sivco, J. N. Baillargeon, A. L. Hutchinson, S.-N. G. Chu, and A. Y. Cho, Appl. Phys. Lett. 68, 3680 (1996)

3. B. F. Levine, J. Appl. Phys. **74** (1993) R1.

4. E. Rosencher and Ph. Bois, Phys. Rev. B **44** (1991) 11415; E. Rosencher, A. Fiore, B. Vinter, V. Berger, Ph. Bois, and J. Nagle, Science **271** (1996) 168.

5. F. Capasso, C. Sirtori, and A. Y. Cho, IEEE J. Quantum Electron. **30** (1994) 1313.

6. H. Hertle, G. Schuberth, E. Gornik, G. Abstreiter, and F. Schäffler, Appl. Phys. Lett. **59** (1991) 2977.

7. M. J. Kane, M. T. Emeny, N. Apsley, C. R. Whitehouse, and D. Lee, Semicond. Sci. Technol. **3** (1988) 722.

8. Y. C. Chang and R. B. James, Phys. Rev. B. **39** (1989) 12672.

9. P. Man and D. S. Pan, Appl. Phys. Lett. **61** (1992) 2799.

10. E. Corbin, K. B. Wong, and M. Jaros, Phys. Rev. B **50** (1994) 2339.

11. F. Szmulowicz and G. J. Brown, Phys. Rev. B **51** (1995) 13203.

12. S. K. Chun, D. S. Pan and K. L. Wang, Phys. Rev. B **47** (1993) 15638.

13. J. S. Park, R. P. G. Karunasiri, and K. L. Wang, Appl. Phys. Lett. **61** (1992) 681; R. P. G. Karunasiri, J. S. Park, and K. L. Wang, ibid. **61** (1992) 2434.

14. B. F. Levine, S. D. Gunapala, J. M. Kuo, S. S. Pei, and S. Hui, Appl. Phys. Lett. **59** (1991) 1864.

15. R. People, J. C. Bean, C.G. Bethea, S.K. Sputz, and L.J. Peticolas, Appl. Phys.Lett. **61** (1992) 1122.

16. G. Bauer, J. Li, and E. Koppensteiner, J. Crystal Growth **157** (1995) 61.

17. L. C. West and S. J. Eglash, Appl. Phys. Lett. **46** (1985) 1156.

18. S. Zanier, J. M. Berroir, Y. Guldner, J. P. Vieren, I. Sagnes, F. Glowacki, Y. Campidelli, and P. A. Badoz, Phys. Rev. B **51** (1995) 14311.

19. P. Boucaud, L. Gao, Z. Moussa, F. Visocekas, F. H. Julien, J.-M. Lourtioz, I. Sagnes, Y. Campidelli, and P.-A. Badoz, Appl. Phys. Lett. **67** (1995) 2948.

20. T. Fromherz, E. Koppensteiner, M. Helm, G. Bauer, J. F. Nützel, and G. Abstreiter, Phys. Rev. B **50** (1994) 15073; Superlatt. Microstruct. **15** (1994) 229.

21. S. J. Allen, Jr., D. C. Tsui, and B. Vinter, Solid State Commun. **20** (1976) 425; T. Ando, ibid. **21** (1977) 133.

22. T. Fromherz, P. Kruck, M. Helm, G. Bauer, J. F. Nützel, and G. Abstreiter, Appl. Phys. Lett. **68**, 3611 (1996); Superlatt. Microstruct. **20**, 237 (1996).

23. *Semiconductor Quantum Wells and Superlattices for Long-Wavelength Infrared Detectors*, ed. M.O. Manasreh (Artech House, Boston, 1993); *Homojunction and Quantum Well Infrared Detectors*, ed. M. H. Francombe and J. L. Vossen (Academic Press, San Diego, 1995).

24. P. Kruck, M. Helm, T. Fromherz, G. Bauer, J. F. Nützel, and G. Abstreiter, Appl. Phys. Lett. **69**, 25 Nov (1996).

25. A. Fenigstein, E. Finkman, G. Bahir, and S. E. Schacham, J. Appl. Phys. **76**, (1994) 1998.

26. H. C. Liu, Appl. Phys. Lett. **60** (1992) 1507.

27. M. Seto, M. Helm, Z. Moussa, P. Boucaud, F. H. Julien, J.-M. Lourtioz, J. F. Nützel, and G. Abstreiter, Appl. Phys. Lett. **65** (1994) 2969.

28. P. Kruck, M. Seto, M. Helm, Z. Moussa, P. Boucaud, F. H. Julien, J.-M. Lourtioz, J. F. Nützel, and G. Abstreiter, Solid State Electron. **40** (1996) 763

29. M. J. Shaw, M. Jaros, Z. Xu, P. M. Fauchet, C. W. Rella, B. A. Richman, H. A. Schwettman, and G. W. Wicks, Phys. Rev. B **50** (1994) 18395.

30. G. Sun, L. Friedman, and R. A. Soref, Appl. Phys. Lett. **66**, 3425 (1995).

A NOVEL INFRARED SiGe/Si HETEROJUNCTION DETECTOR WITH AN ULTRATHIN PHOSPHORUS BARRIER GROWN BY ATOMIC LAYER DEPOSITION

R. Banisch, B. Tilack, M. Pierschel, K. Pressel, R. Barth, D. Krüger, and G. Ritter, Institute for Semiconductor Physics, P.O. Box 409, D-15204 Frankfurt(Oder), Germany, banisch@ihp-ffo.de

ABSTRACT

In strained $Si_{a-x}Ge_x$ heterojunction internal photoemission (HIP) photodiodes the spectral response can be tailored over a wide wavelength range by varying the Ge content. In this paper heavily in situ boron doped SiGe layers with 30% Ge were grown by low pressure rapid thermal chemical vapour deposition (LP(RT)CVD). The detectors exhibit a cut-off wavelength of 8.5 μm. A delta-like P peak, incorporated by atomic layer deposition technique, shifts the cut-off to shorter wavelengths. This shift is related to an increase of the barrier height at the SiGe/Si interface caused by the narrow n^+-doped layer in agreement with device simulation. In this way the trade off between critical film thickness for high Ge content film growth and absorption depth for proper detector response can be overcome.

INTRODUCTION

The SiGe/Si heterojunction internal photoemission (HIP) infrared detector offers the possibility of monolithic integration of large focal plane arrays and for smart sensor systems. A wide spectral range may be covered by changing the energy gap of pseudomorphic SiGe layers through variations in the Ge content. Further possible advantages are improvements in yield due to material uniformity in comparison with compound semiconductors, and the avoidance of thermal expansion mismatch inherent in all hybrid structures.

The HIP detector consists of a heavily doped p^+-SiGe emitter layer on a p-type Si substrate acting as the collector. The detection mechanism involves strong infrared absorption by free carriers in the p^+-SiGe layer, followed by the internal emission of the photo-excited holes over the heterojunction barrier into the silicon substrate. The effective barrier height is determined by the valence band offset on the SiGe/Si interface, and the Fermi-level in the SiGe layer. Because the energy gap in strained SiGe layers depends strongly on the Ge content, the cut-off wavelength and spectral sensitivity of a HIP photodiode can be tailored over a wide range of the IR spectrum (up to about 30 μm). on the other hand the critical thickness of the SiGe decreases with increasing Ge concentration with limits the SiGe-film thickness. This results in a short absorption region and in this way in lower detector response.

First SiGe-HIP detectors were fabricated by molecular beam epitaxy [1,2] and recently by low pressure rapid thermal chemical vapour deposition (LP(RT)CVD) [3].

In this paper presented a novel HIP detector is proposed which uses a narrow n^+-doping spike at the substrate interface, which increases the heterojunction barrier height. In this way the trade off between critical film thickness limitation for high Ge content and absorption depth for proper detector response can be overcome.

N^+ spike doping was first investigated for PtSi/Si [5] and recently applicated in bi-colour PtSi-Schottky-barrier CCD [6] utilizing shallow ion implantation. The n^+ spike was prepared by an atomic layer doping technique [4]. Using the P spike we measured a shift of the cut-off wavelength from 8.2 μm to 4.5 μm for 30% Ge content in agreement with device simulation.

EXPERIMENTAL

The $Si_{1-x}Ge_x$ layers were deposited in a tungsten lamp heated low pressure rapid thermal chemical vapour deposition single wafer reactor at temperatures of 450-500°C and a pressure of 200 Pa with a gas mixture of SiH_4, GeH_4 and H_2. B_2H_6 was added to the source gases for in situ boron doping up to $2x10^{20}$ cm^{-3}.

The deposition was carried out on 100 mm, p-type (12-20 Ωcm) Si (100) wafers. Strained SiGe epitaxial layers were grown with 30% and 50% Ge, 30 nm and 20 nm thick, respectively. The wafers were covered with a boron-doped (10^{19} cm^{-3}) Si cap (50 nm). Between the SiGe and the Si cap a buffer layer of few nm's was grown in which the Ge content was tuned down to zero. A detailed description of the deposition process is published elsewhere [7].

The atomic layer doping technique developed in our lab for doping of SiGe films with B and P [4], has been applied to Si. The main idea of the atomic layer doping technique consists of the separation of doping and film growth. For this purpose the Si deposition was interrupted by switching off the SiH_4 and the heater. Than the surface of the wafer was exposed to PH_3/H_2 at a temperature of 350°C for a certain time. The coverage is controlled by the surface adsorption equilibrium of PH_3 only. After the exposure step the epitaxial growth is continued. This process is still under investigation. First information will be published elsewhere [9]. After the P spike doping we grew a thin undoped Si/SiGe spacer at 550°C and 450°C, respectively. Finally, the boron doped strained SiGe film was grown at 500°C as the emitter for the HIP diode with a thickness of 30 nm.

HIP photodiodes of different area were defined by mesa etching. A low temperature process with low temperature oxide (LTO) passivation, PtSi contact formation and AlCu metallization was used for device preparation. The back side of the wafers was covered with Al for substrate contact. The SiGe layers were characterized by X-ray diffraction (XRD) (Ge content, film thickness, degree of relaxation) and by SIMS (B doping). For device characterization dark current measurements and optical Fourier transformation infrared spectroscopy (FTIR) were applied.

The potential distribution inside the HIP stack including the n^+-doping spike was calculated by a one dimensional TOSCA-simulation [10].

RESULTS AND DISCUSSION

In a system consisting of a narrow n^+-doping layer on p-type material, which is fully depleted, band bending due to space charge in the layer is expected to cause an increase in the barrier height at the p^+-SiGe/p-Si interface. For the device simulation with TOSCA we took silicon material parameters from Green [11] which were scaled and wighted for a Ge content of 30% and a temperature of 100K. For the calculation we assumed a stack consisting of an 1 nm wide phosphorus spike with a concentration of $1x10^{19}$ cm^{-3} and $2x10^{19}$ cm^{-3} on a low doped p-type Si followed by an 5 nm undoped Si/SiGe spacer and the strained $Si_{0.7}Ge_{0.3}$ layer boron-doped with a concentration of $2x10^{20}$ cm^{-3}. The cross section of the structure used for the simulation is included in fig. 1 where the calculated changes of the valence band are represented. In the absence of the doping spike we obtained a barrier height of 175 meV. This value agrees well with the 190 meV change of the energy gap given by Bean [8] for 30%Ge at a temperature of 90 K taking into account that the valence band offset at the SiGe/Si interface is in the order of 90% of the gap narrowing. This result indicates that the extracted material parameters described above are suitable for our calculation. The incorporation of a doping spike increases the barrier to 229meV and to 285meV for the two P concentrations, respectively. To get a fully depleted n^+ spike doped region the total spike concentration should not exceed a value of some $10^{19}$$cm^{-3}$. The performance

of the detector may be additionally improved by a built in drift field resulting from a graded SiGe absorptive layer.
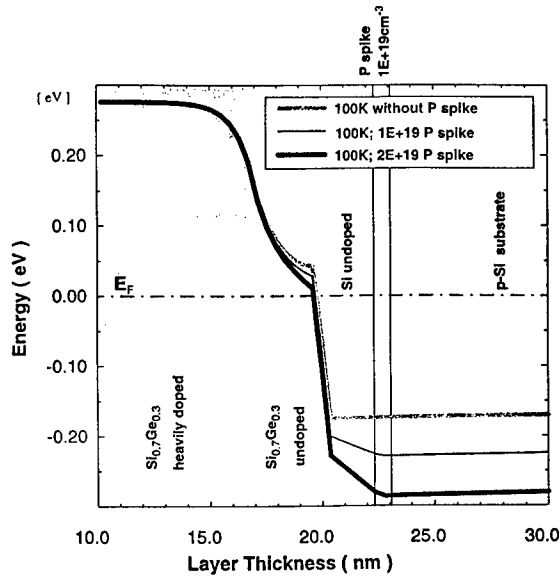
Fig. 1: Valence band edge without and with n$^+$ spike in a p$^+$SiGe/Si stack

In fig.2, a SIMS profile through the layer stack of an HIP diode is shown. The boron concentration inside the SiGe layer was 2×10^{20} cm^{-3}; the Ge content (30%) was estimated by XRD. The samples with the doping spike exhibits a small broaded P peak at the SiGe/Si interface (not shown). This seems be related to the outdiffusion of phosphorus during the following processes. The integration over the P signal gives a concentration of about $1-2 \times 10^{19}$ cm^{-3}.
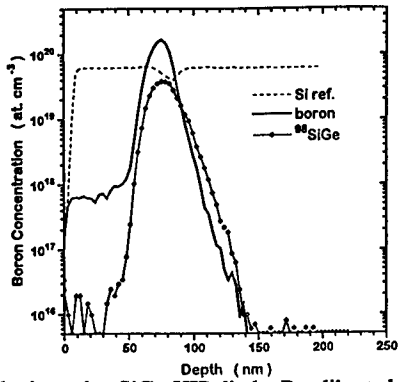
Fig. 2: SIMS profile through a SiGe-HIP diode; B calibrated, Si and SiGe not calibrated

The dark current of the diodes were measured as a function of temperature and Richardson plots were produced as shown in fig.3 for the two different diodes with 30% Ge at a reverse bias of 0.5 V. In fig. 2 I_0 is the reverse current density and T the absolute temperature. The straight

part of the plot results from thermionic emission over the heterojunction barrier. From its slope the barrier height can be estimated, resulting in 153meV and 296meV, without and with a P peak, respectively.
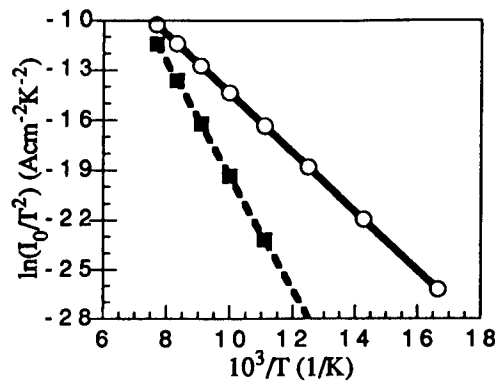
Fig. 3: Richardson plot for the HIP diodes; with (dashed line) and without (full line) the doping spike; reverse bias 0.5V

The spectral photosensitivity of the SiGe HIP diodes were measured with a BOMEM FTIR Spectrometer. The diodes were placed inside the cryostat instead of the spectrometers detector, and spectra were measured at 80 K. In fig. 4, the normalized to the maximum value response spectra for the two 30% Ge diodes and for a 50% Ge diode are shown. All diodes exhibit a strong photoresponse in the infrared. The cut-off (λ_c) is shifted to shorter wavelengths for the diode with the n^+-doping spike as well as for the higher Ge content.
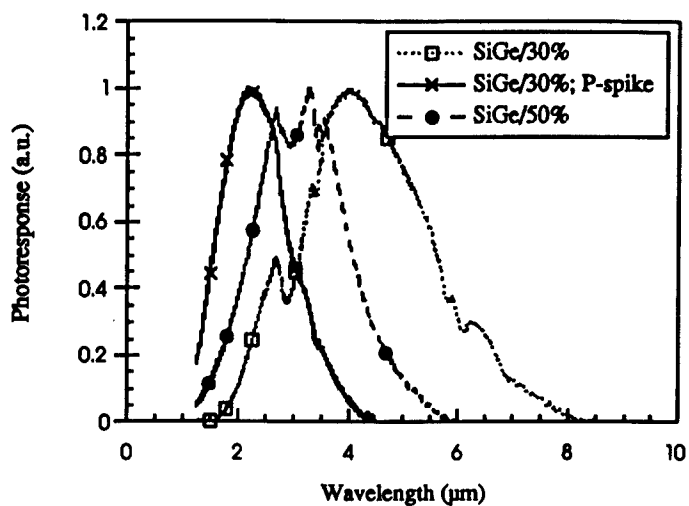
Fig. 4: Spectral photoresponse of the SiGe/Si-HIP; FTIR, 80K; 30% Ge, 30% Ge with n^+ spike, 50%Ge

216

The shift for higher Ge content results from the larger reduction of the energy gap of the strained SiGe layer. The much shorter cut-off for the diode with the P peak is caused by the increase of the barrier at the interface. The realization of a strained SiGe-HIP with such a short λ_c would require a very high Ge content in the order of about 60%. Due to the critical thickness limitation such films can be grown pseudomorphically with a thickness of few nm's only. As a consequence the absorption depth for the IR photons will be reduced, decreasing the detector response.

Table 1 summarizes the cut-off wavelengths λ_c of the HIP diodes, and the corresponding optical (ϕ_o) and thermal (ϕ_t) barrier heights. The results of the simulation are included, too.

Tab.1: Cut-off wavelength λ_c and barrier height Φ for SiGe-HIP-
detectors measured by FTIR at 80 K for different Ge-content

Sample X(%)	d (µm)	λ_c (µm)	Φ optical (meV)	Φ thermal (meV)	Φ calc. (meV)	ΔE(90K) (meV) Bean [8]
30	30	8,2	151	153	175	190
50	20	6,0	207	269		260
30 with P-spike	30	4,5	276	296	285	190

The corresponding variation of the energy gap taken from [8] are given for comparison. The difference between these values and the estimated barrier heights results from the fact that there is a small conduction band offset at the heterojunction. On the other hand, due to the degenerate doping of the SiGe, the Fermi level is shifted into the valence band. Consequently, the carriers see a barrier from the Fermi level and not from the valence band edge.

The shift in the barrier height due to the the n^+ spike doping is in good agreement with the value obtained from the TOSCA simulation assuming a phosphorus concentration of 2×10^{19} cm^{-3}.

The bias dependence of the photoresponse is given in fig. 5. At 80K a high photoresponse occurs already at zero bias. Increasing the bias the signal goes into saturation. This behaviour is simelar for two types of photodiodes, and demonstrates that both detectors can be operated at low biases in the order of 1 volt.
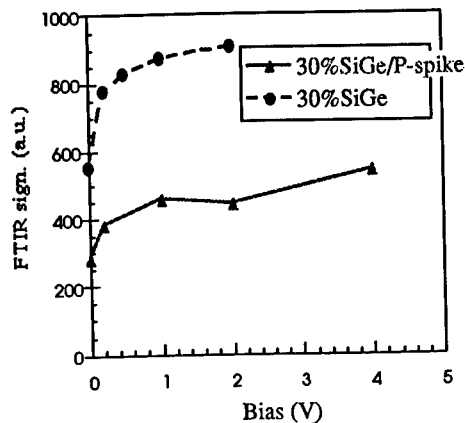
Fig. 5: Bias dependence of the detectors
at 80K; 30% Ge, 30% Ge with n$^+$-spike

217

SUMMARY

A novel SiGe/Si HIP detector is proposed which uses a narrow n^+-doping spike at the substrate interface increasing the heterojunction barrier height. The n^+ spike was prepared by an atomic layer doping technique. Incoporating a P spike the cut-off wavelength was changed from 8.2 μm without P spike to 4.5 μm at a P concentration of about 2×10^{19} cm^{-3} for the same Ge content of 30 %.This result is in agreement with device simulation. In this way the trade off between critical film thickness limitation for high Ge content and high absorption depth for proper detector response can be overcome.

REFERENCES

[1] T. L. Lin and J. Maserjan, Appl. Phys. Lett. 57 (1990) 1422

[2] B-Y. Tsaur, C. K. Chen, and S. A. Marino, IEEE Electron Dev. Lett. 12 (1991) 293

[3] R. Banisch, B. Tillack, K. Pressel, R. Barth, and H. Erzgräber, E-MRS 1996 Spring Meeting, D/P40

[4] B. Tillack, G. Ritter, D. Krüger, P. Zaumseil, G. Morgenstern, and K.-D. Glowatzki, Mater. Science and Technology 11 (1995) 1060

[5] J. M. Shannon, Appl. Phys. Lett. 25 (1974) 75

[6] K. Konuma, Y. Asano, K. Masubuchi, H. Utsumi, S. Tohyama, T. Endo, H. Azuma, and N. Teranishi, IEEE Trans. Electron Devices 43 (1996) 282

[7] B. Tillack, P. Zaumseil, G. Morgenstern, D. Krüger, and G. Ritter, Appl. Phys. Lett. 67 (1995) 1143

[8] C. J. Bean, Proc. IEEE 80 (1992) 571

[9] B. Tillack, D. Krüger, P. Gaworzewski, and G. Ritter, to be publ. in Mater. Science and Eng.

[10] H. Gajewski, H. Langmach, G. Telschow und K. Zacharias: „Der 2D-Bauelementesimulator TOSCA", Handbuch, Berlin 1986, 1993

[11] M. A. Green, J. Appl. Phys. 67 (1990) 2944

DARK CURRENT REDUCTION IN NEAR INFRARED P-I-N DETECTOR DIODES FABRICATED FROM In$_{.75}$Ga$_{.25}$As GROWN BY MOLECULAR BEAM EPITAXY ON InP SUBSTRATES

M. MICOVIC *, W.Z. CAI *, Y. REN *, J. NEAL *, S.F. NELSON **, T.S. MAYER *, D.L. MILLER *
* Electronic Materials and Processing Research Laboratory, Department of Electrical Engineering, The Pennsylvania State University, University Park, PA
** Department of Physics, Colby College, Waterville, ME

ABSTRACT

We have investigated several approaches to improve the material quality of lattice-mismatched In$_{.75}$Ga$_{.25}$As grown by Molecular Beam Epitaxy (MBE) on (1 0 0) InP substrates. They include linear grading of In composition from lattice matched In$_{.53}$Ga$_{.47}$As to In$_{.75}$Ga$_{.25}$As in a 1 μm buffer layer grown at reduced substrate temperature, in combination with various *in situ* annealing and material regrowth steps. The material was used for fabrication of mesa-structure p-i-n photodetectors with 2.2 μm cutoff wavelength. The room temperature dark current density at 1 V reverse bias was approximately 2 mA/cm^2 in all structures that were subjected to anneal and regrowth process, a factor of three improvement over reference samples which were not subjected to annealing and regrowth. The dark current density at 15 V reverse bias (10 mA/cm^2 for the best devices) was at least two orders of magnitude lower in all annealed samples than in reference samples. These results suggest that the MBE grown material can be an attractive alternative to the vapor phase epitaxy (VPE) grown material which is commonly used for fabrication of these detectors.

INTRODUCTION

Indium gallium arsenide (In$_x$Ga$_{1-x}$As) is becoming a material of choice for fabrication of room temperature operated 1-2.8 μm photodetectors.[1] Molecular beam epitaxy is an attractive technique for growth of this material because it offers superior control over layer thickness and composition, and excellent uniformity of these parameters. Detectors which operate at wavelengths that are longer than 1.65 μm must be fabricated from In$_x$Ga$_{1-x}$As layers with $x > 0.53$, which is the value at which the material is lattice-matched to InP substrates. These high- indium-content films are typically grown on InP due to the lack of other more appropriate substrates. Layers for fabrication of photodetectors with a 2.2 μm cutoff wavelength have $x = 0.75$. The lattice mismatch between the InP substrate and In$_{.75}$Ga$_{.25}$As (approximately 1.5 %) is partially accommodated by misfit dislocations, since the detectors must be much thicker (several μm) than the critical thickness (several nm) below which mismatch can be accommodated solely by elastic strain. [2]

The dislocations present in the depletion region of the device may severely degrade its performance. Buffer layers are typically grown between the substrate and the lattice mismatched p-i-n detector structure to reduce the dislocation density in the active region. Composition-graded buffers of In$_x$Ga$_{1-x}$As[3], In$_x$Al$_{1-x}$As[4] or InAs$_y$P$_{1-y}$[5] have been demonstrated to effectively reduce dislocation density in the active region of the mismatched In$_x$Ga$_{1-x}$As/InP, or In$_x$Ga$_{1-x}$As/GaAs material system. The lattice constant of these buffers is usually lattice matched at the substrate epitaxial layer interface, and is brought to the lattice constant of the active region

by a continuous composition grading,[5, 6] a series of abrupt composition steps,[7] or by compositional superlattices.[6] Compositional superlattices and linearly-graded buffer layers are most commonly used in MBE.[5, 6, 8, 7] In this study we investigate linearly-graded buffers since their growth requires fewer shutter operations than the growth of compositional superlattices. Linearly graded buffer layers are commonly grown at low substrate temperatures to avoid island nucleation and the resultant three-dimensional growth.[8]

Elastic strain in linearly-graded buffer layers grown at low temperatures may not be fully relaxed, because nucleation and propagation of misfit dislocations is suppressed at reduced substrate temperatures.[9, 10, 11] If the strain of the buffer is not fully relaxed at the point when the active region growth is initiated, strain energy of the system continues to increase as the active region layers are grown. This may result in the formation of misfit dislocations in the active region in the device, resulting in inferior device performance. Growth of thick buffer layers that would release the elastic strain (7-10 μm is typical for VPE-grown material) is not commercially feasible in MBE because of the slow growth rate, around 1 μm/hour.

Residual strain in linearly-graded buffer layers that were grown by MBE at reduced substrate temperatures can be relaxed by *in situ* thermal annealing.[12, 13] We have observed that p-i-n In$_x$Ga$_{1-x}$As optical detectors with a cutoff wavelength of 2.2 μm grown on annealed, relaxed buffer layers have lower dark currents then devices grown on a similar buffer without an anneal.

We speculate that the observed improvement in electrical characteristics may be due to a reduction in misfit dislocation density in the device active region due to more complete strain relaxation in the underlying buffer.

EXPERIMENT

Layers for fabrication of In$_{.75}$Ga$_{.25}$As detectors were grown on InP (0 0 1) $\pm$ 0.1° substrates in modular Varian GEN II MBE system. The substrate surface was prepared for epitaxial growth by a 5-minute etch in a 4:1:1 H$_2$SO$_4$:H$_2$O$_2$:H$_2$O solution. Substrates were mounted onto wafer holders with indium metal. Prior to initiation of epitaxial growth, the native oxide was desorbed from the substrate surface in a flux of As$_4$ molecules. The pressure of As$_4$ used during the growth was 1.2x10^{-5} Torr, as measured by an ion gage in the beam path. The oxide desorption was monitored by a reflection high energy electron diffraction apparatus (RHEED) and was typically observed at a substrate temperature of 500°C measured by an optical pyrometer. The temperature of oxide desorption was reproducible to within $\pm$ 5°C. The substrate temperature was additionally monitored by a thermocouple located between the heater and the substrate holder. Thermocouple readings were used to estimate substrate temperatures below 450°C, the lower limit for our pyrometer. Substrate temperatures below 450°C were determined by extrapolating a linear fit of the relationship between pyrometer and thermocouple readings obtained at higher temperatures.

The growth rate was 0.78 μm/hour and was kept constant during the growth of the entire structure even when the composition was varied. The fluxes of metal molecules were calibrated with RHEED intensity oscillations. Ternary alloy composition of layers was obtained by selecting the appropriate ratio of the metal fluxes. An arsenic stabilized 2x4 reconstruction was observed by RHEED during the growth and annealing of all structures. Doping in the layers was obtained by Si and Be for p- and n-type doping, respectively.

Table I shows structure of the layers that were used for fabrication of photodetectors. A lattice-matched buffer layer of 0.3 μm In$_{.52}$Al$_{.48}$As and 0.2 μm In$_{.53}$Ga$_{.47}$As was grown on the InP

Table I. Structure of layers for fabrication of p-i-n photodetectors.

Structures A, B, C, F*	Structure D
50 nm In$_{.75}$Ga$_{.25}$As p$^+$	50 nm In$_{.75}$Ga$_{.25}$As p$^+$
50 nm In$_{.75}$Al$_{.25}$As p$^+$	50 nm In$_{.75}$Al$_{.25}$As p$^+$
50 nm In$_{.75}$Ga$_{.25}$As p	50 nm In$_{.75}$Ga$_{.25}$As p
1 μm In$_{.75}$Ga$_{.25}$As S.I.	1 μm In$_{.75}$Ga$_{.25}$As S.I.
.3 μm In$_{.75}$Ga$_{.25}$As n	.3 μm In$_{.75}$Ga$_{.25}$As n
A, F* 1 ⎧ 20 min anneal at 510°C	
B 2 x ⎨ 5x ⎧ 10 nm In$_{.75}$Al$_{.25}$As n	
C 3 ⎩ ⎩ 10 nm In$_{.75}$Ga$_{.25}$As	200 nm In$_{.75}$Ga$_{.25}$As n
80 nm In$_{.75}$Ga$_{.25}$As n	
5x ⎧ 10 nm In$_{.75}$Al$_{.25}$As n	
⎩ 10 nm In$_{.75}$Ga$_{.25}$As	
80 nm In$_{.75}$Ga$_{.25}$As n	
1 μm In$_x$Ga$_{1-x}$As n	1 μm In$_x$Ga$_{1-x}$As n
x = .53 → .75	x = .53 → .75
200 nm In$_{.53}$Ga$_{.47}$As n	200 nm In$_{.53}$Ga$_{.47}$As n
300 nm In$_{.52}$Al$_{.48}$As n	300 nm In$_{.52}$Al$_{.48}$As n
Substrate InP n+	Substrate InP n+

* No annealing

substrate at 490°C for all structures. The substrate temperature was reduced to 400°C during the growth of the last 50 nm of the lattice-matched In$_{.53}$Ga$_{.47}$As layers, and was kept at this temperature during the growth of the linearly-graded buffer layers. Growth was interrupted and samples annealed *in situ* under As flux as indicated in Table 1 during the growth of samples A, B, and C. The substrate temperature was increased to 510°C for 20 min during each growth interruption, after which the substrate temperature was lowered to 450°C and growth was resumed. Attempts to anneal substrates at higher temperatures resulted in excessive re-evaporation of As and nucleation of In droplets. Short-period In$_{.75}$Ga$_{.25}$As/In$_{.75}$Al$_{.25}$As superlattices were introduced into the structures A, B, and C to help protect the surface during high temperature annealing. To separate effects due to the short-period superlatice from effects due to annealing, an additional sample, F, was grown with the structure of sample A but with no growth interruption and annealing steps. The substrate temperature during growth of sample F was increased from 400 to 450°C after the second superlattice was grown, in contrast to samples A, B, and C, where substrate temperature during epitaxial growth was raised to 450°C after the first superlattice and growth interruption. A fifth sample, D, was grown entirely at 400°C without superlattices and growth interruptions. Pieces cleaved from grown layers A, D, and F were reintroduced into the growth chamber and annealed at 510°C to investigate the effects of post growth annealing on material quality.

   Trenches defined by photolithography were etched down to the undoped active layer to form 60x90 mm^2 mesas. Indium on the back of the n+ InP substrates was used as the backside ohmic contact, while Ti/Au contacts were deposited on the top of the mesa structures by thermal

evaporation and lift-off. The electrical characteristics of the devices were measured by an HP4155 parameter analyzer in a dry nitrogen atmosphere shortly after device processing to minimize surface leakage currents at the mesa periphery.

The surface morphology of all samples was examined using an optical microscope and the morphology of the samples C and D was additionally investigated with an atomic force microscope (AFM).

RESULTS

Figure 1 shows typical reverse-bias I-V characteristics of p-i-n detectors fabricated from structures A-F. Results clearly indicate that reverse-bias leakage current is significantly reduced when the active layer is grown on an annealed buffer. The difference is most significant at high
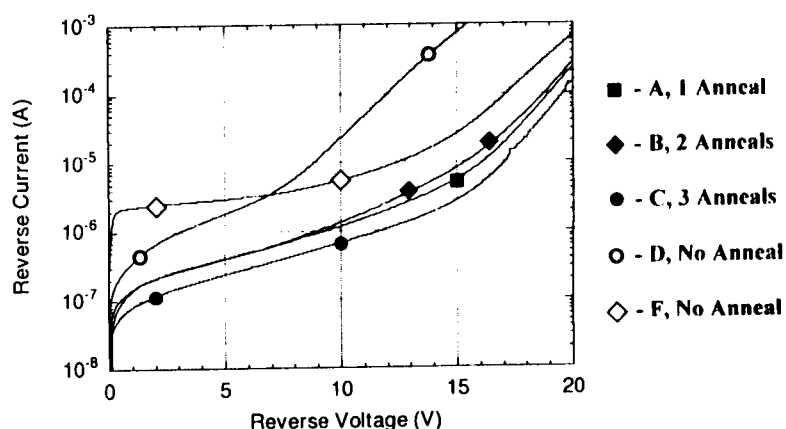
Figure 1. Reverse bias I-V characteristics of photodiodes fabricated from layers A to F.

reverse bias voltages. For a reverse bias voltage of 15 V, the leakage currents of all samples that were grown on annealed buffers (A-C) are two orders of magnitude lower than that of reference sample D which was grown on a non-annealed buffer. The I-V characteristics of the reference sample D are comparable to that of the best samples that were reported in our previous work.[14] The number of growth interruptions and annealing steps in the samples with annealed buffers does not have a significant effect on the reverse-bias I-V characteristics of these layers. The reverse-bias I-V characteristics of the reference sample F, which was grown on a non-annealed buffer with two short period superlattices, displays the highest leakage current of all structures at low reverse bias voltages. The origin of this increase of the leakage current is not clear, but the result suggests that the superlattice without annealing does not improve material quality.

Reverse-bias I-V characteristics of devices which were fabricated from layers that were subjected to a post-growth anneal (pieces of samples A, D, and E) were identical to the characteristics of devices that were fabricated from non-annealed layers of the same samples. This indicates that these structures do not undergo additional changes at temperatures which may be required for device processing. On Fig. 2 a normalized spectral response of a photodetector fabricated from structure C is shown. The cutoff wavelength estimated from the spectral response is around 2.2 μm.
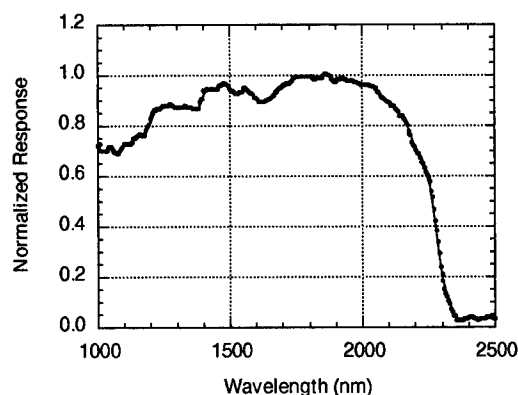
Figure 2. Normalized spectral response of photodiode fabricated from layer C.

Cross-hatch features oriented along the (-1 1 0) and (1 1 0) crystalline axes were observed on all the samples under the optical microscope. The density of the cross-hatch lines was visibly lower in one of the directions on all the samples with annealed buffers (A-C). This asymmetry was

a) sample D, non-annealed buffer   b) sample C, annealed buffer
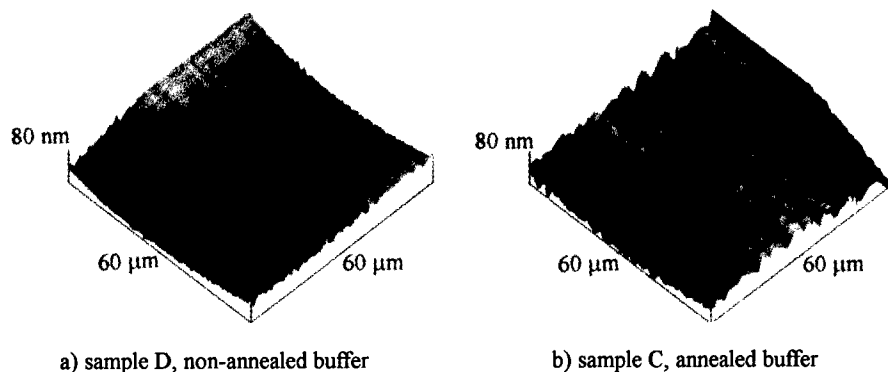
Figure 3. AFM images of surface morphologies of samples a) D and b) C.

not so pronounced on non-annealed samples. Images of the surface morphology of two samples (D - non-annealed buffer and C - annealed buffer) obtained by AFM, shown in Fig. 3, confirm this observation. It can be seen that the sample with the annealed buffer has the rougher surface. A formation of cross-hatch morphology on the surfaces of dislocated interfaces is a known phenomenon.[15] It has been observed that these surface corrugations are correlated to dark line defects and spatial dislocation arrangement.[16,17] The asymmetry of cross hatch pattern is attributed to a difference in nucleation rate or mobility of two types of 60° dislocations that are present in III-V semiconductors.[19,18]

CONCLUSIONS AND DISCUSSION

Results of our study show that reverse bias leakage current of 2.2 μm In$_{.75}$Ga$_{.25}$As p-i-n photodetectors were reduced by a factor of three at low biases and two order of magnitude at high biases when active layers were grown on thermally-annealed low temperature linearly graded buffer layers. This material improvement correlates to a large difference in the cross-hatch pattern between the samples that were grown on annealed buffers and those that were grown on non-annealed buffers. A similar correlation between material quality improvement and formation of cross-hatch has been observed for thermally annealed GaAs films grown on Si substrates, and was attributed to dislocation redistribution due to thermal strains in annealing process.[13]
In our case we attribute material quality improvement and increase in surface corrugation to relaxation of residual elastic strain that was accumulated in the buffer layers during low temperature growth. Absence of metastable strain in the buffer layers, and possible redistribution of dislocations during thermally activated strain relieve may both contribute to the observed material improvement.
In summary, we have demonstrated that material quality In$_x$Ga$_{1-x}$As layers grown on lattice mismatched substrates is improved when they are grown on thermally annealed buffer layers.

ACKNOWLEDGMENTS

REFERENCES

1   G.H. Olsen, Laser Focus 27, 48 (1991).
2   J.W. Matthews, A.E. Blakeslee, J. of Crystal Growth 27, 118 (1974).
3   J.C. Harmand, T. Matsuno, K. Inoue, Japanese J. of Appl. Phys. 28 (7), L1101 (1989).
4   A. Fischer-Colbrie, R.D. Jacowitz, D.G. Ast, J. of Crystal Growth 127, 560 (1993).
5   K. Makita, T. Torikai, H. Ishihara, K. Taguchi, Electron. Lett. 24, 379 (1988).
6   T. Won, S. Agarwala, H. Morkoc, Appl. Phys. Lett. 53, 2311 (1988).
7   S.M. Lord, B. Pezeshki, S.D. Kim and J.S. Harris, Jr., J. of Crystal Growth 127, 759 (1993).
8   P.R. Berger, K. Chang, P. Bhattacharya, J. Singh, K.K. Bajaj, Appl. Phys. Lett. 53, 684 (1986).
9   M.J. Ekenstedt, S.M. Wang, T.G. Andersson, Appl. Phys. Lett. 58, 854 (1991)
10   H. Yaguchi, K. Fujita, S. Fukatsu, Y. Shiraki, R. Ito, Japanese J. of Appl. Phys. 30 (8B), L1450 (1991).
11   J.W. Matthews, A.E. Blakeslee, S. Mader, Thin Solid Film 33, 253 (1976).
12   J.-M. Baribeau, S. Kechang, K. Munro, Appl. Phys. Lett. 54, 323 (1989).
13   T. Nishioka, Y. Itoh, A. Yamamoto, M. Yamaguchi, Appl. Phys. Lett. 51, 1928 (1987).
14   R. Kochar, W.Y. Hwang, M. Micovic, T.S. Mayer, D.L. Miller (unpublished).
15   G. Olsen and M. Ettenberg, Crystal Growth, (Plenum, New York, 1974), Vol. 2, p. 32.
16   E.A. Fitzgerald, D.G. Ast, P.D. Kirchner, G.D. Pettit, J.M. Woodal, J. Appl. Phys. 63, 693 (1988).
17   B.A. Fox and William A. Jesser, J. Appl. Phys. 68, 2739 (1990).
18   K.L. Kavanagh, M.A. Capano, L.W. Hobbs, J.C. Barbour, P.M.J. Maree, W. Schaff, J.W. Mayer, D. Pettit, J.M. Woodal, J.A. Stroscio, R.M. Feenstra, J. Appl. Phys. 64, 4843 (1988).

GROWTH AND CHARACTERIZATION OF INTERFACES IN P-TYPE InGaAs/InP QUANTUM-WELL INFRARED PHOTODETECTORS WITH ULTRA-THIN QUANTUM WELLS

D.K. Sengupta, S. Kim, T. Horton, H.C. Kuo, S. Thomas, S.L. Jackson, A.P. Curtis,
S.G. Bishop, M. Feng, and G.E. Stillman*; Y.C. Chang**, H.C. Liu***
*Center for Compound Semiconductor Microelectronics, ECE Department, University of Illinois at Urbana-Champaign, Urbana, IL 61801
**Materials Research Laboratory, Department of Physics, University of Illinois at Urbana-Champaign, Urbana, IL 61801
***Institute for Microstructural Sciences, National Research Council, Ottawa, Ontario K1A0R6, Canada

ABSTRACT

P-type InGaAs/InP quantum-well infrared photodetectors operated at 4.55 µm require the growth of ultra-thin (10 Å) quantum wells. We report a study of interfaces in QWIPs grown by gas-source molecular beam epitaxy in which we optimized the group V source supply sequence so that a 6 K photoluminescence linewidth as narrow as 8.4 meV was observed from a structure with 10 Å wells. Analysis of the PL suggests that interface roughness was minimized. Cross-sectional scanning tunneling microscopy, double crystal x-ray diffraction, and cross-sectional tunneling electron microscopy confirmed that high-quality interfaces and uniform layers were obtained. Using the derived structural parameters, photocurrent spectral response was theoretically predicted for these QWIPs and then experimentally verified .

INTRODUCTION

GaAs/AlGaAs quantum-well infrared photodetectors (QWIPs) have attracted much attention for use in low-cost high-yield imaging-array applications[1], with recent demonstrations of multiple-color GaAs/AlGaAs QWIPs broadening interest. InP-based QWIPs have also been studied and have been experimentally shown to yield lower dark current and higher responsivies for n-type detectors[2,3]. Intersubband p-type InGaAs/InP QWIPs offer further advantages including the possibility of normal-incidence detection, reduction in dark current, broadening of the absorption spectrum, and shorter wavelength absorption because of the relatively large valence band offset. In addition, combining n- and p-type InGaAs/InP quantum wells offers the possibility of single-device two-color QWIPs for both the 3 - 5 µm and 8 - 14 µm wavelength regimes.

In this article we present GSMBE growth and characterization of p-doped InGaAs/InP QWIPs (operating at 4.55 µm) with ultra-thin wells and excellent interface quality. We first present details of our growth procedures and structural characterization results including photoluminescence (PL), cross-sectional transmission electron microscopy (XTEM), cross-sectional scanning tunneling microscopy (XSTM), and double-crystal x-ray diffraction (DCXRD) measurements. Structural parameters derived from these measurements are used to theoretically predict detector device performance, which is verified with direct measurements of device photocurrent spectral response.

GROWTH AND STRUCTURAL CHARACTERIZATION

Epitaxial growth was performed in a modified Perkin-Elmer 430P GSMBE/CBE system. Cracked AsH_3 and PH_3 were used as the group V sources, while elemental solid sources in effusion cells were used for the group III sources. Details of the MBE system and cracker design are reported elsewhere[4]. All p-QWIP structures (Fig. 1) were grown on semi-insulating (001) Fe-doped InP substrates at 500°C with InP and $Ga_{0.47}In_{0.53}As$ growth rates of 0.59 µm/hr and 1.05 µm/hr, respectively. A two-step procedure (Fig. 2) was implemented for InGaAs-on-InP interfaces, whereby growth of InP was terminated by simultaneously closing the In shutter and switching the PH_3 flow from the growth chamber to a vent line, leaving the InP surface free of flux for a period of time $T_{P'}$. AsH_3 was then introduced, exposing the InP surface to an As_2 overpressure for time T_{As}, thereby providing additional P_2 pumping-out time while preserving the

InP surface from further degradation. Growth of InGaAs was initiated by simultaneously opening the Ga and In shutters. For InP-on-InGaAs interfaces, growth of InGaAs was terminated by simultaneously closing the In and Ga shutters and directing the flow of AsH$_3$ from the growth chamber to the vent line for a period of time $T_{As'}$ during which residual arsenic was pumped from the growth chamber. After $T_{As'}$, InP growth was resumed by opening the In shutter and simultaneously flowing PH$_3$ into the growth chamber. The optimized times 7/10/20 (seconds) were established based on the feedback of PL and DCXRD measurements. The material quality of the optimized p-type InGaAs/InP QWIP structure was then quantified primarily using PL, the results of which were compared to XTEM, XSTM, and DCXRD results.

Photoluminescence

PL measurements were performed at temperatures ranging from 6 to 77 K with 514 nm excitation from an argon ion laser. The PL was dispersed by a 1 m single-grating spectrometer and then detected with a Ge detector. The laser power was varied over the range of 2.4 to 65 mW. Figure 3 shows the PL emission spectra of the p-type QWIP sample as a function both of sample temperature and excitation power. The main emissions from the sample are associated with the recombination of the heavy-hole bound excitons. The line shape of the PL emission is independent of the laser power, indicating that all of the PL is from a single origin. Figure 4 shows the measured PL emission linewidth as a function of sample temperature, as well as calculations of predicted linewidth contributions due to ternary alloy compositional variations and one-monolayer interface roughness. The small value of

Fig. 1. Structure for p-type InGaAs/InP QWIPs used in this work.
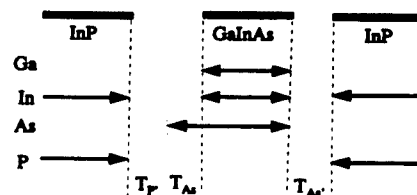
Fig. 2. Gas-switching used for GSMBE growth of InGaAs/InP QWIPs.
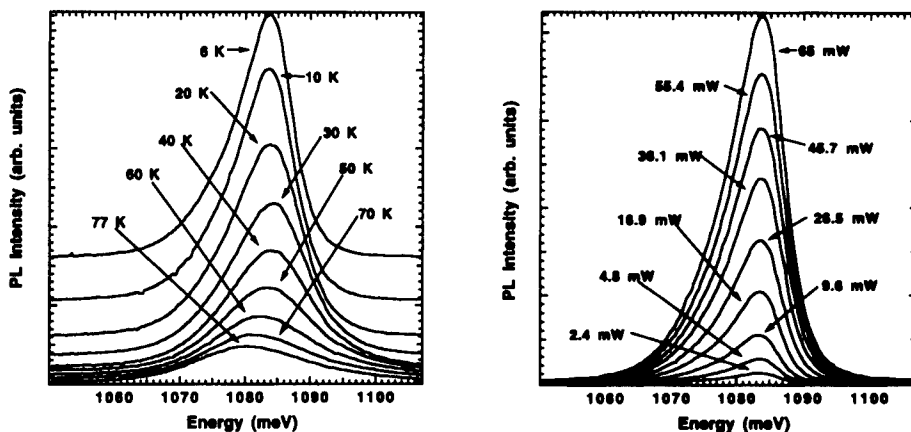
Fig. 3. Photoluminescence spectra for the p-type InGaAs/InP QWIPs, both versus temperature (left hand plot) and versus excitation power (right hand plot).

226
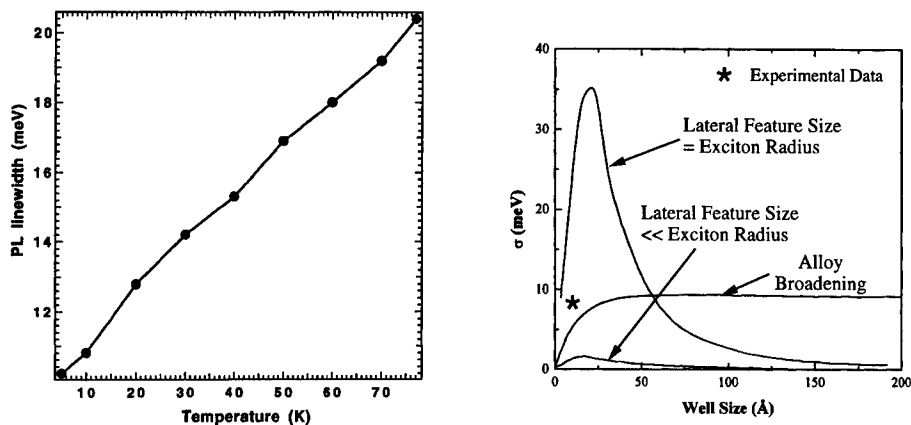
Fig. 4.   Photoluminescence linewidth, both measured (left hand plot) versus temperature, and calculated (right hand plot) versus well-width for one-monolayer interface roughness and two different values of lateral feature size.

measured line broadening at 6 K indicates interface roughness of a monolayer or less and compares very well with previous results by Tsang[5], who showed that these levels of broadening for ultra-thin InGaAs/InP QW structures are likely due to normal statistical variations in the local composition of the ternary well material[6]. Under a simple quantum-well model, the confinement energies for the electron and hole for this structure are 216 and 197 meV, respectively, with the values of the band offsets for the conduction and valence band used being 230 and 380 meV, and effective masses used for the electron and heavy hole being 0.041 m_0 and 0.46 m_0. The difference between the peak position and the summation of the band gap and the confinement energy yields an estimated binding energy of 139 meV for the bound exciton in these samples.

Cross-Sectional Transmission-Electron and Scanning-Tunneling Microscopy

Figure 5 is an XTEM micrograph for this structure showing the quantum-well region plus the InP substrate and thick InGaAs contact regions. The 10 Å wells are well-defined and uniform over a relatively large area and no obvious defects are visible, indicating good material quality. To directly view quantum-well/barrier interfaces, an XSTM micrograph was taken of a single well using an STM design (by Brockenbrough and Lyding[7]) incorporated within an ultra-high vacuum system. The sample was cleaved in-situ to expose the (110) surface for analysis, the results of
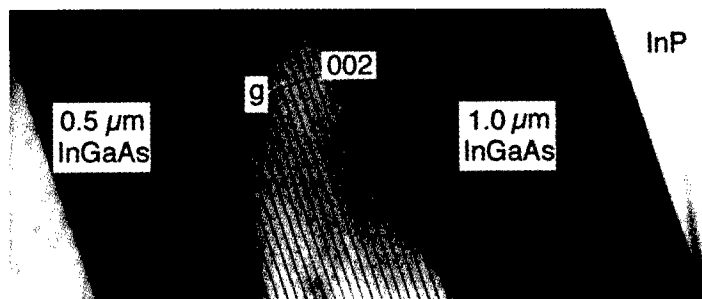
Fig. 5.   XTEM image of p-type QWIP structure showing uniformity of the layers.

which are shown in Figure 6. The InP barriers appear darker than the adjacent InGaAs well regions because of the valence-band offset. The InP barriers are homogenous except in regions close to the interface, while the InGaAs well region displays a mottled appearance throughout, probably due to local alloy fluctuations. The normal interface appears to be sharp, with intermixing less than a monolayer in the [100] direction, while more significant intermixing is observed at the inverted interface. This is attributed to residual As_2 incorporation into the InP layer at the inverted interface, noting that a significant density of As is seen in the InP within 2 monolayers of the interface and scattered As atoms are observed at even 3 and 4 monolayers into the InP barrier.

X-Ray Diffraction

A Philips DCXRD system was used to measure x-ray diffraction patterns for these wafers. All measurements were conducted in θ–2θ mode with a fine collimation of the incident and diffracted x-rays in order to track the evolution of the superlattice harmonics over several degrees. Figure 7 (a) shows the (004) $CuK_{\alpha 1}$ rocking curves for the p-QWIP structure. Superlattice satellites are observed up to the 4th order with an average FWHM of 31 arcsec. The simulations shown in (b) and (c) of Figure 7 were performed by means of the dynamical theory of x-ray diffraction[8] and provided structural information about the thickness and the chemical composition of the MQWs. Figure 7(b) assumes abrupt interfaces for both InGaAs-on-InP and InP-on-InGaAs interfaces, while Figure 7(c) assumes a monolayer of $InAs_{0.5}P_{0.5}$ inserted at each inverted interface as a model for the As intrusion into the InP as seen by XSTM. Since Figure 7(b) yields better agreement with the measured data than Figure 7(c), particularly with respect to the strong first-order satellites, this reaffirms residual As_2 incorporation into the InP barrier layers and subsequent formation of strained InP(As) layers at the interfaces. The combined results of XTEM, XSTM, and DCXRD yield a best

Fig. 6. XSTM occupied-states image of a single quantum well in the p-type QWIP structure. Light areas are InGaAs and dark areas are InP.
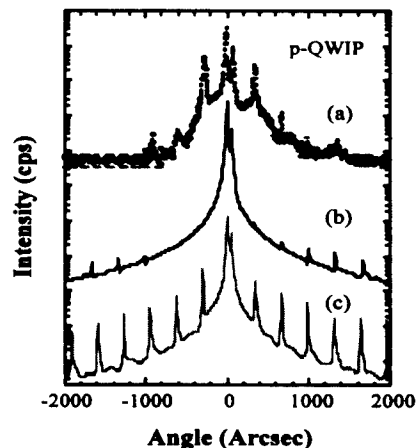
Fig. 7. (a) Measured DCXRD spectrum for the QWIP structure. (b) Results of simulation assuming abrupt interfaces. (c) Results of simulation assuming monolayer InAsP transition at non-inverted interface.

228

fit of 10.5 Å $Ga_{0.525}In_{0.475}As$, 3.04 Å $InAs_{0.5}P_{0.5}$, and 564.3 Å InP, which correspond well with the nominal values of 10/550Å InGaAs/InP.

DEVICE SIMULATION AND EXPERIMENTAL RESULTS

A six-band (two conduction and four valence bands) effective bond-orbital model was used to calculate the absorption coefficient for the p-type QWIPs (model details are presented elsewhere[9]). An $In_{0.53}Ga_{0.47}As$/InP superlattice with 4 monolayers (11 Å) of InGaAs and 68 monolayers (200 Å) of InP in each period was employed. Although the actual layer thickness of InP in each period is 550 Å, the absorption coefficient is believed to be relatively insensitive to the thickness of the barrier as long as it is thick enough to effectively isolate the quantum wells. Optical properties were calculated in the same way as described by Chang et al.[10], and optical transitions from occupied states to unoccupied states were calculated using both inter-subband and inter-band transitions. The 2D carrier density was assumed to be 8×10^{11} cm-2 per well with a valence-band offset of 420 meV[11]. Thus, subbands with energies below 420 meV were considered as continuum states which can lead to photocurrent. With an applied electric field, additional photocurrent due to tunneling through the barrier was accounted for by the WKB approximation.

For device measurements, structures were fabricated into 200 μm diameter mesa diodes by chemical etching and then deposited with non-alloyed Ti/Pt contacts. Devices were polished at 45° for optical coupling and indium-bonded to a copper heat sink. All measurements were performed with the detectors mounted on a stage which was in thermal contact with the cold end of a continuos flow helium cryostat. Photocurrent spectral response measurements were performed at 80K. The results of both simulation and measurements are shown in Figure 8, where all modeled photocurrent spectra have been broadened by a halfwidth of 0.15 eV for comparison to the experimental results. As can be seen, the model results are in good agreement with measurements, particularly in terms of the peak response position close to 4.55 μm.
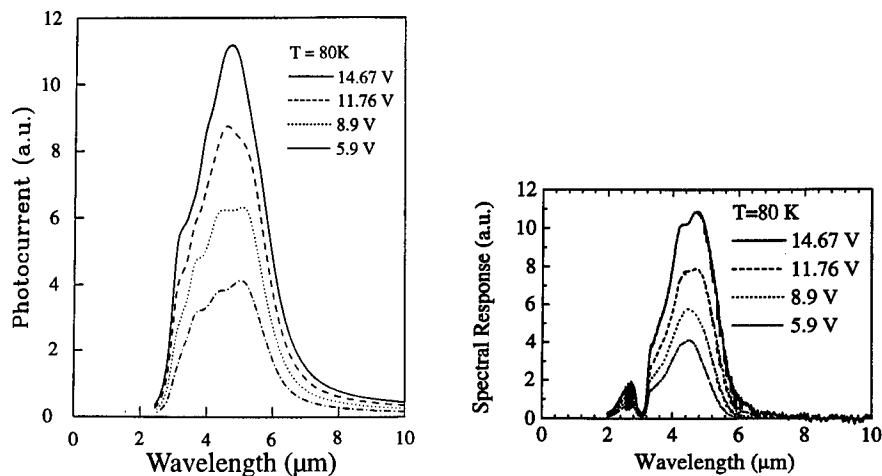
Fig. 8. Photocurrent spectra for the p-type InGaAs/InP QWIPs studied in this work. Modeled spectra using structural parameters independently determined. (b) Measured spectra. (Note: Measured response null close to 3 μm is likely due to water absorption.)

CONCLUSION

In summary, high structural-quality InGaAs/InP QWIPs with ultra-thin (10 Å) QWs were grown by GSMBE. PL measurements, as well as XTEM, XSTM, DCXRD results suggest that

the InGaAs layers were uniformly grown with minimal interface roughness, and that the inverted-interface roughness is very difficult to remove due to As$_2$ carry over. In addition to providing direct evidence of well-defined quantum wells and barriers with abrupt interfaces, the structural analyses yielded precise thickness and compositional parameters for the QWs, which was very important to the simulation of the absorption coefficient and photocurrent spectrum for QWIPs.

ACKNOWLEDGMENTS

REFERENCES

1.   B.F. Levine, J. Appl. Phys. **74**, R1 (1993).

2.   S.D. Gunapala, B.F. Levine, D. Ritter, R. Hamm, and M.B. Panish, Appl. Phys. Lett. **58**, 2024 (1991).

3.   J.Y. Andersson, L. Lundqvist, Z. F. Paska, K. Streubel, and J. Wallin, Proc. of SPIE **1762**, 216 (1992)

4.   S.L. Jackson, J.N. Baillargeon, A.P. Curtis, X. Liu, J.E. Baker, J.I. Malin, K.C. Hseih, S.G. Bishop, K.Y. Cheng, and G.E. Stillman, J. Vac. Sci. Technol. **B 11**, 1045 (1993).

5.   W.T. Tsang and E.F. Schubert, Appl. Phys. Lett. **49**, 220 (1986)

6.   J. Singh, Physics of Semiconductors and Their Heterostructures, pp. 634 - 637, McGraw-Hill, Inc. 1993.

7.   R. Brockenbrough and J.W. Lyding, Rev. Sci. Instrum., **64**, 2225 (1993).

8.   B. K. Tanner, Adv. X-ray Anal. **33**, 1 (1990)

9.   Y.C. Chang, Phys. Rev. **B37**, 8215 (1988)

10.   Y.C. Chang, J. Cheung, A. Chiou, and M. Khosnevisan, J. Appl. Phys. **68**, 4223 (1990)

11.   M. Cardona and N.E. Christensen, Phys. Rev. **B37**, 1011 (1988)

NORMAL INCIDENCE PHOTORESPONSE AS A FUNCTION OF
WELL WIDTH IN P-TYPE GaAs/AlGaAs MULTI-QUANTUM WELLS

G.J. BROWN, M.A. CAPANO, S.M. HEGDE, K. EYINK, F. SZMULOWICZ
Wright Laboratory, Materials Directorate, Wright-Patterson AFB, OH 45433-7707

ABSTRACT

We have performed an optimization study of the mid-infrared photoresponse of p-type GaAs/AlGaAs Quantum Well Infrared Photodetectors (QWIPs) designed for normal incidence detection. In these p-type quantum wells, normal incidence absorption is allowed (by the dipole selection rules for optical transitions) especially for transitions from the heavy-hole ground state to the second light-hole state. Previous theoretical modeling predicted that this transition will produce the strongest bound-to-continuum infrared absorption when the second light-hole state is located very near the top of the GaAs quantum well. For AlGaAs barrier layers with 30% aluminum, our modeling showed that a well width between 45Å and 50Å would optimize the normal incidence photoresponse of this p-type QWIP. In this work, photoresponse spectra are reported for well widths ranging from 40Å to 65Å. A series of samples were studied in which only the GaAs well width was varied in two monolayer increments, from 14 to 20 monolayers. Photoluminescence and X-ray diffraction measurements were used to verify the composition, well width, and structural quality of each sample. This study verified that the spectral range of the normal incidence photoresponse is narrower, as predicted by theory, for well widths in which the second light-hole state approaches the top of the valence band well.

INTRODUCTION

Infrared detectors based on multi-quantum well (MQW) heterostructures are of continuing interest due to the capability of producing large area, high uniformity, two-dimensional imaging arrays. Most previous work has been focused on n-type GaAs/AlGaAs MQWs to take advantage of the low effective mass of the electron, which should provide superior transport properties [1]. However, for these n-type (donor doped) QWIPs, intersubband transitions are limited by dipole selection rules to couple only to radiation with a polarization component perpendicular to the quantum wells (i.e. normal incidence absorption is forbidden) [2]. This limitation then requires the use of gratings on each detector element to bend the incident radiation so that it enters the quantum well stack at an angle to the growth direction. To avoid the complication of processing thousands of small gratings on a two-dimensional array, an alternative approach is to use p-type (acceptor doped) GaAs/AlGaAs QWIPs.

In p-type GaAs/AlGaAs MQW materials, there is strong mixing of the valence bands, especially with the conduction band, which imparts an additional s-like symmetry to the normally p-like valence band wave functions [3]. Transitions between subbands with s-like and p-like symmetry components are not forbidden by symmetry-related quantum mechanical selection rules, such that absorption of radiation at normal incidence is allowed. There are also allowed transitions due to heavy- and light-hole band mixing. This desirable normal incidence photo-excitation of p-type QWIPs has been demonstrated only recently [4,5].

Our previous work measured and theoretically modeled the bound-to-continuum photoresponse in three GaAs/$Al_{0.3}Ga_{0.7}As$ QWIPs with GaAs well widths of 30Å, 35Å and 40Å [3,5]. The 8x8 envelope function approximation model developed for calculating bound-to-

231

continuum absorption spectra was highly successful at matching the measured photoresponse spectra of these three samples. An example of this close agreement between theory and experiment is shown in Fig. 1. This figure also highlights the objective of our recent research. The calculated spectra indicated that a p-type QWIP with a 45Å well width would provide the optimum normal incidence photoresponse at 8.9 microns for $Al_xGa_{1-x}As$ barriers with 30% aluminum. In order to verify this optimized photoresponse, 14 samples were grown and studied in the past two years. This paper covers the results from 6 initial samples grown in-house.

EXPERIMENT

The p-type GaAs/AlGaAs MQW materials for this study were grown by molecular beam epitaxy on semi-insulating (100) GaAs substrates. Four wafers with requested well widths (L_w) of 40Å, 45Å, 50Å and 55Å were grown as a set, and two additional wafers targeting 45Å and 50Å were grown at another time. Each MQW sample had 30 periods and 500Å barrier widths of $Al_{0.3}Ga_{0.7}As$. The MQW stack was sandwiched between two GaAs contact layers. The wells and contact layers were beryllium doped to 1×10^{18} cm^{-3}. The wells were center doped with a 5Å offset at each interface. The structural parameters for each of these samples are given in Table I.

Photoluminescence spectra were taken at 4.5 K using a Bomem Fourier Transform infrared (FTIR) spectrometer. Nearly all of the top contact layer was etched off prior to PL measurements. Photoresponse spectra were taken at low temperature (T<10 K) using a BIO-RAD FTIR spectrometer and a closed-cycle refrigerator. The spectral photoresponse was studied as a function of temperature and applied bias. The etched mesas (5 x 5 mm^2) were mounted perpendicular to the infrared beam with illumination through the top contact layer.
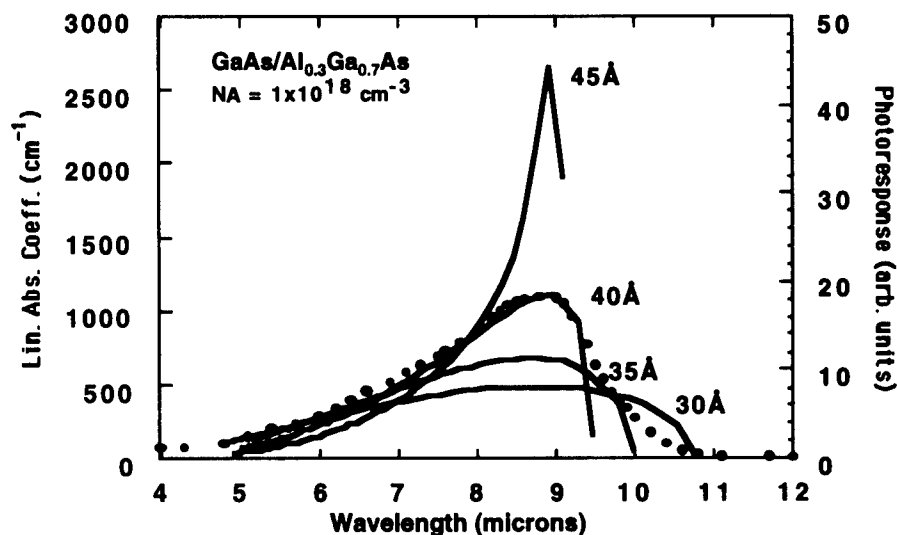
Fig. 1 Comparison of theoretical linear absorption spectra (unbroadened) for 30Å through 45Å well widths, with photoresponse data points (•) for 40Å well width p-type QWIP.

Table I. Structural & Optical Parameters for Samples

	Requested Growth Parameters				X-Ray Fitting Results				
Sample #	L_{well}	$L_{barrier}$	Al%	$N_a(cm^{-3})$	L_{well} (± 5Å)	Period	Al%	E_{cutoff} (meV)	PL peak (meV)
ML-08	50Å	500Å	30	5×10^{18}	56Å	507Å	29	128.7	1610
ML-09	40Å	500Å	30	1×10^{18}	50Å	572Å	26	133.1	1620
ML-10	45Å	500Å	30	1×10^{18}	56Å	592Å	26	123.4	1603
ML-11	50Å	500Å	30	1×10^{18}	58Å	588Å	26	157	1590
ML-12	55Å	500Å	30	1×10^{18}	62Å	602Å	26	----	1574
ML-13	45Å	500Å	30	1×10^{18}	47Å	562Å	31	124.7	1618
QE-03	40Å	500Å	30	1×10^{18}	42Å	575Å	28	131.2	1636

E_{cutoff} corresponds to the wavelength at which the photoresponse intensity drops by 50%.

RESULTS

Photoluminescence and x-ray diffraction measurements were used to verify the composition, well width, and structural quality of each sample. A typical x-ray diffraction spectrum along with the simulated spectrum, used to determine the AlGaAs alloy composition, the superlattice period, and GaAs well width, is shown in Fig. 2. The large number of superlattice peaks and their associated sharpness indicated the high structural quality of the samples. Results from all the x-ray simulations are listed in Table I. These results show that the requested well thickness and alloy composition deviated from nominal values, albeit in a very consistent way. This underscores the necessity of confirming the structural parameters of samples received for characterization.

The photoluminescence (PL) spectra from the set of four consecutively grown MQW samples are shown in Fig. 3. Samples ML-09 and ML-10 had nearly the same peak intensity for the radiative transition between the first conduction and first heavy-hole subbands (c1-to-hh1).
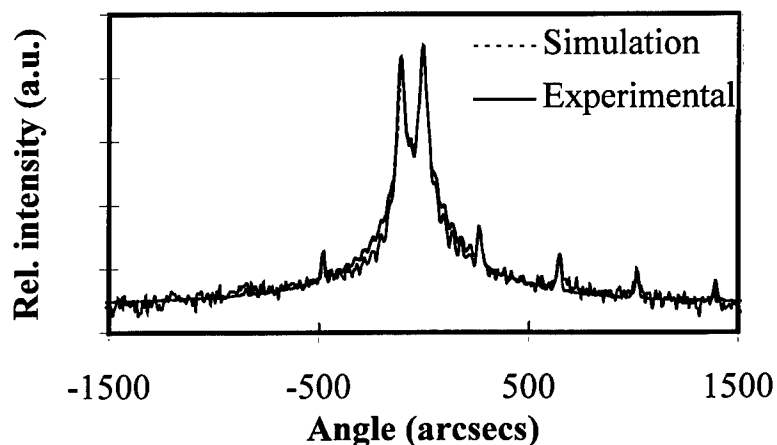
Fig. 2 X-ray diffraction rocking curve for p-type GaAs/$Al_{0.3}Ga_{0.7}As$ multi-quantum well sample (ML-08). The simulated curve used for fitting the structural parameters is included.
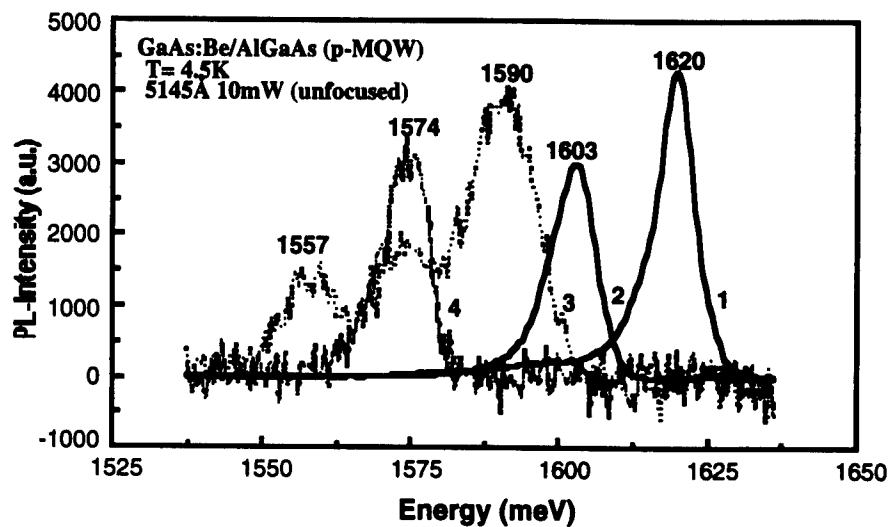
Fig. 3 Photoluminescence spectra of four samples: 1) ML-09, 2) ML-10, 3) ML-11 increased by a factor of 40, and 4) ML-12 increased by a factor of 40.
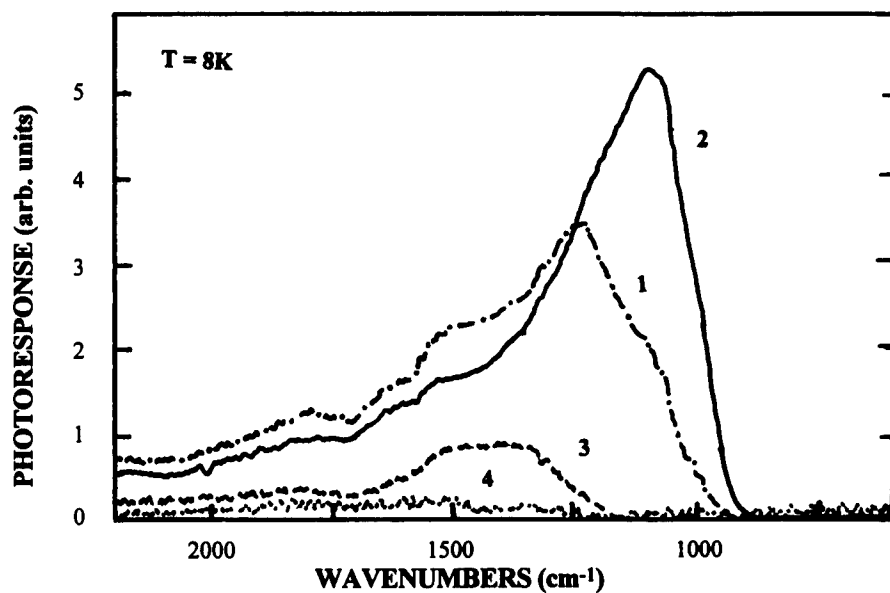
Fig. 4. Normal incidence photoresponse spectra from set of four p-type $GaAs/Al_{0.3}Ga_{0.7}As$ samples: 1) ML-09, 2) ML-10, 3) ML-11 magnified by a factor of 20, and 4) ML-12 magnified by a factor of 20. Nominally only the well width was varied by 2 monolayers between samples.

The peak positions vary as expected for the change in well width, with the peak moving to lower energy for the wider well (ML-10). The same trend toward lower energy is continued in samples ML-11 and ML-12. However, the PL peak intensities for these two samples are over an order of magnitude weaker, as well as broader. The PL spectrum for sample ML-11 even exhibits evenly spaced multiple peaks. The exact cause of the degraded PL spectra for these two samples has not been identified. However, samples ML-11 and ML-12 were grown back-to-back on the same day, while ML-09 and ML-10 were grown on the following day. Obviously, there was some unintentional variation in the growth conditions between these two days.

The photoresponse spectra for the companion set of four MQW samples are shown in Fig. 4. These spectra were taken at 8 K and with an applied bias of +2.7 volts. The photoresponse spectra reflect similar intensity trends to those observed in the PL spectra. The photoresponse spectra for ML-11 and ML-12 are about two orders of magnitude weaker than for ML-09 and ML-10. This is probably the result of a combination of two effects. First, there is the degradation in the quality of these two samples as reflected in the PL spectra. Second, since these wells are much wider, the second light-hole state (lh2) is a bound state. Consequently, charge carriers photoexcited to this state have to tunnel through the barrier for any signal to to be measured. The photoresponse for ML-10 is narrower and more intense than for ML-09. Modeling shows that for the compositions that were actually grown, ML-10 has the lh2 state in the continuum very close to the top of the barrier, which is the optimum absorption condition predicted by theory. The lh2 state for sample ML-09 is pushed farther up into the continuum and therefore, does not couple as strongly to the heavy-hole ground state. Similar effects of well width changes on the intensity and spectral band width have been observed in the photoresponse of n-type QWIPs [6].

Although the samples did not always match the requested structural parameters, there were still a couple of samples that did demonstrate the expected effect of a narrower spectral band width compared to our earlier p-type QWIPs. In each of these samples (ML-08, ML-10 & ML-13), the condition for bringing the resonant lh2 state in the continuum very close to the top of the well was met. Evidence of the narrower photoresponse spectra, as compared to the earlier $L_w = 40Å$ QWIP, is seen in Fig. 5. These narrower photoresponse spectra confirm the theoretical model shown in Fig. 1. These spectra are still broader than the calculated absorption spectra, but a broadening factor was not included in the original calculations and will have a larger impact for these sharp transitions.

As for the predicted increase in photoresponse intensity as the lh2 state approaches the top of the well, we did not achieve a set of samples that would continue the trend specifically shown in Fig. 1. However, some confirmation of the increased bound-to-continuum photoresponse as coupling to the lh2 state increases is observed for the set of samples with 26% aluminum in the barrier layers (see Fig. 4). There is an increase in the measured peak photoresponse intensity between the 50Å and 56Å quantum well widths.

CONCLUSIONS

We have performed a systematic study of MQW samples in which the barrier height was kept constant and only the quantum well width was varied in 2 monolayer (~5Å) increments. This study was to further examine effects of the position of the lh2 resonant state on the normal incidence photoresponse in p-type QWIPs for well widths of 40Å and above. The predicted narrowing of the HH1 to LH2 absorption band as the second light-hole state approaches the top of the well was observed in several samples. However, there is not enough data to make a reliable comparison of the measured photoresponse intensity and the theoretically predicted increase in
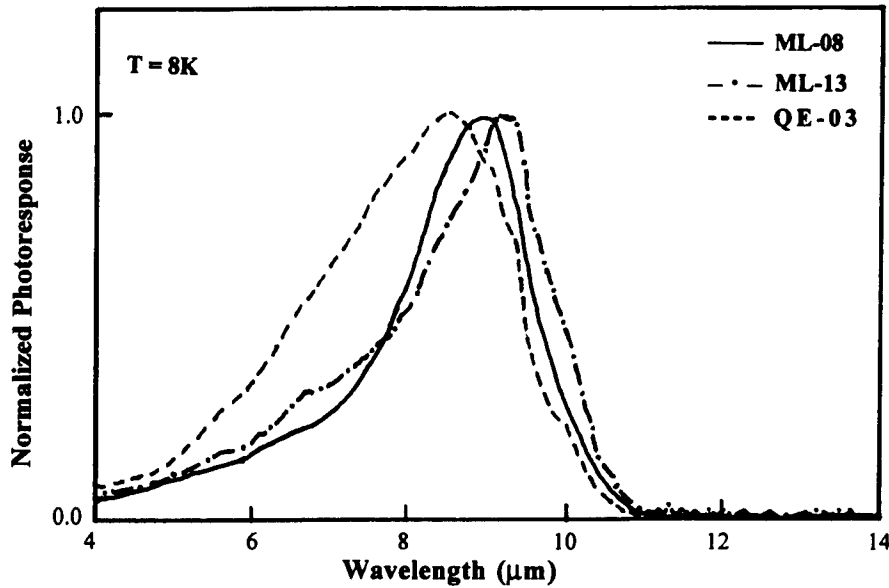
Fig. 5 Normalized photoresponse spectra for two samples where the second light-hole state is near the top of the valence band quantum well, and the spectrum from a previously reported sample with a 40Å well width [5].

the bound-to-continuum absorption as a function of the second light-hole state position. To confirm the magnitude of the increase in photo-excited signal for an optimized p-type QWIP, we would need to achieve a larger set of samples where the change in well width is the only material parameter that is varied. Additional sample sets are currently under study that have been grown by several different sources. Once the optimum design rules have been verified, doping studies will be performed to further enhance the photoresponse of p-type $GaAs/Al_xGa_{1-x}As$ QWIPs.

REFERENCES

1. B. F. Levine, J. Appl. Phys. **74**, p. R1 (1993).

2. D. D. Coon and R. P. G. Karunasiri, Appl. Phys. Lett. **45**, 649 (1984).

3. F. Szmulowicz and G. J. Brown, Phys. Rev. **B51** p. 13203 (1995).

4. B. F. Levine, S. D. Gunapala, J. M. Kuo, S. S. Pei and S. Hui,.Appl. Phys. Lett. **59**, p. 1864 (1991).

5. F. Szmulowicz and G. J. Brown, Appl. Phys. Lett. **66**, p. 1659 (1995).

6. H. C. Liu, J. Appl. Phys. **73**, p. 3062 (1993).

Part IV

HgCdTe–Materials, Devices, and Processing

RESONANT-CAVITY INFRARED DEVICES

J.L. PAUTRAT*, E. HADJI**, G. MULA***, J. BLEUSE, N. MAGNEA
Département de Recherche Fondamentale sur la Matière Condensée/SP2M
CEA Grenoble, 17 rue des Martyrs - 38054 Grenoble CEDEX 9, France
*jpautrat@cea.fr
**present address : NDRE, Division for Electronics, PO Box 25; 2007 Kjeller, Norway
***permanent address : Dip. di Scienze Fisichi; Univ. di Cagliari; via Ospedale 72; 09124
Cagliari, Italy

ABSTRACT

The $Cd_xHg_{1-x}Te$ compounds are well suited to the design of semiconducting devices incorporating an optical microresonator since they display a wide variation of bandgap and refractive index with composition x, while the lattice parameter remains practically unchanged. It is then possible to create a specific optical function by stacking high quality pseudomorphic layers on a crystalline substrate.

Microcavities resonating in the 3-5 μm range have been made by growing a lower Bragg mirror (10.5 periods) and a nominally undoped cavity medium containing a 50 nm active layer (CdTe-HgTe pseudo-alloy). The upper mirror is a gold layer deposited on the cavity. The emission of these Resonant Cavity Light Emitting Diodes has been observed in the 3-4.5 μm range up to room temperature. It coincides with the cavity resonance mode (linewidth 8 meV). With the addition of a ZnS/YF_3 upper mirror, a Vertical Cavity Surface Emitting Laser at 3.06 μm has also been demonstrated.

The microcavity concept appears to be very useful for designing new devices for the 3-5 μm range.

INTRODUCTION

The resonant cavity concept has recently been developped and integrated into optoelectronic devices. A Fabry-Perot cavity is a type of optical resonator defined by two plane parallel mirrors. If the distance between the mirrors is a small number of half wavelengths. this cavity supports a single allowed optical mode: the lightwave of the "resonant" mode, or its harmonics, is able to propagate within the cavity since the light reflected on the mirrors interferes constructively with the main beam. The other wavelengths are not allowed. The density of optical modes is thus greatly modified with respect to free space and it has been shown that the spontaneous emission was correspondingly affected [1,2]. The enhancement or the suppression of radiation is particularly interesting for applications involving emission or detection of radiation. However the main applications have, up to now, been devoted to the emission or detection of light in the visible or near infrared spectrum, mainly designed for silica fiber communication [3].

The $Cd_xHg_{1-x}Te$ compounds are widely used for infrared detection applications. These materials are also potentially useful for emitting devices. The variation of the band-gap with composition x enables them to cover a wide range of wavelengths extending from 0.8 μm (x=1) to more than 12 μm (x=0.2). At the same time the lattice parameter varies by less than 3

239

10^{-3}. These unique properties can be used to build optical resonators, the so-called microcavities, by stacking layers of various composition and optical index.

In this paper we will first describe the design rules and growth of $Cd_xHg_{1-x}Te$ Bragg mirrors and resonant cavities. Then the properties of the Resonant Cavity Light Emitting Diodes (RCLED's) will be described. The last part will be devoted to the laser emission in CdHgTe compounds, and the design and operation of an infrared vertical cavity surface emitting laser will be detailed.

BRAGG MIRRORS AND RESONANT CAVITIES

A Bragg mirror is obtained by stacking several layers, each of optical thickness one quarter of a wavelength, with alternatively high and low refractive index values, respectively n_1 and n_2. At the resonance wavelength, the light beams reflected at each interface add constructively. The higher the refractive index contrast, the smaller the number of bilayers required to reach a given reflectivity. For example when x_{Cd} varies between 0.35 and 0.75, the index varies by more than 20% (from 3.46 to 2.8). All these layers can be prepared by Molecular Beam Epitaxy.

A good mirror is achieved only if the layers do not absorb the light at the working wavelength. This condition can be achieved easily if that wavelength is far enough in the infrared. As an example, the 2 compositions quoted above ($x_1=0.35$ and $x_2=0.75$) can be used at 3 μm and above but for shorter wavelengths x_1 has to be increased. Figure 1 shows an
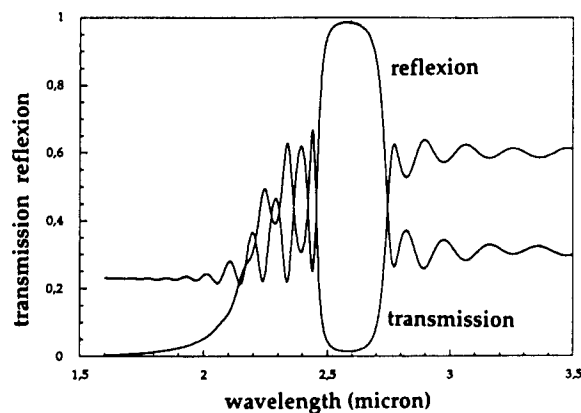
Figure 1. Experimental reflexion and transmission spectra from a Bragg mirror of 17.5 periods of $Cd_{0.47}Hg_{0.53}Te$ /$Cd_{0.75}Hg_{0.25}Te$

example of the reflectivity - transmission spectra of a mirror prepared for a central wavelength of 2.59 μm with $x_1=0.47$ and $x_2=0.75$. The refractive index contrast is of 13.2%. With 17.5 periods, the reflectivity reaches 98.7 %.

It is worth noting that to reach such a reflectivity, the mirror thickness must be fairly high (7.5 μm). For shorter working wavelengths, x_1 must be increased and the index contrast will decrease accordingly. It is then more and more difficult to get high reflectivities. Fortunately, as we shall see in the next section, a reflectivity of 80% is often enough to make an efficient device. However, for very short wavelengths (eg around 1.5 μm) it becomes difficult to design a good mirror made only of a pair of CdHgTe compounds. We have thus prepared mirrors which are based on the lattice matched pair of alloys : CdZnTe-CdMgTe. An example of transmission spectrum obtained on the latter kind of mirror is shown in figure 2 (full line).

It is made of 15 pairs of Cd$_{0.6}$Mg$_{0.4}$Te/Cd$_{0.98}$Zn$_{0.02}$Te whose refractive indices are respectively 2.49 and 2.77 and the central wavelength is 1.4 μm. The reflectivity achieved is 92.5%.

After measurement of the mirror transmission and determination of the central reflectivity wavelength, the sample was reintroduced into the MBE growth chamber and an epitaxial CdTe cavity layer of appropriate thickness was grown.

The final transmission spectrum is shown as the dotted curve of figure 2. It now displays a peak superimposed on the mirror reflectivity. This is the indication of the Fabry-Perot cavity resonance, which is not very sharp in this case since the second mirror is simply the interface between air and the cavity.

With a higher reflectivity mirror the resonance may be very sharp and tailored to the device requirement. Figure 3 shows such a cavity schematically.

The finesse of a Fabry-Perot resonator is given by:

$$F = \Delta\lambda/\lambda = \pi \, (R_1.R_2)^{1/4} \, / \, (1-(R_1R_2)^{1/2}) \tag{1}$$

where λ is the resonance wavelength and $\delta\lambda$ is the resonance width at half maximum.

Figure 2. Transmission spectrum measured on a Bragg mirror of 15 pairs of Cd$_{0.6}$Mg$_{0.4}$Te/Cd$_{0.98}$Zn$_{0.02}$Te layers (full line) and on the Bragg/cavity/air system (dotted line)

Figure 3. Scheme of a typical cavity with 2 epitaxial Bragg mirrors
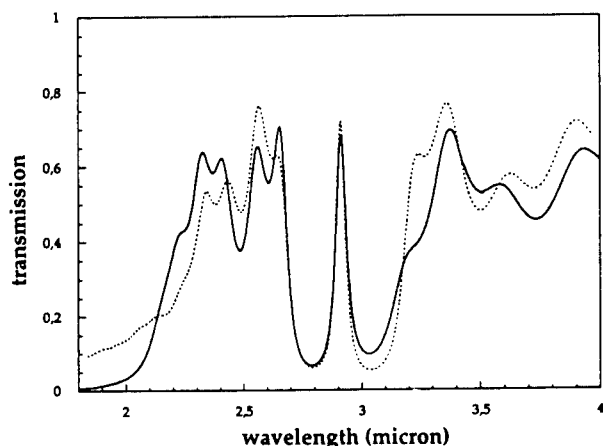
Figure 4. Measured (full line) and calculated (dashed line) transmission spectra of a typical microcavity with 2 epitaxial mirrors of reflectivities of 71 % and 75.2%

The transmission spectrum of a cavity resonating at 2.91 μm and made of 2 epitaxial mirrors is reproduced in figure 4. The substrate is a $Cd_{0.96}Zn_{0.04}Te$ (100) crystal. The bottom mirror (substrate side) consists of 9 periods (reflectivity 71%) and the upper mirror of 6 periods (reflectivity of the mirror/air couple 75.2%). The mirrors are made up of alternate layers of $Cd_{0.47}Hg_{0.53}Te$ and of $Cd_{0.75}Hg_{0.25}Te$ which have an index contrast of 12%.The cavity of $Cd_{0.47}Hg_{0.53}Te$ is half a wavelength thick.

The dashed curve is the simulated spectrum obtained with the nominal growth parameters using standard matrix transfer techniques and the published refractive index data [4]. The calculated spectrum reproduces most of the experimental features. An even better fit could be obtained by slightly adjusting the growth parameters. The experimental finesse of this cavity is 61.

RESONANT CAVITY LIGHT EMITTING DIODES

Description of the device

A microcavity light emitting diode is represented in figure 5 [5,6]. The optical Fabry-Perot resonator consists of a Bragg mirror of 10.5 periods, a λ/2 cavity and an upper metallic mirror. The lower Bragg mirror is grown first, on the $Cd_{0.96}Zn_{0.04}Te$ (100) substrate.

The high and low index layers are respectively $Cd_{0.45}Hg_{0.55}Te$ and $Cd_{0.75}Hg_{0.25}Te$. The thickness of each
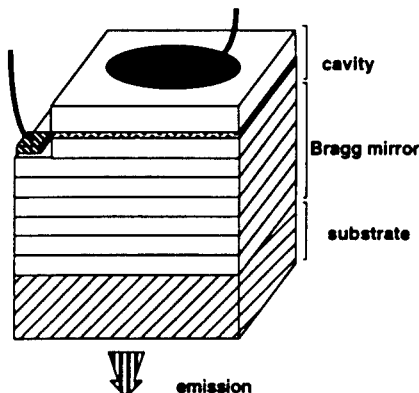
Figure 5. Resonant Cavity Light Emitting Diode (schematic).

layer is again a quarter of the resonance wavelength (3.2 μm in this case). The last period of this mirror is n-type doped with indium to 10^{17} cm^{-3}. The λ/2 cavity medium is made of the high gap $Cd_{0.75}Hg_{0.25}Te$. An active layer consisting of 50 nm of CdTe-HgTe pseudo alloy is inserted in the middle of the cavity. The last 100 nm of the cavity are p-type doped with nitrogen. We added some zinc to the the contact region, in order to enhance the nitrogen activity in the doped zone[7]. The cavity is terminated by a gold mirror which is also used as an ohmic contact to the p-type side. The cavity layer is wet etched in order to contact the n-type layer with indium metal.

Spectral properties

The transmission spectra of the epitaxial mirror and of the full cavity are shown in figure 6. (For measuring the cavity, a semitransparent gold layer has been deposited as a second mirror). The transmission scale has been expanded by a factor 15 for the cavity. The dashed curves give the calculated spectra. The cavity resonance produces the transmission peak at 3.16 μm whose linewidth is 59 nm (7.2 meV). The electroluminescence spectrum measured at room temperature with a current of 6.5 mA is exactly matched to the resonance line.
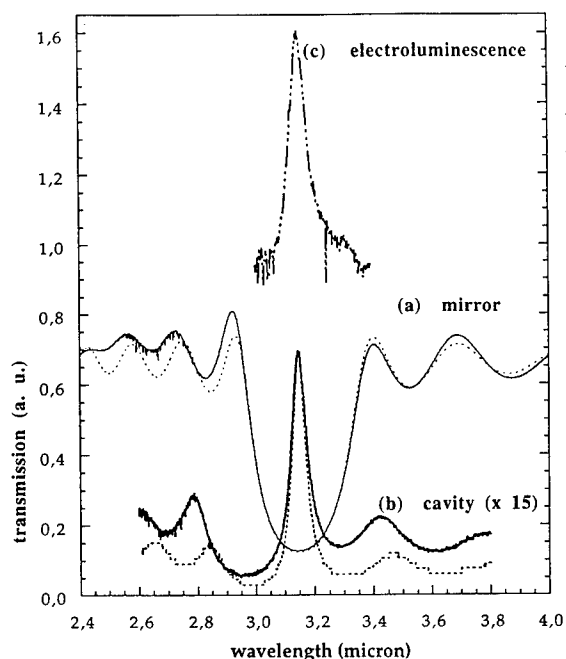
Figure 6. Transmission spectra measured (full line) and calculated (dashed line) for the Bragg mirror (a) and for the full cavity (b). The experimental electroluminescence spectrum was measured with a forward current of 6.5 mA

Detailed measurements of the electroluminescence spectra have been performed and analysed at low temperatures where the emission efficiency is somewhat higher and the linewidth is slightly smaller. All these spectra display the very narrow peak centered on the resonance mode of the cavity (figure 7). The line is much narrower than the emission line of the active medium and its width is independent of the injected current. This rules out any possibility of stimulated emission narrowing. The broad band around 2.4 μm appears to be due to a parasitic recombination in the small gap layers of the mirror.

The predominant role of the cavity on the emission spectrum is further confirmed by the temperature variation of the emission. As is well known, the bandgap of semiconductors varies with temperature. For small gap CdHgTe compounds it increases with increasing temperature. An increase of about 30 meV (corresponding to a decrease of the emission wavelength of 0.25 μm) is then expected between 10 and 300 K. Instead of that we observe a small decrease of the emission wavelength of 0.04 μm (figure 7) which is only due to the shift of the optical constants with temperature.
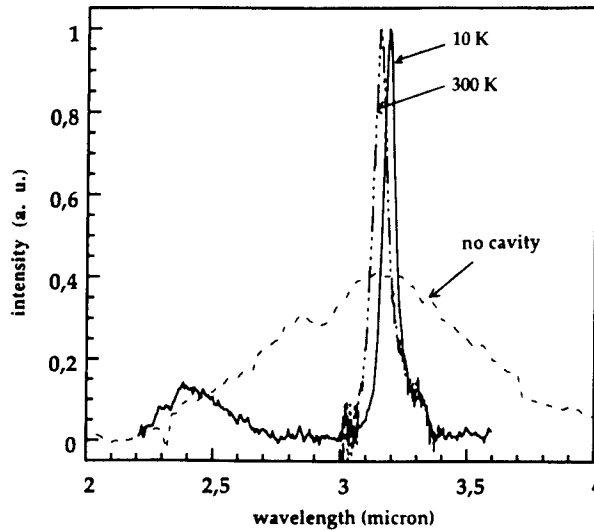
Figure 7. Electroluminescence spectra measured at 10 and 300K on a RCLED and photoluminescence spectrum measured at 300K on a pseudo alloy similar to that in the active layer

In the same figure the room temperature emission spectrum measured on the active material alone is shown for comparison. The narrowing effect of the cavity is clearly seen.

Efficiency and angular variation

The theoretical study of resonant microcavity devices has shown that, in the direction normal to the cavity and for the resonance wavelength, the emission enhancement is given by [8]

$$G= (\xi/2) \, (\tau_{cav}/\tau) \, (1+ R_2^{1/2})^2 (1-R_1) \, (1- (R_1 R_2)^{1/2})^{-2} \qquad (2)$$

With the structure described in figure 6, typical values of the reflectivities are R_1=84%, for the Bragg mirror, and R_2=95%, for the metallic mirror. The antinode enhancement factor ξ is taken as 2, since the active medium is located at the center of the cavity. The cavity radiative lifetime τ_{cav} is only slightly changed with respect to its bulk value τ. The corresponding factor can be taken as 1. With these values the theoretical enhancement factor reaches 55. The experimental enhancement is not easily determined since that would need fabrication and measurement of the emissivity of a similar diode without any cavity. From equation (1) one deduces that, the higher the reflectivities, the higher the enhancement factor. But simultaneously as the cavity finesse increases and the emission band becomes narrower there is a decrease of the emitted power. There is then an optimum value for the reflectivity of the mirror which gives maximum emitted energy. In fact this compromise has to be established for

each application, taking into account the linewidth it requires. From this point of view, the RCLED's devices presented here have not been optimized.

The angular emission diagram is another interesting feature of these devices. Theoretical calculations have been performed [9] which demonstrate that, in addition to the central mode, showing emission enhancement, there is a depletion cone with lower emission than in the non cavity case (see figure 8, where the emission intensity is normalized to the emission in the absence of a cavity).

But for large angles (larger than 28 degrees in the case of the figure), on the average there is no effect of the cavity. In addition, at very large angles, there is a guided or leaky mode which efficiently extracts the light out of the device.

This figure demonstrates that the directivity is improved, in the resonant cavity emitter case. This point has been experimentally verified in the infrared RCLED's [10]. The measurement of the emission under various angles of view shows first a shift of the central line to smaller wavelengths. This is what is expected for a cavity-driven emission (figure 9).

This experimental shift is in good agreement with the theoretical variation as shown in the left part of figure 10. The integrated intensity variation with emission angle (right part of figure 10) displays a full width at half maximum angle of 55°. The same kind of measurements have been done for the parasitic line at 2.4 µm of figure 7. There is no variation of the central wavelength and the FWHM angle is 85°, corresponding to what is expected without a cavity.

The measurement of the external quantum efficiency gives the ratio of the energy emitted in the central cone to the energy injected in the device. This efficiency has been found to vary from $2.4 \ 10^{-3}$ to $2 \ 10^{-4}$ between 15

Figure 8. Calculated spontaneous emission rate as a function of the emission angle for an emitter in a λ cavity with 2 GaAs/AlAs mirrors of 10 periods (from reference [9])
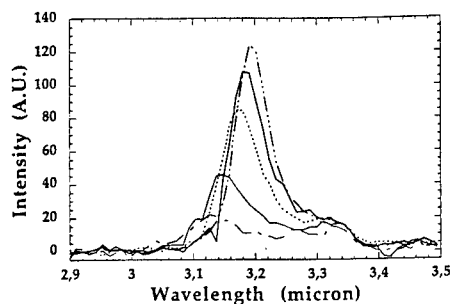
Figure 9. Electroluminescence spectra measured for different collection angles

and 300 K [10]. It is interesting to compare these figures with values published for conventional light emitting diodes, in the wavelength range from 3 to 5.5 µm. This is done in figure 11.

The solid symbols are for the present RCLED's results and other symbols for conventional LED's. For our measurements we have integrated the light in the emission cone (55° FWHM). It is interesting to observe that these first RCLED data are already comparable to the values obtained with other materials and other technologies. In addition, in the RCLED case, the emission is concentated in a narrow spectral band and a narrower emission angle. The quantum efficiency then gives a "useful light" efficiency.

There are several paths of improvement which should lead to even more efficient resonant cavity

Figure 10. Measured and calculated peak wavelength versus angle (full scale radius: 75% to 100% of central wavelength) (left side); diagram of the main and secondary peaks' intensities versus angle, normalized to 100% for normal incidence (right side)

devices. It has recently been demonstrated in the near infrared (0.8 µm) that an external quantum efficiency of 16% was achievable with planar structures [11]. At the same time, general solutions have been proposed to enhance the fraction of the spontaneous emission which is controlled by the microcavity [12] and experimental results were published : increase of the index contrast of the mirrors which enhances the action angle of the Bragg mirrors [13], association of a Bragg mirror and of a metallic one [14], control of the transverse modes in laterally structured devices [15].

VERTICAL CAVITY SURFACE EMITTING LASER

In the previous devices the reflectivity of the mirrors was not set to very high values (82% for the Bragg mirrors) and some losses are expected in the metallic mirror (5%). If one wants to use the resonance of the cavity to produce optical gain, the reflectivity of the mirrors has to be increased while the losses must be kept to a minimum. A first approach to the net gain needed for observing laser emission can be calculated from the following formula, which expresses the fact that the gain at the laser threshold G_{th} compensates for the reflection losses:

$$G_{th} = -(\Gamma L_{act})^{-1} \ln (R_1 R_2)^{0.5}$$

(3)

where Γ is the optical confinement factor and L_{act} is the thickness of the active part of the cavity length.

Figure 11. Diagram of the published quantum efficiency measured for a number of infrared emitting LED's: + : InAsSb (W. Dobbelaere et al., Electron. Lett. **29**, 890 (1993)); Δ : InAsSb (P.J.P. Tang et al., Semicond. Sci. Technol. **10**, 1177 (1995)); **open square** InAlSb (T. Ashley et al., Appl. Phys. Lett. **64**,2433 (1994)); **x** : InGaAs (M.K. Parry et al., Electron. Lett. **30**, 1969 (1994)); **O** : CdHgTe (H. A. Tarry, Electron. Lett. **22**, 416 (1986)); **open diamonds** : CdHgTe (P. Bouchut et al., J. Vac. Sci. Technol. **B9**, 1794 (1991)); • : CdHgTe RCLED's (our results).

We have chosen to start this VCSEL demonstration at a wavelength around 3 μm which is very specific of CdHgTe compounds. The data deduced from measurements on conventional guided lasers give a maximum gain of 100 cm^{-1} at 100K (obtained at a pump power of 100 kW/cm^2) for a GRINSCH structure emitting at 3.1 μm [16,17]. In such a structure the light confinement factor (ratio of the emitting medium width to the light guide width) is less than 0.1. This gives, at this temperature, an intrinsic gain of about 1000 cm^{-1}.

Reducing the temperature allows either an increased gain at the same pump power or a substantial reduction of the pump power. We have then estimated the available gain in the structure, at low temperature, to be about 2000 cm^{-1}. The confinement factor is taken as 0.5 and the active layer thickness $L_{act}=0.1\mu m$. With these data a reflectivity product $R_1 R_2=0.98$ is needed. We have also chosen a photopumping technique. This means that at least one of the mirrors must be transparent to the pump laser, a YAG microlaser emitting at 1.06 μm. The structure of the device is described in figure 12 [18]. The bottom mirror is a 16.5 period
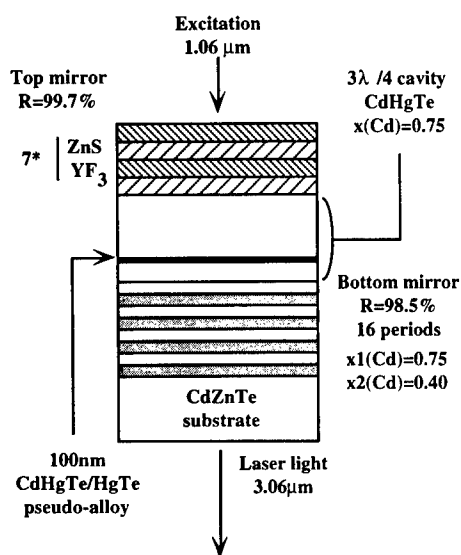
Figure 12. Photopumped vertical cavity surface emitting laser designed for emission at 3.1 μm. The bottom mirror is a MBE grown Bragg mirror of 16.5 periods ($Cd_{0.75}Hg_{0.25}Te$ / $Cd_{0.4}Hg_{0.6}Te$). The $Cd_{0.75}Hg_{0.25}Te$ cavity is 3λ/4 thick and consists of CdTe/HgTe pseudo-alloy. The upper mirror contains 7 periods of ZnS/YF$_3$. It is designed to allow photopumping with a YAG laser at 1.06 μm.

Bragg mirror epitaxially grown on a CdZnTe substrate. The high and low index layers contain respectively 40% and 75% of cadmium. The expected reflectivity is 98.5%.The cavity medium is a $Cd_{0.75}Hg_{0.25}Te$ layer of thickness $3\lambda/4$. The active layer is inserted at the position of maximum electric field. It consists of 100 nm of $HgTe\text{-}Cd_{0.75}Hg_{0.25}Te$ pseudo alloy whose effective band gap is near 4 μm.

The upper mirror is a dielectric stack of ZnS and YF_3 layers. Due to the high index contrast between the two materials (respectively 2.257 and 1.46), the reflectivity of 99.7% is reached with only 7 periods. Both materials are transparent to the excitation laser.

With these reflectivity values the theoretical finesse of the cavity is 350. The expected linewidth for the cavity without losses is then 2 nm. The photoluminescence spectrum measured at 15 K before the deposition of the dielectric mirror is a very broad line extending from 2.95 to 3.7 μm (with a net reinforcement around 3 μm showing that there is already some cavity effect due to the air/cavity interface). The transmission spectrum of the cavity shows the cavity mode at 3.06 μm which has been broadened to 30 nm by the absorption losses in the active layer (absorption coefficient of 7000 cm^{-1} at 3 μm).
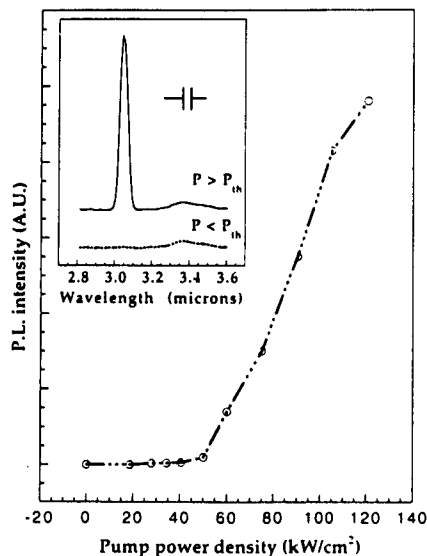
Figure 13. Emission intensity as a function of the pump power. The inset shows the emitted spectrum at low and high excitation powers.

With the complete cavity and under cw excitation the photoluminescence spectrum is hardly detected (figure 13 inset). Indeed the active layer emission is not well centered on the cavity mode. But under pulsed excitation a well defined and intense light emission at 3.06 μm is measured while a weak emission is detected at 3.4 μm.

The linewidth of the laser emission is found to be 13 nm. It is in fact limited by the resolution of the spectrometer (5 nm). It is interesting to note that in this case the line edges are very sharp, much sharper than in the case of the RCLED spectra. This clearly confirms that the light amplification is active only at the maximum of the cavity resonance. A further confirmation is provided by the variation of the light intensity with the pump power shown in figure 13. The threshold for lasing is found at a pump power of 45 kW/cm^2. This is an upper limit calculated with the assumption of a transmission of 50% across the dielectric mirror. The true threshold could be somewhat smaller if the transmission of the mirror is smaller.

The increase of the working temperature leads to a rapid decrease of the emitted light. The laser emission has not been observed above 30 K. There are several reasons for this. First the detuning between spontaneous emission and cavity resonance may become too large to be compensated by the wavelength shift under strong excitation and secondly, as the temperature increases, the non-radiative Auger effect is expected to reduce the optical gain. This can be

understood from recent results obtained on conventional laser structures [16,17]. The recombination of carriers within the active layers is governed by a rate equation:

$$dn/dt = A\, n^2 + C\, n^3 \qquad (4)$$

where the $A\, n^2$ term describes the radiative recombination events while the $C\, n^3$ term is for the non radiative Auger type recombination. The A coefficient decreases slowly with temperature while C is temperature independent. On increasing temperature, to maintain the optical gain above the lasing threshold, n has to increase. The non radiative term, which is in n cubed, then increases faster and faster. This effect may rapidly limit the optical gain in the structure. The Auger coefficient C has been experimentally determined for cadmium mercury telluride layers of various composition, corresponding at various operating wavelengths:

$l = 1.97\ \mu m$ $C = 4.9\ 10^{-28}\ cm^6 s^{-1}$
$l = 2.3\ \mu m$ $C = 2.5\ 10^{-27}\ cm^6 s^{-1}$
$l = 3.25\ \mu m$ $C = 9\ 10^{-26}\ cm^6 s^{-1}$

It is clear that the choice for this VCSEL of an operating wavelength longer than 3 μm was a challenge. There are several ways of reducing the laser threshold: higher reflectivity mirrors, smaller emission wavelength. Also the design of the active medium could lead to a significant reduction of the Auger coefficient as in GaInAs lasers. Some preliminary results have been obtained demonstrating that the use of a strained quantum well significantly reduces the laser threshold [19].

CONCLUSION

The cadmium mercury telluride compounds are well suited to the design and preparation of optoelectronics devices for the mid infrared range. We have prepared resonant cavity light emitting diodes emitting in the 3-4 μm range whose emission efficiency is already above 10^{-4} at room temperature. These devices display a very narrow spectral distribution and a narrower emission cone than conventional LED's. All the properties are quasi insensitive to the temperature variation. VCSEL emission at 3 μm under photopumping has been obtained for the first time.

REFERENCES

1- S. Haroche, D. Kleppner, Physics Today 42 (1), 24-30 (1989).

2- H. Yamamoto, R. E. Slusher, Physics Today, 46 (6), 66 (1993).

3- E.F. Schubert, N.E.J. Hunt, M. Micovic, R.J. Malik, D.L. Sivco, A.Y. Cho, G.J. Zydzik, Science 265, 943 (1994).

4. B. Jensen and A. Torabi, J. Appl. Phys. 54, 5945 (1983).

5. E. Hadji, J. Bleuse, N. Magnea, J.L. Pautrat, Appl. Phys. Lett. 67, 2591 (1995).

6. E. Hadji, J. Bleuse, N. Magnea, J.L. Pautrat, Solid-State Electron. 40, 473 (1996).

7. T. Baron, K. Saminadayar, S. Tatarenko, J. Cryst. Growth 159, 271 (1996).

8. N.E.J. Hunt, E.F. Schubert, R.F. Kopf, D.L. Sivco, A.Y. Cho, G.J. Zydzik, Appl. Phys. Lett. **63**, 2600 (1993).

9. D.G. Deppe, C. Lei, C.C. Lin, D.L. Huffaker, J. Modern Optics, **41**, 325 (1994).

10. J.L. Pautrat, E. Hadji, J. Bleuse, N. Magnea, J. Electron. Mat. **25**, 1387, (1996).

11. J. Blondel, H. De Neve, P. Demeester, P. Van Daele, G. Borghs, R. Baets, Electrn. Lett., **31**, 1286 (1995).

12. Y. Yamamoto, S. Machida, G. Björk, Phys. Rev. A **44**, 657 (1991).

13. D.L. Huffaker, C. Lei, D.G. Deppe, C.J. Pinzone, J.G. Neff, R.D. Dupuis, Appl. Phys. Lett. **60**, 3203 (1992).

14. D.L. Huffaker, C.C. Lin, J. Shin, D.G. Deppe, Appl. Phys. Lett. **66**, 3096 (1995).

15. D.L. Huffaker, D.G. Deppe, Appl. Phys. Lett. **67**, 2594 (1995).

16. J. Bonnet-Gamard, J. Bleuse, N. Magnea, J.L. Pautrat, J. Appl. Phys. **78**, 578 (1995).

17. J. Bonnet-Gamard, J. Bleuse, N. Magnea, J.L. Pautrat, J. Cryst. Growth, **159**, 613 (1996).

18. E. Hadji, J. Bleuse, N. Magnea, J.L. Pautrat, Appl. Phys. Lett. **68**, 2480 (1996).

19. J. Bonnet-Gamard, thesis, Grenoble, France, 1996 (unpublished).

P-TYPE DOPING WITH ARSENIC IN MBE-HgCdTe USING
PLANAR DOPING APPROACH

F. AQARIDEN, P.S. WIJEWARNASURIYA, S. RUJIRAWAT, AND S. SIVANANTHAN
Microphysics Laboratory, Department of Physics (M/C 273), University of Illinois at Chicago,
845 W. Taylor St., Room #2236, Chicago, IL 60607; aqariden@uic.edu

ABSTRACT

The results of arsenic incorporation in HgCdTe (MCT) layers grown by molecular beam epitaxy (MBE) are reported. The incorporation into MBE-MCT was carried out by a technique called planar doping. Arsenic was successfully incorporated during the MBE growth or after a low temperature anneal as acceptors. These results are very promising for in-situ fabrication of advanced optoelectronic devices using HgCdTe material.

INTRODUCTION

MBE-MCT based IR technology has reached a high level of maturity leading to fabrication of sophisticated opto-electrical devices. This technology requires p-n junctions with well controlled concentration level of dopants. For that matter an increased emphasis on replacing native defect doping with extrinsic dopants[1]. Concerning the n-type case, indium (In) has been extensively studied in MCT grown by MBE[2-5]. Indium doped epilayers show excellent electrical properties. Electron mobilities as high as 2×10^5 cm^2/V-s and minority carrier lifetimes in the order of 1μsec at 80 K for Cd composition x=22% are currently obtained. However replacing native acceptor defect doping with extrinsic acceptor dopant at the MBE growth of MCT or after a low temperature anneal not exceeding 250°C has proven to be a serious problem. Using an extrinsic acceptor dopant rather than the native defect acceptor has at least two major advantages. First, the Shockley-Read limited carrier lifetime could be enhanced if an extrinsic dopant whose energy level is closer to the band edge is used. Second, when extrinsic dopants are used, and the native acceptor defect concentration has been reduced well below the concentration of the dopants, the performance of MCT p-on-n heterojunctions has improved[6]. Several attempts were made to use elements of group I to achieve p-type doping of MCT grown by MBE[7-9] and almost all these elements show high diffusivity[7,8], hence, they were deemed to be unsuitable for that matter. On the other hand, group V elements, with their large size and low diffusivity, are expected to result in stable and give well controlled doping level with good electrical activity. Arsenic, which is the dopant of choice for MCT- MBE, has been extensively studied by almost all MCT growth techniques[10,12]. Our main concern in this study is to obtain p-type doped MCT-MBE epilayers using arsenic at the growth temperature or after a low temperature anneal in order to preserve the integrity of the structure, so that MBE will not lose the advantages associated with its low temperature growth, leading to the fabrication of in situ sharp interfaces and avoiding diffusion of dopants that could result from the high temperature annealing. The two major obstacles that we are facing for p-type doped MBE-MCT layers at the growth temperature is two fold. First, arsenic has proven to exhibit an amphoteric behavior in MCT[13]. Second, contrary to what can be achieved in liquid phase epitaxy (LPE), metal-organic vapor phase epitaxy (MOVPE), or bulk growth, the growth of MCT by MBE is taking place under tellurium rich condition[14], hence, the natural and the most probable choice for arsenic is to form a bond with Te by occupying a metallic sublattice site (Cd or Hg) and acts as a donor[10,15]. Many approaches have been tried for achieving p-type doping during the MBE

growth of MCT using arsenic[16-23]. However, none of these approaches could lead to in-situ incorporation of arsenic in MCT-MBE as an acceptor during the growth process.

In this paper we present a novel approach on how to force arsenic to occupy the nonmetallic sublattice site (Te) and act as an acceptor during the growth process or after a low temperature annealing not exceeding 250°C. We will discuss our latest results on arsenic incorporation into (211)B oriented HgCdTe layers grown by MBE at the Microphysics Laboratory at the University of Illinois at Chicago.

EXPERIMENTS

All the MCT epitaxial layers were grown on (211)B oriented CdZnTe substrate in an ISA Riber 2300 MBE machine. The details of growth have been published elsewhere[24]. The cadmium composition and epilayer thickness were determined at room temperature by infrared transmission measurements. The transport measurements of the epilayers (carrier concentration and mobility) were performed by the Van der Pauw technique for temperatures ranging from 300K to 23K, and with magnetic field up to 1.0 Tesla.

Arsenic incorporation into HgCdTe layers was achieved by the planar or delta doping approach. The purpose of this technique is to enhance the arsenic mercury bond formation. This is done by alternating a sheet or plane of arsenic between two thin layers of MCT and repeating this operation until the desired thickness is obtained. An MCT layer of 20 to 200 Å thickness is grown. The growth is then stopped for few seconds while Hg shutter remains all the time open, then the arsenic shutter is opened for only a couple of seconds (3 to 10 sec), then the growth of MCT is restarted. The arsenic concentration in the films was confirmed via secondary ion mass spectroscopy (SIMS) analysis performed at Charles Evans and Associates using a CAMECA primary ion bombardment with a net impact energy of 14.5 KeV

RESULTS AND DISCUSSION

Table 1 summarizes the electrical, material and structural data of the investigated arsenic planar doped epilayers, except for sample #1264 which was grown and doped with arsenic using the conventional approach, in this approach all the shutters are opened at once including arsenic shutter. Comparison of these results with the SIMS results show that we could achieve arsenic p-type doping of $Hg_{1-x}Cd_xTe$ at the MBE growth temperature or after a low temperature anneal using planar doping technique with arsenic activation as high as 85%. We noticed when comparing samples grown with identical growth conditions that SIMS results show that in some cases the smaller the thickness of MCT period, the smaller the average concentration of arsenic in the sample per cm^3. This can be explained by the fact that when the growth conditions are the same, hence the growth rate of $Hg_{1-x}Cd_xTe$ is the same, thus, growing a layer with larger MCT period will require keeping the arsenic shutter closed for longer time. During this time the temperature of the Knudsen cell carrying arsenic could rise slightly and hence the flux of arsenic could increase, leading to a higher concentration of arsenic in the epilayers with larger thickness of MCT period. Another possibility that could explain this unexpected behavior is the SIMS results show that the arsenic profiles are associated with peak structures and we believe that these are due to the periodic nature of arsenic concentration. Higher resolution SIMS measurements need to be performed for further confirmation of these findings.

Table I. Summary of the measured parameters of arsenic planar doped MBE-Hg$_{1-x}$Cd$_x$Te layers

Sample	x(%)	t(μm)	HgCdTe Period(Å)	Hall characteristics as grown or annealed at 250°C		SIMS (cm^{-3})
				N_a-N_d (cm^{-3})	μ at 80K (cm^2/V-s)	
1207*	33.8	2.0	75	6.0×10^{16} (p)	100	5.5×10^{16}
1260	32.6	2.18	61	9.6×10^{15} (p)	208	5.0×10^{16}
1262	35.3	1.75	49	1.8×10^{16} (p)	60	7.0×10^{18}
1263	34	2.59	98	1.0×10^{15} (p)	142	1.7×10^{19}
1264**	32.6	2.49	---	-6.0×10^{16} (n)	4700	1.5×10^{20}
1265	32.2	2.31	88	4.0×10^{16} (p)	185	1.0×10^{18}
1266	32.3	2.44	93	2.0×10^{17} (p)	50	2.5×10^{18}
1267	30.8	1.97	55	6.0×10^{16} (p)	198	3.5×10^{18}

* Sample 1207 is measured as grown.
** Sample 1264 is conventionally doped.

Figure 1 shows the graph of the carrier concentration obtained from the Hall measurements versus inverse temperature for sample 1265, these measurements reveal that we could obtain a p-type conductivity for that sample after an annealing at 250°C under mercury saturated environments with a mobility value at low temperature of 180 cm^2/V-s.
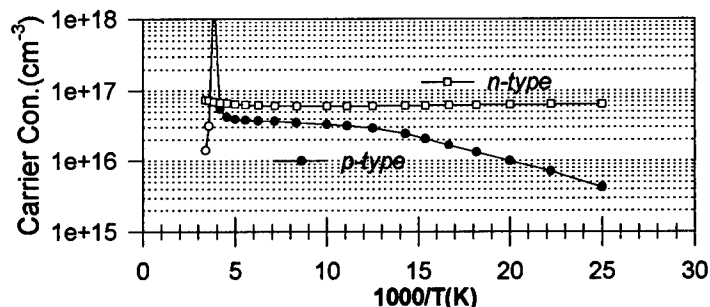
Figure (1) Hall characteristics of arsenic planar doped sample # 1265 (represented with the symbols o,•) and a conventionally doped sample # 1264 (represented with the symbol □); x=33%, after annealing at 250°C. The data was taken at a magnetic field strength of 0.59 Tesla.

Also, figure 1 shows Hall measurement results on a conventionally doped epilayer (sample 1264). After an anneal at 250°C under mercury rich conditions of both samples, the planar doped

layer exhibits a p-type conductivity, while the conventionally doped layer remains n-type. This latter sample converted to p-type with a carrier concentration value at low temperature of $1x0^{18}$ cm^{-3} after an anneal at 450°C followed by a 250°C anneal under mercury saturated conditions.

SUMMARY

        In this work, we used the planar doping technique to incorporate arsenic as an acceptor in HgCdTe layers. The layers were p-type as grown or only required low temperature annealing (not exceeding 250°C). Our tabulated results show SIMS measurements confirm the arsenic incorporation into MBE-MCT epilayers and the results show a good activation of arsenic during the MBE growth when arsenic concentration is in the order of 10^{16} cm^{-3}. This work confirms that arsenic can be an effective acceptor dopant at the MBE growth temperature of $Hg_{1-x}Cd_xTe$. These findings are very promising as an alternative approach to obtain arsenic p-type doped $Hg_{1-x}Cd_xTe$, hence very promising for the IR FPA technology.

REFERENCES
1) M.C. Chen, L. Colombo, J.A Dodge, and J.H. Tregilgas, J. Elec. Materials, 24, 539 (1995)
2) M. Boukerche, J. Reno, I.K Sou, C. Hsu, and J.P. Faurie, Appl Phys. Lett, 48, 1733 (1986)
3) P.S. Wijewarnasuriya, M.D. Lange, S. Sivananthan, and J.P. Faurie,. J. Elec. Materials,24,1211 (1995)
4) J.M. Arias, S.H. Shin, J.G. Pasko, R.E. DeWames, and E.R. Gertner, J. Appl. Phys. 65, 1747 (1989)
5) O.K. Wu, G.S. Kamath, W.A. Radford, P.R. Bratt and E.A. Patten, J. Vac. Sci. Technol. A8, 1034 (1990)
6) H.R. Vydyanath, P.B. Ward, S.R. Hampton, J.B Parkinson and B. Klank, Proc. SPIE 1097, 110 (1989)
7) P.S. Wijewarnasuriya, I.K. Sou, J. Kim, K.K. Mahavadi, S. Sivananthan, M. Boukerche, and J.P. Faurie,. Appl Phys. Lett, 51, 2045 (1987)
8) T.H. Myers, K.A. Harris, R.W. Yanka, L.M. Mohnkern, R.J. Williams, G.K. Dudoff, J. Vac. Sci. Technol. A3, 1438 (1985)
9) D.J. Peterman, M.L. Wroge, B.J. Morris, D.J. Leopold, J.G. Broerman, J. Appl. Phys. 63, 1951 (1988)
10) M. Boukerche, P.S. Wijewarnasuriya, S. Sivananthan, and J.P. Faurie, J. Vac. Sci. Technol. A6, 2830 (1988)
11) M.L. Wroge, et al. J. Vac. Sci. Technol. B4, 1306 (1986)
12) T.C. Harman, J. Electron. Mat. 8,191 (1989)
13) H.R. Vydyanath, J.A. Ellsworth and C.M. Devaney, J. Electron. Mater. 16, 13 (1987)
14) J.P. Faurie, S. Sivananthan, and P.S. Wijewarnasuriya, SPIE Proceedings,1735,141 (1992)
15) P. Capper, J. Vac. Sci. Technol. B9, 1667 (1991)
16) M. Boukerche, S. Sivananthan, P.S. Wijewarnasuriya, I.K. Sou, and J.P. Faurie, J. Vac. Sci. Technol. A7, 311 (1989)
17) H.R. Vydyanath, L.S. Lichtman, S. Sivananthan, P.S. Wijewarnasuriya, and J.P. Faurie, J. Electron. Mat. 24, 625 (1995)

18) S.H. Shin, J.M Arias, M. Zandian, J.G. Pasko, L.O. Bubulac, and R.E. DeWames, J. Electron. Mat. 22, 1039 (1993)
19) J.M. Arias, S.H. Shin, J.G. Pasko, R.E. DeWames, and E.R. Gertner, J. Appl. Phys. 65, 1747 (1989)
20) R.L. Harper, S. Hwang, N.C. Giles, J.F. Schetzina, D.L. Dreifns, and T.H. Myers, Appl. Phys. Lett. 54, 170 (1989)
21) J.W. Han, S. Hwang, Y. Lansiri, R.L. Harper, Z. Yang, N.C. Giles, J.W. Cook, J.F. Schetzina, and S. Sen, Appl. Phys. Lett. 54, 63 (1989)
22) J.M. Arias, M. Zandian, J.G. Pasko, S.H. Shin, L.O. Bubulac, and R.E. DeWames, J. Appl. Phys. 69, 2141 (1991)
23) O.K. Wu, G.S. Kamath, W.A. Radford, P.R. Bratt and E.A. Patten, J. Vac. Sci. Technol. A8, 1034 (1990)
24) J.P. Faurie, S. Sivananthan, and P.S. Wijewarnasuriya, SPIE Proceedings, 1735, 141 (1992)

HIGH PERFORMANCE HgCdTe-DETECTORS GROWN BY MOLECULAR BEAM EPITAXY

R. D. Rajavel, D.M. Jamba, J.E. Jensen and O.K. Wu
Hughes Research Laboratories, Malibu, CA

C.A. Cockrum, J.A. Wilson, E. A. Patten, K. Kosai J. Rosbeck,
P. Goetz, and G. Venzor
Santa Barbara Research Center, Goleta, CA

ABSTRACT

Molecular beam epitaxy (MBE) offers benefits such as the capability for growth of compositionally-tailored heterostructures and in-situ doping of HgCdTe alloys. These capabilities were applied to the growth of long wave infrared unispectral focal plane arrays (FPA) with 480x4 elements. The detectivity (D*) map of the FPA demonstrated performance that was higher than the specification value, with no defective channels. Two-color detectors with the n-p-n architecture, for the simultaneous detection of two closely spaced bands in the midwave infrared spectrum were also grown by MBE. These devices exhibited sharp turn-off and turn-on in both bands. The quantum efficiency was greater than 70% and average R_oA values exceeded 1×10^6 Ω-cm^2 in both bands. These result demonstrate that high performance HgCdTe devices can be grown by MBE.

INTRODUCTION

Molecular beam epitaxy (MBE) technology offers benefits such as in-situ n- and p-type doping capability,[1] low background doping levels,[2] capability for the growth of compositionally-tailored multilayer heterojunction devices, and heteroepitaxial growth of HgCdTe detector structures on Si substrates[3]. As a result MBE has emerged as the premier vapor phase epitaxial growth technique for the growth of HgCdTe detectors. The 77K-performance of unispectral devices currently grown by MBE are on par with those grown by employing the more established liquid phase epitaxial growth technique.[4]

Of the MBE-capabilities mentioned above, p-type doping of HgCdTe alloys is a particularly challenging task. This is due to the low sticking coefficient of As acceptor impurities necessitating growth at low temperatures, coupled with the extreme sensitivity of HgCdTe film properties on growth temperature. As reported first in a patent in 1991, and also in more recent publications, at Hughes we have developed a unique process to address these issues associated with p-type doping of HgCdTe alloys.[1,5] This robust process has been used for the growth of p-type $Hg_{1-x}Cd_xTe$ films (x= 0.8 to 0.22) with good structural properties, and transport properties similar to those reported for films grown by liquid phase epitaxy.[1,6] The electrical activity of arsenic in $Hg_{1-x}Cd_xTe$ films dope with this in-situ direct alloy growth process is between 60-100%, as determined from Hall effect and secondary ion mass spectrometry (SIMS) measurements.

These achievements with in-situ p-type doping of HgCdTe alloys has enabled us to advance the science and technology of HgCdTe-MBE to grow complex devices such as multilayer heterojunction two-color detectors and novel room temperature avalanche photo-detectors.[1,7] In this paper we present some of the highlights of MBE-technology such as the performance of unispectral longwave infrared (LWIR) FPA and simultaneous two-color detectors.

Epitaxial growth of the device structures by MBE was performed in a VG Semicon V-80 system, by using CdTe and elemental Te and Hg as the source materials. The films were grown at a substrate temperature of $\approx$185 °C onto (211)B oriented $Cd_{0.96}Zn_{0.04}Te$ substrates at growth rates that ranged from 1.8-2 μm/hr. As is customary in the growth of narrow gap HgCdTe alloys, an overpressure of Hg was employed during growth. The excess Hg re-evaporates from the surface, and the amount of Hg that is incorporated in the $Hg_{1-x}Cd_xTe$ film is determined by the magnitude of the incident tellurium flux. Hence the alloy composition (the Hg to Cd ratio) dictated by the Te/Cd flux ratio, is determined by the temperatures of the CdTe and Te effusion cells. For this study the beam equivalent pressures of Hg, CdTe, Te were $3-4\times10^{-4}$, 1.5×10^{-6} and 2.5×10^{-6} mBar, respectively. The compositions of the $Hg_{1-x}Cd_xTe$ films were determined from infrared transmission measurements using the empirical expression provided by Hansen, Schmit and Casselman.[8]

RESULTS AND DISCUSSION

Alloy composition control

As reported previously, we have achieved a precision in alloy composition control of $x = \pm 0.003$ for a target composition of $x = 0.225$, for the growth of n-type $Hg_{1-x}Cd_xTe$ layers.[1] Typically, the flux calibration procedure for CdTe and Te involves measuring the individual fluxes and then adjusting the cell temperatures to get the desired flux ratio prior to the growth of a layer. The same procedure for flux calibration was applied for the growth of a series of n-p-n detector structures, the precision in the x-value for the growth of these two-color detectors is $\pm$ 0.005. This value is higher than that previously reported for the growth of unispectral detectors whose thickness is $\approx$9 μm. We believe that changes in the alloy composition are due to minor instabilities in the effusion cell fluxes, and are more pronounced during the growth of devices such as two-color detectors, whose thickness can be > 20 μm. In the near future, we intend to employ in-situ spectroscopic ellipsometry and optical-based flux monitoring techniques to provide information in real-time regarding the x-value of the layer and the magnitude of the constituent flux in order to further enhance the precision in alloy composition control.

Unispectral LWIR detectors

The p-on-n detector structures were grown by depositing $\approx$2 μm thick HgCdTe:As (cap) layer onto 6-8 μm thick HgCdTe:In (base) layers. The composition of the base layer is such that it is appropriate for the detection of the radiation of interest. The alloy composition of the As-doped p-type layer was a wider band gap. The x-ray rocking curve full width at half the diffracted intensity maximum (FWHM) of the base layer is typically < 40 arc-s., and that of the thinner cap layer is between 30-45 arc-s. To determine the dislocation density in the base layer, the cap layer was first removed by a chemical etch. For LWIR layers grown on lattice matched substrates, the typical etch pit density is 5×10^5 cm^{-2}. The etch pit density measured in the base layer was strongly dependent on the growth conditions, specifically the substrate temperature and the Hg/Te flux ratio.

The MBE-grown layers were fabricated as test structures and 480x4 element scanning FPAs with diodes having the mesa architecture. The 77K spectral response characteristic of a representative diode is shown in Fig. 1.
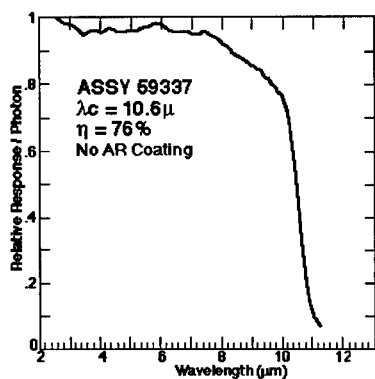
Fig. 1. The spectral response characteristic of a LWIR detector whose absorber layer thickness is 7 μm. Excellent quantum efficiency was observed for these detectors.

The detectors exhibits good short wave response, indicative of long minority carrier lifetime. The average cutoff wavelength for this FPA is 10.6 μm. The quantum efficiency was 76% for these detectors, which had no anti-reflection coating. the 480x4 element FPA was hybridized to a read-out and tested. The normalized detectivity of the FPA is shown in Fig. 2. It is noteworthy that all pixel elements exhibit D* values that are above the lower specification limit, shown by the dotted lines. These performance characteristics demonstrate that high performance FPAs can be fabricated in MBE-grown material. ⸱
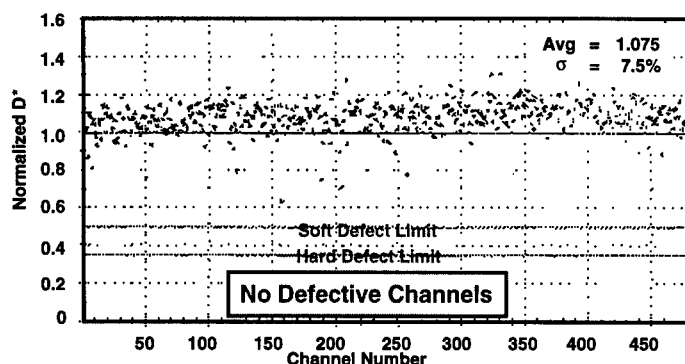
Fig. 2. D* profile for a 480x4 element MBE-grown FPA. There are no defective channels based on D* values.

Two-color detectors

Two color detectors provide an added dimension of contrast that serves as a visual aid in scene interpretation. In addition there is a saving in weight, volume and system complexity, when compared to two individual detectors used for the same application. A schematic of the integrated two-color detector with the n-p-n architecture is shown in Fig. 3.
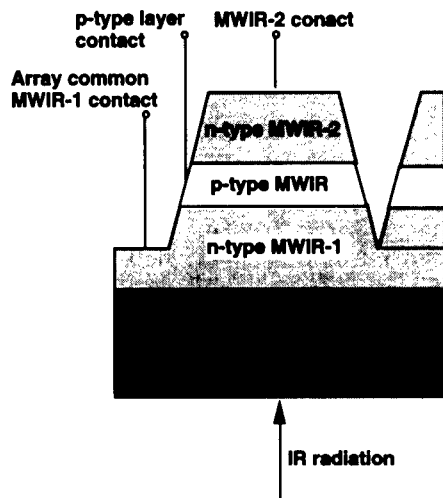
Fig. 3. Schematic of the n-p-n simultaneous two-color detector.

The simultaneous-detection n-p-n device for the detection of two closely spaced bands in the mid wave infrared (MWIR) spectrum is a three terminal device requiring contacts to the top and bottom absorbing layers as well as the middle p-type layer. The alloy compositions of the n-type layer adjacent to the substrate (referred to as the MWIR-1 n-type layer) determines the cut-off for the detector with the shorter cutoff wavelength and the composition of the final n-type layer (MWIR-2 n-type layer) that is deposited on the p-type layer determines the cutoff of the longer MWIR band.

Test structures were fabricated using dry etching to define the mesa architecture. The geometrical area of the MWIR-1 diode was 5.63×10^{-5} cm^2 , while that of the MWIR-2 diode with a longer cutoff was 4.50×10^{-5} cm^2, which provides fill factor of > 80% for the MWIR-2 diode. Fig. 4 shows the spectral response per photon for the integrated two-color detector The diode with a shorter cutoff in the two color detector exhibits a sharp cutoff at 3.7 µm and exhibits good short wave response, an indication of long minority carrier lifetime. Since the base layer of the MWIR-1 diode acts as a band pass filter, the response of the MWIR-2 diode turns on as that of MWIR-1 diode turns off. For this device, the cutoff of the MWIR-2 detector was 4.3 µm.
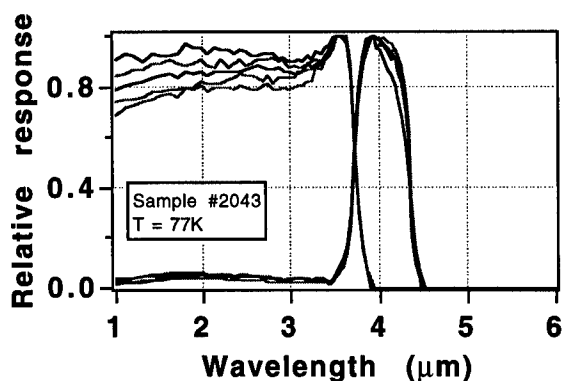
Fig. 4. The spectral response per photon for simultaneous two-color detectors. The cutoff of MWIR-1 is 3.7 μm and that for MWIR-2 is 4.3 μm at 77K.
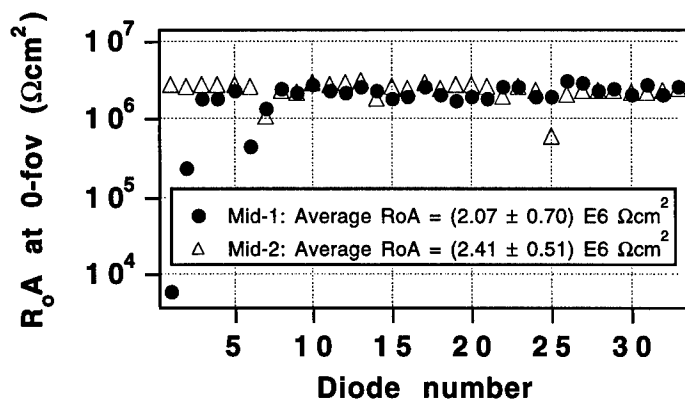
Fig. 5. The RoA distribution for both bands in the two-color detector for 33 diodes in the test structure.

The quantum efficiency of the diodes were determined by employing a calibrated black body source. The quantum efficiency was greater than 70% in both bands for these devices that did not have any anti-reflection coating. The distribution of the R_oA values for all the diodes in the test structure is shown in Fig. 5. Except for a couple of diodes, the R_oA values are quite uniform. The average R_oA for MWIR-1 (λ_{co} = 3.7 μm at 77K) was (2.1 ± 0.7) x10^6 Ω-cm^2 at 0-fov at 77K. The corresponding R_oA values for the MWIR-2 diodes (λ_{co} = 4.3 μm) was (2.4 ± 0.5) x10^6 Ω-cm^2. The results presented here demonstrate that sophisticated devices such as two-color devices can be grown by MBE.

CONCLUSION

The advantages offered by MBE for the growth and doping of HgCdTe heterostructures were applied to the growth of unispectral LWIR FPAs and multispectral detectors for the simultaneous detection of two closely spaced bands in the MWIR spectrum. The performance of the 480x4 element FPA was assessed by detectivity measurements. It is noteworthy that this FPA had no defective channels based on the D* values, and the mean was a factor of 1.075 higher than the specification value. Multispectral devices with the n-p-n architecture were grown and processed as test structures with the mesa geometry. The detectors exhibited sharp cutoff in both bands, and exhibited quantum efficiencies exceeding 70%. The average R_oA for MWIR-1 (λ_{co} = 3.7 μm at 77K) was (2.1 ± 0.7) x10^6 Ω-cm^2 at 0-fov at 77K. The corresponding R_oA values for the MWIR-2 diodes (λ_{co} = 4.3 μm) was (2.4 ± 0.5) x10^6 Ω-cm^2.

REFERENCES

1. R. D. Rajavel, D.M. Jamba, O.K. Wu, J.A. Roth, P.D. Brewer, J.E. Jensen, C.A. Cockrum, G.M. Venzor, and S.M. Johnson, J. Electron. Materials 28, 1410 (1996).

2. J. Arias, paper presented at the Fall 1996 MRS Meeting, Symposium O, Boston, MA, Dec. 2-6, 1996.

3. T.J. de Lyon, R.D. Rajavel, J.E. Jensen, O.K. Wu, S.M. Johnson, C.A. Cockrum, and G.M. Venzor, J. Electron. Materials 28, 1410 (1996).

4. C.A. Cockrum, S.M. Johnson, P.G. Petrowoski, G.M. Venzor, R.D. Rajavel, J.E. Jensen, O.K. Wu, J.D. Benson, J.C. Brown, S.D. Phu, and J.J. O'Neill, Proceeding of IRIS Specialty Group on Infrared Detectors, NIST, Boulder CO, July 1996.

5. G.S. Kamath and O.K. Wu, U.S. Patent 5,028,561 (1991).

6. R.D. Rajavel, O.K. Wu, D.M. Jamba and T.J. de Lyon, J. Vac. Sci. Technol. B14, 2362 (1996).

7. O.K. Wu, R.D.Rajavel, T.J. de Lyon, J.E. Jensen, M. Jack, K. Kosai, G. Chapman, S. Sen, B. Baumgratz, B. Walker, and B. Johnson, to be submitted to J. Electron. Mater.

8. G.L. Hansen, J.L. Schmit, and Y.N. Casselman, J. Appl. Phys. 53, 7099 (1982).

THE ROLE OF ATOMIC HYDROGEN FOR SUBSTRATE CLEANING FOR GROWTH OF CdTe BUFFER LAYERS AT REDUCED TEMPERATURES ON SILICON, CdTe, AND HgCdTe

L. S. HIRSCH, ZHONGHAI YU, M. R. RICHARDS-BABB[*] AND T. H. MYERS
Physics Department, *Chemistry Department, West Virginia University, Morgantown, WV
26506, tmyers@wvu.edu

ABSTRACT

Atomic hydrogen is shown to be efficacious for cleaning CdTe and HgCdTe substrates
for subsequent CdTe growth by molecular beam epitaxy. While single crystal ZnTe and CdTe
growth was obtained on Si substrates that underwent an *ex-situ* HF-based etch, only
polycrystalline CdTe or ZnTe could be obtained on surfaces cleaned using an atomic hydrogen
source. This result is possibly related to gas-phase transport of Te to the Si surface.

INTRODUCTION

Atomic hydrogen has been demonstrated to be effective for cleaning many types of
substrates prior to epilayer growth. Low temperature oxide removal from HgCdTe is of
technological importance. CdTe has been shown to be an effective surface passivation layer for
HgCdTe. Unless the CdTe layer is grown as part of a heterostructure, however, it must be
deposited after the HgCdTe surface has undergone exposure to air and/or chemical etching of the
surface. This allows the formation of an oxide layer, and possibly an amorphous Te layer, which
must be removed prior to CdTe growth. Typical thermal oxide removal requires temperatures
above 180°C in vacuum. Such temperatures can degrade the surface of the HgCdTe. Luo *et
al.*[1] have demonstrated that atomic hydrogen can be used for low temperature oxide removal
and cleaning of CdTe while preserving surface stoichiometry.

Since the first study of the growth of CdTe on Si by molecular beam epitaxy (MBE),[2]
high temperature (>800 °C) thermal desorption has been the primary technique for oxide
removal.[3] Recently, techniques have been developed [4] for *ex-situ* oxide removal from Si
using etchants based on HF. These procedures result in a hydrogen-terminated surface which is
remarkably resistant to further oxidation. The hydrogen can be subsequently desorbed in the
MBE system at temperatures between 550 to 600 °C [5], leaving a clean, ordered Si surface for
subsequent epilayer growth. This technique has been successfully used for the subsequent
growth of ZnTe and CdTe on Si.[6, 7] An alternate, low temperature approach would be to use
atomic hydrogen to remove the oxide, as has been demonstrated for GaAs/Si heteroepitaxy.[8]

In this paper, we demonstrate that atomic hydrogen can be used for low temperature *in-
situ* cleaning of CdTe and HgCdTe. In addition, we present the results of an investigation of the
cleaning of Si substrates using atomic hydrogen.

EXPERIMENT

The oxide-removal experiments and epilayer growths were performed in a custom MBE
system at West Virginia University. [9-11] Substrate preparation is discussed in the individual
sections. Atomic force microscopy (AFM) measurements were made in air using a Digital
Instruments Nanoscope II. A commercial atomic hydrogen source (EPI-AHS-L) was used to

generate atomic hydrogen by thermal cracking of molecular hydrogen on a heated tungsten filament. The filament is heated using a current-regulated power supply, which we typically operate at 9.5 amps to produce a filament temperature of about 2200 °C resulting in a 5% cracking efficiency for H_2. The hydrogen flow used for substrate cleaning typically resulted in a system pressure of 2×10^{-6} Torr. After considering the ion gauge sensitivity for H_2, this represents a flux of about 8.6×10^{14} sec^{-1} cm^{-2} for atomic hydrogen at the above pressure. Assuming a unity accommodation coefficient, the time for a monolayer equivalent impingement is ~ 1.5 sec.

RESULTS - CdTe AND HgCdTe

This section discusses the use of atomic hydrogen to clean CdTe and HgCdTe surfaces. A prior study by Luo *et al.* has shown that atomic hydrogen is very effective at removing oxygen, chlorine, sulfur and carbon from CdTe surfaces while preserving stoichiometry.[1] We show that atomic hydrogen cleaning also results in smooth, 2-D surfaces for subsequent growth.

II-VI, Inc. (Saxonburg, PA) provided both (100) and (211)B-oriented substrates for this study. AFM investigation of the as-received substrates indicated an atomically smooth surface with an rms. surface roughness of less than 0.5 nm. However, we believe that this surface was actually a microscopically-thin disordered layer resulting from residual polishing damage. The surface tended to "smear" under the AFM probe tip, resulting in movement of material. By comparison, this effect was never seen on epitaxial CdTe or etched CdTe or HgCdTe surfaces. When inserted into the MBE system and examined by reflection high energy electron diffraction (RHEED), as-received substrates exhibited only diffuse scattering, even for substrates that were etched in HCl prior to insertion to strip surface oxides. This is consistent with previous LEED studies indicating a thin disordered surface on as-received substrates.[1]

CdTe substrates were then examined after undergoing a chemical etching procedure typical of that used for MBE growth. The substrates were degreased sequentially in trichloroethane, acetone and methanol. The CdTe was then etched for 5 minutes in a 0.5% Br:methanol solution, followed by two methanol dips. The substrates were then blown dry with high purity nitrogen gas, and rinsed in deionized H_2O for 5 minutes. The next step in this procedure was a 30 s dip in 1:9 HCl:deionized water followed by a 5-minute rinse in deionized water, and immediate blow-drying with N_2. AFM examination of a typical (100) CdTe surface from substrates provided at the start of this study after the above procedure indicated a highly textured surface at the microscopic level, with features 50 nm in height and an rms. roughness of 4 nm. Similar roughness was observed for (211)B-oriented substrates. We want to note that II-VI, Inc. has been actively working to improve their polishing process, and have recently achieved much smoother surfaces after this etch procedure (rms. roughness ~ 0.6 nm) indicating significantly less residual damage. RHEED measurements on the as-etched substrates gave irregular, spotty patterns with superimposed rings indicative of a residual Te overlayer, probably from the Br:methanol etch. The substrate had to be heated to temperatures above 200 °C to remove the Te as indicated by disappearance of the diffraction rings. However, the surface remained 3-D in nature, as the diffraction pattern exhibited only spots indicative of the textured surface. This pattern became two-dimensional only after the entire typical thermal treatment, which involved heating up to 300 °C for 10 minutes.

The effect of atomic hydrogen cleaning was investigated at both room temperature and at elevated temperatures. At room temperature, both the diffuse scattering and the rings related to oxides and/or a Te-overlayer disappear after about a 20 minute exposure to atomic hydrogen. A

bright, three-dimensional spot pattern is obtained after a total exposure of about 30 minutes, similar to that observed for the 200 °C thermal pretreatment. For temperatures above about 80 °C, however, the oxide/Te overlayer was rapidly removed and a sharp 2-D pattern with well-defined steaks was observed. AFM examination of the surface of substrates cleaned above 80 °C indicated a microscopically-flat, featureless surface with an rms. surface roughness of less than 0.5 nm.

Surface oxides on CdTe are probably TeO_2 or $CdTeO_3$. [12-14] Removal of these oxides may proceed by reactions of the form:

$$CdTeO_3 + 6H \rightarrow CdTe + 3H_2O \uparrow \qquad (1)$$
$$TeO_2 + 4H \rightarrow Te + 2H_2O \uparrow \qquad (2)$$
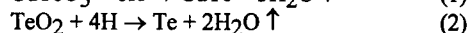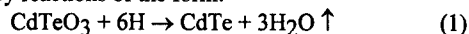
Reaction (2) has the potential to leave behind a Te overlayer, and RHEED also indicates the presence of a Te-overlayer after chemical etching. We believe that the following mechanism is also important for atomic hydrogen cleaning of CdTe:

$$Te + 2H \rightarrow TeH_2 \uparrow \qquad (3)$$
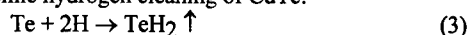
To test this hypothesis, we deposited a polycrystalline Te layer of about 30 Å thickness on a silicon substrate. At 80 °C, this layer was removed by atomic hydrogen irradiation in about 300 s, indicating a Te etch rate of 0.1 Å/sec. Compared to the previously calculated arrival rate for atomic hydrogen, this corresponds to about a 10% efficiency in the use of atomic hydrogen, possibly limited by a kinetic barrier due to the need for two hydrogens to be available at a given Te atom for removal.

We have not been able to directly measure an etch rate for CdTe (or ZnTe) due to atomic hydrogen by either direct exposure of thin layers deposited on silicon substrates or by observation of RHEED oscillations. However, etching must be possible as indicated by the smoothing of textured surfaces. An upper bound for the CdTe etch rate can be inferred from the difference in the CdTe growth rate observed when grown with and without the presence of atomic hydrogen. CdTe grown under an atomic hydrogen flux of 2×10^{-6} Torr exhibited a consistent decrease in growth rate of about 0.1 Å/s, which is comparable to the Te removal rate. The fairly rapid smoothing of the rough, as-etched CdTe surfaces may indicate that atomic hydrogen is more effective at etching three-dimensional structures since edge sites will be more reactive. Temperatures of 80 °C or above may be required to thermally-desorb residual Cd, as there are no stable, volatile hydrides of Cd. Exposing thin ZnTe/Si epilayers to atomic hydrogen also indicated etch rates less than 0.1Å/s.

While low-temperature oxide removal resulting in a sharp, well-ordered interface is of interest for CdTe, it is crucial for CdTe-passivation of HgCdTe for infrared detector fabrication. II-VI, Inc. also provided liquid phase epitaxy (LPE) HgCdTe samples to investigate atomic hydrogen cleaning to HgCdTe. The as-received LPE samples had been chemo-mechanically polished to remove surface features related to the LPE process. Prior to insertion into the MBE system, the LPE layers were degreased in trichloroethylene, acetone and methanol. They were then etched for 5 s in 0.5 % Br:methanol, followed by a methanol rinse and then immediately blown dry.

Results obtained for HgCdTe at room temperature and 80 °C were similar to that observed for CdTe. As-prepared HgCdTe exhibited a diffuse pattern with superimposed rings indicative of an oxide/amorphous Te overlayer. Only after 60 minutes at room temperature did distinct RHEED patterns emerge, indicating removal of the oxide overlayer. The patterns remained spotty, indicative of a rough surface, and there was still diffuse scattering. We believe that the etching process which can lead to a smooth surface is inhibited by Hg and Cd remaining on the surface. Raising the sample temperature to 80 °C dramatically increased the speed of the

process. After a 20 minute exposure to atomic hydrogen, a well-defined two-dimensional pattern exhibiting sharp streaks was observed, as shown in Fig. 1. Continuing exposure to atomic hydrogen eventually resulted in the evolution of the streak patterns into spotty 3-D patterns, indicative of surface roughening.

AFM examination of a HgCdTe surface both cleaned with atomic hydrogen and exhibiting a RHEED pattern similar to that shown in Fig. 1 indicated a microscopically-smooth surface with an rms. surface roughness less than 0.5 nm, with a suggestion of monolayer steps. CdTe grown at 80 °C on such a surface at a rate of 0.1 μm/hr (using a single effusion cell) maintained the sharp, streaky RHEED pattern. The resulting epilayer exhibited the same atomic-level smoothness as the HgCdTe surface when examined by AFM, again with an rms. surface roughness less than 0.5 nm, as shown in Fig. 2.
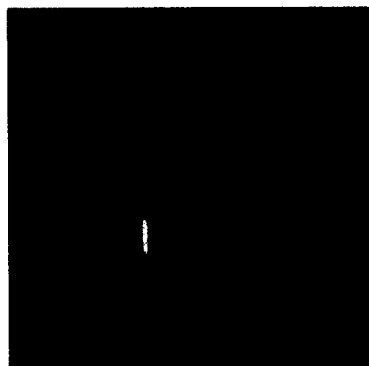
Figure 1. RHEED pattern from HgCdTe cleaned at 80 °C for 20 minutes using atomic hydrogen.
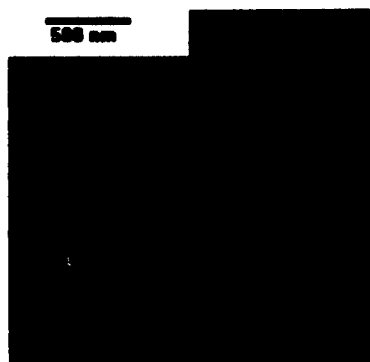
Figure 2. AFM micrograph of an 0.25 μm thick layer of CdTe grown on a HgCdTe surface cleaned using atomic hydrogen. The height scale is 10 nm

RESULTS - Si

Based on prior work by Dhar *et al.*[6] and Lyon *et al.*,[7] we decided to first try growths on (211)-oriented Si substrates cleaned following the procedure outlined by Fenner *et al.* [4] The as-prepared Si substrates gave a RHEED pattern exhibiting diffuse scattering and rings. However, these features disappeared upon heating the substrate above 200 °C, leaving only the sharp, streaky RHEED pattern shown in Figure 3(a). Note the presence of strong Kikuchi lines. The disappearance of the rings may correspond to a desorption of residual carbon from the etch, as reported in a prior study.[15] For comparison, we also investigated the use of atomic hydrogen for cleaning the Si surface. In particular, we found that about a 20 minute exposure of atomic hydrogen at 600 °C removed the oxide layer from a Si substrate etched in a HF:H_2O solution. We also exposed a Si substrate cleaned using the Fenner etch to atomic hydrogen for an equivalent amount of time. Either procedure resulted in a RHEED pattern similar to that obtained by the Fenner etch alone, as shown in Figure 3(b). The only discernible difference was that the samples exposed to atomic hydrogen had a larger amount of diffuse scattering, often indicative of a sub-monolayer thick disordered surface layer. Samples were heated to

<center>(a)   (b)</center>
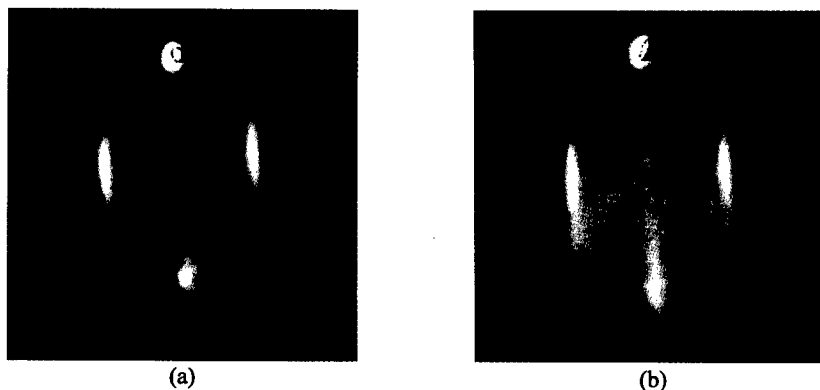
Figure 3. RHEED patterns along the (110) azimuth of (211)-oriented Silicon cleaned using (a) the Fenner procedure and (b) atomic hydrogen

temperatures as high as 700 °C, well above the desorption temperature for hydrogen on Si,[5] without any observation of change from the bulk-like (1x1) RHEED patterns shown in Figure 3 indicating an absence of surface reconstruction.

We obtained only polycrystalline ZnTe and CdTe on a Si surface prepared by either of the three techniques described. It is well known that bare silicon surfaces are highly reactive with the Column VI elements O, S, Se and Te, reacting with similar chemistries. For example, one of the difficulties encountered with the growth of ZnSe on Si [16] was the formation of an amorphous $SiSe_2$ layer at the interface, analogous to SiO_2. We believe that the polycrystalline growth observed was due to the formation of an amorphous $SiTe_2$ layer upon exposure to flux containing Te, analogous to the results observed with Se. Following the lead of Romano [16] *et al.* and Dhar *et al.* [6], we passivated the Si surface by exposure to an As flux during heating to about 550 °C. With the As passivation, we were able to obtain single crystal growth on substrates cleaned by the Fenner process, but growth on substrates exposed to atomic hydrogen continued to result in polycrystalline material. Further investigation indicated that the problem always occurred if the substrate was exposed to atomic hydrogen prior to As-passivation. After As-passivation, atomic hydrogen exposure did not present any deleterious effects.

We believe this effect is not directly related to exposure to atomic hydrogen. As discussed earlier, atomic hydrogen can etch Te (and presumably CdTe and ZnTe) at low temperatures with H_2Te as an etch bi-product. We had a significant coating of Te-bearing compounds in the growth chamber which would see exposure to atomic hydrogen, resulting in a background of H_2Te. Any H_2Te striking the heated Si surface would decompose, allowing Te to react with the surface. Exposure of a Si substrate cleaned with the Fenner process directly to Te did not lead to structural rearrangement in the RHEED pattern. The background diffuse scattering increased, however, consistent with the observations of Fig. 3. Thus, we believe the atomic hydrogen in the system is transporting Te to the Si surface, resulting in a disordered $SiTe_x$ overlayer. Since we do not have the analytical capabilities on our growth chamber to investigate surface contamination, we could not directly confirm this speculation. However, it is consistent with the above results. Thus, our study may indicate that atomic hydrogen cannot be used for oxide removal from Si substrates inside a II-VI MBE chamber. Cleaning in an external preparation chamber may still be feasible.

CONCLUSIONS

We have shown that atomic hydrogen can be used to clean CdTe and HgCdTe for subsequent CdTe growth, removing both oxides and Te overlayers from the surface. However in the case of silicon, hydrogen may transport Te from the walls of the chamber onto the reactive substrate, resulting in an amorphous layer hindering growth. Therefore, hydrogen cleaning can be an effective *in-situ* cleaning method, as long as the environmental contamination does not form a volatile compound with the hydrogen which is subsequently reactive with the substrate.

ACKNOWLEDGMENTS

REFERENCES

1 Y. Luo, D. A. Slater, and R. M. Osgood, Jr., Appl. Phys. Lett. **67**, 55 (1995).
2 Y. Lo, R.N. Bicknell, T.H. Myers, J.F. Schetzina, and H.H. Stadelmeier, J. Appl. Phys. **54**, 4238 (1983).
3 R. Sporken, S. Sivananthan, K.K. Mahavadi, G. Monfroy, M. Boukerche and J.P. Faurie, Appl. Phys. Lett. **55**, 1879 (1989).
4 D.B. Fenner, D.K. Biegelsen and R.D. Brigans, J. Appl. Phys. **66**, 419 (1989).
5 See, for ex., B.S. Meyerson, F.J. Hipsel, and K. J. Uram, Appl. Phys. Lett. **57**, 1034 (1990).
6 N.K. Dhar, C.E.C. Wood, A. Gray, H.Y. Wei, L. Salamanca-Riba and J.H. Diana, J. Vac. Sci. Technol. B **14**, 2366 (1996).
7 T.J. de Lyon, J.A. Roth, O.K. Wu, S.M. Johnson and C.A. Cockrum, Appl. Phys. Lett. **63**, 818 (1993)
8 Y. Okada, T. Fujita, and M. Kawabe, Appl. Phys. Lett. **67**, 676 (1995)
9 Zhonghai Yu, S.L.Buczkowski, M. C. Petcu, N. C. Giles, and T. H. Myers, Appl. Phys. Lett. **68**, 529 (1996)
10 Zhonghai Yu, S.L.Buczkowski, N. C. Giles, and T. H. Myers, Appl. Phys. Lett. **69**, 82 (1996)
11 Zhonghai Yu, S.L.Buczkowski, L.S. Hirsch, and T. H. Myers, to appear in the Dec. 96 issue of J. Appl. Phys.
12 J. G. Werthen, J. P. Haring, and R. H. Bube, J. Appl. Phys. **54**, 1159 (1983)
13 U. Slosbach and H. J. Richter, Surf. Sci. **97**, 191 (1980)
14 M. K. Bahl, R. L. Watson, and K. J. Irgolic, J. Chem. Phys. **66**, 5526 (1977)
15 P.J. Granthaner, F.J. Grunthaner, R.W. Fathauer, T.L. Lin, M.H. Hecht, L.D. Bell, W.J. Kaiser, F.D. Schowengendt and J.H. Mazur, Thin Solid Films **183**, 197 (1989).
16 L.T. Romano, R.D. Bringans, X. Zhou and W.P. Kirk, Phys. Rev. B. **52**, 11, 201 (1995)

IN SITU SPECTROSCOPIC ELLIPSOMETRY FOR MONITORING AND CONTROL OF HgCdTe HETEROSTRUCTURES GROWN BY MOLECULAR BEAM EPITAXY

L. A. ALMEIDA[*], M. J. BEVAN, W. M. DUNCAN, H. D. SHIH

Texas Instruments Incorporated, Corporate Research & Development, P.O. Box 655936, MS 150, Dallas, TX 75265

*Microphysics Laboratory, Physics Department, University of Illinois at Chicago, Chicago, IL 60607

ABSTRACT

A major advantage of vapor phase epitaxial growth techniques is their flexibility to produce $Hg_{1-x}Cd_xTe$ layers with different compositions from one run to the next, as well as the flexibility to produce compositional heterostructures of $Hg_{1-x}Cd_xTe$ in one process step. To take full advantage of this flexibility, reliable, automated control must be introduced. To this end, a phase-modulated spectroscopic ellipsometer (SE) has been implemented for use as a contactless wafer state sensor. In this work SE was used to monitor in real-time the stoichiometry of epitaxial $Hg_{1-x}Cd_xTe$ during growth by molecular beam epitaxy (MBE). SE has provided valuable information about the MBE growth process, by revealing even small fluctuations in x ($\pm$ 0.002). In particular, SE has measured the compositional profiles of both LWIR/MWIR and MWIR/LWIR interfaces. Distinct profiles were revealed for interfaces created by abrupt changes in the CdTe effusion cell set-point and for interfaces created by ramping the cell temperature linearly. Ramping results in a smoothly graded interface, whose thickness may be pre-determined, though typically 2000 Å. An abrupt set-point change results in a sharper transition (~300 Å) followed by oscillations in composition associated with the settling time of the cell (~1500 Å). The thickness of a CdTe passivation layer grown on a LWIR layer was determined. The current status of the SE will be reported through other illustrative examples which demonstrate its utility as a diagnostic tool and as a sensor for real-time, feed-back control of the MBE process.

INTRODUCTION

The narrow bandgap semiconductor $Hg_{1-x}Cd_xTe$ is extensively used for infrared imaging applications in which the relevant spectral regions are those with high transmittance in air. The primary two bands for $Hg_{1-x}Cd_xTe$ use are located at 3-5 µm (MWIR, $x \sim 0.28$) and 8-12 µm (LWIR, $x \sim 0.23$). While liquid phase epitaxy (LPE) is the preferred commercial growth technique, vapor phase techniques such as molecular beam epitaxy (MBE) offer certain advantages; namely, the ability to grow multiple layers in a single process and the flexibility to grow different structures or compositions from run to run. Examples of structures that cannot be easily grown by LPE include dual color detectors based on three or more layers of $Hg_{1-x}Cd_xTe$.[1] In order to achieve reliable control over crucial MBE process parameters, in situ spectroscopic ellipsometry (SE) is being developed as a process sensor for use in a feed-back control system. SE is a non-destructive, contactless probe, which can measure the effective dielectric function $<\varepsilon_1 + i\varepsilon_2>$ of a sample on a time scale commensurate with MBE process control (~ 1s). Previous studies have used SE as an optical sensor in the context of materials processing. Aspnes, et al.[2] demonstrated the first system to control the composition of a growing ternary semiconductor ($Al_xGa_{1-x}As$) using SE as a sensor. Several groups have monitored the epitaxial growth of II-VI semiconductors using SE.[3,4,5,6]

The composition of $Hg_{1-x}Cd_xTe$ is derived from the measured SE data using the effective medium approximation (EMA) of Bruggeman,[7, 8] which approximates the dielectric function of a mixture of materials, given the dielectric functions and volume fractions of each component. Using this analysis, SE will continuously monitor epilayer composition and any detected deviations from a previously determined set point will be adjusted via the CdTe K-cell temperature. This paper demonstrates the feasibility of such a control system by demonstrating the fast and sensitive response of the process sensor (SE) to the process control parameter (CdTe K-cell thermocouple temperature).

EXPERIMENT

An MBE deposition chamber (DCA Instruments), is fitted with a spectroscopic ellipsometer, which was developed at Texas Instruments by Duncan et. al.[9,10]. It has since been licensed to Verity Instruments Corporation and is available commercially. The ellipsometer incorporates phase modulation, as opposed to a more traditional rotating polarizer/analyzer system. Figure 1 shows schematically the details of the experimental setup. Light from a Xe arc lamp is brought to a linear polarizer via a fiber-optic cable. Phase modulation occurs through a fused silica bar, which is attached to a piezoelectric transducer driven at ~ 50 kHz. The resultant strain in the silica bar causes modulated polarization of the beam. The beam then enters the chamber through a strain-free, quartz, bakeable window (Bomco, Inc.), reflects from the sample, and exits the chamber, again through a strain-free window. The reflected light is polarization analyzed before entering a spectrometer, where it is detected by a 46-channel, solid-state detector. The spectral range is from 4074.3 to 8435.7 Å (3.043 to 1.470 eV). The signals are digitized at 1 MHz and a standard fast Fourier transform algorithm converts the signal from the time domain to the frequency domain.

Liquid-nitrogen cooled cryopanels, a cryopump and a nine-inch Hg diffusion pump maintain a vacuum of better than 1×10^{-9} mb in the growth chamber. The MBE growth chamber has a custom-built Hg source and four Knudsen cells (CdTe, Te, In, and As). Two cells (CdTe and Te) have large capacity crucibles (125 cc) and two-zone heating systems. Beam fluxes can be measured with a retractable ion gauge. The temperatures of the cells and the substrate are controlled by a Siemens Simatic TI555 microprocessor. The substrate temperature is monitored and controlled by a backside thermocouple located between the substrate holder and the heating element. Because this thermocouple does not contact the substrate holder, a pyrometer (IRCON) is used to calibrate the temperature.
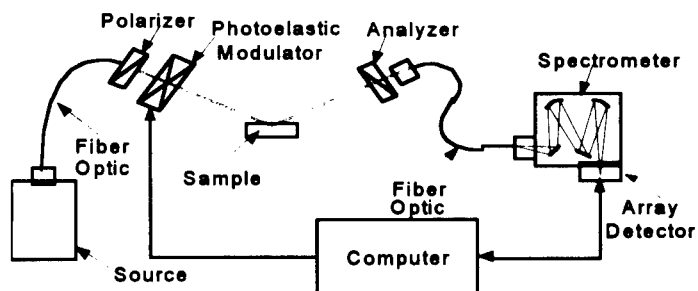
Figure 1. Diagram of current SE, featuring relevant components.

RESULTS

Most of the data were taken using the original 2-inch manipulator that was shown to have a wobble of $\pm 0.16°$. The manipulator was fitted with a sensor which can trigger the acquisition of SE data once per revolution of the manipulator drive motor. The use of this system is referred to as "synchronous data acquisition", which significantly reduced noise introduced by manipulator wobble. Subsequently, the system was retrofitted with a 3-inch, "wobble-free" manipulator, which contained three piezoelectric elements. Appropriate adjustment of these elements reduced wobble to less than $0.05°$. The piezoelectric mechanism can accommodate any variable non-parallelism between substrate wafers which would have the same effect as wobble. Synchronous data acquisition was also used for the 3-inch manipulator.

These improvements (i. e. the wobble-free manipulator and synchronous data acquisition) have substantially reduced the noise associated with SE data acquired while the sample rotated. For MBE growth, monitoring and control of the composition of single and multiple layers of $Hg_{1-x}Cd_xTe$ is most important, especially at the interface between layers. Figures 2a and 2b demonstrate the keen sensitivity of SE to the near-surface ($< 0.1\ \mu m$) composition of the epilayer during the formation of MWIR/LWIR ($x \sim 0.28/x \sim 0.23$) interfaces. In both Figure 2a and 2b the interface was formed without interruption of growth by lowering the CdTe cell temperature by $7°$ C. However, in Figure 2a the cooling occurred at the natural cooling rate of the cell (~ 2 minutes), whereas in Figure 2b the cooling occurred in a more controlled fashion, by linearly ramping the CdTe cell temperature over a 5 minute period. Distinct compositional profiles were detected by SE for each of these processes. In Figure 2a the composition undershot its final equilibrium value by ~ 0.8 % and showed strong oscillations (~ 1.8 % peak to peak) in time with a period of ~ 100 sec. These oscillations were unlikely to be caused by optical interference effects, because of the graded nature of the interface, and since oscillations due to multiple reflections are expected to have a period of ~ 9 minutes, approximately three times the observed period. It is more likely that the observed transients were related to instabilities in the CdTe flux during this abrupt cooling. The CdTe cell thermocouple reading exhibited only a single undershot of ~ 2 °C and stabilized within 4 minutes of the change of set-point, whereas, the composition took ~ 10 minutes to stabilize. As the CdTe cell cannot be cooled faster than at its natural rate, the composition transient seen in

(a)   (b)
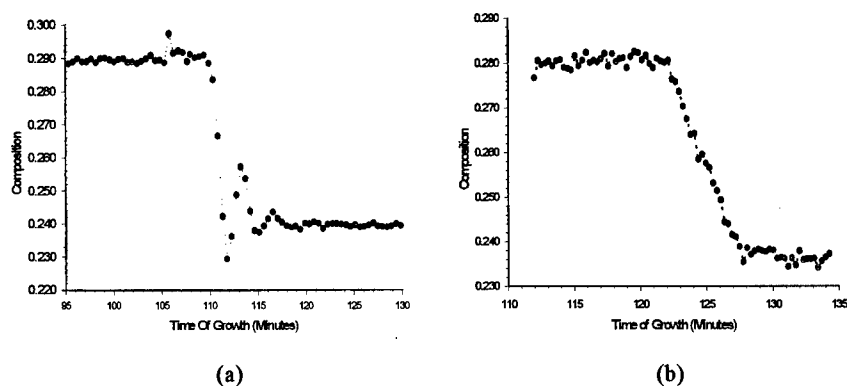
Figure 2. Composition as measured by SE for two types of MWIR/LWIR interfaces. In (a) the CdTe cell was allowed to cool at its natural rate, in (b) the cell was cooled using a linear ramp.

Figure 2a can only be avoided if growth is temporarily stopped to re-establish the new CdTe temperature (abrupt junction) or the CdTe temperature is ramped (graded junction over 2000 Å). Figure 2b illustrates the use of a grading over ~ 2000 Å to avoid a composition transient. By linearly ramping the CdTe cell temperature, the transient was avoided. The SE derived composition was able to track the CdTe effusion cell temperature ramp. The composition showed no undershooting nor oscillation and the CdTe cell thermocouple reading showed undershooting of less than 1 °C.

In Figure 3 is illustrated a triple-layer structure comprising MWIR layers grown on either side of an LWIR film. The interfaces between the MWIR and LWIR layers need to be compositionally graded to avoid the transient shown in Figure 2a but also to minimize misfit dislocations (from lattice mismatch). MBE has the capability to grow these types of structures, and SE has the potential to improve yields of device quality material. Combinations of MWIR and LWIR layers were grown to optimize parameters associated with the growth of the triple-layer structure shown in Figure 3.

In addition to measuring the composition of optically thick $Hg_{1-x}Cd_xTe$ layers, SE measured the thickness of a thin (1500-2000 Å) CdTe layer used to terminate MBE growth and to provide a passivation layer for the $Hg_{1-x}Cd_xTe$ active layer. CdTe is a commonly used passivant for $Hg_{1-x}Cd_xTe$, and films can grown by simply shutting off the Te flux. The Hg flux remains on to prevent Hg loss from the $Hg_{1-x}Cd_xTe$ layer, and the film is likely to have a composition close to $Hg_{0.9}Cd_{0.1}Te$. Figure 4 shows the SE raw data in terms of Ψ and Δ values for CdTe as it deposits onto $Hg_{1-x}Cd_xTe$, also grown in the same growth run. Using a 2-layer model and the optical values for CdTe, its thickness can be obtained as a function of time. There is likely to be a small error in thickness (<5%) as room temperature dielectric functions for CdTe were used since no calibration standards were available at that time. The thickness increased linearly with time until the CdTe shutter was closed, at which point it maintained a constant value. This behavior indicates that SE can be used to control precisely the desired thickness of the deposited CdTe.

Finally, the utility of SE as a diagnostic tool for the MBE process is demonstrated. In this example the Hg flux was disturbed by the condensation of Hg on a cryopanel vane just above the orifice of the Hg source. Over the course of several runs, Hg continuously froze and eventually formed a protrusion which partially blocked the mouth of the Hg source, at which point Hg flux, as recorded by an ion gauge, became erratic. During the growth of a single MWIR layer the
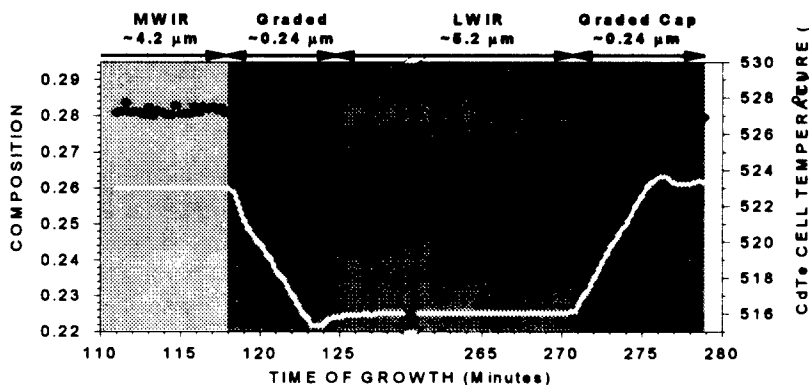
Figure 3. Composition (•) and CdTe cell thermocouple reading (white line) of the graded interface regions of an MWIR/LWIR/MWIR triple layer structure
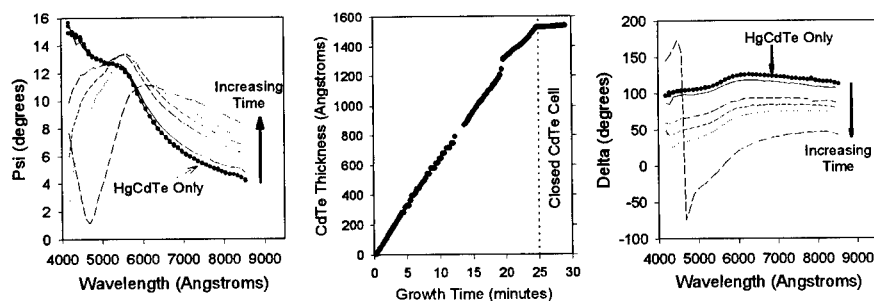
Figure 4. Deposition of a CdTe cap layer (1500 Å) on $Hg_{1-x}Cd_xTe$, both grown in the same run.

formation of such a Hg protrusion occurred. SE data was taken with substrate rotation near the beginning and near the end of the growth run. The resulting compositions are plotted against the time of growth in Figure 5. The beginning of growth proceeds as expected, with strong oscillations in composition for the first ~ 12 minutes associated with multilayer optical effects, followed by a slow drift in composition. By the end of the growth, the solid Hg protrusion had overgrown the mouth of the Hg source, and large fluctuations in composition ($\Delta x \sim 0.01$) were measured. The shape and frequency of these compositional fluctuations corresponded closely to fluctuations in the ambient pressure of the growth chamber. The ion gauge reading is indicated by the solid black line of Figure 5. The spikes in the ion gauge reading coincided with peaks in the scattered Hg flux. This explains the increase in x associated with each spike in the ion gauge reading. The condensed Hg can be removed by a partial warm-up of the cryopanels. This example demonstrates the excellent sensitivity and fast time response of the SE process sensor.

Other minor control problems have been identified by SE. SE revealed small fluctuations in CdTe flux due to poorly tuned temperature control parameters. Re-tuning of these parameters eliminated these fluctuations. Also SE highlighted a problem with the use of hot-lip effusion cells
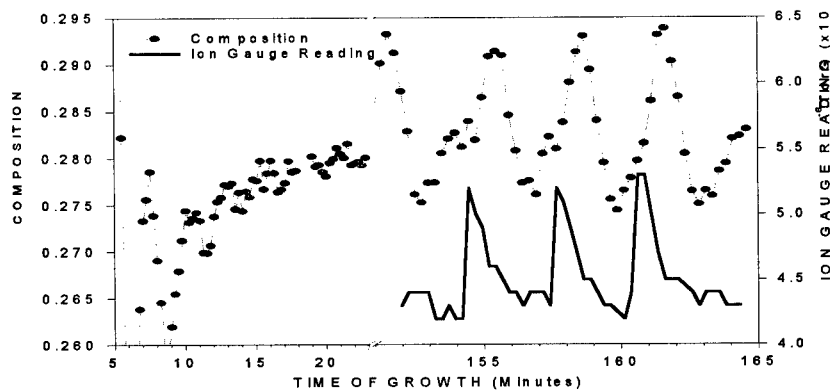
Figure 5. Fluctuations in Hg flux, as indicated by the ion gauge reading, and corresponding fluctuations in composition as measured by *in situ* SE.

273

for Te. A temperature gradient, imposed along the length of the cell to prevent condensation in the mouth of the crucible, caused the Te flux to decrease during a typical growth run. SE detected a gradual composition gradient. This problem was subsequently avoided with the use of a two-zone effusion cell. These anomalies in process control would be difficult to observe if relying on *ex situ* techniques.

CONCLUSIONS

Spectral ellipsometry has enabled the *in situ* measurement of composition during the MBE growth of $Hg_{1-x}Cd_xTe$ single- and multi-layers. Through the incorporation of a "wobble-free" 3-inch manipulator and through the use of synchronous data acquisition, SE data with excellent precision ($\Delta x \sim 0.001$) are routinely taken during growth without the need to stop wafer rotation. SE has aided in the control of composition profiles at the interfaces of multilayer structures by detecting subtle transients associated with the stabilization of the CdTe flux. SE has measured the thickness of optically thin films. Additionally, the improved sensitivity of SE has led to the identification of minor control problems that may have gone unnoticed. Incorporation of SE as a sensor in a compositional control system can now being addressed.

ACKNOWLEDGMENTS

REFERENCES

1. M. B. Reine, P. W. Norton, R. Starr, M. H. Weiler, M. Kestigian, P. Mitra, T. Schimert, F. C. Case, I. Bhat, H. Ehsani and V. Rao, J. Electron. Mats. 24, 699(1995).
2. D. E. Aspnes, W. E. Quinn and S. Gregory, Appl. Phys. Lett., 57, 2707 (1990).
3. Y. Demay, D. Arnoult, J. P. Gailliard and P. Medina, J. Vac. Sci. Tech., A 5, 3140 (1987).
4. R. H. Hartley, M. A. Folkard, D. Carr, P. J. Orders, D. Rees, I. K. Varga, V. Kumar, G. Shen, T. A. Steele, H. Buskes and J. B. Lee, J. Crystal Growth, 117, 166 (1992).
5. B. Johs, D. Doerr, S. Pittal, I. B. Bhat and S. Dakshinamurthy, Thin Solid Films, 233, 293 (1993).
6. J. D. Benson, A. B. Cornfield, M. Martinka, K. M. Singley, Z. Derzko, P. J. Shorten, J. H. Dinan, P. R. Boyd, F. C. Wolfgram, B. Johs, P. He and J. A. Woollam, J. Electronic Mats. (Proceedings of the 1995 U. S. Workshop on the Physics and Chemistry of Mercury Cadmium Telluride and Other IR Materials, in press).
7. D. A. G. Bruggeman, Ann. Phys. (Leipzig) 24, 636 (1935)
8. M. J. Bevan, W. H. Duncan, G. H. Westphal and H. D. Shih, J. Electron. Mats. 25, 1370 (1996).
9. W. M. Duncan and S. A. Henck, Appl. Surface Sci., 63, 9 (1993).
10. S. A. Henck, W. M. Duncan, L. M. Lowenstein and S. Watts Butler, J. Vac. Sci. Technol. A11, 1179 (1993)

CHARACTERIZATION OF THE CH$_4$/H$_2$/Ar HIGH DENSITY PLASMA ETCH PROCESS
FOR HgCdTe

C.R. EDDY, JR.[+], D. LEONHARDT[‡], V.A. SHAMAMIAN, R.T. HOLM, O.J.
GLEMBOCKI, J.R. MEYER, C.A. HOFFMAN AND J.E. BUTLER

U.S. Naval Research Laboratory, 4555 Overlook Ave., SW, Washington, DC 20375
[‡]NRC Postdoctoral Fellow
[+]e-mail: eddy@ccfsun.nrl.navy.mil

ABSTRACT

High density plasma etching of Hg$_{1-x}$Cd$_x$Te in a CH$_4$/H$_2$/Ar chemistry is examined using mass
spectroscopy with careful surface temperature monitoring. The dominant etch products are
monitored as a function of surface temperature (15-200°C), ion energy (20-200 eV), total
pressure (0.5-5 mTorr), microwave power (200-400 W), and flow fraction of methane in the etch
gas mixture (0-30%). In addition, observations are made regarding the regions of parameter space
which are best suited to anisotropic, low damage etch processing. These observations are
compared with previous results in the form of scanning electron micrographs of etched features
for anisotropy evaluation and Hall effect measurements for residual damage. Insights to the
overall etch mechanism are given.

INTRODUCTION

Dry etch processing of narrow band gap semiconductor materials is critically important to
the improved producibility of current infrared devices and the creation of a new and promising
generation of devices based on quantum confinement. In order to generate these devices, it is
imperative to have a more quantitative understanding of the etch process, so that the required
goals: high anisotropy and low damage, may be realized. Recently, there have been several
studies on high density plasma etching of the Hg$_{1-x}$Cd$_x$Te semiconductor [1-7]. High density
plasmas are well suited to low damage processing as a result of the decoupling of plasma density
and ion energy and, therefore, can provide high fluxes of low energy ions (as low as 20 eV) to the
semiconductor surface. A further benefit of high density plasmas is an inherently low operating
pressure (~1mTorr) which promotes highly directional ion energies to the surface and,
consequentially, directional pattern transfer into the semiconductor.
Of the studies on high density plasma etching of Hg$_{1-x}$Cd$_x$Te, few researchers have
examined the process in sufficient detail in order to develop a clear understanding of the surface
processes. Studies of CH$_4$/H$_2$/Ar etching have identified the dominant etch products and shown
that polymer formation is a significant etch rate limiting step[7]. However, a thorough
investigation into the effects of variations in plasma conditions on the formation of etch products
remains to be performed. In this work we examine the effect of variations in ion and neutral
fluxes (both chemical make-up and total flux), ion energy and surface temperature on the
formation of etch products. These experiments are performed in an effort to gain better insight
on process conditions that promote anisotropic, low damage etching in Hg$_{1-x}$Cd$_x$Te.
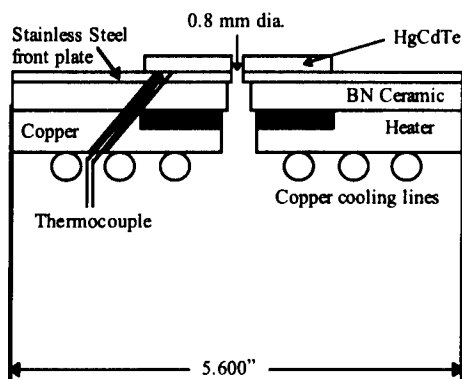
Figure 1. Schematic diagram of mass spectrometer front cap/sampling aperture.

EXPERIMENTAL

Surface chemistry experiments were performed using a thick (~16 μm) $Hg_{1-x}Cd_xTe$ ternary (x = 0.236) film grown by liquid phase epitaxy at II-VI Semiconductors, Inc. (Saxonsburgh, PA). Samples used in the evaluation of etch anisotropy and damage were thin layers ($\leq 1\mu$m) of $Hg_{1-x}Cd_xTe$ ternary (x~0.2) grown by liquid phase epitaxy.

All plasma processing experiments were carried out in an electron cyclotron resonance microwave plasma source configured for reactive ion etching and described in detail elsewhere[3]. Standard etching conditions were: $CH_4/H_2/Ar$ mixtures of 20/55/25 (percent by flow), 15 sccm total flow, 1.0 mTorr total pressure, 300 W coupled microwave power, -50 V rf-induced dc bias of the substrate, a substrate/ECR condition separation of 48-52 cm and substrate temperatures of ~16°C. For surface chemistry experiments, the traditional etching stage was replaced with an Extranuclear ELQ400 quadrupole mass spectrometer with a custom designed front cap/sampling aperture which is shown in Figure 1. The front cap emulates a traditional etching stage with full temperature control (both heating and cooling capabilities). Process conditions were varied for surface chemistry studies as follows: total pressure = 0.5-5 mTorr, coupled microwave power = 200-400 W, and rf-induced dc bias = 0-200 V, methane fraction in the mix (0-30%), and surface temperature (15-200°C).

Since surface chemistry is generally an exponential function of temperature, accurate measurement of this parameter is important to assigning thermal and ion-assisted chemical etch processes occurring at the surface. As anisotropic pattern transfer is desired, ion-assisted chemistry is preferred with minimal variation in thermal chemistry. In this work, diffuse reflectance spectroscopy of a GaAs substrate [8] is used to calibrate the thermocouple embedded in the stainless steel front plate of the front cap/sampling aperture so that the temperature indicated is that of the substrate itself. This is accomplished by measuring the shift in the position of the absorption edge with temperature. This shift corresponds to the change in the band gap which is a well-defined function of temperature[9]. The technique gives 6Å/°C resolution and is described in greater detail elsewhere[8]. Calculations (Fourier's Law with tight mechanical coupling at the interfaces) of the temperature drop from the front surface of the semiconductor to the location of the thermocouple predict a fraction of a degree difference. The diffuse reflectance spectroscopic technique supports this calculation.

The samples used for anisotropy and damage assessment are described elsewhere [3,5]. Anisotropy is evaluated on liquid phase epitaxially grown $Hg_xCd_{1-x}Te$ (x~0.2) thin films on CdTe substrates patterned with AZ photoresist and examined by cross sectional scanning electron microscopy. Changes in carrier properties of $Hg_{0.83}Cd_{0.17}Te$ alloy layers resulting from etch processing are evaluated by Hall effect measurements of a Van der Pauw sample in which the active area had been patterned.

RESULTS

The typical mass spectrum for etch products in the $CH_4/H_2/Ar:HgCdTe$ system is shown in Figure 2. The dominant, unambiguous peaks for each constituent element are Hg, $Te(CH_3)_2$, TeH_2 and $Cd(CH_3)$. When compared to other spectra available in the literature, namely Keller et al. in ref. 7, the TeH_2 peaks are more dominant and the $Cd(CH_3)_2$ and $Te(CH_3)_2$ peaks are much smaller. In the Keller et al. experiment there were two significant differences from this work: 1) direct line of sight sampling of the surface by mass spectroscopy at a fixed distance away; and 2) downstream injection of methane which results in reduced polymer formation at the surface[7]. In this work, mass spectroscopic sampling is through the semiconductor surface and, we believe, less subject to post desorption plasma chemistry and more indicative of surface chemistry. As such, the dominant desorbed etch products are TeH_2, Hg and perhaps $Cd(CH_3)$. In addition, methane is introduced into the plasma reactor in these experiments and not downstream as in the Keller et al. work.

Figure 2. Typical mass spectrum for etch products in high density plasma etching of HgCdTe with $CH_4/H_2/Ar$.

The coupled microwave power controls two factors in determining the plasma flux to the surface, dissociation fraction and ionization fraction. Of these, mass spectral flux characterization [10] shows that ionization fraction is most affected over the 200-400W range. Over this range, CH_3^+ and Ar^+ dominate the spectrum for 300-400 W and CH_3 and Ar dominate for 200-300W. Atomic and molecular hydrogen were not monitored in these studies. As microwave power increases the most dominant etch product change is an increase in Hg. Tellurium hydride shows a slight rise, presumably due to increased atomic hydrogen flux to the surface. However, $Cd(CH_3)$ and $Te(CH_3)_2$ show a slight decrease. When combined with flux characterization results, these observations imply that neutral methyl radicals are preferred over ionized methyl radicals for Cd and Te removal. Further, microwave powers $\leq$ 300 W are sufficient to maximize etch product production. When compared to the work of Keller et al., these results are consistent in that high neutral radical fluxes promote $Te(CH_3)_x$ and $Cd(CH_3)_x$ formation.

As total process pressure is increased, the Hg signal was observed to monotonically increase. Since Hg predominantly evolves from the surface in its elemental form, it is presumed that ion fluxes would enhance its removal through sputtering. However, flux characterizations show a marked decrease in the fraction of the beam that is ionized for pressures > 2 mTorr. Thus, Hg must evolve from the surface for thermodynamical reasons once the Cd and Te are removed. The Te and Cd etch products saturate for P> 2mTorr. Flux characterizations show that for P$\geq$ 2 mTorr, the fraction of dissociated CH_4 in the flux is severely reduced due to gas
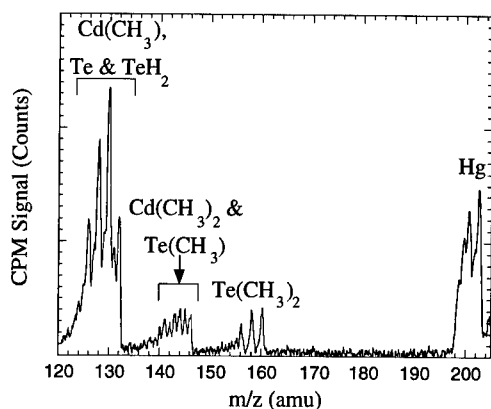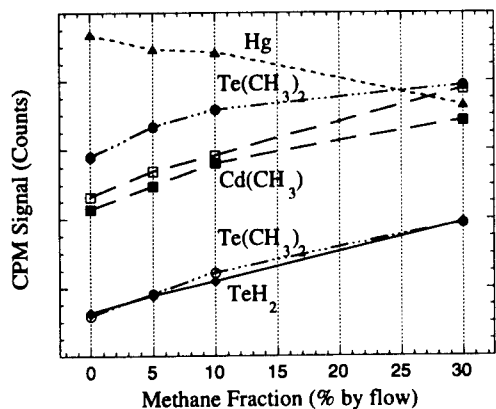
Figure 3. Variation of etch product formation with methane fraction in gas input mix. Other conditions are standard as described in the text.

phase recombination. These results imply that a sufficient flux of CH_x is required to promote surface etching and, thus, pressures $\leq$ 2mTorr are more desirable.

As fraction of methane added to the mix is increased, the $Cd(CH_3)$ and $Te(CH_3)_2$ peaks increase monotonically as expected (see Figure 3). The TeH_2 peaks start to saturate for $\geq$10% CH_4 addition, implying increased Te removal as methyl rather than hydride molecules. However, Hg decreases monotonically. Over the 10-25% range, previous works[3] have shown that the etch rate monotonically increases. Therefore, the decrease in Hg evolution from the surface should be offset by an increase in mercury removal as $Hg(CH_3)_x$, x=1,2. Unfortunately, we were unable to measure these peaks (located at m/z=215 to 234 amu). In general, these observations imply that lower methane fractions (10-20%) are well suited for moderate Cd, Hg and Te removal.

As most applications desire anisotropic pattern transfer, ion-assisted etch chemistry is preferred. Figure 4 shows behavior of etch products as a function of incident ion energy. For $\leq$ 75-100 V there is an increase in etch rate with ion energy consistent with ion-assisted chemistry. For > 100 V, the methyl and hydride etch product peaks saturate or even decrease in intensity. Thus, ion energies less than 75-100 V are preferred. The higher end of this range is associated with higher anisotropy in the perpendicular and transverse ion energies which will result in more anisotropic etching. However, the higher end of this range also brings concern for damage in the semiconductor.

Figure 4. Variation in product peak formation as a function of incident ion energy. Substrate temperature = 50°C, all other conditions standard as described in the text.

Finally, the effect of surface temperature (thermal surface chemistry) on product formation is examined. The elemental Hg peak is observed to increase monotonically, consistent with the thermodynamic removal mechanism discussed above. Metal alkyl and metal hydride products are relatively independent of substrate temperature up to 50°C, then show a slight increase between 50 and 100 °C before saturating at

278

higher levels. Thus, thermal enhancements are not seen until 50°C and keeping the substrate temperature below this level should promote ion-assisted surface chemistry over thermal chemistry and, therefore, etch anisotropy.

In a previous work [3], we have shown that low pressures (<1.0 mTorr) and moderate methane fractions (18%) were optimal for anisotropic pattern transfer. These conditions are consistent with high fluxes of neutral methyl radicals to the surface, shown to be important in the discussion above. These anisotropy results were obtained at substrate biases of 100V, shown here to be at the upper end of the ion-assisted chemistry range. Damage assessment results (of the surface on which ions are impinging, not the sidewall) [5] under these same conditions show a decrease in electron density (3.4×10^{15} to 1.1×10^{15} cm^{-3}) and mobility (3×10^5 to 2.2×10^5 cm^2/V•s), measured at 4.2K. Thus, a bias of 100 V is shown to significantly damage the substrate and slightly lower biases (in the 50-75 V range) are likely to be more suitable to low damage etching.

CONCLUSIONS

Physical and chemical processes occurring at the surface during high density plasma etching of HgCdTe have been examined through mass spectroscopy of evolving etch products while carefully monitoring the substrate temperature. Elemental Hg, TeH$_2$, Te(CH$_3$)$_2$ and Cd(CH$_3$) are identified as the primary etch product species that evolve from the surface during etching. Mercury appears to evolve from the surface for purely thermodynamical reasons. Tellurium and cadmium appear to be removed via chemical reaction with either methyl radicals (preferably neutral) and atomic hydrogen. In general, high degrees of anisotropy in the etch process are obtained by controlling the ion-assisted surface chemistry relative to the thermal chemistry at the surface. Here, they are obtained by controlling the formation of the metal hydrides and metal alkyls. Etch conditions suitable to anisotropic pattern transfer with low damage to the substrate are determined to be: low microwave powers (≤300 W), low total pressures (≤2.0 mTorr), methane flow fractions of 10-20%, substrate biases of 50-75 V, and substrate temperatures of <50°C. Under these conditions there appears to be sufficient neutral methyl and atomic hydrogen fluxes, ion fluxes and ion energy to promote ion-assisted surface chemistry, while minimizing damage to the remaining semiconductor.

ACKNOWLEDGMENTS

REFERENCES

1. G.J. Orloff and P.B. Smith, J. Vac. Sci. & Technol. A **12**, 1252 (1994).

2. C.R. Eddy, Jr., E.A. Dobisz, C.A. Hoffman and J.R. Meyer, Appl. Phys. Lett. **62**, 2362 (1993).

3. C.R. Eddy, Jr., E.A. Dobisz, J.R. Meyer and C.A. Hoffman, J. Vac. Sci. & Technol. A **11**, 1763 (1993).

4. C.R. Eddy, Jr., C.A. Hoffman, J.R. Meyer and E.A. Dobisz, J. Electronic Mater. **22**, 1055 (1993).

5. C.R. Eddy, Jr., R.J. Tonucci, D.H. Pearson, J.R. Meyer and C.A. Hoffman, "ECR-RIE of HgTe/CdTe and InAs/GaSb Heterostructures Patterned using Nanochannel Glass", in Narrow Gap Semiconductors, Proceedings of the 7th International Conference on Narrow Gap Semiconductors, Santa Fe, New Mexico, 8-12 January 1995, (Institute of Physics Conference Series Number 144), edited by J.L. Reno (Institute of Physics Publishing, Philadelphia, PA, 1995), p.364-368.

6. G.J. Oroff, J.A. Woollam, P. He, W.A. McGuhan, J.R. McNeil, R.D. Jacobson and B. Johns, Thin Solid Films **233**, 46 (1993).

7. R.C. Keller, M. Seelmann-Eggebert and H.J. Richter, J. Electronic Mater. **24**, 1155 (1995).

8. T.P. Pearsall, S.R. Saban, J. Booth, B.T. Beard, Jr. and S.R. Johnson, Rev. Sci. Instr. **66**, 4977 (1995).

9. D.E. Aspenes in Properties of Gallium Arsenide (2nd edition), EMIS Datareviews Series No. 2, (INSPEC, The Institute of Electrical Engineers, London, England, 1990), p. 153.

10. C.R. Eddy, Jr., D. Leonhardt, V.A. Shamamian, S.R. Douglass, B.D. Thoms and J.E. Butler, to be published.

HgCdTe(211)B GROWN ON CdTe(211)B/ZnTe(211)B/Si(211) BY MBE

S. RUJIRAWAT, P. S. WIJEWARNASURIYA, Y. P. CHEN, F. AQARIDEN AND
S. SIVANANTHAN
Microphysics Laboratory, Dept. Of Physics (M/C 273), The University of Illinois at Chicago, 845
W. Taylor Street, Room #2236, Chicago, IL 60680; wije@tigger.cc.uic.edu

ABSTRACT

We present preliminary results on HgCdTe(211)B layers grown on CdTe(211)B/ZnTe(211)B/Si substrates by molecular beam epitaxy. As-grown layers show excellent n-type characteristics as measured by Hall effect. Hall mibilities higher than 1×10^5 cm^2/v-s have been measured at 40K for Cd composition ~24% with doping level ~ 3×10^{15} cm^{-3}. Obtained RHEED patterns during the growth shows very smooth surface morphology.

INTRODUCTION

The Microphysics Laboratory (MPL) at the University of Illinois at Chicago (UIC) is recognized as a pioneer in the MBE growth of HgCdTe for infrared focal plane array (IRFPA) manufacturing technology. HgCdTe was grown for the first time by MBE in 1981 on CdTe substrates[1]. Since then, MBE-HgCdTe material has been extensively studied and has reached its maturity to produce device quality material for IRFPA technology[2,3]. As the development of HgCdTe infrared technology has progressed, so has the search for substrates for epitaxial MBE-HgCdTe. Near lattice matched CdZnTe substrates were attractive among researches in MBE-HgCdTe over the last decade. However, CdZnTe substrates have several severe drawbacks such as; lack of large areas, expensive and out diffusion of impurities during the MBE growth etc. Due to this severe drawbacks and interest in large area based IRFPA's, CdZnTe bulk substrates appear to be unrealistic for the near future.

The use of Si substrates is very attractive in IRFPA technology not only because it is less expensive and available in large area wafers but also because in a FPA structure, the coupling of the Si substrates with Si read out circuitry devices and this will allow the fabrication of very large arrays exhibiting long-term thermal cycle reliability. Despite the large lattice mismatched (~19%) between CdTe and Si, MBE has been successfully used for the heteroepitaxial growth of CdTe on Si[4,5]. Previously, we have published results on HgCdTe layers grown on CdTe(111)B/Si(100). In this paper, we will present recent results of CdTe(211)B/ZnTe(211)/Si(211) and HgCdTe(211)B/CdTe(211)/ZnTe(211)/Si(211) layers grown at MPL.

EXPERIMENT

The CdTe growth was carried out in a Riber OPUS 45 prototype manufacturing system, capable of growing up to a 5-inch-diameter wafer. For this work, we used 3 inch diameter Si(211)B. These substrates were cleaned using a modified RCA cleaning method described elsewhere[6,7]. The substrates were first degreased, etched in dilute HF (~2%) then rinsed by deionized water. Finally, a heated solution of $H_2O:HCl:H_2O_2$ (5:1:1) used and this forms a thin protective oxide layer. Then, the wafers are blown dry with N_2 then loaded into vacuum.

The wafers are outgassed at around 400°C in a separate preparation chamber, while at the same time the growth chamber and source material cells are outgassed. The protective oxide is

thermally removed in the growth chamber at around 850°C. The wafer is finally cooled to the appropriate deposition temperature. During the cooling process an As-flux is introduced to modify the surface. A few monolayers of SiTe$_2$ are created by exposing the surface to Te flux during cooling from 450-350°C. Following this predeposition, a thin ZnTe layer is grown at 220°C followed by 10 minute annealing under CdTe and Te flux at 380°C. Finally CdTe layer is grown at temperature of 300°C. Grown CdTe/Si wafers are then cut, characterized and cleaned for the HgCdTe growth.

These wafers are then transferred to Riber 2300 growth chamber for the growth of HgCdTe. The details of the growth procedure have been previously reported. After the growth of HgCdTe, a CdTe cap layer of 0.2μm is deposited. Figure (1) shows the heteroepitaxial structure grown on Si(211)B substrates. Cd composition and layer thickness were determined at room temperature by infrared transmission measurements. The absorption edge was taken to be 500 cm^{-1}. The transport characteristics (carrier concentration and mobility) of the layers were measured by the van der Pauw technique for temperatures ranging from 300K to 30K and with a magnetic field up to 1.0 Tesla.

| CdTe Cap Layer ~ 0.2 μm |
| HgCdTe(211)B ~ 6 μm |
| CdTe(211)B ~ 8 μm |
| ZnTe(211)B ~ 20 nm (Si,Te) compound 2-3 monolayers |
| Si(211)B |
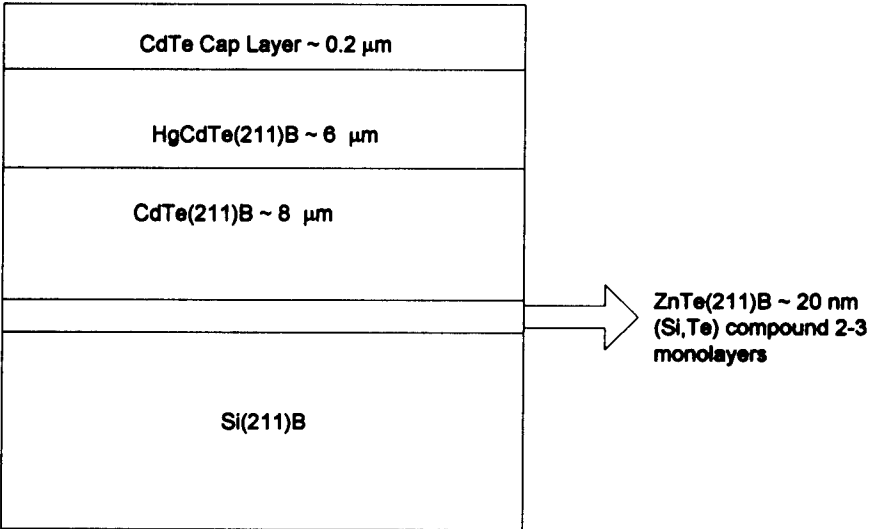
Figure 1. Grown hetero-epitaxial structure by MBE.

RESULTS

The structural quality of the as-grown CdTe(211)B/Si layers was measured by double crystal x-ray diffractometer (DCD) using Si(331) as a monochromator. We examined the rocking curve of {422} diffraction peak. The layer quality is evaluated by the full width at half maximum (FWHM) of double crystal rocking curve. Using the optimized growth condition for Si(211)B substrates, we can routinely obtain CdTe(211)B layers with FWHM below 100 arcsec with the lowest value of 74 arcsec. Etch pit density (EPD) of the as-grown layers using the Everson

solution(lactic: nitric: hydrofluoric acids 25:4:1) were in the low 10^5 cm^{-2} which is about one order lower than the values previously reported on CdTe(111)B/Si system. In order to find out the dependence of EPD on thickness, one of the above grown layer was machined using angle-diamond point turning (DPT)[8]. Everson etch was performed and etch-pit counts were made at several locations along the growth direction of the sample. Figure (2) shows the obtained EPD's against the distance from the interface. As can be seen, heavy misfit dislocation densities near the interface were observed, which rapidly diminish with the distance from the interface. The defect densities approach a constant value at a distance of ~4 μm from the interface.
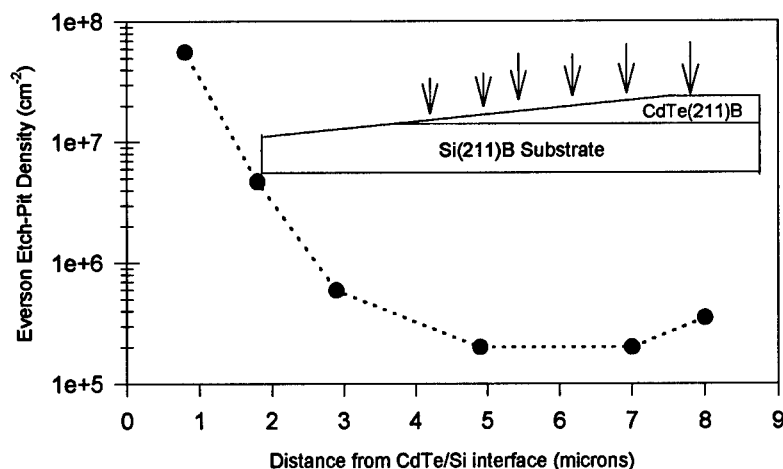
Figure 2. Everson EPD depth profile. the inset shows a cross-sectional schematic of CdTe(211)B/Si(211 sample after angle diamond point turning (DPT). The arrows indicate the approximate positions at which etch-pits were counted.

A series of HgCdTe(211)B layers were grown on these Cd(211)B/ZnTe(211)/Si in RIBER 2300 system. As an example, Table I gives the characteristics of two selected layers grown on CdTe(211)B/Si substrate. Figure (3) shows RHEED pattern obtained during the growth HgCdTe. We have grown ~ 6-8μm thick layers of HgCdTe on CdTe/Si at a growth rate of ~ 6-7 Å/sec. These layers are quite smooth, as is seen from the RHEED pattern. Measured Hall measurements show clear n-type behavior. Figure (4) shows the carrier concentration and mobility curves vs reciprocal temperature of layer #1281. The Cd composition of this layer is 24%. Electron mobility is in the range of 1x10^5 cm^2/v-s at 40K with the doping level of ~ 3x10^{15} cm^{-3}. These values are comparable with the best mobilities reported for HgCdTe for this Cd composition and this doping level. EPD of these layers were mostly in the low 10^6 cm^{-2}.

Table I. Characteristics of selected HgCdTe layers grown on CdTe(211)B/ZnTe/Si(211) by MBE.

Layer #	x (%)	t (μm)	N_d-N_a (cm^{-3})
1277	24.6	8.0	1.0×10^{15}
1281	24.0	5.7	3.0×10^{15}
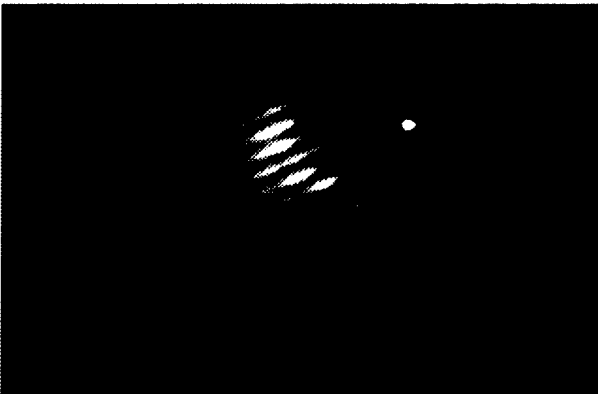
Figure 3. RHEED pattern obtained during the growth of HgCdTe(211)B on sample #1281
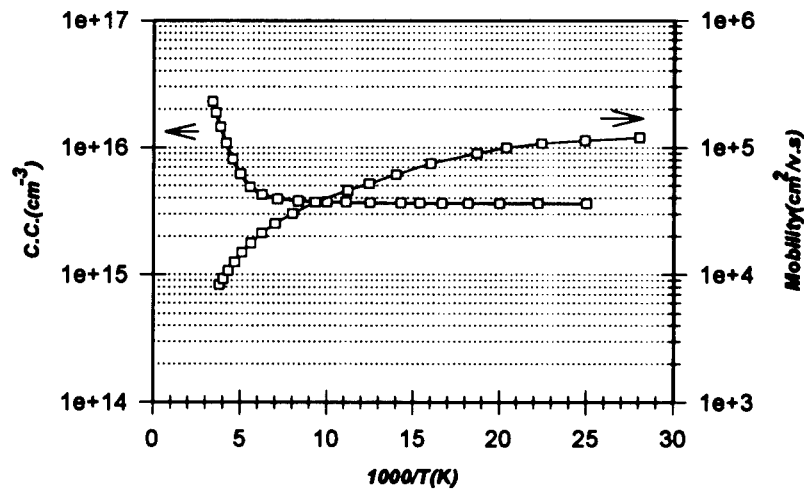
Figure 4. Carrier concentration and mobility vs reciprocal temperature of MBE-HgCdTe(211)B/CdTe/ZnTe/Si layer.

284

CONCLUSIONS

We demonstrated the feasibility to obtain good quality of large-area HgCdTe(211)B on Si. The Hall mobility and the EPD of our HgCdTe layers are comparable to the layers grown on bulk CdTe(211)B. The quality of CdTe(211)B/Si has been significantly improved as shown by the EPD value. We believe that under the optimized growth condition EPD and FWHM could be further reduced. The EPD value will be further reduced to the device-quality (mid 10^5 cm^{-2}) for the layers grown on the lattice-match CdZnTe(211)B/Si substrate which is presently under investigation in the Microphysics Laboratory.

ACKNOWLEDGMENTS

REFERENCES

1. J.P. Faurie and A. Million, J. Crystal Growth 54, 582 (1981)
2. J.M. Arias, S.H. Shin, J.G. Pasko, R.E. DeWames, and E.R. Gertner, J. Appl. Phys. 65, 1747 (1989)
3. P.S. Wijewarnasuriya, M.D. Lange, S. Sivananthan, and J.P. Faurie, J. Elec. Materials, 24, 1211 (1995)
4. R. Sporken, S. Sivananthan, K.K. Mahavadi, G. Monfroy, M. Boukerche and J.P. Faurie, Appl. Phys. Lett. 55, 1879 (1989)
5. R. Sporken, M.D. Lange, S. Sivananthan, and J.P. Faurie, Appl. Phys. Lett. 59, 81 (1991)
6. W. Kern, and D.A. Puotine, RCA Review, 31, pp. 187-206 (1970)
7. Y.P. Chen, S. Sivananthan, and J. P. Faurie, J. Electron. Mater., 22, p. 951 (1991)
8. L.A. Almeida, Ph.D. Thesis University of Illinois 1996.

RAMAN SCATTERING STUDY OF H_2O_2-ETCHED $Zn_{0.1}Cd_{0.9}Te$ SURFACES

Brajesh K. Rai[*], R. S. Katiyar[*], K. -T. Chen[**], H. Chen[**], A. Burger[**]
[*]Department of Physics, University of Puerto Rico, Rio Piedras, P.O. Box 23343, Puerto Rico 00931-3343, USA.
[**]Department of Physics, Fisk University, Nashville, TN 37208, USA.

ABSTRACT

Raman study of as-grown and H_2O_2-etched surfaces of $Zn_{0.1}Cd_{0.9}Te$ single crystal has been performed. A distribution of Te precipitates on the surface of as-grown ZCT, which increases after etching, has been encountered. With high irradiation powers, due to the oxidation of the surfaces, new bands of TeO_3^{2-} are evolved. A downward shift in the peak position, as well as a halfwidth broadening, of all Raman modes has been observed with increasing laser power. The phenomenon, due to the formation of insulating oxide of tellurium in a dispersion of Te precipitates and vice-versa, has been attributed to the quantum confinement of phonons.

INTRODUCTION

Recently, an interesting phenomenon of laser induced quantum confinement in Te precipitates and their oxides, due to spatial localization of excitons and phonons, on the surface of CdTe, has been observed.[1] Localization of electron and hole wave functions in semiconductor nanostructures below a critical size leads to a drastic change in their physical properties as compared to the bulk.[2] Quantum-size effects in several II-VI group semiconductors have been widely studied. Quantum-confined semiconductor nanostructures provide an opportunity to understand the critical-size effect on phonons, exitons, and other small excitations. The non-linear optical phenomenon exhibited by these structures have led to many applied investigations.[3,4]

Single crystals of $Zn_{0.1}Cd_{0.9}Te$ (ZCT) are of interest because of several important applications of the meterial.[5] It is used for fabrication of high efficiency solar cell structures, nuclear radiation detectors, electro-optic modulators, laser windows, as substrate material for HgCdTe based opto-electronic devices, and in the epitaxy of other II-VI compounds for electronic and electroluminescent applications. In addition, the quantum-confined insulating oxides of this material may find potential applications in the development of electronic and opto-electronic devices, such as ultra-fast optical switches etc.

The band gap of amorphous oxygenated CdTe (a-CdTe:O) films grown in a nitrogen atmosphere by the r.f. sputtering deposition technique, have been found to show a wide variation in the range of 1.48 to 3.35 eV.[6,7] Auger analysis of the oxygenated compound shows the existence of an amorphous ternary compound $(CdTe)_{1-x}O_x$. The oxygenation of H_2O_2-etched ZCT surface, under ambient condition, with high laser-irradiation power can be reasonably conceived. The N_2 from air could serve as a catalyst while O_2 will provide necessary oxidation. This process may provide interesting example of nanostructures of $Zn_{0.1}Cd_{0.9}Te$ / $Zn_{0.1}$-$Cd_{0.9}$-Te-O system with dispersion of

semiconductor ($Zn_{0.1}Cd_{0.9}Te$) nanostructures in an insulator $Zn_{0.1}$-$Cd_{0.9}$-Te-O system or vice-versa. A greater electrical insulation of constituent nanostructures, which will lead to the formation of quantum dots (QDs) showing a strong quantum confinement effect, is expected with increased oxidation. Due to the thermal effects caused by high laser irradiation power a study of laser induced exitonic quantum confinement effect, under ambient conditions would be difficult. However, the quantum confinement of vibrational modes and their time dependence, as well as the species formed, can be effectively studied using Raman spectroscopic technique.

We report the controlled oxidation of H_2O_2-etched as well as as-grown ZCT surfaces and its in-situ monitoring using Raman spectroscopy in 80-800 cm^{-1} range. The evolution of TeO_3^{2-} ion on the surface of ZCT is discussed. With high irradiation power, a phenomenon of quantum confinement of Raman modes, due to the formation of insulating oxide of tellurium, is being reported. In addition, the effect of H_2O_2-etching in the creation of QDs is discussed.

EXPERIMENTAL

Crystals of ZCT were grown using the traveling heater method (THM).[8] Surface treatments of the sample was done by H_2O_2 which was preceded by a rinsing in 5% Br/methanol solution—this standard etching procedure is used in fabricating detectors. Two surfaces of ZCT with the H_2O_2 treatment for 5 and 10 minutes, were thus prepared. Coherent Innova 99 CW Ar$^+$ laser was used to provide 514.5, 488.0, and 476.5 nm excitation wavelength. All Raman measurements were performed on the samples kept at room temperature. The normal laser power used in the experiments was ~2 mW to minimize heating and consequent changes in the crystalline state, amorphization, or oxidation of the sample. Higher laser powers in the range of 2 to 22 mW were used to observe the quantum confinement effects. The beam diameter on the sample was less than 2 μm using an 80X eyepiece in the Raman microprobe. Jobin-Yvon T64000 Spectrophotometer with subtractive pre-monochromators coupled to the third spectrograph / monochromator with 1800 grooves/mm grating was used for recording the spectra. Raman measurements were made using a ~180° backscattering geometry. A charge coupled device (CCD at 140 K) detector was employed to detect the Raman signals.

RESULTS AND DISCUSSION

The presence of excess Te on the surface, as well as in the bulk, of CdTe and $Zn_xCd_{1-x}Te$ single crystal is well established and has been widely reported.[5,9-11] The formation of Te aggregates of several nanometer diameter on the surface of CdTe by the treatment of its surface using dilute HNO_3 has been reported by Zitter.[9] Later, with a chemical etchant of Br/methanol solution Amirthraj et al. found a similar precipitation of Te on the surface of CdTe[10]. More recently, the spatial distribution of Te precipitates in the volume of CdTe wafers has been studied by a combination of Raman and Cathodo-luminescence techniques.[5] Thermal annealing of as-grown crystals at 500-600 °C either in

288

Ga melt or in Cd vapor for 2 to 22 hours, results in a dissolution of Te precipitates. After a long-time annealing, the complete disappearance of Te and its oxide from the surface of CdTe, using H_2 plasma, has been reported by Nishibayashi and co-workers.[11] Also, the complete disappearances of Te Raman bands, as a consequence of all of the above mentioned surface treatments, have been reported. In the absence of above mentioned surface treatments, our samples contain a distribution of Te precipitates on the surface of ZCT, moreover, a treatment of their surfaces by H_2O_2 helps in the augmentation of Te precipitates on the surface, which is evident from our experimental results.

Fig. 1 shows the Raman spectra of three ZCT samples: (a) unetched, (b) H_2O_2-etched for 5 min, and (c) H_2O_2-etched for 10 min. Following features are noticeable: (1) The intensity of prominent Raman modes increases after etching. (2) As a result of etching all Raman bands broaden and show a downward shift of their peak positions—a similar behavior of Raman modes is observed with increasing time-duration of etching.

As mentioned earlier, a random distribution of Te precipitates on the surface of ZCT is found, which is further augmented with the H_2O_2-etching. Moreover, the bulk phonons of CdTe and ZnTe, which have far smaller Raman scattering cross section than Te, are masked underneath the stronger Te bands. It is known that the $Zn_xCd_{1-x}Te$ system, with increasing x (> 0.1), shows a two-mode behavior; consequently, four phonons, two each corresponding to

Fig. 1: Raman spectra of three ZCT samples with the excitation line of 476 nm: (a) unetched, (b) H_2O_2-etched for 5 min, and (c) H_2O_2-etched for 10 min.

CdTe (LO_1, TO_1) and ZnTe (LO_2, TO_2), are observed.[12] However, for x less than 0.1, due to the degeneracy of TO_1, LO_2, and TO_2 modes, the system shows a one-mode behavior and accordingly, only two fundamental Raman modes which correspond to LO and TO phonons of CdTe, are observed. Thus, we assign the band near 92, 103, 123, and 141 (partially) to the presence of Te on the surface of ZCT, and the bands at ~140 and ~270 cm^{-1} are assigned to TO phonon of CdTe and its overtone, respectively.

The downward shift and broadening of all Raman modes with etching can be attributed to the increased density of Te precipitates, which helps in the formation of QDs with the creation of insulating oxides of tellurium, as discussed later in this section. Similarly, the intensity of the Raman bands, after etching, increases due to an increase in the density of tellurium on the surface.

In a very recent communication controlled oxidation of CdTe surface, leading to the formation of isolated TeO_3^{2-} ions, was reported.[13] The isolated symmetric bent TeO_3^{2-} ion, for which all of the four normal modes of vibration are Raman active, shows a lifting of degeneracy in crystalline environment, and correspondingly, six Raman bands are

observed. The overtone of asymmetric bending mode, v_4', falling at 381 cm^{-1} have been demonstrated to show Fermi Resonance phenomenon with the totally symmetric v_1 band of TeO$_3^{2-}$. As a result, two intense bands at ~732 and ~777 cm^{-1} have been observed. An exactly similar phenomenon is observed in both H$_2$O$_2$-etched and as-grown ZCT samples. As a result of higher Te precipitation in etched ZCT samples, the intensity of an TeO$_3^{2-}$ mode—similar to that observed for tellurium modes in Fig.1—increases. With higher irradiation power, all TeO$_3^{2-}$ Raman bands in ZCT samples broaden and show a downward shift in their peak positions. A similar, but more thorough, study done with as-grown CdTe single crystal shows the same behavior of all TeO$_3^{2-}$ bands. Therefore, in order to elucidate the phenomenon, we present the results of our experiment done on CdTe with high laser-irradiation power.

Fig. 2 shows the Raman spectra of CdTe single crystal using 514.5 nm excitation line with laser powers—at the sample—of 2, 9, 13.5, 18, and 22 mW, as shown against each spectrum. With increasing irradiation power, the bands become more intense and show a broadening; in addition, a linear downward shift in their peak positions, with increasing irradiation power, is observed.

A study of Te modes in 80-160 cm^{-1} region, with increasing irradiation laser power, shows a similar downward shift and broadening of all Raman modes for all three ZCT samples. The effect of increasing irradiation power on the Raman bands in the region 80-160 cm^{-1}, for 10 min H$_2$O$_2$-etched surface of Zn$_{0.1}$Cd$_{0.9}$Te, is shown in Fig. 3.
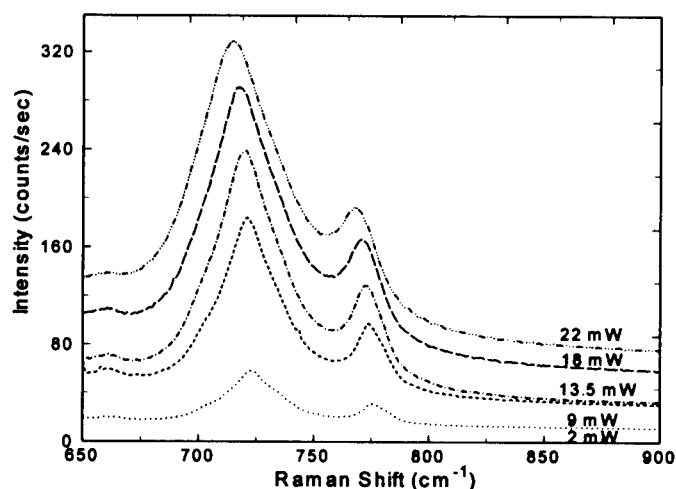
Fig. 2: Raman spectra of CdTe using an excitation line of 514.5 nm with different irradiation power as shown against each spectrum. The two bands, at ~730 and ~775 cm^{-1}, clearly show a downshift and a halfwidth broadening with increasing irradiation power.

The downshift in the peak position of the Raman modes and their halfwidth broadening indicate a size-dependent phenomenon, which is known to occur in spatially confined semiconductor nanostructures. With the laser irradiation, oxide of tellurium, in a dispersion of ZCT, and Te precipitates are formed, resulting in an electrical isolation of Te precipitates, TeO_3^{2-}, and ZCT from each other. Thereby, giving rise to a phenomenon of quantum confinement. In the bulk, $q = 0$ conservation conditions must be fulfilled which almost completely forbids first-order Raman scattering. In the case of nano-clusters, where the cluster-diameter is small compared with the laser wavelength, the dipolar approximation is valid and $q = 0$ conservation condition, due to confinement of the phonons, is totally relaxed. Confinement of Phonons has been observed to cause a broadening and a down-shift in the Raman modes.[14]

The increase in the intensity of the Raman bands, in Fig. 2 and 3, with higher irradiation power can be understood to occur due to an increased precipitation of Te on the surface of the crystal. In addition, more oxidation of the surface takes place with higher irradiation power, and as a result the intensity of the TeO_3^{2-} Raman bands increases. On the other hand, the increased oxidation of the surface results in an increasing electrical isolation of the ZCT nanostructures, Te precipitates and TeO_3^{2-} ions, on the surface. Thus, with the larger downward shift of the Raman peaks and their increased halfwidth broadening, which is evident from Fig. 1 and 2, it is inferred that the size of the QDs decreases with increasing laser-irradiation power.

Fig. 3: Raman spectra of 10 min H_2O_2-etched surface of $Zn_{0.1}Cd_{0.9}Te$, with an excitation line of 476 nm and an excitation power of : (a) 2 mW, (b) 5 mW, and (c) 10 mW, on the sample.

As stated earlier, the Raman measurement of ZCT becomes difficult due to the high precipitation of tellurium, which is known to have a far greater Raman scattering cross-section compared to the ZCT. In addition, a further increase in the density of Te precipitates, after etching and on exposure of the surface with higher irradiation power, make the Raman measurements even more complicated. Therefore, a PL study at low temperature is suggested to investigate the laser induced quantum confinement phenomenon of ZCT nanostructures.

CONCLUSION

With our Raman study, we have found an increased distribution of Te precipitates on the surface of H_2O_2-etched $Zn_{0.1}Cd_{0.9}Te$ single crystals. Raman studies done using high laser irradiation powers show the formation of TeO_3^{2-} ion. A quantum confinement phenomenon—which is manifested by a downward shift of the Raman peaks and their

broadening, with increasing irradiation power—due to the formation of insulating tellurium oxide on the surface, has been observed.

ACKNOWLEDGMENTS

REFERENCES

1. Brajesh K. Rai, R. S. Katiyar, K. -T. Chen, and A. Burger, to be communicated to Appl. Phys. Letts.
2. Al. L. Efros and A. L. Efros, Fiz. Tekh. Poluprovodn. **16**, 1209 (1982) [Sov. Phys. Semicond. **16**, 772 (1982)].
3. F. Capasso, C. Sirtori, and A. Y. Cho, IEEE J. Quantum Electron. **22**, 1853 (1986).
4. V. S. Willims, G. R. Olbright, B. D. Fluegel, S. W. Koch, N. Peyghambarian, J. Mod. Op. **35**, 1979 (1988).
5. N. V. Sochinskii, M. D. Serrano, E Diéguez, F Agulló-Rueda, U pal, J. Piqueras and P. Fernández, J. Appl. Phys **77**, 2806 (1995).
6. F. J. Espinoza Baltrán, F. Sánchez-Sinencio, O. Zelaya-Angel, J.G. Mendoza-Alejo Armenta,C. Vázquez-López, M.H. Farías, G. Soto, L. Cota-Araiza, J.L. Peña, J.A. Azamar barrios & L. Baños, Jpn. J. Appl. Phys. **30**, L1715 (1991).
7. F. J. Espinoza-Beltrán, O. Zelaya, F. Sánchez-Sinencio, J. G. Mendoza-Alvarez, M.H. Farías, L. Baños, J. Vac. Sci. Tech. A **11**, 3062 (1993).
8. R. Triboulet, Proc. 3rd Int. Conf. on CdTe, P. Siffert, A. Cornet (eds.), Strasbourg, p. 171, 1971.
9. R. N. Zitter, Surface Science **28**, 335 (1971).
10. P. M. Amirtharaj and F. H. Pollak, Appl. Phys. Lett. **45**(7), 789 (1984).
11. Y. Nishibayashi, Y. Tokumitsu, T. Imura and Y. Osaka, Jap. J. Appl. Physics part (1), **28** (10), 1919 (1989).
12. L. K. Vodop'yanov, E. A. vinogradov, A. M. Blinov, and V. A. Rukavishnikov, Sov. Phys.—Solid State **14**, 219 (1972).
13. Brajesh K. Rai, H. D. Bist, R. S. Katiyar, K. -T. Chen, and A. Burger, J. Appl. Phys. **80**, 477 (1996).
14. A. Tanaka, S. Onari, and T. Arai, Phys. Rev. B **45**, 6587 (1992).

SPECTROSCOPIC ELLIPSOMETRY STUDY OF HgCdTe EPILAYER SURFACES DURING ELECTRON CYCLOTRON RESONANCE PLASMA ETCHING

J. N. JOHNSON *, J. H. DINAN, K. M. SINGLEY, M. MARTINKA, B. JOHS **
Night Vision and Electronic Sensors Directorate, Ft. Belvoir, VA 22060
*E–OIR Measurements, Inc., Spotsylvania, VA 22553, jjohnson@nvl.army.mil
**J. A. Woollam Co., Inc., Lincoln, NE 68508

ABSTRACT

Spectroscopic ellipsometry has been used to monitor optical characteristics of HgCdTe surfaces during plasma etching in an electron cyclotron resonance reactor. Commonly used process conditions were found to induce changes in the ellipsometric parameters Ψ and Δ. A model was constructed to account for these changes in terms of process-induced roughness and mercury depleted sub-surface layers. An independent characterization of the near-surface region was carried out *ex situ* after etching using Auger spectroscopy and x-ray photoelectron spectroscopy. Plasma process parameters were varied to isolate their influence on surface conditions and a set of parameters is given for which changes are minimized.

INTRODUCTION

Mercury cadmium telluride (HgCdTe) is the detector material of choice for high performance infrared focal plane arrays, and photovoltaic diodes are the favored device configuration. The detector fabrication process begins with the deposition of planar HgCdTe epilayers on CdZnTe substrates. These layers are then etched to form an array of isolated detector elements and to create via holes for electrical contacting.

Liquid phase epitaxy has long been the standard industrial process for deposition of HgCdTe layers. Recently however, a number of advantages of a vapor phase deposition process have been demonstrated [1,2]. The most important of these is control. Because vapor processes are not constrained by thermodynamic equilibrium, the composition, thickness, and electrical characteristics of individual layers and of the junctions between them can be tailored to device applications by adjusting the fluxes of constituent vapors incident on the wafer surface. In addition, for molecular beam epitaxy (MBE), the most advanced form of vapor phase epitaxy, the wafer is in an ultra high vacuum environment and its surface is easily accessible to photon and electron beams for *in situ* analysis and real-time process control. For removal of HgCdTe layers, wet chemical etching in a solution containing bromine is the industrial baseline process. In principal, the advantages that are associated with vapor phase deposition would also hold for vapor phase etching.

Recently, dry etching of HgCdTe has been achieved with a process based on a $H_2/N_2/Ar/CH_4$ plasma generated in an electron cyclotron resonance (ECR) reactor [3]. It has been reported that etched surfaces are smooth, and that heterojunctions formed with CdTe passivating layers exhibit a flat-band electrical condition [3,4]. A first step toward real time process control was taken when a single-wavelength ellipsometer was attached to an ECR reactor to give information on alloy composition and surface roughness [3].

The possibility of real-time control of the IR detector fabrication processes has led us [5,6] as well as others [7-9] to investigate the use of spectroscopic ellipsometry (SE) as a monitor and control for the MBE process. We have also equipped our ECR reactor with a forty-four

wavelength ellipsometer to assess its usefulness as a real-time monitor of the HgCdTe surface during plasma etching. We report here the first results of this investigation.

SE consists of illuminating a sample surface with white light and measuring changes in the polarization state of the reflected radiation. These changes can be related to chemical and structural characteristics of the near-surface region by modeling the ellipsometric data. We have utilized a model based on an effective medium approximation and a graded alloy layer, and have sought to validate the modeling results by carrying out an independent measurement of surface properties using Auger and x-ray photoelectron spectroscopes.

EXPERIMENT

Etching was performed in a PlasmaQuest ECR plasma reactor. The experimental apparatus is shown schematically in Fig. 1. An ASTeX source operating at 2.45 GHz supplied power to the ECR chamber through a quartz window. Microwave reflected power was minimized using a three stub manual tuner. The upper electromagnet produced a 873 G magnetic field to establish the resonance condition. Capacitively coupled RF input from a 40.68 MHz RFPP generator determined the negative self-bias potential. The RF biased mounting stage (chuck) temperature was controlled with a NESLAB recirculator. 10 Torr of helium was applied to the backside of the wafer to facilitate heat transfer during etching. A Balzers 2200 l/s turbomolecular pump maintained a base pressure of 1×10^{-8} Torr between runs.
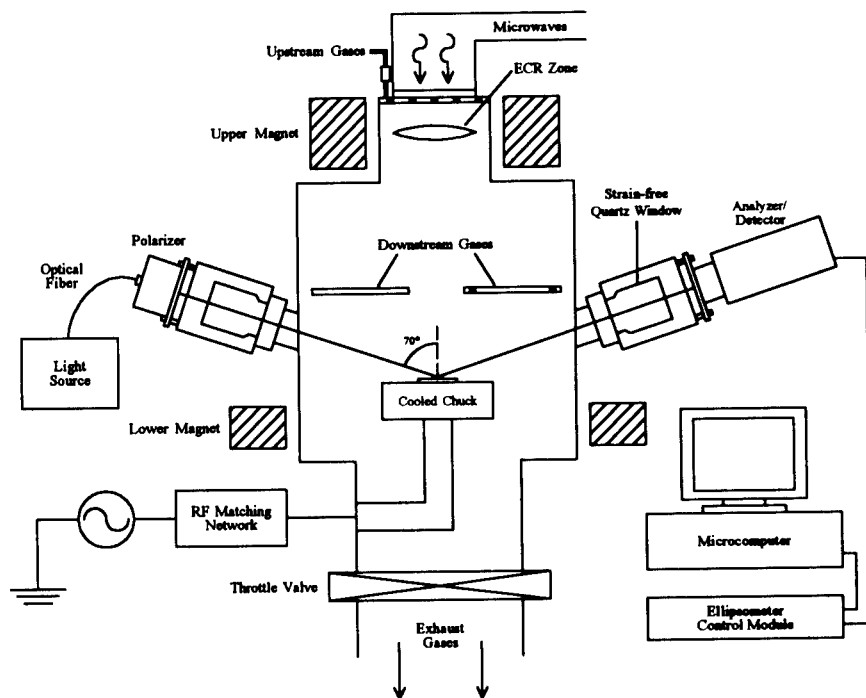
Fig. 1. Schematic representation of ECR/SE experimental setup.

Etching was carried out with H_2, N_2, and Ar introduced above the ECR zone, and CH_4 incorporated into the discharge downstream of the ECR zone (see Fig. 1). Process pressure was 6 mTorr, continuously regulated using the throttle valve. 125 A supplied to the lower collimating magnet enhanced ion directionality. Microwave forward power was 600 W. Spacing between the ECR zone and the sample was fixed at 35 cm. 4 W RF input power established a 3 to 6 V negative self-bias potential. Coolant temperature in the recirculator was 0 °C for all tests. A thermistor embedded in the chuck typically registered an 8 °C increase during a 20 to 30 minute run. Previous experiments performed with a CI Systems noncontact temperature monitor indicated that sample surfaces reached the 15 to 20 °C range.

The HgCdTe near-surface region was monitored during etching using a J. A. Woollam Model M-44 spectroscopic ellipsometer mounted on the ECR reactor. UHV strain-free quartz windows, set at 70° with respect to the normal, transmitted the incident and reflected beams. Alignment was accomplished using vertical and horizontal translation and tilt adjustments on the polarizer and analyzer/detector optical mounts. Light reflected from the sample passed through the analyzer, was dispersed by a diffraction grating, and illuminated the 44 element diode array in the detector. The SE spectral range was 414 to 756 nm. *In situ* system calibrations were performed using a SiO_2 on Si reference standard. A baseline calibration that included the test sample was done before starting the etch process. Ψ and Δ were monitored for each of the 44 wavelengths.

After etching, samples were transferred under vacuum directly from the ECR reactor to the analysis chamber through the interconnecting transport system. *In situ* Auger analysis was conducted using a Physical Electronics single pass cylindrical mirror analyzer (CMA) with the electron beam at normal incidence on the sample surface. A 25 μm diameter fixed beam was used at a current of 10 μA and a primary beam potential of 3000 V. Survey spectra and reduced energy range spectra about each elemental peak were taken to detect residuals and to quantify composition. Data were obtained at a rate of 1 eV/sec from regions of the sample with no prior beam exposure to avoid mercury loss due to beam heating. Composition was referenced against *in situ* results obtained from MBE grown HgTe, HgCdTe, CdTe and CdZnTe.

Ex situ Auger and x-ray photoelectron spectroscopy (XPS) were conducted using a Physical Electronics Model 560 equipped with a double pass CMA and an angular resolving aperture. Angle resolved and integrated data were collected as well as Auger argon ion sputter depth profiles. The electron beam current was 0.4 μA at a potential of 3000 V, and the 1.5 μm diameter beam was rastered over a 0.1 × 0.1 mm area while collecting survey spectra. An effective collection time of 2.25 sec/eV was set to yield a dose similar to the *in situ* data, but distributed over the larger raster area. A reduced dose with a collection time of 1 sec/eV was used for the energy regions of the elements during depth profiles with the beam in spot mode. The electron beam was incident at 55° from the sample surface normal, and angle resolved data were collected along the surface normal at a takeoff angle of 90°, and nearly tangent to the surface at a takeoff angle of 15°. XPS data were generated using a Mg Kα source, and sputter depth profiles were obtained with an Ar ion gun at a potential of 4500 V. The 0.6 mm diameter beam was rastered over 6 × 6 mm and 10 × 10 mm regions to reduce the erosion rate in a controlled manner. Composition and sputter rates were also referenced here against results from MBE grown HgTe, HgCdTe, CdTe and CdZnTe.

RESULTS

During ECR etching, steady state values for Ψ and Δ were obtained by adjusting the process input parameters. A model was then applied to the ellipsometric data in a time slice at the end of the experimental run to determine changes induced by the dry etching. Thus, a set of conditions which resulted in stable Ψ and Δ values was a necessary requirement for this implementation of SE. Previous tests at NVESD have indicated the dependency of ECR etching results on HgCdTe sample orientation, composition, and possibly doping type, emphasizing the importance of SE as a monitoring tool.

Ψ and Δ data acquired during an ECR etching experiment are shown in Figs. 2 and 3. Before starting the etching process, the gas flow rates were set at $H_2/N_2/Ar/CH_4 = 40/30/120/4$ sccm. The initial Ψ and Δ values in these figures are representative of a 30 nm CdTe passivation layer on HgCdTe. Etching started after taking ellipsometric data for 1 minute.
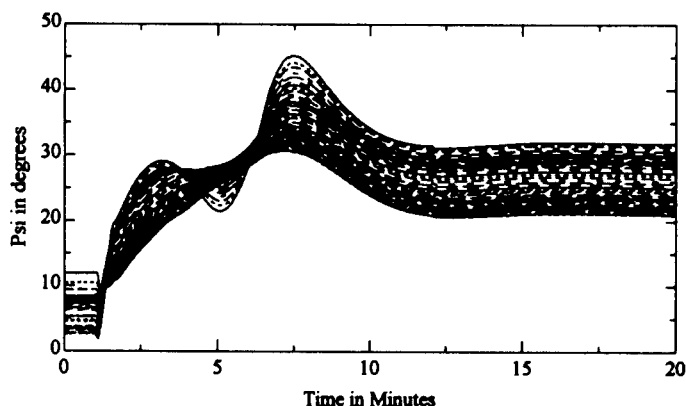
Fig. 2. Psi experimental data versus etch time.
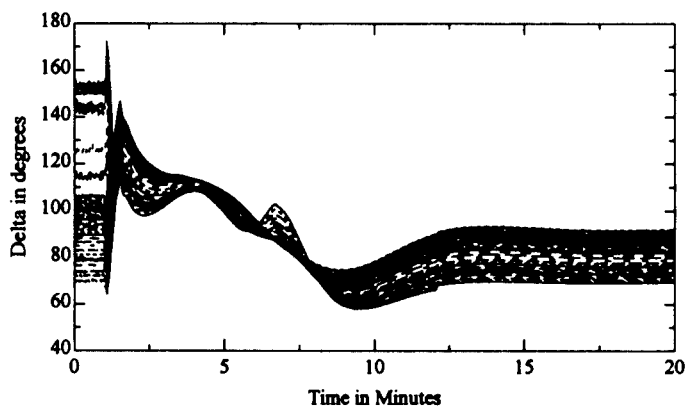
Fig. 3. Delta experimental data versus etch time.

The H_2 flow rate was initially set at 40 sccm to augment the removal of Te by the formation of TeH_2 [3]. This may have resulted in a Cd-rich surface layer, as indicated by the deflections in Ψ and Δ between the 3 and 6 minute marks. The H_2 flow was temporarily increased to 50 sccm, accelerating the deflection of the ellipsometric data. At the 7 minute mark, the H_2 flow rate was then decreased to 35 sccm. This caused Ψ and Δ to approach a more stable set of values. At 15 minutes, the H_2 flow rate was further adjusted to 34 sccm.

After etching, *in situ* Auger results, Fig. 4, show depletion in the surface Hg content similar to that observed in sputter profiles [10]. Surface electron spectroscopy was used in a manner that addressed artifacts specific to HgCdTe [11,12]. The chemical analysis was continued *ex situ* with angle resolved Auger and XPS measurements of the unperturbed near-surface region. The interleaved sampled depths, d, for Auger (0.8 and 3.2 nm) and XPS (1.4 and 5.4 nm) provide reasonable coverage of the region. Sampled depths were for a 0.9 detected signal fraction, $I(d)/I(\infty) = 1-\exp(-d/\lambda\sin\theta)$, where λ is the escape depth [13,14] and θ the takeoff angle. Both techniques detect significant further Hg depletion in the near surface beyond that observed in angle integrated spectra. This is illustrated by the XPS spectra shown in Fig. 5. No unusual chemistry was observed on the short etch duration sample and the carbon residue on the long etch duration sample was not measured by XPS.
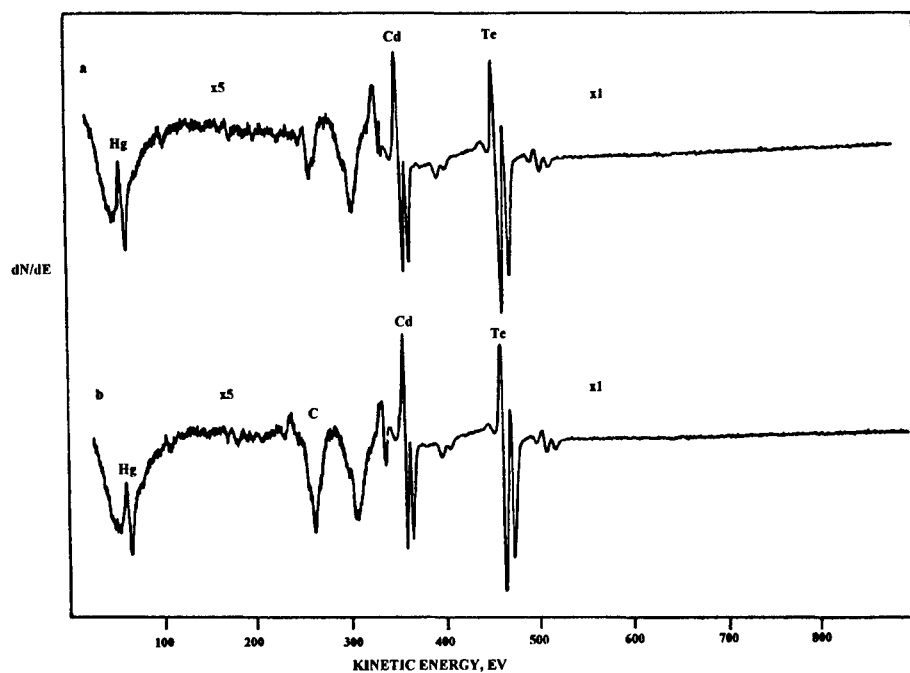
Fig. 4. *In situ* Auger spectra of the Hg depleted surfaces for (a) short and (b) long duration etches showing residual carbon.

297
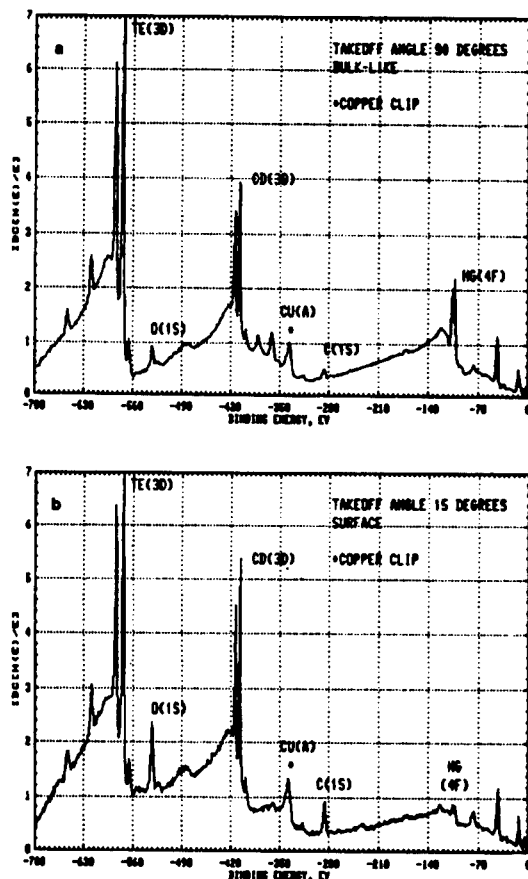
Fig. 5. Angle resolved XPS spectra of the near-surface composition grade for
short duration etch sampled to depths of (a) 5.4 nm and (b) 1.4 nm.

DISCUSSION

A series of models were constructed to account for the ellipsometry data. The model which
gave a best fit to the Ψ and Δ values characteristic of the steady state etching condition consisted
of three regions — a rough surface layer containing CdTe with voids, a HgCdTe layer whose
alloy composition was graded in depth, and a HgCdTe layer with a composition equal to that of
the bulk epitaxial layer. An effective medium approximation (EMA) was applied to the surface
layer. Alloy grading was modeled using five nodes with four slices per node. Variables adjusted
to fit the data were

- thickness and void fraction in the surface layer
- thickness and alloy composition value in the graded HgCdTe layer
- alloy composition of the bulk epilayer.

298

Optimum values for the thickness and void fraction of the surface layer were 50 nm and 58%, respectively. The "roughness" of the sample was independently measured after etching with an optical interference microscope and was found to have an RMS value of 8 nm. This discrepancy is attributed in part to the assumption of uniform composition and void fraction used in the ellipsometric model [15]. In addition, the EMA layer thickness and void concentration are strongly coupled in the model so that values for both can increase proportionally during the iterative fitting process. Results for the graded region are displayed in Fig. 6 in terms of the $Hg_{1-x}Cd_xTe$ x-value.
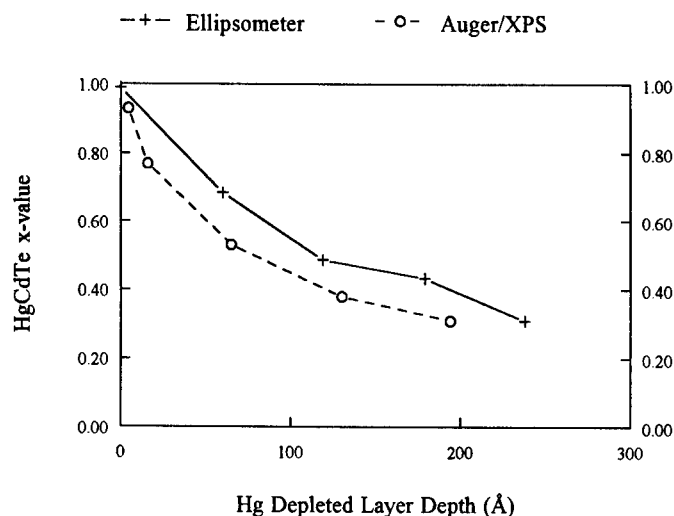
Fig. 6. Results of ellipsometer and Auger/XPS analyses showing changes in x-value versus distance from interface.

Also shown in Fig. 6 are results from the Auger/XPS measurements. These measurements were used to determine the x-value, while sputter equilibrium composition identified the end of the mercury depleted region. Equilibrium is reached during sputtering alone in less than 7.0 nm [11], and the resulting x-value must be scaled to correct for preferential mercury loss in order to reflect the original x-value. To approximate the x-value from the profile data between the near surface and the sputter equilibrium depth, the correction was reduced linearly toward the observed surface composition, e.g., 1 for CdTe. Finally, the sputter erosion rate depends on the x-value [12, 16]. In our system, HgTe erodes at twice the rate of CdTe and MBE layers erode more rapidly than indicated by bulk crater measurements. In order to determine the depth of the graded region in the ECR etched samples, CdTe and HgTe reference erosion data were incorporated in a simple model where the alloy erosion time is the sum of the time to erode the mole fraction of each of the compounds which make up a depth, d, of the alloy. The calculated erosion rate, $R(x) = d/(t_x + t_{1-x}) = [(1-x)/R(HgTe) + x/R(CdTe)]^{-1}$, was used to obtain an average erosion rate and then the thickness of the graded region. In Fig. 6 it can be seen that agreement between the ellipsometry and Auger/XPS results is reasonable.

CONCLUSIONS

The compositional profile for a HgCdTe surface region obtained by modeling spectroscopic ellipsometry data agrees with that from Auger/XPS measurements. This constitutes a validation of the ellipsometric technique and suggests that spectroscopic ellipsometry will be a useful tool for ECR plasma process development. Plasma etching results in a surface that is rougher than the starting material, with a sub-surface layer whose alloy composition is graded in depth. For the process conditions used in this experiment, a steady state is reached for which the depth of the HgTe depleted region is on the order of several hundred angstroms.

ACKNOWLEDGMENTS

REFERENCES

1. J. H. Dinan, J. D. Benson, A. B. Cornfeld, M. Martinka, J. N. Johnson, J. Bratton, and P. Taylor, in Proceedings of the 1996 IEEE/CPMT Int/l Electronics Manufacturing Technology Symposium, Austin, TX, October 1996, p. 205.
2. D. D. Edwall, M. Zandian, A. C. Chen, and J. M. Arias, presented at the 1996 Meeting of the IRIS Specialty Groups on Infrared Materials and Infrared Detectors, Boulder, CO, July-August 1996.
3. R. C. Keller, M. Seelmann-Eggebert, and H. J. Richter, J. Electr. Mater. 25 (8), 1270 (1996).
4. V. Garber, V. Ariel, and G. Bahir, presented at the 1996 International MBE Conference, Peperdine University, Malibu, CA, August 1996.
5. J. D. Benson, A. B. Cornfeld, M. Martinka, K. M. Singley, Z. Derzko, P. J. Shorten, and J. H. Dinan, J. Electr. Mater. 25, 1405 (1996).
6. J. D. Benson, A. B. Cornfeld, M. Martinka, and J. H. Dinan, presented at the 1996 International MBE Conference, Peperdine University, Malibu, CA, August 1996.
7. R. H. Hartley, M. A. Folkard, D. Carr, P. J. Orders, D. Rees, and I. K. Varga, J. Crystal Growth 117, 166 (1992).
8. Y. Demay, J. P. Gailliard, and P. Medina, J. Crystal Growth 81, 97 (1987).
9. M. J. Bevan, L. A. Almeida, W. M Duncan, and H. D. Shih, presented at the 1996 Workshop on the Physics and Chemistry of II-VI Materials, Las Vegas, NV, 1996.
10. V. Garber, V. Ariel, and G. Bahir, presented at the 1996 Workshop on the Physics and Chemistry of II-VI Materials, Las Vegas, NV, 1996 (to be published in J. Electr. Mater.).
11. E. -H. Cirlin, S. Buckingham, P. Ireland, J. Rosbeck, and C. Crosson, J. Vac. Sci. Technol. A 6 (4), 2637 (1988).
12. E. -H. Cirlin, P. Ireland, S. Buckingham, and O. Wu, J. Vac. Sci. Technol. A 6 (4), 2631 (1988).
13. Y. -C. Lu, C. M. Stahle, J. Morimoto, R. H. Bube, and R. S. Feigelson, J. Appl. Phys. 61 (3), 924 (1987).
14. J. P. Williams, S. P. Wilks, R. H. Williams, and H. A. Tarry, J. Vac. Sci. Technol. A 13 (6), 2676 (1995).
15. D. R. Rhiger, J. Electr. Mater. 22 (8), 887 (1993).
16. J. Sheng, L. Wang, G. E. Lux, and Y. Gao, presented at the 1996 Workshop on the Physics and Chemistry of II-VI Materials, Las Vegas, NV, 1996 (to be published in J. Electr. Mater.).

OFF-AREA BONDING OF HgCdTe PHOTOCONDUCTIVE INFRARED DETECTORS USING TRI-LAYER PHOTOLITHOGRAPHY AND WET/DRY ETCHING TECHNIQUES

Sridhar Manthripragada, Kelley Hu*, Frank Peters, Andre Burgess, Sachidananda Babu**, Jack (Zhiqing) Shi*, Danny Krebs, D. Brent Mott, Peter Shu.

NASA Goddard Space Flight Center, Code 718, Greenbelt, MD 20771
*Hughes STX Corp., Lanham, MD 20706
**Ball Aerospace and Technology Corp., Broomfield, CO 80038

ABSTRACT

On-area wire bonding of HgCdTe photoconductive (PC) infrared detectors usually causes material damage underneath the bonding pads. Such damage may propagate into the active area, potentially degrading performance and posing long-term reliability problems. Some off-area bonding fabrication techniques can also induce some degree of semiconductor material damage. In this paper, we report a relatively straightforward off-area bonding scheme that solves these problems. The process uses multiple photolithography and chemical etching steps to create a continuous slope or staircase in the HgCdTe leading down to the epoxy surface. The staircase ensures smooth step coverage for the subsequent metalization. Tri-layer photolithography (resist /metal/resist) and reactive ion etching (RIE) is then used to remove the epoxy in the bonding pad area. Since all areas other than the pad region are protected by the metal film, no RIE radiation damage is induced to the active area. The contact metalization is achieved by using standard liftoff techniques. Our so called staircase off-area bonding fabrication technique can be used to fabricate highly reliable, high density, small-size, detector arrays.

I. INTRODUCTION

The long term reliability of photoconductive (PC) HgCdTe infrared detectors used for space flight applications has always been a concern. Wire bonds on PC HgCdTe detectors, which are a potential weak point in the mechanical integrity of the device, need to withstand the extreme conditions experienced by the spacecraft.

Typical PC detector fabrication involves permanently mounting a HgCdTe wafer onto a substrate with epoxy [1]. The wafer is lapped and polished to a thickness of about 10 microns. After element delineation, contact metalization is applied using standard liftoff techniques. On-area or off-area bonding is then applied to the metal contacts. On-area bonding, shown in Fig. 1(a), refers to bonding on metal that is directly on top of the HgCdTe material. Off-area bonding, shown in Fig. 1(b), refers to bonding on metal that is on top of the substrate.
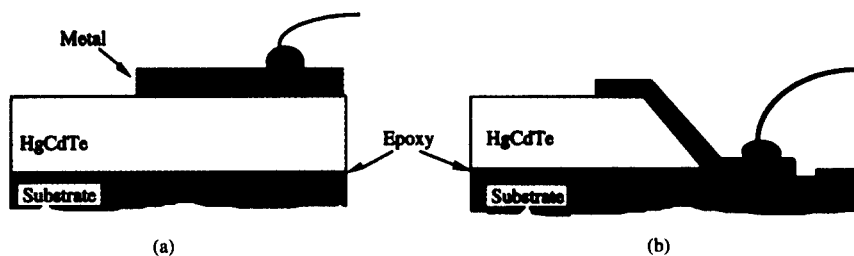
Fig. 1 (a) On-area wire bonding, (b) Off-area wire bonding

On-area wire bonding of PC HgCdTe detectors usually causes semiconductor material damage underneath the bonding pads. Fig. 2 shows crater-like damage caused by on-area wire bonding. Such damage poses long-term reliability problems and potentially introduces noise that degrades the detector performance. To partially mitigate such damage, one has to compromise on the bonding wire size and the force applied for bonding, thus leading to a substantial reduction of bond strength. Using an off-area bonding scheme solves most of these problems.
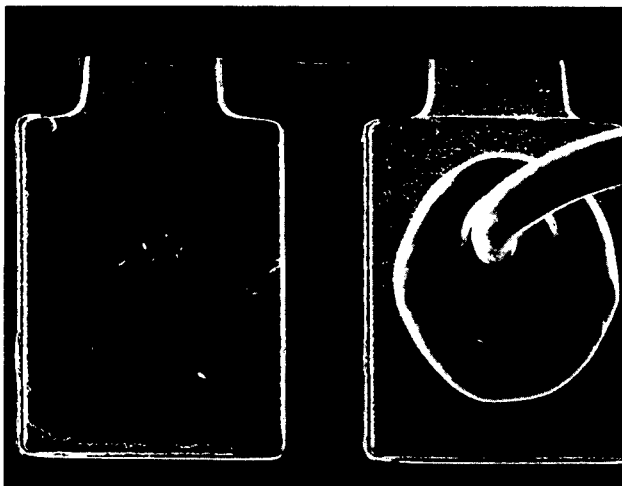
Figure 2 Crater-like damage caused by on-area wire bonding

Off-area wire bonding does not take place on top of the semiconductor; hence, material damage is not an issue. In this case, the bonding is supported by a strong substrate; therefore, a larger diameter bonding wire and greater bonding force can be applied to make the metalization

302

scheme extremely robust. However, off-area bonding techniques can also induce some degree of semiconductor material damage.

II. STAIRCASE OFF-AREA BONDING

We have devised a relatively simple processing recipe for off-area bonding. We have successfully demonstrated the fabrication of a prototype detector using standard photolithography, and wet/dry chemical etching. The process creates a smooth transition in the HgCdTe leading down to the epoxy surface without damaging the semiconductor material. The so called staircase off-area bonding fabrication technique can be easily implemented into an existing process and can be used to fabricate highly reliable, high density, small-size, detector arrays.

The process begins by permanently mounting a HgCdTe wafer onto a substrate with epoxy. The wafer is lapped and polished to a thickness of about 10 microns, (see Fig. 3a). The elements or arrays are delineated using wet chemical etching, (see Fig. 3b). Using a photomask and standard photolithography, the HgCdTe on the edges of the detector is exposed and partially etched, (see Fig. 3c). A second photolithography step exposes the etched area of the edge and some previously unetched HgCdTe. The second etch creates a continuous slope or staircase in the HgCdTe leading down to the epoxy surface, ensuring smooth step coverage for the subsequent metalization, (see Fig. 3d). Tri-layer technique is then used to remove the epoxy in the bonding pad area (see Fig. 3e). This process consists of spinning on and thoroughly baking a thick layer of photoresist, depositing a thin metal film, such as a 2000Å layer of gold, and

a) Lap & Polish HgCdTe to ~10 microns

b) Photomask and Delineate

c) Use first step mask and etch

d) Use second step mask and etch again

e) Use tri-layer lithography and dry etching to etch epoxy

f) Metalize by liftoff

g) Apply off-area wire bonding
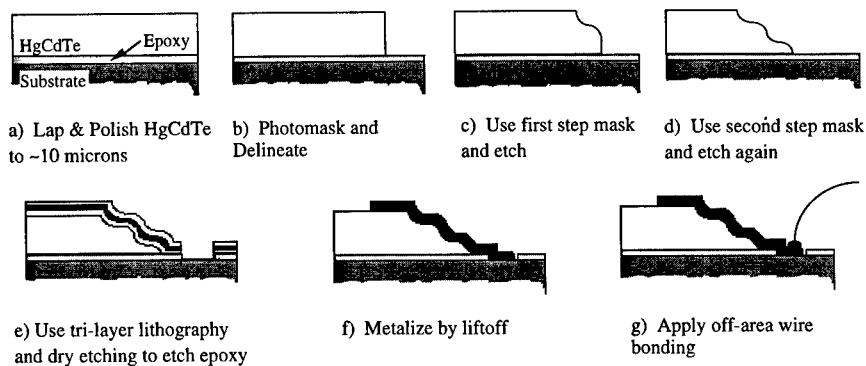
Fig. 3 Detector fabrication sequence using staircase off-area bonding scheme

finally spinning on and soft-baking a second layer of photoresist directly on top of the gold film. Standard photolithography is used to remove the photoresist from the bonding pad area. Wet chemical etching removes the intermediate gold layer. Reactive ion etching (RIE) is then used to remove the first layer of photoresist and the epoxy. The processing conditions include using: an

oxygen plasma, a power of 100W, an operating pressure of 200 mTorr, and an etch time of 20 minutes. Since all areas other than the pad region are protected by the gold film, there is no RIE damage to the detector material. Any standard oxygen plasma asher would be sufficient to reproduce this step. Next, the remaining gold film is stripped off by a simple acetone spray. The contact metalization is achieved by using standard liftoff techniques, (see Fig. 3f). Finally, the device is wire bonded, (see Fig. 3g). The staircase off-area bonding fabrication process described here is not limited to HgCdTe devices. By using the appropriate etchant, this process can be extended to other semiconductor material based devices.

III. TEST DATA

After device fabrication, gold wire bonding is achieved using an ultrasonic wire bonder. Since the wire bonding is directly on the substrate, there is no limit to the maximum acceptable wire diameter that can be used. For the purposes of this test, 1.25 mil diameter gold bonding wire was used. Destructive wire pull tests showed that a 12-14 gram pull was necessary to break the bond. On-area bonding, which is typically limited to 0.7 mil diameter bond wire, has a significantly lower bond strength of 3-4 grams. Table I lists a comparison between typical on-area and the staircase off-area bonding schemes.

Table I Comparison between typical on-area and the staircase off-area bonding schemes.

Bonding Parameter	Staircase Off-area Bonding	On-area Bonding
Maximum acceptable wire size	No limit	Less than 1 mil
Typical bonding strength	12-14 grams using 1.25 mil bonding wire	3-4 grams using 0.7 mil bonding wire
Bonding force	No limit	Limited by semiconductor material properties

To check the mechanical integrity of the metalization under adverse thermal conditions, the devices were subjected to thermal cycling. The detectors were cycled from liquid nitrogen to room temperature 30 times.

Fig. 4 shows a plot of current vs voltage in the operating range of the device. Using a Keithley 236 programmable current/voltage source, the I-V characteristics of the device were measured to verify the metal contact continuity. As expected, the I-V plot is linear, indicating ohmic contacts. The plot also shows a 5 Ohm change in resistance before and after temperature cycling. This device had not undergone a standard metal contact stabilization anneal prior to the temperature cycling, hence, the minor change in resistance can be attributed to a decrease in contact resistance at the metal-semiconductor interface.
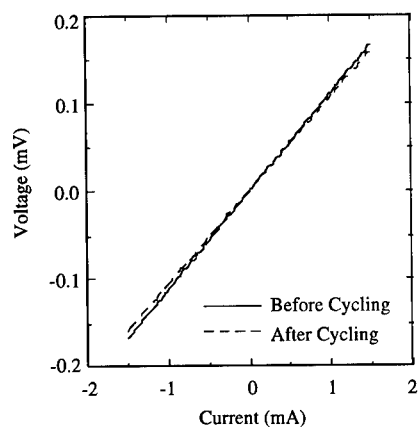
Fig. 4 Current and voltage plot of device before
and after thermal cycling.

Fig. 5 shows a scanning electron microscope (SEM) photo of the GOES-like HgCdTe
detector after the thermal cycling [2]. The metalization of this prototype device, deposited by
sputtering to only 0.8 μm thickness, is continuous and remains robust. The step coverage over
the leg could be further improved by increasing the overall metal thickness.
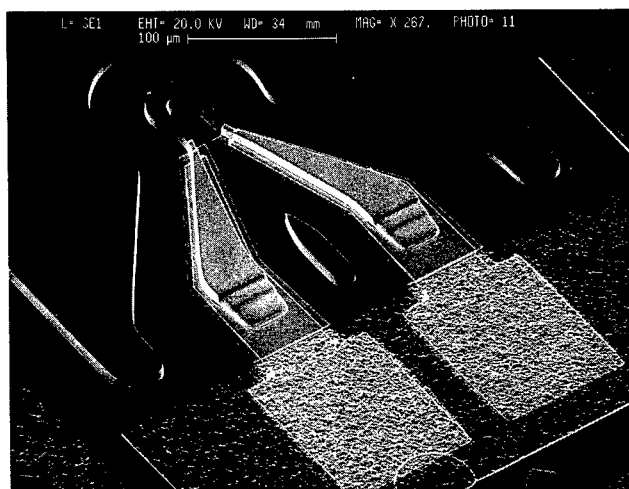
Fig. 5 SEM photo of GOES-like HgCdTe detector [2] using staircase off-area bonding fabrication technique .

IV. CONCLUSIONS

In summary, we have developed a reliable processing recipe, using tri-layer photolithography and wet/dry chemical etching, for the fabrication of PC HgCdTe infrared detectors with off-area bonding. The staircase off-area bonding process allows for the fabrication of highly reliable detectors for commercial, military, space or remote sensing applications. In addition, this process is not limited to HgCdTe devices. By using the appropriate etchant and tailoring the number of steps in the staircase according to the semiconductor substrate thickness, it can also be used for the fabrication of other types of semiconductor laser, detector, or modulator devices, where on-area or other off-area bonding is currently being used.

ACKNOWLEDGMENTS

REFERENCES

1.   R. Martineau, K. Hu, S. Manthripragada, C. Kotecki, S. Babu, F. Peters, A. Burgess, D. Mott, D. Krebs, S. Graham, A. Ewin, A. Miles, V. Bly, T. Nguyen, J. McCloskey, and P.Shu in HgCdTe Detector Technology and Performance for the Composite Infrared Spectrometer (CIRS)/Cassini Mission, edited by L. Horn, (SPIE Proc. 2803, Denver, CO, 1996) pp. 178-186.

2.   R. Martineau, K. Hu, S. Manthripragada, J. Shi, C. Kotecki, F. Peters, A. Burgess, D. Krebs, R. Johnson, D. Mott, and P.Shu in High Performance HgCdTe Infrared Detectors for the GOES Long-Wave Sounder, edited by E.R. Washwell, (SPIE Proc. 2812, Denver, CO, 1996) pp. 490-500.

Part V

Nonlinear and Parametric Oscillator Material

INELASTIC LIGHT SCATTERING IN ZINC GERMANIUM DIPHOSPHIDE CRYSTALS

B.H. BAIRAMOV*, V.K. NEGODUYKO*, YURRI V. RUD*, V.V. TOPOROV*
V.A. VOITENKO**, P.G. SCHUNEMANN***, N. FERNELIUS****, M.C. OHMER****,
H.E. JACKSON*****
*Department of Solid State Physics, A.F. Ioffe Physico-Technical Institute, Russian Academy of
  Sciences, 194021, St. Petersburg, RUSSIA, bairamov@bahish.ioffe.rssi.ru
** Department of Physics, State Technical University, 195251, St. Petersburg, RUSSIA
***Lockheed Sanders Inc., Nashua, NH, USA
****Air Force Wright Laboratory, WL/MLPO, Wright-Patterson AFB, OH, USA
*****Department of Physics, University of Cincinnati, Cincinnati, OH 45221-0011, USA

ABSTRACT

   The inelastic light scattering spectra of chalcopyrite structure $ZnGeP_2$ crystals grown by an
improved low temperature crystallization from the nonstoichiometric solution of this compound
in the liquid Bi or liquid Tl solutions as well as grown by high temperature Bridgman technique
has been investigated together with the optical absorption and electron transport measurements.

INTRODUCTION

   Recently, it has been demonstrated that the investigation of the quasielastic light scattering in
the near infrared spectral range from free carriers in doped III-V semiconductors allows one to
define a lot of information on both the parameters of the band structure as well as the kinetic
characteristics of the current carriers [1-6].
   A natural extension in the search of quasielastic electron light scattering is to examine ternary
compounds exhibiting tetrahedral coordination. Ternary chalcopyrite structure $II-VI-V_2$
compounds are currently of technological interest. They show promise for practical application
for a wide spectral range optoelectronic devices [7-10]. Quasielastic light scattering from free
carriers in chalcopyrite structure compounds are also of interest from a fundamental point of
view since the chalcopyrite structure can be regarded as the simplest ternary analogs of the binary
zincblende structure III-V compounds. They can be derived from the binary phases by ordered
substitution of the Groups II and IV atoms for the Group III atoms.
   An especially good candidate most promising for practical nonlinear optical applications in the
areas of optical parametric oscillators and upconverters in the mid infrared range is the
chalcopyrite structure crystal $ZnGeP_2$ [8-10].
   In this paper, we develop a theoretical model for the free-electron-(hole) gas fluctuations for
the low- concentration limit under the condition of strong screening and derived explicit
expressions for quasielastic light-scattering cross sections. We examine the quasielastic light
scattering from current carriers excitations in the low-concentration n-InP samples. We used
these data as a good model system to study the low temperature (LT) grown from the
nonstoichiometric solution as well as grown by high temperature (HT) directional solidification
from stoichiometric melts and by Bridgmen (nearly stoichiometric) techniques $ZnGeP_2$ single
crystals. with the lowest pseudodirect energy gap of 1.99 eV at room temperature (RT) and n-
InP crystals, isoelectronic analogue of $ZnGeP_2$, with direct energy gap of 1.56 eV (at RT) by
using nonresonant near-infrared excitation with photon energies $\hbar \omega_i$ = 1.17 eV. The absence of

309

an intense background hot luminescence has provided us with an opportunity to carry out quasielastic light scattering measurements in the low frequency range close to the laser line.

THEORY OF QUASIELASTIC ELECTRONIC LIGHT SCATTERING

Spectral lineshape for quasielastic light scattering spectra from charge density fluctuations for small free carrier concentrations

The energy and momentum conservation laws for the elementary process of quasielastic electronic light scattering have the form

$$E_{p'} - E_p = \hbar (\omega_i - \omega_s) = \hbar \omega$$
$$p' - p = \hbar (k_i - k_s) = \hbar q. \tag{1}$$

Here E_p the energy of electron with quasimomentum p; (ω_i, k_i) and (ω_s, k_s) are frequencies and wave vectors of the incident and scattered light, respectively; $\hbar \omega$ and $\hbar q$ are energy and momentum transfer during the scattering process. The energy and momentum transfer are small for scattering by free carriers and there is no electronic scattering if in Eqs. (1) one takes $q = 0$. This is the reason why this type of scattering is called quasielastic.

The scale of quasielastic electronic scattering is set by the squared classical radius of the electron $r_0 = e^2/mc^2 = 2.82 \times 10^{-13}$ cm. This quantity is small which makes the observation of quasielastic electronic scattering very difficult.

The direct information on the spectral lineshape for quasielastic electronic light scattering can be obtained from the integrated light scattering cross section [2]

$$\frac{d^2\Sigma}{d\omega \, d\omega} = \frac{V\omega_i \omega_s^3}{2\pi c^4} \left(e'_k e'_j\right)\left(e'_i e'_n\right)^* < \delta\chi_{ij} \, \delta\chi_{kn} >_q, \tag{2}$$

where the space Fourier component of the equal-time correlation function is

$$< \delta\chi_{ij} \, \delta\chi_{kn} >_q = \int < \delta\chi_{ij}(r)\delta\chi_{kn}(0) >_q e^{-iq \cdot r} d^3r. \tag{3}$$

Further simplifications at high temperatures $T \gg \hbar \omega$ are possible, because classical fluctuations are usually uncorrelated. The correlation function from Eq. (3) then reduces to mean-square fluctuations of basic thermodynamic quantities.

In the case of semiconductors with low concentrations of current carriers and nondegenerate band structure like n-GaAs and p-ZnGeP$_2$ (for which within the quasicubic model the triple degeneracy of the p-like valence band Γ_{15} removed and splits into a nondegenerate level Γ_7 lying above a nondegenerate Γ_6 and Γ_7 levels due to simultaneous effects of the noncubic crystalline field and spin-orbit interaction) the quasielastic light scattering cross section reduces to the Thompson cross section. In the resulting cross section the mass of the free electron is replaced by the effective mass of current carriers.

The spectral lineshape of quasielastic electronic scattering depends on the type of the fluctuations from which scattering occurs. In our case of the low concentrations of free carriers the charge density fluctuations are responsible for the quasielastic electronic scattering. The important aspect of the discussion of quasielastic electronic scattering of light by charge

excitations is the electronic screening of fluctuations. If the concentrations of current carriers is low and the screening radius r_s is large enough to satisfy the following condition

$$q\, r_s >> 1, \qquad (4)$$

then excitations with the wave vectors q are not screened. When there is no screening the single particle fluctuations of the charge density, δn, are the most important in the process of quasielastic scattering. Light is scattered by the single particle excitations only and there are now collective plasmon excitations. The corresponding contribution to the electron susceptibility tensor has the form

$$\delta \chi_{ij} = -\frac{e^2}{m\omega_i^2}\mu_{ij}\delta n. \qquad (5)$$

Here the tensor $\mu_{ij} = m\gamma_{ij}^{\xi\xi}$ is defined by the matrix $\gamma_{ij}^{\xi\xi}$. Diagonal components of the matrix $\gamma_{ij}^{\xi\xi}$ describe intraband scattering . The spatial Fourier component of the electronic density fluctuations δn has the form

$$\delta n = \sum_{\alpha} \exp[iqr_{\alpha}(t)]. \qquad (6)$$

Substitution of Eqs. (6) and (4) to (2) leads to the integrated light scattering cross section given in terms of the correlation function $<\delta n^2>_{q,\omega}$. The correlation of charge density fluctuations (6) is important for separations r large than r_s only. In the opposite case (4), when $r \sim q^{-1} << r_s$, the charge density fluctuations are uncorrelated. There is no interference of the electromagnetic waves, which are scattered from different carriers. The resulting cross section takes the form

$$\frac{d^2\Sigma}{d\omega\, d\omega} = Vr_0^2\left|e_i^I\,\mu_{ij}\,e_j^{s*}\right|^2 n\,\mathrm{Re}\frac{1}{\pi}\int_0^{\infty} d\tau\, e^{i\omega\tau} < e^{iq\Delta r(\tau)}>. \qquad (7)$$

Here $\Delta r(\tau) = r(t+\tau) - r(t)$ is the displacement of the electrons, which is determined by the electron kinematics.

After taking into account the long-range fluctuations in the impurity potential and the integration, one gets the light scattering cross section in the form

$$\frac{d^2\Sigma}{d\omega\, d\omega} = nV\left(\frac{e^2}{m*c^2}\right)^2 (e^I\cdot e^s)^2 \int_{-\infty}^{\infty}\frac{dt}{2\pi}\cos\omega t\,\exp\left\{-\left[\frac{1}{2}(qv_T t^2) + \frac{\rho_0\,q^2 t^4}{24\,m*^2}\right]\right\}, \qquad (8)$$

where $v_T = 2T/m*$, and ρ_0 is mean square fluctuations of the electron chemical potential. If the mean square fluctuation is neglected in Eq. (8), the integration over t leads to the well known Gaussian contour of the quasielastic electronic light scattering spectrum

$$\frac{d^2\Sigma}{d\omega\,d\omega} = nV\left(\frac{e^2}{m^*c^2}\right)^2 (e^I \cdot e^S)^2 \frac{n}{qv_T}\exp-\left(\frac{\omega}{qv_T}\right)^2, \tag{9}$$

where, line width $\Gamma_G = qv_T$. This cross section is well known in classical atomic plasmas. It is apparent that the width of the light scattering cross section [Eq. (9)] reflects the distribution of particle velocities and depends on the fluctuation potential ρ_0, i.e. on the concentration of impurities n.

EXPERIIMENT ASPECTS

Our inelastic light scattering measurements were performed by using as an excitation source the 1064.2 nm line of a cw Nd^{3+}:YAG laser. The scattered light was analyzed by a double grating monochromator with a spectral resolution of 2.1 cm^{-1} and detected with a cooled photomultiplier tube with a photon-counting electronic system. To avoid sample heating effects the incident laser power was maintained at a sufficiently low level of less than 20 mW which was found insufficient to affect the detected spectra.

The LT $ZnGeP_2$ single crystals were obtained by method of vertical bottom-seeded solution growth with the crystallization temperature in the range of 700-750 ^0C which is rather low than the sphalerite-chalcopyrite phase transition temperature [7]. The samples were parallelepipeds oriented along [100] and [001] directions. Our X-ray microprobe study of the LT grown $ZnGeP_2$ single crystals have revealed the same parameters as for samples grown by standard HT method from the directional solidification from stoichiometric melts [8]and by Bridgman (nearly stoichiometric) techniques [9-10].

RESULTS AND DISCASSION

All the LT grown $ZnGeP_2$ samples exhibited p-type conductivity as for the HT grown $ZnGeP_2$ single crystals [8-10]. In Fig. 1 we show the temperature dependence of the hole concentrations for the LT grown p-$ZnGeP_2$ single crystals obtained from liquid <Bi> and <Tl> solutions.
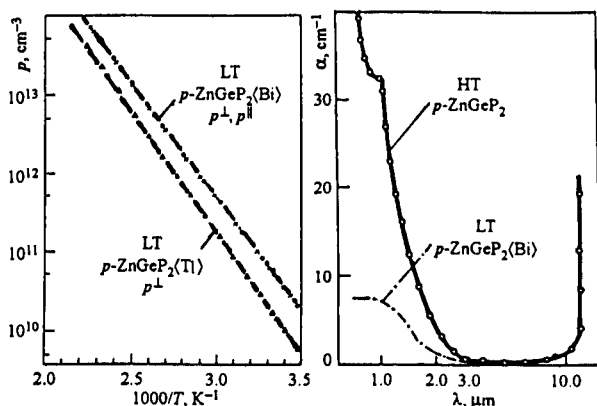
Fig. 1. Temperature dependence of the hole concentrations of the two LT grown p-$ZnGeP_2$ <Bi> and <Tl> samples. Symbols: × and Δ for $p^{\parallel}$, and o for $p^{\perp}$.

Fig. 2. Optical absorption spectra of the LT grown $ZnGeP_2$ <Bi> and HT grown p-$ZnGeP_2$ single crystal obtained by standard technique.

The activation energy $E_A \approx 0.55$ eV for $p = 1.0\times10^{10}$ cm^{-3} at RT is characteristic for deep acceptors. We found that the Hall coefficients and electrical conductivity of the LT grown

ZnGeP$_2$ single crystals were isotropic. This means that the tetragonal compression along the [001] direction is not enough to cause measurable anisotropy of the Hall mobility.

Figure 2 shows the comparison of the optical absorption spectra of the LT and HT grown p-ZnGeP$_2$ single crystals. It is evident that the band edge absorption of the LT grown p-ZnGeP$_2$ single crystals approximately 4 times less. Figure 3 shows typical near infrared quasielastic electronic light scattering spectra observed from doped n-InP samples, binary analogue of ZnGeP$_2$, for different concentrations for polarized scattering configuration. The solid curves are obtained by the subtraction of the two-phonon contributions. Gaussian fit according to Eq. (8) is shown by dots.
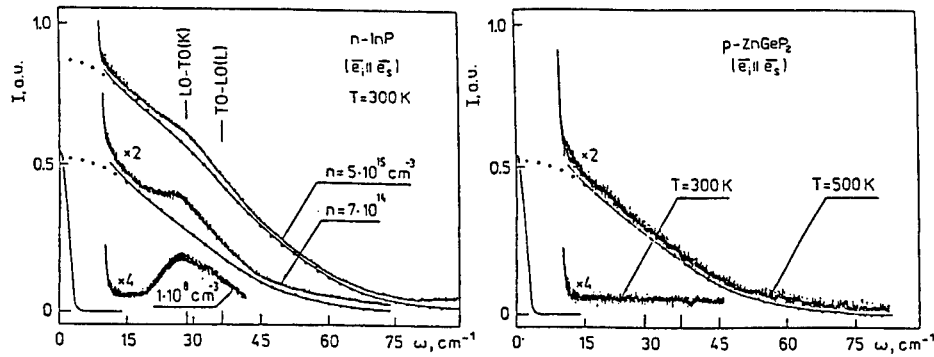
Fig.3. Quasielastic electronic light scattering spectra of n-InP samples in the low concentration range for different concentrations. The excitation of the spectra were performed with laser photon energies $\hbar \omega_i = 1.17$ eV.

Fig. 4. Quasielastic electronic light scattering spectra observed at RT and T = 500 K from the LT grown p-ZnGeP$_2$ single crystal obtained from liquid <Bi> solution. $\hbar \omega_i = 1.17$ eV.

The properly polarization behavior of the Raman scattering spectra obtained from the long-wavelength optical phonons and the sharpness of the lines with the denconvoluated values of full width at half intensity of 1-3 cm^{-1} indicated on high crystalline quality of the LT grown ZnGeP$_2$ single crystals. The typical results of our study of near infrared quasielastic light scattering observed for polarized scattering configuration at RT and T = 500 K for the LT grown ZnGeP$_2$ single crystal obtained from liquid <Bi> solution are presented in Fig. 4. The distortion of the low-frequency occurs at higher temperatures. Temperature was obtained from the Stokes-anti-Stokes intensity ratio. The shape of the spectra at T = 500 K show a new remarkable behavior which is very similar to the ones found in this scattering configuration for n-type InP samples in the low-concentration range (Fig. 3). The analysis of the Gaussian fit of the observed spectral line shape according to Eq. (8) is particularly accurate and similar to that shown in Fig. 3. All these findings strongly suggest that the distorted spectrum arises from the quasielastic light scattering due to the holes charge density fluctuations.

CONCLUSIONS

We have developed a theoretical model and derived an explicit expression for the quasielastic electronic light-scattering cross sections due to the charge density fluctuations under

the condition of rare collisions. We have demonstrated the first direct comparison with experimental results for temperature dependencies of the spectral line shapes for the quasielastic light scattering spectra induced by free hole gas. The experimental verification is performed on the low-concentration n-InP samples, which under the realization of the condition of non-resonant near-infrared excitation when $\hbar \omega_i \leq E_g$, served as a well controlled model system, as well as on the LT grown p-ZnGeP$_2$ single crystals obtained from liquid <Bi> solution. Finally, the theoretical approach to the problem and the observed results provide clear evidence for the existence of strongly temperature-dependent free-hole gas fluctuations and proves the observation of quasielastic light scattering from charge-density fluctuations.

ACKNOWLEDGMENT

REFERENCES

1. B.H. Bairamov, V.A. Voitenko, I.P. Ipatova, and V.V.Toporov, Proceedings of the International Conference Held in Connection with the Celebration of Birth Century C. V. Raman and Diamond Jubilee of the Discovery of Raman Effect, edited by C.P. Banerjee and S.S. Jha, Calcutta, World Scientific, Singapore, 1989, pp. 386-393.

2. B.H. Bairamov, I.P. Ipatova, and V.A. Voitenko, Phys. Reports, **229**, 221 (1993), Phys. Usp. **36**, 392 (1994), [Usp. Fiz Nauk, **163**, 67 (1993)].

3. B.H. Bairamov, V.A. Voitenko, I.P. Ipatova, V.K. Negoduyko, and V.V.Toporov, Phys. Rev. B, **50**, 14923 (1994).

4. B.H. Bairamov, V.A. Voitenko, I.P. Ipatova, V.K. Negoduyko, and V.V.Toporov, Semiconductors, **28**, 531 (1994), [Fiz. Tekh. Poluprovodn. **28**, 913 (1994)].

5. O. Paetzoldt, G. Irmer, J. Monecke, V.V. Toporov, and B.B. Bairamov, Semicond. Sci. Technol. **9**, 81 (1994).

6. B.H. Bairamov, V.A. Voitenko, V.V.Toporov, G. Irmer, and J. Monecke, Proceedings of the International Conference on the Physics of Semiconductors, Berlin, (1996) (accepted for publication).

7. J.L. Shay, and J.H. Wernick, Ternary Chalcopyrite Semiconductors: Growth, Electronic Properties, and Applications, edited by B.R. Pumplin (Pergamon Press, Oxford, 1975), p.244.

8. Yu.V. Rud', Semiconductors, **28**, 1105 (1994), [Fiz. Tekh. Poluprovodn. **28**, 633 (1994)].

9. J.E. McCrae, Jr., M.R. Gregg, R.L. Hengehold, Y.K. Yeo, P.H. Ostedeik, M.C. Ohmer, P.G. Schunemann and T.M. Pollak, Appl. Phys. Lett. **64**, 3142, (1994).

10. N.C. Giles, L.E. Halliburton, P.G. Schunemann, and T.M. Pollak, Appl. Phys. Lett. **66**, 1758, (1995).

MELT GROWTH OF ZnGeP$_2$:
HOMOGENEITY RANGE AND THERMOCHEMICAL PROPERTIES

S. FIECHTER *, R.H. CASTLEBERRY **, M. ANGELOV ***, K.J. BACHMANN **
*Department of Solar Energetics, Hahn Meitner Institute, Glienicker Str. 100,
D-14109 Berlin, Germany, fiechter@hmi.de
**Department of Materials Science & Engineering, North Carolina State University, Raleigh, NC 27695
***Institute for Physics, Technical University, D-98684 Ilmenau, Germany

ABSTRACT

ZnGeP$_2$ crystallized from the melt via horizontal gradient freezing shows the tendency to decompose into Ge and GeP when the equilibrium vapor pressure is not exactly controlled during the entire crystallization process. Using differential thermal analysis (DTA) it was found that ZnGeP$_2$ has a truly congruent melting point of 1311 K. Adding small amounts of the elements and binaries in the ternary system Zn-Ge-P to stoichiometric ZnGeP$_2$ a significant deflection of the liquidus curve was observed at the melting point of ZnGeP$_2$. From DTA, X-ray diffractometry (XRD), photoluminescence (PL), transmission and conductivity measurements it was concluded that the melt grown material was highly compensated. The presence of a broad acceptor and donor band in the band gap could be associated with phosphorous and zinc point defects in the crystal lattice. It is assumed that the defect concentrations are of the order 10^{19} cm^{-3}.

INTRODUCTION

ZnGeP$_2$ crystallizes in the chalcopyrite structure (S.G. I$\bar{4}$ 2d) which can be inferred from the sphalerite lattice by doubling the unit cell of ZnS and ordering the cation lattice. This ordering provoces a small distortion in the direction of the c-axis which substantially affects the optical properties such as birefringence (0.36%) and the direct band gap of 2.34 eV at room temperature. The non-linear optical properties can be used for optical parametric oscillators and for frequency mixing. To gain a high yield from such optical devices a chalcopyrite material of high transparency is in demand, which can only be obtained by a close control of composition during growth. Although the decomposition pressure at the melting point is around 3.5 bars [1] large crystals of high optical quality can be grown from the melt by gradient freezing.

In this paper we present results on the melting behaviour in the vacinity of stoichiometric ZnGeP$_2$ and on the thermal stability of this compound semiconductor. To get insight into the homogeneity range the grown material was investigated by x-ray diffractometry, conductivity and photoluminescence measurements.

EXPERIMENTAL

Crystal Growth

ZnGeP$_2$ was synthesized employing two zone melt synthesis which allows to produce single phase material of 35 g. Starting from the elements of high purity, zinc pellets and germanium lumps were posed into a glassy carbon boat which was placed into a quartz glass ampoule of 30 mm diameter and a length of 300 mm. Prior to evacuating and sealing, the related amount of red phosphorous was placed at the opposit end of the tube to obtain ZnGeP$_2$. In a two zone furnace both sides were heated separately. The carbon boat was brought to 1323 K within 3 h, the phosphorous side was increased to a slightly higher temperature over a period of 24 h to complete reaction under controlled pressure conditions. To prevent decomposition of the melt an additional amount of zinc and phosphorous was added to the ampoule before [2]. To crystallize the material a temperature gradient of 1.7 K/cm was applied along the boat and the temperature decreased by

315

Mat. Res. Soc. Symp. Proc. Vol. 450 ° 1997 Materials Research Society

0.15 K/h. The crystallized ingot was cut into wafers to perform X-ray diffractometry (XRD)-, differential thermal analysis (DTA)- and photoluminescence (PL)- measurements.

Differential Thermal Analysis (DTA) and Thermal Gravimetry (TG)

Melting behaviour and thermal stability were studied using a Netzsch Simultaneous Thermal Analysizer STA 409. Starting materials were stoichiometric $ZnGeP_2$ and mixtures of it with Ge, GeP, GeP_2, ZnP_2 and Zn_3P_2, respectively. Total amounts of 100 mg per run were sealed under vacuum in SiO_2 tubes (3 mm diameter, 10 mm length). The samples were placed in Pt-Ir crucibles in a sample supporting system, consisting of high temperature stable ceramics, and enveloped in platinum foil to ensure uniform temperature. A heating rate of 5 K/min was used. As internal standard the $\alpha \rightarrow \beta$ transition of quartz at 846 K was used as reference. Temperature data were reproducible with a consistancy of $\Delta T \leq 2K$. TG experiments were performed placing the samples in Al_2O_3 crucibles. The samples were heated under N_2 flow (1 bar, 100 sccm) to 1523 K using a heating rate of 5 K/min.

X-ray Diffractometry (XRD), Conductivity and Photoluminescence (PL)- measurements

A SIEMENS X-ray diffractometer D500/5000 with Cukα-radiation was used for XRD measurements. A 112-oriented $ZnGeP_2$ wafer was cut from a grown ingot, polished with diamond paste and etched in brom methanol for 60 s. A standard four point probe system was employed to measure the conductivity. Photoluminescence measurements were performed in an energy range from 0.8 to 2.6 eV varying the temperature T from 4.7 to 195 K, the excitation power P_{ex} from 1 to 300 mW and the excitation wavelength λ_{ex} from 472.9 to 514.5 nm. In the energy range from 0.8 to 1.2 eV a Ge-detector cooled by liquid nitrogen was used, in the range from 1.2 to 2.6 eV a Si-detector was employed.

RESULTS AND DISCUSSION

X-ray Diffractometry (XRD)

The XRD patterns of $ZnGeP_2$ samples were compared with the theoretical diffractogram which was calculated using the lattice constants a = 5.469 Å and c= 10.714 Å taking into account the specific geometry of the SIEMENS diffractometer.
It was found that XRD patterns of $ZnGeP_2$ obtained at the beginning of the horizontal gradient freezing process fitted the line intensities and positions of the ideal diffractogram at best (see Table I). This result also proves the high degree of ordering of the cation sublattice in the chalcopyrite phase. Disordering was detected by comparing the intensity ratio of the 200 and 004 reflexes of each sample with the standard. When in the following crystallization process the melt lost Zn and P in the % mole range Ge and GeP reflexes appeared in the XRD diagrams (figure 1). A disorder of the cation sublattice was observed when the Ge/GeP content succeeded 20 %mole. It is worth mentioning that GeP is a polymorphous material which can crystallize in at least six different modifications [3]. Under ambient conditions it appears in a monoclinic structure. In a $ZnGeP_2$ matrix GeP was stabilized in sphalerite structure a typical high pressure phase which can be obtained by reaction of the elements at 1673 K and 40 GPa [3]. From the XRD measurements the following thermal decomposition process for $ZnGeP_2$ can be described by the equation

$$ZnGeP_2 \Leftrightarrow Zn(g) + (1-x) Ge(c) + x GeP(c) + (0.5-0.25x)P_4(g) \qquad (1).$$

Differential Thermal Analysis (DTA)

In the figures 2 to 3, DTA heating traces are presented which illustrate the influence of GeP/Ge (ratio 5:1), Ge, GeP, GeP_2, ZnP_2 and Zn_3P_2 added to $ZnGeP_2$. The sample BG1-Z1, which

represents single phase material, has a melting peak at 1311 K. The heat of fusion attributed to this peak amounts to 55.2($\pm$ 8)kJ/mole. Solid-solid phase transitions as known from other chalcopyrites such as $CuInS_2$ could not be detected. Adding $\geq$0.25 %mole of the phases mentioned above the melting peak lowers by $\geq$2 K and broadened. Additional peaks appear which will be addressed as peritectic and eutectic temperatures. Adding zinc phosphides the occurrence of a shoulder attached to the left side of the melting peak is typical. Therefore, besides XRD the shape of the DTA traces can be applied to characterize the composition of the grown material.

The results of all measurements are summarized in a pseudobinary cut (figure 4). Remarkable is the deflection of the liquidus around $ZnGeP_2$ which proves that this ternary has a truly congruent melting point. In the work published by Buehler [4] this pronounced melting behaviour was not described. He used cooling curves to construct the phase diagram and the lower temperatures in his liquidus might be due to supercooling effects.

Decomposing a $ZnGeP_2$ powder in a N_2 flow (100 sccm) employing a thermobalance the material lost weight at temperatures higher than 973 K.
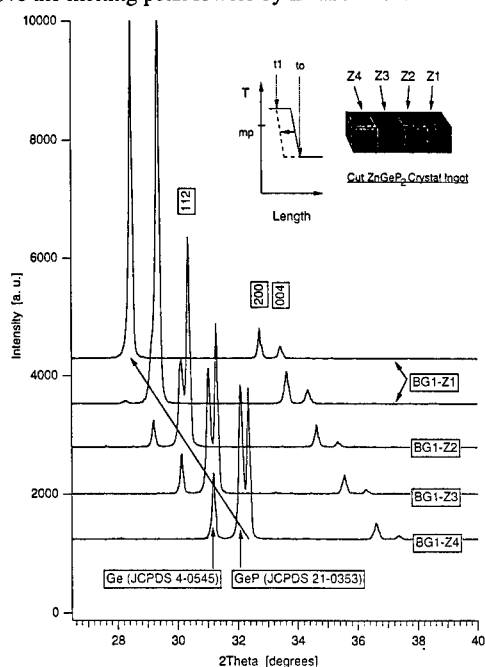
Figure 1. XRD patterns of $ZnGeP_2$-wafers cut from a crystal ingot in the sequence of crystallzation.
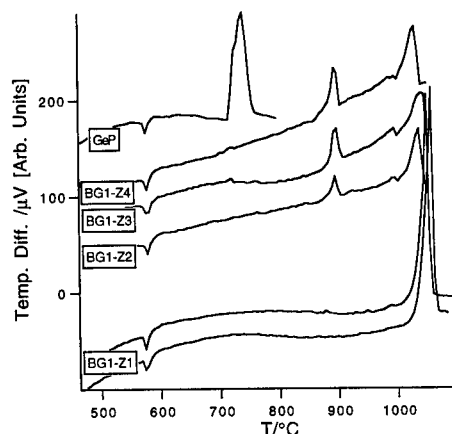
Figure 2. DTA heat traces of $ZnGeP_2$-wafer material cut from a crystal ingot in the sequence of crystallzation.
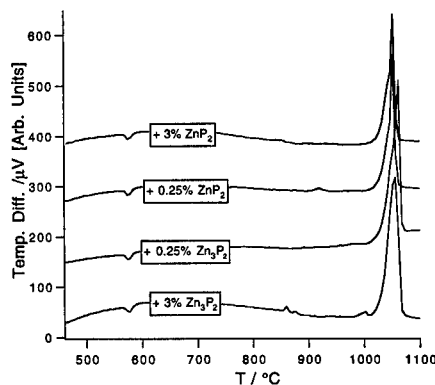
Figure 3. Melt behaviour of $ZnGeP_2$ adding 0.25 to 3 %mole of ZnP_2 and Zn_3P_2, respectively.
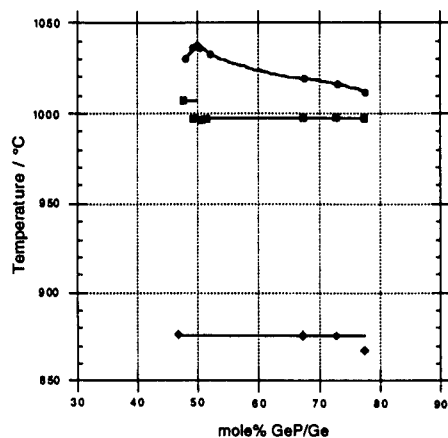
Figure 4. Section of the ZnP$_2$ - Ge/GeP pseudobinary phase diagram.

Table I. Calculated and measured intensities of theXRD lines in ZnGeP$_2$ (a = 5.469 Å, c = 10.714 Å).

hkl	Reflex Intensity (calculated)	Reflex Intensity (measured)
112	100	100
200	10	8.7
004	5	3.5
220	21	21.5
204	40	40.1
312	29	29.8
116	14	8.3
224	4	3.2
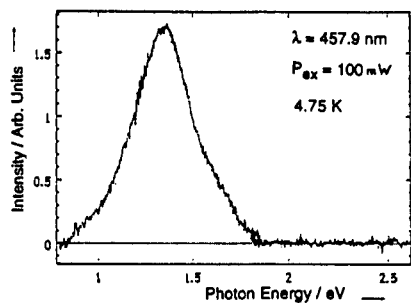
Figure 5. PL emission peak of a 112-oriented ZnGeP$_2$ wafer at T = 4.75 K.
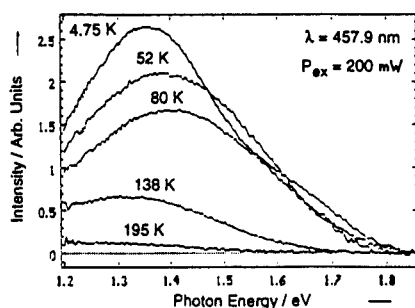
Figure 6. Shift of the emission peak of a ZnGeP$_2$ wafer with temperature.
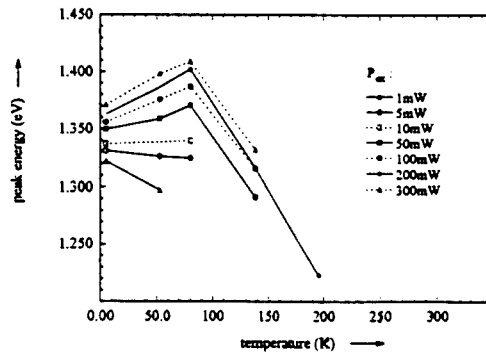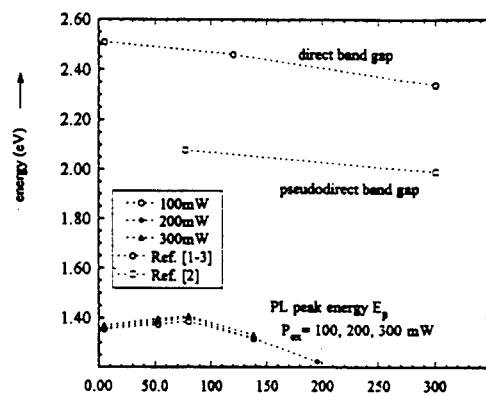
Figure 7. Dependence of the band gap shift of ZnGeP$_2$ with temperature and of the PL peak shift of the emission peak with temperature and excitation power.

Using a heating rate of 5 K/min the weight loss rate dm/dt was highest at 1203 K. At 1573 K decomposition was completed by $\geq 95\%$. The remaining material consisted of Ge and GeP.

To experimentally check the heat of formation ΔH^f of $ZnGeP_2$, which was in a foregoing paper [5] inferred from thermochemical calculations using vapor pressure data, the reaction $ZnP_2 + Ge$ was measured by DTA. The heat of formation inferred from these experiments was $-117.2(\pm 12)$ kJ/mole. This value indicates an exothermic contribution due to the ternary compound formation $\geq 5\%$ compared to the value with the heat of formation of ZnP_2 ($\Delta H^f = -101.1(\pm 4)$kJ/mole.

Conductivity and Photoluminescence (PL) Measurements

All samples were p-type and semi-insulating ($M\Omega$ range). In general, PL measurements showed a broad emission peak (fig. 5). In addition, a shoulder at the high energetic side of the broad band emission appeared when the excitation power was higher than 50 mW. This shape is in agreement with the findings of other authors [6]. The large full width half maximum of this broad emission peak points to the presence of wide acceptor and donor bands in the band gap which are involved in the radiative recombination of excited electron hole pairs. To verify this assumption the influence of the temperature, the excitation power and the excitation energy on the behaviour of the PL peak position was investigated. Figure 6 shows a typical series of curves with a shift of the peak maximum first to higher and with increasing temperature to lower energies. From figure 7 it can be concluded that this tendency only persists at excitation powers higher than 50 mW. The peak shift does not follow the temperature coefficient $\partial E_g/\partial T$ of the direct and pseudodirect band gap. Therefore it was concluded that the emission band is due to donor-acceptor states in the band gap, the recombination energy of which can be described by the equation

$$E_p = E_g - (E_A + E_B) + \frac{e^2}{4\pi\varepsilon_0\varepsilon_r \, r} \qquad (2)$$

where E_p is the maximum of the PL emission peak, E_g the band gap energy, E_A and E_B the acceptor and donor binding energies and ε_r the static dielectric constant. The last term in equation (2) describes the Coulomb interaction between ionized donor-acceptor pairs separated by the distance r on the emission energy. Only pairs, the distance of which are located in a limited interval contribute to the emission peak. The shifts of E_p to higher energies with increasing temperature can be explained with the migration of excited carriers to more favorate positions for radiative recombination which have a small r value. A positive temperature coefficient $\partial E_p/\partial T$ is observed. If the excitation intensities are too small only D-A pairs of larger distance r can contribute. The temperature coefficient $\partial E_p/\partial T$ becomes negative.

In the temperature range from 80 to 195 K at excitation energies ranging from 50 to 195 K E_p shifts to smaller energies which cannot be explained by a negative temperature coefficient $\partial E_g/\partial T$ alone. Under the assumption that the D-A pairs consist of a shallow and a deep state it can be concluded that thermal ionization of the shallow states occurs with increasing temperature which cannot longer contribute to radiative emission. Analysing the emission intensity as a function of temperature it was concluded that the shallow states are related to acceptors. By evaluation of the E_p vs. lg P_{ex} -plot using the equation

$$E_P = E_{P_0} + \beta \, lg(P_{ex}/P_{ex_0}) \qquad (3)$$

the β-values obtained amount to 18, 38.6 and 47.7 meV. Comparing these values with other compound semiconductors of chalcopyrite type structure their size supports again the proposed

defect model and is also in agreement with the high compensation level of the melt grown $ZnGeP_2$ crystals.

The low transparency of the crystal wafers which remain dark even at a thickness of 100 μm supports this result.

CONCLUSIONS

$ZnGeP_2$ grown by horizontal gradient freezing from the melt is highly compensated. In DTA measurements $ZnGeP_2$ exhibits a truly congruent melting point of 1311 K. No solid-solid phase transitions could be resolved in the DTA traces.In the band gap shallow acceptor and deep donor states dominate the PL behaviour. From the thermal dissociation behaviour of the compound where zinc and phosphorous will be released it can be concluded that the high compensation level, the low transparency and the broad PL emission is due to zinc and phosphorous vacancies in the $ZnGeP_2$ lattice.

REFERENCES

1. A.S. Borshchevskii, and T.M. Shantsovoi, Inorg. Chem. **11**, 1853 (1975).

2. S. Fiechter, R.H. Castleberry, N. Dietz and K.J. Bachmann in 7th Int. Symposium on Experimental Methods for Microgravity Materials Science, edited by. R.A. Schiffmann and J.B. Andrews (TMS, 1995) pp. 55-68.

3. J. Osugi, R. Namikawa and Y. Tanaka, Rev. Phys. Chem. Jpn. **37**, 81 (1967).

4. E. Buehler, J.H. Wernick and J.D. Wiley, J. Electron. Mater. **2**, 796 (1973).

5. S. Fiechter, R.H. Castleberry, G. Wood and K.J. Bachmann in 6th Int. Symposium on Experimental Methods for Microgravity Materials Science, edited by R.A. Schiffmann and J.B. Andrews (TMS, 1994) pp.93-100.

6. N. Dietz, I. Tsveybak, W. Rudermann, G. Wood and K.J. Bachmann, Appl. Phys. Lett.**65**, 2759 (1994); see also contribution O7.7 of this conference and references therein.

COMPOSITION OF THE EQUILIBRIUM VAPOR PHASE OVER ZnGeP$_2$ AND THERMAL STABILITY

S. FIECHTER *, A. KURZWEIL*, R.H. CASTLEBERRY ** AND K.J. BACHMANN **
*Department of Solar Energetics, Hahn Meitner Institute, Glienicker Str. 100, D-14109 Berlin,
Germany, fiechter@hmi.de
**Department of Materials Science & Engineering, North Carolina State University,
Raleigh, NC 27695-7919

ABSTRACT

ZnGeP$_2$ can be transported by chemical vapor transport (CVT) using phosphorus or ZnP$_2$ as transporting agent. Since germanium has a seven order of magnitude smaller partial pressure than zinc and phosphorus solely the formation of a volatile GeP$_y$ (y$\geq$1) species can explain the CVT-growth which was observed in a temperature range from 973 to 1573 K. To stabilize this species phosphorus pressures in the bar range are needed. Using absorption spectroscopy to analyze the equilibrium vapor phase composition over P, GeP and ZnGeP$_2$, absorption lines were found adjacent to P$_2$ band heads in the wavelength range from 180 to 260 nm which were addressed as band heads of an unknown GeP$_y$ species. Quadrupole mass spectroscopy (QMS) measurements revealed that this species is not stable at lower pressures decomposing presynthesized GeP and ZnGeP$_2$ in a Knudsen cell. In the temperature range from 550 to 800 K at total pressures of 10^{-7} to 10^{-6} mbar, ZnGeP$_2$ decomposes into Zn and P$_4$ whereas Zn is the dominant gas phase species. Under vacuum ZnGeP$_2$ starts to decompose at 600 K while in a N$_2$ atmosphere decomposition occurs at 923 K. By adding ZnP$_2$ (5mg/cm^3) to polycrystalline ZnGeP$_2$, which was placed in an evacuated and closed quartz glass ampoule, red transparent crystals were yielded in a temperature gradient $\Delta T = 1073\text{-}1023$ K.

INTRODUCTION

Among the I-III-VI$_2$ and II-IV-V$_2$ chalcopyrites ZnGeP$_2$ shows the highest transparency range (0.67 - 12 μm) combined with a relatively high second order susceptibility tensor component (d$_{36}$ = 75 pm/V) and a positive birefringence of 0.36%. Therefore, the material is suited for non-linear optical devices such as optical parametric oscillators. However, high quality material can only be obtained when the growth conditions are very well controlled. The formation of point defects in high concentrations can dramatically decrease transparency. Therefore, the equilibrium pressure over the growing crystal has to be adjusted very precisely. This is the more difficult the higher the growth temperature is, e.g. growing ZnGeP$_2$ from the melt at an equilibrium vapor pressure of ~ 3.5 bar. With increasing temperature the homogeneity range also increases. For that reason, the growth temperature should be as low as possible to obtain crystals of high transparency. Red transparent crystals can be grown by CVT employing phosphorus as transporting agent [1]. Xing et al. [2] have shown that by metal organic chemical vapor deposition (MOCVD) highly conductive, p-type films can be epitaxially deposited on 001-oriented GaP substrates using germane, phosphine and dimethyl zinc as precursors. The type of conductivity is caused by germanium antisites. Kataev et al. [3] grew homoepitaxial, p-type layers on 112-, 100- and 001-oriented ZnGeP$_2$ substrates using ZnCl$_2$ as transporting agent. The layers crystallized in the chalcopyrite lattice but had unusual high concentrations of Ge and Zn. Analyzing phase purity and composition of CVT-grown 112-oriented ZnGeP$_2$ crystals employing phosphorus or zinc diphosphide as transporting agent this method appears suited to produce stoichiometric material of high transparency. Since germanium possesses a far too low vapor pressure an unknown GeP$_y$ gas species has to be assumed to explain the transport rates observed ($\leq$ 3 mg/h).

In this paper we describe the conditions under which this unknown species is stable and investigate the temperature range in which CVT can be obtained. The aim of this work is to identify the conditions for a heteroepitaxial growth of ZnGeP$_2$ (a$_o$= 5.469 Å, c/a= 1.959) on a Si substrate (a$_o$= 5.451 Å).

EXPERIMENT

Optical Absorption Spectroscopy

In this work we used optical absorption spectroscopy to distinguish between different gas species over P(red), ZnP_2, GeP and $ZnGeP_2$. The setup to measure the absorption bands is illustrated in figure 1. A two zone furnace with integrated isothermal furnace liners provided a uniform temperature profile for the quartz glass cuvettes employed (50 and 100 mm length and 10 mm diameter). To overcome the so-called schlieren effect, which contributes to the noise level of the measurement by air turbulences in the heated furnace core, the cuvettes to be measured were placed between two empty quartz glass cuvettes. About 50 mg of the substances were filled into the evacuated and sealed sample cuvettes. Light of a xenon lamp was guided through the quartz glass cuvettes and focused onto the entrance slit of a monochromator using UV-grade quartz lenses. The light intensity was detected by a photomultiplier tube. More details are given in ref. [4].

Mass Spectrometry

The experimental setup is shown in figure 2. A Knudsen cell made from stainless steel with an orifice of 300 μm was filled with P, GeP and $ZnGeP_2$ (20-50 mg), respectively. The effusion cell was heated by a shielded resistance heater and the temperature was controlled by a NiCr/Ni thermocouple. The highest temperature applied was 1000 K. The vapor species formed by decomposition of the precursors were analysed by a quadrupole mass spectrometer (Balzers QMS 420) in cross beam configuration. The pressure in the chamber ranged from 10^{-7} to 10^{-5} mbar corresponding to the temperature of the material in the effusion cell.

Thermal Stability

Thermal stability was studied using a Netzsch Simultaneous Thermal Analysizer STA 409 equipped with a thermobalance. Starting material was stoichiometric $ZnGeP_2$. The total amount per run ranged from 50 to 100 mg. The samples were placed in Al_2O_3 crucibles and heated under N_2 (p = 1 bar, flow rate = 100 sccm) as high as 1523 K using a heating rate of 5 K/min. As internal standard the $\alpha \rightarrow \beta$ transition of quartz at 846 K was used as temperature reference.

CVT-Experiments

3 g pre-synthesized GeP and $ZnGeP_2$ samples were posed in evacuated and sealed quartz glass ampoules (l = 100 mm, $\varnothing$ = 30 mm) adding P or ZnP_2 ($\geq$ 5 mg/cm^3). The ampoules were placed in two zone furnaces and a vertical temperature gradient was applied ($ZnGeP_2$: ΔT =1073-1023 K; GeP: ΔT = 873-773 K).

RESULTS AND DISCUSSION

Absorption Spectroscopy and Mass Spectrometry

Screening the wavelength range from 150 to 1400 nm, absorption lines were only detected in the range from 180 to 270 nm. The detailed band positions were described in ref. [4]. Figure 3 shows the positions of absorption band heads which were attributed to an unknown GeP_y gas species in the equilibrium vapor phase over $ZnGeP_2$. These positions were obtained by carefully comparing the absorption band heads in the vapor phases over GeP, ZnP_2, P(red) and $ZnGeP_2$. Since nothing is known about the geometry of GeP_y gas species in the literature the unidentified UV-spectrum was compared with the spectra of P_2 and other Ge bearing gas species such as GeO and GeS [5]. GeS and P_2 have absorption bands in the same wavelength range as GeP_y. It is interesting to note that P_4 molecules did not show absorption lines in our measurements which were different from P_2 band heads although P_4 was dominant in the vapor phase as QMS measurements elucidated. Investigating the mass spectrum of the vapor phase over $ZnGeP_2$ at 673 K
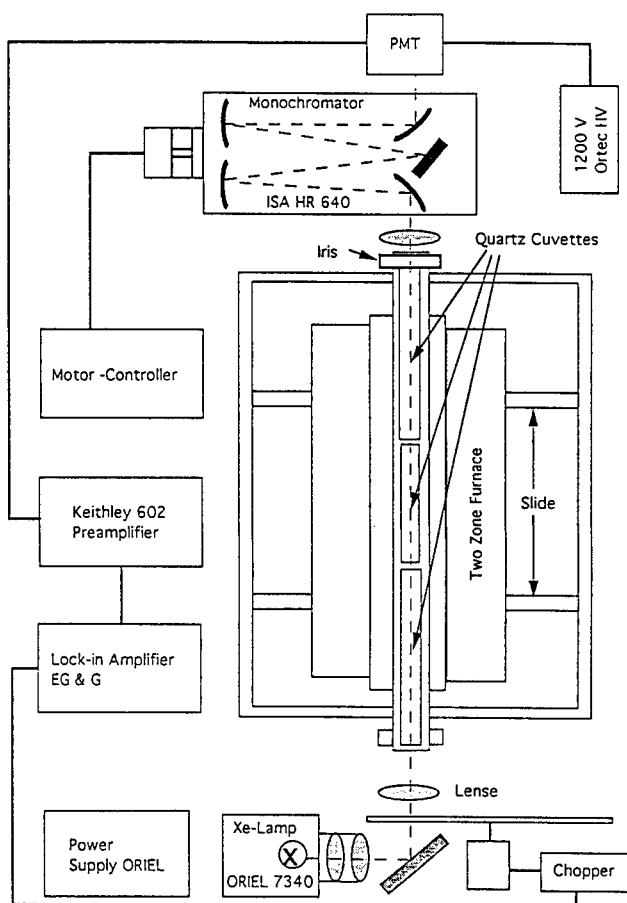
Figure 1. Experimental set-up to measure the optical absorption of the equilibrium vapor phases over $ZnGeP_2$, ZnP_2, GeP and P(red).

(figure 4) only the isotopic distribution of Zn^+ and P_4^+ were detected. The relatively high intensity of the Zn-lines points to fact that under annealing conditions - which can improve the transparency of $ZnGeP_2$ remarkably [6] - preferably zinc will be released.

The QMS measurements of GeP samples merely exhibited the lines of the ionized phosphorus species P_4^+, P_2^+, P_3^+ and P_4^+. This result indicates that the proposed GeP_y gas species, which is in demand to explain CVT of $ZnGeP_2$, is only stable at high pressures.

CVT-Experiments and thermal stability of $ZnGeP_2$

CVT of GeP was studied in a temperature gradient ranging from 873 to 823 K. The formation of a black GeP film in the colder part of the ampoule was noticed in a phosphorus rich atmosphere within 3 days. This phenomenon was first described by Zumbusch, Heimbrecht and Biltz in 1939 [7]. The experiment unequivocally demonstrates the existance of a GeP containing gas species.

323
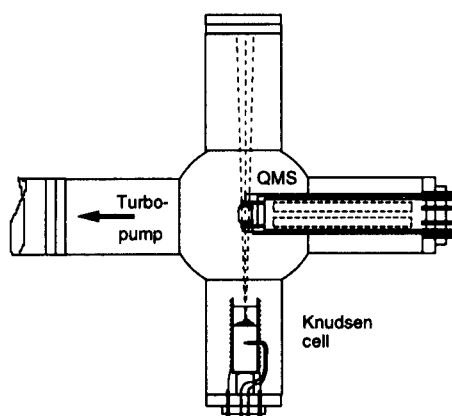
Figure 2. Experimental set-up to study the vapor phase composition by quadrupole mass spectroscopy. The gas molecules were generated using a Knudsen cell.
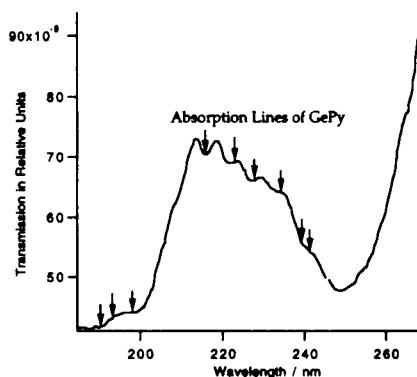
Figure 3. Absorption lines in the vapor phase over $ZnGeP_2$ attributed to the gas species GeP_y.
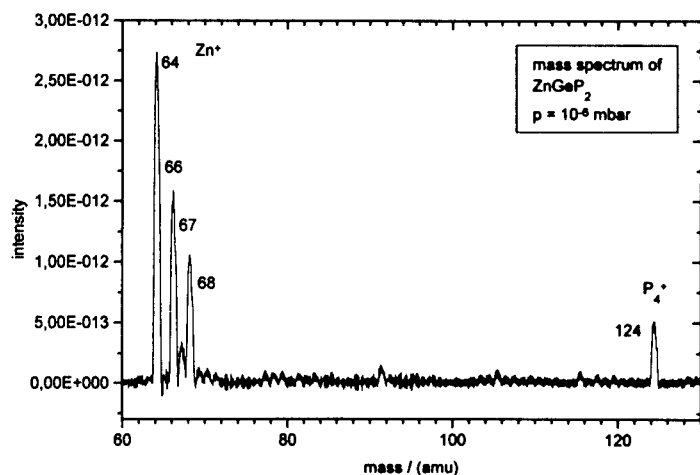
Figure 4. Mass spectrum of the vapor phase over $ZnGeP_2$. At low pressures the vapor phase consists of Zn and P_4.

Flat, 112-oriented, red transparent $ZnGeP_2$ crystals formed within 3 days using ZnP_2 as transporting agent when the transport temperature was higher than 973 K. First experiments with 111-oriented Si wafers showed film formation and the growth of truncated $ZnGeP_2$ pyramids of mm-size on the substrates. A simplified transport equation can be formulated as follows:

$$ZnGeP_2 \text{ (s)} \Leftrightarrow Zn \text{ (g)} + (1\text{-}x)/y \; GeP_y \text{ (g)} + 0.25(1+x) \; P_4 \text{ (g)} \qquad (1).$$
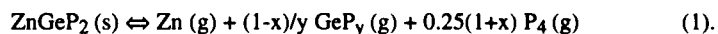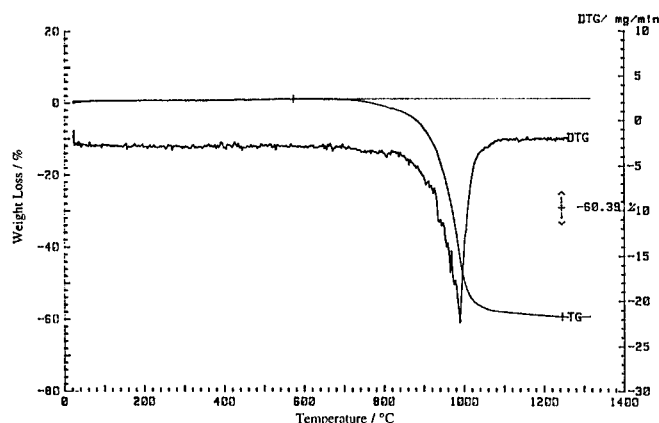
Figure 5. Thermal decomposition of ZnGeP$_2$.
The material starts to decompose at 973 K.

CONCLUSIONS

CVT-experiments with ZnGeP$_2$ and GeP and absorption measurements of their vapor phases indicate the presence of a germanium phosphide gas species. Analysis by mass spectrometry showed that the gass species released from a Knudsen cell at 723 K charged with ZnGeP$_2$ consists of Zn and P$_4$ only. Gaseous GeP$_y$ could not be detected in the vapor phase by QMS measurements. The phosphorus pressure in the Knudsen cell was orders of magnitude lower in comparison with CVT experiments. Therefore, we conclude that the proposed GeP$_y$ species is stable at high phosphorus pressures only. The growth of transparent red ZnGeP$_2$ crystals was observed when ZnP$_2$ was added to the growth system.

REFERENCES

1. G.C. Xing and K.J. Bachmann, Appl. Phys. Lett. **56**, 271 (1990).

2. G.C. Xing, K.J. Bachmann, J.B. Posthill and M.L. Timmons, J. Appl. Phys. **69**, 4286 (1991).

3. Y.G. Kataev, I.A. Bobrobnikova, V.G. Voevodin, E.I. Drigolenko, L.V. Nesterjuk and M.P..Yakubenya, Sov. Phys. J. **31**, 321 (1988).

4. S. Fiechter, R.H. Castleberry, N. Dietz and K.J. Bachmann in 7th Int. Symposium on Experimental Methods for Microgravity Materials Science, edited by. R.A. Schiffmann and J.B. Andrews (TMS, 1995) pp. 57-65.

5. G. Drummond and R.F. Barrow, Proc. Phys. Soc. London **65A**, 277 (1952) and references therein.

6. Y.V. Rud and R.V. Masagutova, Sov. Tech. Phys. Lett. **7**, 72 (1981).

7. M. Zumbusch, M. Heimbrecht and W. Biltz, Z. Anorg. Chem. **242**, 237 (1939).

ELECTRON PARAMAGNETIC RESONANCE AND PHOTOLUMINESCENCE STUDIES OF POINT DEFECTS IN ZINC GERMANIUM PHOSPHIDE (ZnGeP$_2$)

S. D. SETZLER*, L. E. HALLIBURTON*, N. C. GILES*, P. G. SCHUNEMANN**, AND T. M. POLLAK**
*Department of Physics, West Virginia University, Morgantown, WV, 26506
**Sanders, A Lockheed Martin Company, Nashua, NH, 03061

ABSTRACT

Electron paramagnetic resonance (EPR) has been used to monitor native defects, both acceptors and donors, in ZnGeP$_2$ crystals grown by the horizontal gradient freeze technique. These active centers include singly ionized zinc vacancies (V_{Zn}^-), neutral phosphorus vacancies (V_P^0), and neutral phosphorus antisite defects (P_{Ge}^0). The concentration of V_{Zn}^- acceptors correlates with the near-infrared optical absorption present in all ZnGeP$_2$ crystals. A photoluminescence band near 1.4 eV is shown to be polarized and is attributed to donor-acceptor-pair (DAP) recombination. Preliminary time-decay measurements support this assignment. Observation of the EPR spectrum of Mn^{2+} is also reported.

INTRODUCTION

In recent years, considerable progress has been made in the growth of high-quality zinc germanium phosphide (ZnGeP$_2$) crystals for use in frequency conversion applications in the mid-infrared. A suitable birefringence, a large nonlinear optical coefficient, and good thermal conductivity make this material an excellent choice for optical parametric oscillators (OPOs) tunable in the 3 to 9 μm region. However, before ZnGeP$_2$ can achieve its full potential, a broad defect-related absorption band extending from 0.7 to 2.5 μm must be eliminated. This unwanted absorption band overlaps the desirable 2-μm pump region for mid-infrared OPOs and thus limits the maximum pump intensity that can be used in these devices. Several post-growth methods to reduce this absorption have been investigated, including lengthy thermal anneal, high-energy electron irradiation [1], and gamma-ray irradiation [2]. These treatments, although helpful, have not eliminated the absorption problem in ZnGeP$_2$.

Nearly all of the ZnGeP$_2$ crystals described in the literature have been highly compensated, thus indicating nearly equal concentrations of donors and acceptors. There are two competing explanations for the nature of these donors and acceptors. One approach is to assume these defects arise from disorder on the zinc and germanium sublattices, i.e., a zinc antisite defect would be an acceptor and a germanium antisite would be a donor. An alternate approach is to assume that the donors and acceptors are vacancy centers. Magnetic resonance techniques such as EPR, ENDOR, and ODMR make use of hyperfine interactions to identify specific defect models and thus can help to determine whether cation disorder or vacancies dominate in ZnGeP$_2$. Thus far, the zinc vacancy (V_{Zn}^-) [3], the phosphorus vacancy (V_P^0) [4], and the phosphorus antisite (P_{Ge}^0) [5] have been detected by EPR.

EXPERIMENT

The ZnGeP$_2$ crystals used in the present investigation were grown by the horizontal gradient freeze technique at Sanders, a Lockheed Martin Company. Small samples with approximate dimensions of 3 x 3 x 3 mm^3 were cut from larger boules. They had faces perpendicular to the high symmetry directions. The EPR data were taken on a Bruker ESP-300 spectrometer operat-

ing at 9.45 GHz and equipped with an Oxford Instruments helium-gas-flow cryostat for low temperature studies. Slots in the EPR microwave cavity allowed optical access to the samples. In the photoluminescence (PL) measurements, both cw (514.5-nm argon laser) and pulsed (532-nm frequency-doubled Nd:YAG laser) excitation were used. The PL signals were detected with an Instruments SA HR-640 monochromator and a photomultiplier tube with a GaAs(Cs) cathode. For cw excitation, the incident beam was chopped and phase-sensitive detection was used. Time-decay data were recorded using a Tektronix (TDS 684A) digital oscilloscope.

RESULTS

EPR shows the presence of two dominant native defects, a zinc vacancy and a phosphorus vacancy, in all of the $ZnGeP_2$ samples grown by the horizontal gradient freeze technique. The singly ionized zinc vacancy acceptor (V_{Zn}^-) is paramagnetic (S = ½) and is easily seen without photoexcitation at temperatures below 50 K [3]. The unpaired spin is shared nearly equally by two phosphorus nuclei (I = ½, 100% abundant), which gives rise to triplets (1:2:1 line intensity ratios) in the EPR spectra, as shown in Fig. 1(a). This spectrum was taken with the magnetic field along the crystal's c axis, i.e., the four possible crystallographic sites are magnetically equivalent. ENDOR has provided information about the lattice distortion surrounding this defect [6], and has led to its assignment as V_{Zn}^-. This defect is present with slightly varying concentrations (on the order of 10^{19}-10^{20} cm^{-3}) in all samples studied.

Several additional intrinsic defects in $ZnGeP_2$ can be observed during photoexcitation. Laser excitation changes the valence of donors and acceptors, thus converting non-paramagnetic defects into paramagnetic forms. For example, phosphorus vacancies in $ZnGeP_2$ are present as singly ionized donors (V_P^+), but it is their neutral state (V_P^0) which is paramagnetic [4]. These latter centers are observed by illuminating the samples with above-band-gap (514.5 nm) or below-band-gap (632.8 nm) light at temperatures below 10 K. Even at these low temperatures, the neutral state is not stable and decays back to the singly ionized form in a matter of seconds or less. The EPR spectrum from the neutral phosphorus vacancy shows no hyperfine structure, indicating the unpaired spin does not strongly interact with phosphorus neighbors. This defect
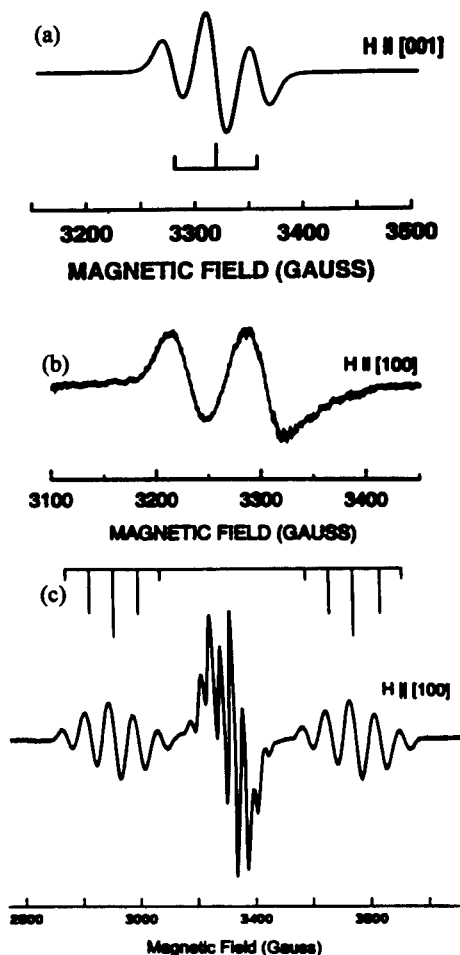
Figure 1. EPR spectra from (a) singly ionized zinc vacancies, V_{Zn}^-, (b) neutral phosphorus vacancies, V_P^0, and (c) neutral phosphorus antisite defects, P_{Ge}^0.

is usually observed at concentrations comparable to that of the zinc vacancies. The EPR spectrum of the V_P^0 center is shown in Fig. 1(b).

Another native paramagnetic defect, the phosphorus antisite, is not usually seen in $ZnGeP_2$ samples grown by the horizontal gradient freeze technique. However a recently grown sample did reveal a significant concentration of this donor. Kaufmann et al. [5] initially reported the presence of P_{Ge}^0 centers during photoexcitation at low temperatures. Figure 1(c) shows the EPR spectrum of the P_{Ge}^0 taken from our recently grown $ZnGeP_2$ sample. This spectrum exhibits a large hyperfine splitting (about 750 G) with the central phosphorus nucleus and smaller ligand hyperfine interactions with the four nearest phosphorus neighbors. We can observe this spectrum at temperatures as high as 40 K, at which point the neutral charge state of the donor becomes unstable and converts back to its singly ionized form. This phosphorus antisite spectrum has only been present in one of the samples grown at Sanders, and for this reason it is not expected to play a major role in explaining the origin of the near-edge absorption in $ZnGeP_2$.

The optical absorption extending from 0.7 to 2.5 μm in $ZnGeP_2$ is commonly assumed to be due to point defects. Figure 2 shows this near-edge optical absorption from four different $ZnGeP_2$ samples. Also, EPR data from two of the samples are included in the figure. The EPR spectra shown are from singly ionized zinc vacancies (V_{Zn}^-), and their relative intensities correlate well with the observed optical absorption. These results strongly suggest that the zinc vacancy acceptors play a direct role in the optical absorption phenomenon. Although not shown, large concentrations of phosphorus vacancy donors were also present in these samples. We conclude that the optical absorption is most likely due to several overlapping bands arising from an acceptor-to-donor transition and band-to-defect transitions. Support for this view comes from PL studies.
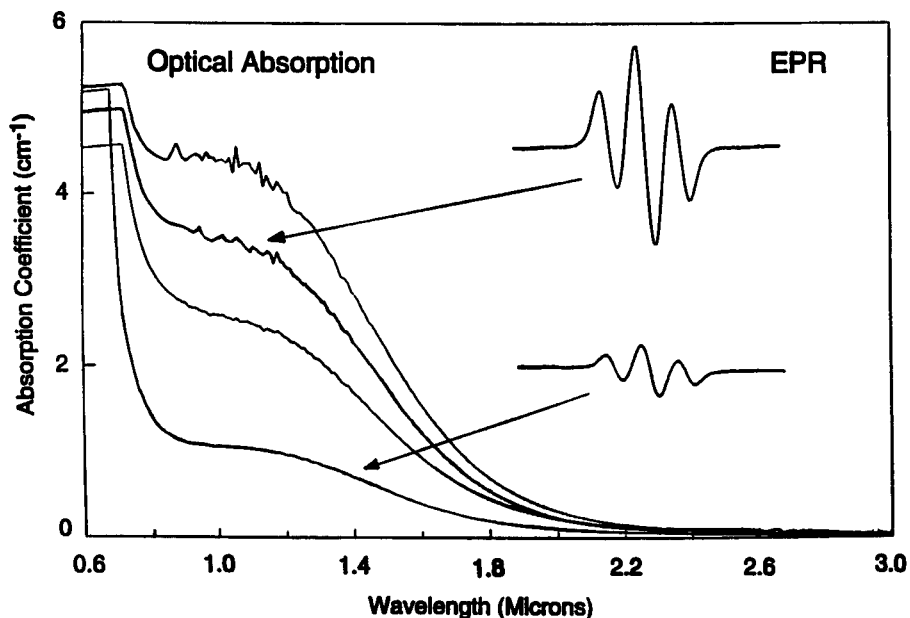
Figure 2. Correlation of near-edge optical absorption and zinc vacancy concentration as measured by EPR.

Results of photoluminescence experiments help to further connect these defects seen by EPR to the near infrared absorption. While PL spectra in $ZnGeP_2$ are often complex [7], measurements taken on our samples indicate only two dominant emission bands at low temperature. Figure 3(a) shows PL spectra taken at 4.8 K with a polarizer placed parallel and perpendicular to the crystal c axis. These spectra have been corrected for the polarization response of the detection system. Subtracting one polarization from the other allowed us to decompose the spectrum into two overlapping bands. One band is partially polarized along the c axis of the crystal (the 1.42 eV band in Fig. 3(b)) and the other band is unpolarized (the 1.62 eV band in Fig. 3(c)). A possible explanation for the two bands is two distinct donor-acceptor-pair (DAP) recombinations. Such a model is not considered likely since EPR data, thus far, have revealed the existence of only one dominant donor (V_P^0) and one dominant acceptor (V_{Zn}^-) in our samples. It is more likely that one of the observed bands is DAP (i.e., the 1.42-eV band) and the other is a band-to-impurity transition, i.e., an (e,A) or (D,h) transition. Since the PL spectra shown in Fig. 3(a) are also observed with below-band-gap light (632.8 nm), we suggest that the 1.62-eV emission is donor-hole (D,h) recombination. We find that the emission and optical absorption exhibit the same polarization behavior and, furthermore, our PL polarization study is at variance with the report of McCrae et al. [8].

From our EPR and PL results, we construct an energy-level diagram in Fig. 4 using a single-donor/single-acceptor model where V_{Zn}^- and V_P^+ are the dominant acceptor and donor defects. We have earlier suggested that a
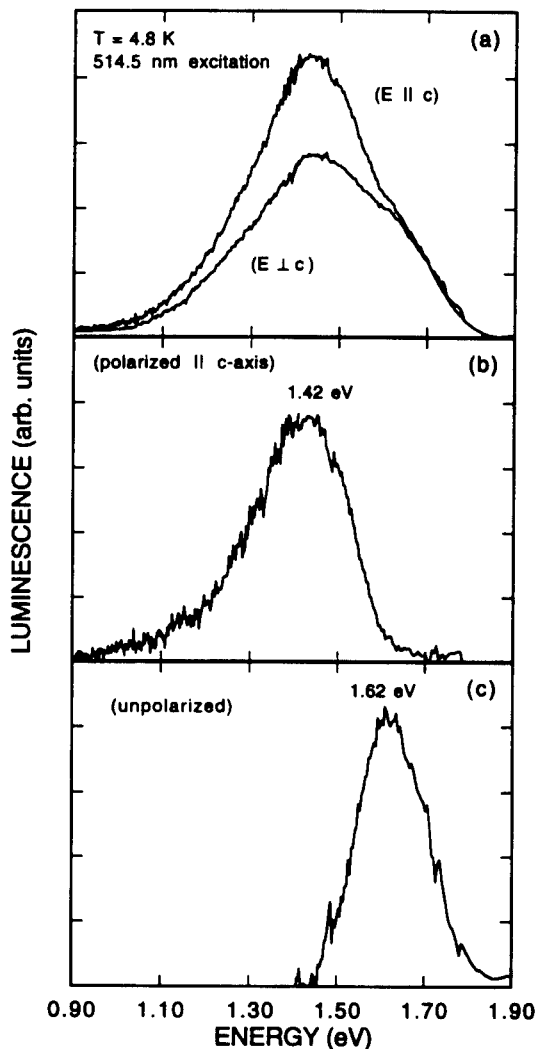
Figure 3. Photoluminescence of $ZnGeP_2$ measured at 4.8 K. (a) Spectra measured with emitted light polarized perpendicular and parallel to the crystal's c axis. These spectra are separated into a polarized part (b) and an unpolarized part (c).

significant DAP emission occurs near 1.4 eV at liquid-helium temperature, and this is illustrated in the figure. Donor-hole transitions, previously assigned to an emission near 1.6 eV, are also illustrated in the figure. The optical absorption, which limits device performance, peaks near 1 μm (1.2 eV) at room temperature, as shown in Fig. 2. A portion of this optical absorption can be attributed to the transitions from the acceptors to the donors. The room temperature absorption and the low temperature emission peaks do not directly coincide, but this is explained in large part by a ~0.1 eV change in band gap with temperature. Additional transitions from the valence band to the donors and from acceptors to the conduction band may be contributing to the high-energy side of the observed broad optical absorption. Likewise, transitions from valence band states to neutral acceptors may give rise to absorption in the region beyond 2 μm.
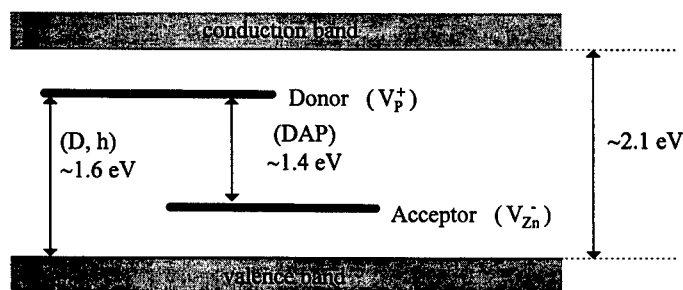
Figure 4. Energy-level diagram based on two dominant native defects.

A preliminary investigtion of the time-decay behavior of the PL bands has been completed. Figure 5 shows the data obtained by monitoring the DAP emission at 1.42 eV after an 8-ns, 532-nm excitation pulse. Because of the low intensity of the emitted light, 1000 decays were accumulated. The decay occurs over a time window extending out to approximately 20 μs and can not be fit by a single exponential. These results support our previous assignment of this emission of DAP recombination in an indirect-gap semiconductor. We also measured the decay of the PL occurring at 1.62 eV and found a similar dependence on time.
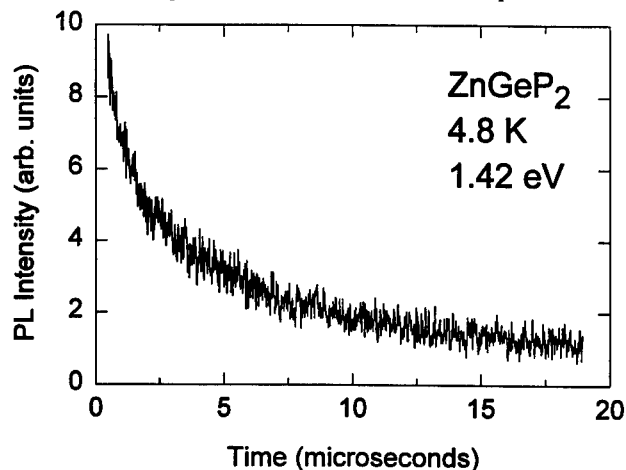
Figure 5. Time decay of the DAP emission at 1.42 eV.

EPR, ENDOR, PL, and time-resolved PL are well suited to study defects in ZnGeP$_2$. Their usefulness, however, is not restricted to studying native defects. Substitutional manganese was reported by Baran et al. [9], and we have recently "rediscovered" this defect in material grown by the horizontal gradient freeze technique. A careful analysis of the Mn^{2+} EPR spectrum, shown in Fig. 6, yields spin-Hamiltonian parameters similar to those reported by Baran, et al. The defect is an S = 5/2 system interacting with an I = 5/2 nucleus (100% abundant). A small crystal field, due to the crystal's tetragonal symmetry, splits the spectrum into five sets of six lines. The three larger lines in the center of the spectrum in Fig. 6 are due to the zinc vacancy. The only sample this manganese spectrum has been seen in was the one in which the antisite P$_{Ge}^0$ was also observed. This piece was cut from the end of a boule, indicating a possible variation in stoichiometry, and photoluminescence studies have not yet been performed on this sample.

Figure 6. EPR spectrum of Mn^{2+} in ZnGeP$_2$.

ACKNOWLEDGEMENTS

REFERENCES

1. P.G. Schunemann, P.J. Drevinsky, M.C. Ohmer, W.C. Mitchel, and N.C. Fernelius in Beam-Solid Interactions for Materials Synthesis and Characterization, edited by D.C. Jacobson, D.E. Luzzi, T.F. Heinz, and M. Iwaki (Mater. Res. Soc. Proc. 354, Pittsburgh, PA, 1994) pp. 729-734.
2. P.G. Schunemann, P.J. Drevinsky, and M.C. Ohmer in Beam-Solid Interactions for Materials Synthesis and Characterization, edited by D.C. Jacobson, D.E. Luzzi, T.F. Heinz, and M. Iwaki (Mater. Res. Soc. Proc. 354, Pittsburgh, PA, 1994) pp. 579-583.
3. M.H. Rakowsky, W.K Kuhn, W.J. Lauderdale, L.E. Halliburton, G.J. Edwards, M.P. Scripsick, P.G. Schunemann, T.M. Pollak, M.C. Ohmer, and F.K. Hopkins, Appl. Phys. Lett. 64 (13), 1615-1617 (1994).
4. N.C. Giles, L.E. Halliburton, P.G. Schunemann, and T.M. Pollak, Appl. Phys. Lett. 66 (14), 1758-1760 (1995).
5. U. Kaufmann, J. Schneider, and A. Räuber, Appl. Phys. Lett. 29 (5), 312-313 (1976).
6. L.E. Halliburton, G.J. Edwards, M.P. Scripsick, M.P. Rakowsky, P.G. Schunemann, and T.M. Pollak, Appl. Phys. Lett. 66 (20), 2670-2672 (1995).
7. N. Dietz, I. Tsveybak, W. Ruderman, G. Wood, and K.J. Bachmann, Appl. Phys. Lett. 65 (22), 2759-2761 (1994).
8. J.E. McCrae, Jr., M.R. Gregg, R.L. Hengehold, Y.K. Yeo, P.H. Ostdiek, M.C. Ohmer, P.G. Schunemann, and T.M. Pollak, Appl. Phys. Lett. 64 (23), 3142-3144 (1994).
9. N.P. Baran, I.I. Tychina, I.G. Tregub, I.Yu. Tkachuk, L.I. Chernenko, and I.P. Shcherbyna, Sov. Phys. Semicond. 9 (12), 1527 (1976).

Defect Characterization in ZnGeP2 by Time -Resolved Photoluminescence

N. Dietz[a,b], W. Busse[d], H. E. Gumlich[d], W. Ruderman[e], I. Tsveybak[e], G. Wood[b] and
K.J. Bachmann[b,c]

[a]Department of Physics, [b]Department of Materials Science & Engineering, [c]Department of
Chemical Engineering, North Carolina State University, Raleigh, NC 27695, [d]Technical
University Berlin, and [e]Inrad, Inc., Northvale, NJ 07647

Abstract

Steady state and time-resolved photoluminescence (PL) investigations on ZnGeP2 crystals
grown from the vapor phase by high pressure physical vapor transport (HPVT) and from the melt
by gradient freezing (GF) are reported. The luminescence spectra reveal a broad infrared
emission with peak position at 1.2 eV that exhibits features of classical donor-acceptor
recombination. The hyperbolic decay characteristic over a wide energy range, investigated from
1.2 eV up to 1.5eV, suggest that this broad emission band is related to one energetic
recombination center. Higher energetic luminescence structures at 1.6eV and 1.7eV were
revealed after annealing of ZnGeP2 crystals in vacuum for a longer period of time. The emission
decay behavior in this energy range is characterized by two hyperbolic time constants, viewed as
the supercomposition of the decay from the broad emission center peaked at 1.2eV and
additional donor-acceptor recombination emissions at 1.6eV and 1.7eV, respectively. ZnGeP2
crystals grown under Ge-deficient conditions by HPVT show an additional emission structure at
1.8 eV with sharp emission fine structures at 1.778 eV related to the presence of additional donor
states.

I. Introduction

Zinc germanium phosphide with a pseudodirect bandgap of ~2.1 eV at room temperature[1]
has an attractive transparency range[2] from 670 nm to 13 μm and a relatively large second order
susceptibility tensor component (d_{36}= 75 pm/V). In view of its substantial positive birefringence
of 0.36%, ZnGeP2 as a suitable material for non-linear optical applications in the infrared, e.g.,
the fabrication of optical parametric oscillators (OPO) and harmonic generation based on
powerful infrared laser sources[3]. In addition to these and other applications in non-linear
optics, ZnGeP2 is of interest in the context of nearly lattice matched heteroepitaxy of compound
semiconductors on silicon (a[Si] = 5.451 Å, a[ZnGeP2] = 5.465 Å, c/a[ZnGeP2] = 1.97) at room
temperature [4].

Recently performed steady-state PL studies revealed a broad emission band with a peak
maxima around 1.2 eV[5]. The origin of this broad band has remained ambiguous, especially
because only the onset of this emission band was known so far. The reported changes in the high
energetic shoulder were investigated as a function of composition. The observed changes in the
PL spectra due to annealing or slightly off-stoichiometric growth[6-8]. They remain still valid,
keeping in mind that the observed shifts of the maxima around 1.3eV might be caused by the
cutoff in the photomultiplier assuming an intensity variation of the emission peaked at 1.2eV.

Even so little is known about the defect chemistry of ZnGeP2 at present, electron paramagnetic
resonance (EPR) measurements[9] support the strong relation of the EPR-signal with an acceptor
band[10] and constricted the possible nature of the defect related acceptor band to be either Zn_{Ge}
sites or V_{Zn} vacancies. From photo-induced EPR results on as grown ZnGeP2 crystals, the deep
PL emission is attributed to D-A transitions associated with V_P-V_{Zn} pairs[11]. However, photo-
induced EPR only probes the near-surface region, while the observed optical brightening is a
bulk effect. In our previous introduced defect related energy band model[5], we assign PL
features to donor-acceptor (DA) recombination processes. In a DA recombination process, after
generation of electron-hole pairs, the electrons and holes are captured by ionized donors and
acceptors. Carriers localized at neutral donors and acceptors separated by a distance, r, may
recombine radiatively emitting photons with an energy of [12]

$$hv = E_G - \left(E_D + E_A\right) + \frac{e^2}{\varepsilon\, r} - \frac{e^2}{\varepsilon}\frac{\alpha^5}{r^6} \tag{1}$$

where E_G is the band gap energy, E_D and E_A the donor and acceptor binding energies, ε the static dielectric constant and α the effective van der Walls coefficient. For very close pairs, the last term of Equ. (1) results in a series of sharp emission lines. However, a large amount of statistically distributed closely spaced pairs may broaden or even suppress the discrete emission lines due to random strain.

Results and Discussion

The energy resolved steady-state PL data in the energy range from 0.7 eV up to 2.5 eV were obtained using a combination of two liquid-N_2 cooled detectors, a GaInAs photomultiplier tube (PMT) and a Ge diode in conjunction with a 0.5 m single-grating monochromator. The excitation was accomplished by an Ar laser with excitation energies of 2.7 eV (λ = 457.8nm), 2.54 eV (λ= 488 nm) and 2.4 eV (λ = 514.8 nm) excitation lines. The system respons of the PMT was corrected to allow the combination of the two spectra, which is essential since the decreasing response of the PMT below 1.3 eV results in a false peak position of the infrared luminescence near 1.3 eV. Time-resolved PL data were obtained by a time-correlated single-photon counting technique. The excitation energy was varied by a XeCl pumped (Eximer laser λ = 308 nm) Dye laser system, Lamda EMG53MSC, in the wavelength range 460-510 nm (Coarin102). The output of the Dye laser was controlled by neutral-filters with an incident power between 100 mW and 3Watt and repetition rates between 200Hz and of 50Hz, respectively. The pulse width is in the order of 18ns. The resulting luminescence was collected and focused in a double monochromator and detected with an S-1 PMT. In lack of fast response detectors in the infrared region below 1.2 eV, the time dependence of the luminescence is carried out only in the energy range from 1.2eV up to 1.8 eV.

Figure 1 shows a typical PL spectrum for an as-grown $ZnGeP_2$ cut from a bulk single crystal grown by the gradient freezing (GF) method. The spectrum is build up from two PL spectra taken with a PMT (1.2 eV up to 2.5 eV) and a Ge-diode (0.7 eV up to 1.3 eV).
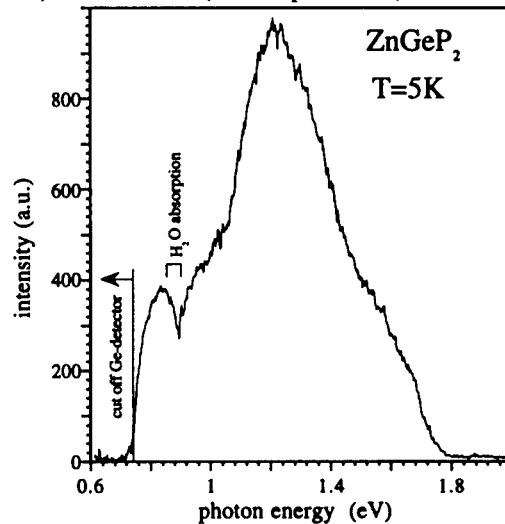
Figure 1:
Photoluminescence spectrum of bulk $ZnGeP_2$ crystal wafers that are cut from a crystal grown by gradient freezing method.

In the energy range from 1.0 eV up to 2.0 eV the spectrum is corrected with that of the PMT and the Ge-diode response function. Below 1.0 eV no correction function for the monochromator and Ge diode response was available. Thus PL spectrum is dominated by the emission peak at 1.2eV with two high energetic shoulders around 1.58 eV and 1.68 eV. The luminescence of all $ZnGeP_2$ samples show a very strong temperature dependence and no luminescence is detected at

room temperature. Figure 2 shows the temperature dependence of the PL spectrum for a ZnGeP$_2$ bulk crystal. With increasing temperature the high energetic emission around 1.6 eV and 1.7 eV decreases rapidly leaving at 100 K the 1.3 eV emission as dominant feature. The time dependence of the observed emission structures in bulk crystals is shown in Figure 3. The spectra are obtained with a S1-PMT in the single-photon counting mode and are not corrected with the PMT response characteristic. The upper curve in fig. 3 shows the emission spectrum of an annealed ZnGeP$_2$ crystal taken without a time window. The emission spectrum obtained in the time window from 0 to 100 µs mainly consists of the high energetic emission structure at 1.68 eV with a small contribution around 1.3-1.4 eV. The emission spectra taken in the time windows 0.1-2ms, 2-18ms and 18-65ms show only one emission contribution with a constant peak maximum around 1.3eV.

Figure 2:
Temperature dependence of the emission of a ZnGeP$_2$ bulk crystal.
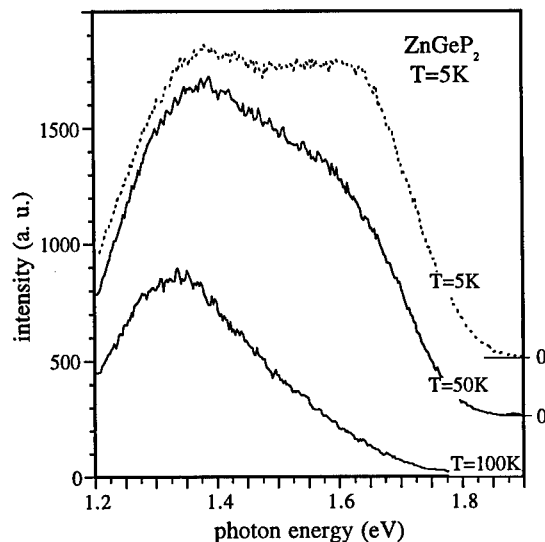
This suggests that the broad emission structure at 1.3 eV is correlated to one transition center. Note, that the peak maximum position is falsed by the cutoff edge of the PMT, as indicated in fig. 1. The decay character analyzed in the energy range of 1.2eV to 1.9 eV is shown in Fig. 4 in a double logarithmic plot for the emission at 1.326 eV, 1.45 eV, 1.574 eV and 1.698 eV in curve (1), (2), (3) and (4), respectively. The decay transients in the energy range 1.2 eV up to 1.7 eV are fitted with the hyperbolic equation I=$\alpha \cdot t^{-\tau}$, with α as a pre-factor and τ the hyperbolic decay factor. The decay factor τ changes form τ=0.81 at 1.326 eV to τ=1.0, τ=1.25 and τ=1.6 at , 1.45 eV, 1.574 eV and 1.698 eV, respectively.

Crystal platelets were grown by horizontal HPVT from molten ZnGeP$_2$ sources with and without additions of excess Zn$_3$P$_2$ to cover the entire range of compositions from Ge- to Zn-rich compositions of the homogeneity range about stoichiometric ZnGeP$_2$[13] The temperature at which nucleation and growth occurred was ~35-50°C below the melting temperature. Since the entire charge was molten and no provisions for replenishment of the molten source by the preferentially evaporating constituents was made, the composition of these platelet crystals changed from the position near to their initial nucleation sites at the fused silica wall to their peripheral parts that are formed in the final stages of growth, that is, at lower Zn partial pressure and higher density of Ge containing precursors to growth than established in the initial phase of growth. HPVT grown ZnGeP$_2$ crystals show therefore a variety of emission structures related to the different stages of growth. Figure 5 shows the photoluminescence spectra obtained in the center of a platelet with different time windows. The emission spectra are similar to that observed for bulk ZnGeP2 (Fig. 3) with one additional sharp emission peaked at 1.778 eV.

Figure 3:
Time dependence of
photoluminescence of a
ZnGeP₂ bulk crystal
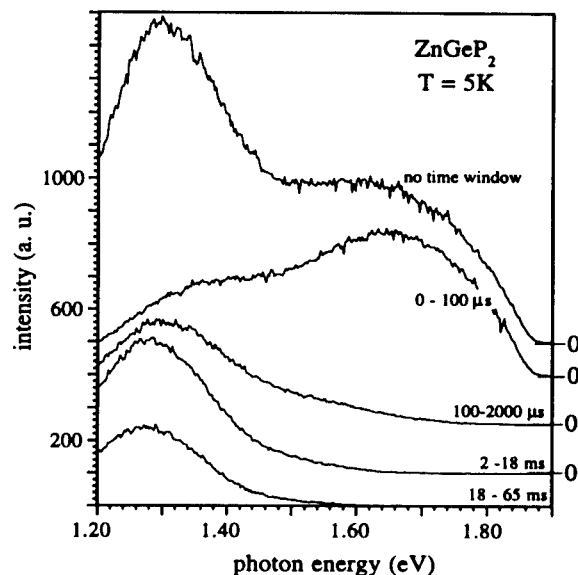
Figure 4:
Decay transients of the PL
emission at 1.326 eV (1),
1.45 eV (2), 1.574 eV (3) and
1.698 eV (4). The exponent τ
in the hyperbolic
approximation changes form
$\tau = 0.81$, $\tau = 1.0$, $\tau = 1.26$ to τ
$= 1.60$ for curve (1), (2), (3)
and (4), respectively.
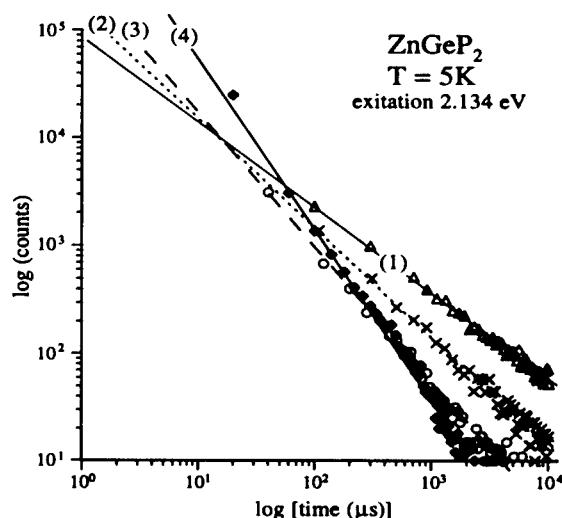
The decay time of the emission in the energy range 1.2 eV upto 1.6 eV is linear in a double logarithmic plot as shown in Fig. 6. The insert in Fig. 5 shows an enlargement of the emission around 1.778 eV with the decay time plotted in a double log. scale in the insert in Fig. 6.

Although the point defect chemistry is thus complex, hints for the predominance of certain defects are obtained by the analysis of the annealing behavior and the behavior associated with specific growth conditions. The parabolic decay time characteristic of the emission in the energy range of 1.2 eV to 1.8 eV can be interpreted in terms of transitions between donor and acceptor states associated with energy subbands in the bandgap of ZnGeP₂, as schematically shown in

336

Fig. 7. Regardless of the as-grown composition, annealing in vacuum depletes the near surface region with regard to the most volatile constituents, that is, phosphorus and zinc. The formation of vacancies on the zinc sublattice reduces the concentration of Zn_{Ge} acceptors and enhances the concentration of Ge_{Zn} donors. The introduction of V_P donors at the surface is associated with the formation of Ge_P acceptors and possibly, but not necessarily, of Zn_P acceptors. Thus the luminescence at 1.6 and 1.7 eV observed in vacuum annealed bulk crystals may be explained tentatively by transitions from V_P donors to V_{Zn} and Ge_P acceptors, respectively. The overall FL shift associated with the generation of V_P and V_{Zn} depends on the values of the equilibrium constants, which are not known at present. The high p-type conductivity observed upon annealing in zinc vapor, has been explained by Rud as an effect of Zn_P antisite defect formation[14]. The n-type conductivity of $ZnGeP_2$ crystals grown under HPVT suggests the formation of relatively shallow donor states that move the fermi level (FL) toward the conduction band edge. Simultaneously emission at 1.78 eV is observed that is neither seen in melt-grown crystals nor for growth from zinc-depleted vapor sources. The high phosphorus pressure used in the HPVT experiments rules out a higher V_P concentration than observed under the conditions of melt growth. Thus the donor responsible for the 1.78 eV emission for HPVT growth from a zinc supersaturated vapor phase must be associated with a different point defect that does not form for HPVT growth from zinc-depleted melt compositions.
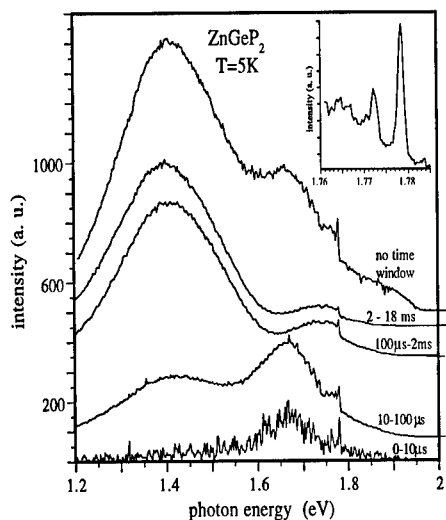
Figure 5:
Time dependence of the emission in the center of a HPVT grown $ZnGeP_2$ crystal. (Insert: Enlarged emission spectrum around 1.77 eV)
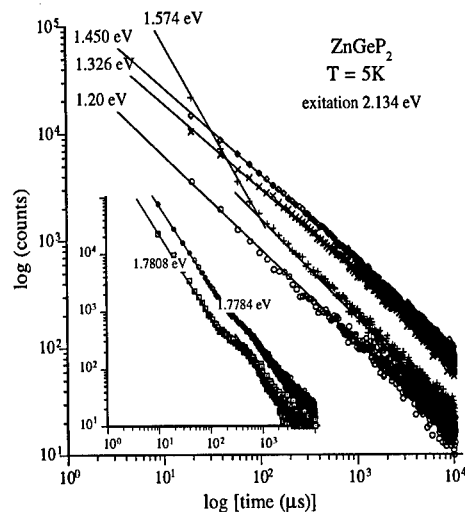
Figure 6:
Decay transients of the PL emission for a HPVT grown $ZnGeP_2$ crystals for various emission energies (Insert: Decay transients of emissions at 1.7784 eV and 1.7808 eV).

The broad deep luminescence in $ZnGeP_2$ crystals observed for crystals grown from the melt and zinc-depleted vapor sources is due to close-spaced D-A pairs , corresponding to the broad donor and acceptor subbands. Accepting the interpretation of the ENDOR measurements [15], the deep acceptor is associated with V_{Zn}. Since these V_{Zn} can be filled by excess Ge atoms under formation of Ge_{Zn} donors, a mechanism is identified by which Ge_{Zn}-V_{Zn} close-spaced D-A pairs can be formed. Also, we prefer the Ge_{Zn} donor over the V_P donors since the presence of Ge_{Zn} antisides upon annealing provides for the simultaneous elimination of V_{Zn} and cation disorder by the reactions (i): $Ge_{Zn} \rightarrow Ge^x + V_{zn}$ and (ii) $Zn_{Ge} + V_{zn} \rightarrow Zn^x$. The associated fermi level motion toward the conduction band edge that results in the filling of residual deep Ge_{Zn} donor states by electrons further enhances the optical brightening. Of course, the simultaneous elimination of P-

337

and Zn-vacancies upon annealing would be also possible, but there exists no obvious linkage in this case. Additional insights are likely to emerge from the results of irradiation studies that permit the controlled formation of defects and their characterization.

Figure 7:

Suggested model of the positions of various donor and acceptor related sub-bands in the bandgap of ZnGeP$_2$. Ef$_p$ is the Fermi level for p-type and Ef$_n$ the Fermi level position for n-type ZnGeP$_2$ crystals.
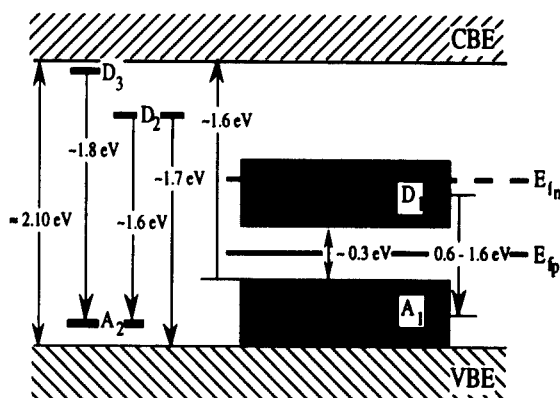
Conclusion

The native defect-related optical properties of ZnGeP$_2$ were studied by steady-state and time-resolved PL. The decay transients for the emission in the energy range 1.2 - 1.6eV show hyperbolic behavior which is interpreted as donor-acceptor pair recombination. Higher energetic luminescence structures at 1.6eV and 1.7eV were revealed after annealing of the ZnGeP$_2$ crystals. ZnGeP$_2$ crystals grown under Ge-deficient conditions by HPVT show additional emission structure at 1.8 eV and a sharp donor-acceptor emission at 1.778 eV associated to the presence of additional donor states.

References:
1. J. L. Shay and J. H. Wernick, Academic Press, New York (1976).
2. G. D. Boyd, H. M. Kasper, J. H. McFee and F. G. Storz, IEEE J. Quantum. Electron. QE 8, 900 (1972).
3. Y. M. Andreev, V. G. Voevodin, A. I. Gribenyukov and V. P. Novikov, Sov. J. Quantum. Electron. 17, 748 (1987).
4. K. J. Bachmann, Mat. Res. Soc. Symp. Proc. 242, 707 (1992).
5. N. Dietz, I. Tsveybak, W. Ruderman, G. Wood and K.J. Bachmann, Appl. Phys. Lett. 65 (22), 2759 (1994).
6. G. K. Averkieva, V. S. Grigoreva, I. A. Maltseva, V. D. Prochukhan and Y. V. Rud, phys. stat sol. (a) 39, 453 (1977).
7. H. M. Hobgood, T. Henningsen, R. N. Thomas, R. H. Hopkins, M. C. Ohmer, W. C. Mitchel, D. W. Fischer, S. M. Hegde and F. K. Hopkins, J. Appl. Phys. 73(8), 4030 (1993).
8. Yu. V. Rud, Semiconductors 28(7), 633 (1994).
9. M.H. Rakowsky, W.K. Kuhn, W.J. Lauderdale, L.E. Halliburton, G.J. Edwards, M.P. Scripsick, P.G. Schunemann, T.M. Pollak, M.C. Ohmer, and F.K. Hopkins, Appl. Phys. Lett. 64(13), 1615 (1994).
10. A. Kiel, Solid State Communications 15, 1021 (1974).
11. N.C. Giles, L.E. Halliburton, P.G. Schunemann and T.M. Pollak, Appl. Phys. Lett. 66, 1758 (1995).
12. J. J. Hopfield, D. G. Thomas and M. Gershenzon, Phys. Rev. Lett. 10, 162 (1963).
13. G. Wood, Master Thesis, North Carolina State University, Raleigh NC 27695 (1994).
14. Y. V. Rud and R. V. Masagutova, Sov. Tech. Phys. Lett. 7, 72 (1981).
15. L. E. Halliburton, G. J. Edwards, M. P. Scripsick, M. H. Rankowsky, P. G. Schunemann and T. M. Pollak, Appl. Phys. Lett. 66, 2670 (1995).

PHOTOLUMINESCENCE STUDY OF p-ZnGeP$_2$ CRYSTALS

YURRI V. RUD*, VASILII YU**, M.C. OHMER***, P.G. SHUNEMANN****
*Ioffe Physico-Technical Institute, 26 Polytekhnicheskaya st., St. Petersburg 194021, Russia
**State Technical University, 29 Polytekhnicheskaya st., St. Petersburg 195251, Russia,
rudvas@uniys.hop.stu.neva.ru
***Wright Laboratory, Wright-Patterson AFB, Ohio 45433
****Lockheed Sanders, Nashua, New Hampshire 03061

ABSTRACT

Photoluminescence (PL) steady-state spectra of p-ZnGeP$_2$ (ZGP) single crystals grown by high- and low-temperature directed crystallization have been investigated. It is determined that the long-wavelength component PL with a maximum in the interval 1.2-1.5 eV for different crystals quenched in the temperature range 77-300 K. The long-wavelength component PL are due to donor-acceptor pair transitions. At room temperature the short-wavelength PL with a maximum near 1.85 eV becomes the determining component. The nature of this band   discussed. The use of low-temperature directed crystallization reduces the concentration of lattice defects in ZGP single crystals and opens up the new possibilities for increasing the conversion efficiencies of nonlinear devices.

INTRODUCTION

Ternary compound of II-IV-V$_2$ ZGP (Eg=1.99 eV [1,2]) crystallized in the chalcopyrite structure which can be inferred from the cubic zincblende lattice by doubling the unit cell and ordering the atoms of cation sublattice. In the tetragonal unit cell a small distortion occurs in the direction of the c-axis which substantially affects on the optical properties of this compound semiconductor. The material is of interest in context of its non-linear optical properties and can be applied as optical parametric oscillator or for frequency mixing [1-4]. The main obstacle impending the realization of the unique possibilities of this ternary diphosphide remains its high optical near infrared absorption [1,2,5,6]. There is therefore, the problem of finding effective ways to decrease the optical absorption in the transmission region of ZGP, on which investigators have focused their efforts [2,5,6].

In the present paper we report results of a systematic study of the photoluminescence of ZGP single crystals in a wide temperature range. Thus far, because of its rapid quenching, radiative recombination in this semiconductor has been investigated in the main at low temperatures (T<80 K) [5-8]. Such investigations could facilitate the development of the physical principles of contact-free diagnostics of optical quality ZGP crystals, which would ultimately make it possible to determine the technological conditions for obtaining material with a highly perfect structure and, correspondingly, make it possible to ensure the required optical quality of this ternary compounds.

EXPERIMENT

ZGP single crystals were grown by high-temperature directed crystallization (HTDC) at the melting point T_{cr} [2]. Some crystals have been prepared by low-temperature directed crystallization (LTDC) which we have developed for the obtaining of ZGP at the range of temperature 600-750°C. These temperatures are considerably below the temperature of the
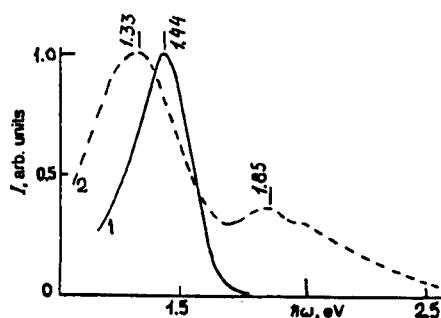
Fig. 1. PL spectra of p-ZGP crystals grown by LTDC (curve 1) and HTDC (curve 2) at T=77 K (λ_{exc} =441 nm).

chalcopyrite→sphalerite phase transition [1]. To increase the optical transmission in the near-IR region of the spectrum, post-growth heat-treatment was also used for a number of crystals [2].

After the mechanical polishing with ≈ 0.05 μm alumina the surface of plates with average dimensions of 2 x 5 x 10 mm was also subjected to chemical polishing in a solution with the composition 5 parts HF: 1 part H_2O: several drops HNO_3 (T=60-100°C, t=1-5 min) followed by washing in deionized water. The surface of single crystals treated in this manner retained the same degree of perfection achieved during prolonged (up to 5 years) storage of the plates under normal conditions. The quality of such treatment did not exhibit any dependence on the crystallographic direction. The X-ray dates show that the lattice parameters of the chalcopyrite prepared by the methods LTDC and HTDC are in agreement with published values for ZGP [1]. The free-hole concentration in the all investigated samples was equal to approximately 10^9-10^{10} cm^{-3} at T=300 K for different processes.

Photoluminescence spectra were obtained at temperatures ranging from 77 K to room temperature. Seven excitation sources were used independently. They were 515, 497, 488, 477, 458 nm lines of a multiline cw Ar$^+$ laser (50 mW output power) extracted by a monochromator, of which the photon energies are 2.41, 2.50, 2.54, 2.60, and 2.71 eV, respectively. We also used a 441-nm line of cw He-Cd laser (10 mW), of which the photon energy are 2.82 eV. The photon energies of these sources are smaller or greater than the direct gap for ZGP. Luminescence light from the sample was analyzed by a greating spectrometer (½ m focal length) and detected by a photomultiplier. An autophase lock-in amplifier was employed. The excitation intensity was changed by a set of neutral density filters. The PL data have been corrected for the system spectral response and the optical tract using a calibrated white light source.

RESULTS

In Fig. 1 we compare the typical spectral dependence of the intensity of the steady-state PL of p-ZGP single crystals made by LTDC and by HTDC. The PL was excited with He-Cd laser, which induces one electron transitions from the higher valence band to the direct minimum of the conduction band $\Gamma_{6v} \rightarrow \Gamma_{6c}$ (the A-transition) [1,9]. As in the case of crystals grown in the high-temperature process, at T=77 K radiative recombination in the impurity region of the spectrum is dominant in the material grown in the low-temperature processes and has a broad PL band. The full-width at half-height $\delta_{1/2}$ (FWHH) of the PL band in the crystals grown by the LTDC is considerably less than for samples grown by the HTDC (Table I), which may be an indication of a lower lattice defect concentration for the low-temperature grown of the ZGP. This reduction in defect may be due to a decreased concentration of antisite defects (Zn_{Ge} and Ge_{Zn}) and/or a narrower region of homogeneity, resulting from the lower crystallization temperature of the ZGP.

340

Table I. PL properties of p-ZGP single crystals.

Methods of preparation	Sample No.	T=77 K			T= 300 K	
		$h\omega_m^L$, eV	$\delta_{1/2}^L$, meV	I^S/I^L	$h\omega_m^S$, eV	$\delta_{1/2}^S$, meV
As-grown LTDC	5	1.44	310 (180-130)	<0.01		
As-grown HTDC	58	1.34	450 (200-250)	0.36	1.83	620 (290-330)
	17	1.38	410 (200-210)	0.02	1.85	640 (310-330)
Post-treatment after HTDC	25	1.38	370 (190-180)	0.02	1.85	660 (310-350
	LS	1.44	410 (210-200)	0.03	1.80	700 (330-370)

Note: The widths of the short- and long-wavelength parts of the band at half-height are indicated in parenthesis. Samples No. 5, 58, 17 and 25 prepared in Ioffe Institute, and sample No. LS— Lockheed Sanders.

The high-temperature process is characterized by a difference of 1.2-1.5 eV in the PL maximum for the crystals grown by the different processes and even within a single boule grown with a single process [7,8,10]. However, for the crystals grown at low temperatures the energy position $h\omega_m$ of the PL band maximum and FWHH are highly reproducible. Here it is fitting to note that the intensity of the long-wavelength PL in the crystals grown below T_{cr} is about an order of magnitude weaker than that of the material obtained at T_{cr}. All this evidence is associated with the energy spectrum of the ensemble of lattice defects, and therefore it is very sensitive to the methods and conditions of growth (Fig. 1).

Using the p-ZGP samples prepared at T<Tcr, we fabricated In/p-ZGP surface-barrier structures in the manner described in [11]. The relative quantum efficiency η in the spectra has a band in the neighborhood of the direct transitions in ZGP, and as the incident photon energy is reduced the photoresponse falls off. If we compare the photosensitivity spectrum of structures made from the low-temperature crystals with the results for structures made with the high-temperature crystals [2,8], we see first a reduction in the photoresponse and the absence of a maximum in η at the long-wavelength edge (hω< 2 eV), which, in addition to the PL dates, is also evidence for the lowered concentration of lattice defects in ZGP as a results of the reduced crystallization temperature.
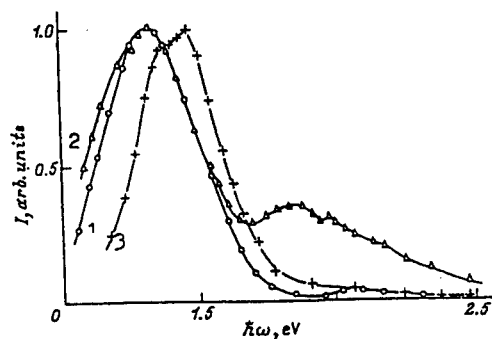

Fig. 2. PL spectra of p-ZGP crystals grown by HTDC at T= 77 K (As-grown samples: curve 1—No. 161, and curve 2—No. 58; post-grown heat-treatment at T_{HT}=500°C and t= 500 h, sample No. 8—curve 3).
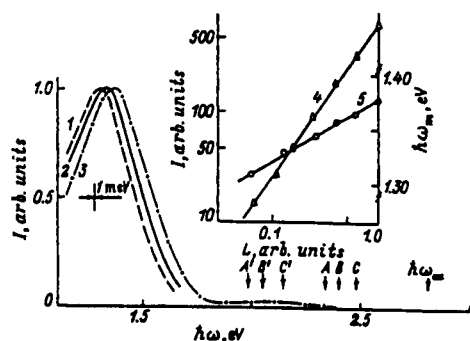
Fig. 3. PL spectra (curves 1-3) and the dependence of the PL intensity (curve 4) at $\hbar\omega_m L$ and the energy $\hbar\omega_m L$ on the relative laser excitation power density L at T=77 K (Sample No. 8, T_{HT}=500°C, t=500 h, energy excitation 2.82 eV. The A',B',C' and A,B,C mark the energies of interband transitions in ZGP [9]).

The results of the PL measurements for the typical samples made by HTDC are presented in Figs. 2-4 and also Table I. They are as follows.

When the PL is excited by radiation with photon energy higher than the energy direct band gap for ZGP [9], the radiative recombination of the typical crystals near 77 K included a wide, dominant, long-wavelength band with a maximum at $\hbar\omega_m$ and an extended short-wavelength shoulder (Fig. 2, curves 1 and 3) or a wide short-wavelength peak near 1.8-2 eV (Fig. 2, curve 2). The maximum of the short-wavelength component lies in the region of pseudodirect interband transitions and could be evidence of the edge radiative recombination, which has thus far not been observed [1,2] . It follows from Table I that the most intense short-wavelength radiation, characterized by the ratio I^S/I^L, is observed, as a rule, in the p-ZGP as-grown crystals (Table I) and post-grown heat-treatment, which results in "bleaching" [2], substantially decreases the intensity of the short-wavelength component of the PL at T=77 K. The large spectral widths $\delta_{1/2}$ at half-maximum of the short- and long-wavelength shows that they are not elementary. It should be noted that in the ZGP crystals subjected to "bleaching" heat-treatment [2] the maximum of the long-wavelength PL band is systematically shifted into the short-wavelength region and the FWHH decreases at the same time (Table I). The $\hbar\omega_m{}^L$ of as-grown ZGP crystals is localized in the region from 1.2 to 1.5 eV, and the PL band in most of these samples is asymmetric, which is manifested in the fact that the long- and short-wavelength half-width $\delta_{1/2}{}^L$ and $\delta_{1/2}{}^S$ are different (Table I). We also call attention to the fact that the parameters of the long-wavelength component of PL excited by radiation with photon energy above the energy of direct A-transitions in ZGP [1,9] were found to be close to the values reported in [7], where PL was excited with a He-Ne laser with the energy photon close to the energy of the pseudodirect A'-transitions for ZGP [9]. This circumstance, together with the fact $\hbar\omega_m{}^L < E_{A'}$, make it possible to associate the long-wavelength radiation to levels of different kinds of lattice defects in ZGP. In this case the change in the position $\hbar\omega_m L$ and the ratio I^S/I^L (Table I) indicate that the density and type of lattice defects in ZGP fluctuate as the conditions under which the single crystals are grown change.

Investigations of the effect of the excitation power density on the PL spectra (Fig. 3, curves 1-3) also support the conclusion that the long-wavelength component of the PL is due to the defects of different nature. It is obvious that as the excitation power density decreases, the energy position of the long-wavelength maximum $\hbar\omega_m{}^L$ and also the long- and short-wavelength wings of this band shift in parallel into the long-wavelength spectral region. The spectral contour of the long-wavelength band is virtually independent of the excitation power density, indicating that the mechanism of the radiative transitions remains essentially the same. As one can see from Fig. 3 (curve 1), in a number of crystals the short-wavelength PL component in the form of an extended
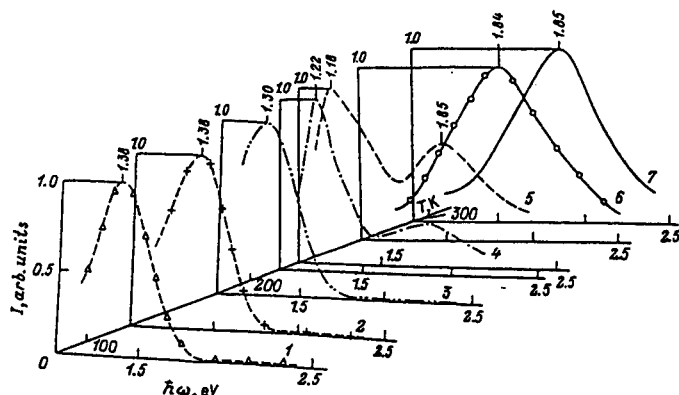
Fig. 4. Temperature dependence of the PL spectra of a p-ZGP crystal (Sample No. 25, L= const, energy excitation hw$_{exc}$=2.82 eV).

shoulder with a broad maximum lies in the region of pseudodirect and direct interband transitions for ZGP [1,9]. The PL intensity at the maximum of the long-wavelength band increases according to a power law I–L$^{1.1}$ (Fig. 3, curve 4), while the shift in the maximum of this band with excitation power density increasing by an order of magnitude (Fig. 3, curve 5) is characterized by the quantity ∂ (hω_m^L)/∂L=30 meV, which makes it possible, after taking into account the results of [12], to conclude that the concentration donors and acceptors, which cancel one another, in ZGP crystals is high. The dependence of the PL spectra on the excitation power density, shown in Fig. 3 (curves 1-3), is the basis for the conclusion that the PL is of a donor-acceptor nature. The changes in the donor and acceptor densities are associated with the crystal growth conditions, which accounts for the fluctuations in hω_mL and I^S/I^L in single crystals grown under different conditions and in the different research groups.

As the temperature increases, another transformation, which is characteristic of the investigated samples, arises in the PL spectra. A typical example of the observed evolution induced in the PL spectra by increasing the temperature of the crystals from 77 to 300 K is shown in Fig. 4. It is obvious that as the temperature increases, the long-wavelength component is quenched and above a certain temperature, which is characteristic of each crystal , a wide asymmetric short-wavelength component is excited and becomes dominant. At room temperature the PL spectra of all investigated samples already includes only the short-wavelength component with a maximum hω_m^S=1.85 eV. The quenching of the long-wavelength component is characterized by a weak temperature dependence in the low-temperatute range and an exponential decrease with several values of the activation energy of the PL quench process, which vary from sample to sample. The temperature dependence of the PL intensity was found to be weaker for the short-wavelength component. As a result, this component is dominant above a certain temperature. The temperature corresponding to the change in the contribution of these bands to the PL is different for the different samples; this is a consequence of the differences in the densities and nature radiative transitions. On the whole, the temperature dependences of the PL for p-ZGP crystals are characteristic been found in the quench processes of these components PL indicate that they could be attributed to the technological conditions. Further investigations could point to possible applications of the PL for rapid diagnostics of the properties and for adjustment of the growth conditions of ZGP single crystals.

CONCLUSIONS

Our experimental results indicate that the use of low-temperature crystallization reduces the concentration of lattice defects in single crystals of zinc germanium diphosphide and opens up new possibilities for increasing the efficiency of radiation converters made from this material. It is determined that the long-wavelength component PL with a maximum in the interval 1.2-1.5 eV for the different crystals is quenched in the temperature range 77-300 K. As a result, at room temperature the short-wavelength component of the PL with a maximum near 1.85 eV becomes the determining component. The nature of the radiative transitions in p-ZGP crystals is discussed on the basis of the obtained dates and it suggested that the PL properties which had been established can be used for diagnostics of optical quality this ternary chalcopyrite compounds.

ACKNOWLEDGMENT

REFERENCES

1. J.L. Shay and J.H.Wernick, Ternary Chalcopyrite Semiconductors: Growth, Electronic Properties, and Applications, Pergamon, New York, 1976, 168 p.

2. Yu.V.Rud', Fiz. Tech. Poluprovodn., 28, 1105 (1984) [Semiconductors, 28, 633 (1994)].

3. P.A. Budni, K. Ezzo, P.G. Schunemann, S. Minnigh, J.C. McCarthy, and T.M. Pollak in OSA Proceedings on Advances Solid State Lasers, edited by G. Dube and L.L. Chase (Optical Society of America, Washington, DC, 1991) 10, p. 335-341.

4. P.G. Schunemann, P.A. Budni, M.G. Knights, T.M. Pollak, E.P. Chicklis, and C.L. Marquardt in Advanced Solid State Lasers and Compact Blue-Green Laser Technical Digest (Optical Society of America, Washington, DC, 1993) 2, p. 131-135.

5. J.E. McCrae, Jr., M.R. Gregg, R.L. Hengehold, Y.K. Yeo, P.H. Ostdiek, M.C. Ohmer, P.G. Shunemann, and T.M. Pollak, Appl. Phys. Lett., 64, 3142 (1994).

6. N. Dietz, I. Tsveybak, W. Ruderman, G. Wood, and K.J. Bachmann, Appl. Phys. Lett., 64, 2759 (1994).

7. G.K. Averkieva, V.S. Grigoreva, I.A. Maltseva, V.D. Prochukhan, and Yu.V. Rud', Phys. Status Solidi (a), 39, 453 (1977).

8. Yu.V. Rud', and I.A.Maltseva, Fiz. Tekh. Poluprovodn., 19, 870 (1977) [Sov. Phys. Solid State, 19, 505 (1977)].

9. G. Babonas, A. Geinrich, V. Cords, J. Moneke, and A. Shileika, Litov. Fiz. Sb., 20, 619 (1990).

10. N.C. Giles, L.E. Halliburton, P.G. Schunemann, and T.M. Pollak, Appl. Phys. Lett. 66, 1758, (1995).

11. V.S. Grigoreva, A.A. Lebedev, K. Ovezov, V.D. Prochukhan, Yu.V. Rud', and A.A.Yakovenko, Fiz. Tekh. Poluprovodn., 9, 1605 (1975) [Sov. Phys. Semicond., 9, 1058 (1975)].

12 I.A. Maltseva, Yu.V. Rud', and Yu.K. Undalov, Fiz. Tekh. Poluprovodn., 10, 400 (1976) [Sov. Phys. Semicond., 10, 240 (1976)].

SELF-TRAPPING OF OPTICAL BEAMS AND LIGHT-INDUCED WAVEGUIDING IN PHOTOREFRACTIVE InP AT TELECOMMUNICATION WAVELENGTHS

M.E. CHAUVET*, S.A. HAWKINS*, G.J. SALAMO*, M. SEGEV**, D.F. BLISS***, G. BRYANT***

* Department of Physics, University of Arkansas, Fayetteville, AR 72701,
  salamo@comp.uark.edu

** Department of Electrical Engineering and Advanced Center for Photonics and Optoelectronic Materials, Princeton University, Princeton, New Jersey 08544

***U.S. Air Force, Rome Laboratory, Hanscom Air Force Base, Massachusetts 01731

ABSTRACT

We demonstrate self-trapping of a two-dimensional beam at 1.3 microns wavelength in resonantly-enhanced InP. The self-trapped beam also induces a two-dimensional optical waveguide in bulk InP, which guides a second beam at 1.55 micron wavelength.

INTRODUCTION

Optical spatial solitons[1-11] in photorefractive crystals offer potential applications in the field of all-optical switching and beam steering. A photorefractive soliton is created when a photo-induced index change exactly compensates for the diffraction of the beam. In this sense the beam is able to create its own waveguide. These effects have been extensively studied in ferroelectric oxide and sillenite oxide crystals for visible wavelengths. For the near infra-red wavelengths used in telecommunications, InP:Fe crystals have already demonstrated interesting photorefractive properties.[12,13] Self-trapping of a laser beam has been reported in InP:Fe.[14] In this paper we report the first observation of the use of a two-dimensional soliton formed at 1.3μm in InP to produce a waveguide to guide a second laser beam at 1.55μm.

EXPERIMENT

For the experiment the beam from a Nd:Yag laser at 1.3μm is collimated and focused with a 5cm focal length lens on the entrance face of an InP:Fe crystal whose temperature is stabilized at

345

Mat. Res. Soc. Symp. Proc. Vol. 450 ° 1997 Materials Research Society

297K. As shown in Figure 1, the electric field, E_0 is applied along <110>, the beam propagates along <1$\bar{1}$0>, and is polarized either horizontally or vertically at 45° from <110>. The beam size at the entrance face of the crystal has a diameter of about 55μm and diverges to a 170μm diameter at the exit face when no field is applied to the crystal. The InP:Fe crystal length is 1cm in the direction of the propagation. When a 12 kV/cm field is applied to the crystal, the beam is trapped and the beam diameter at the exit face is reduced to about 55μm.

RESULTS

Our experiments show that the beam is trapped to the same diameter for either a 1cm or a 0.5cm crystal length, supporting the conclusion that the trapped diameter is the same throughout the crystal. To show that an efficient waveguide is formed in the crystal, we have also propagated a 1.55μm 1mW/cm^2 laser beam collinear to the 1.3μm(1W/cm^2) trapped laser beam. To observe only the 1.55μm beam, a color filter is placed after the crystal. When both beams are vertically polarized, the 1.55μm beam is observed to be guided along the same direction as the 1.3μm beam (Fig. 2a). However, when the polarization of the 1.3μm beam is horizontal and the 1.55μm beam vertical, the 1.55μm beam is guided on the side of the 1.3μm trapped beam (Fig. 2b). While in both cases the 1.55μm beam is effectively guided, we can see that when the 1.3μm beam is horizontally polarized, the 1.55μm beam is efficiently guided and has a near circular profile.

In order to measure the index change responsible for the formation of the waveguide we added an interferometer to the apparatus. This measurement gives an increase of the refractive index in the center of the horizontally polarized 1.3μm beam and a strong decrease (10^{-4}) of the index on one side of beam. This amazingly strong decrease of the index implies that a large photorefractive space charge field is present. We calculate this space charge field to be about 50kV/cm when the applied external field across the crystal is only 5kV/cm. When the polarization of the 1.55μm beam is made vertical, the large index change on the side of the focused 1.3μm beam is seen as an increase in index and the 1.55μm beam is guided.

Despite the small value of the electro-optic coefficient r_{41}, it is clearly possible to induce large index changes. Physically, the large index change is due to the large space charge field which can be created due to the intensity temperature resonance and the low value of the dielectric constant associated with InP.
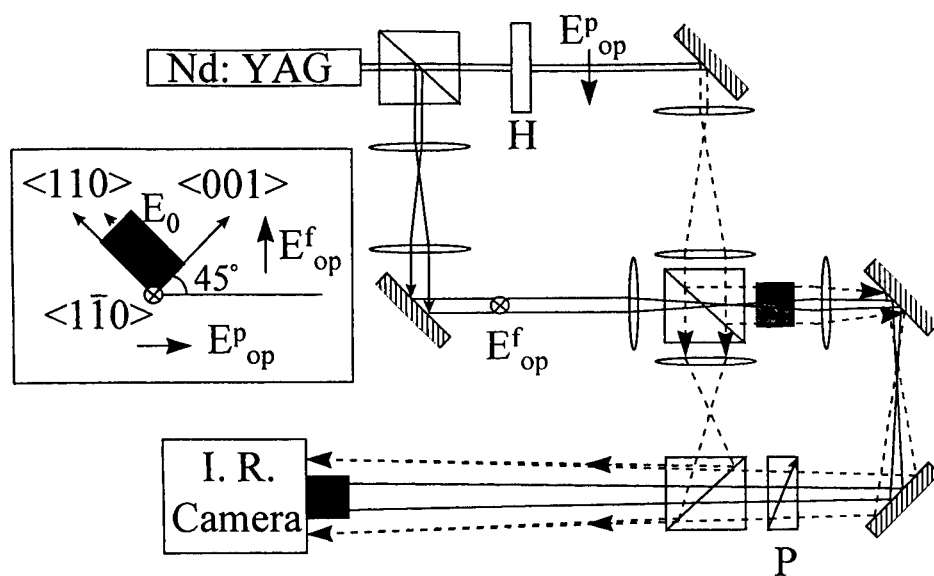
Fig. 1: Optical set-up for the two-dimensional trapping in InP:Fe. View of the entrance face of the crystal for the trapping observation, (a) and for the index change measurements, (b). The dashed beams are only used for the index change measurements. E^p_{op} polarization of the focused beam, E^p_{op}: polarization of the probe beam and reference beam, H: half-wave plate, C: InP:Fe crystal, P: polarizer.
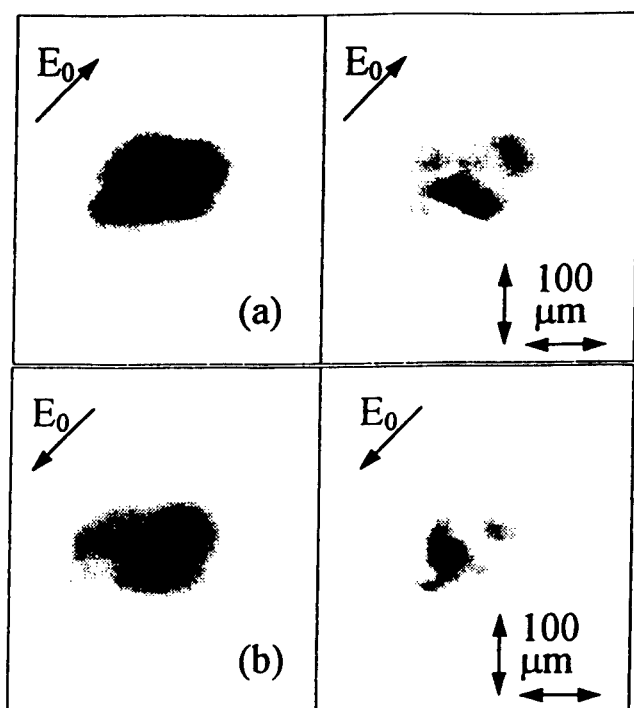
Fig. 2: Image of a 1.55μm wavelength beam at the exit face of the crystal without (left) and with (right) the 1.3μm trapped beam present. Top: both beams vertically polarized; bottom: 1.3μm beam horizontally polarized and 1.55μm beam vertically polarized. E_0=12kV/cm.

CONCLUSIONS

We have shown that two-dimensional optical waveguides can be self-induced in InP:Fe using the photorefractive effect at $1.3\mu m$ wavelength. The intensity dependent phenomenon is related to the intensity temperature resonance found for two-wave mixing measurements in InP:Fe. A refractive index change on the order of 10^{-4} has been measured, showing that a space charge field ten times larger than the applied field E_0 is present in the crystal. The trapping effect described in this paper offers a new way to exploit the photorefractive effect in InP:Fe in the design of reconfigurable optical interconnects.

REFERENCES

(1) M. Segev, B. Crosignani, A. Yariv and B. Fischer, Phys. Rev. Lett. **68**, 923 (1992).

(2) G. Duree, J. L. Shultz, G. Salamo, M. Segev, A. Yariv, B. Crosignani, P. DiPorto, E. Sharp and R^2 Neurgaonkar, Phys. Rev. Lett. **71**, 533 (1993).

(3) G. C. Valley, M. Segev, B. Crosignani, A. Yariv, M. M. Fejer and M. Bashaw, Phys. Rev. A **50**, Rapid Comm., R4457 (1994).

(4) M. Taya, M. Bashaw, M. M. Fejer, M. Segev and G. C. Valley, Phys. Rev. A **52**, 3095 (1995).

(5) M. Segev, G. C. Valley, B. Crosignani, P. DiPorto and A. Yariv, Phys. Rev. Lett. **73**, 3211 (1994).

(6) D. N. Christodoulides and M. I. Carvalho, J. Opt. Soc. Am. B**12**, 1628, (1995).

(7) M. Segev, M. Shih and G. C. Valley, J. Opt. Soc. Am B **13**, 706 (1996).

(9) Steady-state self-focusing effects in a biased photorefractive crystal were first observed by M. D. Iturbe-Castillo, P. A. Marquez-Aguilar, J. J. Sanchez-Mondragon, S. Stepanov and V. Vysloukh, Appl. Phys. Lett. **64**, 408 (1994).

(10) M. Shih, M. Segev, G. C. Valley, G. Salamo, B. Crosignani and P. DiPorto, Elect. Lett. **31**, 826 (1995); M. Shih, P. Leach, M. Segev, M. Garrett, G. Salamo and G. C. Valley, Opt. Lett. **21**, 324 (1996).

(11) Mitchell, Z. Chen, M. Shih and M. Segev, Phys. Rev. Lett. **77**, 490 (1996).

(12) V. Vieux, P. Gravey, N. Wolfer and G. Picoli, Appl. Phys. Lett., **58**, 2880 (1991).

(13) G. Picoli, P. Gravey, C. Ozkul and V. Vieux, J. Appl. Phys., **66**, 3798 (1989).

(14) M. Chauvet, S.A. Hawkins, G.J. Salamo, M. Segev, D.F. Bliss, and G. Bryant, Optics Lett., **21**, 1333 (1996).

Part VI

Interdiffusion in Heterostructures

DIFFUSED QUANTUM WELL STRUCTURES :
ADVANCES IN MATERIALS AND DEVICE REALIZATIONS

E. HERBERT LI
Department of Electrical and Electronic Engineering,
University of Hong Kong, Pokfulam Road, Hong Kong.
Email : ehli@eee.hku.hk

ABSTRACT

The Diffused Quantum Well (DFQW) structures created by both impurity induced and impurity free or vacancy promoted processes have recently been advanced to a higher level. The interdiffusion mechanism is no longer confined to two constituent atoms, but consists of two or multiple phase interdiffusion as well as multiple species, such as three cations interdiffusion and two pairs of cation-anion interdiffusion. Results show that the outcome of these interdiffusions is quite different. For instance, both compressive or tensile strain materials and both blue or red shifts in the bandgap can be achieved dependent on the type of interdiffusion. The advantage of being able to tune the material properties allows the realizations of higher performance lasers and modulators. Two lasing wavelengths (60 nm apart) are produced at $\lambda \approx 1.55\mu m$, on the same substrate, with threshold currents of 290mA, and an extremely large relative reflectance change (over 10000) is predicted with power consumption reduced by 67%. A six fold enhancement of the third order susceptibility over that of the bulk materials can be achieved by using the inter-subband transitions in the DFQW at $\lambda \approx 10\mu m$. Broadband (1000nm) detectors have also been realized due to the wide DFQW spectral bandwidth. Several state-of-the-art results of the DFQW will be summarized with an emphasis on the future developments and directions of the DFQW.

INTRODUCTION

Diffused quantum well (DFQW) is a non-square quantum well produced by interdiffusion of constituent atoms through the heterointerface. In the literature, DFQW is also referred to as quantum well mixing or intermixing (QWI) and quantum well disordering. Extensive work has recently been focused on the application of DFQWs since they provide post-growth tuning of the device operating wavelengths. The DFQWs can also be produced by a controlled interdiffusion process, which allows the rate of diffusion to be varied. This enables a selective area quantum well intermixing technology to laterally confine light for waveguiding. The process of achieving optical lateral confinement includes impurity induced disordering (IID) and impurity-free vacancy diffusion (IFVD). Performance of devices using DFQWs can also be improved and contribute to easy and effective realization of photonic integrated circuits.

The first work [1] on DFQW reported that Zn diffusion into an AlAs-GaAs superlatice, or into $Al_xGa_{1-x}As$-GaAs quantum well heterostructures can enhance the Al-Ga interdiffusion rate at the heterointerfaces and create uniform compositionally disordered $Al_xGa_{1-x}As$ even at lower temperature. Following this, the disk-shaped IR-red GaAs-AlAs superlattice lasers were demonstrated (cw 300K), which were monolithically integrated into rectangular yellow-gap $Al_xGa_{1-x}As$ cavities [2]. This process had become a first patent base on QW mixing.

In recent years, great effort has been put in using DFQW as a tool. Last year, several remarkable papers on lasers and modulators using DFQWs were published. For instance, the fabrication of multiple wavelength lasers and mutli-channel wavelength division multiplexers in GaAs/AlGaAs structures have been achieved using the technique of "selective intermixing in selected area" (SISA), based on IFVD [3]. Buried InGaAs/InP quantum wires with width down to 15mm was fabricated by lateral barrier modulation. The key technique involved was the local removal of the InP top barrier layer of the QW using high resolution electron beam lithography and selective wet chemical etching [4]. Impurity-free

353

Mat. Res. Soc. Symp. Proc. Vol. 450 ° 1997 Materials Research Society

disordering of InP based InGaAs/InGaAlAs QWs induced by three different dielectric thin cap films (SiO$_2$, SiN$_x$, SrF$_2$) has been produced [5]. Detail investigation of the in-plane spatial resolution of the disordering process was also developed [5]. In fact, significant reduction of threshold currents by IID in InGaAs/GaAs QW Ridge-Waveguide Lasers has succeeded [6]. Vertical cavity surface emitting lasers employing a Zn diffused and disordered spatial mode filter were fabricated and tested [61]. Low divergence output beam of surface emission was yielded and it is suitable for short haul optical fiber. Another device which is of interest is the superluminescent diode [8] whose band emission spectrum is broad enough for high sensitivity in fiber optical gyroscopes. In addition, report of reviews have been made on IID by Holonyak in 1988 [9], on the process of DFQW optoelectronics by Weiss in 1990 [10], and on QWI by Marsh in 1993 [11].

In this paper, we aim to make a comprehensive summary on the latest progress and development in DFQWs in different areas ranging from materials, production techniques, diffusion mechanisms, to device applications.

TECHNIQUES FOR MODIFYING INTERDIFFUSION RATES IN QWs

Ion Implantation

Ion Implantation is a technique in which direct injection of ionized, energetic atoms or molecules into a solid is employed. The ions injected will carry energies ranging from a few keV to several MeV, and implant doses from 10^{10} to more than 10^{16} ions/cm^2. Using small implantation energy, the damage introduced to the lattice structure will be reduced but with a decrease in the penetration depth, while with small dose of implants, there will be lesser enhancement of diffusion rate.
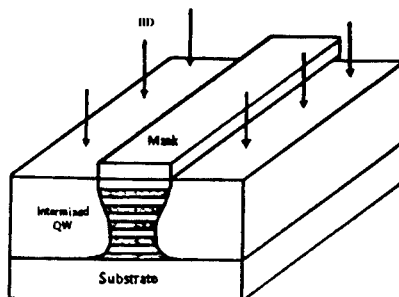
Fig. 1

Ion Implantation will significantly enhance the interdiffusion rate, and control the lateral and vertical depth of diffusion precisely (see Fig. 1). Different combinations of ions and substrates are possible and the most commonly used ones are p-type ions (Zn, Be), n-type ions (Si), neutral type ions (O), and constituent ions (Al, Ga, As) in AlGaAs/GaAs. It was reported that the use of neutral ions (including constituent ions) can prevent the production of free carriers induced by the charged ions (n-type or p-type) which will introduce propagation loss and thus reduce the refractive index of the intermixed QW materials [49]. Recent application of different implants are discussed as follows.

Interdiffusion of Al-Ga in an Al$_{0.3}$Ga$_{0.7}$As/GaAs supperlattice with focused-ion-beam implantation using Si has recently been studied [12]. This implantation technique provides maskless process with high spatial resolution and so, it enables precise patterning on the wafer for optoelectronics integrated circuits (OEIC) applications. Si ions are accelerated to 50 and 100 keV, and with rapid thermal annealing (RTA) at 950 °C for 10s. The diffusion coefficient was extracted to be 4.5x10^{-14}cm^2/s (with a Si ion dose of 1x10^{14}/cm^2) and in comparison with RTA, which can only produce an interdiffusion coefficient of 1.3x10^{-16} cm^2/s. This implies a 2 order magnitude enhancement.

In terms of constituent implantation, implanted gallium into both GaAs/AlGaAs and InGaAs/GaAs QWs have been performed and no significant effect on the diffusion coefficients was found in either systems. For arsenic implantation, the GaAs/AlGaAs system behaved identically to the Ga implanted sample, while in InGaAs/GaAs a region of enhanced interdiffusion was found, where the diffusion coefficient was enhanced by one order of magnitude [13].

Photoluminescence of low-energy, low dose oxygen ion implantation into AlGaAs/GaAs QWs has been studied [14]. Results showed that significant intermixing of both single and multiple

AlGaAs/GaAs QWs has been achieved using 155 keV implantation energy with doses as small as 5 x 10^{13} cm^{-2} after a moderate annealing step. A PL peak shift of 139 meV was observed in a 100Å GaAs QW after implanting 10^{14} cm^{-2} oxygen ions at 155 keV and annealed at 1050 ^{o}C for 40s, while a shift of up to 100 meV was obtained in the MQW with a dose of 8 x 10^{14} cm^{-2} ions at 450 keV with annealing at 950 ^{o}C for 120s.

In spite of these advantages, however, ion implantation technique will introduce more lattice damage and a large amount of defects in the materials. In order to reduce lattice damages, implantation energy is limited and thus, the penetration depth will be reduced.

Impurity Diffusion with Rapid Thermal Annealing

RTA is an essential step in impurity diffusion. Since impurity diffusion process undergoes a very slow rate on its own at conventional conditions, RTA is therefore used to promote its diffusion rate. RTA under temperature ranging from 900 to 1125 ^{o}C leads to substantial increase in interdiffusion rate. Most of the annealing is usually performed in the range from 400 to 1000 ^{o}C, and under a chemical environment with N_2 or even in vacuum to prevent oxidation to occur.

Marsh has demonstrated a method of RTA [11], in which flourine-implanted SCH and GRIN samples were capped with 1000Å of either SiO_2 or Si_3N_4 deposited by plasma-enhanced chemical vapour deposition. RTA is then performed at different temperatures (650 to 750 ^{o}C) in a nitrogen atmosphere. A more recent RTA experiment was performed in 1996 by Bacher which consists of samples annealed for one minute between 450 and 750 ^{o}C under a continuous flux of nitrogen to avoid surface oxidation [15].

Recently, there is a report on an novel application of impurity diffusion [50]. The structure used is a 80-period GaAs/AlAs superlattice with each layer 34 Å thick, Si dopped and annealed at 800 ^{o}C with a carbon source for 3 hours. PL spectra showed that the magnitude of the intermixing of Al and Ga increases with depth which is in contrast with the intermixing mechanism considering vacancy injection from the surface. This is because in theory, the diffusion coefficient of carbon is very small and hence carbon remains mainly at the surface of the MQW. Reduction of Si diffusion speed is mainly due to the combination of Si and carbon. As a result, the intermixing coefficient is small at the surface and increase gradually with depth.

In general, flexibility of easy alteration of the compositional profile inside the material is made possible in impurity diffusion. However, unintentional intermixing may take place in regions other than those implanted and precise depth control cannot be achieved with this diffusion method. The volume concentration of impurity drops during interdiffusion and will eventually drop below the threshold concentration at which the implantation enhanced disordering occurs.

Impurity Free Vacancy Diffusion (IFVD)

The mechanism of IFVD requires the encapsulation of MQW samples by a dielectric cap such as SiO_2 or Si_3N_4 (see Fig. 2) and then annealing at high temperature around 850 ^{o}C ~ 900 ^{o}C for 30 to 180 seconds. This will lead to out-diffusion of Ga into the cap and vacancies are generated on the group III sublattice that diffuse to the barriers and promote the interdiffusion in the MQWs. By using different combination of caps, selective area bandgap control is possible.
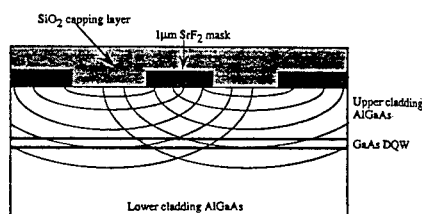

Fig. 2 [3]

A recent experiment on IFVD [16] was performed to investigate whether Ga vacancy are generated during SiO_2 capping and annealing. A uniformly Si doped GaAs epilayer of 10um thick with n = 4.8 x 10^{18} cm^{-3} grown by MBE was studied using photoluminscence and cathodoluminescence. As a

result, an increase in the strength of the emission at 1.2 eV is observed which is attributed to the Ga vacancy. This evidence shown that Ga vacancy is the species responsible for IFVD.

The advantage of using IFVD is that it is a simple method which requires much less equipment to perform. As discussed above in using ion implantation, only neutral species IID can circumvent the large optical propagation losses associated. However, neutral impurities still introduce substantial changes in material resistivity and trap concentrations. IFVD can create large bandgap energy shifts without these disadvantages of IID. However, using IFVD will increase the number of etching steps needed to control the thickness of SiO_2. Moreover, control of oxygen composition in SiO_xN_y is complex.

Laser Assisted Disordering

Laser assisted disordering is a direct write process that can pattern impurity induced layer disordering. This new technique employs a highly focused Ar^+ laser beam (see Fig. 3). For fabrication of AlGaAs-GaAs DFQW [17], the laser beam with lasing wavelength of 488 nm, is scanned through the heterostructure sample which is encapsulated with a 90 nm layer of $Si-Si_3N_4$. Its scan speed can be as high as 85 μm/s. The laser beam interaction region will result in a smooth cylindrical section on the micron scale. Annealing is then applied to drive the Si into the as-grown crystal, resulting in a local mixing of the crystal layers.

In a more recent report, pulsed photoabsorption-induced disordering technique was used to selectively intermix GaInAs/GaInAsP QW structure, which was studied by the use of high spatial resolution time-resolved PL. Measurements showed that a reduction in the non-radioactive recombination time of nearly two orders of magnitude as a result of this intermixing technique [53].

The laser assisted technique is a flexible process for optoelectronic device and circuit fabrication. However, a direct-write system is not an optium configuration for many application. For example, commercial production of diode lasers is based upon high yield, high throughput techniques such as photolighography. Further improvement is required.
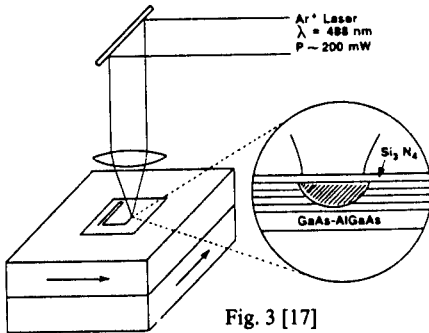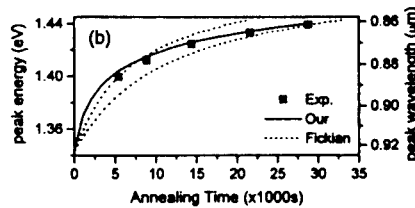
Fig. 3 [17]   Fig. 4 [19]

DIFFUSION MECHANISM

One Phase, Group III in $A_xB_{1-x}C$ system

Simple calculations were made under Fick's Law of diffusion to determine the composition profile x(z) for $Al_xGa_{1-x}As/GaAs$ and $In_xGa_{1-x}As/GaAs$ QWs [18]. This simple model leads to error function solutions :

$$x(z) = x_0 \left\{ R_1 - \frac{1}{2}R_1 \left[erf\left(\frac{L_z + 2z}{4L_d}\right) + erf\left(\frac{L_z - 2z}{4L_d}\right) \right] \right\}$$

where z is the growth axis, x_0 is the as-grown composition of the QW material, L_D is the interdiffusion length and L_z is the well thickness. For AlGaAs/GaAs QW, $R_1 = R_2 = 1$ and for InGaAs/GaAs QW, $R_1 = 0$

& $R_2 = -1$. It has been reported that this equation accounts for a wide range of diffusion coefficient values obtained in various III-V semiconductor systems [51,52].

On the other hand, it has been found recently that the above Fick's diffusion equation may not properly describe the interdiffsuion in the InGaAs/GaAs QW with strain [19]. The strain is believed to introduce changes in crystal defect concentration and thus diffusivity is also influenced by strain. Therefore, the non-Fickian equation, which is an expanded form of Fick's second law, is introduced :

$$\frac{\partial C}{\partial t} = \frac{\partial}{\partial z}\left(D_0 \exp(\kappa\ C)\frac{\partial C}{\partial z}\right)$$

where C is the indium concentration, D_0 is the diffusivity when no stress is applied, κ is the parameter indicating the degree of strain enhancement and is also a function of In concentration.

This equation has included the effects of strains empirically. The experimental PL peak shifts as a function of annealing time were well fitted by this equation, as shown in Fig. 4. Useful parameters, such as diffusivity of InGaAs/GaAs QW were found using this equation.

One Phase, Group III only in $A_xB_{1-x}C_yD_{1-y}$

Cation interdiffusion results in the formation of an InGaP/InGaAs abrupt interface from as-grown InGaAs/InP QW. Theoretical analysis [25] indicates that a large strain was built up across the well during early stage of interdiffusion. The strain and its effect on the bandgap profile of the disordered structure produces a distinctive quantum confinement profile which remains abrupt even after significant interdiffusion. This phenomenon together with a diffused well width which equals to that of the as-grown QW are in contrast to other material systems such as AlGaAs/GaAs and InGaAs/GaAs. The effect of strain results in a potential buildup in the barrier near the interface at the top of the well, while it gives rise to two miniwells at the bottom of the wells. The HH and LH band-edge splitting results in two distinct HH and LH confinement profiles with different depths.

One Phase, Group III plus V in $A_xB_{1-x}C_yD_{1-y}$ system

The effect of interdiffusion on the confinement profile of the quaternary material systems has been reported recently [20]. The intermixing of $In_{0.53}Ga_{0.47}As/InP$ has been modeled, taking into account different interdiffusion rates on the group III and group V sublattice. Error function distribution discussed above was used to represent the composition profile. A strained QW was resulted after intermixing. Theoretical results showed that when the cation interdiffusion rate is faster than that of the anion, the ground-state (C1-HH1) transition shifts to longer wavelengths. For prolonged interdiffusion, this shift to longer wavelengths, saturates and then decreases. This is in good agreement with the reported experimental results of Zn-diffused disordering [21-23] as well as thermal annealing of InGaAs/InP QWs [24]. When the anion diffusion rate is faster, results showed that the effective bandgap of the diffused QW would be the C1-LH1 ground state transition which shifts to shorter wavelength with interdiffusion. The tensile strain that is induced under these disordering conditions which moves the LH ground state above the HH ground state. Results obtained from these calculations showed that the control of relative extent of cation and anion interdiffusion offers different possiblities for optoelectronic device fabrication.

Two Phase, Group V in $A_xB_{1-x}C_yD_{1-y}$ system

Mukai [26] has derived a formula that describes the two-phase interdiffusion mechanism of the quaternary material system which includes the different interdiffusion coefficients between layers and interfacial discontinuity of interdiffused species. The formula was applied to analyze the dependence of an interdiffusion induced energy shift on annealing time, annealing temperature and well width in InGaAsP/InP QWs. Good agreement was achieved between the calculated and measured values.

Two phase Group V sublattice interdiffusion in $In_{0.53}Ga_{0.47}As/InP$ QW was also theoretically investigated [27] using the same formulation with a pseudo time dependence. This model has been

validated with an even better agreement with experimental results. However, perfect fitting can not be obtained and further work must be continued.

Multiple Species, Group III

The most recent analysis on multiple cations interdiffusion in $In_{0.53}Ga_{0.47}As/In_{0.52}Al_{0.48}As$ is performed using a model base on the expanded form of Fick's second law [28]:

$$\frac{\partial C_i}{\partial t} = \sum_{j=1}^{n-1} D_{ij} \nabla^2 C_{ij}$$

where n = the number of diffusable species, C is the indium concentration, D_0 is the diffusivity when no stress is applied. The model is fitted to the measured concentration data in order to determine their diffusion coefficients. It was found that the Ga-Ga diffusion coefficient is relatively large in comparison to the other rates so that the Ga concentration profiles show a more broadened distribution after annealing (see Fig. 5). The In-Ga diffusion is fund to be negative which gives rise to the inverse process of diffusion, causes sudden abrupt change in the In profiles at the interfaces. Again, further experimental work should be done to enable a large set of data to be fully analyzed.
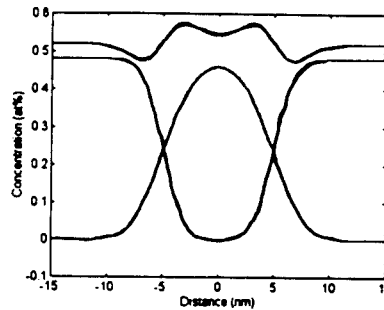

Fig. 5

BAND STRUCTURE

Effects of interdiffusion on the subbands in an AlGaAs/GaAs QW has been investigated theoretically [29] in which the subband energies and wave functions in an interdiffusion-induced AlGaAs/GaAs single quantum well structure were calculated. The confinement profile was modeled by an error function. The spatially dependent electron effective mass was taken into consideration using a non-parabolic band model derived from a fourth-order expansion in k with the coefficients determined using a 14-band calculation. The valence subband mixing between the heavy and light holes were also considered. It was found that subband properties of the nonsquare QW was different from that of the conventional SQW. First of all, the subband-edge energy will initially increase and then decrease with interdiffusion, which could be explained by the evolution of the nonsquare QW shape in terms of crossover point, which is defined as the confinement profile intersection at the well barrier interface of the as-grown and interdiffused QWs. Enhancement of interband transition is predicted for the off-diagonal selection rule at the initial stages of interdiffusion, and a reduced confinement of the wave function was also observed. Lastly, the enhancement of the lowest energy light-hole negative mass was also obtained. The non-monotonic behavior of the subband-edge energies suggested hat when only the lowest interband energy was used to characterize the interdiffusion process, errors are likely to occur. Analysis has also been done on InGaAs/GaAs QW and InGaAs/InP QW structures [30,31].

FAR-IR OPTICAL PROPERTIES

The first theoretical study of the linear and nonlinear intersubband absorption coefficients in AlGaAs/GaAs DFQW was reported by Li [59] following the first observation of an interdiffusion shifted intersubband transition energy by Ralston [60], see Fig. 6. Results indicated that the well shape variation can provide a large tuning wavelength range in the far IR region with an almost constant absorption. This DFQW structure can be used to produce a wide bandwidth detector. The DFQW structure can also provide lower leakage currents due to reduced tunneling between the wells since the barrier thickness at the ground state energy is always thicker than that at the excited state energy. Effects of interdiffusion on the intersubband optical properties in a modulated doped QW structure have also been investigated

theoretically [32]. Linear and nonlinear intersubband electroabsorption and the change in refractive index with different well width, doping concentration, Aluminium concentration ration in AlGaAs/GaAs QW were studied. A wide tuning range has been predicted which can be applied to the realization of multi-color and broadband photodetector. More recently, a DFQW has been employed to predict the enhancement of the third-harmonic susceptibility to an extent that it is six times better than the case of GaAs [33]. The obtained $\chi^{(3)}$ enhancement is as high as 2700 $(nm/V)^2$, as shown in Fig. 7, and may also be carefully varied to produce a tuning range. However, there are still technical problems in fabricating with a high yield and low price.
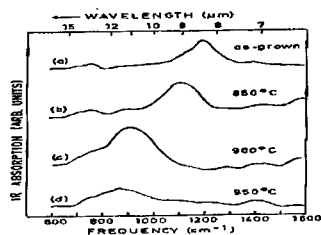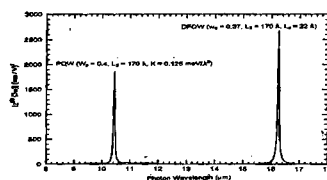

Fig. 6 [60]   Fig. 7 [33]

Fig. 6 and 7 show the enhancement of $\chi^{(3)}$ in which shifting of intersubband absorption resonance occurs.

INTER-BAND IR OPTICAL PROPERTIES

Absorption

The most recent experimental work of partially intermixed QW waveguides is performed in 1989 [34], with the incident focused laser beam polarized both parallel (TE) and perpendicular (TM) to the plane of the QW layers. These spectra show the polarization anisotropy characteristic of QW absorption. In the TE spectra, both the lh and hh excitons appear while in the TM spectra, the hh exciton disappears and the lh exciton absorption strength increases. The intermixing induced band-edge shifts are clearly seen. There are theoretical studies in which a hyperbolic function has been used to model the confinement profile of a disordered $Al_{0.3}Ga_{0.7}As/GaAs$ QW [54] and results predict a different absorption spectra for the TE and TM polarization, and which is in good agreement with published measurements near the absorption edge. In a more recent investigation, theoretical calculations are performed on polarized absorption coefficients of interdiffused AlGaAs/GaAs MQW [55]. Calculations were made without any approximation or presumption of the eigenstates. Results showed that for diffusion length ranging from 10Å to 30Å, the blue shift of the absorption edge is larger. The two dimensional QW properties were strongest in the beginning of interdiffusion.

Refractive Index

The effect of boron and fluorine IID on n_R of AlGaAs MQW was studied experimentally [39]. Substantial changes of > 1% in the refractive index were obtained in partially disordered material over the measured wavelength range. This implies that fluorine produces larger change than boron for similar annealing conditions. A few years later, experiment has been performed to investigate the effect of Zn IID on the refractive of AlGaAs/GaAs MQWs [38]. This is a structure consisting of several uncoupled MQW ridge waveguides with tapered disordering across the transverse direction was employed. The refractive index changes have been deduced as a function of the Ga/Al interdiffusion length by the use of an interference technique. A maximum index change of 0.083 and 0.062 was measured for significant disordering (L_d = 6.6 nm) at 35 and 100 meV below the band edge energy of the as-grown MQW respectively.

Moreover, the polarization dependent refractive index for both $Al_{0.3}Ga_{0.7}As$/GaAs and $In_{0.2}Ga_{0.8}As$/GaAs single QWs are calculated [36,37]. The confinement profile for the $Al_{0.3}Ga_{0.7}As$/GaAs DFQW is modeled by an error function and n_R is determined by the real and imaginary parts of the dielectric function including contributions from the Γ, X and L Brillouin zones. It was found that at longer wavelengths, n_R decreases with increasing interdiffusion which normally provides a positive index step with respect to a less interdiffused QW. For shorter wavelengths, the wavelength range for a positive refractive index step increases as the extent of disordering between two interdiffused QWs is increasing. Polarization dependent n_R of disordered, strained InGaAs/GaAs single QWs was also calculated using the same method applied to $Al_{0.3}Ga_{0.7}As$/GaAs QW. In this calculation, decrease in refractive index with increase in the extent of disordering at longer wavelengths was observed. These structures also exhibit birefringence in a range of wavelengths from the QW band-edge to barrier band-edge, which decreases with interdiffusion.

Electro-absorption and Electro-Optic

There has been one experimental measurement on perpendicular field electroabsorption in GaAs/AlGaAs QW structures [34] which have been modified via partial interdiffusion of the well and barrier layers. Quantum well Stark effect has been observed in the DFQW where the room temperature exciton peaks are blue shifted by at least 40 meV via partial layer interdiffusion. On the other hand, the Quantum well Stark effect has also been analyzed theoretically in an AlGaAs/GaAs DFQW. Results showed a twofold enhancement of the Stark shift for the interdiffused QW over that of the square QW for the same 50 kV/cm applied field [56]. Excitonic absorption peak also shows a much larger reduction with increasing applied field in the more extensively DFQWs. These characteristics may be used to realize optical modulators with high on/off ratio and lower drive voltage.

In 1995, electric field induced refractive index change and absorption coefficient change in TE polarization are analyzed at room temperature for various interdiffusion modified $Al_{0.3}Ga_{0.7}As$/GaAs QWs was also studied [35]. For small and medium interdiffusion lengths with fields of 100 and 50 kV/cm, respectively, improved chirping and electroabsorption can be obtained. In addition, in a selected set of interdiffusion lengths and fields, the material can be used for an electroabsorption modulator with reduced chirping in a wide range of operation wavelengths.

Optical Gain

Analyses are performed on laser gain and current density at room temperature for intermixed $Al_{0.3}Ga_{0.7}As$/GaAs single quantum well structures [41]. It was observed that small amount of intermixing will not affect the lasing quality much. Both the peak gain and current density remain about the same strength. However, for larger amount of intermixing, the lasing will diminish. A wide wavelength tuning range of 55 nm can be obtained without greatly affecting the quality of the lasing properties. Application of selective disordering to integrated optoelectronics devices on a planar substrate can be achieved.

DEVICES

Distributed Feedback (DFB) Lasers

The realization of gain coupled DFB lasers using the method of masked implantation induced QW intermixing was demonstrated [57]. The combination of Electron Beam Lithography and the implantation enhanced intermixing was successfully applied in the fabrication. It was found that the GaInAs/AlGaInAs material system has a high potential for tunable optoelectronic devices. A detail investigation on the integration processing steps such as implantation, subsequent annealing and re-growth with InP (MOVCD) was presented. Enhancement of side mode suppression ratio (SMSR) in λ/4 shifted DFB laser using DFQW is also proposed (Fig. 6). The suppression ratio can be increased significantly by introducing diffusion step along longitudinal direction of QW active region. Results

show that large κL (>2.6) devices with step refractive index profile will exhibit stable, single-mode operation. The maximum power for single mode operation is obtained for >50 mW [42].

Vertical-cavity surface-emitting lasers (VCSEL)

In the past two years the performance of VCSELs has dramatically improved. Following the discovery of using IID for carrier confinement in edge-emitting lasers, recently, there is an investigation on the dielectic-apertured VCL structure (see Fig. 8) using Zn IID to modify the perimeter of the QW active region for achieving enhanced carrier confinement [7].

Top contact
Polyimide
p-type GaAs/AlGaAs DBR
Zn diffusion
Laterally etched AlAs layer
Active region
n-type AlGaAs/AlAs DBR
n⁺ GaAs substrate
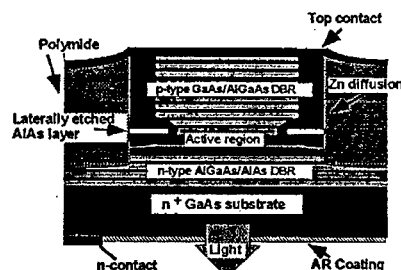n-contact
Light
AR Coating

Fig. 8 [7]

The laser is tested and it was found that threshold currents as low as 0.67 mA is obtained for IID-defined VCLs. The performance of IID-VCLs has been compared to air-gap apertured VCLs fabricated from adjacent material from the same wafer. SEM images of the active region and near field EL measurements indicated that the Zn-IID has resulted in confinement of the carriers in the lasers and such confinement should enable the generation of smaller diameter VCLs in the future.

Fabry-Perot Lasers

A multiple wavelength Fabry-Perot Laser was fabricated by vacancy enhanced QW disordering which involves the use of a dielectric cap annealing. The device structure consists of a Si doped GaAs substrate, followed by a 1.1 μm thick large gap $Al_{0.8}Ga_{0.2}As$ cladding layer and a 165 nm small gap $Al_{0.3}Ga_{0.7}As$ core containing single GaAs QW (7nm). Lasing wavelength was selectively shifted by 20nm compared with fabrication by as-grown material. SrF_2 capped laser will consume 14 mA but only 10 mA for SiO_2 capped laser [43]. Theoretical analysis was also performed in which Fabry Perot semiconductor laser with periodic change in the extent of interdiffusion along the longitudinal direction of the Quantum Well active region is proposed to improve the discrimination between cavity modes [58].

IID Ridge-waveguide (RW) Lasers

Si-induced disordering is used in producing the InGaAs/GaAs QW ridge-waveguide lasers via lateral confinement. The ridge stripe is etched by pure Cl_2 plasma to form a ridge stripe. Zn diffusion is processed at 620 °C for 20 minutes. Threshold current as low as 0.7 mA for pulsed operation and 0.9 mA for cw operation was achieved. Comparing with the IID RW laser with conventional ones, great improvement in internal loss can be seen although there is a reduction of the internal quantum efficiency with respect to the conventional ones. Leakage current and threshold current for IID RW are both lower than that of conventional RW laser [6].

Vertical-cavity Fabry-Perot reflection modulator

A Fabry-Perot reflection type modulator which uses interdiffused AlGaAs/GaAs quantum wells as the active cavity material has been studied and optimized theoretically [44]. An asymmetric Bragg reflector structure (modeled by transfer matrices), with a doped depletion layer in the heterostructure, has been considered. This is the first study to model such material system in this type of modulator, and the results show improvement in modulation property over the conventional rectangular quantum well modulator. In particular, the change of reflectance in the diffused quantum well modulator is almost 0.6 to 0.7, which is higher than that of the typically available values (~0.4 to 0.6), while the OFF-state on-resonance reflectance is almost close to zero. The operation voltage is also reduced by more than half, due to a higher tunneling rate of electrons, in the large extensively diffused quantum wells. The finesse of the more extensively diffused quantum well also improves. Both of these features improve the change

361

of the reflectance in the modulator. The operation wavelengths can be adjusted over a range of 100nm. However, the absorption coefficient change of the diffused quantum well increases only when there is a small amount of interdiffusion.

Superluminescent Diodes

A broad-spectrum LED was fabricated by high-energy ion implantation (1MeV P^+-ions) using a SiO_2 mask (a few micron of thickness) [8]. Annealing is then performed at 700 °C for 90 seconds. The device (Fig. 9) is then etched into a ridged structure to improve guiding. An increase in the emission full-width-half-maximum from 28 nm to 90 nm was observed. Emitted power of the diode will increase with the current.
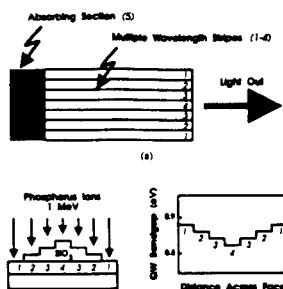

Fig. 9 [8]

Waveguide

In 1994, a novel waveguide polarization mode splitter using refractive index changes induced by superlattice disordering has been produced [45]. The operation principle of this splitter is based on the polarization-dependent refractive index changes induced by disordering InGaAs/InP sulerlattices using Si_3N_4 cap-annealing method. One attractive feature of this slpitter is that it requires no electrical control and is suitable for semiconductor monolithic integrated circuits. In 1995, a report [46] on an InGaAs/InP QW waveguide which is intermixed by using MeV phosphorous ion implantation. The bandgap is blue shifted by 90 nm in all planar process.

Infrared Photodetector

The barrier layer and well of an infrared photodetector are partially intermixed and peak detection wavelength is red shifted [47]. Successive annealing at 850 °C were used to tune the 8.13μm detector to 9.13 μm continuously. The layer structure is grown by MBE on semi-insulating GaAs substrate. Each of the 32 periods of QW consists of 346Å AlGaAs barriers and 58Å GaAs well. The peak absorption strength reduces with increasing annealing time fom 6% to 4%, but the overall quantum efficiency remains steady. The increase in dark current is mainly due to the details of subband energies and diffusion of Si through the layer structure can lower the device resistivity. The peak detection wavelength of the DFQW detector is beyond the half maximum point of that of the as-grown QW device. This indicates a clear-cut band-gap tuning between the two structures without crosstalk noise. The modified detector has responsivity comparable to as-grown material with larger spectral linewidth.

There is also a theoretical analysis of the intersubband infrared photodector performance for various stages of interdiffusion in AlGaAs/GaAs QW [40]. It was found that the absorption strength and responsivity are enhanced for certain extents of interdiffusion and the peak detection wavelength red shifts continuously with a large tunable range from 7 to 38.4 um. The dark current is at an acceptable value for small diffusion extent.

Solar Cell

Enhancement of energy conversion efficiency and spectral response by using interdiffused III-V semiconductor QW in photovoltaic device is proposed (see Fig.10). Calculations were based on an ideal solar cell model. The spectral response and energy efficiency are enhanced significantly by the DFQW structure.
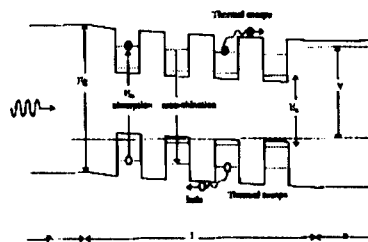

Fig. 10 [48]

Therefore, in view of the advances in the MBE and MOCVD growth techniques, DFQW photovoltaic device could provide a new approach to the high efficiency solar cell [48].

CONCLUSION

It can bee seen that DFQW has introduced a very promising future in optoelectronics. In fact, development has advanced not only in improving performance, reliability, and integration of existing optical components, but also for cultivating novel optical functions. A planar, compatible OEIC in which a variety of different optical and electronic devices are composed of a common MQW structure, is proposed. It has been demonstrated that this concept is expected to be applicable to long-wavelength materials such as AlInAs/InGaAs and InGaAsP/InP MQW and is believed to focus an important direction of OEIC structure towards high performance and productivity. Another aspect which is of interest will be photonic integrated circuits. Integration of InGaAs/InP MQW laser and a low-loss waveguide in the long-wavelenght region with high coupling efficiency using a cap-on-source-annealing technique has succeeded. This integration technique does not require a re-growth process, and it should prove useful for a variety of integrated devices, including mode-locked lasers and lasers integrated with optical modulators. In the future, further device enhancement and progressions are expected. In addition, wavelength demultiplexing moduator is foreseen as a new area of development.

ACKNOWLEDGEMENT

Reference

[1]   W. D. Laidig, N. Holonyak, Jr., and M. D. Camras, Appl. Phys. Lett. **38**, 776 (1981)
[2]   N. Holonyak, Jr., W. D. Laidig, and M. D. Camras, Appl. Phys. Lett. **39**, 102 (1981)
[3]   B.S.Ooi, S.G.Ayling, A.C.Bryce, and J.H.Marsh, IEEE Phot. Tech. Lett. **7**, 944 (1995)
[4]   K.Kerkel, J.Oshinowo, A.Forchel, J.Weber, and E.Zielinski, Appl. Phys. Lett. **67**, 3456 (1995)
[5]   S.Sudo, H.Onishi, Y.Nakano, Y.Shimogaki, K.Tada, M.J.Mondry, and L.A.Coldren, Jpn. J. Appl. Phys. **35** 1276 (1996)
[6]   S.Y.Hu, M.G.Peters, D.B.Young, A.C.Gossard, and L.A.Coldren, Phot. Tech. Lett. **7**, 712 (1995)
[7]   P.D.Floyd, B.J.Thibeault, J.Ko, D.B.Young, L.A.Coldren and J.L.Merz., LEOS anneal meeting, 207 (Boston, Nov 1996)
[8]   P.J.Poole, M.Davies, M.Dion, Y.Feng, S.Charbonneau, R.D.Goldberg, and I.V.Mitchell, Phot. Tech. Lett. **8**, 1145 (1996)
[9]   D. G. Deppe, and N. Holonyak, J. Appl. Phys. **64**, R93 (1988)
[10]   B. L. Weiss, Ed., Special Issue, Opt. Quantum. Electron. **23**, S799 (1991)
[11]   J. H. Marsh, Semicond. Sci. Technol., **8**, 1136 (1993)
[12]   P. Chen and A. J. Steckl, J. Appl. Phys. **77**, 5616 (1995)
[13]   I.V.Bradley, W.P.Gillin, K.PHomewood, and R.P.Webb., J. Appl. Phys. **73**, 1686 (1993)
[14]   B. L. Weiss, I. V. Bradley, and N. J. Whitehead, J. Appl. Phys. **71**, 5715 (1992)
[15]   G. Bacher, D. Tonnies, D. Eisert, and A. Forchel, J. Appl. Phys. **79**, 4368 (1996)
[16]   S.J.Lycett, A.J.Dewdney, M.Chisoni, C.E.Norman and R.Murray, J. Elect. Mat. **24**, 197 (1995)
[17]   J. E. Epler, R. L. Thornton, and T. L. Paoli, Appl. Phys. Lett. **52**, 1371 (1988)
[18]   S.Burkner, M.Maier, E.C.Larkins, W.Rothemund, E.P.O'Reilly, and J.D.Ralston, J. Elec. Mat. **24**, 805 (1995)
[19]   S. W. Ryu, I. Kim, and B. D. Choe, Appl. Phys. Lett. **67**, 1417 (1995)

[20]   W. C. Shiu, J. Micallef, I. Ng, and E. H. Li, Jnp. J. Appl. Phys. **34**, 1778 (1995)

[21]   I.J.Pape, P.LiKamWa, J.P.R.David, P.A.Clazton, P.N.Robson and D.Sykes, Electron. Lett. **24**, 910 (1988)

[22]   K. Nakashima, Y. Kawaguchi, Y. Kawamura, Y. Imamura and H. Asahi, Appl. Phys. Lett. **52**, 1383 (1988)

[23]   S. A. Schwarz, M. Koza, L. Nazar, and B. J. Skromme, Appl. Phys. Lett. **53**, 1051 (1988)

[24]   C. Francis, M. A. Bradley, P. Boucaud, F. H. Julien and M. Razeghi, Appl. Phys. Lett. **62**, 178 (1993)

[25]   J. Micallef, E. H. Li, and B. L. Weiss, J. Appl. Phys. **73**, 7524 (1993)

[26]   K. Mukai, M. Sugawara, and S. Yamzaki, Phy. Rev. B. **50**, 2273 (1993)

[27]   E. H. Li, J. Micallef, and W. C. Shiu, Mat. Res. Soc. Symp. Proc. **417**, 289 (1996)

[28]   Y.Chan, W.C.Shiu, W.K.Tsui, and E.H.Li, MRS FALL O8.4 (Boston, Dec 1996)

[29]   E. H. Li, B. L. Weiss and K. S. Chan, Phy. Rev. B. **46**, 15181 (1992)

[30]   J.Micallef, E.H.Li, K.S.Chan, and B.L.Weiss, Proc SPIE **1675**, 211 (1992)

[31]   M.C.Y.Chan, K.S.Chan, and E.H.Li, Proc SPIE **2886**, 140 (1996)

[32]   E. H. Li (to be published)

[33]   E. H. Li, Appl. Phys. Lett. **69**, 460 (1996)

[34]   J.D.Ralston, W.J.Schaff, D.P.Bour, and L.F.Eastman, Appl. Phys. Lett. **54**, 534 (1989)

[35]   E. H. Li and W. C. H. Choy, IEEE Phon. Tech. Lett. **7**, 881 (1995)

[36]   E. H. Li, B. L. Weiss, K. S. Chan, and J. Micallef, Appl. Phys. Lett. **62**, 550 (1993)

[37]   J. Micallef, E. H. Li, and B. L. Weiss, Appl. Phys. Lett. **62**, 3164 (1993)

[38]   S. K. Han, S. Sinha, and R. V. Ramaswarmy, Appl. Phys. Lett. **64**, 760 (1994)

[39]   S.I.Hansen, J.H.Marsh, J.S.Roberts, and R.Gwilliam, Appl. Phys. Lett. **58**, 1398 (1991)

[40]   A. S. W. Lee, and E. H. Li, Appl. Phys. Lett. **69**, 1 (1996)

[41]   E. H. Li, and K. S. Chan, Elect. Lett. **29**, 1233 (1993)

[42]   S. F. Yu and E. H. Li, IEEE Phot. Tech. Lett. **8**, 482 (1996)

[43]   D. Hofstetter, H. P. Azppe, J. E. Epler, and P. Riel, Appl. Phys. Lett. **67**, 1978 (1995)

[44]   W. C. H. Choy and E. H. Li, IEEE J. Quantum Elec. **33**, no.3 (1997)

[45]   Y. Suzuki, H. Iwamura, T. Miyazawa, and O. Mikami, IEEE J. Quantum Elec. **30**, 1794 (1994)

[46]   J. J. He, Y. Feng, E. S. Koteles, P. J. Poole, M. Davies, M. Dion, R. Goldberg, I. Mitchell and S. Charbonneau, Elect. Lett. **31**, 2094 (1995)

[47]   A.G.Steele, M.Buchanan, H.C.Liu, and Z.R.Wasilewski, J. Appl. Phys. **75**, 8234 (1994)

[48]   Y.Cheng, A.S.W.Lee, and E.H.Li, IEEE TENCON'95, 81 (1995); Y. Cheng, *MPhil Thesis* (University of Hong Kong, 1997)

[49]   I. V. Bradley, W. L. Weiss, and J. S. Roberts, Opt. Quantum Elect. **23**, S823 (1991)

[50]   Y.T.Oh, S.K.Kim, Y.H.Kim, T.W.Kang, and C.Y.Hong, J. Appl. Phys. **77**, 2415 (1995)

[51]   T. E. Schlesinger and T. Kuech, Appl. Phys. Lett. **49**, 519 (1986)

[52]   G. P. Kothiyal and P. Bhattacharya, J. Appl. Phys. **63**, 2760 (1988)

[53]   S. J. Fancey, G. S. Buller, J. S. Massa, A. C. Walker, C. J. McLean, A. McKee, A. C. Bryce, J. H. Marsh, and R. M. De La Rue, J. Appl. Phys. **79**, 9390 (1996)

[54]   E. H. Li and B. L. Weiss, IEEE J. Quantum Elect. **29**, 311 (1993)

[55]   E. H. Li, B. L. Weiss, and K. S. Chan, IEEE J. Quantum Elect. **32**, 1399 (1996)

[56]   E. H. Li, K. S. Chan B. L. Weiss, and J. Micallef, Appl. Phys. Lettl **63**, 533 (1993)

[57]   J. Kuhn, C. Kaden, V. Harle, H. Bolay, F. Scholz, H. Schweizer, H. Hillmer, R. Losch, and W. Schlapp., Nuclear Instru. Meth. Phys. Res. **B106**, 471 (1995)

[58]   C.W.Lo, S.F.Yu, and E.H.Li, IEEE Electron Devices Meeting, 30 (Hong Kong, 1995)

[59]   E. H. Li, B. L. Weiss, and A. Laszcz, Elect. Lett. **28**, 885 (1992)

[60]   J.D.Ralston, M.Ramsteiner, B.Dischler, M.Maier, G.Brandt, P.Koidl, J. Appl. Phys. **70**, 2195 (1991)

[61]   P.D.Floyd, M.G.Peters, L.A.Coldren, and J.L.Merz, IEEE Phot. Tech. Lett. **7**, 1388 (1995)

Interdiffusion in Quantum Wells: Mixing Mechanisms and Energy Levels

Richard G Gass and Howard E Jackson
Department of Physics, University of Cincinnati
Cincinnati, OH, 45220-0011, USA

and

P J Hughes and Bernard L Weiss
Department of Electronic & Electrical Engineering
University of Surrey, Guildford, SURREY GU2 5XH, UK

Abstract

Compositional interdiffusion in $Al_{0.3}Ga_{0.7}As$/GaAs superlattice structures with equal 3.5 nm barrier and well widths induced by Si focused ion beam implantation and subsequent rapid thermal annealing has been modeled. A strong depth dependence of the mixing process is observed at a Si^{++} energy of 100 keV and at a dose of $1x10^{14}$ cm^{-2}; this depth dependence is modeled by considering the second derivative of the vacancy profile. That is the maximum in the vacancy injection generated by the transient vacancy concentration gradient. We have included the dynamics of the spatial vacancy profile in the model and find good agreement with experimental results.

Interdiffusion across the well/barrier interfaces modifies the subband structure in AlGaAs/GaAs single quantum well (QW) structures. We have investigated the interrelated changes in both confinement energy of the subband states and the composition dependence of the bandgap energy in the QW, both of which are a strong function of the initial well width. Higher order transitions are found to be more sensitive than the ground state transitions to interdiffusion especially during the early stages of interdiffusion. These calculations model the experimental measurements (photoluminescence and photoreflectance) which are used to characterize interdiffused QW structures.

I.   Introduction

The modification of the optical properties of quantum well (QW) structures by post growth thermal techniques is of both intrinsic importance and of direct relevance for the fabrication and integration of QW devices for optoelectronic applications. Compositional and confinement profiles, and thus the subband and optical properties of the QW, for instance, can be tailored by the controlled thermal interdiffusion of atoms across the QW heterointerfaces.

A key to understanding the nature of interdiffusion and its use in the design of devices is the understanding of the variation of the optical properties of QW structures with interdiffusion. We have studied the effects both the nature of compositional diffusion and the effect of interdiffusion on the carrier confinement profile for a series of AlGaAs/GaAs single QW (SQW) structures. We briefly review some of our recent modeling efforts on the nature of compositional mixing in AlGaAs/GaAs superlattices and report on modeling calculations of the subband energy level structure after interdiffusion in SQWs.

II. Modeling of Compositional Mixing

The understanding of compositional mixing is important for the design and fabrication of a wide range of nanostructures, from optical waveguides, to DBR and DFB lasers, to quantum wires. The compositional mixing discussed here is that induced by ion implantation followed by rapid thermal annealing. The Al diffusivity in implanted AlGaAs/GaAs superlattices may be enhanced in by orders of magnitude, leading to its use in creating optoelectronics structures.

We very briefly review two models that have been advanced to explain compositional intermixing and identify a new phenomenological term in the interdiffusion description that is necessary to explain data obtained by several research groups [1-3]. Each of these models proceeds in two steps. Firstly the distribution of implanted ions and vacancies (a key to the mixing mechanism) are calculated, and the effects of the rapid thermal annealing is calculated by solving the diffusion equations simultaneously for the Al and vacancy distributions, which have been given by, Kahen and Rajeswaren [3], are :

$$\frac{\partial C_v}{\partial t} = \frac{\partial}{\partial x}(D_v \frac{\partial C_v}{\partial x}) - \frac{(C_v - C_{v,eq})}{\tau},$$ (1)

$$\frac{\partial C_{Al}}{\partial t} = \frac{\partial}{\partial x}(D_{Al} \frac{\partial C_{Al}}{\partial x}),$$ (2)

where D_v is the vacancy thermal equilibrium diffusion constant, C_{Al} is the Al lattice site concentration, and the transient Al diffusion coefficient is given by :

$$D_{Al}(x,t) = D_{Al,eq}(C_v/C_{v,eq})$$ (3)

where $D_{Al,eq}$ is the thermal equilibrium Al diffusion coefficient. This model provides a description of many of the salient experimental results.

However, Chen and Steckl [4] noted that the depth dependence of the intermixing, as seen in secondary ion mass spectroscopy (SIMS) results, was not accurately predicted. In particular, the measured depth dependence displayed a region of greater mixing (a "pinch-off" region) near the region where the second derivative of the vacancy concentration was a maximum. Thus they were led to propose a modification to the Al diffusivity, replacing Eq. 3 above with :

$$D_{Al}(x,t) = D_{Al,eq} \frac{C_v}{C_{v,eq}} \exp\left(\alpha \frac{\partial^2 C_v(x,t)}{\partial x^2} - \phi \right). \tag{4}$$

Physically, this equation suggests that the interdiffusion during rapid thermal annealing is affected by the movement of vacancies due to the implantation-induced gradient. Although no calculations were carried out using this equation, the dependence on the second derivative of vacancy concentration clearly provides for a pinch off region in the depth dependence of the intermixing. Calculations using the Kahen et al. [3] model cannot provide the observed pinch off region.

We suggest a different phenomenological equation for the Al diffusivity:

$$D_{Al}(x,t) = D_{Al,eq} \exp\left(\beta \frac{\partial C_v}{\partial t} \right), \tag{5}$$

This diffusivity is different from that in Eq 3 since here the rate of change of the vacancy concentration is important, but is connected to the diffusivity of Eq 4 in that *enhanced interdiffusion* will be predicted at certain depths.

Gass and Jackson have carried out extensive numerical calculations of the interdiffusion versus depth as a function of time [5]. For example, for a superlattice of 3.5 nm $Al_{0.3} Ga_{0.7}$ As barriers and 3.5 nm GaAs wells (similar to that used by Chen and Steckl), we predict a largely unmixed region near the surface, followed by a pinch-off region, followed by an increasingly unmixed region as the depth increases, a result distinctively in contrast to the model of Kahen et al. Figure 1 displays a snapshot of the

367

interdiffusion at t = 4s using the parameters $D_{Al,eq}$ = 0.1 nm^2/s, D_v = 1000 nm^2/s and $C_{v,eq}$ = (1/250)/nm^3 calculated with the two models.
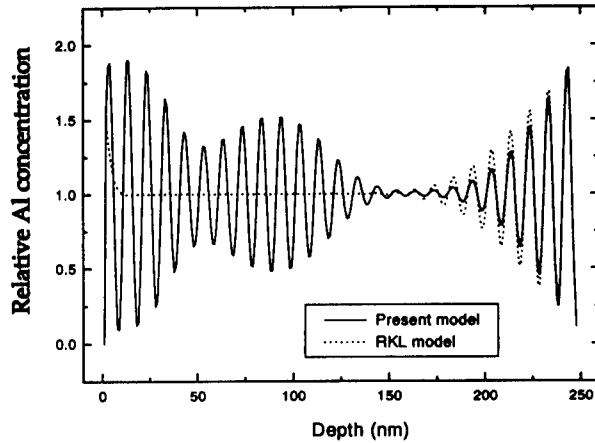

Fig. 1 : Plot of relative aluminum concentration versus depth (nm) after 4 seconds of interdiffusion, using the parameters given in the text. The dotted line is the result of calculations using the Kahen, Rajeswaran, Lee model and the solid line is the result of calculations using the model of Gass and Jackson (see text).

III. Energies of Interdiffused Single Quantum Well Structures

Interdiffusion across the well/barrier interfaces modifies the subband structure in AlGaAs/GaAs single quantum well structures. The modification of material properties that accompanies such interdiffusion is the basis for a variety of devices from optical channel waveguides to laser diode structures. We have investigated the interrelated changes in both the confinement energy of the subband states and the composition dependence of the bandgap energy in the QW; they are a strong function of the initial QW width. To simply the problem we considered only SQW structures in these calculations. An understanding of interdiffusion in QWs provides a detailed understanding of the widely used experimental characterization probes of photoluminescence and photoreflectance.

The theoretical model of Li et al. [6] was used to calculate the effects of interdiffusion on the subband states and thus the interband transitions of AlGaAs/GaAs SQW structures. This model structure has a GaAs SQW with varying well widths (L_z) bounded on both sides by 100 nm $Al_{0.3} Ga_{0.7}$ As barrier layers. Changes in the subband energy states were calculated for different values of the interdiffusion length L_d (where L_d = (D t)$^{1/2}$, D is

the temperature dependent Al-Ga interdiffusion coefficient, and t the annealing time), by solving the Schrodinger equation using a finite difference method.

An example of our results is shown in Figure 2, where we show the transition energies for the ground state transition as a function of the normalized diffusion length (L_d/L_z) where L_z is 2.5 nm.
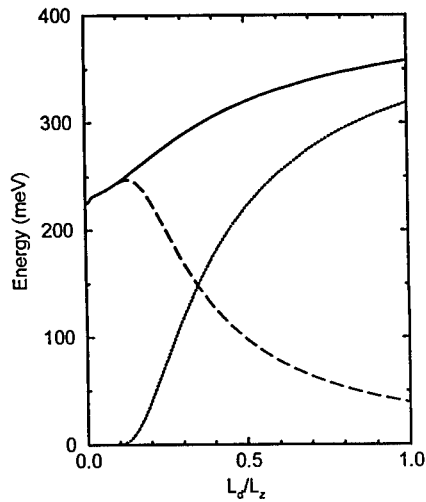
Fig. 2 : The variation of the ground state transition energy (solid line) as a function of the normalised diffusion length. The dashed and dotted lines represent the contributions of the confinement and compositional energy changes to the ground state transition energy.

The measured transition energy includes changes in both the confinement and compositional energies. These two competing effects, essentially the effective interdiffused well width and the effective interdiffused well depth, dominate for differing L_d and differing L_z, but initially changes in the confinement effect dominate.

Similar calculations have been carried out for the higher order transitions where we find increased sensitivity and a dependence on the electron-hole spatial probability distributions. A more detailed description of these results is presented elsewhere [7].

IV. Summary

We have explored theoretical modeling of both the nature and effects of compositional interdiffusion on the energy subbands of an SQW structure. We suggest that the observed depth dependence of compositional interdiffusion may require a new description which includes an additional term to describe an enhanced interdiffusion region. Calculations of interdiffusion in an AlGaAs/GaAs SQW provide the explicit dependence on the interdiffusion length L_d, identify regions where either the confinement or the concentration effects dominate, and suggest that higher order transitions are more sensitive to these effects.

References:

1. K. B. Kahen, G. Rajewaran and S.-Tong Lee, Appl. Phys. Lett., **53**, 1635 (1988).
2. S.-Tong, G. Braunstein, P. Fellinger, K. B. Kahen, and G. Rajeswaran, Appl. Phys. Lett., **53**, 2531 (1988).
3. K. B. Kahen and G. Rajeswaran, J. Appl. Phys., **66**, 545 (1989).
4. P. Chen and A. J. Steckl, J. Appl. Phys., **77**, 5616 (1995).
5. R. Gass and H. E. Jackson, to be published.
6. E. H. Li, B. L. Weiss and K. S. Chan, Phys. Rev. **B46**, 15181 (1992).
7. P Hughes, B. L. Weiss and H. E. Jackson, submitted for publication.

POLARIZATION INSENSITIVITY IN INTERDIFFUSED, STRAINED InGaAs/InP QUANTUM WELLS

Joseph Micallef, James L. Borg, and Wai-Chee Shiu[*]
Department of Microelectronics, University of Malta, Msida MSD06, Malta
[*] Department of Mathematics, Hong Kong Baptist University, Waterloo Road, Hong Kong

ABSTRACT

Theoretical results are presented showing how quantum well disordering affects the TE and TM absorption coefficient spectra of $In_{0.53}Ga_{0.47}As$/InP single quantum wells. An error function distribution is used to model the constituent atom composition after interdiffusion. Different interdiffusion rates on the group V and group III sublattices are considered resulting in a strained structure. With a suitable interdiffusion process the heavy hole and light hole ground state, excitonic transition energies merge and the absorption coefficient spectra near the fundamental absorption edge become polarization insensitive. The results also show that this polarization insensitivity can persist with the application of an electric field, which is of considerable interest in waveguide modulators.

INTRODUCTION

There is increasing interest in polarization independent modulators for optical communication systems since optical signals propagating along optical fibres do not usually maintain light polarization. New high-speed applications such as in-line optical pulse reshaping and retiming, and optical demultiplexing [1] require polarization insensitivity. Semiconductor quantum well (QW) optical modulators, which utilize the quantum–confined Stark effect (QCSE), offer the potential of enhanced device performance such as high on/off ratios, low driving voltages, and small device sizes [2,3], and are suitable for monolithic integration with other semiconductor optical devices [4]. However, in waveguide modulators where light propagates parallel to the QW plane, optical absorption exhibits strong polarization dependence since TE polarization interacts mainly with heavy holes while TM polarization interacts with light holes. This polarization sensitivity can be reduced if degeneracy of the heavy- and light-hole exciton peaks is achieved through bandgap engineering.

QW disordering in III-V semiconductors, which results in the interdiffusion of constituent atoms across the well-barrier heterointerfaces, offers the potential of continuous modification of the material bandgap, and hence of varying the absorption edge, in localized areas. The extent of interdiffusion and thus of the bandgap modification can be controlled by the post-growth QW disordering process parameters. This process has been used to produce lateral photon confinement in lasers and optical waveguides [5], shift the emission wavelength of an InP-based quantum well laser structure [6] and it has the potential to improve modulation performance by enhancing the on/off ratio and lowering the drive voltage [7].

Tensile strain in InGaAs/InP QW structures can be used as a tool to obtain polarization independent electroabsorption [8]. Coherent tensile strain reduces the energy gap between the conduction band and both the degenerate valence bands and the spin-orbit split-off band, and

at the same time causes the LH band to move towards the conduction band edge and the HH band to move away from the conduction band edge. One approach that can lead to the merging of the heavy-hole (HH) and light-hole (LH) ground state transition energies is to grow lattice-matched InGaAs/InP QWs and then use post-growth QW interdiffusion to introduce the required tensile strain.

Experimental results of the disordering of $In_{0.53}Ga_{0.47}As/InP$ QW structures have been interpreted in terms of three different interdiffusion processes: i) comparable interdiffusion rates on both group III and group V sublattices, ii) interdiffusion on group III sublattice only, and iii) interdiffusion on both sublattices but with different interdiffusion rates [9-12]. In this paper the effects of different interdiffusion rates on the two sublattices in an $In_{0.53}Ga_{0.47}As/InP$ single QW on the fundamental absorption edge for TE and TM polarizations are modelled, taking into consideration the graded compositional profiles and the strain build up that result in the interdiffused QW structure.

COMPUTATIONAL CONSIDERATIONS

An $In_{0.53}Ga_{0.47}As$ layer sandwiched between thick InP barriers is considered here. The interdiffusion processes on the two sublattices are modelled by two different interdiffusion lengths [12]. The interdiffusion of In and Ga atoms is characterized by a diffusion length L_d, which is defined as $L_d = (Dt)^{1/2}$, where D is the diffusion coefficient and t is the diffusion time; the interdiffusion of As and P atoms is characterized by a different diffusion length L_d'. Lattice-matching to InP only exists for $In_xGa_{1-x}As_yP_{1-y}$ materials with $y \approx 2.2(1 - x)$ [13], so that for the case being considered here, with $L_d' \neq L_d$, a strained QW structure results. After disordering, the composition of the interdiffused atoms across the QW is assumed to have an error function distribution [14]. The constituent atom compositional profiles can, therefor, be represented as follows:

(i) in the group III sublattice, the In concentration after interdiffusion. $\tilde{x}(z)$, is described by

$$\tilde{x}(z) \quad = \quad 1 - \frac{1 - x}{2} \left[erf\left(\frac{L_z + 2z}{4 L_d}\right) \quad + \quad erf\left(\frac{L_z - 2z}{4 L_d}\right) \right]$$

where L_z is the as-grown well width, z is the growth direction, and the QW is centred at z = 0.

(ii) in the group V sublattice, the As compositional profile after interdiffusion. $\tilde{y}(z)$, is given by

$$\tilde{y}(z) \quad = \quad \frac{y}{2} \left[erf\left(\frac{L_z + 2z}{4 L_d'}\right) \quad + \quad erf\left(\frac{L_z - 2z}{4 L_d'}\right) \right]$$

where y = 1 is the As concentration of the as-grown structure.

The compositional profiles in the disordered QW structure imply that the carrier effective mass, the bulk bandgap, the strain and its effects vary continuously across the QW. Consequently, the carrier effective mass. $m^*_r(z)$, is now z-dependent and is obtained from $m^*_r(z) = m^o_r(\tilde{x},\tilde{y})$, where $m^o_r(x,y)$ is the respective carrier $In_xGa_{1-x}As_yP_{1-y}$ bulk effective mass, and r denotes either the electron (C), heavy hole (HH), or light hole (LH). The unstrained (bulk) bandgap in the well, $E_g(\tilde{x},\tilde{y})$, is also a function of the compositional profile, so that the

unstrained potential profile after interdiffusion, $\Delta E_r(\tilde{x},\tilde{y})$, varies across the well and is given by $\Delta E_r(\tilde{x},\tilde{y}) = Q_r \Delta E_g(\tilde{x},\tilde{y})$, where Q_r is the band offset and ΔE_g is the unstrained bandgap offset.

The carrier confinement profile after interdiffusion, obtained by modifying the bulk postprocessing potential profile with the variable strain effects, is determined from [15]:
$U_r(z) = Q_r [\Delta E_g(\tilde{x},\tilde{y}) - S_\perp(\tilde{x},\tilde{y})] \pm S_{||r}(\tilde{x},\tilde{y})$, where $S_\perp(\tilde{x},\tilde{y})$ is the change in the bulk bandgap due to the biaxial component of strain, and $S_{||r}(\tilde{x},\tilde{y})$ is the potential corresponding to the HH–LH band edge splitting induced by the uniaxial component of strain. $S_{||HH}(\tilde{x},\tilde{y})$ and $S_{||LH}(\tilde{x},\tilde{y})$ are asymmetric due to the coupling between the LH and split off band, and $S_{||C}(\tilde{x},\tilde{y}) = 0$. The detailed expressions for $S_{||HH}(\tilde{x},\tilde{y})$ and $S_{||LH}(\tilde{x},\tilde{y})$ are derived in [15].

The electron and hole subband edge structure is obtained using the envelope function scheme by introducing these variations in the appropriate one-electron Schrödinger equation, which is then solved numerically to obtain the subband energy levels, the interband transition energies, and the envelope wave functions. Details of the calculations are given in [15]. The absorption coefficient spectrum near the fundamental absorption edge is next calculated taking into consideration the ground state interband and 1 S exciton optical absorption in the interdiffused structure, where the HH and LH related 1 S exciton binding energies and wave functions are determined by a perturbative-variational method. Details of these calculations are reported in [16].

RESULTS AND DISCUSSION

The structure considered here is an undoped $In_{0.53}Ga_{0.47}As/InP$ single QW layer, with an as-grown width $L_z = 6$ nm, lattice-matched to thick InP barriers. The interdiffusion process is represented by the condition $L_d' = 2L_d$.

The compositional profile, in-plane strain, and carrier confinement profiles for $L_d' = 2L_d = 1.41$ nm are shown in Fig. 1. The interdiffusion on the group V sublattice is faster than that on the group III sublattice, with the result that the well becomes InGaAsP, Fig. 1(a), with constituent atoms compositional profiles that give rise to a tensile strain in the interdiffused QW, Fig. 1(b). For the structure and interdiffusion conditions considered here a tensile strain of about 0.6% is induced in the centre of the well. The compositional profile also causes a compressive strain in the barrier close to the interface. The combination of the unstrained bandgap and the effects of the strain distribution on this bandgap gives rise to the confinement profiles in Fig. 1(c). The LH potential profile is shifted towards the electron (C) potential profile, while the HH potential profile is shifted away from the electron potential profile. Under these conditions the C–HH and C–LH ground state transition energies coincide. The effects of the tensile strain induced in the interdiffused QW on the HH and LH confinement profiles compensate the energy level splitting of the HH and LH ground states due to the different hole masses.

The TE and TM absorption coefficient spectra near the fundamental absorption edge are shown in Fig. 2, without the application of an electric field and for an applied field $F = 100$ kV/cm. The exciton peaks shift to longer wavelengths with the application of the electric field reflecting the QCSE, and at the same time decrease in value. In the interdiffused QW an enhanced Stark shift can result compared to the as-grown QW [7]. The effective width of the tilted confinement profile experienced by the electron and hole ground states under the action of the applied field is larger in the interdiffused QW than in the as-grown QW. As a result the applied field lowers the ground state subbands, and thus the ground state transition energy, to a greater extent in the interdiffused QW. The figure also shows that the fundamental

Fig. 1(a). Composition profile
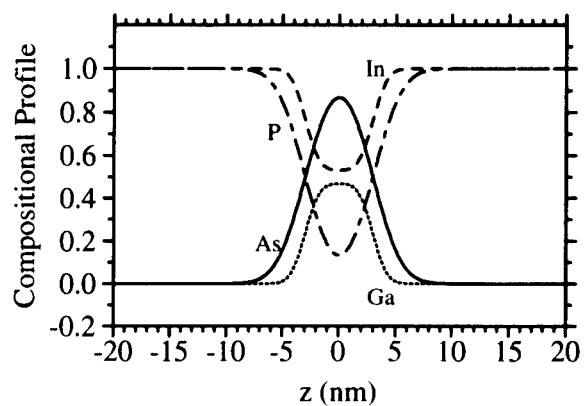for L_z = 6 nm, L_d' = 1.41 nm,
with well centre at z = 0.

Compositional Profile

1.0
0.8
0.6
0.4
0.2
0.0
-0.2

In

P

As

Ga

-20 -15 -10 -5 0 5 10 15 20

z (nm)

Fig. 1(b). In-plane strain for
the interdiffused QW.

In-Plane Strain %

1.0
0.5
0.0
-0.5
-1.0

-20 -15 -10 -5 0 5 10 15 20

z (nm)
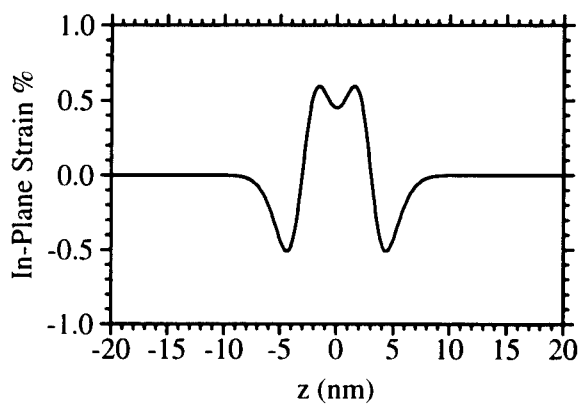
Fig. 1(c).   Carrier confinement
profiles for electron (C), heavy
hole (HH) and light hole (LH).

Confinement Profile (eV)

1.5
1.0
0.5
0.0
-0.5

C

LH

HH

-20 -15 -10 -5 0 5 10 15 20

z (nm)
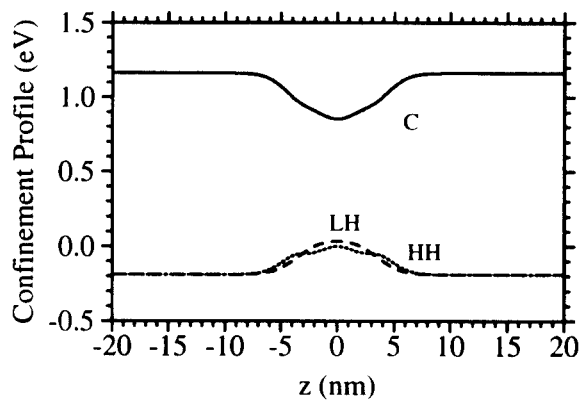
absorption edges for the two polarizations are quite close to each other for both F = 0 and F = 100 kV/cm, indicating that polarization insensitive electroabsorption is possible in the interdiffused InGaAsP QW structure.
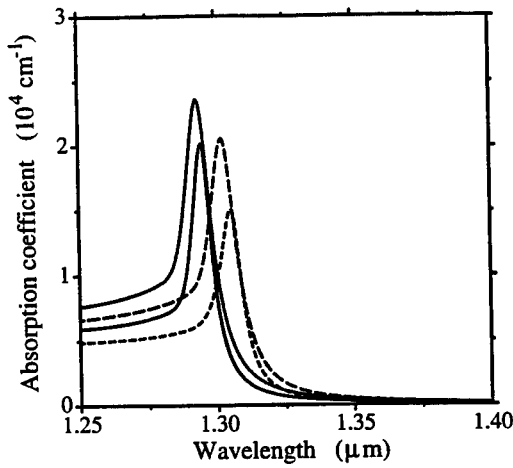

Fig. 2. Absorption coefficient spectra for TE and TM polarization for the interdiffused InGaAs/InP quantum well at $L_d' = 1.41$ nm, calculated for applied electric field F = 0 kV/cm, solid line for TE, dotted line for TM, and F = 100 kV/cm, short-dash for TE, and long-dash for TM.

Fig. 3 shows the electric field dependence of the absorption coefficient change $\Delta\alpha$ for TE and TM polarizations at the wavelength $\lambda = 1.305$ μm for the interdiffused QW structure, where $\Delta\alpha = \alpha_F - \alpha_{F=0}$. With the application of an electric field the absorption change increases consistently and a significant increase in $\Delta\alpha$ results at F = 100 kV/cm. For the InGaAs/InP QW disordering process parameters considered here, the polarization characteristics of the absorption coefficient change are quite controlled and the polarization insensitivity persists even at the higher electric fields.
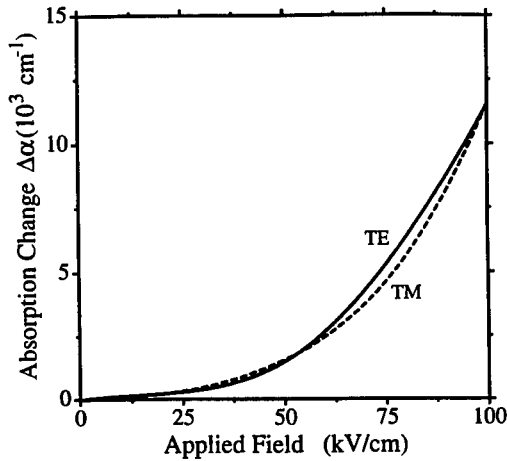

Fig. 3. Absorption coefficient change $\Delta\alpha$ with applied electric field, where $\Delta\alpha = \alpha_F - \alpha_{F=0}$, for TE and TM polarization, for $\lambda = 1.305$ μm

CONCLUSIONS

The interdiffusion of $In_{0.53}Ga_{0.47}As$/InP QWs as an approach for controlling the polarization-sensitive characteristics of the absorption coefficient and the absorption change due to the QCSE has been investigated theoretically. When the group V sublattice interdiffusion rate is greater than the group III sublattice interdiffusion rate a tensile strain results in the interdiffused QW, leading to degeneracy of the heavy- and light-hole transition energies. Results presented for absorption coefficient spectra near the fundamental absorption edge, and for the electric field dependence of the absorption coefficient change, indicate that optimization of the interdiffusion process can lead to polarization-insensitive modulation at particular wavelengths. For the QW structure and interdiffusion parameters considered here polarization insensitivity can be achieved around 1.3 μm, by inducing a 0.6% tensile strain in the centre of the interdiffused InGaAsP well. This can be a promising approach for polarization-insensitive electroabsorption devices.

ACKNOWLEDGEMENT

REFERENCES

1. M. Suzuki, H. Tanaka, N. Edagawa, and Y. Matsushima, J. Lightwave Technol. **LT-10**, 1912 (1992).
2. I. Kotaka, K. Wakita, K. Kawano, H. Asai, and M. Naganuma, Electron. Lett. **27**, 2162 (1991).
3. T. Ido, H. Sano, D.J. Moss, S. Tanaka, and A. Takai, IEEE Photon. Technol. Lett. **6**, 1207, (1994).
4. T.L. Koch, J. Quantum Electron. **27**, 641 (1991).
5. W. Xia, S.C. Lin, S.A. Pappert, C.A. Hewett, M. Fernandes, T.T. Vu, P.K.L. Yu, and S.S. Lau, Appl. Phys. Lett. **55**, 2020 (1989).
6. P.J. Poole, S. Charbonneau, M. Dion, G.C. Aers, M. Buchanan, R.D. Goldberg, and I.V. Mitchell, IEEE Photon. Technol. Lett. **8**, 16 (1996).
7. J. Micallef, E.H. Li, and B.L. Weiss, Appl. Phys. Lett. **67**, 2768 (1995).
8. T. Aizawa, K.G. Ravikumar, S. Suzaki, T. Watanabe, and R. Yamauchi, IEEE J. Quantum Electron. **30**, 585 (1994).
9. M. Razeghi, O. Archer, and F. Launay, Semicond. Sci. Technol. **2**, 793 (1987).
10. I.J. Pape, P. Li Kam Wa, J.P.R. David, P.A. Claxton, P.N. Robson, and D. Sykes, Electron. Lett. **24**, 910 (1988).
11. S.A. Schwarz, P. Mei, T. Venkatesen, R. Bhat, D.M. Hwang, C.L. Schwarz, M. Koza, L. Nazar, and B.J. Skromme, Appl. Phys. Lett. **53**, 1051 (1988).
12. H. Sumida, H. Asahi, S.J. Yu, K. Asami, S. Gonde, and H. Tanoue, Appl. Phys. Lett. **54**, 520 (1989).
13. GaInAsP Alloy Semiconductors, ed. T.P. Pearsall, Wiley, New York, 1982, p. 295.
14. T.E. Schlesinger and T. Kuech, Appl. Phys. Lett. **49**, 519 (1986).
15. J. Micallef, E.H. Li, and B.L. Weiss, J. Appl. Phys. **73**, 7524 (1993).
16. J. Micallef, E.H. Li, and B.L. Weiss, Superlatt. & Microstructures **13**, 315 (1993).

Multiple Cations Interdiffusion in $In_{0.53}Ga_{0.47}As/In_{0.52}Al_{0.48}As$ Quantum Well

Y. Chan* , W.C. Shiu** , W.K. Tsui* , and E. Herbert Li*

* University of Hong Kong, Department of Electrical and Electronic Engineering, Pokfulam
  Road, Hong Kong.
**Hong Kong Baptist University, Department of Mathematics, Kowloon, Hong Kong.

Abstract

Multiple cations interdiffusion in $In_{0.53}Ga_{0.47}As/In_{0.52}Al_{0.48}As$ quantum well (QW) structure is investigated by using the model of expanded form of Fick's second law. The model is fitted to the measured concentration data in order to determine their diffusion coefficients. Once the concentration distribution is obtained, the types of strain and their variation across the QW can be determined, thus the subbands and transitions can be gathered. Result shows interesting phenomena due to this three species interdiffusion.

1. Introduction

There are immense interests in the InGaAs/InAlAs QW which are lattice matched to InP substrate. This is because of their application in the fabrication of optoelectronic devices operating in the 1.3 -1.6 μm spectral range, as well as for high field devices. Recently InGaAs/InAlAs heterostructures have been grown by molecular beam expitaxy (MBE) on InP substrates in single and multiple quantum wells[1]. This new material system have so far been concentrated on the transport properties of high mobility two-dimensional electron gas at single interfaces[2], the achievement of laser action[3], and the variation of luminescence energy as a function of quantum well thickness[4]. The application of thermal processing of QW materials is now extended to both multiple species and phases. Recent reports have been put effort towards two species interdiffusion considering only one effective diffusion coefficient[5,6]. Although, after diffusion, this system only confines to the III metals but it consists of three interdiffused elements. This complicates the diffusion process because it cannot be described by the simple one diffusion coefficient model. To understand the interdiffusion mechanism in this multiple species, all the three diffused elements (Al, In, Ga) should be described by their own diffusion rate together with the cross rates.

2. Modeling

A. Effects of disordering

A number of models have been presented for investigating interdiffusion involving the use of only one error function in approximating the compositional profiles. $In_{0.53}Ga_{0.47}As/In_{0.52}Al_{0.48}As$ Diffused QW (DFQW) can be complicated by the fact that the interdiffusion of the group III metals cannot necessarily be described by a single effective diffusion coefficients. In order to give a comprehensive DFQW of this model, we have modeled the above system by the expanded form of Fick's second law:

$$\frac{\partial C_1}{\partial t} = \frac{\partial}{\partial z}\left(D_{11}\frac{\partial C_1}{\partial z}\right) + \frac{\partial}{\partial z}\left(D_{12}\frac{\partial C_2}{\partial z}\right) \qquad (1)$$

$$\frac{\partial C_2}{\partial t} = \frac{\partial}{\partial z}\left(D_{21}\frac{\partial C_1}{\partial z}\right) + \frac{\partial}{\partial z}\left(D_{22}\frac{\partial C_2}{\partial z}\right) \qquad (2)$$

where t is time, C_1, and C_2 are concentrations of In, and Ga respectively, t is time, D_{ij} (i,j=1,2) are the diffusion coefficients, D_{ii} is the diffusion rate of species i and D_{ij} is the cross diffusion rate between species i and j, z is the growth position, and the QW is centered at z=0 The diffusion coefficients are obtained by fitting the diffusion model to the measured concentration data [6] by using least square to minimize the error. Then, by discretizing the diffusion equations into time and position steps, and by using the as-grown profile as the initial condition, the partial differential equations are solved. The solution to the finite difference method gives rise to the concentrations of the diffused species as a profile across the system normalized over the system. The concentration of Al, C_3 , is obtained by $C_3 = 1 - C_1 - C_2$ which is the stoichiometry boundary condition.

The compositional profiles in the DFQW structure imply that the carrier effective mass, the bulk band gap, the strain and its effects vary continuously across the QW if the well is within the critical thickness regime. Subsequently the carrier effective mass $m_r^*(z)$ will z-dependent and it is in the form $m_r^*(z) = m_r^*(C_1,C_2)$, where $m_r^*(x,y)$ is the respective carrier $In_xGa_yAl_{1-x-y}As$ bulk effective mass, and r denotes either the electron C, heavy hole (V=HH) or light hole(V=LH). The unstrained (bulk) band gap in the well, $E_g(C_1,C_2)$, is also a function of the compositional profiles, so that the unstrained potential profile after interdiffusion, $\Delta E_r(C_1,C_2)$, varies across the well and is given by

$$\Delta E_r(C_1,C_2) = Q_r \Delta E_g(C_1,C_2), \qquad (4)$$

where Q_r is the band offset and ΔE_g is the unstrained bandgap offset.

B. Effects of strain

The in-plane strain, $\varepsilon(C_1,C_2)$, across the well will vary so that the strain effects are also z-dependent. Assuming that the growth direction z is along <001>, then for the biaxial stress parallel to the interface the strain components, after interdiffusion, are given by[7]:

$$\varepsilon_{xx} = \varepsilon_{yy} = \varepsilon(C_1,C_2)$$

$$\varepsilon_{zz} = -2[c_{12}(C_1,C_2)/c_{11}(C_1,C_2)]\varepsilon(C_1,C_2) \qquad (5)$$

$$\varepsilon_{xy} = \varepsilon_{yz} = \varepsilon_{zx} = 0$$

where $\varepsilon(C_1,C_2)$ is misfit factor between the well and the barrier and is defined to be negative for compressive strain, and $c_{ij}(C_1,C_2)$ are the elastic stiffness constants. The change in the bulk bandgap, $S_\perp(C_1,C_2)$, due to the biaxial component of strain is given by[7]:

$$S_\perp(C_1,C_2) = -2a(C_1,C_2)[1-c_{12}(C_1,C_2)/c_{11}(C_1,C_2)]\varepsilon(C_1,C_2) \tag{6}$$

where $a(C_1,C_2)$ is the hydrostatic deformation potential calculated from[7]:

$$a(C_1,C_2) = -\frac{1}{3}[c_{11}(C_1,C_2)+2c_{12}(C_1,C_2)]\frac{dE_g(C_1,C_2)}{dP} \tag{7}$$

where dE_g/dP is the hydrostatic pressure coefficient of the lowest direct energy gap E_g The splitting energy, $S_{//}(C_1,C_2)$, between the HH and LH band edges induced by the uniaxial component of strain is given by[7]:

$$S_{//}(C_1,C_2) = -b(C_1,C_2)[1+2c_{12}(C_1,C_2)/c_{11}(C_1,C_2)]\varepsilon(C_1,C_2) \tag{8}$$

where $b(C_1,C_2)$ is the shear deformation potential. The parameters a, b, c_{ij}, dE_g/dP in above equations are assumed to obey Vegard's law[8], so that their respective values depend directly on the compositional profiles across the QW. In the case of InGaAs/GaAs it is assumed that the LH and spin-orbit band are coupled due to the presence of the stress while the HH state remains uncoupled. The valence band splitting at Γ for the HH band and for the LH band are given by:

$$S_{//HH}(C_1,C_2)=S_{//}(C_1,C_2) \tag{9}$$

$$S_{//LH}(C_1,C_2)= 1/2[S_{//}(C_1,C_2)+\Delta_o(C_1,C_2)]+1/2[9\{S_{//}(C_1,C_2)\}^2$$
$$+\{\Delta_o(C_1,C_2)\}^2-2S_{//}(C_1,C_2)\Delta_o(C_1,C_2)]^{1/2} \tag{10}$$

respectively, where $\Delta_o(C_1,C_2)$ is the spin-orbit splitting. The QW confinement potential after the disordering process, $U_r(C_1,C_2)$, is obtained by modifying the unstrained potential profile after processing, $\Delta E_r(C_{In},C_{Al})$, by the variable strain effects, and is given by:

$$U_r(C_1,C_2)=\Delta E_r(C_1,C_2) - S_{\perp r}(C_1,C_2) \pm S_{//r}(C_1,C_2) \tag{11}$$

where $S_{\perp r}(C_1,C_2)=Q_r S_\perp(C_1,C_2)$, the '+' and '-' signs represent the confined HH and LH profiles, respectively, and $S_{//c}(C_1,C_2)=0$.

C. Sub-band-edge calculation

To calculate the electron and hole wave function in QW, we use the multiband effective mass theory. A parabolic bands model and Luttinger-Kohn- Hamiltonian with strain components are used for the conduction and valence bands respectively. The electron states near the conduction subband edge are assumed to be almost purely s-like and nondegenerate (excluding spin), while the hole states near the valence subband edge are almost purely p-like and four-fold degenerate (including spin). The envelope function scheme is adopted to describe the slowly varying (spatially extended) part of the wavefunction.

379

The wavefunctions of the electron and hole subband edge at the zone centre of Γ valley symmetry can be calculated separately, using the Ben-Daniel and Duke model by the one-dimensional Schrodinger-like equation, which is written as follows:

$$-\frac{\hbar^2}{2}\frac{d}{dz}\left[\frac{1}{m_r^*(z)}\frac{d\Psi_{rl}(z)}{dz}\right] + U_r(z)\cdot\Psi_{rl}(z) = E_{rl}\Psi_{rl}(z) \tag{12}$$

where $\Psi_{rl}(z)$ is the wavefunction of the lth subband for electrons($r=cl$) or holes ($r=vl$), respectively; $m_r^*(z)$ is the corresponding carrier effective mass in the z direction; E_{rl} is the subband-edge energy. Equation (12) is solved numerically using a finite difference method with the above confinement profile.

3. Results and Discussion

Table 1 shows the fitted interdiffusion coefficients which gave a rather surprising results in that the In-Ga diffusion coefficient is negative which means that the gradient of Ga will cause the inverse process of diffusion in In. Figure 1(a) shows Group III alloy concentration profile of as-grown $In_{0.53}Ga_{0.47}As/In_{0.52}Al_{0.48}As$ DFQW with 100Å well width and 250Å thickness barrier. The In and Al as-grown content are set under lattice matched condition. Figure 1(b) and Figure 1(c) show the concentration profiles of the system with diffusion time of 1 hour and 3 hours at a temperature of 812°C respectively. It can be seen that both Al and Ga show smooth interdiffusion profiles. However, the In profile in Figure 1(b) shows a bouncing behavior at the interfaces. This is due to the fact that an inverse process of diffusion has been developed in In at the interfaces. At long diffusion time, all three species become smoothly distributed and the profiles are being lifted up at the well center implying all species have been diffused throughout the entire QW structure.

The confinement profiles show a double-welled structure in the well lager and a double barrier structure very similar to a resonant tunnel structure. This is because a consequence due to the frustration of In profiles. Eigen states exist both in the double-welled bottom potential and in the upper well top region. Well-to-well coupling does occur for the low energy states and tunneling enhancement also apply to the top most states. The transition energy C1-HH1 is shown in figure 3. A slow rate of increase of the bandgap occurs before 1 hour diffusion time and becomes quite rapidly after 3 hours.

The diffusion process can be used to tune the wavelength of InGaAs/InAlAs QW material in the region of 1.5µm which is the optimum wavelength for operation of fiber optic systems with the lowest attenuation. In addition to shifting the operating wavelength, the effect of tensile strain QW on the laser application which is the first light-hole subband as the top valence subband can perform a smaller threshold current density as well as compressive strained QW. Moreover, this material system can also be used to develop both electro-absorptive and electro-refractive modulators in the optimum wavelength so that an integration of these optoelectronic devices can be developed in next stepped.

Table 1	The experimental data fitted interdiffusion coefficients of $In_{0.53}Ga_{0.47}As/In_{0.52}Al_{0.48}As$			
	In-In	In-Ga	Ga-In	Ga-Ga
D_{ij}	2.98	-4.01	0.18	6.69
Unit:	$10^{-18} cm^2 \cdot s^{-1}$			
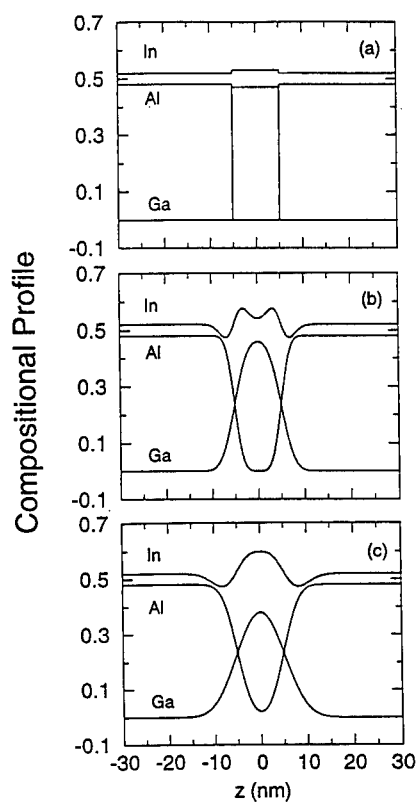
Figure 1. Compositional Profiles of $In_{0.53}Ga_{0.47}As/In_{0.52}Al_{0.48}As$ with well width 100Å at 812 °C. (a) As-grown; (b) diffused for 1 hour; (c) diffused for 3 hours.
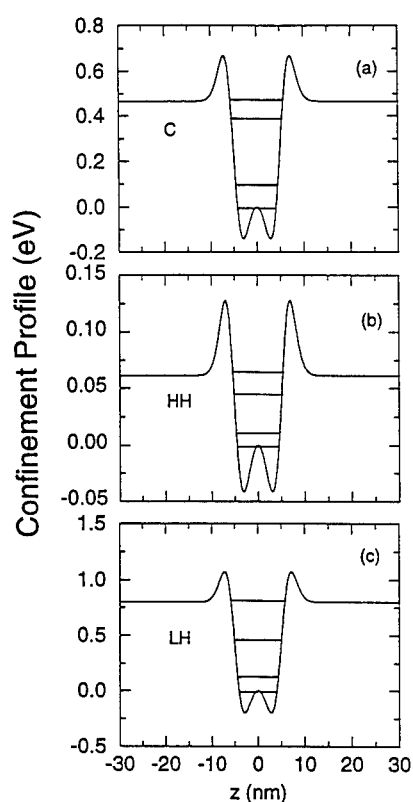
Figure 2. The Confinement profiles, and confined subband states for (a) electron, (b) HH, (c) LH of $In_{0.53}Ga_{0.47}As/In_{0.52}Al_{0.48}As$ interdiffusion for 1 hour.

381
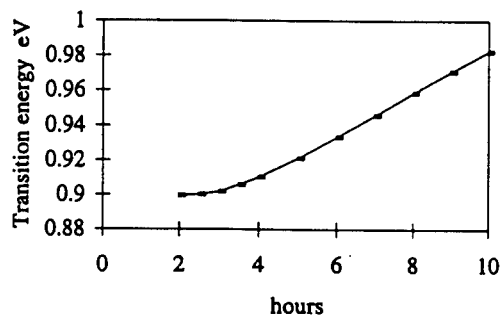
Figure 3. The transition energy C1-HH1 of $In_{0.53}Ga_{0.47}As/In_{0.52}Al_{0.48}As$.

4. Conclusions

In this work, the three species cations interdiffusion has been modeled base on the expanded Fick's second law. Results were fitted with experimental data and individual diffusion coefficients were determined. It is found that the Ga-Ga diffusion coefficient is relatively large in comparison to the other rates so that the Ga concentration profiles show some broadening on annealing. It is also found that the In-Ga diffusion coefficient is negative which gives rise to the inverse process of diffusion, causes sudden abrupt change in In profiles at the interfaces. All this would have important consequence in the understanding of the interdiffusion mechanism in multiple species of multiple alloy QW materials.

5. Acknowledgment

6. References

[1]   K. Y. Cheng, A. Y.Cho, T. J. Drummound, and H. Morkoc, Appl. Phys. Lett. **40**, 147 (1982).
[2]   A. Kastalasky, R. Dingle, K. Y. Cheng, and A. Y. Cho, Appl. Phys. Lett. **41**, 274 (1982).
[3]   H. Temkin, K. Alavi, W. R. Wagner, T. P. Pearsall, and A. Y. Cho, Appl. Phys. Lett. **42**, 845 (1983).
[4]   D. F. Welch, D. W. Wicks, and L. F. Eastman, Appl. Phys. Lett. **43**, 762 (1983).
[5]   K. S. Seo, P. K. Bhattacharya, G. P. Kothiyal, and S. Hong, Appl Phys. Lett. **49** 966(1986).
[6]   R. J. Baird, T.J. Potter, G.P. Kothiyal, P.K. Bhattacharya, Appl. Phys. Lett. **52** 2055(1988).
[7]   H. Asai and K. Oe, J. Appl. Phys. **54** 2052 (1983).
[8]   R. People, Phys. Rev. B. **32** 1405 (1985).

PHASE MODULATOR DEFINED BY IMPURITIES INDUCED DISORDERING

K. M. Lo*, W. C. H. Choy**, E. H. Li***
* Quincy, MA
** Department of Electronic and Electrical Engineering, University of Surrey, U.K.
*** Department of Electrical and Electronic Engineering, University of Hong Kong, H.K.

ABSTRACT

Optical waveguide type phase modulators defined by impurities induced disordering (IID) are investigated. To achieve a better optical confinement, a two steps ion implantation process is carried out to introduce additional impurities with respect to depth in the cladding region. A more uniform refractive index profile in deeper lateral confined region is obtained after thermal annealing. The refractive index different between the core and cladding can be adjusted by controlling the extension of interdiffusion in the cladding. This provide tuning of single mode operating region. For present IID phase modulator with 25 period of 100Å/100Å $Al_{0.3}Ga_{0.7}As$/GaAs multiple quantum wells single mode operating at $0.88\mu m$, a normalized phase shift of 362°/Vmm, chirping parameter of 47, and absorption loss less than $120cm^{-1}$ are achieved theoretically.

INTRODUCTION

Different III-V semiconductor quantum wells (QWs) materials have been intensely investigated in electro-optical phase modulator [1, 2]. The use of QWs material has an advantage of large variation in the electric field induced refractive index change due to the quantum confined Stark effect in the QW around the excitonic absorption edge as compared to those in conventional materials like bulk III-V semiconductors and $LiNbO_3$. However, most of the QW phase modulator are single insulated component [1, 2]. In order to obtain an efficient way of monolithic integration of optoelectronics components on a single substrate, a technique of impurities induced disordering has been utilized to integrate optoelectronics [3, 4]. Impurities are introduced selectively by masked implantation followed by diffusion into the desired regions of a QW structure, a modification of the bandgap and a refractive index step would be result between the as-grown and the disordered regions [5]. The IID process therefore enables a planar process to be used to fabricate and insulate different optical devices such as laser [6], modulator [7] and waveguide [8] on single substrate and makes optoelectronic integration a reality.

A theoretical model is developed to investigate IID lateral confined AlGaAs/GaAs QW phase modulators. The modulators are single mode operation. To increase optical confinement and phase modulation, twice ion implantation with different implantation energies are introduced. The model of IID by ion implantation, optical guiding and modulation properties will be given in the next section. In the third section, results on single mode phase modulation and modulation performance will be presented.

COMPUTATION CONSIDERATIONS

Impurities Induced Disordering by Ion Implantation

For present phase modulator, the active region consists of stacked $Al_{0.3}Ga_{0.7}As$/GaAs as-grown QWs. With a core region presisted by a mask, two lateral regions of the QWs are ion-implanted by Ga ions for cladding. After thermal annealing, the QWs structure with the implanted impurities has lower refractive index than the intrinsic region, hence provide a lateral optical confinement to the active cavity.

The impurity density is computed in a two dimensional structure. The distribution of impurities after implantation $W(x,y)$, where x and y is defined as the lateral direction and depth of the structure respectively, is described by an error function relation based on the experimental and simulation results [10]. The total impurities distribution $W_T(x,y)$ is obtained by linear summation of each, i.e.

$$W_T(x,y) = \sum_{i=0}^{M} W_i(x,y), \tag{1}$$

where $W_i(x,y)$ is the i-th impurities profile of the total M times of implantation. A classical diffusion law is used to described the the motion of the impurities during annealing time t

$$\frac{\partial W_T(x,y,t)}{\partial t} = D_{ion}\nabla^2 W_T(x,y,t). \tag{2}$$

For short annealing time, the diffusion of impurities is assumed to be independent of the motion of Al/Ga atoms and the diffusion coefficient D_{ion} is a constant through out the annealing. Moreover, the interdiffusion coefficient of Al/Ga, D_{atom}, is assumed to be depend on local defect density only, i.e. $D_{atom}(x,y,t) = \alpha D_{ion}(x,y,t)$. α is a numerical factor determined from experimental data. The diffusion equation for Al/Ga atoms is given by

$$\frac{\partial C(x,y,t)}{\partial t} = \nabla[D_{atom}\nabla C(x,y,t)], \tag{3}$$

where $C(x,y,t)$ is the Al/Ga concentration. Solving (3), the Al/Ga concentration profile can be obtained from which its corresponding diffusion length L_d [11] is determined. Using a developed model [11], a refractive index profile $n(x,y)$ is calculated for different L_d.

Scalar Wave Equation

Given the refractive index profile of IID phase modulator, its optical guiding properties are studied by means of solving the scalar wave equation

$$\left[\frac{\partial^2}{\partial x^2} + \frac{\partial^2}{\partial y^2} + k^2 n^2(x,y) - \beta^2\right]\Psi(x,y) = 0, \tag{4}$$

where $\Psi(x,y)$ denotes the transverse modal electric field, $k = 2\pi/\lambda$, where λ represents the free-space wavelength and β is the associated propagation constant. (4) is solved by an improved Fourier decomposition method [13].

Performance Measurement by Modulation parameters

The modulation performance of the phase modulator is interpreted in terms of several measuring parameters. The first one is modulation efficiency of the phase modulation which can be measured from the phase change per modulation length and applied voltage or in normalized phase shift as $\Delta\theta_N = 2\pi\Delta n_{eff}/(V\lambda_{op})$, where $\Delta n_{eff} = \Delta\beta/k$ is change of effective refractive index, λ_{op} is the operating wavelength and V is the applied voltage which is calculated by the Poisson's equation [12]. For present phase modulator, the selected λ_{op} (in eV) is less than the bandgap energy of the $Al_{0.3}Ga_{0.7}As/GaAs$ cladding layers. Therefore, it is assumed that only the optical power confined in the active cavity will be absorbed. Since the active cavity is constructed from QWs material, the optical confinement factor Γ can be defined as the ratio of optical electric field in QWs (active cavity) and the whole structure.

The effective absorption coefficient is given by $\alpha_{eff} = \int_{QWs}\alpha(x,y)\Psi^2 dA/\int_{\infty}\Psi^2 dA$, where $\alpha(x,y)$ is material absorption coefficient of the $Al_{0.3}Ga_{0.7}As/GaAs$ QWs structure. Under non-bias condition, α_{eff} is considered as the absorption loss of the modulator.

The chirping parameter is a crucial indicator to the performance of the modulator. Under bias, both n_{eff} and α_{eff} will change, the static chirping parameter β_{mod} is given as $\beta_{mod} = 4\pi\Delta n_{eff}/(\lambda_{op}\Delta\alpha_{eff})$, where $\Delta\alpha_{eff}$ is the change of effective absorption. From this relation, β_{mod} can be considered as a measure of the relative strength of the phase modulation to that of intensity modulation. To be a good phase modulator, the chirping parameter should greater than 10 [14].

RESULTS AND DISCUSSIONS

The active region of the proposed IID electro-optical phase modulator consists of multiple periods of 100Å/100Å $Al_{0.3}Ga_{0.7}As/GaAs$ as-grown QWs. Results of two active cavity of $0.5\mu m$ thick (25 QW periods) and $1\mu m$ thick (50 QW periods) are presented in this section. The top and bottom layer of the modulator are heavily p and n doped $Al_{0.3}Ga_{0.7}As$ to form a p-i-n structure. The whole device is fabricated on a n^+-GaAs substrate. The modulation under applied field F of 50kV/cm and 100kV/cm are studied at λ_{op} of $0.88\mu m$.

A typical refractive index profile after single step of ion implantation is shown in Fig. 1(a). The modification of the refractive index near the top and bottom of the ion implanted cladding layer is small such that optical power leaks out from these regions as shown in Fig. 1(b) and weakening the guiding property. In order to improve the optical confinement, ion implantation is carried out twice, one with shallower and one with deeper penetration depth to produce a combined impurities distribution with greater uniformity in the depth of the cladding layer. By carefully adjusting the implantation energies, the region with uniform refractive index clearly extends as shown in Fig. 2(a). Optical field profile of the corresponding guiding mode is shown in Fig. 2(b). The guiding property of this twice ion-implanted structure improves as comparing with field profile of the one step ion-implanted structure in Fig. 1(b).

The ion-implanted diffusion is carefully designed to adjust the refractive index for single mode operation. Present results shown that a range of material refractive index profile can serve for single modal modulation at the selected λ_{op} of $0.88\mu m$. This is illustrated by plotting the normalized propagation constant $b = ((\beta/k)^2 - n_{min}^2)/(n_{max}^2 - n_{min}^2)$, where n_{max} and n_{min} are the maximum and minimum refractive index of the active cavity, against annealing time t (which stands for the refractive index profile) as shown in Fig. 3.
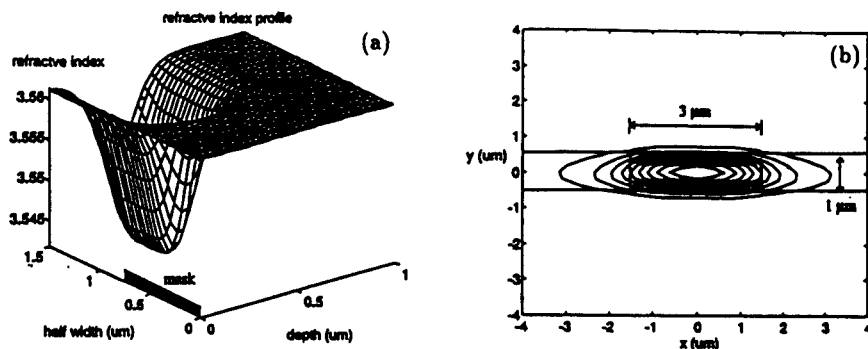
Figure 1: (a) The refractive index profile of half cross-section device structure provided by one ion implantation. (b) Contour of optical field of the corresponding guiding mode.
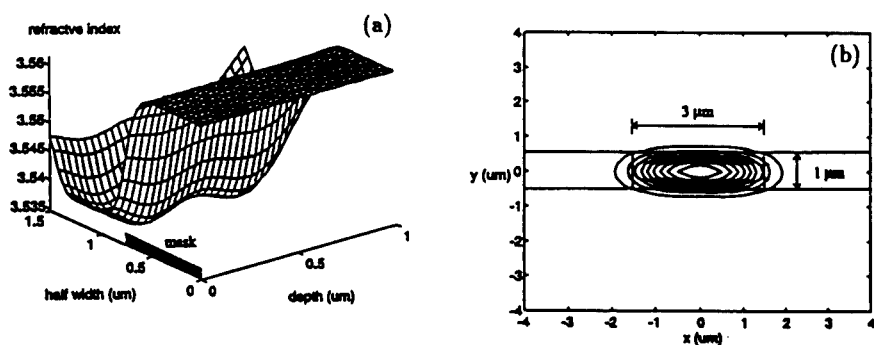

Figure 2: (a) The refractive index profile of half cross-section device structure provided by twice ion implantation. (b) Contour of optical field of the corresponding guiding mode.
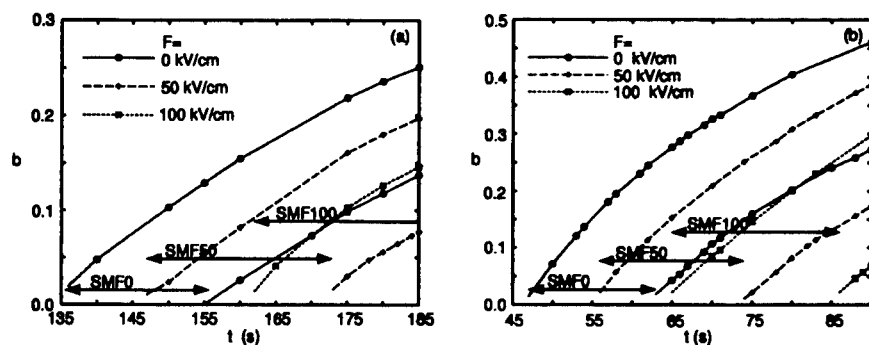

Figure 3: Normalized propagation constant b against annealing time t for cavity thickness of (a) $0.5\mu m$ and (b) $1.0\mu m$. Annealing time is shorter for fundamental mode .

Table 1: Modulation parameters of two phase modulators with cavity thickness of $0.5\mu m$ (25 QW periods) and $1\mu m$ (50 QW periods).

Thickness (μm)	0.5		1	
bias field (kV/cm)	0	50	0	50
bias voltage (V)	0	2.54	0	5.04
Γ	0.843	0.839	0.919	0.911
n_{eff}	3.5138	3.5116	3.5421	3.540
Δn_{eff}	-	-2.22×10^{-3}	-	-2.40×10^{-3}
depletion width (μm)	-	0.507	-	1.01
$\Delta\theta_N$(°/Vmm)	-	362	-	194
α_{eff} (cm^{-1})	117.3	110.7	132	123.6
$\Delta\alpha_{\text{eff}}$ (cm^{-1})	-	-6.6	-	-8.4
β_{mod}	-	+47	-	+41

The intervals SMF0, SMF50 and SMF100 corresponds to single mode operation under field strength of 0, 50 and 100kV/cm. With an applied field, the refractive index profile, and thus the propagation mode, is modified. The interval therefore modifies as shown in Fig. 3. The waveguide modulator may support single mode or multiple mode guiding at the selected λ_{op}. In order to maintain single mode operation, only the overlapping region between two intervals with different applied fields, such as the overlapping region between SMF0 and SMF50 of Fig. 3, can provide a single mode phase modulation. In fact, the modulation can also work between SMF50 and SMF100 which provide a much larger overlapping range for operation. However, there must have some resistance loading in an electrical circuit for electro-optical modulation, in order to reduce the power consumption of the phase modulation, the one without bias requirement is selected, i.e. the case without a d.c. offset. Between SMF0 and SMF100, there are no overlapping meaning that single modal phase modulation up to a bias field of 100kV/cm does not exist. In fact, present phase modulator can provide a large enough modulation between 0 and 50kV/cm.

The performance of the two modulators is listed in Table 1. The normalized phase shifts $\Delta\theta_N$ are large enough that over 180° phase modulation can be obtained. For the $0.5\mu m$ thick cavity, a two fold increase of $\Delta\theta_N$ is seen when compared with $1\mu m$ thick cavity while maintain a low absorption loss of less than 150cm^{-1}. This shows that applied field of 50kV/cm is large enough to bias the modulator with an useful phase modulation. For the $1\mu m$ thick cavity, its phase modulation under 50kV/cm is larger than that of $0.5\mu m$ one since the optical confinement increase in the thicker cavity and also in which twice number of QWs contribute for modulation. However, its active thickness is two times of the thinner structure meaning that twice bias voltage is required for the same amount of applied field. This results in a weaker normalized phase shift. The β_{mod} obtained indicates that the phase modulation is at least 40 times greater than the intensity modulation at the selected λ_{op}, this is four fold large than the basic requirement of phase modulator. Under the 50kV/cm applied field, the depleted thickness of both cases are thicker than their corresponding cavity thickness and hence, during operation, the QWs structures produced for phase modulation are completely and effectively used.

CONCLUSION

Optical waveguide type phase modulators with $0.5\mu m$ and $1\mu m$ thick QWs active cavity using masked ion-implantation to selective induce disordering to the QWs have been investigated. These devices are carefully designed to achieve single mode operation at $0.88\mu m$. For the $1\mu m$ thick cavity, twice ion implantation is introduced to provide a wider cladding region with uniform refractive index. This improve the optical confinement and hence the phase modulation under same amount of bias as compared to the $0.5\mu m$ one. However, in terms of the normalized phase shift and power consumption, thin cavity provide better modulation performance. In summary, the two phase modulators can provide large phase change, normalized phase shift of $362°/Vmm$ and $194°/Vmm$ for the $0.5\mu m$ and $1\mu m$ thick cavity respectively. Chirping parameter of more than 40 with frequency compression property is achieved and absorption loss is less than $150cm^{-1}$. This make present phase modulator become a competitive among the QW phase modulation devices.

REFERENCES

1. S. Yoshida, Y. Tada, I. Kotaka, and K. Wakita, Electron. Lett. **30**, 1795 (1994).

2. H.K. Tsang, J.B.D. Soole, H.P. Le Blane, R. Bhat, M.A. Koza, and I.H. White, Appl. Phys. Lett. **57**, 2285 (1990).

3. S.R. Andrew, J.H. Marsh, M.C. Holland, and A.H. Kcan, IEEE Photon. Technol. Lett. **4**, 426 (1992).

4. T. Miyazawa, H. Iwamura, and M. Naganuma, IEEE Photon. Technol. Lett. **3**, 421 (1991).

5. C. Vien, M. Schneider, D. Mailly, R. Planel, H. Launois, H.Y. Marzin and B. Descouts. J. Appl. Phys. **70**, 1444 (1991).

6. P.J. Poole, S. Charbonnesu, M. Dion, G.C. Aers, M. Buchana, R.D. Golderb, and I.V. Mitchell, IEEE Photon. Technol. Lett. **8**, 16 (1996).

7. D.G. Deppe, L.H. Guido, M. Holonyak Jr., K.C. Hsieh, R.D. Burnham, D.L. Thornton and E.L. Paoli, Appl. Phys. Lett. **49**, 510 (1986).

8. E. Kapon, N.G. Stoffel, E.A. Dobisz, and R. Bhat, Appl. Phys. Lett. **52**, 351 (1988).

9. P. J. Bradley and G. Parry, Electron. Lett. **25**, 1349 (1989).

10. D. Briggs and M. P. Seah, Eds., Ion and Neutral Spectroscopy, vol. 2 of Practical Surface Analysis, Wiley, Chicheater, 2nd (1992).

11. E.H. Li, B.L. Weiss, K.S. Chan, and J. Micallef, App. Phys. Lett. **62**, 550 (1993).

12. W.C.H. Choy, and E.H. Li, IEEE J. of Quantum Electron., to be appeared.

13. S. J. Hewlett, and F. Ladouceur, J. Lightwave Technol. **13**, 375 (1995).

14. T. Hausken, R. H. Yan, R. I. Simes, and L. A. Coldren, Appl. Phys. **55**, 718 (1989).

ANALYSIS OF THREE TYPES OF INTERDIFFUSION PROCESS IN INGAAS/INP QUANTUM-WELL AND THEIR DEVICES IMPLICATIONS

MICHAEL C.Y.CHAN**, K.S.CHAN* and E. HERBERT LI**
*City University of Hong Kong, Department of Physics and Materials Science, Kowloon, Hong Kong
**University of Hong Kong, Department of Electrical & Electronic Engineering, Pokfulam, Hong Kong

ABSTRACT

The optical properties of $In_{0.53}Ga_{0.47}As/InP$ single quantum well (QW) (with an as-grown well width of 60Å structures) interdiffused with different cation and anion interdiffusion rates have been theoretically analyzed for applications in optoelectronics. The interdiffusion of InGaAs/InP QW structures is complicated as interdiffusion can occur for either (i) only group-III (In,Ga), (ii) group-V (As,P), or (iii) both group-III and group-V sublattices. Depending on the resulting composition profiles, the shifts (blue or red) of the transition energies can be tuned to wavelengths between 1.3μm to 1.55μm for device applications. The results show that the control of the rates of cation and anion interdiffusion offers interesting possibilities for designing optoelectronic devices such as modulators and lasers.

INTRODUCTION

Currently InGaAs/InP quantum-well (QW) structures are actively studied for the fabrication of a variety of optoelectronic devices, such as modulators, detectors, waveguides, and lasers, for operation in the 1.3μm-1.55μm wavelength region[1]. By exploiting the strain effects on the band-gap, the bandstructure of the device can be engineered to optimize the device characteristics. Apart from this, interdiffusion of constituent atoms, the rate of which depends on lattice distortion, impurities, defects and the process temperature, is a versatile technique to modify the device bandstructure. Using this technique, the QW compositional profiles, the confinement potentials and the optical properties can be modified as a result of the diffusion of constituent atoms. The interdiffusion processes in InGaAs/InP QW system is more complex than those in AlGaAs/GaAs and InGaAs/GaAs because both group-III and group-V atoms can participate in the interdiffusion process. Although some theoretical[2] and experimental[3] studies were undertaken on (In,Ga)(As,P)/InP QWs, the mechanism of interdiffusion in these systems is not well understood. In order to predict the interdiffused compositional profiles, some hypotheses have to be made. The interdiffusion processes of group-III and group-V atoms are assumed to be independent and there are three categories of interdiffusion: (i) only group-III diffusion, (ii) only group-V diffusion, and (iii) both group-III and group-V diffusion. It has been reported that group-V atoms is more easily interdiffused than group-III atoms. Arsenic and phosphorus atoms begin to interdiffuse at about 500 °C while group-III atoms are known to interdiffuse above 800 °C[4]. The control of diffusing atoms is determined by the impurities in the structure. It is thus important to understand the effects of interdiffusion on the optical characteristics of InGaAs/InP QWs for integration and optimization of devices. In this paper, we model the interdiffusion processes in an undoped InGaAs/InP single QW and study their effects on the optical properties.

MODEL FORMULATION

It is assumed that for diffusion processes (i) and (ii) the group-III and group-V interdiffusion processes can be modeled by two different diffusion lengths. The interdiffusion of group-III atoms is characterized by a diffusion length L_d^{III}, which is defined as $L_d^{III} = \sqrt{(D^{III}t)}$, where D^{III} is the diffusion coefficient of group-III atoms and t is the diffusion time; the interdiffusion of group-V atoms is characterized by the diffusion length L_d^V. The structure modeled here consists of an as-grown $In_{0.53}Ga_{0.47}As$ square well with thickness 60Å sandwiched between thick InP barriers. After intermixing, the concentration of the interdiffused atoms across the QW structure has an error function profile. For the group-III atoms, the In concentration after interdiffusion is described by

$$x_{In}(z) = 1 - \frac{1-x}{2}[erf(\frac{L_z + 2z}{4L_d^{III}}) + erf(\frac{L_z - 2z}{4L_d^{III}})] \qquad (1)$$

where L_z is the as-grown well width, z is the growth direction, and the QW is centered at z=0. For the group-V atoms, the As concentration after interdiffusion is given by

$$y_{As}(z) = \frac{y}{2}[erf(\frac{L_z + 2z}{4L_d^V}) + erf(\frac{L_z - 2z}{4L_d^V})] \qquad (2)$$

where y=1 is the As concentration of the as-grown structure. For diffusion of group V atoms only, Mukai et al[4] studied in details the diffusion of group-V atoms in InGaAs/InP and found that the diffusion coefficients are different in the barrier and well layers and the concentration of group-V atoms is discontinuous across the interface. Here in the present work, we model the diffusion process (iii) using the two phase model described in Mukai et al.

In this paper, we consider the interdiffusion of $In_{0.53}Ga_{0.47}As$/InP QW, in which the QW layer is lattice-matched to the barrier layers. After interdiffusion, the chemical compositions deviates from the lattice-matched condition leading to a non-uniform strain in the lattice. To calculate the electron and hole wave functions in QW, we use the effective mass theory. For most III-V semiconductors, it is a good approximation that the conduction and valence bands are decoupled. A parabolic band model and the Luttinger-Kohn- Hamiltonian with strain components are used for the conduction and valence bands respectively. The electron states near the conduction subband edge are assumed to be s-like and nondegenerate (excluding spin), while the hole states near the valence subband edge are p-like and four-fold degenerate (including spin). The envelope function scheme is adopted to describe the slowly varying (spatially extended) part of the wavefunction. The wavefunctions of the electron and hole subbands at the zone centre can be calculated separately by solving the one-dimensional Schrodinger-like equation as follows:

$$-\frac{\hbar^2}{2}\frac{d}{dz}\left[\frac{1}{m_{lr}^*(z)}\frac{d\psi_{rl}(z)}{dz}\right] + U_r(z)\cdot\psi_{rl}(z) = E_{rl}\psi_{rl}(z) \qquad (3)$$

where $\psi_{rl}(z)$ is the wavefunction of the lth subband for electrons(r=cl) or holes (r=vl), respectively; $m_{lr}^*(z)$ is the corresponding carrier effective mass in the z direction; E_{rl} is the subband-edge energy. Equation (3) is solved numerically using a finite difference method with

the above confinement profile. For valence band sturcture, it is necessary to diagonalize the Luttinger-Kohn Hamiltonian with appropriate confinement potentials for heavy and light holes. The hole envelope functions depend on $k_{//}$ as a result of the mixing of the heavy and light hole bands. In this work, the effective Hamiltonian approach described in Chan[5] is used to solve the Luttinger-Kohn Hamiltonian to obtain the valence subband structure.

The polarization dependent absorption coefficient and optical gain are calculated using the following equations, where the orientation of the polarization is also considered:

$$g(\omega) = \frac{e^2 M_b^2}{\pi \varepsilon_o n_R c_o m_o^2 \omega L_z} \sum_{p,q} \int |\langle \Psi_{Cp} | \Psi_{Vq} \rangle|^2 L(E_p(k) - E_q(k) - \hbar\omega)[f^c(E_p(k)) - f^v(E_q(k))]dk$$

(4)

$$\alpha(w) = \frac{e^2 M_b^2}{\pi \varepsilon_o n_R c_o m_o^2 w L_z} \sum_{p,q} \int |\langle \Psi_{Cp} | \Psi_{Vq} \rangle|^2 L(E_p(k) - E_q(k) - \hbar w)dk \qquad (5)$$

where L_z is QW width, n_R is the refractive index, c_o is the velocity of light in vacuum and ε_0 is the permittivity of free space; e and m_0 are the electron charge and rest mass respectively; $M_b^2 = (m_o^2 P^2/3\hbar)M^2(\theta)$ where P is given by Kane's model, and $M(\theta)$ is a factor due to the difference in orientation between the confined carrier in-plane wave vector and the optical polarization vector (represented by θ); k is the transverse wave vector in the direction parallel to the QW layer; E_p and E_q are the electron and hole subband energy respectively; ψ_c and ψ_v are the envelope wavefunctions for the electrons and holes respectively; L is the Lorentzian broadening factor with HWHM Γ_b = 5meV. The summation in (4) and (5) includes all the bound states in the conduction (p) and valence (q) bands. The Fermi functions , f^c and f^v, are solved numerically for the quasi-Fermi levels at a fixed carrier injection (n^{2D} = 3× 10^{12} /cm^2).

RESULTS AND DISCUSSIONS

In the present study, we consider a 60Å-thick undoped $In_{0.53}Ga_{0.47}As$ single quantum well layer sandwiched between 300Å-thick InP barriers. All the parameters are determined by interpolating between the binary parameters at room temperature. A general parameter T for the quaternary material $A_xB_{1-x}C_yD_{1-y}$ can be related to the parameters of four binary compounds AC, AD, BC, and BD using the following interpolation formula

$$T(x,y) = (1-x)yT_{BC} + xyT_{AC} + x(1-y)T_{AD} + (1-x)(1-y)T_{BD} \qquad (6)$$

The compositional dependence of bulk bandgap in eV is given by[6]

$$E_g(x,y) = 1.35 - 1.17y + 0.668(1-x) - 0.069(1-x)y + 0.18y^2 + 0.03(1-x)y^2$$
$$+ 0.758(1-x)^2 - 0.322(1-x)^2y \qquad (7)$$

while the spin-orbit splitting, in eV, is given by[7]

$$\Delta_0(x,y) = 0.34(1-x)y + 0.43xy + 0.1(1-x)(1-y) + 0.1x(1-y) \qquad (8)$$

The conduction band offset Q_c of InGaAs/InP heterostructures is taken to be 0.6.

The optical gain results of interdiffused lattice-matched InGaAs/InP QW for different diffusion processes are shown in figure 1. In fig.1(a), we show the gain of QW with interdiffusion of only group III sublattice. The peak gain energy shifts to lower energies as interdiffusion proceeds and the peak gain magnitude increases with the degree of interdiffusion.

This is due to the deepening of the QW potential and the increase in confinement when the group-III atoms interdiffuse. The gain spectra of wells with interdiffusion of both group-III and group-V sublattices are shown in figure 1(b). The error function confinement profile of this kind of interdiffused QW shifts the peak of the gain spectrum to higher energies and reduces the peak height. Figure 1(c) shows the gain after interdiffusion of group V sublattice. It is noticed that the peak gain energy shift to higher energies when the well is interdiffused.

The absorption coefficients of interdiffused InGaAs/InP QWs calculated in the present study include the 1s heavy and light hole exciton transitions. The 1s bound exciton wavefunction is determined by a perturbative-variational method[8], and the exciton envelope function is given by:

$$\psi_{1s}(\rho) = \frac{4\lambda}{\sqrt{2\pi}a^*} e^{-\frac{2\rho\lambda}{a^*}} \qquad (9)$$

where $a^* = \frac{4\pi\varepsilon\hbar^2}{\mu_{//}e^2}$ is the exciton Bohr radius, ρ is the relative distance between the electron and (heavy or light) hole in the quantum well along the transverse direction, which is denoted by // and is parallel to the quantum well layer. $\mu_{//}$ is the reduced effective mass in the transverse direction. ε is the static dielectric constant. The variational parameter λ is obtained by minimizing the following expression:

$$\iint dz_e dz_v |\Psi_{c1}(z_e)|^2 |\Psi_{v1}(z_v)|^2 \left\{ \frac{1}{4}a^* + z - \frac{1}{2}\pi z \left[H_1(\frac{4\lambda z}{a^*}) - N_1(\frac{4\lambda z}{a^*}) \right] \right\} \qquad (10)$$

where z_e and z_v are the electron and hole positions, $z=|z_e-z_v|$, ψ_{c1}, ψ_{v1} are the electron and hole envelope wavefunctions, H_1 and N_1 are the Struve and Neumann functions of order 1, respectively. The binding energy E_b of the 1s bound exciton is obtained by the parameter λ and is defined by:

$$E_b = -4\lambda^2 R \qquad (11)$$

where $R = \frac{\mu_{//}e^4}{32\pi^2\varepsilon^2\hbar^2}$ is the Rydberg energy. The exciton absorption coefficient, $\alpha_{1s}(\omega)$, is given by:

$$\alpha_{1s}(\omega) = \frac{A\omega}{c_o n_R} |\Psi(\rho=0)|^2 \frac{\Gamma_b}{\pi(E_{exc} - \hbar\omega)^2 + \Gamma_b^2} \qquad (12)$$

where $A = \frac{e^2\hbar^2}{3\varepsilon_o m_e^* E_{cv}^2 L_z} M_0 |\langle \Psi_{c1}|\Psi_{v1}\rangle|^2 \wp$, $E_{exc}=E_{c1}+E_{v1}+E_g+E_b$, and Γ_b is the exciton linewidth (half width half maximum) broadening factor. For the 1s exciton only $\rho=0$ is allowed and hence $\wp^{TE}=3/2$(hh), ½(lh) and $\wp^{TM}=0$(hh), 2(lh). The calculated exciton binding energies are shown in tables 1-3 as a function of the diffusion lengths.

Table 1 Exciton Binding Energies of interdiffused InGaAs/InP QW (Group III only)

Group-III diffusion length (Å)	$L_d=0$	$L_d=10$	$L_d=20$	$L_d=30$	$L_d=40$
HH Binding Energy (meV)	4.84	4.38	4.07	3.80	3.62
LH Binding Energy (meV)	5.92	5.33	4.91	4.57	4.34

Table 2 Exciton Binding Energies of interdiffused InGaAs/InP QW (Group III&V, $L_d^{III} = L_d^V = L_d$)

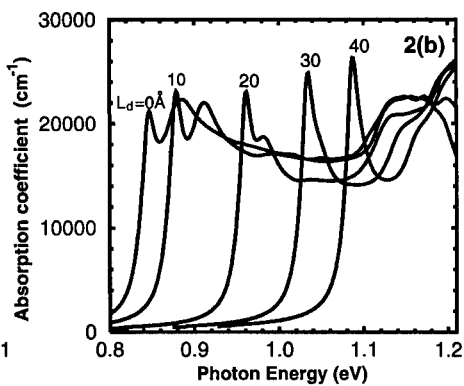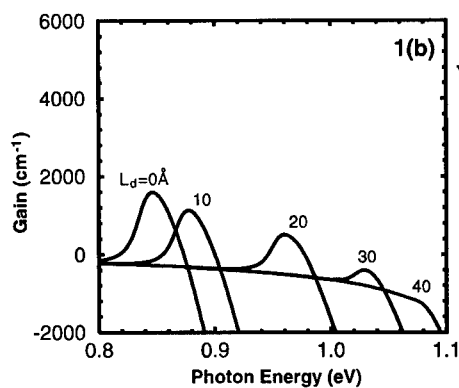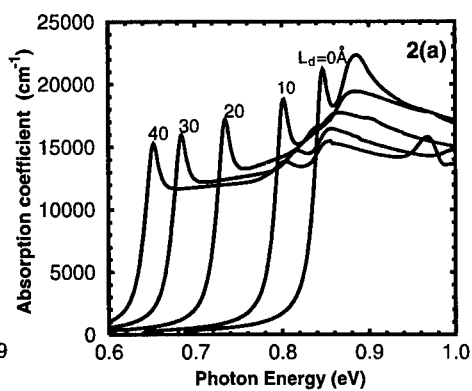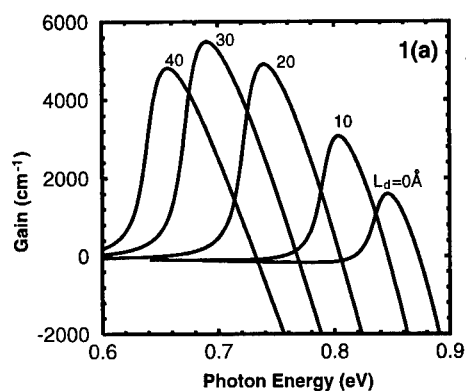| diffusion length (Å)	$L_d=0$Å	$L_d=10$	$L_d=20$	$L_d=30$	$L_d=40$
HH Binding Energy (meV)	4.84	5.98	6.33	6.62	6.71
LH Binding Energy (meV)	5.92	6.91	7.43	7.56	7.74
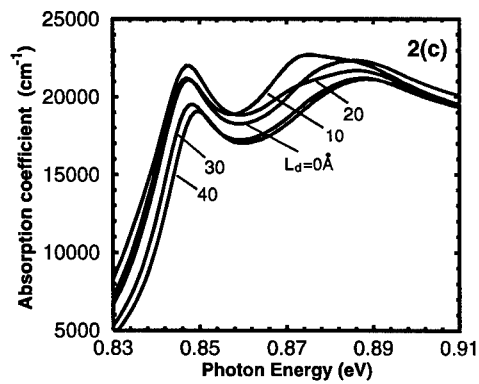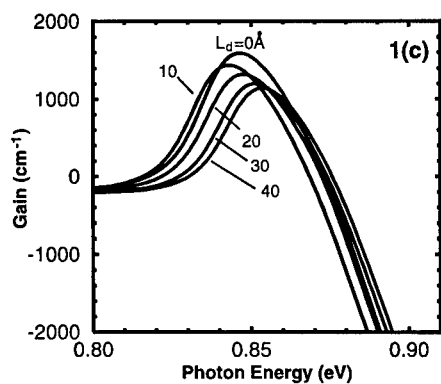
Fig. 1 Optical gain for (a) group-III, (b) group-III & v, and (c) group-V interdiffusion.

Fig. 2 Absorption coefficient for (a) group-III, (b) group-III & V, and (c) group-V Interdiffsion.

Table 3 Exciton Binding Energies of interdiffused InGaAs/InP QW (Group V)

Group-V diffusion length (Å)	$L_d=0$	$L_d=10$	$L_d=20$	$L_d=30$	$L_d=40$
HH Binding Energy (meV)	4.84	4.85	4.86	4.87	4.88
LH Binding Energy (meV)	5.92	5.93	5.94	5.95	5.97

In these table, the exciton binding energy decreases (increases) as the diffusion length increases for the only group-III (group-III & V) diffusion. The changes in exciton binding energy for these two diffusion processes are mainly due to the change in the transverse electron and hole effective masses in the well layers. For the two-phase group-V diffusion, the binding energy slight increases as the diffusion length increases.

The absorption coefficients of lattice-matched InGaAs/InP QWs for different diffusion lengths are shown in figure 2. In fig.2(a), we show the absorption of QW with interdiffusion of only group III sublattice. The absorption peak energy also shifts to lower energies as interdiffusion proceeds and the 1s exciton absorption peak decreases with the degree of interdiffusion. The absorption coefficients of wells with interdiffusion of both group-III and group-V sublattices are shown in figure 2(b). This kind of interdiffused QW has the exciton absorption peak shifted to higher energies and increased in the peak height. Figure 2(c) shows the absorption coefficients after the interdiffusion of group V sublattice. It is noticed that the 1s exciton peaks for all the diffused wells have approximately the same energy and the heights of absorption peaks are slightly reduced by interdiffusion.

CONCLUSION

The effects on the optical gain and absorption coefficient of a lattice-matched InGaAs/InP quantum well due to various interdiffusion processes are reported. It is shown that the interdiffusion of group-III sublattice increases the peak gain leading to improved performance in lasers and the interdiffusion of group-III & V sublattices increases the exciton absorption coefficients, which can be used to optimize optical modulators.

ACKNOWLEDGMENT

REFERENCES

1. R.J.Deri, E.Kapon, R.Bhat, M.Seto and K.Kash, Appl. Phys. Lett., 54,1737 (1989)
2. Joseph Micallef, E.Herbert Li and Bernard L.Weiss, J. Appl. Phys., 73,7524 (1993)
3. I.J.Pape, P.Li Kam Wa, J.P.R.David, P.A.Claxton and P.B.Robson, Electron. Lett., 24, 1217 (1988)
4. K.Mukai, M.Sugawara and S.Yamazaki, Phys. Rev. B, 50, 2273 (1994)
5. K.S.Chan, J.Phys. C: Solid State Phys., 19, L125 (1986)
6. R.E.Nahory, M.A.Pollack, W.D.Johnston,Jr., and R.L.Barns, Appl. Phys. Lett., 33, 659 (1978)
7. S.Adachi, J. Appl. Phys., 53, 8775 (1982)
8. J.F.Jiang, Solid State Comm., 50, 589 (1984)

OPTICAL PROPERTIES OF DIFFUSED AlGaAs/GaAs MULTIPLE QUANTUM WELLS AND THEIR APPLICATIONS IN HIGH POWER LASER

Yi Luo, Ai-Qing Jiang, Zhi-Biao Hao, and Jian-Hua Wang
State Key Lab on Integrated Optoelectronics, Department of Electronic Engineering,
Tsinghua University , Beijing, China

Terry W. K. Lai and E. Herbert Li
Department of Electrical and Electronic Engineering, University of Hong Kong,
Pokfulam Road, Hong Kong, e-mail : ehli@eee.hku.hk

Abstract

We will present results for an $Al_{0.24}Ga_{0.76}As$/GaAs diffused multiple quantum well with five periods of 100/100 Å thick well/barrier layers grown in between $Al_{0.24}Ga_{0.76}As$ guiding layers and cladded on top by a 1μm thick p-$Al_{0.44}Ga_{0.56}As$ layer and on the bottom by an n-$Al_{0.44}Ga_{0.56}As$ layer of equal thickness, on a n^+-GaAs buffer layer and n^+-GaAs substrate. Vacancy enhanced QW diffusion is employed where a 2000 Å thick layer of SiO_2 is deposited on top of the diffused multiple quantum well structure. Photoluminescence measurement and photovoltage measurement at room temperature show that after rapid thermal annealing for 30 sec at 1000 °C to 1040 °C, a bandgap shift of 30 nm is obtained for the exciton edge. Further, this technique is applied to a ridge waveguide laser structure to make two windows for high power output up to 36 mW. This device shows that the diffusion process may have practical applications.

Introduction

Impurity free vacancy diffusion (IFVD) is a simple way to control the mixing in quantum wells [1]. Multiple quantum wells (MQW) intermixing using IFVD has been becoming very attractive recently for modifying optical properties of materials as this method is able to tune the bandgap of the MQW wafer and at the same time it can be used for making window structures for high power laser operation.

Diffused multiple quantum wells (DF-MQW) can be obtained by intermixing the alloy composition of barriers and the wells through their heter-interfaces. In an AlGaAs/GaAs system, SiO_2 is selectively capped on the MQW structure to enhance the intermixing. The sample then undergoes Rapid Thermal Annealing (RTA) at temperatures above 850 °C for 30 sec. These procedures induce the out-diffusion of Ga into the capping SiO_2 layer which results in the generation of vacancies in the QWs, enhancing the interdiffusion of Al and Ga atoms, so that the diffusion coefficient becomes larger. The resulting increase in bandgap can be evidenced by the blue shift of photoluminescence (PL) measurement and photovoltage measurement.

DF-MQW can be applied to high power lasers with quite a few advantages [2]: (1) An increase in the band shift to shorter wavelengths of the band edge can be obtained, thereby improving the operation of the high power lasers. (2) DF-MQW can be easily obtained by using the existing fabrication technologies.

High output power lasers are receiving a lot of attention for several different applications [3,4] such as free-space communications, optical storage, high-density optical disk memory systems and high-speed laser beam printers. The optical output power of semiconductor lasers is however limited by catastrophic optical damage (COD) [3-6] which results from local degradation of laser mirrors by laser light absorption in depleted regions as a consequence of thermal runaway. Moreover, larger threshold current is necessary for high power lasing operation. Consequently, the thickness of the active layer has to be increased and lower output power will be obtained [5]. Thus the COD threshold optical power density has to be increased to cater for high power laser operation. There are two possible solutions to increase the COD threshold optical power density: (1) Increase the lasing cavity stripe width or (2) use 'window' structure. The former method has the problem of instability and nonfundamental far-field patterns [3]. The latter method was proposed to have the property of less absorption adjacent to the mirror surface since evidence shows that decrease in adjacent mirror absorption will increase the COD threshold optical power density [5].

The 'window' at two ends of the sample are produced by using IFVD on the sample. The size of the 'window' is controlled by the size of the SiO_2 cap. IFVD and annealing promote the degree of interdiffusion of Ga and Al atoms, which results in a modification of bandgap energy and thus the refractive index . This implies that a tunable operation wavelength and high laser output power can be obtained. The 'window' structure therefore provide a mean to improve the reliability of the device by reducing facet degradation.

In this work, we report full steps of fabrication procedures and the use of IFVD to obtain the diffused AlGaAs/GaAs MQW. We also present the results of PL measurement and photovoltage measurement of the diffused AlGaAs/GaAs MQW for determining the 'window' performance in the high power ridge waveguide laser diode. In addition, limitation on the maximum output power has been determined.

Fabrication and Experiment

Undoped AlGaAs/GaAs MQW structure was grown on a n^+-GaAs buffer layer and n^+-GaAs substrate by Molecular Beam Epitaxy (MBE) in this experiment as shown in Fig. 1. The MQW consisted of five periods of alternating $Al_{0.24}Ga_{0.76}As$/GaAs layers with both of the $Al_{0.24}Ga_{0.76}As$ barriers and GaAs QWs having equal thickness of 100Å. The MQW was surrounded by $Al_{0.24}Ga_{0.76}As$ guiding layers. It was then cladded on the top by p-$Al_{0.44}Ga_{0.56}As$ (Be doped) and on the bottom by n-$Al_{0.44}Ga_{0.56}As$ (Si-doped) layers of equal thickness of 1 μm.

A SiO_2 layer of 2000Å was deposited on the surface of the sample by sputtering. The obtained sample was then put in a quartz box for RTA at temperatures ranging from 1000 °C to 1040 °C for 30 sec in flowing nitrogen at a rate of 2.5 litre/min. After annealing, the SiO_2 cap was removed in a buffered HF solution.

PL measurements were performed at room temperature. Blue shift of about 30 nm from 849.4 nm to 818.6 nm was obtained which implies that a good tunable operation wavelength has been achieved. Room temperature photovoltage measurements was also used to measure the

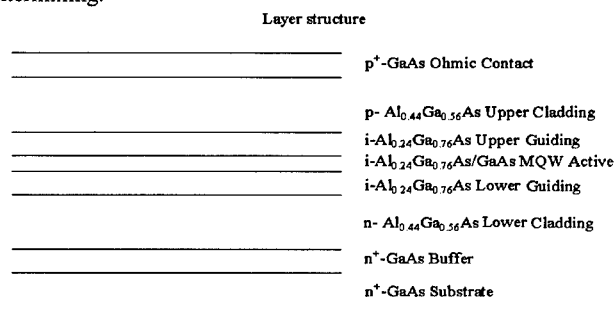blue shift of the bandgap. These two measurements show the tuning of bandgap by quantum wells intermixing.

Layer structure

p⁺-GaAs Ohmic Contact

p- Al₀.₄₄Ga₀.₅₆As Upper Cladding
i-Al₀.₂₄Ga₀.₇₆As Upper Guiding
i-Al₀.₂₄Ga₀.₇₆As/GaAs MQW Active
i-Al₀.₂₄Ga₀.₇₆As Lower Guiding

n- Al₀.₄₄Ga₀.₅₆As Lower Cladding

n⁺-GaAs Buffer

n⁺-GaAs Substrate

Fig. 1. Schematic diagram of the diffused multiple quantum wells structure.

The high power ridge waveguide laser diode has the same structure as the as-grown sample, but the window structure has been adopted to its ends and p⁺-GaAs ohmic contact was deposited, as shown in Fig. 2. The ridge is 5 μm wide and 1.1 μm deep. Light outr t power versus current characteristics are obtained to determine the maximum output power and the threshold current.

Window region   P-electrode
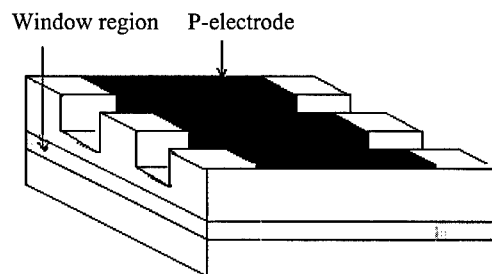
Fig. 2. Schematic diagram of the high power ridge waveguide laser with window structure.

Results and Discussion

PL spectra was used for monitoring the degree of compositional disordering and the transition energy between the first heavy hole and electron states in the AlGaAs/GaAs system. The PL measurements at room temperature are shown in Fig. 3. For the as-grown sample, Fig. 3 curve (a), an emission peak at 849.4 nm and a lower emission peak of shorter wavelength of 843 nm has found due to heavy hole (HH) and light hole (LH) excitonic transitions respectively. Fig. 3 curve (b) is the PL spectrum of sample after RTA at 1000 °C for 30 sec. The highest emission peak has shifted to a lower wavelength of 832.5 nm. The shoulder peak has disappeared. It is due to the broadening of PL spectrum. Such phenomenon shows the intermixing of the barriers and the wells which tunes the bandgap of the material. Fig. 3 curve (c) refers to another sample treated under RTA at 1020 °C for 30 sec. Its emission peak has

shifted to 829.4 nm with broadening. The broadening can be explained by the increased intermixing of the well and barrier layers together with the well width fluctuation [7].
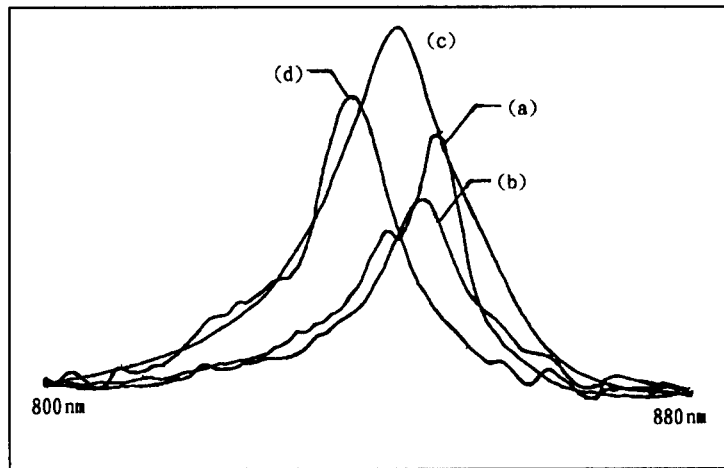

Fig. 3. Photoluminescence spectra of the DF-MQW sample, for (a) the as-grown sample, (b) RTA at 1000 °C shows a blue shift of 16.9 nm, (c) RTA at 1020 °C and (d) RTA at 1040°C show larger blue shift up to 30.8 nm.

Fig. 3 curve (d) shows the sample under RTA at 1040 °C for 30 sec. Its PL spectrum shifts further to the left, from 849.4 nm to 818.6 nm, giving 30.8 nm blue shift for its sample. The degree of intermixing depends on the annealing temperature. From the measurements, intermixing is enhanced with increasing temperature.

To verify the above result, photovoltage measurements have been performed using different samples treated at different RTA temperatures, and shown in Fig. 4. The spectra shown in the figure are the as-grown sample and those at different RTA temperature for 30 sec. Three absorption edges can be observed where the one at longer wavelength represents the band gap [8]. Such absorption edge has the trend of shifting to shorter wavelength as the annealing temperature increases. The as-grown sample has an absorption edge at 851 nm (1.458 eV) in Fig. 4 curve (a). If RTA is applied at 1000 °C for 30 sec in Fig. 4 curve (b), blue shift of absorption edge to 839 nm (1.479eV) results. For higher temperatures 1020 °C in Fig. 4 curve (c) and 1040 °C in Fig. 4 curve (d), the blue shift is enhanced up to 38 nm and 30 nm respectively. Thus, bandgap enlargement can be characterized by the blue shift of absorption edge. However, the measured absorption edge wavelength at 1020 °C is shorter than at 1040 °C. Such result is unexpected and which may be due to an error in measurement.

The high power ridge waveguide laser diode used in this experiment adopts the DF-MQW structure as the windows at the two ends. Fig. 5 shows the light output power versus current characteristics of high power ridge waveguide laser diode. Fig. 5 curve (a), shows the output power of a window structure laser diode with a threshold current at 85 mA and maximum power of 36 mW. For the conventional laser diode without the window structure,

Fig. 5 curve (b), a lower threshold current at 60 mA and maximum power at 30 mW result. The increase in higher output power is due to the tuning of the bandgap at the output window as a result of the intermixing of MQW which blue shifts the output wavelength. Also, the threshold
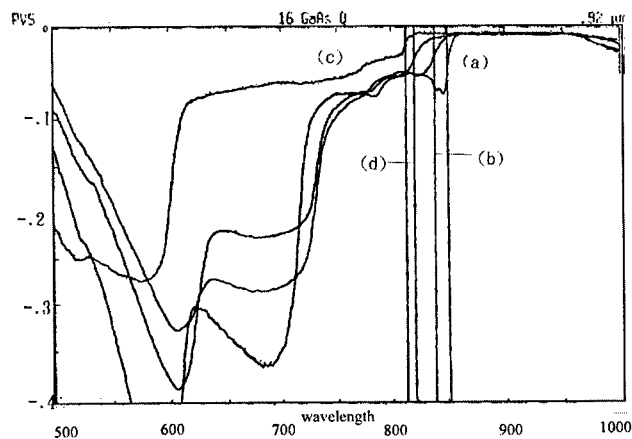

Fig. 4. Photovoltage spectra recorded at room temperature. The curves (a), (b), (c) and (d) represent the as-grown sample, RTA at 1000 °C, 1020 °C and 1040 °C respectively.
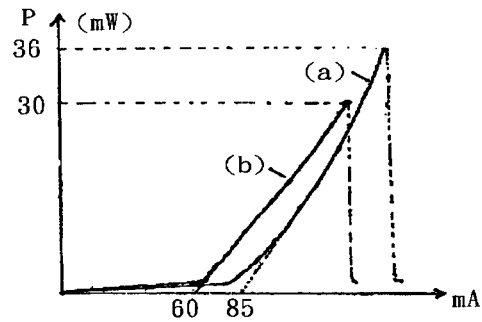

Fig. 5. Light output power (P) versus current curve characteristics of the high power ridge waveguide laser diode. (a) is the laser diode with window structure and (b) conventional laser diode without window structure.

COD power is observed to increase by 20% showing the potential of the window structure made by IFVD technique to obtain high power laser output.

399

Conclusion

Diffused multiple quantum wells can be easily obtained by IFVD under RTA at about 1000 °C for achieving a good tunable operation wavelength range. Results presented here show such ability by a large blue shift of more than 30 nm at an annealing temperature of 1040 °C. This diffused QW structure has been utilized to produce a window for high power ridge waveguide laser diode with an enhanced COD threshold power up to 20%. Therefore, the DF-MQW window structure made by IFVD technique is a very attractive technology to produce high power output in lasers.

Acknowledgement

Reference

[1] J. Marsh, Semicond. Sci. Technol., vol. 8, pp.1136-1155, 1993.
[2] S. F. Yu and E. H. Li, IEEE Photon. Tech. Lett., vol. 8, pp.482-484, 1996.
[3] J. Ungar, N. Bar-cham and I. Ury, Electron. Lett., vol 22, pp.279-280,1986.
[4] Y. Ueno, K. Endo, H. Fujii, K. Kobayashi, K. Hara, T. Yuasu, Electron. Lett., vol.26, pp.1726-1728, 1990.
[5] H. O. Yonezu, M. Ueno, T. Kamejima, and I. Hayashi, IEEE J. Quantum Electron., vol. 15, pp.775-781,1979.
[6] M. Ueno, IEEE J. Quantum Electron.,vol 17, pp2113-2122, 1981.
[7] K. Kash, B. Tell, P. Grabbe, E. A. Dobisz, H. G. Craighead, and M. C. Tamargo, J. Appl. Phys., vol. 63, pp.190-194, 1987.
[8] M. Gail, J. Brunner, J. Nutzel, G. Abstreiter, J. Engvall, J. Olagos and H. Grimmeiss, Semicond. Sci. Technol., vol. 10, pp.319-325, 1995.

INTEGRATED ALL-OPTICAL DEVICES FABRICATED USING AREA-SELECTIVE DISORDERING OF MULTIPLE QUANTUM WELL STRUCTURES

Patrick LiKamWa[†], Ayman Kan'an[*], Mitra-Dutta[‡] , Jagadeesh Pamulapati[**]
Center for Research and Education in Optics and Lasers (CREOL), University of Central Florida
4000 Central Florida Blvd., Orlando, FL 32816-2700. E-mail: likamwa@creol.ucf.edu

[†] also with the Electrical and Computer Engineering, University of Central Florida, Orlando, FL 32816.

[*] now at the School of Electrical and Computer Engineering, Purdue University, Lafayette, IN 47907-1968, E-mail: kanan@ecn.purdue.edu

[‡] US Army Research Office, Research Triangle Park, 4300 Miami Blvd, NC 27709-2211, E-mail: dutta@aro.ncren.net

[**]US Army Research Labs, 2800 Powder Mill Road, Adelphi, MD 20783-1145, E-mail; jpamulapati@arl.mil

ABSTRACT

We describe a method of silicon oxide capped disordering of GaAs /AlGaAs multiple quantum wells (MQW) and its application to the fabrication of passive waveguides integrated with nonlinear switching sections. The silicon oxide cap in this work was formed by spinning a solution of glass forming compound and curing it. The characteristics of the disordering process has been studied by monitoring the shift of the photoluminescence as a function of rapid thermal annealing temperature and fitting the n=1 electron heavy-hole level to that calculated from an error function diffusion profile. Our results indicate a Ga-Al inter-diffusion constant of $8x10^{-16}$ cm^2s^{-1} at 980°C and an activation energy of 4.4eV which is similar to values reported by other researchers.

The disordering process is then used to define selected areas of disordered and non-disordered MQWs and ridge waveguide structures were fabricated by conventional photolithography and wet chemical etching. Two structures have been studied. One is the nonlinear zero-gap directional coupler with disordered input and output branching waveguides, and the other is the symmetric nonlinear integrated Mach-Zehnder interferometer with one arm containing a non-intermixed MQW section. The devices investigated using a pump-probe set-up, exhibited strong all-optical switching behavior with a contrast ratio of 15:1.

INTRODUCTION

Multiple Quantum Well (MQW) structures have attractive electro-optic and nonlinear properties at optical frequencies close to the band-gap frequency. Many devices, such as optical modulators and monolithic bandgap tuned lasers, rely heavily on quantum confinement for their operation and offer improved performance over their bulk counterparts. Other components, such as interconnects and strip-loaded waveguides, need to operate at optical frequencies that are non-resonant with the bandgap frequency of the semiconductor so that the waveguide is effectively transparent at the operating wavelength. To achieve monolithic integration of several optoelectronic devices on a single MQW wafer, one should be able to define materials with different optoelectronic properties (absorption coefficient, material resistivity and refractive index) at different locations. Although MQWs with different compositions and thicknesses can be realized during growth, this method of integrating optoelectronic devices requires extensive

growth capabilities and the growth conditions are very critical for the realization of high quality structures and achieving reproducible results.

Post-growth disordering of MQW layers have been investigated for some time now and that process holds great promise in the realization of integrated optical devices[1]. MQW's can be selectively disordered in a variety of ways, such as impurity induced disordering[2], laser induced disordering[3, 4], ion-implantation-enhanced interdiffusion[5,6] and vacancy induced disordering[7,8]. Of these processes, the impurity-free vacancy induced disordering (IFVD) appear to have the best characteristics. Since it is an impurity-free process, waveguides fabricated in such disordered materials do not experience attenuation due to free-carrier absorption. We have developed a simple means of achieving disordering of MQW structures that is also fully compatible with other semiconductor device fabrication techniques. The process is affordable, area-selective, and highly reproducible. Room temperature photoluminescence (PL) characterization indicates a 40nm possible blue shift in the peak emission wavelength as a result of the disordering process. We used this process to realize two devices: One is an all-optical switch that has a nonlinear mode-beating section coupled with low-loss branching waveguides. The other is an integrated Mach-Zehnder optical modulator that has one non-intermixed arm while the other arm and the rest of the structure are made of disordered MQW structure. Pump-probe measurements were done on the devices to study the switching characteristics of these integrated devices.

EXPERIMENTAL PROCEDURE

The MQW waveguide structure used in this work consists of 38 periods of 70Å GaAs layers alternating with 70Å $Al_{0.3}Ga_{0.7}As$ layers. The MQW waveguide core was clad by a 0.5μm thick $Al_{0.3}Ga_{0.7}As$ layer on the top and a 2μm thick $Al_{0.3}Ga_{0.7}As$ layer on the bottom. The structure was grown by molecular beam epitaxy(MBE) on an undoped GaAs substrate. In order to achieve controlled intermixing between the GaAs quantum wells and the AlGaAs barriers, the surface of the sample was coated with a thin film of "spin-on-glass" which is a commercially available solution of glass (SiO_x) forming compound. The thin film was deposited by spinning the liquid on the sample surface at a speed of 3000 rpm for 30 seconds, this resulted in a film thickness of 230 nm. The film was then cured at 400°C for 30 minutes in a constant flow of ultra high purity air (78% nitrogen and 22% oxygen). Localized compositional disordering was then induced by photolithographic definition and removal of the SiO_x film in selected regions followed by rapid thermally annealing. The rapid heating of the sample was carried out in a flowing nitrogen atmosphere in an AG Associates Heatpulse 210 rapid thermal annealer. The sample was placed face down on a mechanical grade undoped GaAs substrate to protect the face of the sample and to provide overpresure of As so as to minimize its desorption. The silicon oxide cap at the surface promotes out-diffusion of Ga atoms into the cap layer, thus generating group III vacancies at the surface of the sample. The intermixing is caused by the inter-diffusion of the these vacancies with Ga and Al atoms, with a subsequent diffusion of the vacancies into the MQW region and the ensuing disordering of the quantum wells. There have been previous reports on the use of SiO_2 to enhance the intermixing of group III-V multiquantum well structures[9,10,11]. Rapid thermal annealing of a sample that is encapsulated by an SiO_x cap layer deposited on the surface by either chemical vapor deposition or electron beam evaporation results in a significant blue shift of the band-edge. The magnitude of the blue shift is a function of the annealing time and temperature. The main difference between this work and the previously reported work is the simplicity of the current technique that is used to generate the vacancies and enhance the impurity free vacancy diffusion in the heterostructure.

In order to characterize our method of IFVD, different samples measuring 3x4 mm^2 of the MQW structure described above were first cleaned with solvents, and then coated with spin-on

glass and cured at 400°C for 30 minutes in a nitrogen/oxygen atmosphere. Conventional photolithography and photoresist masking was then used to etch off the SiO_x layer from the surface of one half of each sample by immersing them in a buffered oxide etchant (BOE) (1:9 $HF:H_2O$) for 30 seconds. The samples were then annealed separately for 20 seconds at temperatures of 960, 970, 980, and 1000°C respectively. The degree of disordering was measured by comparing the room temperature PL of the SiO_x-capped region, the uncapped region, and an as-grown sample. The samples were excited by a focused 15mW He-Ne laser beam (632.8nm), and the PL was collected by a lens onto a monochromator connected to an optical multichannel analyzer. As the Al atoms diffuse into the quantum well region, the abruptness of the interfaces is destroyed and the subband energies move apart, resulting in an increase in the n=1 electron to heavy-hole transition energy. The thermal annealing was carried out for 20 seconds over a range of temperatures and the PL shift as a function of temperature was plotted as shown in figure 1. The heavy hole (hh) and light hole (lh) exciton transitions that are clearly resolved for the as-grown remain clearly resolved after the annealing for the uncapped sample. The measurement indicates that the MQW intermixing using this method results in a difference of 37 nm or more between the blue shifted effective band edge of the coated and that of the uncoated samples.
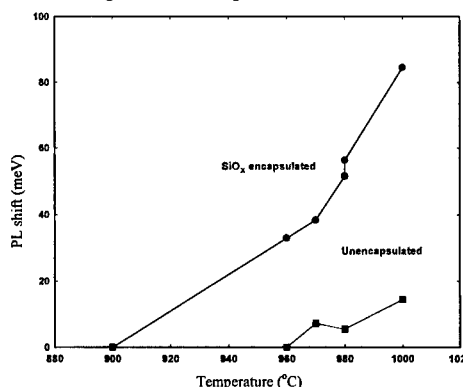

Figure 1. Plot of PL shift as a function of anneal temperature (anneal time was 20s in all cases).

THEORETICAL MODELING

To model the interdiffusion of Al and Ga atoms in a single QW, Fick's equation is solved assuming constant diffusion coefficients, D, that is independent of the initial Al composition of the barrier layers

$$\frac{\partial x(z,t)}{\partial t} = D\frac{\partial^2 x}{\partial z^2}$$

where $x(z,t)$ is the Al concentration at position z after annealing for t seconds. The Al composition varies across an intermixed centered at $z=0$ is given by

$$x(z) = x_0\left[1 + \frac{1}{2}erf\left(\frac{z-L/2}{2\sqrt{Dt}}\right) - \frac{1}{2}erf\left(\frac{z+L/2}{2\sqrt{Dt}}\right)\right]$$

where x_0 is the initial Al composition of the barrier, L is the initial well width, D is the diffusion, t is the annealing time, and erf is the error function. As a result of this alteration of this potential profile, the quantized energy levels inside the QW are increased. This increase is dependent on the initial width of the QW, the annealing time, the initial concentration of the Al atoms, x_0, and finally and most importantly the diffusion coefficient which depends of the number of vacancies at the surface.

To find the diffusion coefficient at a given annealing time and temperature, we assume that the quantum well closest to the surface contributes to the part of the PL at its peak wavelength. We also assume that there is no coupling between the neighboring quantum wells, this assumption is valid because the barrier separating the wells is thick enough to prevent any noticeable interaction between the wave functions of the eigenstates inside the QWs. Thus, we

403

can safely assume that the calculated e1-hh1 transition energy of a single well corresponds to that of our MQW structure. In the calculations of the electron and heavy-hole subband energies, the following parameters were used: the effective masses of the electron and the hh were considered to be $0.067m$ and $0.48m$, respectively (where m is the free electron mass). The bandgap energy as a function of the Al composition, $x(z)$, was approximated by

$$E_g(eV) = 1.43 + 1.44x(z)$$

and the energy offset ratio of the conduction to the valence band was taken to be 65:35.

The n=1 e-hh transition wavelength for the 80Å QW was calculated to be 834.6nm, this value agrees with the measured PL of the structure which was found to peak at $\lambda=835$nm. The values of the diffusion coefficient that correspond to the blue shift at the annealing temperatures were calculated by an iterative procedure. For an assumed value of D, the e1-hh1 transition energy of the intermixed QW was calculated using the transmission matrix method[12] and compared to the measured value until they are less than 0.5 meV apart.

Figure 2 shows the deduced values of D plotted as a function of (1/kT) for both the capped and the uncapped samples. A curve fit of the data gives a single activation energy of $E_a \approx 4.4$eV. This value is in good agreement with the results reported in the literature[10,13]. The fact that almost identical activation energies were obtained for both curves implies that the dissimilarity in disordering behavior between the SiO_x capped and uncapped sample is due to the difference in the number of vacancies generated at the surface of the samples. It is evident that the diffusion coefficient for the SiO_x capped sample is one order of magnitude greater than that for the uncapped samples.

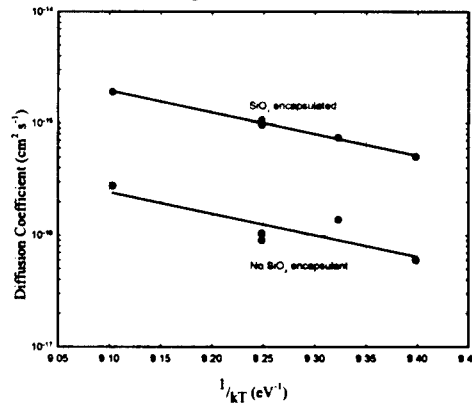

Figure 2. Plot of the deduced values of the diffusion coefficient vs. 1/kT for both the capped and the uncapped samples.

A single-mode ridge waveguide was fabricated from an intermixed sample and the waveguiding losses were measured using a thermally scanned Fabry-Perot transmission technique. For this measurement, a cw Ti:sapphire laser with an intracavity frequency narrowing etalon was employed for stable narrow linewidth operation. The measurements of the Fabry-Perot fringes indicated that scattering losses due to the vacancy induced disordering was around 10dB/cm. While this value is still too high for the technique to be applicable to the integration of several devices, a simple demonstration of its intended use has been performed with the integrated all-optical devices described in the next section.

ALL-OPTICAL DEVICES EMPLOYING RESONANT NONLINEARITIES

The first device described in this paper is the zero-gap nonlinear directional coupler (NLDC) which consists of a single mode input waveguide, a dual-mode coupling section and two single-mode output waveguides. Except for the mode-beating section, all regions of the MQWs were intermixed to blue shift the band-edge away from the device operating wavelength. After the silicon oxide was spun on the surface, the film was cured as described above. Then using a contact mask photolithographic process to define windows measuring 100x500 μm^2 in positive photoresist, a buffered oxide etch (BOE) was used to remove the oxide film within the exposed

windows. After removing the photoresist, the sample was subjected to rapid thermal annealing at 980°C for 20 seconds to diffuse the vacancies into the MQW region. Thus the whole sample except for the windowed sections, was intermixed. The zero-gap directional coupler was defined using a second step photolithography and aligned carefully so that the double-mode waveguide sections are exactly within the non-intermixed windows. Using a wet chemical etch consisting of H_3PO_4:H_2O_2:H_2O solution in the ratios of 1:1:10, a 350 nm thickness of the cladding layer is etched off to form cladding ridges for 3.4μm wide double-mode switching sections with 1.7μm wide single mode waveguides. Finally the GaAs substrate was polished down to 100μm thickness and the sample was cleaved to a total length of 1.7mm assuring good facets.

The switching characteristics of the devices were measured using an optical pump-probe set-up. Wavelength tunable, sub-picosecond pulses were obtained from a self-modelocked Ti:sapphire laser pumped by a cw argon ion laser. The control beam was polarized in the TE (horizontal) configuration while the mechanically chopped signal beam was polarized in the TM (vertical) direction. The two beams were recombined co-linearly and focused into the input waveguide. The light at the output of the device was collected by a microscope objective lens and imaged onto a CCD camera. A polarizer placed at the output of the waveguide was used to filter out the control beam. The throughput of the signal beam from either output port was measured by a silicon photo-detector with a small aperture. Lock-in detection was used to measure the signal beam at the output port as a function of time delay between the control and signal beam.
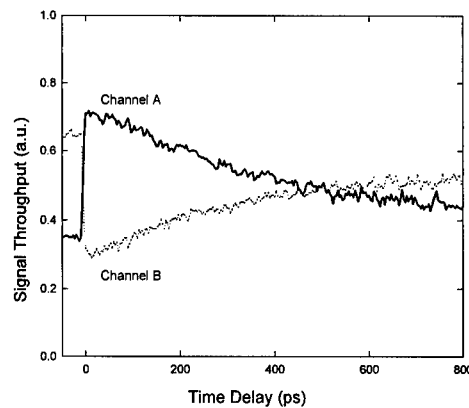

Figure 3. Switching of the transmission of the signal pulses through the output channels A and B as a function of the time delay with the control pulses.
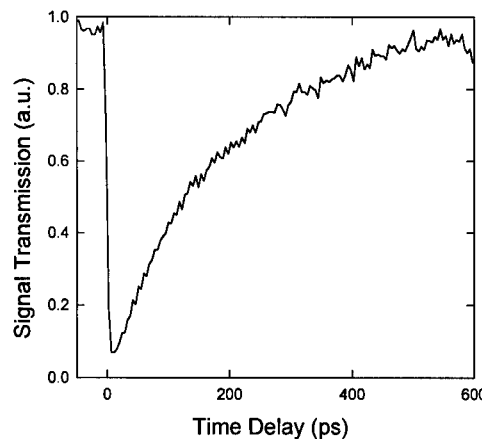
Figure 3 shows the transmission of the signal in the two output ports of the NLDC as a function of the delay between the pump and the probe beams. The initial 63:37 split ratio of the output ports was switched to 30:70 with an exponential recovery time constant of around 300 ps. The total power through the two output ports remained constant and hence indicated that negligible nonlinear absorption took place.

The second device is the integrated Mach-Zehnder (MZ) optical modulator. It contains a 500μm long active switching region of non-intermixed MQW in one arm, while the other arm and the rest of the structure were made of disordered MQW. The same process described for the above was also used in the fabrication of this device except that in this case the defined windows measured 20x500(μm)². PL

Figure 4. Probe transmission in an integrated Mach-Zehnder interferometer as a function of the delay between the signal and the control pulses.

405

measurements showed a distinctive difference between the peak wavelengths of the luminescence from the windowed (non-intermixed) and the intermixed regions. This indicates that the technique is highly area-selective. The same optical setup was used to measure the switching performance of the integrated Mach-Zehnder device. Figure 4 shows the output power being modulated by the injection of a strong optical pump pulse. The device has a switch contrast of 15 to 1 and it too exhibited an exponential recovery time constant of about 300 ps.

CONCLUSIONS

We have developed an inexpensive and reliable process for the area-selective disordering of MQW structures. The scattering losses due to the vacancy induced disordering was measured to be less than 10dB/cm and work is currently underway to further improve on the waveguiding quality of the disordered MQWs. This technique has been applied to the fabrication of two integrated optical devices. In both devices, the mechanism for the switching is the nonlinear refractive index that is caused by photo-generated carriers. Since this mechanism entails absorption of some of the pump beam, it is hence very important that the optical absorption be confined to the active sections only. Selective area disordering is shown to be very effective at defining regions of different bandgap energies. Hence it can be ensured that the energy of the pump laser beam is too low in comparison to the bandgap energy of the passive regions to be absorbed and the free carriers are only created in the non-intermixed active sections. The controlled selective area intermixing of MQW structures will potentially play a significant role in the advancement of photonic integrated circuits.

REFERENCES

1. P. Li KamWa, Optical and Quantum Electron., 23, pS925, 1991.
2. W. D. Laidig, N. Holonyak Jr., M. D. Camras, K. Hess, J. J. Coleman, P. D. Dapkus, J. Bardeen, Appl. Phys. Lett., 38, p776, 1981.
3. D. Kirillov, J. L. Merz, P. D. Dapkus, J. J. Coleman, J. Appl. Phys., 55, p1105, 1984.
4. J. E. Epler, R. D. Burnham, R. L. Thornton, T. L. Paoli and M. C. Bashaw, Appl. Phys. Lett., 49, p1447, 1986.
5. Y. Hirayama, Y. Suzuki, and H. Okamoto, Jpn. J. Appl. Phys., 24, 1498 (1985).
6. J. Cibert, P. M. Petroff, D. J. Werder, S. J. Pearton, A. C. Gossard and E. English, Appl. Phys. Lett., 49, p223, 1986.
7. E. S. Koteles, B. Elman, P. Melman, J. Y. Chi, C. A. Armiento, Optic. Quantum Electron. 23, pS779, 1991.
8. D. G. Deppe, L. J. Guido, N. Holonyak, Jr., K. C. Hsieh, R. D. Burnham, R. L. Thornton, and T. L. Paoli, Appl. Phys. Lett., 49,510 (1986).
9. M. Ghisoni, P. J. Stevens, G. Parry, and J. S. Roberts, Opt. and Quantum Elect., 23 (1991) S915-S924.
10. I. Gontijo, T. Kraus, J. H. Marsh, and R. M. De La Rue, IEEE J. of Quantum Elect., V. 30, no. 5 (1994) 1189.
11. S. Shi, P. Li Kam Wa, A. Miller, J. Pamulapati, P. Cooke, and Mitra Dutta, Appl. Phys. Lett., 66 (1), 1995, p79.
12. Y. Zebda and A. M. Kan'an, J. of Appl. Phys., 72 (1992) 559.
13. J. D. Ralston, S. O'Brien, G. W. Wicks, and L. F. Eastman, Appl. Phys. Lett. 52, p1511, 1988.

MODELING OF Be DIFFUSION IN InGaAs EPITAXIAL STRUCTURES

S. Gautier*, S. Koumetz*, J. Marcon*, K. Ketata*, M. Ketata* and P. Launay**
*LCIA-INSA de Rouen, Place Emile Blondel, B.P.08, F76131 Mont Saint Aignan, France
**CNET de Bagneux, 196 av. H. Ravera, B.P.107, F92225 Bagneux, France

ABSTRACT

The subject of this work is the simulation of Be diffusion during post-growth Rapid Thermal Annealing (RTA) of InGaAs epitaxial layers grown by Chemical Beam Epitaxy (CBE). This diffusion may occur during thermal treatments of InGaAs/InP Heterojunction Bipolar Transistors (HBT's), which contributes to limit the frequency performances of these devices. In order to characterize the Be depth profiles, Secondary Ion Mass Spectrometry (SIMS) has been used. The concentration dependent diffusivity has been covered to perform an improved data fitting of Be diffusion profiles. In a first step, the solid state diffusion mechanisms have been developed, including the Substitutional-Interstitial Diffusion (SID) and, in particular, Kick-out mechanism. To explain the observed concentration profiles and related diffusion mechanisms, a Generalized Substitutional-Interstitial Diffusion model is proposed. A simultaneous diffusion by Dissociative and Kick-out mechanisms is suggested. Good agreements between experimental depth profiles and simulated curves have been obtained.

INTRODUCTION

The device performances of InGaAs/InP Heterojunction Bipolar Transistor could be strongly improved by reduction of the InGaAs base sheet resistance using high p-type doping level. However, an excessive diffusion of such dopants from the base to the emitter during post-growth technological processes can cause severe degradations of HBT's [1]. Consequently, the base dopant diffusion control during epitaxial growth and post-growth technological processes is essential. Be and Zn diffusion in GaAs compounds have been extensively studied in the past [2-8]. They have been found based on Dissociative [2,3] or Kick-out [4,5] mechanisms. Comparing the two models, some authors found that the second one have an advantage over first [5,6]. In contrast, investigations on p-type dopant diffusion in InP based epitaxial compounds, particularly Be in InGaAs, are still limited [7,8].

The aim of this work is to investigate the Be diffusion during post-grown annealing in order to control the concentration profiles of this dopant in InGaAs epitaxial layers. This requires reliable fitting operations of the Be redistribution during RTA.

EXPERIMENT

A rigorous optimization of the growth conditions has been already performed at the CNET laboratories which has allowed to minimize the Be diffusion from InGaAs base layer during growth [9]. Epitaxial layers were grown by Chemical Beam Epitaxy on a $<100>$ oriented semi-insulating InP substrates in a Riber 2300 CBE apparatus [9]. At first, $0.1\mu m$ InP buffer layer was grown, followed by $0.5\mu m$ undoped $In_{0.53}Ga_{0.47}As$ layer and then $0.2\mu m$ Be-doped $In_{0.53}Ga_{0.47}As$ layer with different Be doping levels $\left(5\times10^{18}, 1\times10^{19}\text{ and }3\times10^{19}\text{cm}^{-3}\right)$. Finally, an undoped $In_{0.53}Ga_{0.47}As$ layer of $0.5\mu m$ was grown on the Be doped layer. The undoped layers were grown at a rate of $1.76\mu m / h$ and doped ones at $2.40\mu m / h$ with a V/III flux ratio of 2 and a substrate temperature of $500°C$. This combination of flux ratio and growth temperature gives

the best material quality, improving its electrical proprieties. The low flux ratio is necessary to ensure the "arsenic stabilized surface" at 500°C.

The post-growth Rapid Thermal Annealing was performed in a halogen lamp furnace ADDAX XM. The wafers were annealed in flowing $(Ar+10\% H_2)$ gas. The temperature cycles were monitored by a thermocouple attached to the sample holder. RTA was carried out at temperatures in the range of 500-800°C using a heating rate of about 28°C / s.

The resulting samples were depth profiled in Cameca IMS-4F SIMS apparatus, equipped with oxygen source, using a primary beam of 3.5KeV impact energy.

RESULTS

We have observed that there is no significant Be diffusion during the post-growth annealing for all doping levels $(5 \times 10^{18}, 1 \times 10^{19}$ and $3 \times 10^{19} cm^{-3})$ if RTA is performed at 500 and 600°C during time lower than 1 min. The same observation has been made for the samples doped to $5 \times 10^{18} cm^{-3}$ and annealed at 700°C during 30s. In contrast, in the case of $3 \times 10^{19} cm^{-3}$ Be concentration, an important Be diffusion occurs for temperatures and times higher then 700°C and 1 min respectively (solid lines in Figs. 1(a,b)).
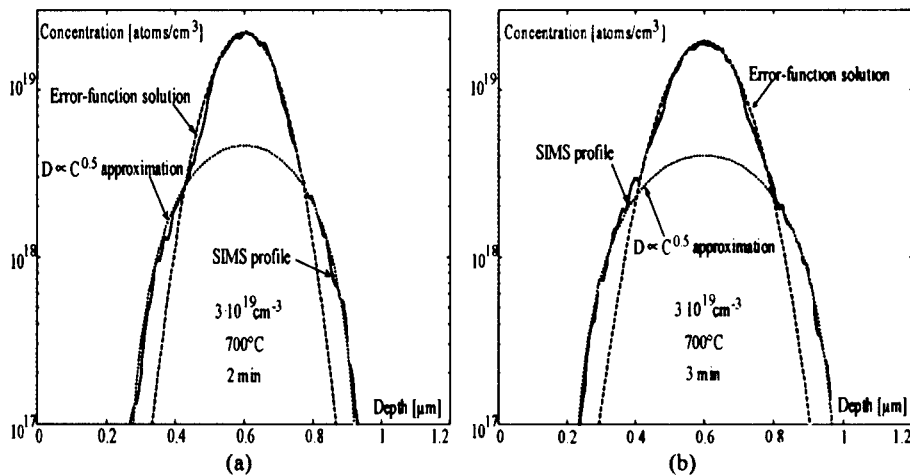
Figs. 1(a,b). SIMS diffusion profiles (solid lines) and calculated curves (dashed and dotted lines) for $3 \times 10^{19} cm^{-3}$ Be doping level, 700°C annealing temperature and annealing time of : (a) 2 min and (b) 3 min.

I. A General SID model in the case of time independent Be effective diffusivity.

If the Be diffusion coefficient is a function of the Be concentration only and the total dopant of finite source (initially close to a thin layer) remains invariant with diffusion time, a modified version of the Boltzmann-Matano analysis could be used for obtaining a functional dependence between the diffusivity of beryllium and its concentration [10]. The Boltzmann-Matano technique has been applied to our depth profiles and so, permitted to deduce that the Be effective diffusion coefficient D_{eff} is approximately constant for the high part of the experimental curves and proportional to the square root of concentration for the low part [11,12]. Thus, the high

concentration profile portions have been fitted by error-function distribution [13]. We used the value of $1.8 \times 10^{-13} \mathrm{cm}^2 \mathrm{s}^{-1}$ for the parameter D_{eff} (dashed curves in Figs. 1).

Assuming that the Be effective diffusivity is proportional to the square root of Be concentration for low concentration profile part, we substituted its expression $D_{eff} = D_{max} \sqrt{C(x,t)/C_{max}}$ into Fick's second law and solved numerically the resulting differential equation by finite-difference explicit scheme [14] using the maximum effective diffusion coefficient $D_{max} = 1.28 \times 10^{-12} \mathrm{cm}^2 \mathrm{s}^{-1}$ corresponding to the maximum concentration $C_{max} = 1.1 \times 10^{19} \mathrm{cm}^{-3}$ of Be species in the doped layer at $t = 0$, which contribute in the $D_{eff} \propto \sqrt{C}$ dependence mechanism (dotted curves in Figs. 1).

To explain these results, a General SID model has been proposed combining a simultaneous diffusion by Dissociative and Kick-out mechanisms. On the other hand, the Fermi-level effect is used to explain the functional dependence variation of the effective diffusion coefficient of Be with concentration [11,12].

II. Kick-out diffusion model adapted to our experimental conditions.

Under point defect nonequilibrium, the Kick-out mechanism with the neutral beryllium interstitial species Be_i^o and the singly ionized Ga and In self-interstitials I_{III}^+, given by reaction

$$Be_i^o \overset{K}{\Leftrightarrow} Be_s^- + I_{III}^+ \qquad (1)$$

(where Be_s^- is the singly negatively charged Be substitutional species) could be used to obtain quantitative data fits. We suggested that local instantaneous equilibrium between interstitial and substitutional Be is reached at any location and any moment. Consequently, the law of mass action applied to reaction (1) gives :

$$\frac{C_i}{C_s C_I} = \frac{C_i^{eq}}{C_s^{eq} C_I^{eq}} = K \qquad (2)$$

where K is the reaction constant and $C_i^{eq}, C_s^{eq}, C_I^{eq}$ denote the equilibrium concentrations of $Be_i^o, Be_s^-, I_{III}^+$ species respectively in the doped layer at initial instant. Taking into account Fermi-level and electric build-in effects, we obtained the following differential equation system :

$$\begin{cases} \dfrac{\partial C_i}{\partial t} + \dfrac{\partial C_s}{\partial t} = D_i \dfrac{\partial^2 C_i}{\partial x^2} & (3) \\[2ex] \dfrac{\partial C_I}{\partial t} = D_I \dfrac{\partial^2 C_I}{\partial x^2} + \dfrac{\partial C_s}{\partial t} - k_I \times \left[C_I - C_I^{eq}(p) \right] - D_I \dfrac{\partial}{\partial x}\left(\dfrac{C_I}{p} \dfrac{\partial p}{\partial x} \right) & (4) \end{cases}$$

Eq. (3) gives the increase rate of the Be atoms supposing the diffusion coefficient of the substitutional beryllium D_s negligible in comparison with the diffusion coefficient of the interstitial beryllium D_i. Eq. (4) gives the rate of increase (for in-diffusion) or decrease (for out-diffusion) of the Ga and In self-interstitials, where the first term on the right hand side represents self-interstitials losed (gained) by the diffusion of these last with the self-interstitial diffusivity D_I ; the second term represents gain of self-interstitials due to interstitial Be transforming into substitutional ; the third term is the bulk annihilation (production) of self-interstitials by dislocation climb with the coefficient of annihilation (production) k_I ; the fourth term is due to the

electric field produced by the charge distribution (with the negative sign because of the positively charged nature of the I_{III}^+ species). The I_{III}^+ thermal equilibrium concentration $C_I^{eq}(p)$ changes with Be concentration according to Fermi-level effect [15] :

$$C_I^{eq}(p) = C_I^{eq}(n_i) \times \frac{p}{n_i} \qquad (5)$$

where $C_I^{eq}(n_i)$ is the I_{III}^+ thermal equilibrium concentration under intrinsic conditions (n_i denotes intrinsic carrier concentration) and p is the local hole concentration, given by :

$$p = \frac{1}{2}\left(C_a + \sqrt{C_a^2 + 4n_i^2}\right) \qquad (6)$$

Eqs. (2)-(6) have been solved simultaneously numerically using finite difference explicit scheme. The experimental profiles have been fitted with the calculated curves using the simulation parameters listed in Tab. I.

C_a^{eq} $[cm^{-3}]$	C_i^{eq} $[cm^{-3}]$	n_i $[cm^{-3}]$	$C_I^{eq}(n_i)$ $[cm^{-3}]$	D_i $[cm^2 \cdot s^{-1}]$	D_I $[cm^2 \cdot s^{-1}]$	k_I $[s^{-1}]$
3×10^{19}	3×10^{17}	2×10^{17}	1.4×10^{15}	9×10^{-11}	3×10^{-12}	0.6

Table I. Simulation parameters used for obtaining the theoretical curves (dashed lines) in Figs. 2.

The results of this simulation are given in Figs. 2. We were not able to obtain satisfactory fitting using the Kick-out model with the charged interstitial Be because of the strong influence of electric build-in effect [5]. It has been also impossible to fit the depth profiles using Dissociative diffusion model with charged or neutral interstitial Be and charged or neutral Ga and In vacancies.
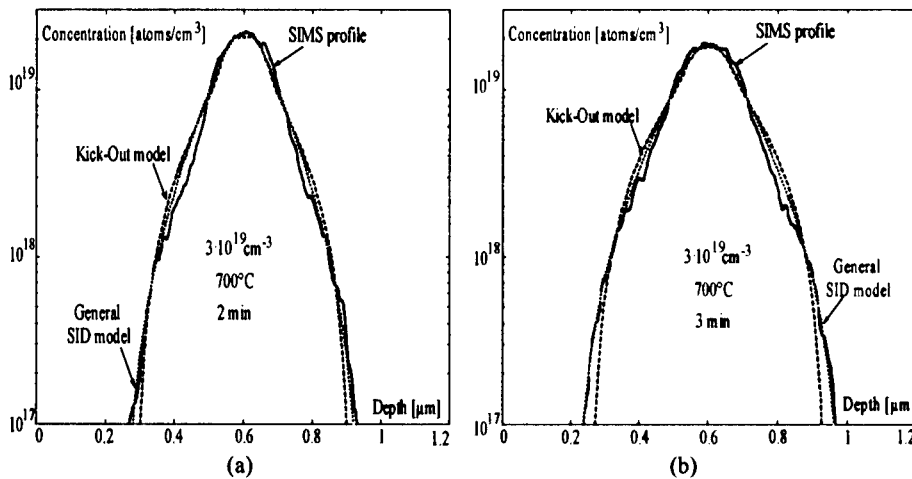
Figs. 2(a,b). SIMS diffusion profiles (solid lines) and calculated curves (Kick-out model : dashed lines, Generalized SID model : dotted lines) for $3 \times 10^{19} cm^{-3}$ Be doping level, $700°C$ annealing temperature and annealing time of : (a) 2 min and (b) 3 min.

III. A General SID model in the case of time dependent Be effective diffusivity.

Assuming the point defect nonequilibrium, we suggested that the Be diffusion in InGaAs is governed by Kick-out and Dissociative mechanisms simultaneously with neutral beryllium interstitial species Be_i^o, singly ionized Ga and In self-interstitials I_{III}^+ and singly negatively charged Ga and In vacancies V_{III}^- :

$$\begin{cases} Be_i^o \Leftrightarrow Be_s^- + I_{III}^+ & (7) \\ \gamma Be_i^o + \gamma V_{III}^- \Leftrightarrow \gamma Be_s^- & (8) \end{cases}$$

These reactions combine to give the following expression :

$$(1+\gamma)Be_i^o + \gamma V_{III}^- \overset{K'}{\Leftrightarrow} (1+\gamma)Be_s^- + I_{III}^+ \tag{9}$$
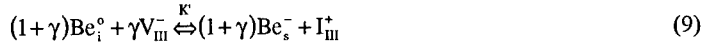
In general case the coefficient γ, which characterizes the dissociative part in diffusion, depends on x and t. In a first approximation, it has been considered constant and equals to 1 (equiprobability of two mechanisms on average). So, Eq. (9) transforms into :

$$2Be_i^o + V_{III}^- \overset{K'}{\Leftrightarrow} 2Be_s^- + I_{III}^+ \tag{10}$$
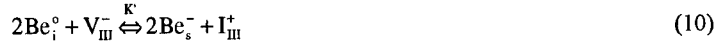
giving rise (assuming the condition of instantaneous equilibrium between Be_i^o and Be_s^- species) to the mass action relation :

$$\frac{C_i^2 C_v}{C_s^2 C_I} = \frac{\left(C_i^{eq}\right)^2 C_v^{eq}}{\left(C_s^{eq}\right)^2 C_I^{eq}} = K' \tag{11}$$

where K' is the reaction constant and C_v^{eq} is the V_{III}^- equilibrium concentration in the doped layer at $t = 0$. The reaction (8) add to the system of Eqs. (3) and (4) the following differential equation:

$$\frac{\partial C_v}{\partial t} = D_v \frac{\partial^2 C_v}{\partial x^2} - \frac{\partial C_s}{\partial t} - k_v \times \left[C_v - C_v^{eq}(p)\right] + D_v \frac{\partial}{\partial x}\left(\frac{C_v}{p}\frac{\partial p}{\partial x}\right) \tag{12}$$

This last gives the decrease rate (for in-diffusion) or increase (for out-diffusion) of the Ga and In vacancies, where the first term on the right hand side represents vacancies gained (losed) by diffusion (with the vacancy diffusivity D_v), the second represents loss of vacancies due to interstitial Be going substitutional, the third term is the bulk production (annihilation) of vacancies by dislocation climb with the coefficient of production (annihilation) k_v , the fourth term is due to the electric field produced by the charge distribution (with the positive sign because of the negatively charged nature of the V_{III}^- species). The V_{III}^- thermal equilibrium concentration $C_v^{eq}(p)$ changes with Be concentration according to Fermi-level effect [15] :

$$C_v^{eq}(p) = C_v^{eq}(n_i) \times \frac{n_i}{p} \tag{13}$$

where $C_v^{eq}(n_i)$ is the V_{III}^- thermal equilibrium concentration under intrinsic conditions. Eqs.(3)-(6),

(11)-(13) have been solved simultaneously numerically using finite difference explicit scheme. The depth profiles have been fitted with the simulation parameters listed in Table II :

$C_\bullet^{eq}$ $[cm^{-3}]$	C_I^{eq} $[cm^{-3}]$	n_i $[cm^{-3}]$	$C_I^{eq}(n_i)$ $[cm^{-3}]$	D_i $[cm^2 \cdot s^{-1}]$	D_I $[cm^2 \cdot s^{-1}]$	K_I $[s^{-1}]$	$C_v^{eq}(n_i)$ $[cm^{-3}]$	D_v $[cm^2 \cdot s^{-1}]$	k_v $[s^{-1}]$
3×10^{19}	3×10^{17}	2×10^{17}	3.5×10^{14}	5×10^{-10}	1×10^{-10}	1.1	1.7×10^{17}	7×10^{-11}	0.1

Table II. Simulation parameters used for obtaining the theoretical curves (dotted lines) in Figs. 2.

It could be seen that the Generalized SID model gives better simulation results than Kick-out diffusion model (see Figs. 2).

CONCLUSIONS

In summary, a General Substitutional-Interstitial Diffusion model in the case of point defect nonequilibrium is proposed to explain the experimental profiles of Be diffusion in InGaAs compounds. This model, based on simultaneous diffusion by Dissociative and Kick-out mechanisms, gives the better simulation of experimental data in comparison with the Kick-out diffusion model modified according to our experimental conditions.

ACKNOWLEDGMENTS

REFERENCES

1. N. Jourdin, F. Alexandre, C. Dubon-Chevalier, J. Dangla, and Y. Gao, IEEE Trans. Electron. Devices 39, p. 767 (1992).
2. F.C. Frank and D. Turnbull, Phys. Rev. 104, p. 617 (1956).
3. R.L. Longini, Solid State Electron. 5, p. 127 (1962).
4. U. Gösele and F. Morehead, J. Appl. Phys. 52, p. 4617 (1981).
5. S. Yu, T.Y. Tan and U. Gösele, J. Appl. Phys. 69, p. 3547 (1991).
6. A.H van Ommen, J. Appl. Phys. 54, p. 5055 (1983).
7. E.G. Scott, D. Wake, G.D.T. Spiller and G.J. Davies, J. Appl. Phys. 66, p. 5344 (1989).
8. R.A. Metzger, M. Hafizi, W.E. Stanchina, T. Lin, R.G. Wilson and L.G. McGray, Appl. Phys. Lett. 63, p. 1360 (1993).
9. J.L. Benchimol, M. Juhel, M. Petitjean, A. Ancilotti, J. Vac. Sci. Technol. B13, p. 1 (1995).
10. M. Ghezzo, J. Electrochem. Soc. 119, p. 977 (1972).
11. S. Koumetz, J. Marcon, K. Ketata, M. Ketata, C. Dubon-Chevalier, P. Launay, and J.L.Benchimol, Appl. Phys. Lett. 67, p. 2161 (1995).
12. S. Koumetz, J. Marcon, K. Ketata, M. Ketata, F. Lefebvre, P. Martin, P. Launay, Mater. Sci. and Eng. B37, p. 208 (1996).
13. M. Ilegems, J. Appl. Phys. 48, p. 1278 (1977).
14. W.H. Press, S.A. Teucolsky, W.T. Vetterling, B.P. Flannery, Numerical recipes in C, Cambridge University Press, 1992, pp. 847-851.
15. T.Y. Tan and U. Gösele, J. Appl. Phys. 61, p. 1841 (1987).

QUANTUM WELL INTERMIXING IN GAINAS/GAINASP AND GAAS/ALGAAS STRUCTURES USING PULSED LASER IRRADIATION

A.C. BRYCE*, R.M. DE LA RUE*, J.H. MARSH*, B.S. OOI**, B.QIU*, C.C. BUTTON*** and J.S. ROBERTS***
*University of Glasgow, Department of Electronics and Electrical Engineering, Glasgow, G12 8QQ Scotland, UK, acbryce@elec.gla.ac.uk
**Present Address Department of Electrical and Electronic Engineering, Block B1, Nanyang Technical University, Nanyang Avenue, Singapore, 639791
***Department of Electronic and Electrical Engineering, University of Sheffield, Mappin Street, Sheffield, S1 3JD, England, UK

ABSTRACT

An essentially impurity free, direct write and potentially high spatial resolution quantum well intermixing technique using pulsed laser irradiation is reported. This technique uses a Q-switched Nd:YAG laser emitting at 1.06 μm with a pulse length of ~20 ns and repetition rate of 10 Hz. The typical energy densities used for both GaInAs/GaInAsP and GaAs/AlGaAs structures were ~ 5 mJ mm^{-2}. Multiphoton interactions with carriers lead to phonon emission, the phonons interact with the lattice thus generating point defects which diffuse during a subsequent annealing stage in a rapid thermal annealer and cause intermixing. Photoluminescence measurements have demonstrated that the spatial resolution of the process is better than the resolution of the PL measurement (ie better than 25 μm) and the technique has been used to write directly a grating of period 1.25 μm into a GaInAs/GaInAsP quantum well structure. This was achieved using a grating of period 2.5 μm etched into the surface of the substrate; when illuminated by the Q-switched pulses this grating generated a volume hologram of point defects within the sample at half the etched period. A clear dip in the transmission spectrum of the waveguide which had been processed in this way was observed at 1.525 μm. Differential bandgap shifts of up to 40 meV have been observed in GaAs/AlGaAs double quantum well samples. 3 μm wide ridge waveguide lasers were fabricated from the intermixed and control samples. The threshold currents of the intermixed and the control lasers were comparable. The slope efficiency of the intermixed lasers showed insignificant changes when compared to the as-grown lasers.

INTRODUCTION

Laser induced quantum well intermixing (QWI) processes for the fabrication of photonic integrated circuits (PICs) have been investigated for some time. In the GaAs/AlGaAs quantum well system, both annealing of implanted samples [1] and transient melting of multiple layers by pulsed excimer or cw Ar laser irradiation [2] have been shown to be effective. Transient melting using scanned cw lasers, with a power density of ~250 kW mm^{-2}, has been utilised to introduce encapsulant Si into the epitaxial layers. This Si then acts as an impurity induced disordering source which takes place during a subsequent annealing stage [3]. Quantum well wires have also been fabricated using a tightly focused spot [4] (intensity ~30 kW mm^{-2}). Laser induced processes have advantages over other QWI processes, such as impurity induced disordering (IID) and impurity free vacancy disordering (IFVD)[5], in that they are potentially impurity free and offer the possibility of direct writing. However, they may require high power densities to melt the material, may introduce thermal shock damage if used in a pulsed mode and may cause an undesirable redistribution of dopants outwith the active region of the device.

Photo-absorption induced disordering (PAID) is a laser induced QWI technique developed in the GaInAs/GaInAsP system [6]. The laser radiation is absorbed in the quantum well region generating heat and causing thermal intermixing, with the resulting material being of high optical and electrical quality [7, 8]. However, the spatial selectivity of the technique is limited by lateral heat flow. For monolithic integration of optical devices, the limited spatial selectivity leads to poor performance as the interface abruptness is ~100 μm.

A new technique, which involves irradiating multiple quantum well (MQW) material with high energy laser pulses and producing transient heating in the crystal, is reported here and its application to both InGaAs/InGaAsP and GaAs/AlGaAs laser structures is demonstrated. In both material systems, disruption to the lattice resulting from rapid thermal expansion leads to a localised increase in the density of point defects. The absorption mechanism in the two materials varies slightly. The InGaAs/InGaAsP having a bandgap energy lower than the photon energy, allows the direct absorption of single photons whereas in the GaAs/AlGaAs system, where the bandgap is larger than the photon energy, and two photon absorption is to generates hot free carriers. The laser pulses are also absorbed by free carriers already present in the samples of both material systems, such absorption also contributing to the generation of heat within the samples. The point defects generated during the irradiation subsequently diffuse during a high temperature anneal, thereby enhancing the quantum well intermixing rate.

In the InGaAs/InGaAsP system, measurements of the spatial resolution of the process are presented, along with the transmission spectrum from a grating feature which has been realised in a waveguide by the direct-write technique. In the GaAs/AlGaAs system, bandgap-tuned lasers which have been fabricated from intermixed material are demonstrated.

EXPERIMENT

All samples were grown by metal organic vapour phase epitaxy. The InGaAs/InGaAsP samples took the form of a waveguide structure grown on an InP substrate; were undoped and lattice-matched throughout. The MQW layer consisted of five GaInAs wells separated by 120 Å GaInAsP barriers and was bounded by two graded index (GRIN) GaInAsP confining layers and capped with an InP cladding layer. The structure being essentially a laser structure without the doping and the contact layer. For the studies on GaAs/AlGaAs double quantum well (DQW) laser samples, a separate confinement heterostructure (SCH) structure was used. The DQW region was undoped and consisted of two 10 nm wide GaAs quantum wells, separated by a 10 nm $Al_{0.2}Ga_{0.8}As$ barrier. The top and bottom $Al_{0.2}Ga_{0.8}As$ barriers were 0.1 µm thick. The upper and lower cladding $Al_{0.4}Ga_{0.6}As$ layers were doped to 5×10^{17} cm^{-3} using carbon and silicon respectively and were 0.9 µm and 1.5 µm thick. The top contact epitaxial layer consisted of 0.1 µm of GaAs doped with 5×10^{18} cm^{-3} of zinc.

A Q-switched Nd:YAG laser, generating pulses ~ 20 ns long was employed with a repetition rate of 10 Hz. Samples were irradiated with the Q-switched laser, at room temperature and at normal incidence to the surface, with between 600 and 9000 pulses. The energy densities used were ~ 5 mJ mm^{-2} for the InGaAs/InGaAsP samples and 1.25 mJ mm^{-2} for the GaAs/AlGaAs samples. The energy densities were chosen so that the surface of the semiconductor did not exhibit visible damage, even after 10 min of exposure. The InGaAs/InGaAsP samples were capped with a 200 nm thick layer of SiO_2 during laser irradiation in order to prevent the desorption of the phosporus; some of the GaAs/AlGaAs samples were left uncapped in order to determine the effect of the cap on the intermixing. After irradiation, samples were annealed in a rapid thermal processor (RTP). The annealing temperatures and times were 700 °C and 180 s for the InGaAs/InGaAsP samples and 925 °C and 60 s for the GaAs/AlGaAs samples. The SiO_2 cap was left on the InGaAs/InGaAsP samples during annealing to prevent the desorption of P. Before annealing the GaAs/AlGaAs samples the SiO_2 capping layer, if present, was removed to avoid any IFVD effects. These samples were placed face down on a piece of fresh GaAs and another piece of GaAs was placed over the back to provide an As overpressure. Photoluminescence (PL) measurements performed at 77 K were carried out to study the bandgap shift after intermixing.

To measure the spatial resolution of the intermixing, material was irradiated for 20 minutes under the above conditions but, in this case, a portion of the sample was shielded from the laser with a metal mask suspended a few hundred microns above the surface. After annealing, the 77 K PL peak wavelengths were measured along a line perpendicular to the masked interface.

1:1 mark-space ratio gratings with period of 2.5 µm were defined using photography on the substrate side of a sample of the InGaAs/InGaAsP material. The sample was wet-etched using P_3HO_4:HCl to produce the grating as V-grooves on the substrate. The resist was removed and the samples were irradiated using the pulsed Nd:YAG laser at normal incidence to the

surface for 5 minutes. The grating on the surface generates a volume hologram within the sample, with a period half that of the surface grating, thus generating heat spikes in the quantum well layer with a spatial resolution of the order of 1 µm. After exposure to the laser, the samples were annealed using RTP at 700°C for 60 s. The transmission spectrum of a 5 mm long slab waveguide was measured.

Ridge waveguide lasers were fabricated from samples of the GaAs/AlGaAs structure, a pulsed-PAID intermixed sample, a control sample which had not been irradiated but had been annealed and an as-grown sample. The ridge was 3 µm wide and was dry-etched to a depth of 0.8 µm. The lasers were tested under pulsed current conditions at room temperature. Measurements of the light/current (L/I) characteristics and lasing spectra were performed.

RESULTS

In the InGaAs/InGaAsP material, shifts of up to 130 nm (80 meV) were measured (Fig. 1). It can be seen that most of the shift was produced after irradiation by as few as 300 pulses at the energy density used here. Irradiation by a larger number of pulses produced only slightly greater increases in the bandgap. Therefore, in order to limit the possibility of surface damage and the formation of extended defects which would inhibit intermixing, the number of pulses used in the process was kept to a minimum.

A measurement of the spatial resolution of the process is shown in Fig. 2. The plot shows the variation in the peak wavelength as a function of position across the interface in steps of 25 µm. It can be seen that there is a very sharp interface between the disordered and nondisordered areas which indicates that the spatial resolution is at least as good as 25 µm. Measurement of the ultimate resolution is limited by the probe size of the PL arrangement. The undulations in the plot may be evidence of edge diffraction of the laser beam at the mask interface, an effect which would be reduced by using gold reflective masks evaporated directly onto a silica coated surface.

Fig. 3 shows the resulting transmission spectrum from the sample which had been irradiated through the grating etched into the substrate. Also shown is a spectrum measured from an unirradiated sample which had been annealed in the RTP at the same time. Two features are apparent: firstly, the absorption edge has shifted to shorter wavelength in the grating sample as a result of exposure to the Q-switched laser pulses, indicating that a certain amount of intermixing has taken place throughout the area where the grating has been defined. Secondly, there is a clear
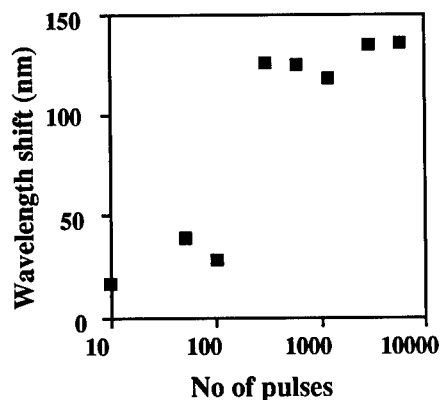
Fig. 1   Shift in peak PL wavelength after irradiation and annealing as a function of the number of laser pulses.
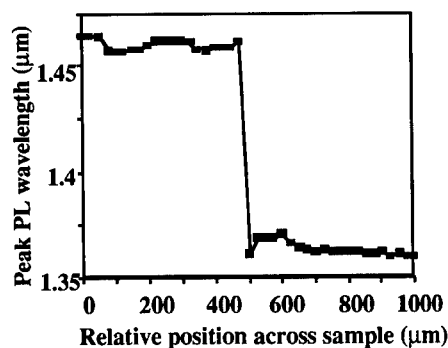
Fig. 2   Spatially resolved PL across and interface between intermixed and nonintermixed areas of a sample.
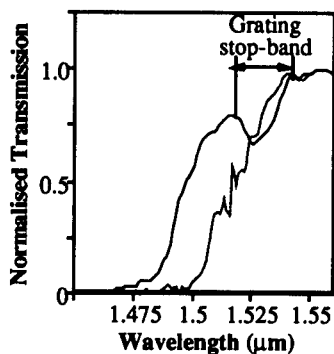
Fig. 3: Transmission spectra through slab waveguide samples without a grating (dotted) and with a grating (solid line).

transmission dip around 1.525 μm. The feature is relatively broad for several reasons—the grating itself is weak because there are only 5 QWs in the waveguide and so the refractive index difference between the intermixed and nonintermixed regions of the grating is small, a slab waveguide sample was assessed which would allow a range of incident angles on the grating leading to Bragg reflection over a range of wavelengths, and the grating period will not be completely constant because of undulations in the surface on the substrate side of the sample. The presence of the transmission dip does, however, provide evidence that a grating has been formed within the waveguide.

Figure 4(a) shows the bandgap energy shift as a function of laser exposure time. It can be seen that a differential bandgap shift of up to 40 meV has been obtained. Samples exposed to a large numbers of pulses (6000, 10 min irradiation time) seem to exhibit less intermixing. A similar effect has been observed using B implantation, where it was found that increasing the dose above an optimum value led to smaller bandgap shifts. Transmission electron microscope (TEM) studies showed that the point defects, at the higher doses, coalesced to form extended defects such as dislocation loops [9]. Such extended defects are stable and trap point defects, so inhibiting the interdiffusion of Ga and Al.

The blue shift in wavelength as a function of annealing temperature was also investigated. DQW samples, both with and without the protection of a SiO_2 layer during laser irradiation, were subjected to laser exposure for 2 min (1200 pulses) and annealed at temperatures in the range 850 to 925°C for 60 s. As-grown samples without laser exposure were also included to act as control samples. The results are shown in Figure 4(b), where it can be seen that the samples which had a bare surface during irradiation show larger degrees of intermixing than those protected with a SiO_2 layer. Laser irradiation creates point defects by generating a hot carrier plasma which then emits a sufficiently high concentration of phonons that the crystal structure is disrupted[10]. The Nd:YAG laser emits at a wavelength of 1.06 μm, so the photon energy is below that of the bandgap of any part of the GaAs/AlGaAs structure. The hot carrier plasma, therefore, is created

Fig. 4 (a) Bandgap energy shift of samples subjected to various number of pulses. Samples were annealed at 925°C for 60s. (b) Bandgap shift of the as-grown, bare surface and SiO_2 capped (during laser irradiation) samples as a function of RTP temperature. Samples were exposed to the laser for 2 min annealed for 60 s.

by free carrier absorption due to carriers produced by the grown-in dopants and, given that the pulse intensity is around 6.25×10^{10} W m^{-2}, by two photon absorption[11] followed by free carrier absorption. For the samples with SiO_2 caps, the absorption of photons and, hence, the creation of point defects is expected to be approximately uniform throughout the semiconductor.

Analysis of the dependence of the QWI rate on laser intensity suggests that between 3 and 5 photons are involved in creating a point defect. In the case of the uncapped samples, the laser pulse was directly incident on the surface of the semiconductor. The laser pulse possesses a high enough peak intensity and energy density to break the bonds between atoms of the semiconductor, ablating the surface atoms and creating point defects at the surface. These point defects could subsequently diffuse and induce QWI during annealing at high temperature. It is therefore suggested that the combined effect of laser ablation and multiphoton absorption is responsible for QWI in the uncapped samples.

The L/I characteristics of 1 mm long lasers, together with lasing spectra, from the as-grown, the control and the intermixed samples are given in Figure 5(a) and 5(b). The lasing spectra were recorded at a current of about 1.5 times the threshold current of the lasers.

It can be seen in Figure 5(a) that the threshold current of the intermixed lasers increased by about 15%, however the processed control laser also exhibit a similar increase. Any change in the slope efficiency of the intermixed lasers compared to the as-grown devices was found to be insignificant. The small increase in the threshold current of the intermixed lasers is probably related to depletion of As, since the samples were only proximity capped during annealing. This shortcoming could be overcome by using a dielectric cap during the RTP stage. (No dielectric cap was used in this experiment to eliminate IFVD effects). The control sample was found to have shifted by about 10 nm relative to the as-grown laser (Fig. 5(b)). This wavelength shift is undesirable and can also be prevented if an intermixing mask such as SrF_2 or P-doped SiO_2 is used [1, 12]. In short, the lasers intermixed using the pulsed-PAID process are still of high quality.

CONCLUSION

In conclusion, pulsed PAID, an intermixing process using light from a Q-switched Nd:YAG laser, has been developed. The technique has been used to produce shifts of over 100 nm (60 meV) in GaInAs/GaInAsP quantum well structures and spatially selective
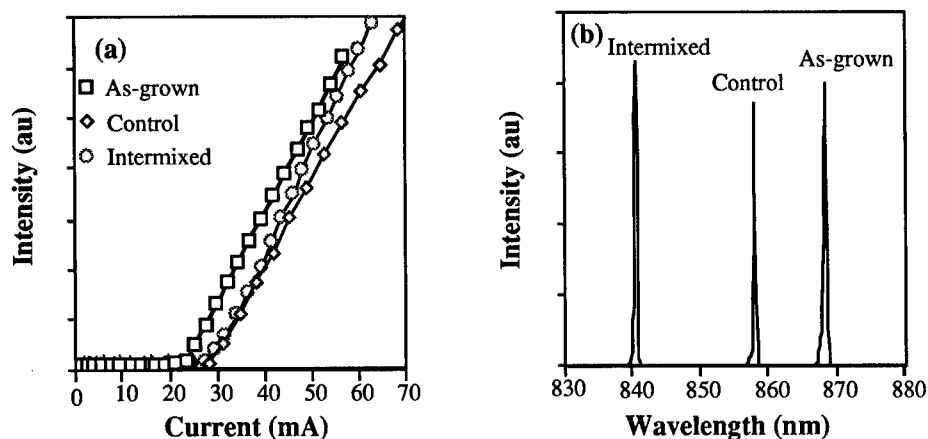
Fig. 5 (a) The light/current characteristics and (b) the lasing spectra from 3 μm wide stripe lasers fabricated from the as-grown, control (RTP, without laser exposure) and the pulse-PAID intermixed samples.

intermixing with a resolution better than 25 μm has been demonstrated. The process has also been used to define a grating within a slab waveguide after epitaxial growth. The period of the grating is 1.25 μm, demonstrating that the pulsed PAID process can be used to define features of less than 1 μm.

The process has also been demonstrated to induce QWI in GaAs/AlGaAs structures, producing differential bandgap shifts of up to 40 meV. Bandgap tuned lasers have been fabricated, confirming that processed material is of high electrical and optical quality.

ACKNOWLEDGEMENTS

REFERENCES

1.   A. Rys, Y. Shieh, A. Compaan,. H. Yao and A. Bhat, Optical. Eng., 29, pp. 329-338 (1990).

2.   J. Ralston, A.L. Moretti, R.K. Jain and F.A. Chambers, Appl. Phys. Lett., 50, pp. 1817-1819 (1987).

3.   J.E. Epler, R.D. Burnham, R.L. Thornton, T.L. Paoli and M.C. Bashaw, Appl. Phys. Lett., 49, pp. 1447-1149 (1986).

4.   K. Brunner, G. Absreiter, M. Walther, G. Böhm and G. Tränkle, Surface Science, 267, pp. 218-222 (1992).

5.   J.H. Marsh and A.C. Bryce, Material Science and Engineering, B24, pp. 272-281, (1994)

6.   C.J. McLean, J.H. Marsh, R.M. De La Rue, A.C. Bryce, B. Garrett and R.W. Glew, Electron. Lett., 28, pp. 1117-1119 (1992)

7.   A. McKee, C.J. McLean, A.C. Bryce, R.M. De La Rue and J.H. Marsh, Appl. Phys. Lett., 65, pp. 2263-2265 (1994).

8.   G. Lullo, A. McKee, C.J. McLean, A.C. Bryce, C.C. Button, and J.H. Marsh, Electron. Lett., 30, pp. 1623-1625 (1994).

9.   B.S. Ooi, A.C. Bryce, J.H. Marsh and J. Martin, Appl Phys Lett , 65, pp. 85-87 (1994).

10.   R.M. Wood, Laser Damage in Optical Materials, IOP Publishing, 1986, Bristol, UK., pp. 1-41.

11.   F.R. Laughton, J.H. Marsh and J.S. Roberts, Appl. Phys. Lett., 60, pp. 166-8 (1992)

12.   P. Cusumano, B.S. Ooi, A. Saher Helmy, S.G. Ayling, B. Vögelle, A.C. Bryce, J.H. Marsh and M.J. Rose, accepted by J. Appl. Phys.

IMPURITY FREE VACANCY DISORDERING USING PHOSPHORUS DOPED SiO$_2$ AND PURE SiO$_2$ CAPS

P. CUSUMANO*, A. SAHER HELMY, B. S. OOI, R. M. DE LA RUE, A. C. BRYCE,
J. H. MARSH,
Department of Electronics and Electrical Engineering, University of Glasgow,
Glasgow G12 8QQ, Scotland, U K, E-mail:cusumano@elec.gla.ac.uk

*on leave from: Dipartimento di Ingegneria Elettrica, Università degli Studi di Palermo,
Viale delle Scienze, I-90128 Palermo, Italy

ABSTRACT

A spatially selective quantum well intermixing process, using phosphorus-doped silica (SiO$_2$:P) containing 5 wt% P to inhibit intermixing and pure SiO$_2$ to enhance intermixing, is presented. The SiO$_2$:P cap has been found to suppress bandgap shifts in both *p-i-n* and *n-i-p* GaAs/AlGaAs quantum well laser structures, with bandgap shift differences as large as 100 meV observed from samples capped with SiO$_2$ and with SiO$_2$:P after rapid thermal processing at temperatures as high as 950 °C for 60 s. Extended cavity ridge lasers exhibited low threshold currents with TE losses of 3.2 cm^{-1} measured in the passive waveguide sections at the lasing wavelength using the Fabry-Perot resonance method. This value is among the lowest reported so far using an impurity-free disordering technique.

INTRODUCTION

The impurity-free vacancy disordering (IFVD) [1] of GaAs/AlGaAs quantum well (QW) laser structures using SiO$_2$ capping and rapid thermal annealing (RTA) is based on the fast out-diffusion of Ga atoms into the cap layer creating group III vacancies. The diffusion of these vacancies toward the QW active layer, during the annealing step, promote Al-Ga exchange between barriers and wells leading to QW shape modification from abrupt to gradual with a subsequent energy increase of the quantized levels. As arsenic desorption from GaAs surface layers takes place at annealing temperatures around 700 °C [2], the use of a dielectric mask is crucial for preserving the surface quality of the samples and, more important, for achieving selective intermixing across a wafer during the annealing step.

While SrF$_2$ [3], [4] is an effective mask for QW intermixing suppression, our experience is that, due to thermal stress on the GaAs surface, damage and cracks are induced when the annealing temperature is higher than 930 °C, limiting the maximum degree of selective intermixing achievable. High purity Si$_3$N$_4$ films, deposited by plasma enhanced chemical vapour deposition (PECVD), have also been reported [5] as dielectric masks but they are difficult to deposit reproducibly because of the systematic incorporation of O$_2$, resulting in SiO$_x$N$_y$ which, however, can be an effective cap for inducing Ga out-diffusion [6]. A surface passivation technique using a hydrogen plasma has recently been demonstrated [7] as an effective mask for QW intermixing suppression in undoped structures. The main limitation of this technique is that it is only effective at relatively low temperatures (900 °C), and the possibility of transferring it to the more common *p-i-n* doped laser structures used in optoelectronics is still under investigation.

Recently, Rao et al. [8] reported the use of SiO$_2$ doped with phosphorus (SiO$_2$:P) as a 'universal' intermixing source for III-V compounds. SiO$_2$:P with only 1% by weight of P [9] was used to induce intermixing in nominally undoped GaAs/AlGaAs shallow multiple QW structures by furnace annealing at a temperature of 850 °C and no masking dielectric cap was used to prevent intermixing or for surface protection during annealing.

As the amount of P incorporated into SiO$_2$ increases, the thermal expansion coefficient increases [10] and a decrease in the glass softening temperature [11] takes place. Moreover the built-in stress of PECVD SiO$_2$:P films is reduced as the P doping concentration increases and the

419

films become more dense and void-free compared with undoped SiO_2 [10]. Thus, by choosing an increasing amount of P doping, SiO_2:P films can be tailored to be less permeable to Ga atoms. In this paper, we demonstrate that SiO_2 doped with 5% wt P can be used effectively to suppress the out-diffusion of Ga, and hence can selectively mask intermixing, in p-i-n and n-i-p GaAs/AlGaAs double QW laser structures. Encapsulants with a higher P content were not considered due to their increasingly hygroscopic nature [10], affecting the IFVD process reliability. Large differential shifts between regions masked with SiO_2 and SiO_2:P have been observed with excellent surface morphology and a high degree of reproducibility. Results from CW operated extended cavity ridge lasers are presented and the influence of the losses in the passive sections on threshold current and slope efficiency is addressed. TE losses in the transparent integrated waveguides at the lasing wavelength are as low as 3.2 cm^{-1} for a differential shift of 30 nm obtained by IFVD.

EXPERIMENT

Two wafers having a similar, separate-confinement heterostructure configuration were grown by molecular beam epitaxy in the form of p-i-n and n-i-p double QW laser structures. The p-i-n wafer consisted of a 0.5 µm GaAs buffer layer grown on a Si doped n-type GaAs substrate. The double QW region was undoped and consisted of two 10 nm wide GaAs quantum wells, separated by a 10 nm $Al_{0.2}Ga_{0.8}As$ barrier. The top and bottom $Al_{0.2}Ga_{0.8}As$ barriers were 0.1 µm thick. Both the upper and lower cladding $Al_{0.4}Ga_{0.6}As$ layers were 1.5 µm thick and doped at a concentration of 5×10^{17} cm^{-3} using Be and Si respectively. The top contact layer consisted of 0.1 µm of GaAs doped with 5×10^{18} cm^{-3} of Be. The structure of the n-i-p wafer was similar to that of the p-i-n, apart from the fact that a semi-insulating GaAs substrate was used and the growth sequence was inverted.

Dielectric films of SiO_2:P and SiO_2, about 200 nm thick, were deposited at a temperature of 330 °C using a conventional PECVD apparatus equipped with a separate PH_3 flow line for P doping. The P content was measured by energy dispersive X-ray (EDX) spectroscopy, giving an estimated value of 5% by weight, with a 1:2 atomic concentration ratio between Si and O. After deposition of the oxides, the samples were cleaved into squares of area 2×2 mm^2 and rapid thermal annealed for 60 s in flowing N_2 at temperatures between 800°C and 950°C. Uncapped samples were annealed at the same time to study the thermal stability of the wafer. Samples were sandwiched face-down between two pieces of fresh GaAs to provide proximity capping during annealing. The 77 K photoluminescence (PL) spectrum of the annealed samples was measured to assess the degree of intermixing.

RESULTS

The blue wavelength shifts in the 77 K PL peak, as compared with the as-grown material, plotted versus the anneal temperature for the p-i-n and n-i-p structures are shown in Figures 1 (a) and (b) respectively. It can be seen from these figures that SiO_2:P acts as a very effective mask for preventing Ga out-diffusion, limiting the bandgap widening to no more than 5 nm for both n-i-p and p-i-n samples at temperatures up to 950 °C. Moreover, no surface damage was produced by this dielectric cap under the annealing conditions studied here. In contrast, the blue shifts for both p-i-n and n-i-p samples capped with SiO_2 increase with temperature and are always greater than those for uncapped samples, demonstrating the enhanced disordering promoted by SiO_2 capping as compared with uncapped samples.

To further validate our experiments, the SiO_2:P film was partially removed from p-i-n double QW laser samples, cleaved from a wafer grown by metalorganic chemical vapor deposition (MOCVD), using optical lithography and wet etching in buffered HF solution, and the samples were capped with 200 nm of SiO_2 and rapid thermal annealed under the conditions described above. Figure 2 (a) shows the PL shift versus the annealing temperature and again the masking properties of the SiO_2:P film are quite evident.
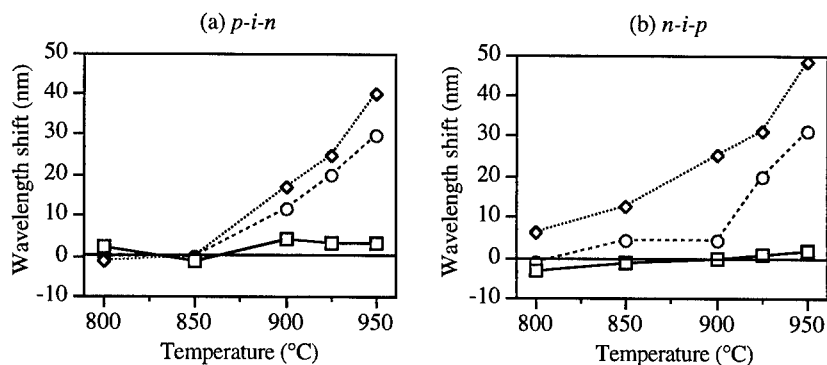
Fig. 1. Wavelength shifts of the 77 K PL peak for SiO₂:P capped (—□—),
SiO₂ capped (⋯◇⋯) and uncapped (⋯○⋯) (a) *p-i-n* and (b) *n-i-p* samples
as a function of annealing temperature with a duration of 60 s.

It can be witnessed here that differential bandgap shifts larger than 40 nm can be obtained easily in samples partially masked with SiO_2:P and capped with SiO_2, with excellent surface morphology, in particular at the edge interface between SiO_2:P and SiO_2. To demonstrate the use of this new masking technique for fabrication of integrated devices, extended cavity ridge (3 µm wide, 0.7 µm deep) lasers were fabricated on *p-i-n* MOCVD samples with a differential shift of 30 nm after RTA at 940 °C for 60 s (Fig. 2 (b)).

Light/current curves and related spectra, in CW operation at T=20 °C, for a solitary 400 µm long laser and for an integrated device with 400 µm/2.73 mm long active/passive sections, reflecting the typical behaviour of the fabricated devices, are shown in Fig. 3. The extended cavity lasers showed equal power output levels from both active and passive ends, with emission wavelengths between 853 and 855 nm. As shown in Fig. 3, due to the losses introduced by the integrated waveguide, the threshold current increases by 14%, from 7 mA for the solitary laser to 8 mA for the extended cavity laser, and the slope efficiency decreases by 40%, from 0.32 W/A per facet to 0.19 W/A per facet. We directly measured the losses in the passive waveguides cleaved from the same sample, as a function of the wavelength and for TE polarization, using the Fabry-Perot resonance method [11] and the results are shown in Fig. 4. The losses exhibit a broad minimum of about 3 cm⁻¹ around the lasing wavelength of 855 nm, increasing for both
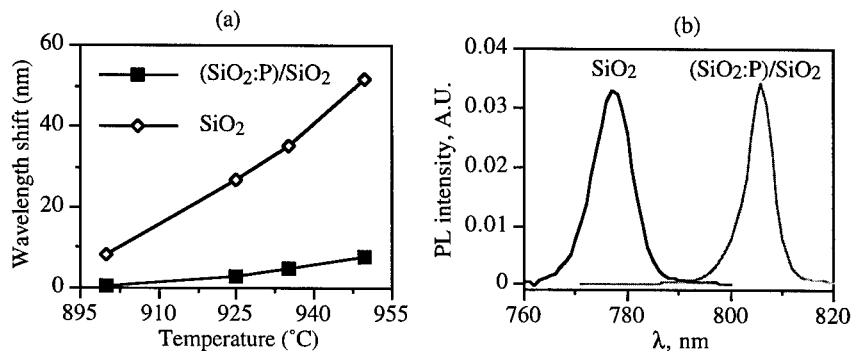
Fig. 2. (a) PL wavelength shift versus temperature of rapid thermal annealing for 60 s in *p-i-n* MOCVD samples containing both masked and intermixed regions and (b) PL spectra for sample used for extended cavity laser fabrication (RTA @ 940 °C for 60 s).

longer and shorter wavelengths due to free carrier absorption in the doped cladding layers and resonant absorption in the partially intermixed QW, respectively.

Assuming a logarithmic dependence of the gain on the current density [13], from the balance between gain and losses at threshold the following formulae are obtained:

$$\frac{I_{ex}}{I_{nor}} = \exp\left(\frac{\alpha_p L_p}{n\Gamma g_0 L_a}\right)$$
(1)

$$\frac{\eta_{ex}}{\eta_{nor}} = \frac{g_{nor}^{th}}{g_{ex}^{th}} = \frac{\alpha_a + \dfrac{1}{L_a}\ln\dfrac{1}{R}}{\alpha_a + \dfrac{1}{L_a}\ln\dfrac{1}{R} + \alpha_p\dfrac{L_p}{L_a}}$$
(2)

where α_a, L_a and α_p, L_p are the losses and length, respectively, of the active and passive section, Γ is the optical overlap factor and g_0 the gain constant per well, and n the number of wells. In deriving (1) and (2), coupling losses between the active and passive waveguide have been assumed to be zero because no mode mismatch due to refractive index change is introduced by the IFVD process. From (2), assuming a modal reflectivity R of 0.32, we calculate the losses α_a in the active section to be 3.4 cm-1, in good agreement with the value of 3 cm-1 obtained from broad area lasers fabricated in the as-grown material. The mirror losses are 28.5 cm-1 and the losses $\alpha_a(L_p/L_a)$ introduced by the integrated waveguide amount to 22 cm-1 due to the high ratio L_p/L_a of 6.8. This explains the 40% decrease in slope efficiency. Due to the high quality material and the logarithmic gain current density relation in quantum wells, leading to higher differential optical gain as compared with bulk material, the threshold gain in the extended cavity lasers is attained with only a 14% increase in threshold current.
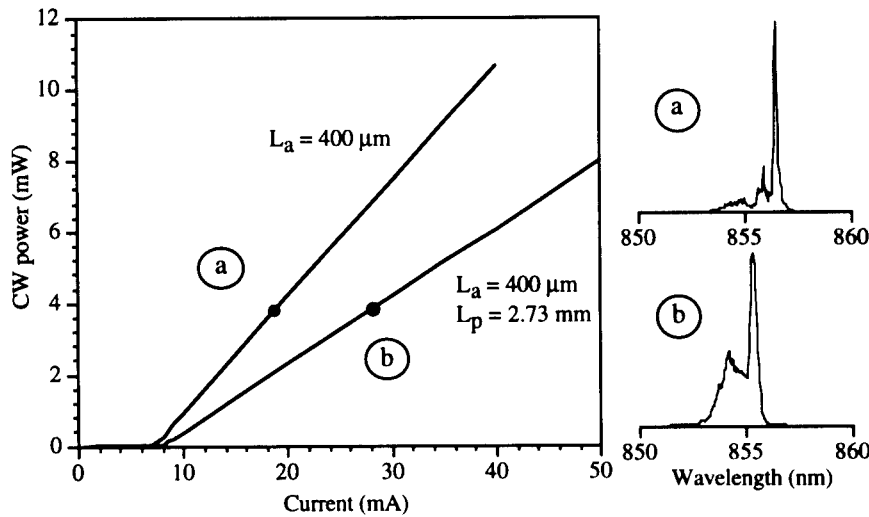
Fig. 3. Light-current curves and spectra of (a) normal and (b) extended cavity ridge lasers.
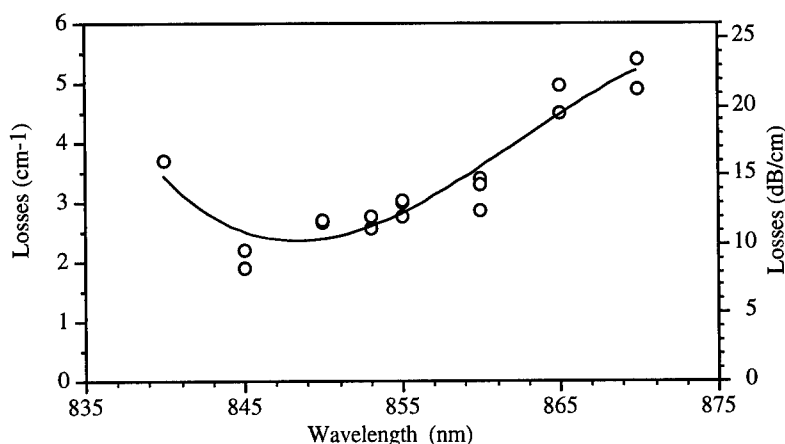
Fig. 4. TE polarization losses versus wavelength in the integrated ridge waveguides.

CONCLUSIONS

There are at least two possible explanations for the masking properties of SiO_2:P films with high P content. Beside the fact that PECVD SiO_2:P films are more dense and void-free than SiO_2 [10] and, as such, they have a better masking behaviour against Ga out-diffusion [14], strain at the interface between GaAs and dielectric films used as capping material can also play an important role during the IFVD process. The thermal expansion coefficient of GaAs is about ten times larger than SiO_2 and, as a consequence, the SiO_2 film is under tensile strain and the GaAs surface layer is under compressive strain. Under these conditions, because of the high diffusion coefficient of Ga in SiO_2, the out-diffusion of Ga atoms into the SiO_2 film is an energetically favourable process because it minimises the strain in the system. The addition of P into the SiO_2 film leads to an increase in the thermal expansion coefficient [10] and a decrease in the glass softening temperature [11]. Therefore, less compressive strain will be induced during the annealing step in the GaAs surface layer and, as a result, the number of Ga vacancies will be reduced due to reduced Ga out-diffusion.

It can be seen from Fig 1 (a) and (b) that p-i-n and n-i-p wafers have similar degrees of intrinsic thermal stability since the uncapped samples from these wafers shifted to about the same wavelength under similar annealing conditions. Comparing Fig 1 (a) and (b) shows that SiO_2 capped n-i-p samples exhibited larger degrees of QW intermixing than the p-i-n samples. This result may be due to the rise in energy of the crystal Fermi level [15] in n-type material, leading to a reduction in the formation energy of group III vacancies and, hence, to a larger equilibrium Ga vacancy concentration in n-type material than in p-type material From the point of view of photonic devices integration, the above results suggest that the growth of n-i-p structures would give a higher degree of intermixing than the conventional p-i-n structures typically used in QW intermixing processes.

The losses achieved in the integrated passive waveguides at the lasing wavelength are about the same as those in the active sections, indicating little band-edge absorption in the partially intermixed QW, which basically exhibits a transparency behaviour, but with no current injection. Transparency could be also achieved by current injection in a non-intermixed QW but this, for long integrated devices, requires a second contact, electrically insulated from the active region, and the subsequent increase in the total injected current is not always compatible with CW operation. Losses in the integrated waveguides are limited mainly by p-type free carrier absorption, with a possible contribution from acceptor-like Ga vacancies [16] that have diffused into the active region. A simple way to reduce the losses would be by tailoring the doping

profiles together with the structural parameters of the laser structure [17]. Although no systematic lifetime measurements were performed, we could not see any degradation of laser performance during the measurements, an indication that the optical and electronic properties of the laser material are still of sufficiently high quality after the selective IFVD process. This technique is being currently used for the fabrication of a range of integrated devices including mode-locked laser diodes and optical space switches comprising passive 3 dB couplers and laser diode amplifiers operating as optical gates.

ACNOWLEDGEMENTS

REFERENCES

[1] D. G. Deppe, L. J. Guido, N. Holonyak Jr., K. C. Hsieh, R. D. Burnham, R. L. Thornton and T. L. Paoli, Appl. Phys. Lett. 49, 510 (1986).

[2] T. E. Haynes, W. K. Chu and S. T. Picraux, Appl. Phys. Lett. 50, 1071 (1987).

[3] J. Beauvais, J. H. Marsh, A. H. Kean, A. C. Bryce and C. Button, Electron. Lett. 28, 1670 (1992).

[4] H. H. Yee, S. Ayling, R. M. De La Rue, B. Vogele and Y. P. Song, IEE Proc. Optoelectron. 143, 94 (1996).

[5] L. J. Guido, K. C. Hsieh, N. Holonyak Jr., R. W. Kaliski, V. Eu, M. Feng and R. D. Burnham, J. Appl. Phys. 61, 1329 (1987).

[6] M. Kuzuhara, T. Nozaki and T. Kamejima, J. Appl. Phys. 66, 5833 (1989).

[7] C. J. Hamilton, S. E. Hicks, B. Vogele, J. H. Marsh and J .S. Aitchison, Electron. Lett. 31, 1393 (1995).

[8] E. V. K. Rao, A. Hamoudi, Ph. Krauz, M. Juhel and H. Thibierge, Appl. Phys. Lett. 66, 472 (1995).

[9] E. V. K. Rao (private communication).

[10] S. K. Ghandhi, VLSI fabrication principles, 2nd ed. (John Wiley & Sons, New York, 1994), pp. 530-532 and references therein.

[11] T. Y. Tien and F. A. Hummel, J. Am. Ceram. Soc. 45, 422 (1962).

[12] R. G. Walker, Electron. Lett. 21, 581 (1985).

[13] P. W. A. McIlroy, A. Kurobe and Y. Uematsu, IEEE J. Quantum Electron. QE-21, 1958 (1985).

[14] S. Singh, F. Baiocchi, A. D. Butherus, W. H. Grodkiewicz, B. Schwartz, L. G. Van Uitert, L. Yesis and G. J. Zydzik, J. Appl. Phys. 64, 4194 (1988).

[15] D. G. Deppe and N. Holonyak Jr., J. Appl. Phys. 64, R93 (1988).

[16] S. O'Brien, J. R. Shealy, F. A. Chambers and G. Devane, J. Appl. Phys. 71, 1067 (1992)

[17] R. G. Waters, D. S. Hill and S. L. Yellen, Appl. Phys. Lett. 52, 2017 (1988)

THE CONFINEMENT PROFILE OF AS-GROWN MOVPE AlGaAs/GaAs QUANTUM WELL STRUCTURES

W.C.H. CHOY, P.J. HUGHES, B.L. WEISS
Department of Electronic and Electrical Engineering, University of Surrey, Guildford, Surrey, GU2 5XH, UK

ABSTRACT

Interband transitions of a series of as-grown AlGaAs/GaAs quantum well structures grown by MOVPE have been studied using photoreflectance to determine their well shape. The transition energies calculated using three different quantum well profiles are compared to those obtained using photoreflectance. The results show that the shape of these structures is best represented by an exponential potential profile.

INTRODUCTION

The ability to determine the compositional/confinement profile of quantum well (QW) structures is important since it is this profile that determines their optical properties. In general, QWs structures are ideally grown to give rectangular profiles, where the composition changes abruptly at the well/barrier interfaces, which is known to occur in practical QW structures.

In this paper, the effects of compositional grading on a series of MOVPE grown AlGaAs/GaAs QW structures is investigated using photoreflectance (PR). Photoreflectance is used here since this technique can determine all the interband transition energies in QW structures which are determined by the QW confinement profile. A previous report of these structures based on a rectangular shape profile model, showed that the higher order transitions corresponded to wider as-grown well widths than those determined by the ground-states [1]. This suggested that the change in the Al composition at the interfaces of these QWs was not abrupt but somehow graded. To investigate these results further, trapezoidal and exponential compositional/confinement grading profiles were studied here. The first was a linearly graded trapezoidal profiles at both interfaces while the second had exponentially graded profiles at both interfaces, both being symmetric about the well center.

EXPERIMENT

The samples studied here form part of a continuing investigation into their properties [1]. They were grown by MOVPE at Sheffield University and consist of four single QWs, clad by 1000 Å $Al_xGa_{1-x}As$/GaAs barrier layers. Two samples have barrier compositions (x) of 0.2 and the other two other have x = 0.3. Each pair of samples have nominal GaAs well thicknesses (L_z) of 50 Å and 100 Å. For reference, these structures are referred to by the notation (x/L_z), i.e. 0.3/50, 0.3/100, 0.2/50 0.2/100.

The PR system used here is the standard arrangement and is described elsewhere [2]. The PR spectrum of each sample was measured at 300 K and is shown in Figure 1. The transition energies were determined using a lineshape fitting model based on Aspnes third derivative functional forms (TDFF) [3]. The model also incorporated an oscillatory term which was characteristic of Franz-Keldysh oscillations (FKO) [4] associated with an inherent built-in electric field in all of these samples [2].

425
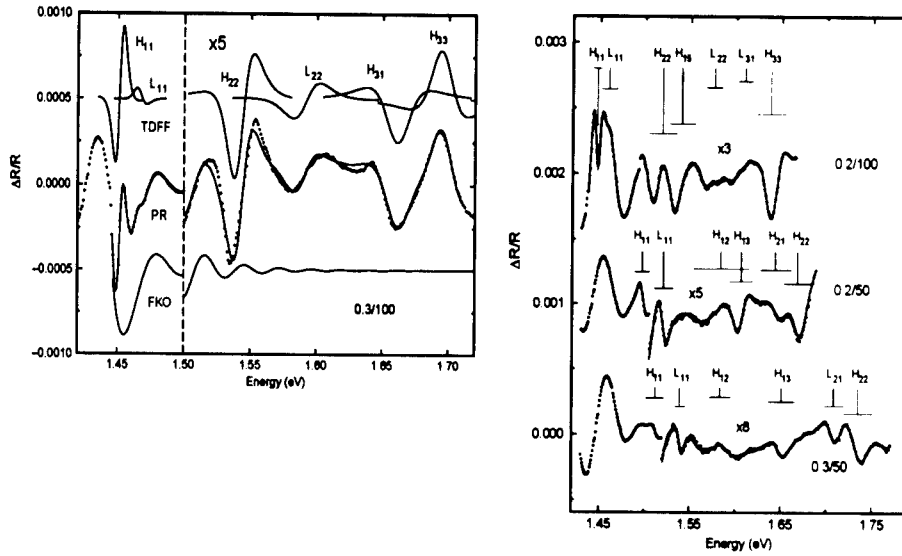
Figure 1. The PR fit to and spectrum of structure 0.3/100 showing profiles of the FKO and TDFF components and of structures 0.3/50, 0.2/50 and 0.2/100. The baselines have been shifted vertically from each other for clarity. The energy positions of the TDFF components are shown by vertical lines, the length of which represents the intensity of the TDFF. The horizontal lines represent the half-width-half maxima of the TDFFs.

MODEL

The theoretical model developed by Li et al [5] was used to identify the QW transitions which were determined from the fitting analysis of the PR spectra. A summary of these revised results is presented in Figure 1 where transitions from electron (m) to heavy- and light-hole (n) are referred to here by the notation H_{mn} and L_{mn} respectively.

The material parameters, including band offset, carrier effective masses, bandgap and binding energies are similar to those used previously [1] except for heavy hole effective mass (m_H) which is given by [6]:

$$m^\Gamma_H(x) = (0.50 + 0.2x)m_o \tag{1}$$

In addition, the bandgap energy (E_g in eV) for $Al_xGa_{1-x}As$ is given by [7]:

$$E_g(x) = 1.424 + 1.594 + x(1-x)(0.127-1.31x) \tag{2}$$

The trapezoidal profile and exponential profile are symmetric. Consequently, the profiles of these structures with a center point at z = 0 are defined as follows.

Trapezoidal profile:

$$x = 0, \quad 0 \leq z \leq |\tfrac{1}{2}L_z^{bottom}| \tag{3a}$$

$$x = x_0(z - L_z^{bottom}/2)/(L_z^{top}/2 - L_z^{bottom}/2), \quad |\tfrac{1}{2}L_z^{bottom}| < z \leq |\tfrac{1}{2}L_z^{top}| \tag{3b}$$

$$x = x_0, \quad z \geq |\tfrac{1}{2}L_z^{top}| \tag{3c}$$

Exponential profile:

$$x = x_0 \exp[-\beta/(z^2 - (L_z^{bottom}/2)^2], \quad |z| \geq 0 \tag{4}$$

where β is the curvature parameter, L_z^{bottom} and L_z^{top} are the widths of the bottom and top of the well respectively, z and x_0 are the growth direction and the Al concentration in the barrier layers. In the trapezoidal well, the potential is graded linearly at the well/barrier interface between L_z^{bottom} and L_z^{top}. The energy states for this profile is dependent upon the gradient of the interface which is a function of the difference between L_z^{bottom} and L_z^{top}. The exponential profile is defined by the curvature parameter β, so that a large value of β corresponds to a steep exponential profile.

RESULTS AND DISCUSSION

Our previous investigation of these structures showed that the fit between the experimental and model transition energies implied that the value of L_z determined from the higher order transitions was greater than the value of L_z determined for the ground-states by ~10 Å. In this paper, the values of L_z have been determined as a function of transition energy for structure 0.3/100, see Figure 2. From the graph, it is seen that the calculated transition energies agree with the experimental results for values of L_z, which show increases as the order of the transition increases. The trapezoidal and exponential QW profiles were therefore studied to achieve an improved fit between the experimental and modelling results. Both of these profiles produce graded interfaces, where the Al composition (x) varies along the z direction.

To demonstrate the effects of these different potential profiles, the deviation between the experimental and theoretical transition energies for these structures are shown in Table 1, for the rectangular, trapezoidal and exponential profiles; where L_z^{bottom} = 100 Å (wider wells) and L_z^{bottom} = 45 Å (narrow wells) using a band offset of 65:35.

In each case the values of L_z and the profile parameters were optimized for the best fit between the calculated and measured transition energies. For all structures, the difference between the measured and calculated transition energies for the rectangular profiles are large, especially for the higher order transitions. In the case of structure 0.3/100, this deviation is reduced to an acceptable level ($\pm$2 meV) for the ground state transitions of the trapezoidal profile, where L_z^{top} = 124 Å. However, for the higher order transitions the deviation is still large and positive. This suggests that the gradient of the interface should be decreased, (i.e. an increased L_z^{top}). However, we found that increasing L_z^{top} resulted in an unacceptable difference in the ground state transitions. In contrast, the exponential profile with β = 3.5 shows that the deviation is further reduced for the higher order transitions. This is explained by the fact that this profile produces a larger effective well width in the upper half of the well thus enabling the energy states, and therefore the deviation, to be reduced. This effect is shown in Figure 3, where the conduction and valence band confinement energy profiles as a function of L_z are plotted. The

energy decrease of the electron (m = 3) state is the largest for the exponential profile in comparison to the trapezoidal profile. This decrease is not as pronounced for the heavy- and light-hole states which suggests that any variation in the transition energy is dominated by changes in the conduction band.
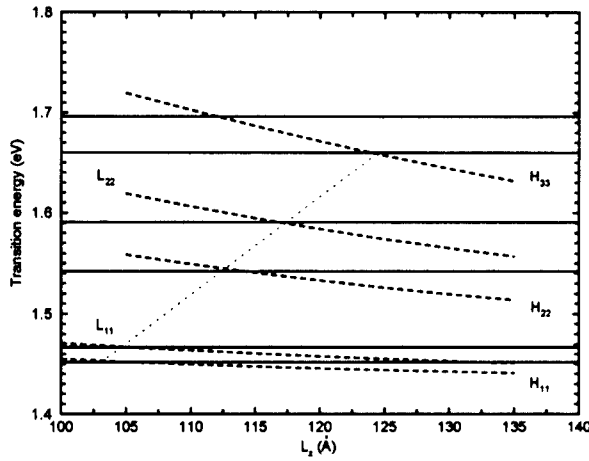
Figure 2. Comparisons between the calculated transition energies (dashed line) of the rectangular QW for different well widths and that of the experimental transition energies (solid line) for structure 0.3/100. The dotted line shows the trend of the intersection between the experimental and modelled transition energies.
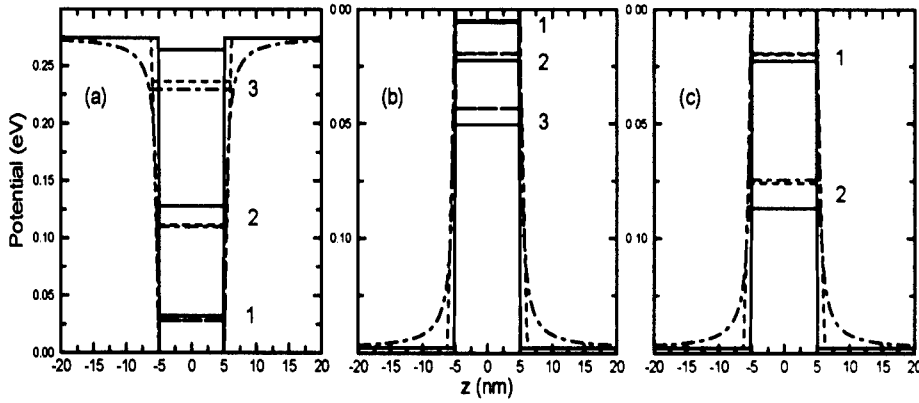
Figure 3. The potential profile and confined energy states of calculated rectangular (solid line), trapezoidal (dashed line) and exponential (dot-dashed) QWs of structures 0.3/100 for (a) conduction band, (b) valence band - heavy-hole, (c) valence band - light-hole.

428

The same behavior is found in the other three structures, see Table 1. For structure 0.2/100, a good match is obtained using the exponential profile for $\beta = 5$. For the narrow well structures the average differences are larger but are considered acceptable since the QW subband energies are more sensitive to material parameters, particularly L_z. The values of β used here are 0.9 and 1.2 for 0.3/50 and 0.2/50 respectively. The values of β are smaller for the narrower well structures because the energy states are more sensitive to the confinement profile. However, the difference in β between the narrow and wider well structures is insignificant in the model. This suggests that the growth profile, which we consider to be exponential, is consistent from one structure to another.

The effect of changing the band offset ratio to 70:30 was also considered. In general, it resulted in an increase in the average deviation for the higher order transitions, particularly for the narrow well structures. However, these results do not provide any conclusive evidence for the value of Q_c.

In both narrow well structures a number of PR features were observed which were identified as "forbidden" transitions in the QW [1]. The presence of these features is attributed to the non-rectangular profile of these QW structures since it is known that the selection rules are relaxed for non-rectangular profiles. The deviation of these "forbidden" transitions is also larger than those of the allowed transitions, see Table 1.

Table 1. List of the difference between the experimental and the theoretical transition energies for the rectangular QW (RQW), trapezoidal (TRAP) and the exponential (EXP).

Sample	Difference of Transition (meV)						
0.3/100	H_{11}	L_{11}	H_{22}	L_{22}	H_{31}	H_{33}	-
RQW, $L_z = 100$ Å	+3	+5	+27	+42	+31	+41	-
TRAP, $L_z^{bottom} = 100$ Å, $L_z^{top} = 124$ Å	-2	-2	+9	+15	+2	+7	-
EXP, $L_z = 100$ Å, $\beta = 3.5$	-2	-2	+7	+12	+3	0	-
0.2/100	H_{11}	L_{11}	H_{22}	H_{15}	L_{22}	L_{31}	H_{33}
RQW, $L_z = 100$ Å	+6	+7	+38	-	+35	-	-
EXP, $L_z = 100$ Å, $\beta = 5$	-1	-2	+13	-2	+2	-4	+5
0.3/50	H_{11}	L_{11}	H_{12}	H_{13}	H_{21}	H_{22}	-
RQW, $L_z = 45$ Å	+10	+20	-16	-15	+2	+22	-
EXP, $L_z = 45$ Å, $\beta = 0.9$	-1	+5	-21	-26	-9	+8	-
0.2/50	H_{11}	L_{11}	H_{13}	H_{21}	L_{21}	H_{22}	-
RQW, $L_z = 45$ Å	+6	+12	-	-	-	-	-
EXP, $L_z = 45$ Å, $\beta = 1.2$	-1	+3	-1	+18	-6	-3	-

CONCLUSION

In this paper the effects of graded interfaces in four as-grown AlGaAs/GaAs QW structures has been investigated. Using both a trapezoidal and exponential potential profiles, a good fit has been obtained between the experimental and calculated transition energies. These results show that the QW is best represented by an exponential profile rather than by the more traditionally accepted rectangular profile. The results also demonstrate that PR is a useful characterization method for the determination of the QW shape as it enables all of the allowed interband transitions in a given QW structure to be obtained.

ACKNOWLEDGEMENTS

REFERENCES

1. P.J. Hughes, T.J. Hosea and B.L. Weiss, Semicond. Sci. Technol. **10**, p. 1339 (1995).

2. P.J. Hughes, B.L. Weiss and T.J.C. Hosea, J. Appl. Phys. **77**, p. 6472 (1995).

3. D.E. Aspnes, Surf. Sci. **37**, p. 418 (1973).

4. H. Shen and M. Dutta, Appl. Phys. Rev. **78**, p. 2151 (1995).

5. E.H. Li, B.L. Weiss and K.S. Chan, Phys. Rev. B **46** p. 15181 (1992).

6. J.S. Blakemore, J. Appl. Phys. **53**, p. 10 (1982).

7. D.E. Apsnes, S.M. Kelso, R.A. Logan and R. Bhat, J. Appl. Phys. **60**, p. 745 (1986).

Part VII

Papers Concerning Related Topics

ADVANCES IN IR-LED TECHNOLOGY

R. HÖVEL, E. WOELK* , M. DESCHLER, D. SCHMITZ, H. JÜRGENSEN,
AIXTRON GmbH, Kackertstraße 15-17, 52072 Aachen, Germany
*AIXTRON Inc. 1569 Barclay Blvd., Buffalo Grove, IL 60089, USA

ABSTRACT

Due to the world wide demand for IR emitting devices like IR-LED, printhead for laser printers, readout of optical storage devices, serial and parallel fibber/guided wave optical links and free space optical interconnects for remote controllers there is a great interest in multiwafer technology. In this paper we present growth results with respect to IR applications with the Planetary Reactor® system using AlGaAs/GaAs and longer wavelength material. For the mass production of LEDs the Planetary Reactor® system fulfills not only to grow high quality films with excellent uniformities, which results on high yield on wafer, but also to grow with high precursor utilization efficiency and wafer throughput. This is proven for thick layers by an excellent growth stability and a thickness uniformity better than ±2%. These high uniformities are achieved at conditions of growth efficiency in the range of 30-50% for group III materials and a comparatively low V-III ratio. To increase the intensity of LEDs GaAs/AlAs Bragg reflectors were grown. Reflectivity characteristics measurement and high resolution X-ray diffractometer measurements confirmed the thickness uniformity in the order of ±1% on 4" wafers. The excellent thickness uniformity is also achieved on a 9x6" configuration. For the first time in this study also the 7 x 2" performance of InP based materials is reported.

INTRODUCTION

Beside other applications for IR emitting devices mainly data links will be the next big growth area. For this purpose the IR-LED is the most important compound semiconductor device. Today its most important applications are in products such as TV remote controls. But in near future the important application is computers and office equipment [1]. In order to realize very fast data transfers (10 Mb/s transfer rates) the LED will be replaced by a IR vertical surface emitting laser (VCSEL) because VCSEL offer the coherent output and high modulation rates of a laser, features which are necessary to achieve high data rates.

For such kind of devices the epitaxial growth of high quality films with excellent uniformities is necessary. To meet the requirement of mass production a high yield, the growth with high precursor utilization efficiency and high wafer throughput is also required. As a mass production technology the MOVPE fulfills these requirements. In this paper the concept of the Multiwafer Planetary Reactor® will be described. To prove that this reactor is an excellent tool for the growth of epitaxial layers for IR-applications new growth results will be demonstrated .

THE REACTOR SYSTEM

The requirements on the reactor technique for production include the capability of producing material with highly uniform distributions of properties as well as the cost efficient handling of large volume growth. The basis for scaleable processes is the availability of reproducible results and profound theoretical knowledge about all growth parameter influences. Such an approach to multiwafer reactor techniques has been first described in the Planetary Reactor concept. The Multiwafer Planetary Reactor® developed by P. M. Frijlink is based on the Gas Foil Rotation® Technique [2]. A graphite susceptor plate supporting the wafers is levitating on a layer of H_2. The same gas flow is also causing the rotation of the wafer support by means of shear forces. Each individual wafer is rotating by the same technique, thus causing planetary motion. The speed of rotation is directly controlled by computerized mass flow controllers. The 2", 3", 4" or 6"capability of the reactors is only defined by the geometry of the graphite discs and thus can be changed in a simple procedure between the runs.
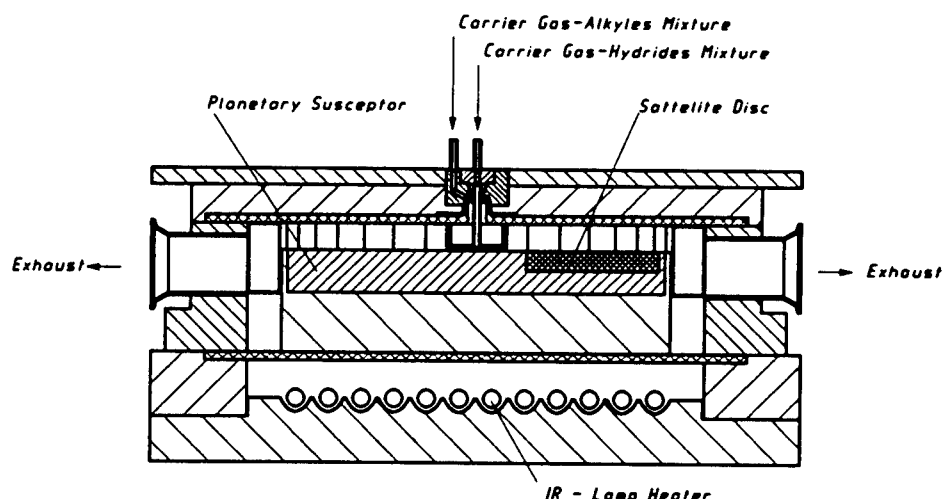
Fig.1: Schematic of Planetary Reactor®

In this horizontal reactor, the wafers are aranged on a circular susceptor which rotates around its central axis, through which the gas flow of group III organometallics with the dopants and a hydrogen carrier flow with the group V hydrides is provided. Because of the rotation of the susceptor platform as a whole as well as of each individual wafer, one gains the high compositional and thickness uniformity. A schematic of the reactor cell is given in Fig. 1. The cross section shows the main graphite susceptor, the satellite discs, the IR lamp reflector underneath, the double O-ring leak integrity monitoring system, and water cooling of the entirely

metal contained reactor. This reactor type is also available with RF-heating and an automated cassette to cassette wafer handling system.

The growth uniformity of such a reactor simulated and verified in a binary material system is shown in Fig. 2. A modeling of GaAs growth rate distribution over the susceptor radius in an AIX2000 Planetary Reactor® cell, capable for up to 7x2" or 5x3" wafers. Parameter of the scale of curves is the total gas flow at a constant initial concentration of TMGa. Marked in the radius axis is the area in which the rotating substrates are placed. The growth efficiency is represented by integration of the growth rate over the radius. So in the case of the growth rate coming to zero within the reactor radius, the efficiency is at its maximum. For obtaining a uniform thickness distribution, the rotation of the single wafers is used to equilibrate the growth rate decrease shown in this static case. Thus, a certain shape of the depletion curve over the radius must be adjusted by choosing the proper flow pattern. The growth efficiency of this reactor is approximately 35% to 45% at its optimum load. Increasing the wafer capacity of the reactor by enlargement of the susceptor radius and reactor cell the growth efficiency is increased. The largest MOVPE reactor AIX 3000 shows a growth efficiency of more than 50% for the TMGa consumption at the growth of GaAs.

growth rate [λ/s]   relative thickness [1 %]

radius [cm]   position [mm]
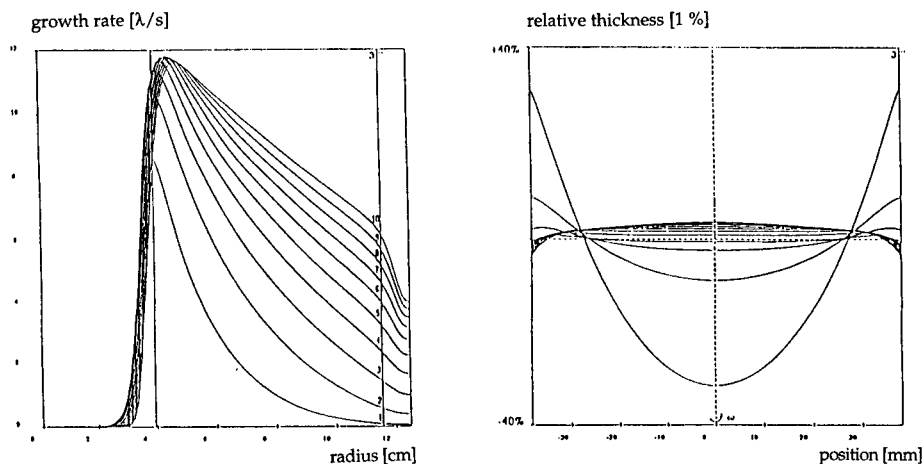
Fig. 2:3" applications: (left) growth rate profiles of the deposit for various sets of carrier flow, (right) normalized thickness profiles on rotating wafer for various sets of carrier flow

MATERIAL QUALITY

GaAs/AlAs Bragg reflectors

In order to improve the output power of IR-LED the growth of GaAs/AlAs Bragg reflector as a mirror was investigated. Furtherone such Bragg reflectors are used as DFB mirrors in VCSELs which become important for IR data links. These kind of structures are very sensitive against thickness uniformity and can be used to prove the growth uniformity of the reactor.
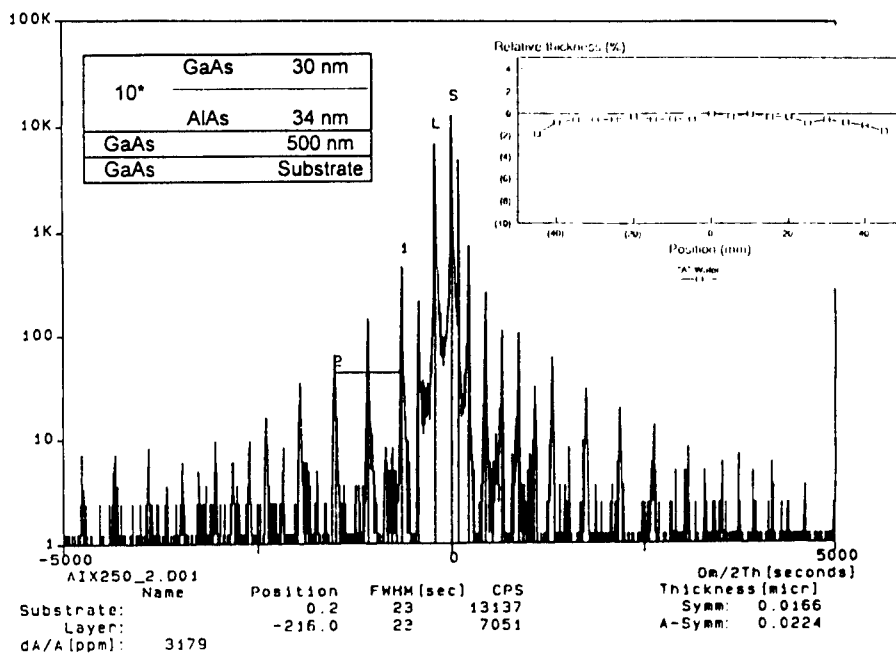
Fig. 3:4-Crystal HRXRD Measurement of GaAs /AlAs Bragg Reflector Structure. Insert: Thickness uniformity ±1 % across 4" Wafer Diameter.

Fig. 3 shows a typical spectrum of a 4-Crystal HRXRD measurement of a 10 period alternating structure of 33nm GaAs/41nm AlAs. The appearance of multiple satellite peaks demonstrates the high quality of the superlattices. The evaluation of Pendellösung-fringes measured over the area of a 4" wafer revealed a uniformity of 1- 1.5% on the 4" wafers. This is also proven by an automatic mapping reflectometer. This excellent value is achieved on 5 x 4" inch wafer in one run in a AIX 2400.

Growth of GaAs/AlGaAs on 6" wafers

For the last ten years there is a steady increase from 2" to 6"technology for the GaAs material technology. Although the growth on 6" wafers is not so attractive for mass production of IR light emitting devices the growth of GaAs, GaAlAs and GaInP was carried out on 6" GaAs substrates. However, the growth on large substrates demonstrates the potential of the Planetary Reactor® and today at least three substrate manufacturers offer 6" GaAs wafers. The thickness uniformity achieved in a 9 x 6" Multiwafer Planetary Reactor across a full 6" GaAs substrate area is better than ±2%.
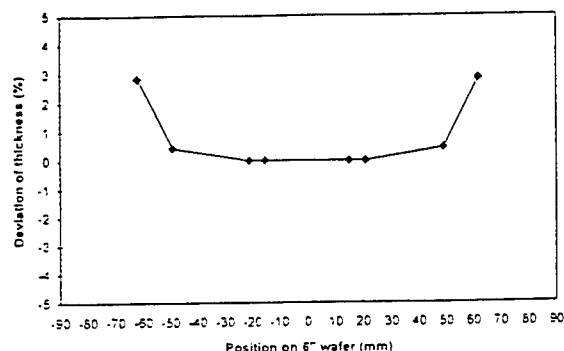
Fig. 4 Deviation of thickness versus 6" wafer

InP based material

Growth experiments of InP based material were carried out on an AIX 2400 reactor with a reactor configuration of 9 x 2". On a Si doped InP layer and a quaternary InGaAsP layer the thickness uniformity was observed. The film thickness was measured using the scanning reflectance technique. The layers were too uniform and the thickness variations were tow low to be detected and translated into a map by this technique. However, single point measurements in the center and approximately at 20 mm radius were carried out and the maximum deviation for all 7 x 2" wafers was 0.087 μm for a 1.9 μm thick Si-doped InP layer and 0.069 μm for a 1.5 μm GaInAsP layer. The variation from wafer to wafer is 2.2 % for the data measured in the center indicating that all wafers are exposed to an identical gas phase composition.

To determine the inhomogeneities in doping concentration the sheet resistivity of the structures was measured. Although the measured value is a convolution of thickness and carrier concentration, the trends are easy to detect. N -type (Si) and p-type (Zn) InP was grown. The variation from wafer to wafer is only 3,5% while the variation from wafer to wafer is 5,5%. The non-uniformity in the Zn-doped structures is much less than that was found in the Si-doped layers. This may allow the conclusion that a further improvement by optimizing the growth parameters is possible. Nevertheless it can be concluded that the doping homogeneity is rather uniform.

In order to investigate the composition homogeneity of quaternary layers the PL emission wavelength was measured. The PL results of the undoped quaternary is excellent. The standard deviation across each wafer is less than 2 nm (Fig. 4). The difference between the minimum and maximum of the wafer average of one growth run is only 2.3 nm. The histograms for each of the wavelength maps reveal a total wavelength spread of only 8 nm.

437
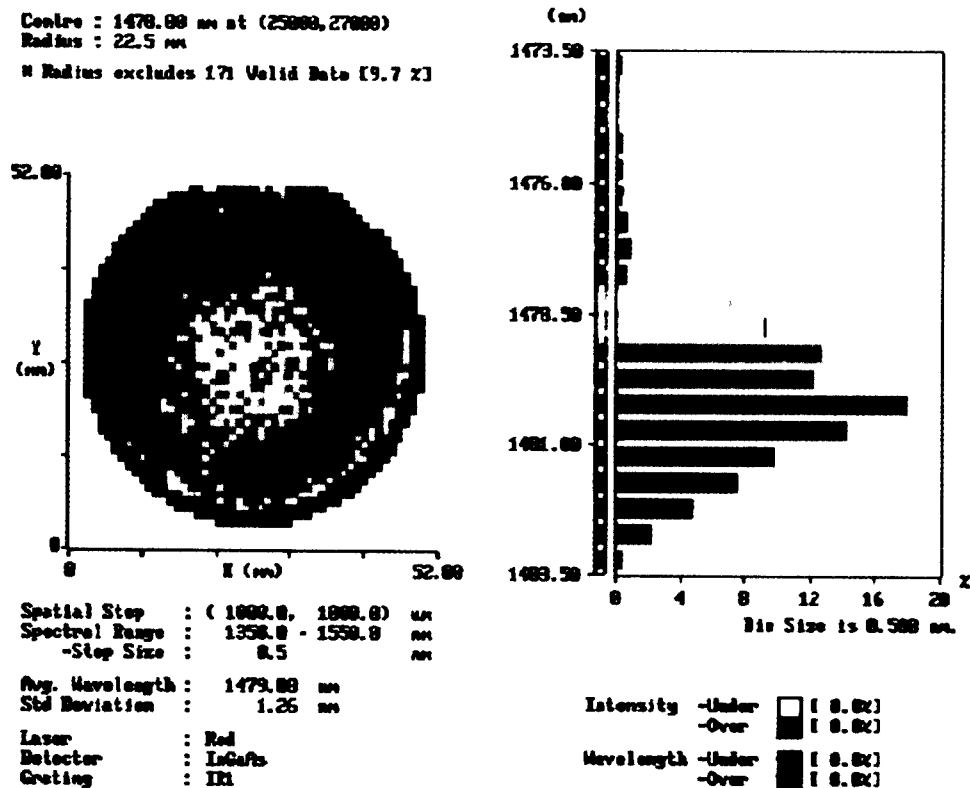
Fig 5. Room temperature PL map of a InGaAsP layer

SUMMARY AND CONCLUSION

Due to the world wide demand of IR devices we have investigated the growth of GaAs and InP-based material with a multiwafer reactor. For the mass production the Planetary Reactor system fulfills not only to grow high quality films with excellent uniformity, which results on high yield on wafer but also to grow with high precursor utilization efficiency and wafer throughput. The excellent thickness uniformity is also achieved on a 9 x 6" configuration and is also better than 2%. The growth of InP based material with a reactor configuration of 7 x 2" was carried out. Excellent homogeneities in thickness, sheet resistivity and PL wavelength were achieved. All these results prove the Planetary Reactor concept as an efficient tool for the production of layer structures for IR devices.

REFERENCES

1. Marie Meyers, Compound Semiconductor May/June 1996 , p. 39.
2. P. M. Frijlink, J. of Crystal Growth 93, 1988, pp. 207-215

NUMERICAL SIMULATION OF ELECTRONIC BEHAVIOR IN A FINITE SUPERLATTICE WITH A TAMM STATE: A POSSIBLE SUBMILLIMETER WAVE EMITTER WITHOUT OPTICAL PUMPING

J. E. MANZOLI*, O. HIPÓLITO**
*Ciência e Engenharia de Materiais - Universidade de São Paulo (USP), CX 369, ZIP-13560-970, São Carlos, SP, Brazil, manzoli@ifqsc.sc.usp.br
**Universidade de Mogi das Cruzes, Departamento do Núcleo de Pesquisas Tecnológicas, Mogi das Cruzes, SP, Brazil

ABSTRACT

We propose a semiconductor heterostructure consisting of six coupled quantum wells of GaAs plus a larger one, all inside $Al(x)Ga(1-x)As$, x=0.35. Our simulation prevents that the localized electronic eigen-state at the large well, the Tamm state, will oscillate when the voltage applied across these "finite superlattice" varies fast. We include exchange and correlation effects in the local density approximation and made the self-consistent calculations to the electrons at 77K varying the voltage in a gate contact of the device. We obtain the effective potential, the sub-bands (mini-bands) and respective electronic densities which enable us to simulate the temporal evolution of an electronic wave-packet when the gate-voltage is switched fast. Such a switching turns the Tamm eigen-state in a wave-packet. By the simulation we conclude that this wave-packet oscillates a Tera-Hertz frequency that can emit electromagnetic radiation as a charge oscillator. We estimate the finite superlattice capacitance and it confirms the possibility of changing the Hamiltonian faster than the period of the oscillation.

INTRODUCTION

Oscillations and Tamm (localized) states [1, 2, 3, 4, 5] in semiconductor superlattices and the coherent submillimeter-wave emission observed from charge oscillations in a double-well potential[6] has pointed out to a revolution in photodetectors, optical switchers and infra-red emitters. The infra-red radiation is explained as a simple charge oscillation[7] whose frequency is related to the electric field through the heterostructure. Some characteristics of the system with two wells[6] are that away from resonance the oscillating signal becomes quickly weaker and the optical generation require large and expensive femtosecond laser system.

Trying to avoid such inconveniences we simulate a new heterostructure reporting a self-consistent numerical calculation of the electronic structure in a finite superlattice (FSL) with the presence of a Tamm state in order to localize the electrons initially. As far as we know this is the first calculation for the profile of an infra-red emitter without optical pumping which we expected to be an alternative for the femtosecond laser system and, as the states in the mini-band are more delocalized than in a double-well, we believe that the oscillating signal becomes stronger even a little more far from resonance. The opto-electronic applications are obvious.

In our proposal the oscillating package stays initially in the Tamm well and will oscillate, by applying a sudden voltage Vg. This gate voltage makes the large well at a higher electron potential than the FSL. At the first alignment of the Tamm eigen-state with

the bottom of the mini-band, we set it free to obey the Schrödinger equation (1) where the initial condition (function) is the Tamm state at Vg = 0.0V. We observe its temporal evolution in this new Hamiltonian. It is an oscillation in the Terahertz domain to which we can associate an electromagnetic emission. A schematic view of the FSL is shown in *figure 1*.
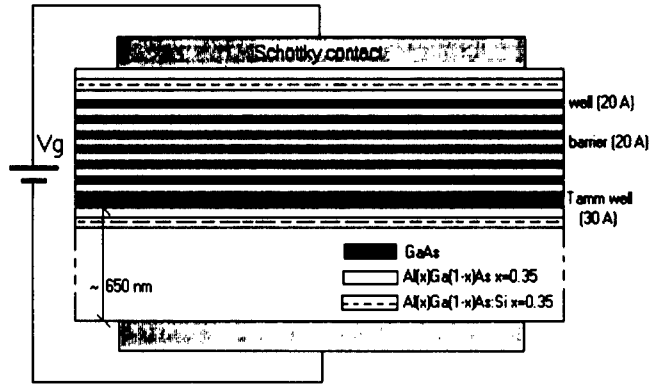
Figure 1: Sketch of the finite superlattice heterostructure. The system consists of 6 periods of GaAs quantum wells (20A) in $Al_{0.35}Ga_{0.65}As$, barriers of 20A, plus a wide well of GaAs (30A) - a Tamm well. On top and down of the wells the donor doping layers limits are shown by the different shadow layers with donor densities of $8.25 \times 10^{12} cm^{-2}$ (top-110A) and $7.5 \times 10^{11} cm^{-2}$ (down-50A). In the whole structure the residual acceptor doping density is $5 \times 10^{15} cm^{-3}$.

We can't observe such oscillation if the packet finds scattering ions. Therefore the doping layers, suppliers of electrons, must not be in the FSL. Our alternative was to put the doping in sandwich layers. This choice limitates the number of layers in the FSL, if we desired to maintain a linear alignment of the wells in energy and minimize the lost of coherence of the waves which constitute the packet as they pass through interfaces. Of course we are considering a very pure interface between different materials, in such a way that a phase delay time of each wave of the packet won't be effective in the lost of coherence until a few periods of oscillation were completed.

The fast switching in the gate voltage will change the effective potential at which the electron are submitted to. We made a simple estimate, explained late, of the time delayed to the stabilization of the effective potential and conclude that it is smaller than the oscillation period of the wave packet, what is necessary to cause the oscillations.

THE SIMULATION MODEL

We solve the time-dependent Schrödinger's *equation (1)* for z (growth) direction, considering plane waves for the electrons in x and y ones:

$$H\Psi_n(z,t) = \left[-\frac{\hbar^2}{2}\frac{\partial}{\partial z}\frac{1}{m^*(z)}\frac{\partial}{\partial z} + V_{eff}(z,t) \right]\Psi_n(z,t) = i\hbar\frac{\partial}{\partial t}\Psi_n(z,t) \qquad (1)$$

We use in such solution the Split Operator technique[9] in the so called imaginary time:

$$\begin{aligned}\Psi(t+\Delta t) &\cong e^{\frac{\Delta t}{i\hbar}[\frac{V_{eff}}{2}+\frac{1}{2}P_z\frac{1}{m^*}P_z+\frac{V_{eff}}{2}]}\Psi(t) \cong \\ &\cong e^{\frac{\Delta t}{2i\hbar}V_{eff}}e^{\frac{\Delta t}{2i\hbar}[P_z\frac{1}{m^*}P_z]}e^{\frac{\Delta t}{2i\hbar}V_{eff}}\Psi(t) \cong \\ &\cong e^{\frac{\Delta t}{2i\hbar}V_{eff}}\frac{1+\frac{\Delta t}{4i\hbar}(P_z\frac{1}{m^*}P_z)}{1-\frac{\Delta t}{4i\hbar}(P_z\frac{1}{m^*}P_z)}e^{\frac{\Delta t}{2i\hbar}V_{eff}}\Psi(t)\end{aligned} \qquad (2)$$

where $V_{eff} = V_h + V_{exc} + V_s$ is the effective potential, V_h is the Hartree potential, V_{exc} is the exchange and correlation potential, and V_s is the FSL conduction band profile.

The Hartree potential, V_h, is obtained, as usually, through:

$$\frac{\partial}{\partial z}\epsilon(z)\frac{\partial}{\partial z}V_h = -4\pi e^2[n(z) - N_d(z) + N_a(z)] \qquad (3)$$

where ϵ is the electric permeability, N_d and N_a are the donor and acceptor densities respectively and $n = \sum_n N_n\Psi_n^*\Psi_n$ is the electronic density with

$$N_n = \frac{m_m^*KT}{\pi\hbar^2}\ln\left[1 + e^{\frac{E_F-E_n}{KT}}\right] \qquad (4)$$

where E_F is the Fermi energy calculated for the bulk semiconductor by assuming the charge neutrality, E_n is the eigen-energy of subband n and $m_m^* = \int m^*\Psi^*\Psi dz$.

The exchange and correlation effects are (parametrized by [8]):

$$V_{exc}(z) = \frac{-e^2}{\epsilon(z)a_0^*\pi\alpha r_s}[1 + 0.7734\ln(1 + X^{-1})] \qquad (5)$$

where $\alpha = \left(\frac{4}{9\pi}\right)^{\frac{1}{3}}$; $r_s = \left(\frac{4\pi a_0^{*3}n}{3}\right)^{\frac{-1}{3}}$; $X = \frac{r_s}{21}$; $a_0^* = \frac{\hbar^2 4\pi\epsilon}{m^*e^2}$ (effective Bohr's radius)

In the Split Operator method we change (t) by $(-it)$ and end up with the *imaginary time* evolution. In doing so we change the Schrödinger's *equation (1)* to a diffusion-equation like where a wave function converges to the ground-state. By starting with a certain number of initial wave functions ortonormalized themselves at every time step, they converge to the first, second, etc. eigen-states.

"Freezing" the effective potential at the gate voltage which causes the desired resonance, we made the *real temporal* evolution of the chosen wave packet, with the above algorithm.

RESULTS

The calculation is performed for seven wells, for many combinations of the FSL parameters, temperatures and doping densities.

These combinations of the parameters were tested in order to get only the "Tamm" sub-band, in the wide well, populated without the applied voltage Vg.

Many systems haven't the desired characteristics because not only the Tamm State is populated or they haven't a satisfactory oscillation under resonant voltage.

To achieve the resonant tunneling oscillation we choose the heterostructures parameters whose potential profile is indicated in *figure 2*. The voltage at which resonances of populated sub-bands occur are obtained by the scan viewed in the corner down-right of *figure 2*.
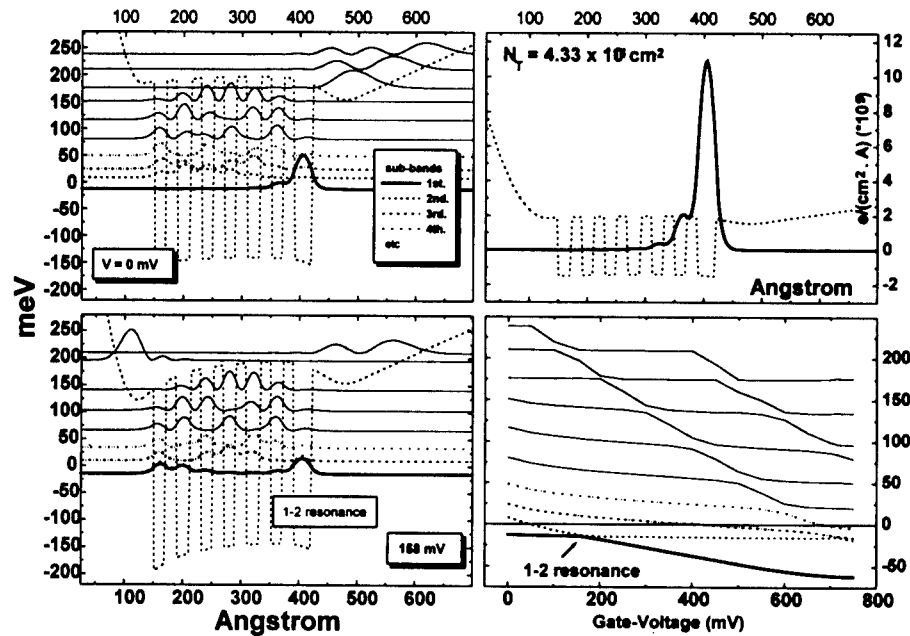
Figure 2: Left: potential profile and the electronic probability densities aligned with the respective sub-band at the indicated voltages. Top right: the electronic charge density in the "Tamm" sub-band. Down right: sub-band changes with gate-voltage (Fermi Level at 0meV).

Using the effective potential profile of the *figure 2* at 158 mV we make the temporal evolution of the Tamm state whose initial electronic density is also shown in *figure 2* . This wave packet realize the movement (oscillation) of *figure 3*.

This wave packet represents the electrons which are localized initially in the largest well and then will experience a charge oscillation whose frequency will be the same as that of the emission (0.6 THz).

This oscillation is possible only if the effective potential changes its profile faster than the oscillation's period. In order to over-estimate this time we compare the FSL as a capacitor in a simple RC-circuit, where the capacitance is function of its charge. We consider the total charge in the FSL as:
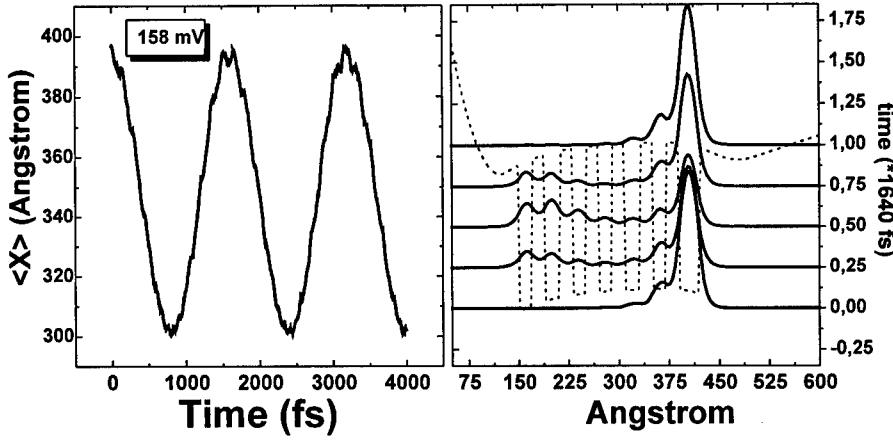
Figure 3: FSL under the first resonance (first and second sub-bands). Left: the expected position of the Tamm state as function of time. Right: the probability density of this wave package in some selected instants.

$$Q = eA \int_0^{6500} n(z) dz \qquad (6)$$

Where e is the electron charge, A is the contact area and n(z) is the electronic density.

This charge is function of the gate voltage, and the capacitance of the FSL is:

$$C = \frac{\partial Q}{\partial V} \qquad (7)$$

In a simple RC-circuit we have, by the Kirchhoff's law:

$$V = \frac{Q}{C} + R\frac{\partial Q}{\partial t} \qquad (8)$$

Where R is the internal and external resistances of the experimental apparatus.
So we have:

$$dt = \frac{RC}{VC - Q} dQ \qquad (9)$$

The time delayed to change the charge from 0 to Q is:

$$\Delta t = R \int_0^Q \frac{C}{VC - Q} dQ \qquad (10)$$

Using this equation, where $C(C(V_g)$ or $C(Q))$ is calculated by the equation (7) , R$\simeq$50Ω, V=158 mV (the gate voltage of resonance) and a contact area of two μm^2 we obtain Δt=1.56ps, lower than the 1.6ps of the oscillation period, as desired. A small contact area guarantee a small time. So we believe that oscillations are possible.

443

CONCLUSIONS

Here we exposed a theoretical prediction of a far-infra-red emission without optical pumping but with a "fast switching" the gate voltage instead. A more precise heterostructure could be thought, if its effective potential profile was more fast changed when the gate voltage turned on. An estimate of dephasing times due to interface imperfections will be important too.

We use the usual self-consistent calculations but with the Split-Operator, technique which is very versatile in the solution of Schrödinger's equation to many different heterostructures.

The initial "eigen-Tamm-State" becomes a state which could be thought as a sum of the new eigen-states of the changed Hamiltonian, mainly by the eigen-states in resonance. It could exist a situation where the wave packet is a sum of Stark ladder states, allowing the frequency of emission to be tuned linearly by the electric field (or by the gate voltage) and not in a very few range near the resonance. In such situation the oscillation is a kind of Bloch - Oscillation and the emission's wave-length could be tuned by the voltage.

References

[1] I. Tanaka, M. Nakayama, H. Nishimura, K. Kawashima and K. Fujiwara, *Solid-State Electronics* **37** (4), 863 (1994).

[2] E.E. Mendez and G. Bastard, *Physics Today* , 34 (1993).

[3] C. Waschke, H.G. Roskos, K. Leo, H. Kurz and K. Köhler, *Semicond. Sci. Technol.* **9**, 416 (1994).

[4] C. Waschke, H.G. Roskos, R. Schwedler, K. Leo, H. Kurz and K. Köhler, *Physical Review Letters* **70** (21), 3319 (1993).

[5] H. Ohno, E.E. Mendez, J.A. Brum, J.M. Hong, F. Agulló-Rueda, L.L. Chang and L. Esaki, *Physical Review Letters* **64** (21), 2555 (1990).

[6] H.G. Roskos, M.C. Nuss, J. Shah, K. Leo, D.A.B. Miller, A.M. Fox, S. Schmitt-Rink and K. Köhler, *Phys.Rev.Lett.* **68** (14), 2216 (1992).

[7] C. Dean, *Am. J. Phys.* **27**, 161, (1959).

[8] L. Hedin, B.I. Lundqvist - *J.Phys.C: Solid St. Phys.* 4 (14), 2064 (1971).

[9] M.H. Degani, *Appl. Phys. Lett.* **59** (1), 57 (1991).

THE PROFILE DESIGN OF STRAINED SiGe-CHANNEL P-TYPE MODULATION DOPED FET

KLAUS Y.J. HSU and S.M. HUANG
Department of Electrical Engineering, National Tsing Hua University, Hsinchu, Taiwan 300,
R.O.C., yjhsu@ee.nthu.edu.tw

ABSTRACT

To improve the performance of p-type SiGe-channel FET's is important for Si-based high-speed/high-frequency applications. This work discusses the design of germamium profiles in the strained $Si_{1-x}Ge_x$ channel region of p-type SiGe modulation doped FET's and studies its effect on device performance. Two-dimensional device simulator is used to simulate the large-signal device performance for various Ge distributions including triangular, trapezoidal, and flat profiles. In particular, the thickness of the strained SiGe channel layer is 15 nm and a 5 nm thick Si cap layer is on top of the channel. It is found that with the same integrated Ge content in the strained channel, graded Ge profiles lead to higher transconductances and larger threshold voltage windows than those of flat profiles, due to deeper potential wells and better carrier confinement ability. For triangularly graded profiles, the peak position must be located in the upper half portion of the channel layer to result in superior performance. By adding more Ge to extend the peak region, triangular profiles become trapezoidal ones. However, more Ge content does not necessarily produce better performance. If the well depth of trapezoidal profile is the same as that of triangular profile and if the trapezoid plateau begins at the same position as that of triangle peak, the device performance is almost the same for both profiles.

INTRODUCTION

High-speed silicon devices are strongly demanded by the rapid growth of communication and computer markets. For Si technology to fit in the high-speed/high-frequency area, Si/SiGe heterojunction devices have been developed [1]-[6]. The Si/SiGe heterojunction bipolar transistors (HBT's) provide advantages in device operation speed, but the power consumption becomes a potential problem when integration density increases. Introducing SiGe material into CMOS design makes both low power consumption and high speed possible. While problems such as process integration are still asking for efficient solutions for Si/SiGe CMOS technology, the profile design in the devices is another important issue in the development process. For example, it is essential to increase the speed of p-type devices in order to improve the overall circuit performance. Studying the device structures also provides physical insight toward optimal device design as well as potential problems in device operation. For p-type SiGe modulation doped FET (p-MODFET), how to design a good Ge profile is an important issue. In this work, the effect of germanium concentration profiles on the electrical properties of SiGe p-MODFET is systematically investigated by using a two-dimensional device simulator. Based on the simulations, guidelines for designing superior profiles are derived.
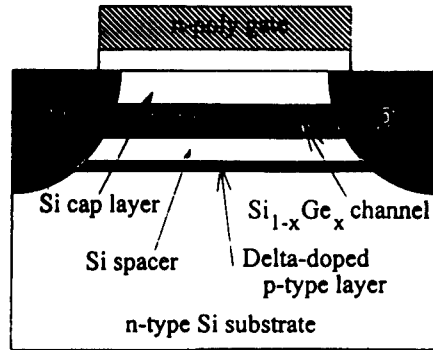
Fig. 1 Illustration of the simulated SiGe p-MODFET.
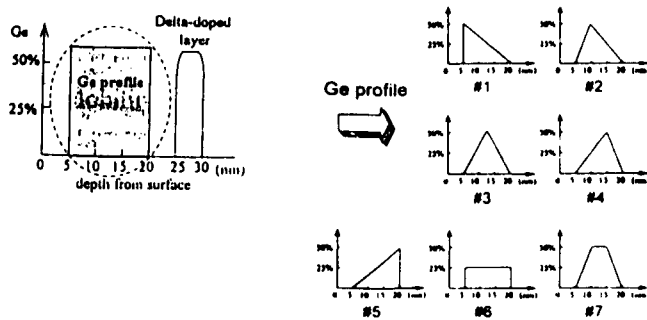
Fig. 2 Ge concentration profiles under study.

ANALYSIS METHOD AND CONDITIONS

Unlike SiGe HBT's, grading the Ge profiles in the SiGe channels of MODFET does not introduce longitudinal electric field to accelerate carriers. It is another reason that requires the study of Ge profile design in SiGe MODFET's, namely carrier confinement. Grading affects the carrier concentration in the SiGe channel and has influence on the turn-on of other parasitic channels. Therefore, the device current and transconductance are strongly dependent on the Ge profile design. The purpose of the paper is to access this issue by simulation.

In order to concentrate on the effect of different Ge profiles and to avoid the influence of short channel effect, a long channel p-MODFET (l=1.8 μm) is devised for the study. The structure of the simulated p-MODFET is schematically illustrated in Fig. 1. Several parameter also need to be fixed in advance. The gate material is set to be n^+-poly Si to suppress turning on the parasitic channel in the Si cap layer. The oxide thickness is chosen as 10 nm. The thicknesses of the Si cap layer, the $Si_{1-x}Ge_x$-channel layer and the Si buffer layer are 5 nm, 15 nm and 5 nm, respectively, and these three layers are all undoped. To obtain a threshold voltage of the SiGe-channel of about -0.5 V, the δ-doped layer is set to have a thickness of 5 nm and a doping concentration of about 6×10^{17} cm^{-3}, and the background doping of the n-type

substrate is 10^{16} cm^{-3}. In this work, after the study of Ge profiles, the substrate doping and the δ-doping are also varied under a fixed Ge profile to study the leakage current property.

Seven Ge profiles in the SiGe-channel region, as shown in Fig. 2, are devised for electrical property simulations. Profiles #1 to #5 are all triangles and only differ at the peak positions. Profile #6 is a rectangle and has the same Ge dose as those of profiles #1 to #5. Profile #7 is a trapezoid with the plateau beginning at the same position and the same height as those of the peak of profile #2. Therefore, the dose of profile #7 is larger than the other profiles. All the doses are within the critical thickness limit. As a reference, Si MOSFET with the same device dimensions and the same threshold voltage (-0.5 V) is also simulated.

The TMA MEDICI 2D device simulator [7] is used for the simulations. Drift-diffusion model is employed to account for the DC characteristics. Impact ionization model is also included to analyze the hot carrier and punch-through phenomena. The material parameters of $Si_{1-x}Ge_x$ are set equal to those of Si except the energy bandgap and mobility. From the simulations, large-signal electrical characteristics are obtained. Potential contours and carrier concentration contours can also be plotted. The quantities we concentrate our notice on are transconductance and threshold voltage.

RESULTS AND DISCUSSION

Threshold Voltage

There are two threshold voltages defined for the MODFET's with cap layers: One is the SiGe-channel threshold voltage (V_{TH}) and the other is the parasitic surface-channel threshold voltage (V_{TS}). In order to confine more carriers in the high-mobility SiGe-channel region, good profile designs must maximize the gate voltage window (ΔV_T) which is defined as the difference between V_{TH} and V_{TS}. Fig. 3 shows the threshold voltage behavior of the Ge profiles under study. For triangular profiles, V_{TS} varies significantly (from -1.77 V to -1.19 V) as the Ge peak shifts from the interface between Si cap layer and SiGe-channel toward the interface between SiGe-channel and Si buffer layer. V_{TH} also changes but with slight amount (from -0.50 V to 0.46 V). Therefore, the triangular peaks near the upper interface give larger ΔV_T. This can be explained by considering the effect of the Ge concentration slope on
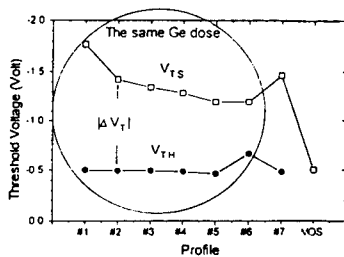
Fig. 3 Threshold voltages for various Ge profiles.
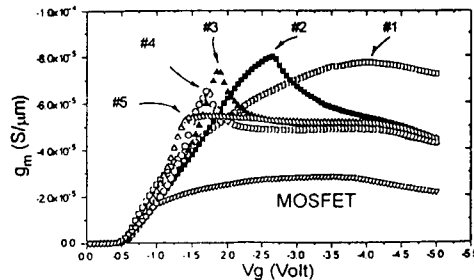
Fig. 4 The g_m-V_g curves of profiles #1 to #5 and of Si MOSFET.

447

confining holes in the triangular potential wells. Larger slope at the top portion of triangle offers larger reverse electric field to hinder the holes from jumping into the surface-channel. So profile #1 has the largest V_{TS}. Since the delta-doping concentration and the peak value of Ge profile dominate the hole concentration in the potential well, the five profiles have similar values in V_{TH}. Profile #6 has small Ge peak concentration (25%), therefore, its V_{TH} is much larger. Interestingly, this profile has the same V_{TS} as that of profile #5. This confirms the interpretation mentioned above since profile #5 has the same effective top barrier height as that of profile #6. For profile #7, it is noted that its threshold voltages are nearly the same as those of profile #2, which can be understood with the same reasoning. Although profile #1 gives the largest gate voltage window, it is uneasy to fabricate in reality. On the other hand, profile #7 owns 25% more Ge dose but provides only the second largest ΔV_T. Thus profile #2 is the best choice in the views of threshold voltage window requirement and process feasibility.

Transconductance

The g_m-V_g curves for the various profiles are calculated at a drain bias of -3 V. It is found that the peak transconductance of profile #6 (25% Ge, rectangle) is 1.7 times larger than that of Si MOSFET, and the other profiles have even larger values. This is consistent with the trend that higher Ge mole fraction gives higher carrier mobility.

The transconductance peak degrades and moves to higher gate bias when the Ge concentration peak shifts from the top interface to the bottom interface, as shown in Fig. 4. Also, these transconductance peaks are sharper than that of Si MOSFET. Because the SiGe-channel is turned on first in SiGe p-MODFET as the gate bias sweeps, its transconductance ramps up faster than in Si MOSFET. Although profile #5 has the smallest V_{TH} and its g_m rises most rapidly, its hole confinement capability is the worst and thus the surface-channel takes over the conduction at the smallest gate bias, which in turn leads to the smallest transconductance peak value among the five cases. At higher bias, the p-MODFET's show similar transconductance behavior as Si MOSFET does, due to the existence of surface-channel conduction. Because holes experience more severe interface scattering in profile #1, the transconductance is a little smaller than in profile #2.

Profile #7 has more Ge dose than profile #2, but their transconductance curves differ from each other only slightly, as shown in Fig. 5. The slight difference lies in that the larger bottom Ge concentration slope of profile #7 corresponds to a smaller V_{TH} and thus the g_m
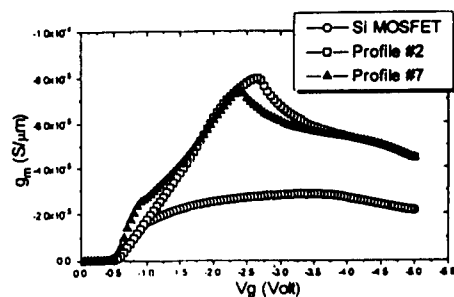
Fig. 5 Comparison between the g_m-V_g curves of profiles #2 and #7.
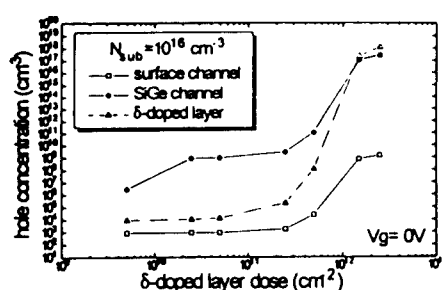
Fig. 6 Hole concentration v.s. δ-doping level in three regions.

448

ramps faster in the -0.5 V to -1 V bias range. Similar hole confinement abilities in both profiles give similar g_m curves for most of the gate biases. Therefore, more Ge does not guarantee better performance. The important point is where the Ge is added.

Doping Consideration

In SiGe p-MODFET's, several paths may exist for hole leakage current at zero gate bias: the surface-channel, the SiGe-channel, and the modulation-doped layer. Here, we monitor the hole concentrations in these layers at sub-threshold condition to study the effect of changing the doping levels in the modulation-doped layer and the substrate. Profile #2 is chosen for the study.

Simulation results show that the SiGe-channel dominates the leakage current by several orders in magnitude than the other two regions at moderate δ-doping levels (Fig. 6.) Although smaller δ-doping is helpful in reducing leakage, it is harmful in maintaining ΔV_T because V_{TH} will be significantly changed. Increasing the substrate doping could be a better way, because V_{TH} and V_{TS} change synchronously with the substrate doping and ΔV_T can be kept constant. The substrate doping can be chosen according to the δ-doping level so that the δ-doped layer can be fully depleted and the leakage current can be effectively suppressed. Fig. 7 shows that the hole concentrations in the δ-doped layer and in the SiGe-channel can be reduced by increasing the substrate doping without sacrificing ΔV_T. Of course, the absolute value of V_{TH} sets a criterion to the choice of substrate doping.
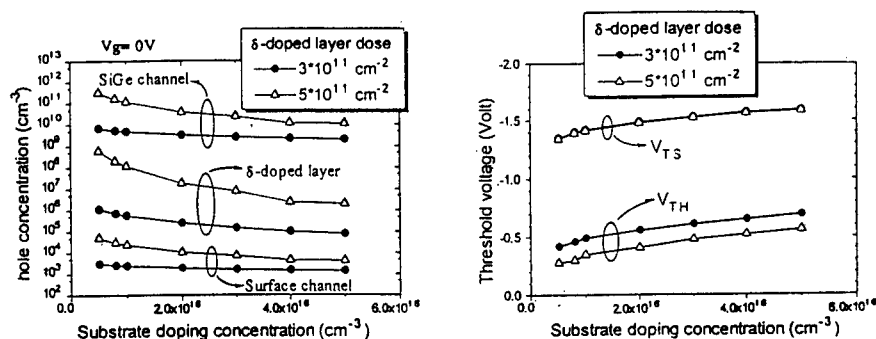
Fig. 7 (a) Hole concentration v.s. substrate doping level in
three regions. (b) Dependence of threshold voltages
on substrate doping.

SUMMARY

The Ge profile design in SiGe-channel p-MODFET is studied. The top gradient of the graded Ge profiles plays the key role in carrier confinement. Triangular profiles with large peaks located in the upper region of the SiGe-channel provide best device characteristics. Adding more Ge near the δ-doped layer can not enhance device performance and thus can be excluded. The substrate doping and the δ-doping must be tailored together to suppress leakage current. Optimal profile can be obtained according to these guidelines.

REFERENCES

1. G.L. Patton *et al.*, "Silicon-Germanium-Base Heterojunction Bipolar Transistors by Molecular Beam Epitaxy," IEEE Electron Dev. Lett. 9, (1988), pp. 165-167.

2. T. Tatsumi *et al.*, "Si/Si$_{1-x}$Ge$_x$/Si Heterojunction Bipolar Transistor Made with Si Molecular Beam Epitaxy," Appl. Phys. Lett. 52, (1988), pp. 1089-1091.

3. H. Temki *et al.*, "Si$_{1-x}$Ge$_x$ Strained-Layer Heterostructure Bipolar Transistors," Appl. Phys. Lett. 52, (1988), pp. 895-897.

4. P.M. Garone *et al.*, "Carrier Confinement in MOS gated SiGe/Si Heterostructures," IEDM Tech. Digest, (1990), pp. 383-387.

5. S.V. Vandebroek *et al.*, "High-Mobility Modulation-Doped Graded SiGe-Channel p-MOSFET's," IEEE Electron Dev. Lett. 12, (1991), pp. 447-449.

6. S.V. Vandebroek *et al.*, "SiGe-Channel Heterojunction p-MOSFET's," IEEE Electron Dev. Lett. 41, (1994), pp. 90-101.

7. Technology Modeling Associates, Inc., TMA MEDICI Two Dimensional Device Simulation Program User Manual Version 2.0, (1994), vols. 1 & 2.

NO-PHONON AND PHONON-ASSISTED INDIRECT TRANSITIONS
IN Si$_{1-x}$Ge$_x$ SINGLE CRYSTALS

A. GERHARDT
Institut für Kristallzüchtung, D-12489 Berlin, Rudower Chaussee 6, Germany
FAX: +049 (30) 63923003   Phone: +49 (30) 63923091   e-mail: donecker@ikz-berlin.de

ABSTRACT

The absorption properties of high quality bulk Si$_{1-x}$Ge$_x$ single crystals ($0 \leq x < 0.16$) are studied. Transmission measurements were performed at the indirect absorption edge. The shape of the absorption edge is characterized by structures attributed to the onset of no-phonon and phonon-assisted indirect optical transitions. Threshold energies have been determined using a differential method. A corrected calibration function for the dependence of the excitonic energy gap on composition is presented for the compositions, where x ranges from 0 to 0.16 . The presented calibration function can be used for the composition analysis by an optical method. The analysis is independent of absolute transmission values.

A simulation of the absorption spectra by calculations based on second order perturbation theory was used to fit the experimental data. This procedure allows to estimate the oscillator strength of the no-phonon transition in dependence on x.

INTRODUCTION

Si$_{1-x}$Ge$_x$ belongs to the relevant material systems for applications in the near-infrared spectral range. A potential use is the development of advanced electronic and optoelectronic devices. A particular interest is in the field of silicon-based photovoltaics to enhance the photovoltaic response in the infrared[1]. The fundamental quality of the Si$_{1-x}$Ge$_x$-system is to control the gap energy by the variation of the Ge concentration x. The gap energy is closely connected with the optical band gap. The knowledge of the spectral behavior of the absorption coefficient in dependence on x is of particular interest.

The transmission of Si$_{1-x}$Ge$_x$ was studied first by Braunstein et al.[2]. For increasing Ge concentrations the absorption edge was found to shift towards lower photon energies. The authors derived their composition dependence on the gap energy from a fit of a one phonon expression. In the present paper the transmission in the vicinity of the absorption edge was measured using Fourier Transform (FTIR) spectroscopy. A corrected calibration function for the dependence of the energy gap on composition is presented for the x-range from 0 to 0.16 Only high quality single crystals were investigated. The gap energy can be determined by using the threshold position of transitions instead of the intensity ratios of the transmission, which depends on thickness and effective reflectivity. The derivative of the transmission at the absorption edge reveals several characteristic features attributed to different types of indirect transitions.

Rutherford backscattering (RBS) was used to determine the Ge concentration in the Si$_{1-x}$Ge$_x$ samples.

A theoretical model for the absorption of electromagnetic radiation at the optical edge in an indirect semiconductor includes several indirect transitions. The fit of the theory to the experimental data allows to draw conclusions about the x dependence of the oscillator strengths.

EXPERIMENT

$Si_{1-x}Ge_x$ single crystals have been grown using the float zone (FZ) and the Czochralski (Cz) technique[3,4]. The samples had a thickness of d=0.05cm and were polished at both sides. The wafer diameter amounts up to 4cm. Typical Ge contents are in the 0-16 at per cent range. The carrier density was below $1 \cdot 10^{17} cm^{-3}$.

Transmission spectra have been obtained employing the BRUKER IFS 66v FTIR spectrometer in the spectral range of the indirect absorption edge in the 0.8-1.3eV region. The configuration of the FTIR spectrometer was a tungsten source, a CaF_2 beam splitter and a Ge detector. The maximal resolution was 0.1cm. The measurements were performed at temperatures from 77K to 300K.

The RBS random spectra were measured using $^4He^+$ ions at 1.4MeV with a detector angle of 170°.

RESULTS

The interactions between the indirect semiconductor $Si_{1-x}Ge_x$ and electromagnetic radiation are the subject of the investigations. The valence band (VB) maximum and the conduction (CB) minimum occur at different points in the momentum (k) space. Transitions of electrons from the VB to the CB require a participation of phonons to conserve the momentum. The energy is changed by the absorption of photons. The energetic position of an indirect transition is characterized by the band gap energy E_g and the energy of the participating phonon E_{ph}:

$$\hbar \omega_i = E_g \pm E_{ph,i} \qquad (1)$$

Band-to-band transitions with the absorption (a) or the emission (e) of several phonons $E_{ph,i}$ occur. Assuming parabolic energy bands at the critical points, the second order perturbation theory leads to a quadratic dependence of the absorption coefficient α on the photon energy $\hbar \omega$ for these electronic transitions:

$$\alpha_{el,i} = A_{el,i} \left[\hbar \omega - \left(E_g \pm E_{Ph,i} \right) \right]^2 \qquad \text{for:} \qquad \hbar \omega > \left(E_g \pm E_{Ph,i} \right) \qquad (2)$$

$$\alpha_{el,i} = 0 \qquad \text{for:} \qquad \hbar \omega \leq \left(E_g \pm E_{Ph,i} \right)$$

The electrostatic interaction and the local correlation of the electron-hole pair manifest themselves by excitonic states. The excitonic contributions can be described by a hydrogen like series of states below the conduction band edge. For these transitions into excitonic states, α follows the square root law:

$$\alpha_{exc,i} = B_{exc,i} \left[\hbar \omega - \left(E_g \pm E_{Ph,i} - E_{exc} \right) \right]^2 \qquad \text{for:} \qquad \hbar \omega > \left(E_g \pm E_{Ph,i} - E_{exc} \right) \qquad (3)$$

$$\alpha_{exc,i} = 0 \qquad \text{for:} \qquad \hbar \omega \leq \left(E_g \pm E_{Ph,i} - E_{exc} \right)$$

The strengths of the transitions are expressed by A and B. Different kinds of phonons $E_{ph,i}$ (TO, LO, LA, TA) are involved. The ultimate shape of the indirect absorption edge is formed by

a superposition of contributions from the electronic and excitonic transitions. The onset of distinctive transitions manifests itself by weak changes of the slope of the absorption spectrum.

The first and second derivative of the transmission spectra were calculated to reveal these weak changes. This was done, because the changes in the shape of the transmission are more developed than in the shape of the absorption. The transmission τ is given by:

$$\tau(\omega) \approx (1-R)^2 \exp\left(-\alpha(\omega) d\right). \tag{4}$$

The spectral dependence is conserved in the first derivative of the transmission as well as in the first derivative of the absorption, if it is assumed that the derivative of the effective reflectivity (R) is small

$$\frac{\tau'(\omega)}{\tau(\omega)} = -\alpha'(\omega) \ d - \frac{2R'(\omega)}{1-R(\omega)} \tag{5}$$

As shown in fig.1, in the first derivative of a FZ-Si transmission spectra several structures become well visible. The shape of these structures corresponds to the shape of the derivative of
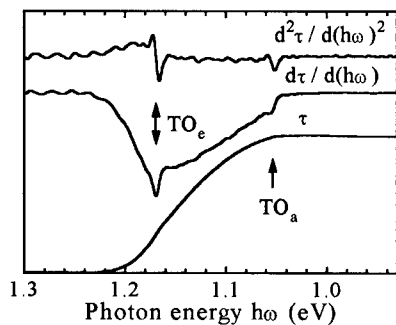
figure 1. The transmission τ of a FZ Si sample at room temperature and the first and the second derivative. The extrema in the derivatives can be attributed to thresholds of TO phonon assisted transitions (absorption and emission).
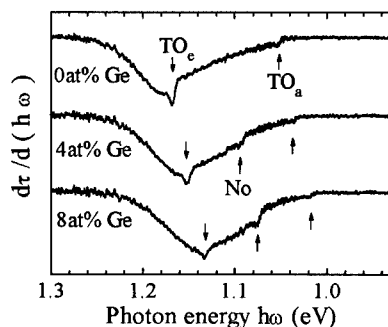
figure 2. The first derivatives of 3 samples with different compositions. For increasing Ge content the absorption edge with the characteristic thresholds shifts toward lower energies. For x>0.002 a no-phonon transition occurs.

a transition into excitonic states described by equation (3). The exact position of a threshold can be determined by evaluating the energetic position of the corresponding minima at the first and second derivatives. The example in fig. 1 reveals two transitions, which are separated by an energy of 115.6meV (932cm^{-1}). Because this value equals twice the TO-phonon energy of Si of 57.8meV (466cm^{-1})[5], one transition can be identified as a transition with TO-phonon absorption and the other with TO-phonon emission. In this manner, the TA-phonon thresholds can be determined, too. The TA-phonon energy of Si is 18.4eV (148cm^{-1}) by evaluating the derivatives.

For the Si$_{1-x}$Ge$_x$ samples the absorption edge was found to be shifted towards lower photon energies, when the Ge content increases. The derivatives of the edge show the shift of the structures mentioned (fig. 2). The energy interval between the thresholds, which were identified

as onsets of TO-phonon assisted transitions, remains constant. No significant change in the TO-phonon energies was observed for the investigated compositions. A further threshold appears positioned exactly at half the energy between the TO-phonon thresholds for samples with Ge contents of more than 0.2at per cent. This structure can be attributed to a no-phonon transition. It is caused by the perturbation of the translation symmetry of the lattice due to the incorporated Ge atoms.

The excitonic gap energy ($E_{gx}=E_g-E_{exc}$) can be derived directly from the position of the no-phonon threshold. The calibration function of the excitonic gap energy in dependence on the composition was performed utilizing the more pronounced TO threshold. Because of the constant energy interval between the TO-thresholds, the phonon energies of Si can be applied. The linear regression of the room temperature data leads to the function:

$$E_{gx}(x) = \left(1.110 - 0.382\,x \right) eV \qquad (6)$$

The position of the threshold can be determined with an accuracy of ± 1.3meV. The transitions broaden for inhomogenous samples. The Ge concentration can be determined with an accuracy of $\Delta x = \pm 0.005$.
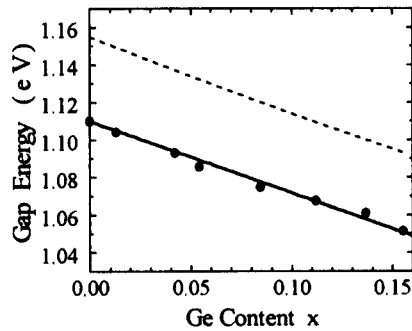
figure 3. Excitonic band gap of Si$_{x-1}$Ge$_x$ alloys as a function of the composition. The circles ($\bullet$) and the solid line are the excitonic gap at room temperature. For comparison the dashed line represents the excitonic gap energy from photoluminescence spectra at 4K[8].
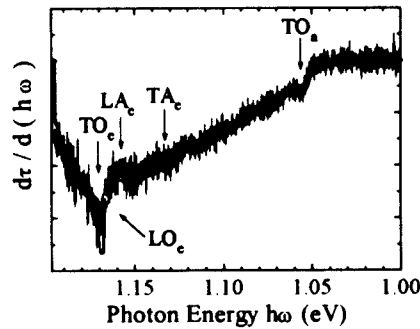
figure 4. The first derivative of the transmission (black) and the derivative of the fitted transmission (white). TO-, LO-, LA- and TA-phonon assisted transitions were considered. The thresholds become better visible at the derivative of the best simulation.

The composition dependence of the gap data, which were measured at room temperature, has the same slope as the function obtained from low-temperature luminescence data [6]. The difference on the energy scale (fig.3) is given by the well-known temperature shift of the Si band gap [7]. The comparison of the presented calibration function with the function of Braunstein et al.[2] revals a minor difference in the slope of the function and a more pronounced difference in absolute energy values. This may be caused by the inaccurate one phonon aproximation, which was used to determine the gap energy. They also investigated samples, which partly were polycrystalline. In this paper the transmission of high quality single crystals were measured.

RBS measurements

Due to the fairly different masses of Si and Ge and the high backscattering cross-section of Ge, RBS is a suitable method for the element analysis of Ge in $Si_{1-x}Ge_x$. Random spectra of different Ge concentrations show a different signal level depending on the Ge in content. Both surfaces were measured, because of the low accessible depth of about $1\mu m$. Then the spectra were added to give a spectrum with an average composition to make the results comparable with the bulk analysis from the transmission measurements.

Data analysis

The data analysis has been performed by a simulation procedure, which is based on second order perturbation theory. The model describes the spectral shape by adding the contributions of the involved indirect transitions. Band to band as well as excitonic transitions are included (equ.2 and 3). The positions of the transitions have to be exactly determined by evaluating the first and second derivative of transmission, since they are sensitive parameters of the fit. Then each contribution is fitted separately by a variation of the factor, which represents the oscillator strength. If the contribution of a transition is determined, it will be subtracted from the data. All contributions are characterized in this way to answer the following questions: Which phonons are involved? What kinds of processes occur? What is the oscillator strength of each transition?. The example (fig.4) shows the first derivative of the experimental transmission and the fitted transmission of a FZ Si sample. Additionally to the thresholds observed in the derivatives further contributions can be identified and determined in the course of the fit. The positions of these thresholds are strongly related to absorption and emission transitions involving LO, LA and TA phonons, because the energetic position of the thresholds corresponds to the Si phonon energies [5].

In order to test the fitting process and to consider temperature effects, the absorption spectra of a Si sample measured at various temperatures were fitted first. The temperatures range from 77K up to 300K. As expected the coefficients according to the strength of contributions from transitions involving absorption or emission of phonons show a temperature behavior in accordance with the Bose-Einstein statistics of the phonons.

Fitting the data of $Si_{1-x}Ge_x$ mixed crystals with different Ge content reveals the changing share of each contribution represented by the coefficients $A_{el,i}$ and $B_{exc,i}$. Regarding the temperature the coefficients are related to the oscillator strengths. As an example the coefficient B_{no} of the no-phonon transition is shown in fig.5 . B_{no} seems to be mainly determined by a linear dependence of the oscillator strengths on the considered part of composition.

Profiling and mapping

The optical properties of the $Si_{1-x}Ge_x$-system can be used to get information about the composition of a $Si_{1-x}Ge_x$ sample very rapidly, simply and without destruction of the sample [8]. Further it is a very cost efficient method to determine the Ge content, because no preparation of the sample is necessary. This procedure may be applied without a detailed knowledge of the exact thickness and the surface quality. Thus wafer with a defined surface and thickness as well as thick bulky samples in the as grown state can be analyzed. It is possible to scan along the crystal growth axis (fig.6) or to perform a lateral composition map of a wafer.
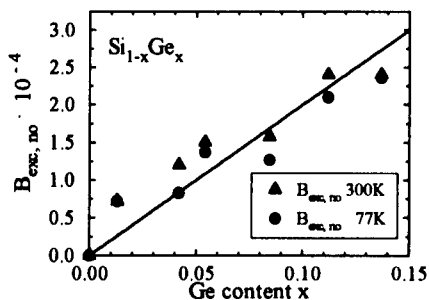
figure 5. Coefficients of the no-phonon assisted transition into excitonic states in dependence on composition x. The coefficients for two different temperatures are related to the oscillator strengths.
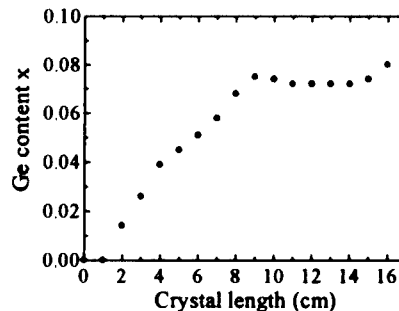
figure 6. A scan along the crystal axis of a $Si_{1-x}Ge_x$ single crystal in the as-grown state. The growth of the crystal starts with a Si seed, then Ge is added.

CONCLUSIONS

Threshold energies of the transitions at the indirect absorption edge can be determined by examining the first and second derivative of the transmission. For the $Si_{1-x}Ge_x$ single crystals the TO phonon energy of Si is constant in the range $0 \leq x < 0.16$. A simulation of the absorption edge can be performed considering the threshold positions and phonon energies. Coefficients, which are related to oscillator strengths are a result of the data analysis.

The shift of the gap energy of $Si_{1-x}Ge_x$ was determined by evaluating a certain threshold position. The presented calibration function between the alloy composition and the excitonic band gap can be used for optical composition analysis at room temperature.. It is a bulk analysis of $Si_{1-x}Ge_x$ material. The method is nondestructive, independent of absolute transmission values. There is no special sample preparation required. A profiling and mapping of samples can be performed.

ACKNOWLEDGMENTS

REFERENCES

[1] J. M. Ruiz, J. Casado, and A. Luque, in Proc. 12th European Photovoltaic Conf., Amsterdam, 1994, p. 572.
[2] R. Braunstein, A. R. Moore, and F. Herman, Phys. Rev. 109, 695 (1958).
[3] J. Wollweber, D. Schulz, and W. Schröder, J. Crystal Growth 163, 243 (1996).
[4] N. V. Abrosimov, S. Rossolenko, V. Alex, A. Gerhardt, and W. Schröder, J. Crystal Growth 166, 657 (1996).
[5] M. Asche and O. G. Sarbei, Phys. Stat. Sol. (b) 103, 11 (1981).
[6] J. Weber and M. I. Alonso, Phys. Rev. B 40, 5683 (1989).
[7] W. Bludau, A. Onton, and W. Heinke, J. Appl. Phys. 45, 1846 (1974).
[8] J. Donecker, A. Gerhardt, and J. Wollweber, Mat. Sci. Engineerg. B 28, 18 (1994).

XPS STUDY OF THE PbSe/CaF$_2$(111) INTERFACE GROWN ON Si BY MBE

X.M. FANG *, W.K. LIU **, P.J. McCANN *, B.N. STRECKER* and M.B. SANTOS **
* School of Electrical and Computer Engineering and Laboratory for Electronic Properties of
  Materials, University of Oklahoma, Norman, OK 73019
** Department of Physics and Astronomy and Laboratory for Electronic Properties of Materials,
   University of Oklahoma, Norman, OK 73019

ABSTRACT

The initial stages of MBE growth of PbSe on CaF$_2$/Si(111) were studied by *in situ* XPS.
The surface reaction between CaF$_2$ and elemental Se is also studied as a comparison. Ca 2p, F 1s,
Pb 4f and Se 3d peaks all shift to lower binding energies (1.2 - 1.6 eV) with increasing PbSe
coverage. This indicates a strong interaction between the PbSe overlayer and the underlying CaF$_2$
and the formation of Pb-F and Ca-Se interfacial bonds. No chemically graded reaction products
are detected at the PbSe/CaF$_2$ interface. A transition layer of about 6 ML is observed which can
be partially accounted for by the open 3D structure of CaF$_2$ where three layers of atoms are
available for bonding with the deposited material. This structure allows interpenetration of the
PbSe and CaF$_2$ layers which necessarily leads to a thin transition layer. Based on our XPS results,
we propose a model for the bonding arrangements at the PbSe/CaF$_2$(111) interface.

INTRODUCTION

Epitaxial growth of high quality PbSe/CaF$_2$/Si(111) heterostructures is an important materials
technology for fabricating infrared detector arrays and tunable diode lasers [1,2]. The large band
edge discontinuities (>3eV) may also be utilized in the fabrication of quantum effect
heterostructure devices composed of thin layers of these materials. For these heterostructures,
the bonding arrangements and stoichiometry during interface formation can have a significant
impact on the ultimate device performance. While the CaF$_2$/Si(111) interface has been extensively
investigated [3], little has been reported on the PbSe/CaF$_2$ interface. In this work, we use *in situ*
XPS to study the initial stages of MBE growth of PbSe on CaF$_2$/Si(111) and propose models for
the bonding arrangements at the PbSe/CaF$_2$ heterointerface.

EXPERIMENT

Epitaxial growth of PbSe/CaF$_2$/Si(111) heterostructures was carried out in a single growth
chamber of an EPI modular GEN-II MBE system. Three-inch diameter p-type Si(111) substrates
were cleaned using a modified Shiraki etch [4] followed by a 2min. HF(10%) dip. We have
shown that high quality single crystalline CaF$_2$ can be grown on Si(111) by removing the
hydrogen-passivated layer at temperatures as low as 500°C and thereby minimizing undesirable
interfacial reactions arising from the high Se background [5]. PbSe films were grown on 200Å of
CaF$_2$ at substrate temperatures of 280°C by evaporating bulk PbSe in a low temperature effusion
cell held at 600°C. This corresponds to a BEP of 6.0×10^{-7} Torr and a growth rate of 0.054ML/s
as inferred from RHEED intensity oscillations [5]. For the deposition of Se, an EPI valved

cracker was used to produce a BEP of 1.1×10^{-7} Torr ($T_{bulk}/T_{cracker} = 220/425°C$). High structural quality of PbSe was confirmed by sharp (1×1) streaks in the RHEED patterns and smooth surfaces revealed by SEM and Nomarski microscopy.

To study the interface formation, PbSe growth was interrupted at various coverages and samples were transferred under UHV to an adjoining analysis chamber for XPS experiments. This chamber is equipped with a VG100AX hemispherical analyzer and an XR3E2 twin-anode X-ray source used in conjunction with a VGX900 data acquisition system (Fisons Instruments). The base pressure of this chamber was kept below 10^{-9} Torr during the experiments. XPS spectra were obtained by running the Alk$\alpha_{1,2}$ source (hυ = 1486.6eV) at a 15keV potential and a 10mA emission current. The constant analyzer energy mode was used with a pass energy of 20eV. All binding energies (BE) are referenced to F $1s$ = 685.0eV for bulk CaF_2.

RESULTS AND DISCUSSIONS

XPS Results

Fig. 1 shows the evolution of photoemission intensities of Ca $2p$, F $1s$, Pb $4f$ and Se $3d$ core level transitions after sequential deposition of PbSe onto the CaF_2/Si(111) surface. The Ca $2p$ and Pb $4f$ peaks are spin-orbit split into j = 1/2, 3/2 and j = 5/2, 7/2 doublets, respectively. Energy shifts of ~0.4eV were observed for the CaF_2 peaks after the deposition of less than 0.5ML of PbSe (plots (a) and (b) in Fig. 1). This probably arises from band-bending caused by charge transfer between the semiconductor and the insulator.

With increasing coverage, the Pb and Se peaks grow as well as shift to lower BE. Corresponding shifts and reduction in intensities can be observed in the Ca and F spectra. The Ca and F core levels are broadened with noticeable shoulders developed on the lower BE side at ~1ML coverage (encircled in plot (c) of Fig. 1). At this early stage, no preferential segregation of Ca nor F was detected, suggesting that the interfacial bonding involves both Ca and F atoms. These observations are indicative of PbSe overlayer–CaF_2 interaction and can be attributed to the formation of Pb-F and Ca-Se interfacial bonds. The ratio of F $1s$ to Ca $2p$ signals drops at higher coverages, probably due to the more effective shielding of the F atoms by the bigger Pb atoms.

Above 1ML, the Ca, F, Pb and Se peaks all shift in tandem to lower BE without any significant broadening of the peaks. This suggests that these atoms are now in a continuously changing environment at different stages of interface evolution. For CaF_2, this represents a progressive dilution of Ca and F in an increasingly PbSe-rich matrix. At the same time, the Pb $4f_{7/2}$ and Se $3d_{3/2}$ peak energies approach the bulk values of 136.55 and 52.85eV, respectively at ~6ML.

Earlier work involving LPE growth of PbSe on BaF_2 substrates revealed that selenium vapor reacts with BaF_2 to form reaction compounds [6]. During MBE growth of PbSe on BaF_2/CaF_2 buffer layers on Si, evidence of interfacial reactions is manifested as blisters formed when the CaF_2 layer is greater than the critical thickness of 20Å [7]. It was speculated that reaction with BaF_2 allowed migration of Se to the CaF_2 layer where it penetrated threading dislocations and reduced the plasticity of the layer. To investigate the possibilities of reaction product formation at the PbSe/CaF_2 interface, we examined the core level transitions during Se deposition on CaF_2/Si(111) surface. Clear breaks in the Se peak intensity against coverage plot (Fig. 2a) can be seen, suggesting the presence of interfacial compounds with different stoichiometries. This is consistent with LPE results where BaSe and $BaSe_3$ are formed when BaF_2 surface is exposed to Se vapor. In contrast to elemental Se deposition, PbSe deposition leads to a much smoother
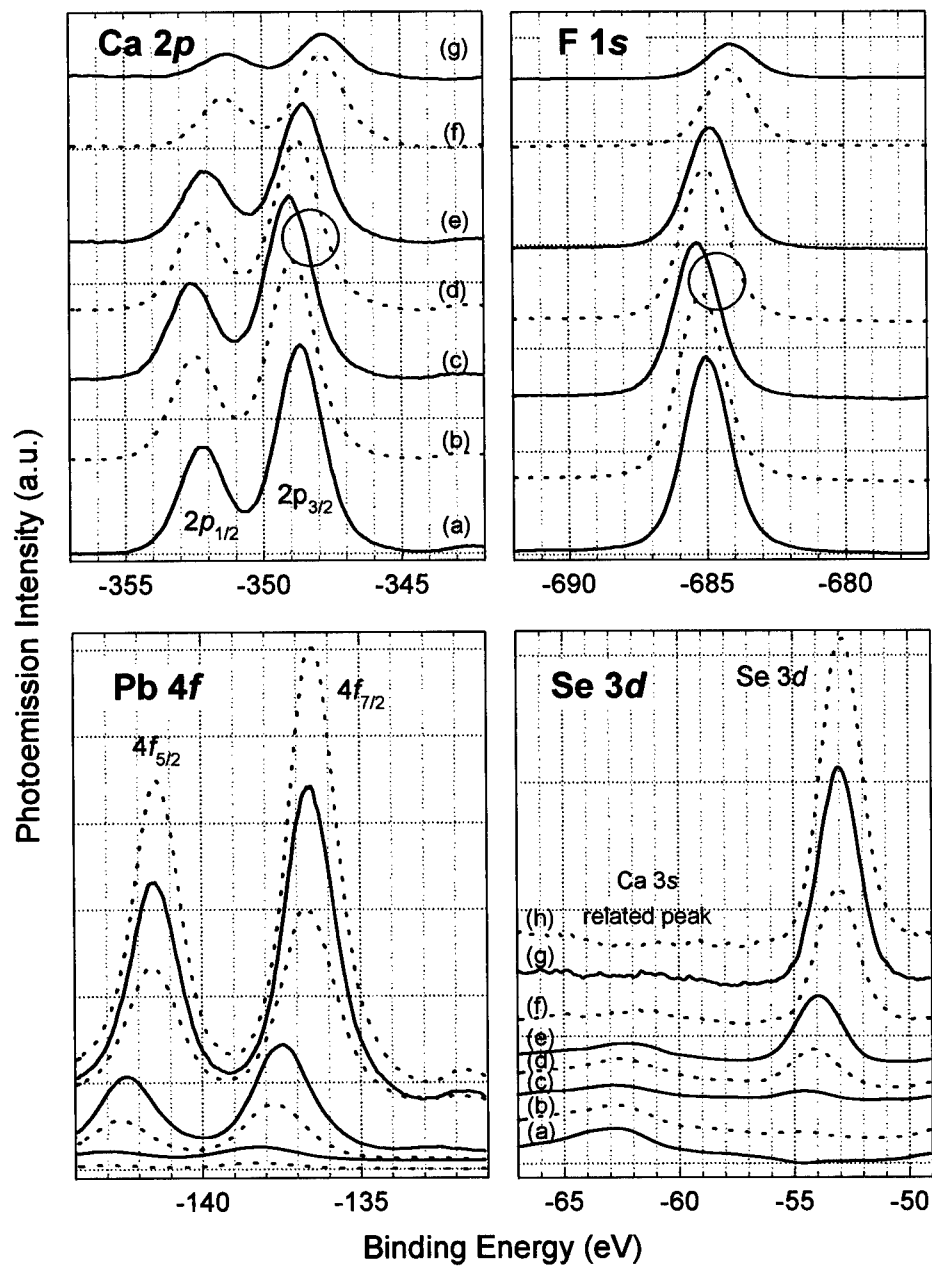
Figure 1. Evolution of photoemission intensities during sequential deposition of PbSe on CaF$_2$/Si(111). PbSe coverages: (a) 0, (b) 0.27ML, (c) 0.81ML, (d) 1.6ML, (e) 3.25ML, (f) 6.5ML, (g) 13ML and (h) 26ML.
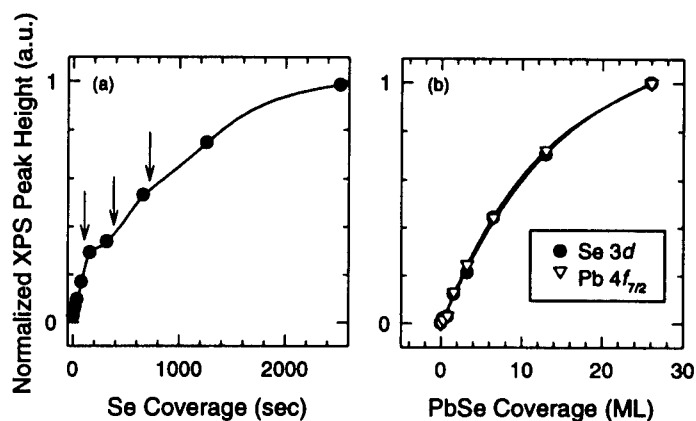
Figure 2. Variation of the normalized XPS overlayer peak heights as a function of coverage during the deposition of (a) Se and (b) PbSe on CaF₂/Si(111).
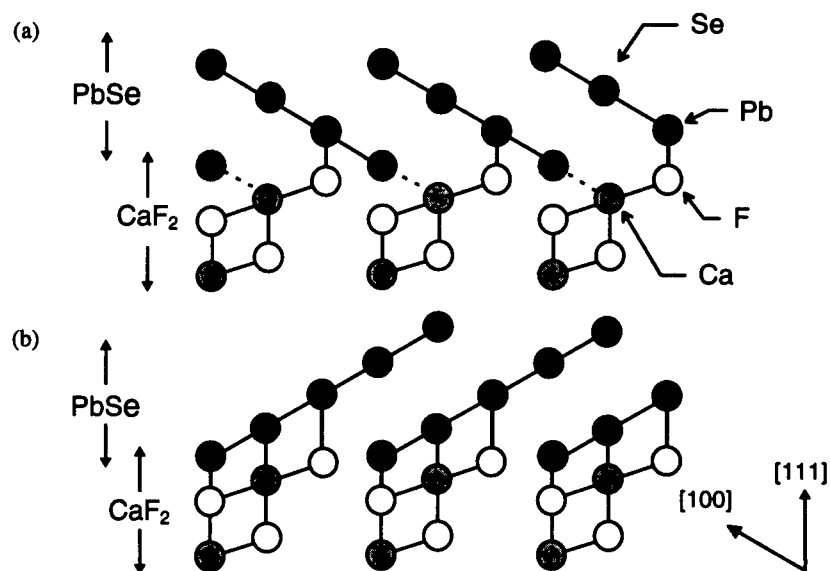
Figure 3. Models for the bonding arrangements at the PbSe/ CaF₂ (111) interface along the (01̄1̄) plane: (a) Pb atoms directly bonded to top-layer F atoms while Se atoms share bonds with three surrounding Ca atoms, (b) Pb atoms directly bonded to lower-layer F atoms and Se atoms bonded to Ca atoms residing directly below. The bonding arrangement in (b) is more energetically favorable [10].

variation of the Se (as well as Pb) peak intensity (Fig. 2b), indicating that the PbSe/CaF$_2$ interface is much more abrupt, with no evidence for the existence of chemically graded reaction products at the interface.

PbSe/CaF$_2$ Interfacial Bonding Arrangements

The fact that the CaF$_2$ and the PbSe overlayer BE shift in tandem implies that there is an orderly compositional transition through the PbSe/CaF$_2$ interface. The thickness of this transition layer, about 6ML, can be partially accounted for by the open three-dimensional structure of the CaF$_2$(111) surface. Three layers of atoms are available for bonding with deposited material: (1) a layer of F at the surface, (2) a layer of Ca 0.79 Å below the surface, and (3) another layer of F 1.58 Å below the surface. This structure allows interpenetration of the PbSe and CaF$_2$ layers which necessarily lead to a thin compositional transition layer.

Based on electrostatic arguments, it is reasonable to assume that only Pb-F and Ca-Se bonding occurs at the PbSe/CaF$_2$ interface. In addition, both PbF$_2$ and CaSe have stable cubic phases with lattice parameters (5.927Å and 5.924Å, respectively) [8,9] and hence bond lengths that lie between those of CaF$_2$ (a=5.464)Å and PbSe (a=6.126Å). This leaves two possible bonding arrangements for the interface as shown in Fig. 3. One consists of Pb atoms residing directly over and bonding to the top-layer of F atoms and of Se atoms residing directly over the lower-layer of F atoms but bonding to the three surrounding Ca atoms (Fig. 3a). The second consists of Pb atoms residing directly over and bonding to the lower-layer of F atoms and of Se atoms residing directly over and bonding to the layer of Ca atoms (Fig. 3b). Coexistence of these two bonding arrangements results in the growth of PbSe epilayers with twinned domains azimuthally rotated by (2n-1)π/3 with respect to each other. Diffraction from such a layer would show sixfold symmetry. This was not observed in the our RHEED patterns indicating that only one bonding arrangement exists for our structures. Our present XPS data, which supports the simultaneous formation of Pb-F and Ca-Se bonds at the interface, is consistent with both of these bonding arrangements but cannot unambiguously differentiate between them. It has, however, been suggested that equilibrium interactions favor the second bonding arrangement [10].

CONCLUSIONS

In situ XPS has been used to investigate the interfacial chemistry and bonding configurations between PbSe and CaF$_2$ grown on Si(111) substrates. Ca 2p, F 1s, Pb 4f and Se 3d peaks all shift to lower binding energies (1.2 - 1.6 eV) with increasing PbSe coverage. This indicates a strong interaction between the PbSe overlayer and the underlying CaF$_2$ surface and the formation of Pb-F and Ca-Se interfacial bonds. Unlike the Se/CaF$_2$ interface where interfacial compounds with different stoichiometries are present, no chemically graded reaction products are detected at the PbSe/CaF$_2$ interface. Instead, a transition layer of about 6 ML is observed which can be partially accounted for by the open 3D structure of CaF$_2$ where three layers of atoms are available for bonding with the deposited material. This structure allows interpenetration of the PbSe and CaF$_2$ layers which necessarily leads to a thin transition layer.

ACKNOWLEDGMENTS

REFERENCES

1. H. Zogg, A. Fach, C. Maissen, J. Masek, and S. Blunier, Optical Eng. **33**, 1440 (1994).
2. D.L. Partin, IEEE J. Quantum Electronics, **24**, 1716 (1988).
3. D. Rieger, F.J. Himpsel, U.O. Karlsson, F.R. McFeely, J.F. Morar, and J.A. Yarmoff, Phys. Rev. B, **34**, 7295 (1986).
4. A. Ishizaka and Y. Shiraki, J. Electrochem. Soc. **133**, 666 (1986).
5. P. J. McCann, X. M. Fang, W. K. Liu, B. N. Strecker and M.B. Santos, accepted for publication in J. Cryst. Growth (1996).
6. P. J. McCann and C. G. Fonstad, J. of Electr. Mater. **20**, 915 (1991).
7. V. Mathet, P. Galtier, F. Nguyen-Van-Dau, G. Padeletti, and J. Olivier, J. Cryst. Growth, **132**, 241 (1993).
8. G. Harbeke, in Landolt-Börnstein Numerical Data and Functional Relationships in Science and Technology, III/17f, edited by O. Madelung, H. Schulz and H. Weiss (Springer-Verlag, Berlin, 1983) p. 220.
9. P. Eckerlin and H. Kandler, in Landolt-Börnstein Numerical Data and Functional Relationships in Science and Technology, III/17f, edited by O. Madelung, H. Schulz and H. Weiss (Springer-Verlag, Berlin, 1983) p. 220.
10. D. K. Hohnke, H. Holloway, and M. D. Hurley, Thin Solid Films, **38**, 49 (1976).

GROUP II-VI DOWNCONVERTING PHOSPHORS

V. VALDNA, T. GAVRISH, J. HIIE, E. MELLIKOV, A. MERE
Tallinn Technical University, Tallinn, EE-0026, Estonia, vello@opto.ttu.ee

ABSTRACT

The efficiency of group II-VI solid solutions doped with chlorine and copper as X-ray downconverting phosphors for photodetectors is investigated. It is found that the phosphors based on the group II-VI compounds and prepared in oxygen-free medium can increase the photodetectors sensitivity to X-ray radiation more than one order of magnitude and enhance the photodetectors photovoltage versus X-ray radiant flux characteristic linearity.

INTRODUCTION

Wide bandgap group II-VI compounds ZnS, ZnSe and CdS are one of the most effective luminescence materials which enable to cover the spectral range from blue-green to near infrared, if solid solutions are formed. These materials can be used in electroluminescent displays [1, 2], for short-wavelength visible light emitting diodes and lasers [3-7] and as X-ray downconverting coatings on the photodetectors [8,9]. Recently, we investigated the Zn(SeTe) solid solutions and found that from these materials effective red phosphors can be fabricated, if Te excess which is formed at a thermal treatment, is removed [10].

In II-VI compounds two intense luminescence bands exist which are usable at room temperature. (1) Self-activated (SA) luminescence band which is formed due to the intrinsic host defects and one dopant. (2) Donor-acceptor pair (DAP) luminescence band which is formed when donor and acceptor codopants are used. Different background impurities in the initial material can supress or enhance the intensity value of these bands. The nearby located SA and DAP luminescence bands form one broad band whose spectral curve shape and band peak location can be varied by the used dopants, fluxing medium concentration and mixture composition.

The doping of luminescence materials with rare earth elements has attracted much attention last years [1, 11]. Rare earth elements have partially filled 4f shells which are well screened by outer closed orbitals $4s^2$ and $5p^6$. The intracentre transition of 4f electrons give rise to sharp emission spectra in various host materials [11].

The aim of this work was to investigate the efficiency of doped with Cl and Cu (ZnCd)S, (ZnCd)Se and Zn(SeTe) phosphors as X-ray downconverting coatings for photodetectors.

EXPERIMENT

ZnS, CdS, ZnSe, CdSe and ZnTe powders of semiconductor purity as starting materials were used. Mixed powders were heated with 5 wt% $ZnCl_2$ or $CdCl_2$ at 1250 K in the evacuated quartz ampoules, then cooled down to room temperature together with a tube furnace at a rate of ~ 1.2 Kmin^{-1}. $CuCl_2$ solution in water was used for the copper doping. Residual $ZnCl_2$ or $CdCl_2$ were removed from phosphors by the vacuum annealing at 800 K.

Scintillator caps for measurements were made from black paper. The inner side of the cap was coated with a phosphor layer on white paper using epoxy glue. X-ray tube 0.5BSV2-Cu with a copper anode was used as a X-ray source. The X-ray radiant flux value was determined with a X-ray dose meter DRG3-02. The photovoltage of the silicon photodiode S1336-8BK coated with a scintillator cap was registered with the electrometer ITN-6, with a 100 MΩ load resistance.

RESULTS

Photodiode S1336-8BK photovoltage U_F without and with the scintillator caps of different phosphors at the radiant flux value 23.5 μRs^{-1} (14.5 keV) is presented in Table I. The highest U_F values were achieved with the ZnS and ZnSe-based phosphors.

Table I
Photodiode S1336-8BK photovoltage U_F with the caps of different phosphors at radiant flux 23.5 μRs^{-1} (14.5 keV). Load resistance 100 MΩ.

No	Phosphor	Dopants	U_F, mV
1	-	-	1.22
2	$Zn_{0.8}Cd_{0.2}S$	Cl, Cu	46.2
3	$Zn_{0.7}Cd_{0.3}S$	Cl, Cu	46
4	$Zn_{0.6}Cd_{0.4}S$	Cl	25.6
5	$Zn_{0.6}Cd_{0.4}S$	Cl, Cu	38.8
6	$Zn_{0.98}Cd_{0.02}Se$	Cl, Cu	26.5
7	$Zn_{0.915}Cd_{0.085}Se$	Cl, Cu	29.5
8	$Zn_{0.85}Cd_{0.15}Se$	Cl, Cu	24.5
9	ZnSe	Cl	5.7
10	ZnSe	Cl, Cu	24.7
11	$ZnSe_{0.98}Te_{0.02}$	Cl, Cu	26.5
12	$ZnSe_{0.95}Te_{0.05}$	Cl	23.5
13	$ZnSe_{0.95}Te_{0.05}$	Cl, Cu	31.8
14	$ZnSe_{0.9}Te_{0.1}$	Cl, Cu	20.8

The dependence of a photodiode photovoltage upon a X-ray radiant flux value is presented in Fig. 1. The diode photovoltage versus X-ray radiant flux characteristics with and without (ZnCd)S phosphor coatings, measured at different times, were different. In Sept. 1994 we measured with the (ZnCd)S phosphor coatings nearly linear characteristics up to the X-ray radiant flux values of 10^4 μRs^{-1}. Some sublinearity of the characteristics can be caused by the phosphor to photodiode conversion losses (photodiode has a glass window). In May 1996 with the same (ZnCd)S phosphors and with (ZnCd)Se and Zn(SeTe) phosphors diode photovoltage began to
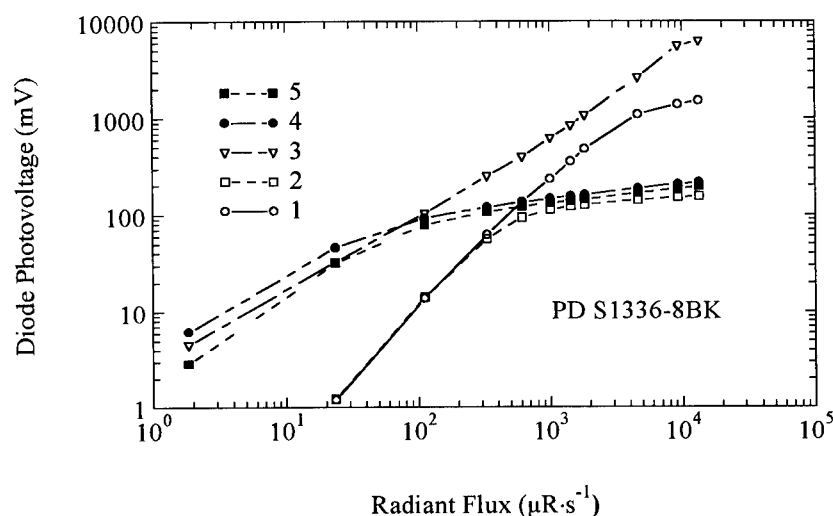
Fig. 1. *Photodiode S1336-8BK photovoltage versus X-ray radiant flux. (1) and (2)*
Without coating. (3) and (4) With $Zn_{0.8}Cd_{0.2}S:Cu:Cl$ phosphor cap. (5) With
$ZnSe_{0.95}Te_{0.05}:Cu:Cl$ phosphor cap. (1) and (3) are measured in Sept. 1994.
(2), (4) and (5) are measured in May 1996.

saturate from the X-ray radiant flux value of $\sim 10^2 \ \mu Rs^{-1}$ whereas the results were the same at low
X-ray radiant flux values. After the checkup of the X-ray tube we concluded that the earlier
measurements at high X-ray radiant flux values caused some alterations in the photodiode
structure. From the group II-VI solid solutions ZnS-based phosphors have the highest conversion
efficiency. Doped with copper and chlorine ZnS-based phosphors have remarkable afterglow
whereas afterglow is not detected at doped with only one dopant chlorine ZnS-based phosphors.
However, its conversion efficiency is smaller too. ZnSe-based phosphors can be superior at low X-
ray radiant flux levels due to a much smaller time constant of these phosphors.

II-VI photoconductive cells have oxide layer on the cell surface due to a fabrication
technology. We measured the enhancement of the sensitivity up to 2 orders of magnitude and
much better linearity of the cell resistance vs. X-ray radiant flux characteristics using the Cd(SeTe)
photoconductive cell with a phosphor cap.

CONCLUSIONS

We have investigated the efficiency of (ZnCd)S, (ZnCd)Se and Zn(SeTe) solid solutions as
downconverting phosphors for the photodetectors. We have found that these compounds enabled
more than one order of magnitude to enhance the silicon photodiode sensitivity to a X-ray radiant

465

flux and to improve the linearity of the photodiode photovoltage versus X-ray radiant flux characteristic.

ACKNOWLEDGMENTS

REFERENCES

1. P.D. Rack, A. Naman, P.H. Holloway, S-S. Sun and R.T. Tuenge, MRS Bulletin 21, 49 (1996).

2. S. Shionoya, Materials Forum 15, 132 (1991).

3. W. Gebhardt, B. Hahn, H. Stanzl and M. Deufel, J. Crystal Growth 159, 238 (1996).

4. H. Kukimoto, Materials Science Forum 143-147, 385 (1994).

5. D. Olego, Europhys. News 26, 112 (1995).

6. A. Ishibashi, J. Crystal Growth 159, 555 (1996).

7. A.V. Nurmikko, H. Jeon, R.L. Gunshor and J. Han, J. Crystal Growth 159, 644 (1996).

8. M.M. Blouke et al., Applied Optics 19, 3318 (1980).

9. C.I. Coleman, Applied Optics 20, 3693 (1981).

10. V. Valdna, J. Hiie, U. Kallavus, A. Mere and T. Piibe, J. Crystal Gowth 161, 177 (1996).

11. P.N. Favennec, H. L'Haridon, M. Salvi, D. Moutonnet and Y. LeGuillou, Electronics Letters 25, 718 (1989).

SPUTTER DEPOSITION OF SEMICONDUCTOR SUPERLATTICES FOR THERMOELECTRIC APPLICATIONS

ANDREW V. WAGNER, RONALD J. FOREMAN, JOSEPH C. FARMER,
TROY W. BARBEE JR.
Chemistry and Materials Science Department, Lawrence Livermore National Laboratory
7000 East Avenue, Livermore, CA 94550 USA

ABSTRACT

Theoretical dramatic improvement of the thermoelectric properties of materials by using quantum confinement in novel semiconductor nanostructures has lead to considerable interest in the thermoelectric community. Therefore, we are exploring the critical materials issues for fabrication of quantum confined structures by magnetron sputtering in the lead telluride and bismuth telluride families of materials. We have synthesized modulated structures from thermoelectric materials with bilayer periods of as little as 3.2 nm and shown that they are stable at deposition temperatures high enough to grow quality films. Issues critical to high quality film growth have been investigated such as nucleation and growth conditions and their effect on crystal orientation and growth morphology. These investigations show that nucleating the film at a temperature below the growth temperature of optimum electronic properties produces high quality films. Our work with sputter deposition, which is inherently a high rate deposition process, builds the technological base necessary to develop economical production of these advanced materials. High deposition rate is critical since, even if efficiencies comparable with CFC based refrigeration systems can be achieved, large quantities of quantum confined materials will be necessary for cost-competitive uses.

INTRODUCTION

The thermoelectric effect uses the thermal energy transported by charge carriers to produce solid-state cooling with electrical current flow or, conversely, to take advantage of thermal diffusion of charge carriers in a thermal gradient to produce a current. The use of thermoelectric materials to generate current has a wide range of applications, ranging from temperature sensing "thermocouples" to electrical power generators for interplanetary spacecraft. The application of thermoelectrics for cooling or heating is primarily limited by its efficiency which is lower than that of conventional gas cycle refrigeration. However, since thermoelectric devices have no moving parts, they can easily be made very small and relatively inexpensively. They also produce no vibrations, making them ideal for coupling with optical or infrared sensors. Although they have not replaced CFC and related refrigeration systems for large-scale cooling of food or buildings where efficiency is very important, thermoelectric coolers are being mass produced for portable food coolers where their small size and light weight are important.

Recently developed semiconductor technology and theory may provide a route to engineering higher efficiency materials, which could greatly expand the use of thermoelectric materials bringing the advantage of solid-state coolers to a substantially broader range of applications. Theoretical predictions by Hicks and Dresselhaus suggest that using 2D quantum confinement of the charge carriers in multilayer thermoelectric materials may lead to a substantial increase in the thermoelectric figure of merit, Z.[1,2] The figure of merit is defined as:

$$Z = \frac{S^2}{\Lambda \rho} \qquad (1)$$

where ρ, S, and Λ are the electrical resistivity, Seebeck coefficient, and the thermal conductivity, respectively. Multiplying by temperature, T, gives the dimensionless figure of merit, ZT: the materials parameter which characterizes the optimal performance of the material in a device, both in terms of efficiency as well as maximum achievable cooling. High Z material could enable the use

of thermoelectric cooling for important applications which are currently beyond the accessible temperature range for thermoelectric materials such as high temperature superconductor devices. The increase in efficiency would also be of great benefit to cooling infrared detector and night vision equipment which are battery powered.

Enhanced thermoelectric properties have been recently reported in the quantum well layers of PbTe/Pb$_{1-x}$Eu$_x$Te multilayer samples synthesized by molecular beam epitaxy.[3,4] However, to make thermoelectric multilayer materials commercially viable, it is essential to extend the MBE work and grow structures with a high Z by established high deposition rate techniques. The expertise necessary to grow such materials by sputter deposition has been developed at Lawrence Livermore National Laboratory through extensive work on multilayer x-ray optics and other novel multilayer materials.[5,6] At LLNL, we apply this multilayer sputter deposition technology to demonstrate the effectiveness of magnetron sputtering to synthesize thermoelectric multilayer materials with potential for 2D quantum well behavior. The ability to synthesize state-of-the-art thermoelectric materials in thin film form is essential to using thin film technology to engineer the properties of these materials. We thus begin our work by focusing on the understanding and control of the composition and structure of thin films of the individual materials needed for the well and barrier in the multilayer sample. We present parallel work on two families of semiconductor materials which are good candidates for achieving improved ZT through quantum confinement in multilayer films. One system is based on the good thermoelectric material lead telluride, PbTe, where a compatible barrier material, necessary for making quantum well structures, can be made by the partial substitution of Eu for Pb which widens the bandgap. The other system considered here is the bismuth telluride solid solution with antimony and selenium, $(Bi_{1-x}Sb_x)_2(Te_{1-y}Se_y)_3$, which is presently the best room temperature thermoelectric material. In this system the bandgap can be widened to form barrier material for quantum well structures by changing the ratios of the constituent materials.

EXPERIMENTAL PROCEDURE

We synthesized all the films for these experiments using magnetron sputtering. The sputter system is cryogenically pumped and achieves base pressures of approximately 1×10^{-7} torr prior to sputtering. Substrates are mounted on an electrically-isolated heated stage which rotates below two or more magnetron sputtering guns. The sputter sources are usually operated at an Ar pressure around 16 millitorr at a power of 10 W giving deposition rates of about 5 Å/s directly under the gun. Multilayer samples are synthesized by alternately positioning the substrates under the two magnetron sputter sources. Single-layer films are made by positioning the substrate directly below a single source. Sample doping is achieved by periodically passing a growing film under a second magnetron source sputtering dopant material at a low rate. A computer controls the position and slew rate of the stage, as well as the power to the sputter sources, allowing automated deposition of complex layered structures. Temperature, gas pressure, and gun parameters are logged by the computer during the deposition.

Shields are mounted around the guns to reduce cross contamination between the sputter sources. These shields are heated to form a hot walled environment around the deposition area which serves two purposes. First, it helps maintain the substrate temperature at the deposition temperature, which is important for thin mica or kapton substrates which are in radiative equilibrium with their surroundings. Second, re-evaporation of Te from these hot surfaces maintains an overpressure of this high vapor pressure element above the substrate. The combination of the hot wall technique and excess Te incorporated in the target is required for the growth of stoichiometric films.

RESULTS

This section presents the results from investigation of the single-layer and multilayer films of two families of thermoelectric materials. High quality single-layer films must be synthesized and understood in order to effectively fabricate multilayer films. Therefore, we first present work on
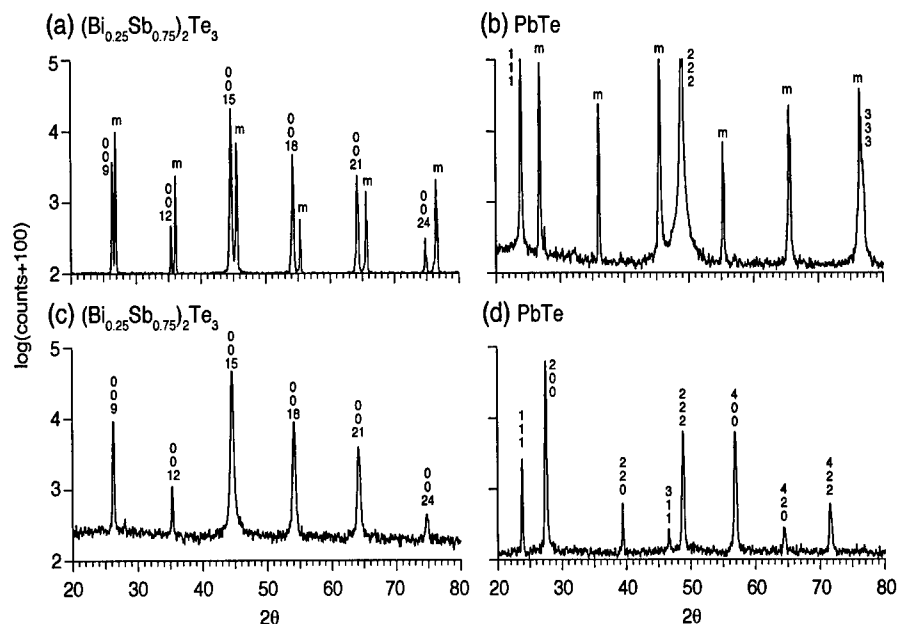
Figure 1: X-ray diffraction scans. a) $(Bi_{0.25}Sb_{0.75})_2Te_3$ film on mica showing strong c axis orientation. b) PbTe film on mica showing a well textured (111) film. c) $(Bi_{0.25}Sb_{0.75})_2Te_3$ film on glass showing strong c axis orientation. d) PbTe film on glass showing random texture. Mica substrate reflections are labeled m.

control of growth morphology and electrical quality of PbTe and $(Bi_{1-x}Sb_x)_2(Te_{1-y}Se_y)_3$ single-layer films. Then, preliminary results are presented for the PbTe/Pb$_{1-x}$Eu$_x$Te multilayer system, and our success with the synthesis of compositionally modulated $(Bi_{1-x}Sb_x)_2(Te_{1-y}Se_y)_3$ multilayers.

Control of growth morphology for single-layer films

Single-layer film growth morphology is critical to the subsequent growth of two component multilayer films. It is important that growth be controlled in such a way as to maintain a planar growth surface since growth topography dictates both interfacial and quantum well layer quality in multilayer films. Increasing growth temperature was found to improve electrical properties in both systems considered here as long as stoichiometry was maintained. Above an optimal temperature, however, surface morphology was observed to degrade. Increased surface mobility at high temperatures leads to faceting of individual grains. This was found to be a limiting problem in the $(Bi_{1-x}Sb_x)_2(Te_{1-y}Se_y)_3$ system where occasional misoriented grains quickly grew into large platelets at high temperatures.[7] Surface grooving along grain boundaries is also observed in films grown at high temperatures. Not only does the temperature affect crystal growth, it also has a strong effect on nucleation of the films. At low deposition temperatures, a large number of small grains nucleate and films are observed to grow with a fine-grained columnar crystal structure. Films grown at higher temperatures have higher atomic surface mobility and are observed to have a larger grain size. Increasing the temperature even more led to degradation of the crystallographic texture.

In both material systems, it was found that the optimal growth sequence was to nucleate the films at a temperature below that used for growth. For PbTe, smooth well oriented films were nucleated at a temperature of 250°C and then the temperature was raised to 315°C during growth. Higher temperatures were found to work best for $(Bi_{1-x}Sb_x)_2(Te_{1-y}Se_y)_3$ with nucleation at 350°C and growth at 380°C.

use	material	thickness	Seeb.	resistivity	thermal conductivity	ZT	Hall mobility
		μ	$\mu V/K$	$10^{-3}\Omega cm$	$W/cm^2 K$		$cm^2/V\ sec$
reference	PbTe	bulk	-200	1.5	0.02	0.4	1600
well	PbTe	1	-125	1.25	1	0.19	320
reference	$Bi_{0.5}Sb_{1.5}Te_{2.9}Se_{0.1}$	bulk	220	1.0	0.014	1.0	300
well	$Bi_{0.5}Sb_{1.5}Te_3$	0.88	118	0.53	1	0.56	130
barrier	$Bi_{0.5}Sb_{0.5}Te_{1.5}Se_{1.5}$	0.56	210	5.3	1	0.18	37
multilayer	$(Bi_{1-x}Sb_x)_2(Te_{1-y}Se_y)_3$	0.7	140	1.4	1	0.30	50

Table 1: Measured electrical properties of single layer and multilayer films. State of the art bulk values are also listed as a reference for comparison with measured values of the films. The thermal conductivity used for calculation of ZT was that of the bulk. This is only a rough guide in the $(Bi_{1-x}Sb_x)_2(Te_{1-y}Se_y)_3$ system since the thermal conductivity will depend on the composition as well as doping levels.

Films were grown on BaF_2, Mica, glass, silicon nitride and kapton substrates. Those deposited on freshly cleaved (111) BaF_2 and Mica under these conditions have a mirror like surface. SEM investigation at 30,000X showed a flat featureless surface on these specular films only occasionally interrupted by a misaligned grain. X-ray diffraction on the specular films shows they are well oriented. Bi_2Te_3 has a rhombehedral structure related to that of Bi, and is composed of planes of Bi and Te atoms.[8] As shown in Figure 1a, films are found to grow along the c direction (with respect to the hexagonal representation of the structure). The inplane crystal structure of films grown on mica was found by plan view TEM electron diffraction to be a mosaic single crystal. Conversely, Figure 1b shows PbTe which has the NaCl structure grows with a strong (111) texture. While BaF_2 is a good choice for a substrate being nearly lattice matched with both films, we show here that excellent growth morphology can also be achieved on mica. Mica is a good substrate for our thermoelectric investigations since it cleaves into large atomically smooth surfaces with hexagonal symmetry and is much easier to work with than BaF_2. It also makes a good substrate for device work since it can be cleaved into very thin sheets. This is important for thin film devices since thermal conduction in the substrate degrades device performance.[9]

Growth of oriented films on the amorphous substrates was more difficult. As shown in Figure 1c, oriented growth has been achieved in the $(Bi_{1-x}Sb_x)_2(Te_{1-y}Se_y)_3$ system. However for PbTe films grown on amorphous substrates, the x-ray diffraction shows a nearly random orientation of the film (Figure 1d). The differing growth rates of the different crystalline orientations then cause the surface to become faceted and rough at deposition temperatures required to achieve the best thermoelectric performance.

Electrical properties

Doping is a critical issue for electrical performance in semiconductor thermoelectric materials. For both of these materials Te tends to re-evaporate from the surface during growth so maintaining an excess supply of Te to the growth surface is critical in achieving stoichiometry. The measured Seebeck coefficient and resistivity of otherwise undoped films is a powerful method for monitoring the stoichiometry since excess of either component in compound semiconductors will act as a dopant. $(Bi_{0.25}Sb_{0.75})_2Te_3$ films were found to be p-type showing that they were always slightly Te deficient despite the excess Te. Changing the Te overpressure by changing the temperature of the shields around the guns, however, was used as a means of controlling the doping level.

Undoped PbTe films were of very high resistivity and either n or p-type depending on exact growth conditions, demonstrating good stoichiometry. To optimize the thermoelectric properties of PbTe, a small amount of Bi was added to the film during deposition by occasionally sweeping the growing film under a second sputtering gun which was depositing Bi at a low rate. With Bi
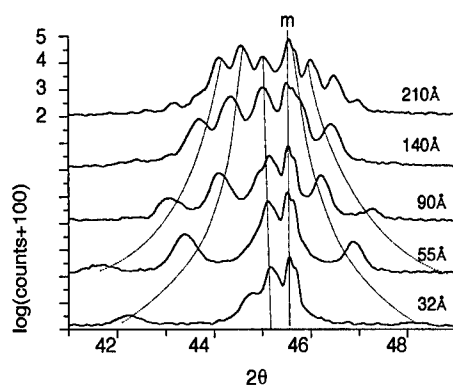
Figure 2: X-ray diffraction of a series of $Bi_{0.5}Sb_{1.5}Te_3/Bi_{0.5}Sb_{1.5}Te_{1.5}Se_{1.5}$ multilayer films of varying thickness. The mica substrate peak is labeled m. The central peak is the films (0,0,15) peak with multilayer satellite peaks on either side.

Figure 3: Bright field TEM micrograph of the 140Å period $Bi_{0.5}Sb_{1.5}Te_3/Bi_{0.5}Sb_{1.5}Te_{1.5}Se_{1.5}$ multilayer film. Diffraction contrast with a Fresnel defocus condition clearly shows the layering.

doping, the film resistivity dropped by about three orders of magnitude and showed consistent n type conductivity. Although the doping was introduced in a periodic very thin layer, there is no evidence it did not diffuse uniformly into the film either by segregation at the growth surface or by bulk diffusion.

Table 1 lists values for the electrical properties of single layer films measured at room temperature. Care was taken to use insulating substrates and AC measurement techniques while making these measurements as previously reported[10]. Preliminary results from in-plane thermal conductivity measurements of these thin films indicate that for PbTe films the thermal conductivity is very close to that of the bulk. For $(Bi_{0.25}Sb_{0.75})_2Te_3$, however, the thermal conductivity in the thin film samples measured was higher than reported for optimized bulk material, presumably as a result of the very high doping level in the particular samples investigated. For this reason, bulk values of the thermal conductivity will be assumed in calculating the dimensionless figure of merit in Table 1 until these results can be confirmed.

Multilayer systems

Having achieved the desired growth surface in single layer PbTe films, an effort was made to grow $PbTe/Pb_{1-x}Eu_xTe$ multilayer films. Unfortunately, only weak evidence for multilayer structure was found by x-ray diffraction in these films. This has been attributed to oxidation of the Eu which is thought to have occurred during preparation of the sputter target by powder processing.

In the $(Bi_{1-x}Sb_x)_2(Te_{1-y}Se_y)_3$ system, we have achieved considerable success in growing multilayer structures by varying the Te:Se ratio between layers. It was thought that by exchanging Se for Te in this solid solution the bandgap could be widened to form a barrier material for a thermoelectric quantum well structure. Multilayer structures have been grown using the optimum deposition parameters determined from the single-layer experiments discussed earlier. Satellite peaks in the high angle x-ray diffraction patterns (Figure 2) show that multilayer materials have been grown with evidence of periodicity in structures with bilayer repeat lengths as small as 32Å. In Figure 3, TEM of a 140Å bilayer repeat length film shows clear layering with approximately equal layer thickness. These results show that it is possible to grow multilayer structures in the $(Bi_{1-x}Sb_x)_2(Te_{1-y}Se_y)_3$ system by magnetron sputtering and that they are stable at the temperatures which have been determined necessary to grow optimal electrical quality films.

471

DISCUSSION

For single layer films, the dimensionless figure of merit of sputter deposited films is below that of optimum bulk material. This difference is a result of additional charge carrier scattering in these thin films as can be seen from Hall mobility measurements shown in Table 1. Charge carrier scattering either from impurities or from matrix or dopant atoms on the wrong site are thought to be the cause of the reduced mobility. Considerable improvement in the figure of merit is expected by the reduction in chamber background pressure during deposition, which is caused by outgasing from the heated shield assemblies.

In Table 1 the electrical properties of the $(Bi_{1-x}Sb_x)_2(Te_{1-y}Se_y)_3$ multilayer films are listed besides those of the single layer films. The failure to achieve enhancement in the dimensionless figure of merit in these films can be attributed to insufficient barrier height of the barrier material. Infrared spectroscopy has been used to examine barrier height in these materials and little difference between proposed barrier and well materials is observed. Results of our IR investigation are difficult to interpret, however, because of high doping levels combined with interference fringes in these thin films.

Although the barrier composition chosen in the work to date is not adequate to produce quantum confinement it is possible that by changing the composition a wider bandgap material can be found. Several other elements also form limited solid solutions with this system and are potential candidates as barrier materials.

CONCLUSIONS

The conditions for the growth of PbTe and $(Bi_{1-x}Sb_x)_2(Te_{1-y}Se_y)_3$ thermoelectric thin films by magnetron sputtering have been optimized. By nucleating the film at a temperature below the growth temperature, smooth well oriented films have been grown on both BaF_2 and mica. Structures with the appropriate dimensions for quantum confinement have been fabricated from thermoelectric materials using sputtering. These structures have been shown to be stable at deposition temperatures necessary to grow high quality materials. In order to achieve quantum confinement in the $(Bi_{1-x}Sb_x)_2(Te_{1-y}Se_y)_3$ system, higher bandgap barrier materials are needed which are compatible with the growth of quality thin film thermoelectric materials developed here.

ACKNOWLEDGMENTS

REFERENCES

1. L.D. Hicks, M.S. Dresselhaus, *Phys. Rev. B* **47**, 12727 (1993).
2. L.D. Hicks, M.S. Dresselhaus, *Appl. Phys. Lett.* **63**, 3230 (1993).
3. L.D. Hicks, T.C. Harman, X. Sun, and M.S. Dresselhaus, *Phys. Rev. B Rapid* **53**, 10493 (1996).
4. T.C. Harman, D.L. Spears and M.J. Manfra, *Journal of Electronic Materials* **25**, 1121 (1996).
5. T.W. Barbee, Jr., in *Synthetic Modulated Structures*, ed. L. Chang and B.C. Giessen, (Academic Press, New York, 1985) pp. 313-337.
6. T.W. Barbee, Jr., *Physica Scripta*, **T31**, 147 (1990).
7. A.V. Wagner, R.J. Foreman, L.J. Summers, T.W. Barbee, J.C. Farmer, in *Proc. of the XV International Conference on Thermoelectrics*, Pasadena, CA 1996 (IEEE, Piscataway, NJ) pp. 459-463.
8. A. Krost, P. Grosse, in *Physics of Narrow Gap Semiconductors*, edited by E. Gornik, H. Heinrich, L. Palmetshofer (Lecture Notes in Physics, **152**, NY : Springer, 1982) pp 49-53.
9. A.V. Wagner, R.J. Foreman, L.J. Summers, T.W. Barbee, J.C. Farmer, in *Proc. of the XV International Conference on Thermoelectrics*, Pasadena, CA 1996 (IEEE, Piscataway, NJ) pp. 269-273.
10. A.V. Wagner, R.J. Foreman, L.J. Summers, T.W. Barbee, J.C. Farmer, in *Proc. 30th Intersociety Energy Conversion Engineering Conference* **3**, Orlando, FL (ASME, NY, 1995) pp. 87-92.

SURFACE CHARGE GRATING IN THE TRANSVERSE GEOMETRY HOLOGRAPHIC RECORDING THIN FILM DEVICES

QINGNAN WANG, DOYLE A. TEMPLE
Department of Physics, Hampton University, Hampton, VA 23668,
wong@gprc.hamptonu.edu

ABSTRACT

We have used a two-dimensional charge transport model to study edge effects in photorefractive thin films. Our result shows that in addition to the bulk space charges, the large surface charges near the edges make a significant contribution to the space charge field. Quadratic electro-optic material were used as an example to study the surface-charge-layer-field quantitatively. The conditions for the device performance be dominated by either surface charge or bulk trap charges are clearly demonstrated .

INTRODUCTION

Transverse-applied-field thin film photorefractive gratings have been studied extensively in both the transmission and reflection geometry [1-4]. Typically, one-dimensional transport equations are used to calculate the space charge field [1,5,6]. However, the thin film devices such as multiple quantum well structures, very often may be operated with a fringe spacing much larger than the film thickness. This requires a two dimensional charge transport model to fully understand the device characteristics. For the transverse geometry, Aguilar, et.al. recently studied the impact of thin film edge effects on the initial photorefractive recording rate within the short time approximation and their result exhibited the important role of the vertical field components introduced by edge effects of the material [7]. However, their theory is limited to an initially short time period and no information about the steady state was obtained. In this paper, a model is developed for the charge transport in which the two dimensional nature of the device is explored. Our result indicates the presence of a large surface charge layer near the boundary causing the several key figures of merits of the device, such as the trap limiting field, to have different physical meanings from that of the bulk case.

THEORY

Consider two plane waves I_r and I_s intersecting in a photorefractive thin film in the transverse geometry in which both of the external electric field E_0 and the wave grating vector $\mathbf{K}$ are along x direction which is in parallel to the film plane. Starting from the standard charge transport rate equations for one photocarriers, we have [5]

$$\frac{\partial N_D^i}{\partial t} = (sI + \beta)(N_D - N_D^i) - \gamma n N_D^i \tag{1}$$

$$\frac{\partial n}{\partial t} - \frac{\nabla \cdot \mathbf{J}}{e} = \frac{\partial N_D^i}{\partial t} \tag{2}$$

$$\mathbf{J} = e\mu n\mathbf{E} + \mu k_B T \nabla n \tag{3}$$

$$\nabla \cdot \mathbf{E} = -\frac{e}{\varepsilon_0 \varepsilon}(n - N_D^i + N_A) \tag{4}$$

$$J_y = 0, \quad \text{for } y = \pm \frac{L}{2} \tag{5}$$

where $I(x) = I_0[1 + m \cos(Kx)]$ is the fringe pattern, $I_0 = I_r + I_s$ is the total optical intensity, m is the modulation index, N_D^i is the density of ionized donors, N_A is the density of shallow acceptors, n is the density of free electrons, γ is the electron recombination constant for donors, J is the current density, E is the total electric field, μ is the electron mobility, and the photovoltaic effect is assumed to be zero. The boundary condition Eq.(5) assumes that there is no current flow perpendicular to the grating at the edges.

Within the small modulation approximation, the solution of the rate equations takes the form

$$\begin{pmatrix} n \\ N_D^i \end{pmatrix} = \begin{pmatrix} n_0 \\ N_{D0}^i \end{pmatrix} + e^{i(\omega t + Kx)} \begin{pmatrix} n_1 \\ N_{D1}^i \end{pmatrix}. \tag{6}$$

It is easy to show that the zero order solution remain the same as the bulk case while the first-order solutions compose of three terms.

$$n_1 = n_a + 2n_b \cosh(gKy) + 2n_c \sinh(gKy), \tag{7}$$

$$N_{D1}^i = N_a + 2N_b \cosh(gKy) + 2N_c \sinh(gKy), \tag{8}$$

where n_a and N_a are the solutions for the bulk case and

$$g = \sqrt{\frac{(i\omega - i\Gamma_{Ee} + \Gamma_{De} + \Gamma_{Re} + \Gamma_{die})(i\omega + \Gamma_{Ie}) + \Gamma_{Re}(\Gamma_{die} - \Gamma_{Ie})}{(i\omega + \Gamma_{Ie})\Gamma_{De}}} \tag{9}$$

The rates in the above expression is given in Ref. 5.

In order to get the analytic expression for the first-order solutions, the relation between the first harmonics of the space charge density and the space charge field is required. In the bulk case, Poisson's equation is easily solved since the gradient operator can simply be replaced by iK. However, the situation here becomes much more complicated when the two-dimensional nature of thin film devices is included. The first harmonic of the potential for the space charge densities of Eq.(8) is given by

$$\phi_1 = \phi_a + \phi_b \tag{10}$$

where

$$\phi_a = \frac{eN_a}{K^2\varepsilon_0\varepsilon}[1 - \cosh(Ky)e^{-\delta}] \tag{11}$$

$$\phi_b = \frac{eN_b}{K^2\varepsilon_0\varepsilon}[e^{-\delta}(\frac{e^{g\delta}}{g-1} - \frac{e^{-g\delta}}{g+1})\cosh(Ky) - \frac{2}{(g^2-1)}\cosh(gKy)] \tag{12}$$

ε is dielectric constant, and δ is defined as

$$\delta = \frac{KL}{2}. \tag{13}$$

Applying Eq.(10) to the boundary conditions Eq.(5), we get

$$\frac{N_a}{N_b} = 2ge\delta \frac{\sinh(g\delta)}{\sinh(\delta)} (\frac{\Gamma_{De}(i\omega + \Gamma_{Ie})}{\Gamma_{Re}\Gamma_{die}} - \frac{1}{g^2-1}) + (\frac{e^{g\delta}}{g-1} - \frac{e^{-g\delta}}{g+1}) \tag{14}$$

STEADY STATE SURFACE CHARGE LAYERS

Many of the experiments in transverse geometry have been performed under the steady state conditions. Therefore, only the steady state solution is considered in detail here. Taking $\omega = 0$ for Eq. (14) gives

$$\frac{N_a}{N_b} = 2ge\delta \frac{\sinh(g\delta)}{\sinh(\delta)} (\frac{E_D}{E_q} - \frac{1}{g^2-1}) + (\frac{e^{g\delta}}{g-1} - \frac{e^{-g\delta}}{g+1}) = 2ge\delta \frac{\sinh(g\delta)}{\sinh(\delta)} \frac{-iE_0}{E_q} \frac{1}{g^2-1} + (\frac{e^{g\delta}}{g-1} - \frac{e^{-g\delta}}{g+1}) \quad (15)$$

where the relevant parameters above are given in TABLE I.

TABLE I. The parameters for the steady state

$g = \sqrt{\frac{E_q}{E_d} + 1 - \frac{iE_0}{E_d}}$	Trap-limited-field for bulk $\quad E_q = \frac{eN_T}{\varepsilon\varepsilon_0 K}$
Diffusion field $\quad E_d = K\frac{k_B T}{e}$	Effective-trap-density $\quad N_T = \frac{N_A(N_D - N_A)}{N_D}$
Debye Length $\quad L_D = \sqrt{\frac{\varepsilon\varepsilon_0 k_B T}{e^2 N_T}}$	Trap-limited-field for thin film $\quad E_{q0} = \frac{eN_T L}{2\varepsilon\varepsilon_0}$

The N_b term in Eq. (8) is truly a surface charge term because its space charge is concentrated within a small thickness ΔL, defined as

$$\Delta L \approx \frac{1}{|g|K} \approx \begin{cases} L_D = \sqrt{\frac{\varepsilon\varepsilon_0 k_B T}{e^2 N_T}} & , \text{ for } E_0 \ll E_q \\ \sqrt{\frac{k_B T}{e E_0 K}} & , \text{ for } E_0 \gg E_q \end{cases} \quad (16)$$

where L_D is the Debye screening length. When the applied field E_0 is much smaller than the bulk trap limiting field E_q, ΔL is equal to the Debye screening length and is independent of both the fringe spacing and applied field. For an effective trap density of $10^{16}/cm^3$ in GaAs/AlGaAs multiple quantum wells, ΔL has a value of 0.04 μm, which is very small and is only a small percent of the sample thickness devices (a few μm) [1]. Therefore, this can be said to be a true surface charge layer.

PHOTOREFRACTIVE GRATINGS

The calculation of the photorefractive grating from the space charge field can be quite complicated if both linear electro-optic and nonlinear band edge electro-optic effects are included [8]. The linear electro-optic coefficient can be significantly different from its bulk value due to the elasto-optic effect. Here, a simple situation is considered, where the linear electro-optic effect is negligible compared with the quadratic Franz-Keldysh effect [1]. This is used to illustrate the impact of edge effects on the photorefractive grating. Under such a condition, the photorefractive grating is proportional to the square of the total electric field, which implies that only the cross product term between the applied field and E_x contributes to the first harmonic of the dielectric grating. Consider the average value of E_x over the y-direction inside the thin film. Combining the contributions from both N_a and N_b, gives

$$\bar{E}_x = -\frac{m(E_0 + iE_d)}{(1 + \frac{iE_0 - E_d}{E_q})} \{[1 - \frac{1-\exp(-KL)}{KL}] + \frac{1}{[\frac{\delta e\delta}{\sinh(\delta)}(\frac{-iE_0}{E_{q0}})(\frac{g}{g+1}) + 1]}[\frac{1-\exp(-KL)}{KL} - \frac{2}{g(g+1)KL}]\}$$

$$(17)$$

The first term in the brackets corresponds to the contribution from the bulk space charge density and it is proportional to a geometry function f(KL)

$$f(KL) = 1 - \frac{1-\exp(-KL)}{KL} . \tag{18}$$

From Eq.(17), we can see the transition between the two-dimensional case and the three-dimensional case as KL becomes large. The second term in Eq.(17) comes from the surface charge. In the small K limit, it reaches the value

$$\overline{E}_x = \frac{-mE_0}{(\frac{-iE_0}{E_{q0}} + 1)} \{1 - \frac{KL}{2}[1 + (\frac{2L_D}{L})^2]\} \tag{19}$$

Where E_{q0} is given by TABLE I. Also notable is that E_{q0} is independent of K, which is the result of the two dimensional nature of the device and has a totally different physical meaning from that of the bulk case. In the large K limit Eq. (17) gives the result for the bulk case, as expected.

Numerical studies have been done of the space charge field as a function of fringe spacing when the applied field is much less than $\overline{E}_{q0}$. The results are shown in Figure 1. For large Λ, the contribution from bulk charge is negligible and the surface charge dominates the device behavior. The transition in dimensionality of the device can be clearly seen as Λ increases.
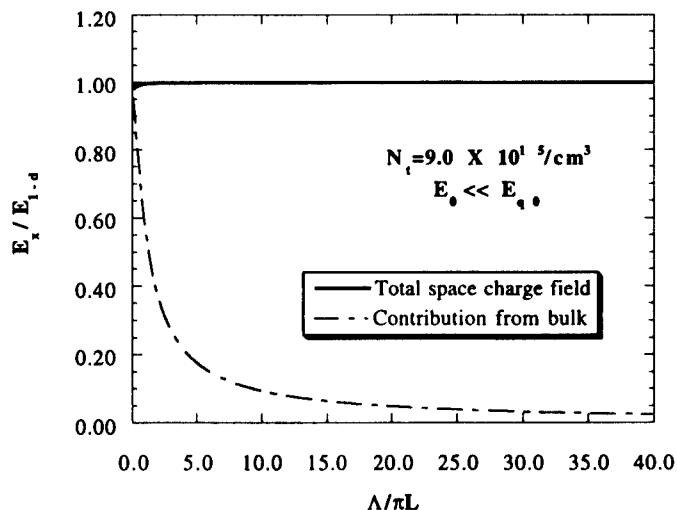
FIG. 1 Space charge field as function of fringe spacing. The contribution from bulk charge is negligible for large Λ. The transition of the dimensionality of the device can be clearly seen as Λ increases. E_{1-d} denotes the solution for one dimension transport model.

For an applied field E_0 up to around E_q, the field dependence of the space charge field is shown in Figure 2. The experimental apparent trap limited field here is actually E_{q0}

instead of E_q and the contribution from surface charge is reduced significantly by a high applied field.
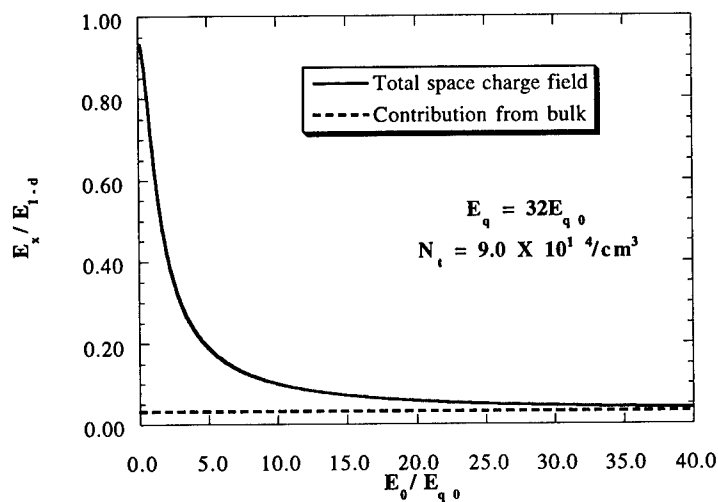
FIG. 2 Space charge field as a function of applied field for a fixed fringe spacing. Notice the apparent trap limited behavior is observed when E_0 is much less than E_q. If the effective trap density is small, the contribution from bulk charge may become important when the device is trap limited by E_{q0}.

CONCLUSION

It has been shown that the photoinduced charge density inside the film is uniform except to within a few Debye lengths of the surface and this surface charge layer may dominate the device performance. The space charge field within thin film photorefractive devices has distinct features in both the large applied electric field limit and the small K limit. It is also an illustration of the importance of the boundary conditions and the need for more work to fully explore the rich practical meaning associated with the surface charges.

REFERENCES

1. Q. Wang, R. M. Brubaker and D. D. Nolte, J. Opt. Soc. Am. B **9**, 1626 (1992).
2. G. Montemezzani, P. Rogin, M. Zgonik and P. Günter, Phys. Rev. B **49**, 2484 (1994).
3. A. Partovi, A. Kost, E. Garmire, G. Valley and M. Klein, Appl. Phys. Lett. **56**, 1089 (1990).
4. M. Kwolek, M. R. Melloch, D. D. Nolte and G. A. Brost, Appl. Phys. Lett. **67**, 736 (1995).

5. P. Günter and J.-P. Huignard, Photorefractive materials and their applications I (Spring-Verlag, Berlin, 1988). Chap. 3.
6. L. F. Magana, F. Agulló-López and M. Carrascosa, J. Opt. Soc. Am. B. **11**, 1651 (1994).
7. M. Aguilar, M. Carrascosa, F. Agulló-López and L. F. Magana J. Appl. Phys. **78**, 4840-4844 (1995).
8. G. Fogarty and M. Cronin-Golomb, Optics Lett. **20**, 2276 (1995).

AUTHOR INDEX

Abstreiter, G., 201
Ahoujja, M., 79
Allerman, A.A., 23, 43
Almeida, L.A., 269
Angelov, M., 315
Aqariden, Fikri, 251, 281
Ashley, T., 103

Babu, Sachidananda, 301
Bachmann, K.J., 315, 321, 333
Baek, Jong-Hyeob, 159
Balramov, B.H., 309
Banisch, R., 213
Barbee, Jr., Troy W., 467
Barth, R., 213
Bauer, G., 201
Beckham, C., 61
Beling, C.D., 165
Berger, V., 111, 135
Beswick, J.A., 103
Bevan, M.J., 269
Biefeld, R.M., 23, 43
Bishop, S.G., 225
Bleuse, J., 239
Bliss, D.F., 345
Boggess, T.F., 85
Borg, James L., 371
Boucaud, P., 111, 135
Braithwaite, G., 129
Bredthauer, R., 79
Brown, G.J., 195, 231
Bryant, G., 345
Bryce, A.C., 413, 419
Burger, A., 287
Burgess, Andre, 301
Busse, W., 333
Butler, J.E., 275
Button, C.C., 413

Cai, W.Z., 219
Capano, M.A., 231
Castleberry, R.H., 315, 321
Chan, K.S., 389
Chan, Michael C.Y., 389
Chan, Y., 377
Chang, Y.C., 225
Chauvet, M.E., 345
Chen, H., 153
Chen, H., 287
Chen, K-T., 287
Chen, Y.P., 281
Choi, H.K., 3, 55
Choy, W.C.H., 383, 425
Chung, S.J., 73
Cockrum, C.A., 257
Connolly, J.C., 91
Connors, M.K., 3
Curtis, A.P., 153, 225

Cusumano, P., 419

De La Rue, R.M., 413, 419
Deschler, M., 433
Diaz, J., 13
Dietz, N., 333
Dinan, J.H., 293
Duboz, J-Y., 123, 135
Ducloux, E., 135
Duncan, W.M., 269
Dutta, Mitra, 401

Eddy, Jr., C.R., 275
Elliot, C.T., 103
Emeny, M.T., 129
Eyink, K., 231

Fang, X.M., 457
Farmer, Joseph C., 467
Felix, C.L., 31
Feng, M., 225
Feng, Z.C., 61
Ferguson, I., 61
Fernelius, N., 309
Fiechter, S., 315, 321
Flatté, Michael E., 85
Foreman, Ronald J., 467
Fromherz, T., 201
Fung, S., 165

Garbuzov, D.Z., 91
Gass, Richard G., 365
Gauthier-Lafaye, O., 111, 135
Gautier, S., 407
Gavrish, T., 463
Gerhardt, A., 451
Giles, N.C., 327
Glembocki, O.J., 275
Glotin, F., 111
Goetz, P., 257
Goldammer, K.J., 97
Grein, C.H., 85
Gumlich, H.E., 333
Guziewicz, Marek, 67

Hadji, E., 239
Halliburton, L.E., 327
Han, Won Seok, 159
Hao, Zhi-Biao, 395
Hardaway, H.R., 73
Hart, L., 73
Hauenstein, R.J., 97
Hawkins, S.A., 345
Hegde, S.M., 231
Helm, M., 201
Helmy, A. Saher, 419
Hlie, J., 463
Hipólito, O., 439

479

SUBJECT INDEX

quantum well(-), 97, 111, 147, 371, 377,
383, 389, 413, 425
confinement, 287, 467
infrared photodetectors, 195
intermixing, 413, 419
mixing, 353
QWIPs 225

Raman, 287
rapid thermal annealing, 395
rapid thermal processing, 419
regrowth, 219
resonance, 293
resonant cavity light-emitting
diodes, 239
RIE, 67

second-harmonic generation, 201
self-consistent, 439
(8 x 8)-k $\bullet$ P model, 173
semiconducting antimonide
compounds, 67
SID, 407
$Si_{1-x}Ge_x$, 213, 451
silicon, 263
SIMS, 407
simulation, 439
single crystals, 339
Si/SiGe quantum wells, 201
spectroscopic(-), 293
ellipsometer, 269
sputtering, 467
stabilization method, 165
stimulated gains, 111
strained(-), 371
layer superlattices, 73
multiple quantum wells, 153
$Si_{1-x}Ge_x$ channel , 445
subband states, 365
superlattice(-), 97, 439
structures, 365
surface(-)
charge, 473
recombination, 129

Tera-Hertz, 439
tertiarybutylarsine, 55
thermal stability, 321
thermoelectric, 467
thermophotovoltaics, 55
thin
E-O devices, 473
films, 473
threshold(-)
current densities, 85
voltage windows, 445
time(-)
delay, 327
resolved photoluminescence, 333
transconductances, 445
transport in thin device, 473
tri-layer photolithography, 301
tunneling, 189
two(-)
color(-)
detectors   257
quantum-well infrared
photodetectors, 173
dimensional optical
waveguide in bulk InP, 345
II-VI compound, 463
type-II, 31

vacancy profile, 365
vapor phase by high-pressure physical
vapor transport (HPVT), 333
VCSEL 159
vertical(-)
cavity surface emitting
laser, 147, 239
quantum wells, 135
virtual substrate, 49

wavefunction engineering, 31
wave-packet, 439
whispering gallery modes, 135

x-ray, 463

ZGP, 339
ZnCdTe, 287
$ZnGeP_2$, 315, 321, 327, 333